

Catchment-scale spatial targeting of flood management measures to reduce flood hazard: An end-to-end modelling approach applied to the East Rapti catchment, Nepal

PEARSON, CALLUM,JAMES

How to cite:

PEARSON, CALLUM,JAMES (2020) *Catchment-scale spatial targeting of flood management measures to reduce flood hazard: An end-to-end modelling approach applied to the East Rapti catchment, Nepal*, Durham theses, Durham University. Available at Durham E-Theses Online: <http://etheses.dur.ac.uk/13794/>

Use policy

The full-text may be used and/or reproduced, and given to third parties in any format or medium, without prior permission or charge, for personal research or study, educational, or not-for-profit purposes provided that:

- a full bibliographic reference is made to the original source
- a [link](#) is made to the metadata record in Durham E-Theses
- the full-text is not changed in any way

The full-text must not be sold in any format or medium without the formal permission of the copyright holders.

Please consult the [full Durham E-Theses policy](#) for further details.

Academic Support Office, Durham University, University Office, Old Elvet, Durham DH1 3HP
e-mail: e-theses.admin@dur.ac.uk Tel: +44 0191 334 6107
<http://etheses.dur.ac.uk>

CATCHMENT-SCALE SPATIAL TARGETING OF FLOOD MANAGEMENT MEASURES TO REDUCE FLOOD HAZARD

AN END-TO-END MODELLING APPROACH APPLIED TO THE EAST RAPTI CATCHMENT,
NEPAL

CALLUM JAMES PEARSON



THESIS SUBMITTED FOR THE DEGREE OF DOCTOR OF PHILOSOPHY

DEPARTMENT OF GEOGRAPHY

DURHAM UNIVERSITY

2020

ABSTRACT

Globally, practical approaches to managing flood hazards are moving away from mitigation solely at the point of the impact, and towards an integrated catchment-scale approach which considers flood source areas, flow pathways of flood waters and impacted communities. The current method for managing the fluvial flood risk in Nepal, however, generally involves localised structural interventions in affected areas using a static and reactive approach. This method does not create long term resilience to the hazards. There is therefore the need to rely less on these large-scale structural measures and focus instead on sustainable and non-structural measures for flood mitigation that allow the catchments and communities within them to be more resilient.

The three-stage, end-to-end approach developed in this thesis provides a process to help shift towards an integrated catchment management for flood hazard reduction in Nepal. The approach centres on identifying flood water source areas within the catchment and spatially targeting flood management measures in these locations. Consideration is also given to the potential impact of future, flow magnitude increasing, land cover change such as deforestation and the abandonment of terraced agriculture that is evident in many Nepali catchments.

Stage 1 adopts SCIMAP-Flood, a catchment-scale decision support framework that identifies critical source areas for flood waters. The framework uses maps flood water generating areas based on spatial rainfall patterns and land cover, the incorporation of travel times across a catchment, and modelling of hydrological connectivity. Outputs are used to create catchment-scale flood management scenarios which target flood source areas; tested flood management measures include targeted afforestation, check dams in key sub-catchments and abandoned terrace restoration.

In Stage 2 the flood management scenarios are assessed using CRUM3, a physically-based, spatially distributed, catchment-scale hydrological model. The impact of the flood management measures can be evaluated throughout the catchment using the modelled change in discharge. Stage 3 uses LISFLOOD-FP, a 2D flood inundation model, to establish the change flood inundation patterns at key flood impacted communities within the catchment from the created flood management scenarios. Stage 2 and Stage 3 utilise a coupled hydrological-hydraulic modelling approach with the results from the CRUM3 model entering the LISFLOOD-FP model as inflow hydrographs.

The approach is applied to the East Rapti catchment, a 3,084 km² sub-catchment of the Nayarani River in southern central Nepal. The catchment contains three river flow gauges (Lothar Khola [catchment area - 169 km²], Manahari Khola [427 km²] and Rapti River [471 km²]) placed within the main sub-

catchments and eight rainfall gauges. Additional data used to drive the approach was attained from global datasets and acquired during fieldwork.

This thesis has researched the potential effectiveness of the implementation of flood management interventions at the catchment-scale and evidences an alternative approach to flood management that is applicable in both Nepal and the wider Himalayan Region. Based on the integrated modelling approach, the results predict that the high flow magnitudes in the East Rapti catchment can be reduced through a catchment-scale approach.

However, even with a combined approach of large scale spatially targeted afforestation and check dam implementation ($\overline{Q99.9}$ decrease of $\leq 5.3\%$), the use of solely catchment-scale flood management approaches to combat flood hazard might not be effective at reducing the flood impact to at-risk communities. A significant outcome from the catchment-scale modelling work was that there is a far greater potential for land use change to increase, rather than reduce through mitigation, flow magnitudes in the East Rapti catchment. The model results suggest that any land within the East Rapti catchment that is altered from existing forest will contribute to increasing the flow magnitude ($\overline{Q99.9}$ increase of up to 48.2%).

CONTENTS

Abstract	i
Figures	vii
Tables	xvii
Appendices	xx
Abbreviations	xxiii
Declaration of copyright	xxv
Acknowledgements	xxvi
Acknowledgement of funding.....	xxvi
1 Introduction	1
1.1 The impacts and management of fluvial flooding in Nepal	1
1.2 Research aim and objectives	8
1.3 Research approach: An overview of the end-to-end process for the spatial targeting of flood management measures at the catchment-scale	8
1.3.1 Stage 1 – Identifying flood water generating areas using SCIMAP-Flood	9
1.3.2 Stage 2 – Catchment-scale scenario modelling using CRUM3.....	10
1.3.3 Stage 3 – Inundation modelling at flood impact points using LISFLOOD-FP	10
1.4 Thesis structure.....	11
1.5 Background literature	12
1.5.1 Current and future approaches to flood management in Nepal	12
1.5.2 Land use change and the hydrological impact in Nepal and the wider Himalayas	14
1.5.3 Geo-spatial analysis for spatial targeting flood management measures at the catchment-scale	18
1.5.4 The use of hydrological models to assess flood hazard reduction through catchment- based management techniques and interventions	20
1.5.5 Modelling the impact of catchment-scale flood management through flood inundation extent change using coupled approach	22
1.5.6 Uncertainty throughout hydrological modelling	24
1.6 Summary	27
2 The East Rapti catchment	28
2.1 Introduction	28
2.2 Location.....	28

2.3	Catchment characteristics	29
2.3.1	Geology	29
2.3.2	Topography	32
2.3.3	Soils	34
2.3.4	Land cover	34
2.4	Climate	36
2.5	Catchment hydrology.....	39
2.5.1	Hydrological regime	39
2.5.2	Flood events in the East Rapti catchment	41
2.6	Evaluation of the gauged climate and river flow data for the East Rapti catchment.....	42
2.6.1	Rainfall data	42
2.6.2	Temperature data	43
2.6.3	River flow data	43
2.6.4	Justification of gauged data used in the CRUM3 hydrological modelling	48
2.7	East Rapti catchment summary	51
3	Identifying flood water source areas for the spatial targeting of flood management measures at the catchment-scale.....	53
3.1	Introduction	53
3.2	Methods.....	55
3.2.1	SCIMAP-Flood.....	55
3.2.2	East Rapti catchment data for SCIMAP-Flood.....	57
3.2.3	The SCIMAP-Flood Fitted approach used to determine land cover risk weightings	70
3.2.4	East Rapti catchment data for SCIMAP-Flood Fitted	71
3.2.5	SCIMAP-Flood methods summary	78
3.3	Results.....	80
3.3.1	SCIMAP-Flood Fitted results to determine the land cover weightings.....	80
3.3.2	SCIMAP-Flood results.....	83
3.4	Discussion.....	101
3.4.1	Determining flood source areas in the East Rapti catchment using SCIMAP-Flood ...	101
3.4.2	Identifying locations for catchment-scale flood management measures in the East Rapti catchment using SCIMAP-Flood.....	105
3.4.3	Assessing the impact of land cover on the flood regime in the East Rapti catchment using SCIMAP-Flood Fitted.....	107
3.4.4	The influence of the spatial data inputs on the SCIMAP-Flood output	110

3.4.5	The application of the SCIMAP-Flood approach in data sparse catchments.....	112
3.5	Conclusions	114
4	Assessing the change to the high flow regime under catchment-scale flood management scenarios using simulation modelling	116
4.1	Introduction	116
4.2	Methods.....	119
4.2.1	CRUM3	119
4.2.2	East Rapti catchment data for CRUM3 model setup	126
4.2.3	CRUM3 parameter sensitivity analysis	128
4.2.4	East Rapti data for CRUM3 model assessment and calibration.....	131
4.2.5	CRUM3 GLUE approach	132
4.2.6	Spatial representation of land cover in CRUM3	138
4.2.7	The development of catchment-scale scenarios using CRUM3.....	141
4.2.8	CRUM3 methods summary	154
4.3	Results.....	155
4.3.1	East Rapti GLUE results	155
4.3.2	East Rapti catchment-scale scenario results.....	161
4.4	Discussion.....	189
4.4.1	The potential impacts of future land use change and degradation on the flood regime in the East Rapti catchment	189
4.4.2	The potential for flood risk reduction through catchment-scale flood management in the East Rapti catchment.....	192
4.4.3	The representation of the East Rapti catchment in the CRUM3 hydrological model	196
4.5	Conclusions	199
5	Determining the impact of catchment-scale land use change on local-scale inundation patterns.....	201
5.1	Introduction	201
5.2	Methods.....	204
5.2.1	LISFLOOD-FP.....	205
5.2.2	LISFLOOD-FP model setup.....	206
5.2.3	Sensitivity analysis of the LISFLOOD-FP model parameters	211
5.2.4	Modelled catchment-scale flood management scenarios.....	213
5.2.5	LISFLOOD-FP methods summary	215
5.3	Results.....	216

5.3.1	Baseline inundation extents for the 2009 and 2010 high-flow events.....	216
5.3.2	LISFLOOD-FP sensitivity analysis results	220
5.3.3	LISFLOOD-FP catchment-scale scenario inundation modelling results	224
5.4	Discussion.....	249
5.4.1	The impact of catchment-scale change on the localised inundation characteristics within the East Rapti catchment.....	249
5.4.2	The need for a coupled modelling approach and the use of localised inundation extents in flood impacted areas when developing a catchment management scenario.....	253
5.4.3	The representation of the channel and floodplain at localised flood-impacted areas within the East Rapti catchment.....	257
5.4.4	Sources and impacts of uncertainty in the LISFLOOD-FP results.....	261
5.5	Conclusions	264
6	Research summary and conclusions	266
6.1	Introduction	266
6.2	Original contributions to knowledge	266
6.3	Research conclusions.....	267
6.3.1	The end-to-end approach used to determine the impact of spatially targeted catchment-scale flood management measures.....	267
6.3.2	Stage 1 – Identifying flood water generating areas using SCIMAP-Flood	270
6.3.3	Stage 2 – Catchment-scale scenario modelling using CRUM3.....	271
6.3.4	Stage 3 – Inundation modelling at flood impact points using LISFLOOD-FP	273
6.4	Recommendations for future work	274
7	Appendices.....	277
8	References	297

FIGURES

Figure 1.1: The major river basins in Nepal	3
Figure 1.2: An illustration of the main geomorphic zones occurring in a cross-section through Nepal..	3
Figure 1.3: District level totals of people affected (both directly and indirectly) due to flooding across Nepal	5
Figure 1.4: District level totals of houses destroyed or damaged due to flooding across Nepal.....	6
Figure 1.5: Population density across Nepal	7
Figure 1.6: A conceptual overview of the three modelling stages used in the end-to-end approach for the spatial targeting of flood management measures at the catchment-scale.	9
Figure 1.7: Examples of terraced agriculture in Nepal	16
Figure 1.8: The conceptual structure used in the FLEXT decision matrix to determine the locations for changes in the landscape with flood protection benefits	20
Figure 1.9: An example of the spatial scales used in a coupled modelling approach from Felder et al..	23
Figure 1.10: A conceptual overview of the uncertainty cascade through a coupled modelling approach looking at medium range flood forecasting.....	26
Figure 2.1: The main channel network in the East Rapti catchment and the catchment location within Nepal	29
Figure 2.2: The geology of the East Rapti catchment.....	31
Figure 2.3: A regional geomorphic map of Nepal with the East Rapti catchment	31
Figure 2.4: A DEM showing the elevation variation throughout the East Rapti catchment based on the ALOS Global Digital Surface Model (AW3D30) 30 m dataset.	33
Figure 2.5: A slope map of the East Rapti catchment based on the ALOS Global Digital Surface Model (AW3D30) 30 m dataset.....	33
Figure 2.6: A map of the main land cover categories in the East Rapti catchment based on supervised classification of Landsat 8 imagery	35
Figure 2.7: A selection of photos taken by the author of the different land covers within the East Rapti catchment	36
Figure 2.8: The location of the DHM rainfall and river flow gauges within, or in close proximity to, the East Rapti catchment	38

Figure 2.9: Average monthly rainfall totals in mm (1998-2016) for three DHM rain gauges distributed across the East Rapti catchment.....	39
Figure 2.10: Average daily flows in $\text{m}^3 \text{s}^{-1}$ at the DHM river flow gauges in the East Rapti catchment (1998 to 2016).....	41
Figure 2.11: The Rapti River at Rajaiya gauge	44
Figure 2.12: The Lothar Khola at Lothar average daily flow data for each year between 1998 and 2015.	46
Figure 2.13: The Manahari Khola at Manahari average daily flow data for the year 2009.....	47
Figure 2.14: The Rapti River at Rajaiya average daily flow data for the year 2004.....	48
Figure 3.1: A diagram outlining the SCIMAP-Flood and SCIMAP-Flood Fitted approaches used in Chapter 3.....	56
Figure 3.2: A diagram illustrating the processes used in SCIMAP-Flood to calculate relative flood risk at a catchment-scale	56
Figure 3.3: The location of selected flood impact points in the East Rapti catchment.....	59
Figure 3.4: An example of the overland flow travel time spatial data to the Sauraha flood impact point.	60
Figure 3.5: The overland flow contributing area for the split Hetauda flood impact points shown in Figure 3.3.	60
Figure 3.6: An example of the gridded daily rainfall output for the East Rapti catchment with the final combination of DHM rain gauges and TRMM satellite points used to obtain the daily rainfall grids overlain.	65
Figure 3.7: The cumulative bias-adjusted rainfall spatial rainfall patterns associated with the 2001 and 2003 high flow events.....	67
Figure 3.8: An overview of the SCIMAP-Flood Fitted inverse modelling approach to derive the top land cover parameter sets for the East Rapti catchment using the August 2017 storm event.....	70
Figure 3.9: The locations within the East Rapti catchment from which the August 2017 peak flows were estimated.	73
Figure 3.10: A comparison of the pre- (left) and post-event (right) Planet satellite imagery for a section of the East Rapti catchment.....	74
Figure 3.11: The location of the 25 flow gauging locations broken down by the method used at each location.	76
Figure 3.12: An example of one of the dry tributaries (site 19 in Figure 3.11) in which field-based observations were made	77

Figure 3.13: The Seafloor HyDrone RCV with attached ADCP for gauging wider and deeper channels	77
Figure 3.14: Measuring the flow across a cross-section using the handheld flow meter	78
Figure 3.15: Dotty plots from all 15,000 (left) and the top 750 (5%) (right) of the SCIMAP-Flood Fitted model simulations showing the Pearson correlation coefficient compared to the SCIMAP-Flood land cover weighting value for each of the seven land cover classes in the East Rapti catchment.....	81
Figure 3.16: A boxplot showing the SCIMAP-Flood land cover weightings for the top 10 weightings sets based on the Pearson’s correlation coefficient and the SCIMAP-Flood Fitted inverse modelling approach	83
Figure 3.17: SCIMAP-Flood output for the East Rapti catchment created using the rainfall patterns associated with the top 10 flow events, the top 10 land cover weighting sets and 6 flood impact points.	84
Figure 3.18: A focused view on one of the key areas with the highest potential to generate flood waters within the East Rapti catchment taken from Figure 3.17.	84
Figure 3.19: SCIMAP-Flood output for the East Rapti catchment created using TRMM satellite-only rainfall patterns associated with the top 10 flow events, the top 10 land cover weighting sets and 6 flood impact points	86
Figure 3.20: A comparison of the distribution of SCIMAP-Flood flood risk generation scores across the SCIMAP-Flood output created using the scaled rainfall patterns (Figure 3.17) and the TRMM satellite-only rainfall patterns (Figure 3.19)	86
Figure 3.21: Point density analysis of SCIMAP-Flood output using the scaled rainfall data (top) and TRMM-only rainfall data (bottom) showing the areas of with the highest flood water generation weighting.	87
Figure 3.22: SCIMAP-Flood output for the East Rapti catchment created using TRMM satellite only rainfall patterns for each monsoon period (May to September) between 1998 and 2016, the top 10 land cover weighting sets and 6 flood impact points.	89
Figure 3.23: A comparison of the distribution of SCIMAP-Flood flood risk generation scores across the SCIMAP-Flood output created using the TRMM storm even rainfall patterns (Figure 3.19) and the TRMM monsoonal rainfall patterns (Figure 3.22)	89
Figure 3.24: Point density analysis of SCIMAP-Flood output using TRMM-only rainfall data for the top 10 storm events (top) and the TRMM-only rainfall data for the monsoon periods between 1998 and 2016 (bottom) showing the areas of with the highest flood water generation weighting	90

Figure 3.25: SCIMAP-Flood output for the East Rapti catchment created using the rainfall patterns associated with the top 5 flow events, the top 10 land cover weighting sets and 6 flood impact points..	92
Figure 3.26: A comparison of the distribution of SCIMAP-Flood flood risk generation scores across the SCIMAP-Flood output created using the top 10 storm event rainfall patterns (Figure 3.17) and the top 5 storm event rainfall patterns (Figure 3.25).....	92
Figure 3.27: Point density analysis of SCIMAP-Flood output using the rainfall spatial patterns from the top 10 flow events (top) and the rainfall spatial patterns from the top 5 flow events (bottom) showing the areas of with the highest flood water generation weighting	93
Figure 3.28: Point density analysis of SCIMAP-Flood output comparing the removal of the Andrauli flood impact point (a), the removal of the Hetauda flood impact point (b), the removal of the Lothar flood impact point (c), the removal of the Manahari flood impact point (d), the removal of the Madi Bridge flood impact point (e), the removal of the Sauraha flood impact point (f) and the use of all 6 flood impact points (g).....	95
Figure 3.29: SCIMAP-Flood output for the East Rapti catchment created using the rainfall patterns associated with the top 10 flow events, the top 10 land cover weighting sets and split flood impact points at Sauraha and Hetauda with the 4 other flood impact points also used in Figure 3.17	97
Figure 3.30: A comparison of the distribution of SCIMAP-Flood flood risk generation scores across the SCIMAP-Flood output created using the original flood impact point placement (Figure 3.17) and the split flood impact point placement (Figure 3.29)	97
Figure 3.31: Point density analysis of SCIMAP-Flood output using the 6 selected flood impact points (top) and alternative flood impact points (bottom) showing the areas of with the highest flood water generation weighting.....	98
Figure 3.32: The overall sensitivity of areas having a flood risk score of (a) > 0.50 and (b) > 0.75. Based on the point density analysis of SCIMAP-Flood output and the percentage appearance of an area across the sensitivity scenarios.....	100
Figure 3.33: The percentage distribution of slope (left) and Network Index (right) values throughout each of the land cover categories in the East Rapti.....	103
Figure 3.34: SCIMAP-Flood output for the East Rapti catchment (as presented in Figure 3.17) reinterpreted to help with the spatial targeting of flood management measures.....	106
Figure 4.1: A diagram outlining the CRUM3 simulation modelling approach taken in Chapter 4.	119
Figure 4.2: A conceptual representation of the CRUM3 model structure	120
Figure 4.3: A conceptual diagram of the hydrological processes in CRUM3.....	122

Figure 4.4: Average percentage change in discharge for Q01, Q05, Q95 and Q99 for each CRUM3 model parameter	131
Figure 4.5: The 150 m base land cover spatial pattern resampled from the supervised classification land cover data	139
Figure 4.6: The blanket coverage of the catchment using the Forest land cover class.....	142
Figure 4.7: The deforestation land use change scenario with areas of Forest around the populated part of the catchment replaced with Shrubland	143
Figure 4.8: The urban expansion scenario with Built-Up Area increased around four settlements using a 1 km buffer	144
Figure 4.9: The terrace abandonment land use change scenario with 50% of the Rainfed Agriculture in the catchment converted to Shrubland.....	145
Figure 4.10: The combined urban expansion, deforestation and terrace abandonment scenario within the East Rapti catchment.....	146
Figure 4.11: The targeted afforestation scenario areas of the catchment with a SCIMAP-Flood value > 0.50	147
Figure 4.12: The targeted afforestation scenario areas of the catchment with a SCIMAP-Flood value > 0.50 derived from point density analysis.....	148
Figure 4.13: Examples of four different check dams.....	149
Figure 4.14: The distribution of sub-catchments with check dams implemented in based on the point density analysis of the SCIMAP-Flood output.....	150
Figure 4.15: The combined spatially targeted afforestation and check dam flood management scenario using point density analysis of the SCIMAP-Flood output (SCIMAP-Flood values > 0.50).....	151
Figure 4.16: Offsetting the combined land use change (urban expansion, deforestation and terrace abandonment) through the use of targeted afforestation from point density analysis of the SCIMAP-Flood output (SCIMAP-Flood value > 0.50).....	152
Figure 4.17: Simulated and observed average daily flow hydrographs at the Lothar gauge based on the calibration using the Rapti gauged data (top) and Lothar gauged data (bottom).....	159
Figure 4.18: Simulated and observed average daily flow hydrographs at the Rapti gauge based on the calibration using the Rapti gauged data (top) and Lothar gauged data (bottom).....	160
Figure 4.19: A combined boxplot and swarmplot showing the blanket land cover change scenarios and the corresponding percentage change in Q99.9 at the six flood impact points	166
Figure 4.20: A comparison of median flow for the six flood impact points for the base (blue) and BLA_F (red) scenarios	167

Figure 4.21: A comparison of median flow for the six flood impact points for the base (blue) and BLA_IA (red) scenarios.	167
Figure 4.22: A combined boxplot and swarmplot showing the DEF_IA and DEF_S scenarios and the corresponding percentage change in Q99.9 at the six flood impact points.....	169
Figure 4.23: A comparison of median flow for the six flood impact points for the base (blue) and DEF_S (red) scenarios.	169
Figure 4.24: A combined boxplot and swarmplot showing the URB_BUA and the corresponding percentage change in Q99.9 at the six flood impact points	171
Figure 4.25: A comparison of median flow for the six flood impact points for the base (blue) and URB_BUA (red) scenarios.....	171
Figure 4.26: A combined boxplot and swarmplot showing the TER_BG and TER_S scenarios and the corresponding percentage change in Q99.9 at the six flood impact points.....	172
Figure 4.27: A comparison of median flow for the six flood impact points for the base (blue) and TER_S (red) scenarios.	173
Figure 4.28: A combined boxplot and swarmplot showing the NEG_S scenario and the corresponding percentage change in Q99.9 at the six flood impact points.....	174
Figure 4.29: A comparison of median flow for the six flood impact points for the base (blue) and NEG_S (red) scenarios.	174
Figure 4.30: A combined boxplot and swarmplot showing the AFF50_F and AFF75_F scenarios and the corresponding percentage change in Q99.9 at the six flood impact points.....	176
Figure 4.31: A combined boxplot and swarmplot showing the AFF50_PDA_F and AFF75_PDA_F scenarios and the corresponding percentage change in Q99.9 at the six flood impact points	176
Figure 4.32: A comparison of median flow for the six flood impact points for the base (blue) and AFF50_F (red) scenarios.....	177
Figure 4.33: A comparison of median flow for the six flood impact points for the base (blue) and the AFF50_PDA_F (red) scenarios	177
Figure 4.34: A combined boxplot and swarmplot showing the DAM50 and DAM75 scenarios and the corresponding percentage change in Q99.9 at the six flood impact points.....	179
Figure 4.35: A comparison of median flow for the six flood impact points for the base (blue) and the DAM50 scenario (red) scenarios.....	179
Figure 4.36: A combined boxplot and swarmplot showing the TER_F scenario and the corresponding percentage change in Q99.9 at the six flood impact points.....	180
Figure 4.37: A comparison of median flow for the six flood impact points for the base (blue) and the TER_F (red) scenarios.....	181

Figure 4.38: A combined boxplot and swarmplot showing the POS50 and POS75 scenarios, and the corresponding percentage change in Q99.9 at the six flood impact points.....	182
Figure 4.39: A comparison of median flow for the six flood impact points for the base (blue) and the POS50 (red) scenarios.....	182
Figure 4.40: A combined boxplot and swarmplot showing the AFF75_PDA_F_NEG_S and AFF50_PDA_F_NEG_S scenarios and the corresponding percentage change in Q99.9 at the six flood impact points.	184
Figure 4.41: A comparison of median flow for the six flood impact points for the base (blue) and the AFF50_PDA_F_NEG_S (red) scenarios.	184
Figure 4.42: A combined boxplot and swarmplot showing the DAM50_NEG_S and DAM75_NEG_S scenarios and the corresponding percentage change in Q99.9 at the six flood impact points	186
Figure 4.43: A comparison of median flow for the six flood impact points for the base (blue) and the DAM50_NEG_S (red) scenarios.....	186
Figure 4.44: A combined boxplot and swarmplot showing the POS50_NEG_S and POS75_NEG_S scenarios, and the corresponding percentage change in Q99.9 at the six flood impact points	188
Figure 4.45: A comparison of median flow for the six flood impact points for the base (blue) and POS50_NEG_S (red) scenarios.....	188
Figure 5.1: Outline of the process used in Chapter 5 to provide a detailed assessment of the impacts of a given catchment management scenario.....	204
Figure 5.2: The LISFLOOD-FP model extent and inflow locations for Sauraha.....	207
Figure 5.3: The LISFLOOD-FP model extent and inflow locations for Hetauda	207
Figure 5.4: The CRUM3 modelled hydrographs from the downstream end of the Sauraha LISFLOOD-FP model for the chosen 2009 (blue) and 2010 (red) high-flow events.	209
Figure 5.5: A flood probability map for Sauraha using the baseline parameters and 2009 event hydrograph.....	217
Figure 5.6: A flood probability map for Hetauda using the baseline parameters and 2009 event hydrograph.....	217
Figure 5.7: A flood probability map for Sauraha using the baseline parameters and 2010 event hydrograph.....	219
Figure 5.8: A flood probability map for Hetauda using the baseline parameters and 2010 event hydrograph.....	219
Figure 5.9: The median inundation extents at Sauraha from the model ensemble 2009 event hydrographs for the flow magnitude increasing scenarios and the baseline extent	225

Figure 5.10: A cumulative histogram comparison of the 10th (orange), 50th (blue) and 90th (grey) percentile inundation depths occurring in areas of Built-Up Area throughout the Sauraha model extent using the 2009 event hydrograph..... 227

Figure 5.11: The median inundation extents at Hetauda from the model ensemble 2009 event hydrographs for the flow magnitude increasing scenarios and the baseline extent. 229

Figure 5.12: A cumulative histogram comparison of the 10th (orange), 50th (blue) and 90th (grey) percentile inundation depths occurring in areas of Built-Up Area throughout the Hetauda model extent using the 2009 event hydrograph. 230

Figure 5.13: The median inundation extents at Sauraha from the model ensemble 2010 event hydrographs for the flow magnitude increasing scenarios and the baseline extent 232

Figure 5.14: A cumulative histogram comparison of the 10th (orange), 50th (blue) and 90th (grey) percentile inundation depths occurring in areas of Built-Up Area throughout the Sauraha model extent using the 2010 event hydrograph..... 233

Figure 5.15: The median inundation extents at Hetauda from the model ensemble 2010 event hydrographs for the flow magnitude increasing scenarios and the baseline extent 235

Figure 5.16: A cumulative histogram comparison of the 10th (orange), 50th (blue) and 90th (grey) percentile inundation depths occurring in areas of Built-Up Area throughout the Hetauda model extent using the 2010 event hydrograph 236

Figure 5.17: The median inundation extents at Sauraha from the model ensemble 2009 event hydrographs for the flow magnitude decreasing scenarios and the baseline extent 238

Figure 5.18: A cumulative histogram comparison of the 10th (orange), 50th (blue) and 90th (grey) percentile inundation depths occurring in areas of Built-Up Area throughout the Sauraha model extent using the 2009 event hydrograph..... 239

Figure 5.19: The median inundation extents at Hetauda from the model ensemble 2009 event hydrographs for the flow magnitude decreasing scenarios and the baseline extent 241

Figure 5.20: A cumulative histogram comparison of the 10th (orange), 50th (blue) and 90th (grey) percentile inundation depths occurring in areas of Built-Up Area throughout the Hetauda model extent using the 2009 event hydrograph 242

Figure 5.21: The median inundation extents at Sauraha from the model ensemble 2010 event hydrographs for the flow magnitude decreasing scenarios and the baseline extent 244

Figure 5.22: A cumulative histogram comparison of the 10th (orange), 50th (blue) and 90th (grey) percentile inundation depths occurring in areas of Built-Up Area throughout the Sauraha model extent using the 2010 event hydrograph..... 245

Figure 5.23: The median inundation extents at Hetauda from the model ensemble 2010 event hydrographs for the flow magnitude decreasing scenarios and the baseline extent	247
Figure 5.24: A cumulative histogram comparison of the 10 th (orange), 50 th (blue) and 90 th (grey) percentile inundation depths occurring in areas of Built-Up Area throughout the Hetauda model extent using the 2010 event hydrograph	248
Figure 5.25: A comparison of areas in the Hetauda model in which the inundation depth has been reduced (> 0.05 m) between the BLA_F and POS50 scenarios.....	252
Figure 5.26: A comparison of areas in the Sauraha model in which the inundation depth has been reduced (> 0.05 m) between the BLA_F and POS50 scenarios.....	252
Figure 5.27: The relationship between the percentage change in median LISFLOOD-FP model inundated area and the average median percentage change in Q _{99.9} flow magnitude from the CRUM3 catchment-scale modelling for the ten scenarios.....	254
Figure 5.28: The potential impact of the channel and floodplain morphology on the inundation extent. This example uses the 10 th and 90 th percentile extents at Sauraha from the BLA_F scenario and highlights areas that have a slope < 2 degrees.....	256
Figure 5.29: The potential impact of the channel and floodplain morphology on the inundation extent. This example uses the 10 th and 90 th percentile extents at Hetauda from the BLA_F scenario and highlights areas that have a slope < 2 degrees.....	256
Figure 5.30: Slope analysis of the 5 m ALOS AW3D elevation data highlighting areas of higher slope gradient around the flood defences in Hetauda.	259
Figure 5.31: The Sauraha LISFLOOD-FP model extent overlaid on the HEC-RAS produced flood extent for a return period of 50 years (2% AEP) (red/orange) and 100 years (1% AEP) (blue) adapted from Singh (2013).	260
Figure 5.32: The Sauraha LISFLOOD-FP model extent overlaid on the HEC-RAS produced flood extent and depths for a 5-year return period (20% AEP) event for the main East Rapti channel adapted from the Asian Development Bank (2016)	260
Figure 5.33: A comparison of the 10 th , 50 th and 90 th percentile flood extents for the 2009 high-flow event across the model ensemble from the BLA_F scenario in the Sauraha model.	263
Figure 5.34: A comparison of the 10 th , 50 th and 90 th percentile flood extents for the 2010 high-flow event across the model ensemble from the BLA_F scenario in the Sauraha model.	263
Figure 6.1: An overview of the three stages used in the end-to-end approach for the spatial targeting of flood management measures at the catchment-scale.....	268

Figure 6.2: A conceptual overview of the uncertainty cascade through the end-to-end approach....
..... 270

TABLES

Table 2.1: Percentage coverage of the main land covers in the East Rapti catchment in 2016 based on supervised classification of Landsat 8 imagery.....	35
Table 2.2: DHM rainfall gauge information that shows the data period available for the rainfall gauges around the East Rapti catchment	49
Table 2.3: DHM river flow gauge information that shows the data period available for the gauges within the East Rapti catchment.....	50
Table 3.1: A comparison of the monthly and daily R^2 values comparing the DHM gauged rainfall and the TRMM satellite rainfall totals at the gauges within, or in close proximity, to the East Rapti catchment	63
Table 3.2: Periods of rainfall data used that are associated with the top 10 flow events in the East Rapti catchment	66
Table 3.3: The main land cover categories in the East Rapti catchment that were classified during the creation of the land cover map.....	69
Table 3.4: A confusion matrix of the supervised land cover mapping for the East Rapti catchment..	69
Table 3.5: Peak flow estimates and corresponding data used to obtain the estimated risk indicators for SCIMAP-Flood Fitted..	76
Table 3.6: The SCIMAP-Flood land cover weighting values for each land cover in the top 10 weighting sets, based on the Pearson’s correlation coefficient and the SCIMAP-Flood Fitted inverse modelling approach	82
Table 3.7: The percentage coverage of the land covers within the East Rapti catchment and respective average and standard deviation (SD) of the slope gradient and Network Index values	102
Table 4.1: Parameter values for sensitivity analysis.....	129
Table 4.2: An example of a rescaled parameters across the different land covers for one of the top GLUE model runs.....	141
Table 4.3: A description of each catchment-scale scenario for the East Rapti catchment and the corresponding scenario ID.	153
Table 4.4: The top 8 model runs based on a formal statistical approach to model evaluation and using the Lothar gauge, ranked by MAE.	156
Table 4.5: The top 8 model runs based on a formal statistical approach to model evaluation and using the Rapti gauge, ranked by MAE.....	156

Table 4.6: The top 8 model runs based on an informal approach using hydrological signatures for model evaluation and using the Lothar gauge	158
Table 4.7: The top 8 model runs based on an informal approach using hydrological signatures for model evaluation and using the Rapti gauge.	158
Table 4.8: Median percentage change in Q99.9 for the catchment scenarios across all six flood impact points.	163
Table 4.9: Mean percentage change in Q99.9 for the catchment scenarios across all six flood impact points	164
Table 5.1: The baseline parameters used for the Sauraha LISFLOOD-FP model.....	211
Table 5.2: The baseline parameters used for the Hetauda LISFLOOD-FP model.....	211
Table 5.3: The model runs used to undertake a sensitivity analysis of the main LISFLOOD-FP parameters for the Sauraha model.....	212
Table 5.4: The model runs used to undertake a sensitivity analysis of the main LISFLOOD-FP parameters for the Hetauda model.....	213
Table 5.5: The median percentage change in flow magnitude (Q99.9) for the catchment scenarios modelled using CRUM3 (see Chapter 4) at Hetauda and Sauraha..	214
Table 5.6: A comparison of inundation extent percentage and areal change in comparison to the baseline extent under different LISFLOOD-FP model sensitivity analysis scenarios for the Sauraha model	221
Table 5.7: A comparison of inundation extent percentage and areal change in comparison to the baseline extent under different LISFLOOD-FP model sensitivity analysis scenarios for the Hetauda model.	223
Table 5.8: A comparison of inundated area extent change across the model ensemble for flow magnitude increasing catchment-scale scenarios at Sauraha using the 2009 event hydrograph.	226
Table 5.9: A comparison of inundated area extent change across the model ensemble for flow magnitude increasing catchment-scale scenarios at Hetauda using the 2009 event hydrograph.....	229
Table 5.10: A comparison of inundated area extent change across the model ensemble for flow magnitude increasing catchment-scale scenarios at Sauraha using the 2010 event hydrograph.	232
Table 5.11: A comparison of inundated area extent change across the model ensemble for flow magnitude increasing catchment-scale scenarios at Hetauda using the 2010 event hydrograph.....	235
Table 5.12: A comparison of inundated area extent change across the model ensemble for flow magnitude decreasing catchment-scale scenarios at Sauraha using the 2009 event hydrograph. ...	238

Table 5.13: A comparison of inundated area extent change across the model ensemble for flow magnitude decreasing catchment-scale scenarios at Hetauda using the 2009 event hydrograph....	241
Table 5.14: A comparison of inundated area extent change across the model ensemble for flow magnitude decreasing catchment-scale scenarios at Sauraha using the 2010 event hydrograph. ...	244
Table 5.15: A comparison of inundated area extent change across the model ensemble for flow magnitude decreasing catchment-scale scenarios at Hetauda using the 2010 event hydrograph....	247
Table 5.16: The relationship (r value) between the median percentage change values from the ten scenarios across the 32 run model ensemble, for both the catchment modelling (Chapter 4) and the inundation modelling (Section 5.3).....	254
Table 6.1: An overview of the shared data (shaded red) across the different stages of the end-to-end approach	269

APPENDICES

Appendix 7.1: DHM daily rainfall time series for the Amlekgunj (top) and Beluwa (bottom) gauges for 1998 to 2016	277
Appendix 7.2: DHM daily rainfall time series for the Daman (top) and Dunkauli (bottom) gauges for 1998 to 2016	277
Appendix 7.3: DHM daily rainfall time series for the Hetauda gauge (top) for 1998 to 2017 and Jhawani gauge (bottom) for 1998 to 2016.	278
Appendix 7.4: DHM daily rainfall time series for the Makwanpur Gadhi (top) and Rampur gauges (bottom) for 1998 to 2016.....	278
Appendix 7.5: DHM daily average discharge time series for the Lothar gauge for 1998 to 2016 (top) and for 2009 to 2011 (bottom)	279
Appendix 7.6: DHM daily average discharge time series for the Manahari gauge for 1998 to 2016 (top) and for 2009 to 2011 (bottom)	279
Appendix 7.7: DHM daily average discharge time series for the Rapti gauge for 1998 to 2016 (top) and for 2009 to 2011 (bottom).	280
Appendix 7.8: DHM daily rainfall and discharge totals from the 2009 monsoon period (June to September) comparing the Lothar flow gauge and Beluwa rainfall gauged data.	280
Appendix 7.9: DHM daily rainfall and discharge totals from the 2010 monsoon period (June to September) comparing the Lothar flow gauge and Beluwa rainfall gauged data.	281
Appendix 7.10: DHM daily rainfall and discharge totals from the 2009 monsoon period (June to September) comparing the Rapti flow gauge and Hetauda rainfall gauged data.	281
Appendix 7.11: DHM daily rainfall and discharge totals from the 2010 monsoon period (June to September) comparing the Rapti flow gauge and Hetauda rainfall gauged data.	282
Appendix 7.12: The cumulative bias-adjusted rainfall spatial rainfall pattern associated with the 1998 high flow event.	282
Appendix 7.13: The cumulative bias-adjusted rainfall spatial rainfall pattern associated with the 2002 high flow event.	283
Appendix 7.14: The cumulative bias-adjusted rainfall spatial rainfall pattern associated with the 2004 high flow event.	283
Appendix 7.15: The cumulative bias-adjusted rainfall spatial rainfall pattern associated with the 2009 high flow event.	284
Appendix 7.16: The cumulative bias-adjusted rainfall spatial rainfall pattern associated with the 2010 high flow event.	284

Appendix 7.17: The cumulative bias-adjusted rainfall spatial rainfall pattern associated with the July 2011 high flow event.	285
Appendix 7.18: The cumulative bias-adjusted rainfall spatial rainfall pattern associated with the August 2011 high flow event.	285
Appendix 7.19: The cumulative bias-adjusted rainfall spatial rainfall pattern associated with the 2014 high flow event.	286
Appendix 7.20: Literature values for CRUM3 land cover parameters.	287
Appendix 7.21: Literature values for CRUM3 soil parameters.....	288
Appendix 7.22: Literature values for CRUM3 soil parameters.....	289
Appendix 7.23: Parameter ensembles from the top 8 ranked GLUE runs using a formal statistical approach and the Rapti gauged data.....	290
Appendix 7.24: Parameter ensembles from the to 8 ranked GLUE runs using a formal statistical approach and the Lothar gauged data.....	290
Appendix 7.25: Parameter ensembles from the top 8 ranked GLUE runs using an informal hydrological signatures approach and the Rapti gauged data.	291
Appendix 7.26: Parameter ensembles from the to 8 ranked GLUE runs using an informal hydrological signatures approach and the Lothar gauged data.....	291
Appendix 7.27: The median flood extents of the 32 CRUM3 model inflow hydrographs from the channel friction value sensitivity analysis runs of the Sauraha LISFLOOD-FP model	292
Appendix 7.28: The median flood extents of the 32 CRUM3 model inflow hydrographs from the floodplain friction value sensitivity analysis runs of the Sauraha LISFLOOD-FP model.....	292
Appendix 7.29: The median flood extents of the 32 CRUM3 model inflow hydrographs from the downstream boundary slope value sensitivity analysis runs of the Sauraha LISFLOOD-FP model. ..	293
Appendix 7.30: The median flood extents of the 32 CRUM3 model inflow hydrographs from the sub-grid channel geometry parameter value sensitivity analysis runs of the Sauraha LISFLOOD-FP model.	293
Appendix 7.31: The median flood extents of the 32 CRUM3 model inflow hydrographs from the model DEM grid resolution sensitivity analysis runs of the Sauraha LISFLOOD-FP model.....	294
Appendix 7.32: The median flood extents of the 32 CRUM3 model inflow hydrographs from the channel friction value sensitivity analysis runs of the Hetauda LISFLOOD-FP model.....	294
Appendix 7.33: The median flood extents of the 32 CRUM3 model inflow hydrographs from the floodplain friction value sensitivity analysis runs of the Hetauda LISFLOOD-FP model.....	295
Appendix 7.34: The median flood extents of the 32 CRUM3 model inflow hydrographs from the downstream boundary slope value sensitivity analysis runs of the Hetauda LISFLOOD-FP model. ..	295

Appendix 7.35: The median flood extents of the 32 CRUM3 model inflow hydrographs from the sub-grid channel geometry parameter value sensitivity analysis runs of the Hetauda LISFLOOD-FP model. 296

Appendix 7.36: The median flood extents of the 32 CRUM3 model inflow hydrographs from the model DEM grid resolution sensitivity analysis runs of the Hetauda LISFLOOD-FP model 296

ABBREVIATIONS

AC	Autocorrelation
ADCP	Acoustic Doppler current profiler
AEP	Annual exceedance probability
ALOS	Advanced Land Observing Satellite
ASTER	Advanced Spaceborne Thermal Emission and Reflectance Radiometer
CRUM3	Connectivity of Runoff Model v.3
DHM	Department of Hydrology and Meteorology
ESA CCI	European Space Agency Climate Change Initiative
FDC	Flow duration curve
GDP	Gross Domestic Product
GIS	Geographic Information System
GLUE	Generalised Likelihood Uncertainty Estimation
GPCC	Global Precipitation Climatology Centre
GPM	Global Precipitation Measurement
ICIMOD	International Centre for Integrated Mountain Development
JAXA	Japanese Aerospace Exploration Agency
MAE	Mean absolute error
mASL	Metres above sea level
MSE	Mean square error
NASA	National Aeronautics and Space Administration
NFI	National Forest Inventory
NPR	Nepalese Rupee
NSE	Nash-Sutcliffe efficiency
PBIAS	Percent bias
PD	Peak distribution
RLD	Rising limb density
Q	Flow
Q99.9	99.9 th percentile flow
$\overline{Q99.9}$	Mean 99.9 th percentile flow
$\widetilde{Q99.9}$	Median 99.9 th percentile flow
RMSE	Root mean square error
SD	Standard deviation

SCIMAP	Sensitive Catchment Integrated Modelling and Planning
SRTM	Shuttle Radar Topography Mission
TRMM	Tropical Rainfall Measuring Mission
UN	United Nations
USD	United States Dollar

DECLARATION OF COPYRIGHT

I confirm that no part of the material presented in this thesis has been previously submitted by me or any other person for a degree in this or any other university. In all cases, where it is relevant, material from the work of others has been acknowledged.

The copyright of this thesis rests with the author. No quotation from it should be published without the prior written consent, and information derived from it should be acknowledged.

Callum J. Pearson

ACKNOWLEDGEMENTS

This thesis would not have been possible without the many people that have helped make this research project what it is and made the PhD experience a thoroughly enjoyable journey.

Firstly, I would like to thank my main supervisor Sim Reaney for all the advice, support, and encouragement he has provided over the last three and a half years. He has been a great help from the start, helping transition the early ideas into the final product and helping navigate the many challenges that were faced on the way.

I would also like to thank Nick Rosser and Andy Large, my secondary supervisors, who have both provided expert guidance throughout. Nick has been fantastic in helping me acclimatise and navigate the trials faced when working in Nepal. It was a significant step up in fieldwork logistics from my previous experiences in Cumbria! Andy helped facilitate my (temporary) escape to Newcastle and was always willing to catch up over a coffee to discuss how things were going.

Thanks go to my examiners Jeff Warburton and Nick Chappell for an informative and interesting viva. It was a fitting end to my PhD process and the discussions opened up many possibilities for taking the research forward.

With regards to the fieldwork side of project I would like to thank help that came in a variety of forms from Matt, Borbala, Ed, Ivo, and Jack whilst out in Nepal. This ranged from wading into the streams for flow gauging purposes to introducing me to the joys of getting your momos fried rather than steamed.

I would like to thank my friends (Simon, Ed, Pope, Bertie, and Josh amongst others) from Department of Geography at Durham for the daily coffee-fuelled distractions in the Manley Room and for the (predominantly cycling- and pub-based) activities beyond the confines of work. Further thanks go to those in Newcastle and the IAPETUS DTP for the enjoyable time spent working whilst away from Durham.

My final thanks go to my family and my girlfriend Abi for their support throughout the project. Abi in particular has had to endure my occasional on-off love affair with the East Rapti catchment and I cannot thank her enough for her all-round amazingness that helped get me through the project.

ACKNOWLEDGEMENT OF FUNDING

This research was funded by the Natural Environment Research Council as part of the IAPETUS Doctoral Training Programme (NE/L002590/1).

Additional financial support for fieldwork was provided by the Faculty of Humanities and Social Sciences Bid Preparation Fund at the University of Newcastle and through the Institute of Hazard, Risk and Resilience at Durham University from a donation by Charles Wilson.

1 INTRODUCTION

1.1 THE IMPACTS AND MANAGEMENT OF FLUVIAL FLOODING IN NEPAL

Nepal is a country heavily impacted by disasters with extensive loss of life, property, and economic damage caused by flooding, earthquakes, droughts, landslides, famines, and epidemics (Government of Nepal, 2010; DesInventar, 2019). Flooding has the most regular impact of the disasters on the Nepali population, accounting for 39.1% of the 128 disasters recorded between 1954 and 2019 flooding related (EM-DAT, 2019). Flood-related disasters account for > 46% of the 11.9 million people affected and > 19% of the 45,447 people injured or killed by natural disasters in the same time-period (EM-DAT, 2019). Between 1971 and 2013 the combination of floods and rainfall-induced landslides have killed over 8,500 people in Nepal with the mountain and hill regions susceptible to landslides and the lowland regions prone to fluvial flooding (DesInventar, 2019). There have been 30 significant flood events between 1950 and 2019 that have each been confirmed to have killed over 100 people (EM-DAT, 2019).

Recent major flood events include the 1993 central Nepal floods, the 2008 western Nepal floods, the 2008 Koshi embankment failure, the 2013 Mahakali floods, 2014 Karnali floods, and the 2017 southern Nepal floods; all bar the 2008 Koshi embankment failure were caused due to consistent heavy rainfall (ISET-International, 2015; Smith et al., 2016; Government of Nepal, 2017; EM-DAT, 2019). Merz et al. (2006) and the UNDP Nepal (2009) note, however, that lesser flood events are an annually reoccurring issue for the lowland regions in Nepal. In addition to the loss of human life, there are economic and social costs to the hydrological disasters with over 5,000,000 people affected, over 115,000 houses destroyed with further 140,000 damaged, and an estimated 600 km of the road network damaged between 1971 and 2013 (DesInventar, 2019). The 2017 southern Nepal floods alone caused NRP 60,716 million (USD 584.7 million) in damage and losses, excluding personal household losses, which amounts to approximately 3% of Nepal's GDP (Government of Nepal, 2017). With many communities in the Terai region relying on subsistence agriculture the floods can have a devastating impact on an individual level; the 2008 Koshi flood, for example, killed 14,571 livestock and deposited sand on agriculturally productive land (Gautum and Dulal, 2013; Smith et al., 2016).

There are five major mechanisms that trigger flooding in Nepal: 1) rainfall-generated fluvial floods, 2) glacial lake outburst floods, 3) landslide dam outburst floods, 4) pluvial (surface water) flooding, and 5) flooding associated with infrastructure failure (WECS, 2011). During the monsoon season (June to September) Nepali catchments receive between 70% and 90% of the annual rainfall total and, correspondingly, 80% of the total annual flow occurs in this period (Gautum and Acharya, 2011,

Andermann et al., 2012a). It is in the monsoon period that 88% of the EM-DAT (2019) categorised flood events occur; a sub-type within the hydrological disasters group, the flood category comprises of coastal, riverine, flash and ice jam flood events. Of the flood events categorised in the EM-DAT (2019) disaster inventory 78% were fluvial in nature with rainfall-generated fluvial flooding predominantly occurring in the latter stages of the monsoon season when the ground is saturated and saturation excess overland flow happens (Gilmour et al., 1987; Merz et al., 2006; WECS, 2011). Merz et al. (2006) establishes that the largest rainfall-runoff events occur with high volume, long duration, and medium intensity rainfall events.

The locations of the major catchments throughout Nepal are shown in Figure 1.1 with a conceptual overview of the geomorphic zones that Nepal comprises of shown in Figure 1.2. The largest catchments (Koshi, Nayarani, Karnali and Mahakali) are a mixture of snow- and rain-fed (Bookhagen and Burbank, 2010; Smith et al., 2016). The flooding within the many of the medium-sized rain-fed catchments, such as the Bagmati, West Rapti and Babai rivers originating from the Mahabharat Range, occurs from both continuous, long duration rainfall causing an overtopping of the banks along the main channel network and from intense rainfall causing flash flooding in the small tributaries originating in the Siwalik Range (Government of Nepal, 2010; Asian Development Bank, 2016; Smith et al., 2016; Government of Nepal, 2017). Extreme rainfall has the potential to cause flash flooding and is most likely to occur in the hills of the Siwalik Range where smaller catchments have a rapid time-to-peak (ADPC, 2010). Continuous rainfall-driven floods along the main channel network of the medium-sized catchments are often characterised by a gradual rise and fall of the flood levels with a low velocity (Singh, 2013). During the severe July 1993 flooding in central Nepal, a maximum 24-hour rainfall of 540 mm was recorded at Tistung; including an hourly maximum rainfall of 70 mm (Dhital et al., 2011). The high intensity and large volume of rainfall was spread over an area of 530 km² during the July 1993 event; resulting in widespread flash flooding and landslides that killed 160 people in highland areas and 815 in lowland areas with over 60,000 people displaced (Chalise and Khanal, 2002). The August 2014 Karnali flood was generated by a 24-hour rainfall totals of up to 500 mm recorded across the catchment (ISET-International, 2015). This rainfall resulted in an estimated 1-in-1000 year (0.1% annual exceedance probability (AEP)) flood event and the Karnali River rising by an estimated 9 m at a gauging station in the northern part of the Terai region (ISET-International, 2015).

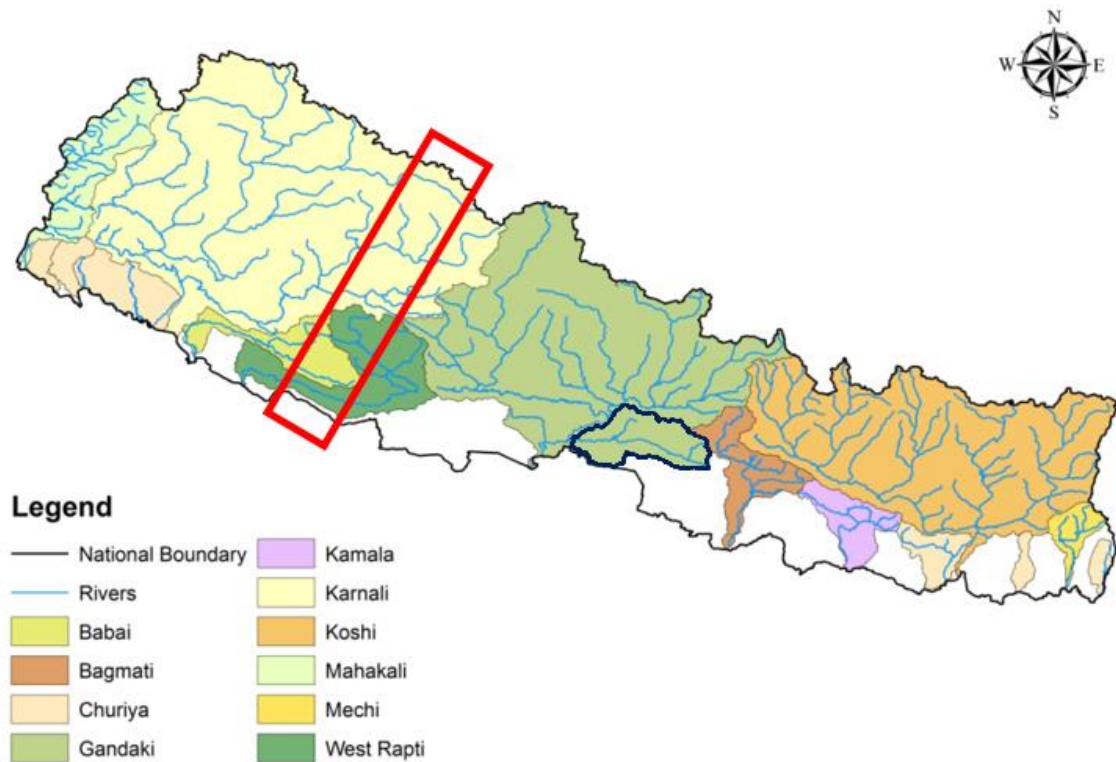


Figure 1.1: The major river basins in Nepal (from Smith et al., 2016 [pp. 2]). Red polygon shows an example spatial coverage of illustration in Figure 1.2 below. The East Rapti catchment, the case study catchment, is a sub-catchment of the Gandaki/Nayarani catchment illustrated with a dark blue outline. Note: presented national boundary does not account for updates made in June 2020.

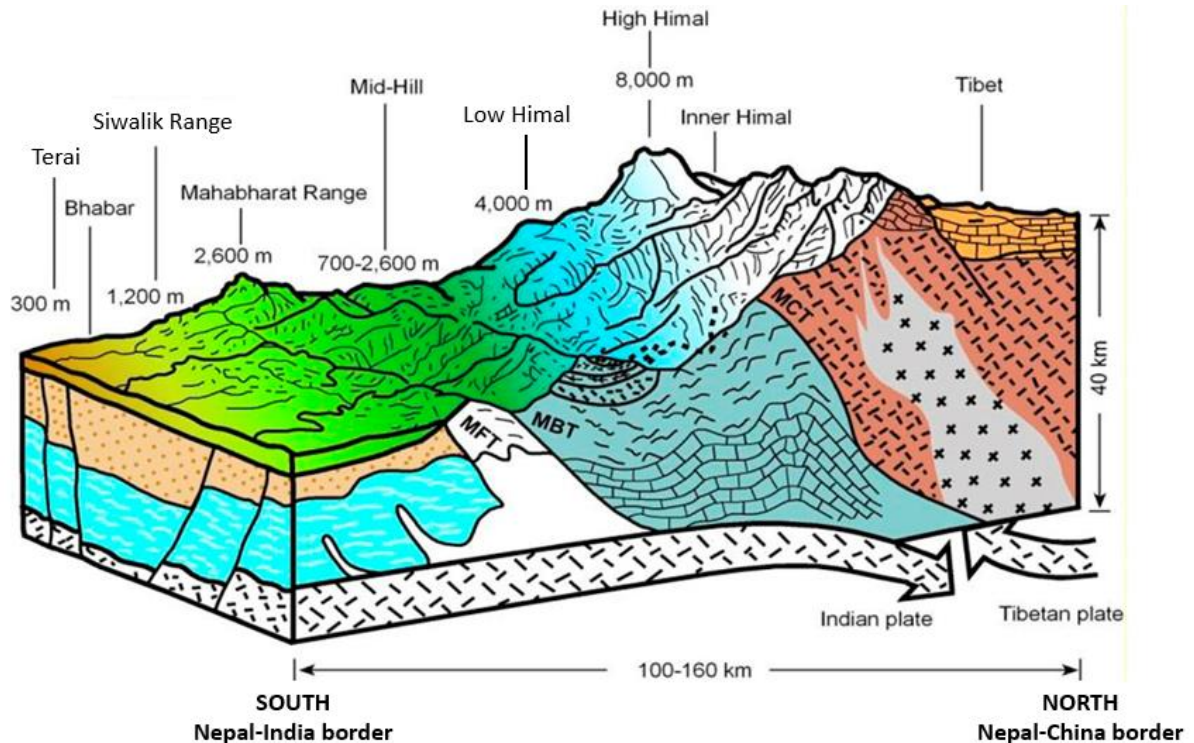


Figure 1.2: An illustration of the main geomorphic zones occurring in a cross-section through Nepal (modified from Bricker et al., 2014 [pp. 13]). See red polygon in Figure 1.1 for an example coverage of the cross-section.

The spatial distribution of two of the impacts of flooding are shown in Figure 1.3 (persons affected) and Figure 1.4 (houses destroyed or damaged). The figures show that the majority of the flooding causes the greatest number of deaths and damage in the more densely populated Terai plains and Siwalik Range regions. The largest numbers of deaths have occurred in the Bagmati, Kamala and Narayani catchments. Seen in Figure 1.5, the mountainous regions have the lowest population densities with the highest, outside of the Kathmandu Valley, seen across the central and eastern parts of Terai region (Government of Nepal, 2010). There are, however, other areas in the Middle Hills (including the Mahabharat Range) and the mountains of the Lesser Himalayas that have experienced deaths and economic damage due to flooding. This spatial variation of flood damage can be attributed to geomorphology and population distribution. The steep valleys and gorges in the mountainous regions constrain flows and limit the potential area of flooding in addition to determining where the population can inhabit with few settlements on the valley bottom. Conversely, the flat Terai region has minimal restriction on the flow once the embankments are overtopped (Government of Nepal, 2010). Additionally, due to sedimentation, the beds of many rivers in the Terai erode and aggrade by between 100 mm and 300 mm a year; many communities are therefore located at lower elevations than the neighbouring river (ISET-International, 2015).

The current method for managing the fluvial flood risk in Nepal generally involves localised interventions in affected areas using a static and reactive approach (Dhakal, 2013). This reactive approach largely fails to consider the interactions between source and impact areas of flood waters across the catchment (Dhakal, 2013; Nepal et al., 2014). To improve flood management, there is therefore a need to consider the catchment as a connected system and explore measures that address the sources and movement of flood water and associated mitigation features to reduce the flood hazard (POST, 2014). Notably, many of the existing structural measures, such as embankments along the channel, are often poorly maintained and prone to failure, resulting in large-scale inundation in areas considered to be protected (Government of Nepal, 2017). As noted in response to recent flood events by Dhakal (2013) and the Government of Nepal (2017), there is the need to rely less on large-scale structural measures and focus instead on sustainable, non-structural measures for flood mitigation that allow the catchments and communities within them to be more resilient. The impact and resilience of any adopted flood management approaches within many Nepali catchments will be placed under stress with possible widespread future land use change (e.g. the abandonment of agricultural terraces, deforestation and urban expansion) having a potential detrimental impact on the hydrological regime and leading to higher flood peaks for the same rainfall event (e.g. Ives and Messerli, 1989; Singh, 2013; Chaudary et al., 2016; Rimal et al., 2019).

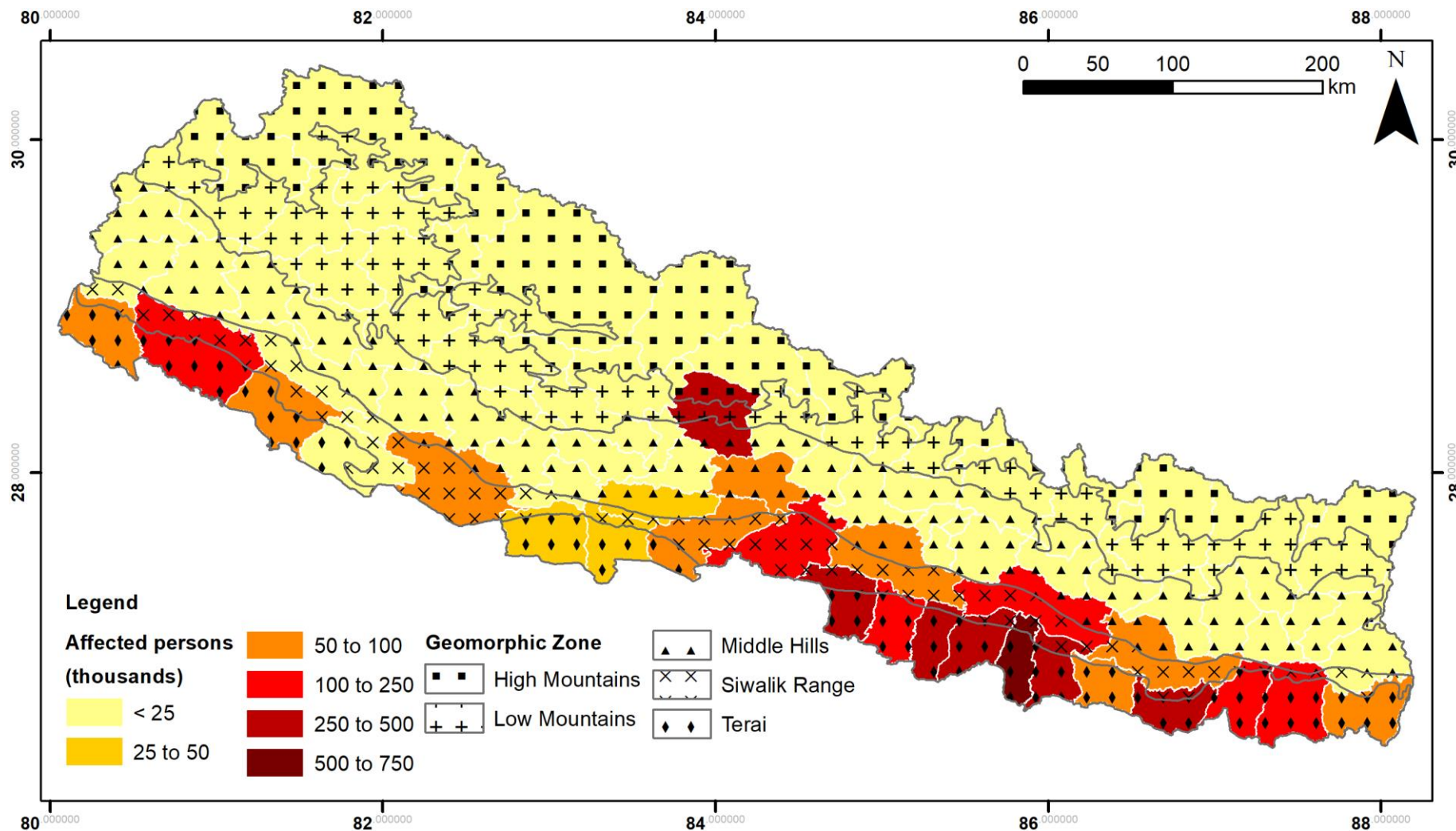


Figure 1.3: District level totals of people affected (both directly and indirectly) due to flooding across Nepal (data from DesInventar, 2019). A simplified distribution of the geomorphic zones is overlaid (data from ESA, 2013). The Mahabharat Range is situated immediately to the north of Siwalik Range within the Middle Hills zone. Note: presented national boundary does not account for updates made in June 2020.

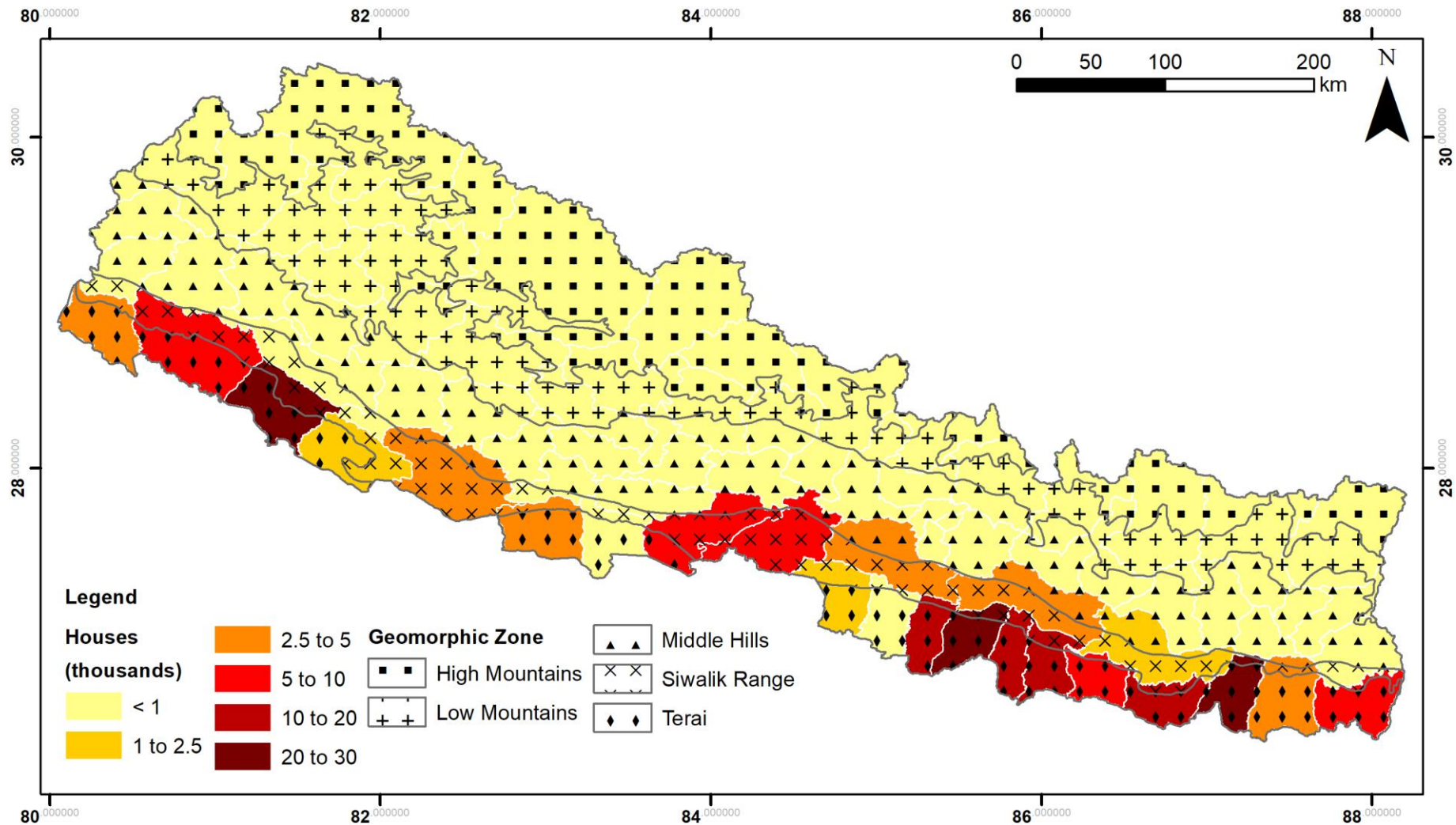


Figure 1.4: District level totals of houses destroyed or damaged due to flooding across Nepal (data from DesInventar, 2019). A simplified distribution of the geomorphic zones is overlaid (data from ESA, 2013). The Mahabharat Range is situated immediately to the north of Siwalik Range within the Middle Hills zone. Note: presented national boundary does not account for updates made in June 2020.

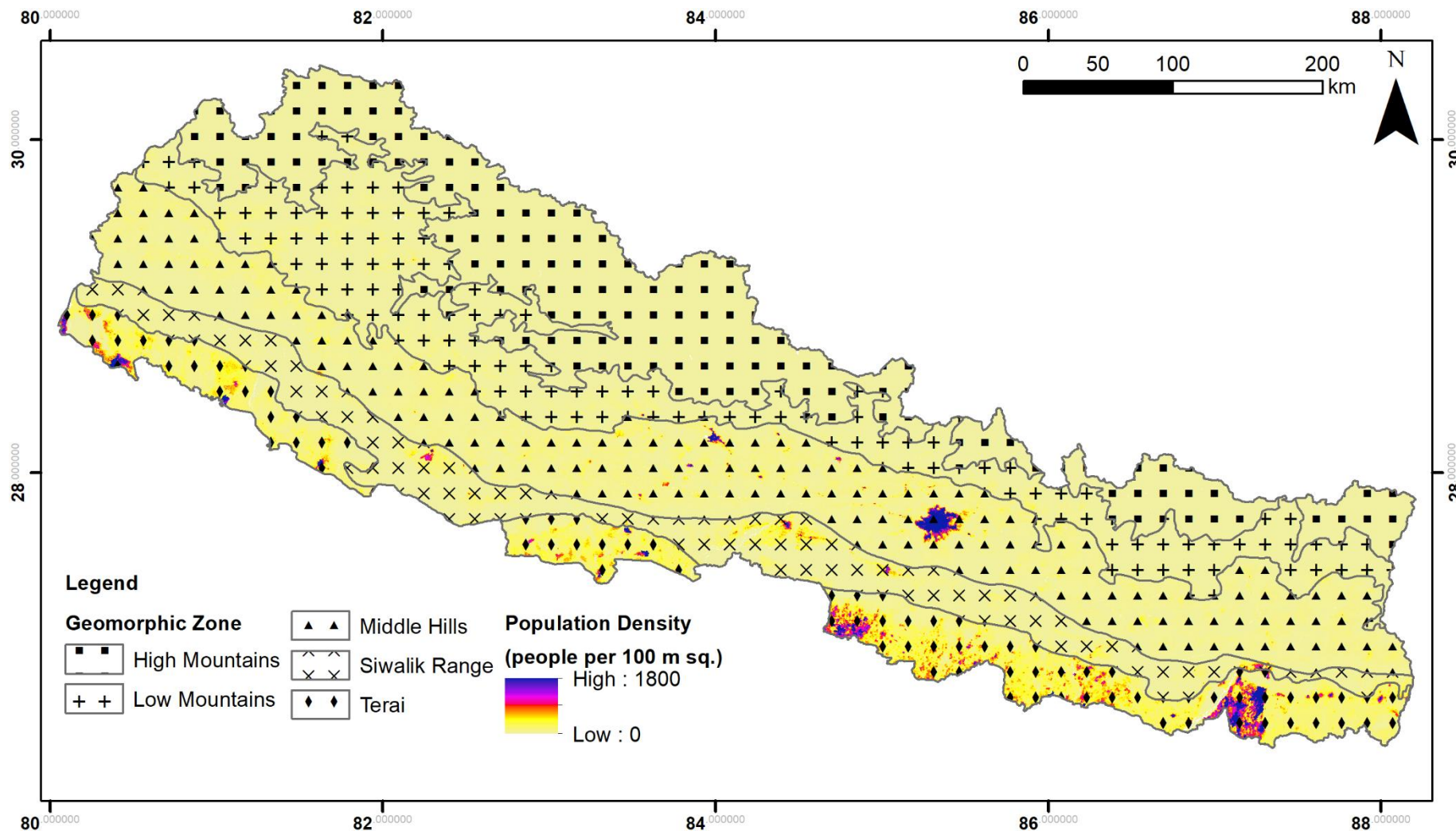


Figure 1.5: Population density across Nepal (data from UN OCHA, 2019). A simplified distribution of the geomorphic zones is overlaid (data from ESA, 2013). The Mahabharat Range is situated immediately to the north of Siwalik Range within the Middle Hills zone. Note: presented national boundary does not account for updates made in June 2020.

1.2 RESEARCH AIM AND OBJECTIVES

The aim of this thesis was *to evaluate the potential for spatially targeted catchment-scale flood management measures in the East Rapti catchment, Nepal*. This evaluation was made using a combination of field data and exploratory numerical modelling. The process developed in this research is applicable to catchments beyond the presented case study and allows policy makers, catchment managers, and scientists to gain an understanding into the potential contribution of future land cover change and the implementation of flood management measures on the high flow regime at key flood impacted areas within a catchment.

To meet the aim the research has the following objectives:

- 1. To establish the spatial distribution of source areas that contribute to flooding at the catchment-scale.**
- 2. To ascertain where to spatially target flood management measures within a catchment.**
- 3. To quantify the potential impact of spatially targeted flood management measures on the hydrological regime at the catchment-scale.**
- 4. To quantify the potential impact of land use change on the hydrological regime at the catchment-scale.**
- 5. To determine the effect of spatially targeted flood management measures on altering the inundation patterns at key flood impact points.**
- 6. To determine the effect of land use change and degradation on altering the inundation patterns at key flood impact points across the catchment.**

1.3 RESEARCH APPROACH: AN OVERVIEW OF THE END-TO-END PROCESS FOR THE SPATIAL TARGETING OF FLOOD MANAGEMENT MEASURES AT THE CATCHMENT-SCALE

This research has investigated the potential effectiveness of the implementation of flood management interventions at the catchment-scale. It evidences an alternative approach to flood risk management applicable in Nepal, the wider Himalayan Region and beyond. The process developed throughout this project will also attempt to quantify the potential impact on the flood regime of future land use change.

This approach is applied to the East Rapti catchment in southern Nepal with the research process applicable in other catchments. Representative of a typical medium-sized Nepali catchment, many of the communities in the East Rapti catchment experience annual flooding (UNDP Nepal, 2009). The East Rapti catchment was heavily impacted by the 2017 flood event that, as a result of continuous

monsoonal rainfall, was responsible for 12 deaths within districts that make up the catchment (Chitwan and Makwanpur) (Government of Nepal, 2017).

Figure 1.6 provides an overview of the end-to-end approach developed in this research to meet the overall project aim. The approach is capable of testing spatially targeted flood management scenarios at the catchment-scale. The end-to-end approach is split into three stages that combine to create a catchment-scale flood management toolkit that functions at a range of spatial scales.

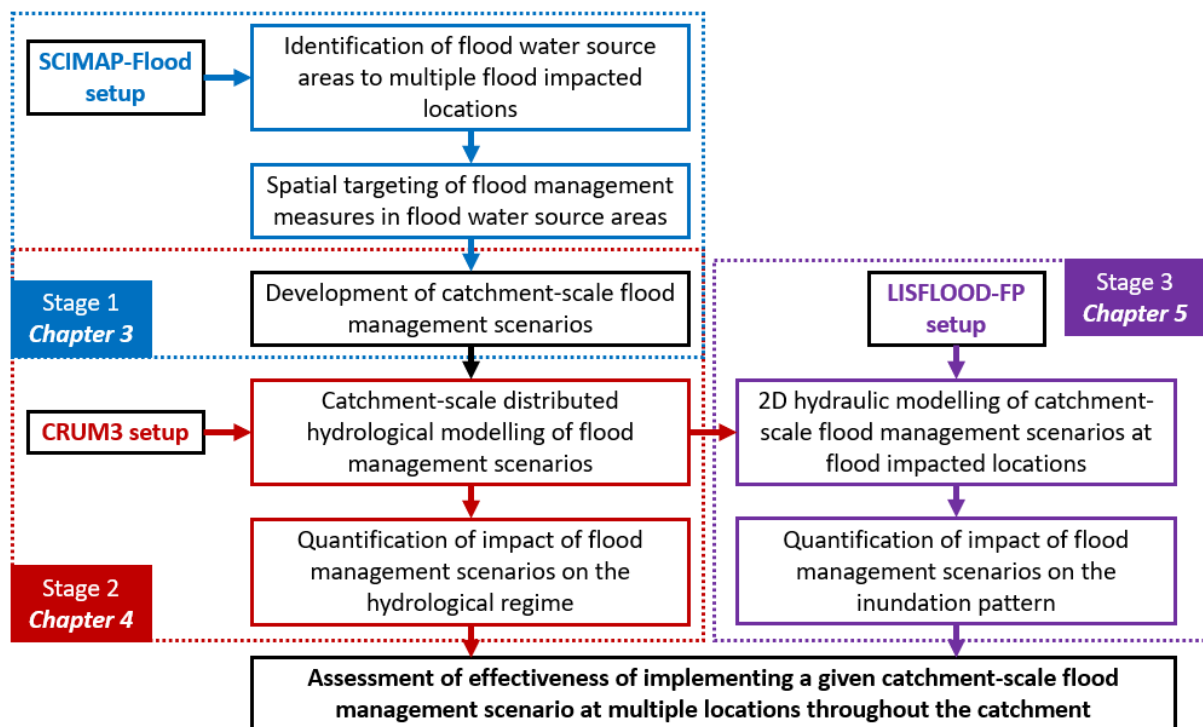


Figure 1.6: A conceptual overview of the three modelling stages used in the end-to-end approach for the spatial targeting of flood management measures at the catchment-scale.

1.3.1 Stage 1 – Identifying flood water generating areas using SCIMAP-Flood

The first stage of the process involves identifying the flood source areas and impact areas at the catchment-scale. This stage will be achieved using SCIMAP-Flood (Reaney, *in prep.*), a risk-based decision support framework, to help inform and develop flood management scenarios. SCIMAP-Flood identifies flood water generating areas based on analysis of spatial rainfall patterns and land cover, the incorporation of transmission times across a catchment, and modelling of hydrological connectivity. The SCIMAP-Flood output identifies locations where flood management measures would be most suitable to have a positive effect, if implemented, for multiple flood impacted communities across the catchment. SCIMAP-Flood requires minimal input data to operate and can be run using global datasets and can therefore be applied to catchments with limited or no available local data.

This research presents the development of the SCIMAP-Flood Fitted approach. An extension of SCIMAP-Flood that uses inverse modelling to determine the land cover risk weightings within the

SCIMAP-Flood framework. Additionally, this is the first application of SCIMAP-Flood in a data sparse context, with an approach established to develop a system suitable for application in other catchments with poorer data availability.

1.3.2 Stage 2 – Catchment-scale scenario modelling using CRUM3

The second stage of the process aims to quantify the impact of the flood management measures and land use change on the flow regime using a physically-based, fully distributed hydrological model, CRUM3 (Lane et al., 2009). Spatially targeted catchment-scale scenarios are created using the SCIMAP-Flood output and then modelled in detail using CRUM3. The spatially explicit scenarios, in which individual catchment cells can be altered, provides a more accurate picture of the hydrological impact of catchment-scale land use change and possible flow magnitude reduction scenarios than a lumped or semi-distributed model. The CRUM3 output shows the impact of a given scenario on the flow hydrographs at multiple locations throughout the catchment. This approach allows for the assessment of the impact on the hydrological regime from a given catchment-scale management scenario at all the flood impacted areas and hence enables a catchment-wide consideration of the effect of mitigation measures. Within the East Rapti case study the modelled flood management scenarios involve targeted afforestation and the implementation of check dams in key flood water generating sub-catchments. Additional scenarios were modelled to simulate future land use change (e.g. deforestation and urban expansion) across the catchment.

The presented CRUM3 research covers one of the first detailed catchment-scale flood management studies using a distributed hydrological model in a Nepali catchment. The findings evidence an approach that can be used to consider the effect of a mitigation scenario on the flow regime across multiple points of flood impact within a catchment. Additionally, the approach used is the first study using the CRUM3 model to have spatially distributed rainfall with a scaled rainfall grid providing individual daily rainfall totals for each cell in the catchment.

1.3.3 Stage 3 – Inundation modelling at flood impact points using LISFLOOD-FP

The third stage of the process uses a coupled modelling approach that applies the hydrograph output from the flood management and land use change scenario modelling (Stage 2) as inflows in a hydraulic inundation model. The hydraulic model used in the final stage of the end-to-end approach is LISFLOOD-FP which represents the 2D water flow and flood inundation (Bates and De Roo, 2000). The output of the LISFLOOD-FP hydraulic modelling determines the inundation patterns, as a result of implementing a given catchment-scale scenario, at key flood impacted areas within the catchment. The results of the hydraulic modelling can help determine if the flow magnitude changes produced from the CRUM3 catchment modelling provide a benefit with regards to the inundation extent at key flood impact areas.

The LISFLOOD-FP research, in addition to the CRUM3 modelling, outlines one of the first coupled hydrological/hydraulic modelling approaches undertaken in a Nepali catchment. The coupled modelling approach is the first to investigate the potential impacts from implementing a catchment-scale flood management approach within the region.

1.4 THESIS STRUCTURE

The structure of this thesis follows the conceptual overview of the end-to-end approach outlined in Figure 1.6 and contains six chapters which combine to meet the research objectives presented in Section 1.2.

Chapter 2 provides an overview of the East Rapti catchment, the case study catchment used to explore the application of the end-to-end approach. This chapter also includes an evaluation of the climate and river flow data that has been used throughout the research process.

Chapter 3 presents the development and application of the SCIMAP-Flood framework in the first stage of the approach. The research in this chapter establishes the source areas within the East Rapti catchment that generate flood waters to key flood impacted communities and helps meet both the first and second research objective.

Chapter 4 presents the findings of the CRUM3 catchment-scale hydrological modelling for the East Rapti catchment. The CRUM3 model results help address the third and fourth research objectives and provide an indication as to the impact of both catchment-scale flood management measures on reducing the flow magnitude throughout the catchment and the impact of future land use change and land degradation on increasing the flow magnitude.

Chapter 5 presents the outputs from the LISFLOOD-FP inundation modelling. The third and final stage of the approach allows for the comparison of inundation patterns at key flood impacted areas. This stage builds on the results of catchment modelling in Chapter 4 using the hydrographs from the catchment-scale scenarios. The approach used in this chapter provides evidence to answer the fifth and sixth research objectives.

Chapter 6 summarises the overall end-to-end approach created to meet the research aims and discusses the implications arising from the East Rapti case study. This chapter also includes the main conclusions, recommendations, and proposed future work that is based on the findings of the research.

1.5 BACKGROUND LITERATURE

1.5.1 Current and future approaches to flood management in Nepal

Globally, investment in flood defences has been dominated by a paradigm of hard-engineering solutions to protect urban areas from inundation (Thorne et al., 2007; Howgate and Kenyon, 2009). Within Western Europe, the cost of implementation and maintenance of concrete defences coupled with limited budgets and increasing flood risk has led to need to a focus on more sustainable, cheaper, flood management on a catchment-wide scale (Nisbet et al., 2011). This approach is often referred to as a catchment-based flood management. The approach aims to alter the river flow at certain locations (e.g. a settlement or vital infrastructure) during the flood peak whilst considering the entire catchment as a whole system (Lane, 2017). A notable aspect of the approach is a reliance on the reintroduction of more natural hydrological processes within the catchment through soft-engineering (POST, 2014; Iacob et al., 2017; Lane, 2017). Under the catchment-based flood management approach, it is necessary to consider the variability of flow at any given point in the catchment as a consequence of two contrasting processes: attenuating flow or increasing tributary flow (Lane, 2017). The catchment-based flood management approach then works through optimising the balance between flow attenuation and increasing tributary flow input.

The flood management approach currently taken in Nepal contrasts with this catchment-based approach. Research by Nepal et al. (2014) concludes that an integrated land and water management approach undertaken at both the basin and catchment-scale is necessary to ensure sustainable development and reduced detrimental impacts. This recommended shift to a more integrated approach would bring the flood management process in Nepal in line with the global trend, especially with the soft engineering solutions perhaps best utilised where they can improve and aid the effectiveness of the traditional hard-engineering approach (Lane, 2017). There is research within Nepal that investigates the implementation of an integrated catchment management approach. Through modelling using HEC-RAS (Brunner, 1995), Singh (2013) establishes that, in addition to well-designed river training structural measures, targeted afforestation and controlled deforestation in Chitwan could reduce the flood hazard. The impact of check dams to attenuate flow in the upper parts of the catchment is noted in both Singh (2013) and Asian Development Bank (2016).

The International Centre for Integrated Mountain Development (ICIMOD) detail that the advised approach for flood risk management, in particular flash flood risk management, in the Himalaya Region involves both non-structural aspects and structural interventions (Shrestha et al., 2012). The non-structural elements to flood risk management include education, training, the raising of awareness and localised early warning systems; it is noted, however, that non-structural methods are

most effective with a responsive population and an organised network. Singh (2013) highlights socio-economic interventions such as public awareness campaigns on the importance of forest resources as a flood mitigation device and on the diversification of fuel sources to reduce reliance on fuelwood. There are differences in the perceived value of the forest as an ecosystem service in Nepal at present with those in the upland source areas of the catchment placing priorities on fuel and soil conservation and not for its flood control potential (Acharya et al., 2019). Adhikari (2013) notes that there should be better enforcement of, and education around, the riverbed sediment mining that takes place across the Terai region which has the potential to increase localised flood inundation. Shrestha and Bajracharya (2013) state that there is ongoing testing of flood forecasting models in Nepal. The flood forecasting models will help develop an early warning system. There is additional research on localised community-based early warning systems by Smith et al. (2016) which investigates similar early warning system approaches used in the Terai region of India (Shukla and Mall, 2016). Through NGO Practical Action, community based early warning systems are operational in eight Nepali catchments; the system should give between two and six hours for a community to prepare for a flood event (Smith et al., 2016).

The structural interventions outlined in Shrestha et al. (2012) are comparable to those used in other countries and involve a variation of soft- and hard-engineering methods. Localised hard-engineering interventions include levees and embankments, terracing for slope control and check dams for sediment and discharge control (Shrestha et al., 2012; Shrestha, 2014). Hard-engineering, such as gabion embankments and other river training interventions, is often employed in the Terai region but, due to rapid sediment deposition, often have a limited lifespan (Dhakal, 2013). Furthermore, the use of dams for flood storage is illustrated; this method has the potential benefit of hydropower production and water resource storage (Dhawan, 1993; Shrestha et al., 2012; Sharma and Awal, 2013). It should be noted that, despite strong seasonal river flow variation, the majority of existing hydropower stations in Nepal are run-of-the-river types and do not store water. Sharma and Awal (2013) suggest that a mixture of run-of-the-river and storage dams should be built to store water and reduce the diurnal and seasonal variation in sediment supply. Soft-engineering techniques and interventions include the use of vegetation for slope control and retaining soil to maintain or increase the infiltration capacity (Shrestha et al., 2012). Dhawan (1993) and Nepal et al. (2014) highlight that, with deforestation being a potential cause of increased flood risk in the Himalayas, that afforestation could reduce the risk of flooding.

The implementation of flood management schemes in Nepal has generally been reactive with the localised implementation failing to consider the hydrological regime at the catchment-scale. Within the available literature there is guidance and case studies on the flood risk reduction approaches from

organisations such as ICIMOD. However, there is limited literature on the quantification and relative effectiveness for a proper analysis of the implementation of a catchment-scale approach.

1.5.2 Land use change and the hydrological impact in Nepal and the wider Himalayas

With many Nepali catchments land use change and degradation, including the abandonment of agricultural terraces, extensive deforestation and urban expansion, are key factors that have a potential detrimental impact on the hydrological regime (Ives and Messerli 1989; Nepal, 2012; Paudel et al., 2014; Chaudary et al., 2016; Rimal et al., 2019). Section 1.5.2.1 outlines the effects of deforestation on the hydrological regime with Section 1.5.2.2 providing an overview of the impact of terraced agriculture, and consequent agricultural abandonment, on the catchment hydrology.

1.5.2.1 *Deforestation*

Within Nepal the forests are the largest natural resource and an important factor in the economy (Chaudhary et al., 2016). Deforestation within Nepal has occurred largely due to population pressure with a growing population requiring more fuelwood, more timber for construction and more agricultural land (Ives and Messerli, 1989; Metz, 1991; Gerrard and Gardner, 2002; Neupane et al., 2015; Chaudary et al., 2016). Chaudary et al. (2016) ascertain that the overall forest cover in Nepal has steadily declined with an annual deforestation rate of 1.7% during the 1980s and 1990s. Ives and Messerli (1989) determine that between 1950 and 1980 over half the forest reserves within Nepal were lost. This annual rate of change is deemed to have slowed to between 0.06% and 0.18% between the 1990s and 2010 and preventative measures such as the Community Forest intervention have been undertaken (Chaudary et al., 2016). However, Rimal et al. (2019) through land use change modelling predict that deforestation will continue towards the 2030s due to continued urban expansion throughout Nepal.

The hydrological impact of deforestation in the Himalayan region, at the plot-scale, can be seen through a range of research. Haigh et al. (1990) ascertain that during the monsoon season in Uttarakhand, the pine forests intercepted 22% of rainfall and the denser Sal forest intercepted 34%. Working in the Middle Hills of Nepal, Gardner and Gerrard (2003) establish that the monsoon runoff coefficient was 33% for degraded forest cover and 1% for good status secondary forest cover. This runoff coefficient for forest is comparable to the 0.2% to 1.3% measured by Pathak et al. (1985). Land converted to terraced agriculture had a runoff coefficient of between 5% and 26% (Gardner and Gerrard, 2003). Sastry et al. (1986) found that the cumulative impact on runoff in a catchment experiencing deforestation converted to agriculture resulted in the volume of runoff increasing by 15% with a 72% increase in peak runoff rate.

Ives (1989) and Ives and Messerli (1989), when discussing the theory of 'Himalayan environmental degradation', state that deforestation disrupts the normal hydrological regime and increases river flow with a reduced infiltration capacity increasing surface run-off entering the river system and an increase in sedimentation rates from deforested areas removing the storage capacity of the channel network. An additional impact of deforestation is the reduced evapotranspiration within the catchment from the reduced forest cover (Zhang et al., 1999; Nepal et al., 2014). A Nepali Government Department of Water Induced Disaster Prevention study in the Lothar Khola in southern Nepal determined that uncontrolled deforestation was the primary cause of sediment aggradation and consequent reduced channel capacity (Singh, 2013). There is also a perceived risk of deforestation causing flooding within Nepal, ranking as the second biggest cause of flooding after 'rainfall patterns changing due to climate change' in socio-hydrological analysis by Devkota (2014). Modelling undertaken by Rai and Sharma (1998) supports this with land use change in a catchment from forestry and agro-forestry to open agriculture increasing streamflow predictions by 11%.

The role of deforestation on the flood regime in Nepal is, however, contested with some research concluding that deforestation would have only a minor, if any, role in monsoonal flooding (e.g. Gilmour et al., 1987; Hamilton and Pearce, 1988; Thomson et al., 2007; van Dijk et al., 2009; Nepal, 2012). Gilmour et al. (1987) and van Dijk et al. (2009) establish that, whilst the surface soil infiltration capacity increases through transition from grazed grassland to forest, the cumulative impact is not likely to reduce flooding downstream but could reduce localised overland flow and gully erosion. This localised impact is more likely to have an impact in small sub-catchments but not across larger catchments where flow synchronisation and spatial and temporal variation in rainfall and land use will reduce the impact that deforestation has on the hydrological regime (Metz, 1991; Beschta, 1998; Bruijnzeel, 2004; van Dijk et al., 2009).

1.5.2.2 Agricultural terracing and consequent abandonment

Agriculture in mountainous regions is dominated by the use of terraces, particularly in economies reliant on subsistence agriculture such as Nepal (Lasanta et al., 2001; Arnaez et al., 2015). The terracing system provides a larger surface area of flat land for crop production through the creation of a cultivated section and a riser (van Dijk and Bruijnzeel, 2004; Arnaez et al., 2015; Wei et al., 2016). Figure 1.7 illustrates examples of different terrace types across Nepal. The global variety in formation, structure and usage of agricultural terraces has resulted in numerous terrace classification systems (Wei et al., 2016). Within Nepal there are two forms of terrace system; 'bari', outward sloping rain fed terraces and 'khet', irrigated terraces generally found near a valley bottom (Gerrard and Gardner, 2000). Gardner and Gerrard (2003) found that, for a rain fed terraced catchment in the Middle Hills of Nepal, terrace widths were between 2 m and 10 m and the terrace risers were approximately 2 m in

height. Terraced agriculture increases soil infiltration rates, reduces the risk of soil erosion and decreases runoff; this results in more water being retained on the hillslopes and potentially has an impact on flood generation (Wheaton and Monke, 2001; Arnaez et al., 2015).

The development of agricultural terraces impacts significantly on the local hydrological processes. The construction of terraces reduces the slope, irrigation ditches alter the drainage network, and the soil characteristics change as infiltration rates increase and soil water saturation may occur (Arnaez et al., 2015). Vegetation type and coverage has a significant impact on the runoff coefficient of agricultural terraces; with a coefficient of between 5% and 50% in a monsoonal climate, between 5% and 25% in a drier climate and between 20% and 40% in abandoned terraces (Gardner and Gerrard, 2003; van Dijk et al., 2005; Seeger and Ries, 2008; Arnaez et al., 2011). Irrigation ditches are needed in areas of high annual rainfall to prevent additional water flowing over the terrace risers and causing excessive soil erosion (Gardner and Gerrard 2003). There is a reduction of the strength of the hydrological connectivity within a terraced catchment with the terrace construction interrupting overland flow and altering the runoff contribution dynamics with a catchment (Cammeraat, 2004; Arnaez et al., 2015; Wei et al., 2016).

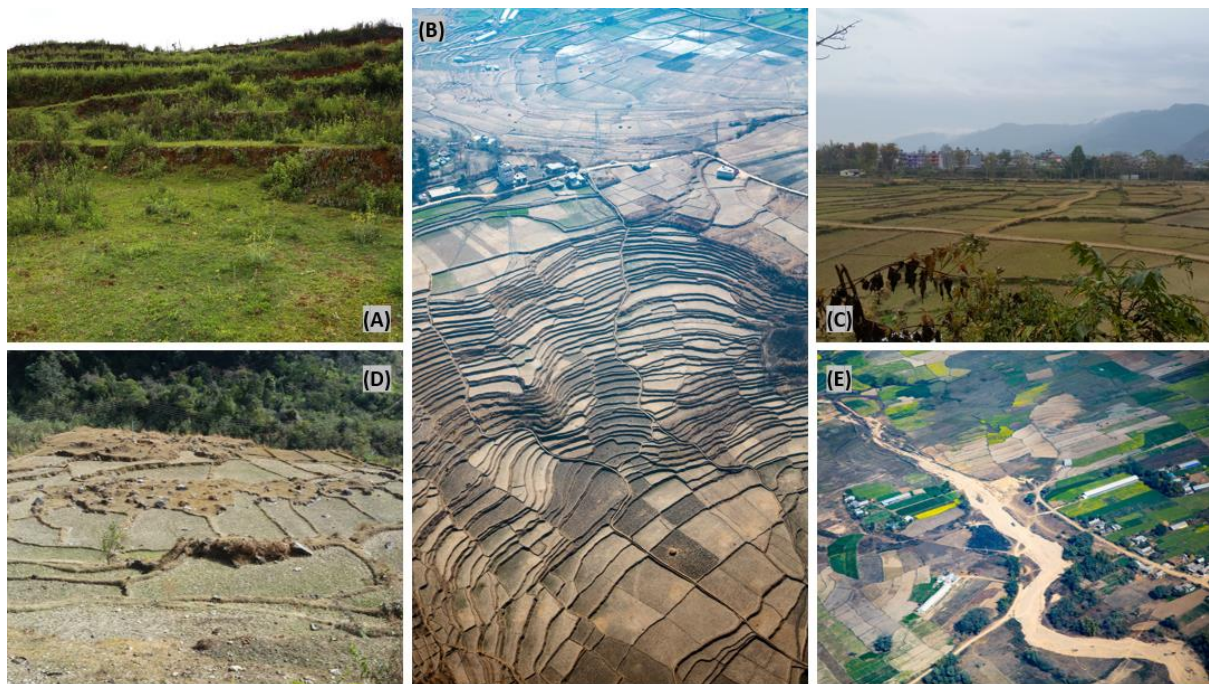


Figure 1.7: Examples of terraced agriculture in Nepal. (a) abandoned hill terraces, (b & d) a network of hill terraces and (c & e) lowland, irrigated terrace network. Photos taken by the author between January 2017 and May 2018.

Taking a global perspective from areas with similar agricultural practices, Bellin et al., (2009) illustrate that terraces decrease the hydrological connectivity and slowed runoff for rainfall events with a return period of less than 10 years in Murcia, Spain. Wei et al. (2016) state that terracing increases soil moisture and water holding capacity through increased soil roughness. A study of the Yun-Gui Plateau,

a dryland area in the Southwestern China, saw mean soil moisture increasing from 15.7% in the slopes to 29.7% in terraced slopes; other studies indicate that the water holding capacity under terraces could be 5.0 to 6.2 times higher than under unaltered slopes (Li et al., 2006). In Uttarakand, India, Haigh et al. (1990) establish that well maintained back-sloping terraces provide the best practice for soil and water conservation. The study found an average infiltration rate of 33.6 mm hr⁻¹ in terraced cropland compared to 21.5 mm hr⁻¹ with grassland. From a catchment-scale runoff and flow generation potential perspective, Lesschen et al. (2009) use a 30 km² semi-arid upland Spanish catchment to determine that terracing across the catchment produced 20% of the total runoff produced from the scenario with no terracing.

Due to social and economic changes, there is a global trend towards the abandonment of labour intensive, low production terraced agriculture (Arnaez et al., 2015). In Europe, technological developments, and the corresponding increase in agricultural productivity, have seen farming concentrated on accessible and fertile land; the usage of marginal regions such as the terraced areas has accordingly reduced (Giupponi et al., 2006; Garcia-Ruiz, 2010; Garcia-Ruiz and Lana-Renault, 2011). In Nepal, outmigration as foreign labour to India and the Middle East, has seen a neglect of subsistence farming with access to alternative income sources and also an increase in the preference for livestock over crop farming (Maharjan et al., 2013; Jaquet et al., 2016). In parts of the Nepali Himalayan area, up to 30% of previously cultivated land has been abandoned (Khanal and Watanabe, 2006; Paudel et al., 2014; Jaquet et al., 2015; Ojha et al., 2017).

Abandoned terraces, often in a poorly maintained condition, cause significant changes to the hydrological dynamic of hillslopes (Arnaez et al., 2015). A broken wall/riser will create concentrated runoff and faster flows and thus result in an increased catchment peak discharge (Arnaez et al., 2015). The increased hydrological connectivity that follows the abandonment of a terraced area can result in a larger area contributing overland flow to a river network. Meerkerk et al. (2009) highlight that terrace abandonment causes a threefold increase in area contributing to river flow in 1-in 8-year (12.5% AEP) return period events. This is change in hydrological connectivity due to abandoned or broken terraces can increase the runoff generation at the catchment-scale. Lesschen et al. (2009) determine that, in a small semi-arid catchment with 127 out of 500 terrace walls collapsed, there was a 25% increase in total catchment runoff due to the degraded nature of the land when compared to a 'fixed' terrace wall scenario. It should be noted, however, that the change in vegetation once a terrace has been abandoned can have a greater impact on connectivity than the deconstruction of the terrace itself (López-Vicente et al., 2013).

There is a large volume of research investigating the role of agricultural terraces in runoff reduction, water conservation, soil conservation and increased productivity (e.g. Chow et al., 1999; Castro et al., 2002; Luedeling et al., 2005; Aquino et al., 2015; Stavi et al., 2015). Several studies, such as Lesschen et al. (2009), focus on runoff generation at the catchment-scale. However, it is apparent that there is minimal literature on the role of terracing and terrace abandonment from a flood management perspective. With agricultural terracing, and the abandonment of the terrace network, a key issue in Nepal is the impact on the hydrological regime at the sub-catchment-scale and the potential cumulative benefits of using the land use system for flood risk reduction purposes at the catchment-scale should be investigated.

1.5.3 Geo-spatial analysis for spatial targeting flood management measures at the catchment-scale

Spatial targeting using spatial analysis has become an essential tool in environmental policy design and planning with measures such as water quality, flood risk reduction and carbon sequestration targeted within a catchment or landscape (O'Connell et al., 2007; van der Horst, 2007; Jackson et al., 2013). Mapping through GIS analysis has the advantage of using basic, often freely available, data to provide an initial assessment at a variety of scales (Nedkov and Burkhard, 2012). GIS analysis is notably prevalent in the spatial targeting of sites when determining cost-benefit ratios for payment for ecosystem services (Wünscher et al., 2008; Jackson et al., 2013). The analysis can be used to indicate the spatial distribution of an ecosystem service, for example where service occurs already or where the service can be implemented (Mogollón et al., 2016). Spatial targeting is also used to locate sites for agri-environment measures that are used to help mitigate diffuse water pollution at a variety of scales (van der Horst, 2007; Reaney et al., 2011; Naden, 2013). At the catchment-scale, Naden (2013) used spatial targeting to identify pollutant hotspots and connectivity in the context of pollutant sources and pathways; mitigation measures can then be created to target key locations within the catchment.

From a flood management perspective, there is a significant amount of research on the rapid assessment and mapping of flood hazard areas using GIS-based weighted multi-criteria decision analysis (e.g. Kourgialas and Karatzas, 2011; Kazakis et al., 2015; Abdelkareem, 2017; Xiao et al., 2017; Mahmoud and Gan, 2018; Patrikaki et al., 2018; Tang et al., 2018). However, with regards to the implementation of flood management measures at the catchment-scale, there are few tools that provide an assessment, especially a rapid assessment, of areas within a catchment that generate the flood water and would benefit from having flood management measures implemented. There is research investigating the prioritising and targeting of sub-catchments for flood management purposes (Saghafian and Khosroshani, 2005; Roughani et al., 2007; Diakakis, 2010; Saghafian et al.,

2010; Sulaiman et al., 2010) through the assessment of geomorphic unit hydrographs. However, much of the research does not consider the combination of the spatial and temporal variability in patterns of rainfall, land cover, and hydrological connectivity across a catchment. Further research has used geospatial data-driven frameworks to determine critical runoff source areas within catchments (Juracek, 2000; Hlaing et al., 2008; Leh and Chaubey, 2009; da Silva et al., 2012; Ameri et al., 2018). However, this is from the perspective of land management and not from the view of flood management.

SCIMAP-Flood is a one decision support framework focussed on determining critical runoff source areas from a flood management perspective. The framework has previously been applied in the United Kingdom for the River Eden catchment, a 2300 km² catchment (Reaney and Pearson, 2016), and the River Roe catchment, a 69 km² rural catchment a sub-catchment of the River Eden (Pearson, 2016). In both these studies, the SCIMAP-Flood output was utilised to help locate areas within the catchment that were responsible for generating flood waters to areas impacted by flooding. Catchment-scale flood management scenarios created from the SCIMAP-Flood output were then tested using a physically-based, distributed hydrological model. Developed to explore the spatial interaction and trade-offs between ecosystem services, Polyscape (now called LUCI) (Jackson et al., 2013) contains a flood mitigation tool that uses elevation, land cover and soil data to assess the storage and permeability capacity of elements within the landscape and assign a flood risk priority category; mitigating measures can be placed in the identified high-risk areas. Polyscape was used for the Pontbren catchment in the UK to establish areas with a high (> 500 m² of grassland with a non-mitigated contribution area), moderate (125 to 500 m²) and negligible (< 125 m²) flow accumulation potential, in addition to areas already providing flood mitigation (deep permeable soils, forest land cover, ponds) (Jackson et al., 2013). Benavidez et al. (2016) used LUCI in a similar capacity to establish areas with flood mitigation potential for a catchment in the Philippines. A similar, ecosystem services-based, approach is used by Nedkov and Burkhard (2012) for a catchment in Bulgaria using a combination of watershed modelling and an ArcGIS-led assessment matrix. Mogollón et al. (2016) use river flow records to estimate the relative importance of selected landscape features in regulating flooding. The outcomes are used to map both the relative biophysical (runoff, evapotranspiration, and infiltration) and relative technological (flood mitigation measures) capacity of a catchment to help regulate floods. Wilcke et al. (2006) used the FLEXT decision matrix (see Figure 1.8) to find suitable locations for agriculture to have an impact on flood protection at the catchment-scale for the Mulde catchment in Germany. The FLEXT decision matrix evaluated factors such as the seasonal land use, slope, water storage potential for agricultural and urban surfaces to identify areas where the soil

treatment methods, such as a change in tillage method or land cover change, can help retain precipitation in the landscape.

There is available research that explores the benefits of using the landscape to help mitigate flooding. This is predominantly done under the guise of ecosystem services and with a view towards cost-benefit ratios. It was apparent through reviewing the literature on spatial targeting for flood management at the catchment-scale that, in an attempt for rapid assessment using a minimal dataset, storm rainfall patterns and overland flow travel times were not considered.

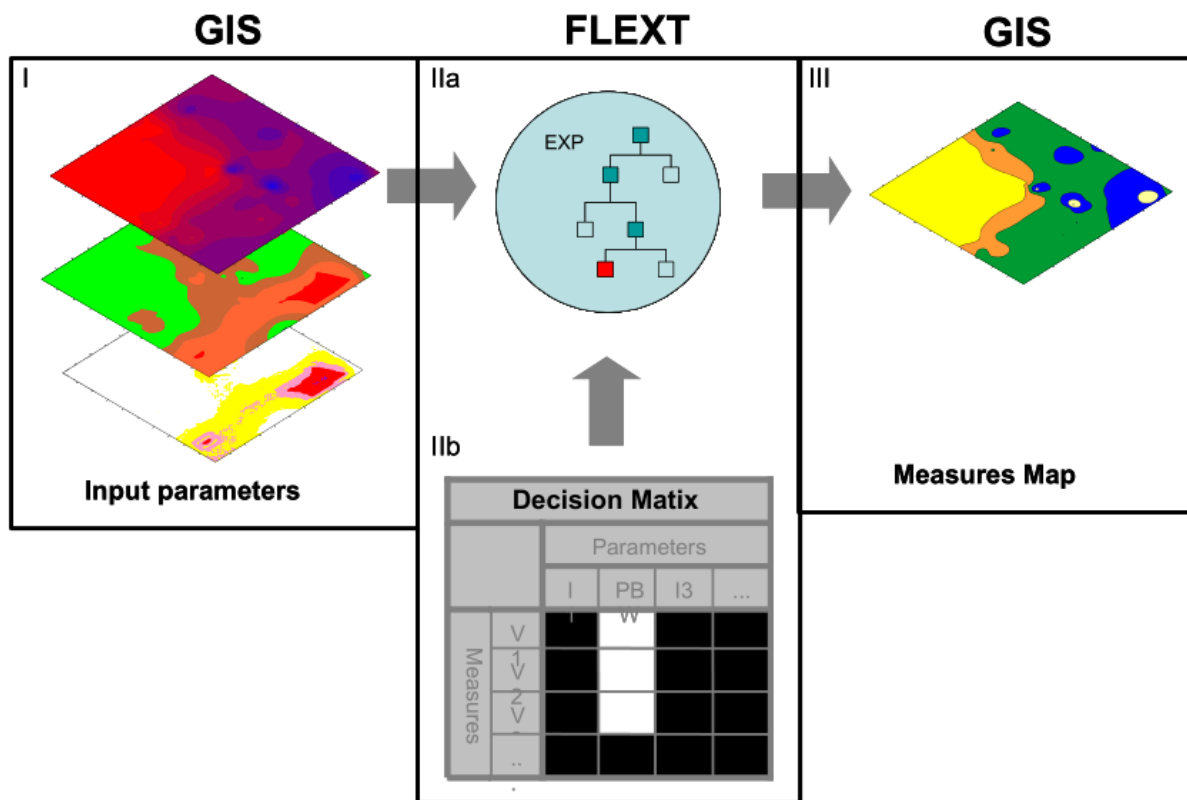


Figure 1.8: The conceptual structure used in the FLEXT decision matrix to determine the locations for changes in the landscape with flood protection benefits (Wilcke et al., 2006 [pp. 4]). Input parameters (e.g. agricultural land cover and elevation data) are then assessed against the FLEXT decision matrix (IIb) to determine suitable locations where conservational agriculture will have a positive effect for flood protection purposes. A map of the suitable locations is produced in III.

1.5.4 The use of hydrological models to assess flood hazard reduction through catchment-based management techniques and interventions

Hydrological models have an extensive range of applications including water resource management, flood risk assessment and management, hydropower assessment and climate change prediction (Pechlivanidis et al., 2011). Models can help develop greater understanding of the hydrological system and allow the extrapolation of both time and space; assisting the identification of dominant processes involved and the assessment of the impact of change (Singh and Woolhiser, 2002). Modelling provides

a method of investigating and quantifying changes of a catchment's hydrological regime through simulating land use alteration without having to physically alter the land (Mulligan, 2004).

Increased availability of powerful computers, fine-scale spatially distributed datasets and information on the physical properties of a catchment has witnessed an uptake in the usage of distributed models (Blöschl et al., 2008; Pechlivanidis et al., 2011). Distributed models have been applied in mountainous watersheds, including study catchments within the Himalayas, to investigate a variety of research aims. The research applications of distributed modelling in mountainous watersheds include the impact of projected climate change on the hydrological regime (e.g. Mauser and Bach, 2009; Rahman et al., 2012), the impact of snow and glacial melt on the hydrological budget (e.g. Marks et al., 1999; Luo et al., 2012; Pelliccioti et al., 2012), hydrological processes in mountainous catchments (e.g. Lehning et al., 2006; Li et al., 2014; Nepal et al., 2014) and flash flooding (e.g. Zocatelli et al., 2010; Nikolopoulos et al., 2011). Spatially distributed models have been utilised to model a range of spatial scales in mountainous catchments. Mauser and Bach (2009), for example, use a large-scale distributed model to investigate the impact of climate change on water flow in the Upper Danube Basin with a study catchment size of 77,000 km². Marks et al. (1999) model the impact of snowmelt on a hydrological regime in mountainous catchments across the USA that range from 1 km² to 2,500 km².

With regards to modelling flood management techniques and interventions at the catchment-scale, spatially distributed models have predominantly been used to investigate the impact of catchment-scale afforestation and land use change (De Roo et al., 2001; Fohrer et al., 2001; Calder et al., 2003; Bronstert et al., 2007; Bathurst et al., 2011; Nepal, 2012; Salazar et al., 2012; Nepal et al., 2015; Neupane et al., 2015; Dixon et al., 2016). Other multi-benefit catchment-scale flood management techniques, such as woody debris dams (e.g. Liu et al., 2004; Dixon et al., 2016; Pearson, 2016; Metcalfe et al., 2017; Hankin et al., 2019) and soil aeration (Pattison, 2010; Smith, 2011; Pearson, 2016), have also been modelled using distributed hydrological modelling. Bronstert et al. (2007) used a multi-scale nested approach, and varying levels of model conceptualisation, to compare different land use impacts and the effects of river training interventions. Salazar et al. (2012) modelled, in addition to spatial targeted afforestation, the effectiveness of flood management structures, such as micro-ponds and small reservoirs, to retain water in the landscape. Pearson (2016) quantifies spatially targeted flood management interventions at the catchment-scale using CRUM3, a distributed model, in a small (69 km²) upland catchment in Cumbria, UK. Chappell et al. (2017), also working in a small upland Cumbrian (16 km²) catchment, use a catchment-scale 2D model (JFLOW) to assess the potential impact on flow magnitude from hillslope tree planting and leaky dams during a 1-in-30 year (3.3% AEP) flow event. Hankin et al. (2019) used a coupled modelling approach to assess the impact of runoff

attenuation features in a small UK catchment. This integrated approach is also used in Metcalfe et al. (2017) to explore the impact of leaky debris dams on flood hazard reduction.

Hydrological modelling has been undertaken in a few catchments across Nepal. These studies are predominantly to help understand catchment processes, but models have also been used to predict the impact of future catchment change. Nepal et al. (2014) used J2000, a distributed, process-orientated hydrological model, to model future climate change scenarios in the Dudh Kosi River catchment. J2000 was also used in Nepal (2012) to model simple land use change scenarios in the same catchment. It must be noted that the creation of hydrological models in the Himalayan region are often hampered by a lack of representative data with a sparse gauging network and data uncertainty due to the practical difficulties of maintaining the network (Kattelmann, 1987, Sharma et al., 2000; Nepal, 2012; Nepal et al., 2014).

Spatially distributed hydrological models have been used for a range of purposes to model hydrological processes in mountainous catchments and to model a range of catchment-scale flood management interventions. It was apparent from reviewing the available literature that most of the research into modelling catchment-scale flood management interventions has predominantly been undertaken in rural upland European catchments. There is limited literature on applying the interventions in both mountainous catchments and regions outside of Western Europe.

1.5.5 Modelling the impact of catchment-scale flood management through flood inundation extent change using coupled approach

Within hydrology, model coupling is a process in which the outputs of one model are fed into another as boundary conditions or input parameters. This information exchange could be either the hydrograph outputs of a hydrological model fed into a hydraulic model as input boundary conditions (e.g. Grimaldi et al., 2013; Mateo et al., 2014; Nguyen et al., 2016; Zope et al., 2016; Felder et al., 2017) or the predictions of a meteorological model fed into a hydrological model (e.g. Bartholmes and Todini, 2005). From a flooding perspective, Felder et al. (2017) note that a hydrological model is often used to determine the conversion of rainfall to runoff; the corresponding modelled flood event hydrograph is then used as the inflow condition in a hydraulic flood inundation model. The model chain can be extended to include all three modelling stages or additional stages such as a reservoir operation module used in Mateo et al. (2014).

A coupled modelling approach for flood inundation mapping has been used in prior research. Examples include Biancamaria et al. (2009) who use a combination of a flow routing scheme (TRIP) and a land surface scheme (ISBA) to represent the landscape processes of the snow-covered Ob catchment in Siberia with the outputs used as lateral inflows into the LISFLOOD-FP hydraulic model.

Bonnifait et al. (2009) use n-TOPMODELS to model rainfall runoff with the flow output entering a 1D hydraulic model (CARIMA) to recreate a historic flood event in the Gard region of France. An approach using the Generalised Likelihood Uncertainty Estimation (GLUE) methodology is applied by McMillan and Brasington (2008) to produce an end-to-end flood risk assessment. Applied to the Upper Granta catchment in the UK, the end-to-end approach combines a stochastic rainfall model to generate design storm events, a rainfall-runoff model to convert the rainfall into a hydrograph and a 2D floodplain inundation model similar to LISFLOOD-FP (McMillan and Brasington, 2008). A similar three stage approach is evident in Rodriguez-Rincon et al. (2015) who investigate the uncertainty propagating through the model cascade to derive flood inundation extents. Nguyen et al. (2016) model the inundation extents of flash floods in Oklahoma using a rainfall runoff model (HL-RDHM) and a hydraulic model (BreZo). Felder et al. (2017) use a catchment-scale hydrological model (PREVAH) to create hourly flow hydrographs for multiple sub-catchments for the Aare River in Switzerland. The created hydrographs are entered into a hydraulic model (BASEMENT) as lateral inflows. This is coupled approach is spatially represented in Figure 1.9.

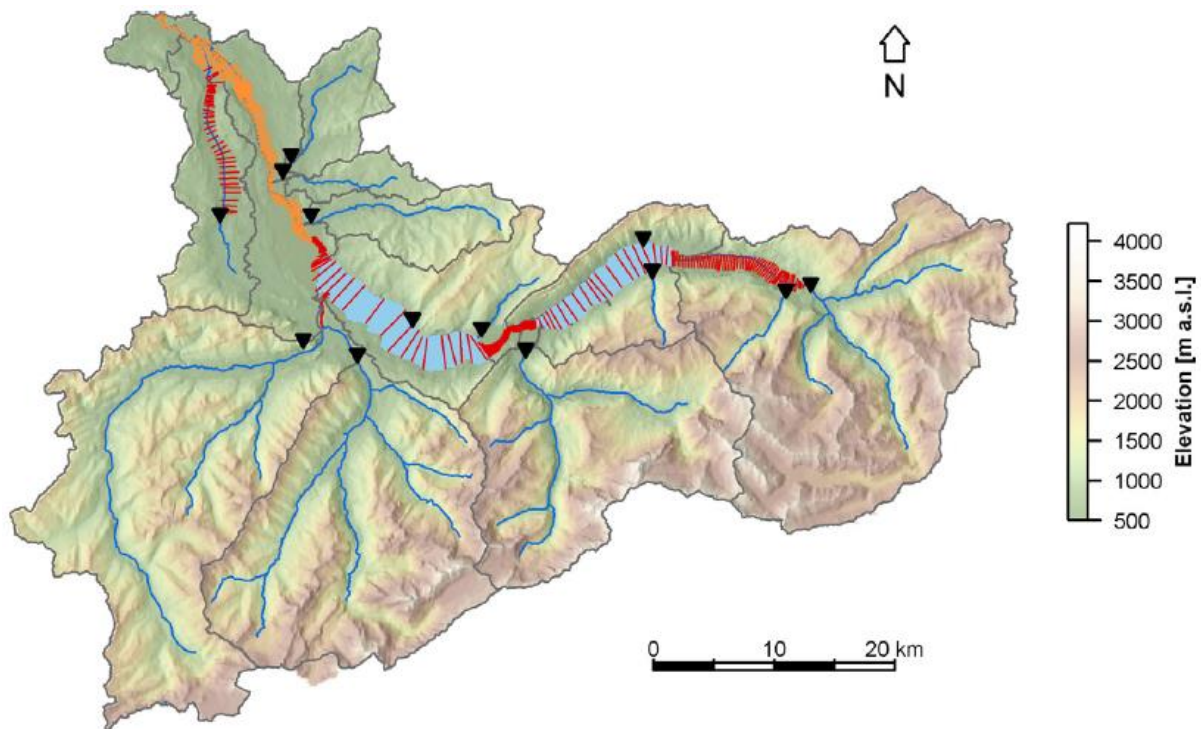


Figure 1.9: An example of the spatial scales used in a coupled modelling approach from Felder et al. (2017 [pp. 159]). The black triangles indicate coupling points between the sub-catchment-scale hydrological models and reach scale hydraulic model. At these points, the outputs of the hydrological model are used as lateral inflows into the hydraulic model. The red and orange lines indicate the hydraulic model extents used for the flood inundation modelling.

Whilst many studies use a coupled modelling approach for flood inundation mapping there is limited research using the approach to test the impact of catchment flood management measures. Hankin et al. (2019) integrate a hillslope runoff model (Dynamic Topmodel) and a 2D hydrological model (both

JFlow and HEC-RAS) to model the impact of runoff attenuation features. In a small, upland UK catchment the study looks at the potential storage of a large attenuation feature and corresponding change in flood extent downstream. A similar method is employed in Metcalfe et al. (2017) who assess the impact of in-channel attenuation features across a catchment through using a hillslope runoff model (Dynamic Topmodel) and a 1D hydraulic model; the output of this research looks at hydrograph change as opposed to flood inundation extent due to the 1D nature of the hydraulic modelling. At a large scale, Linde et al. (2010) model the effectiveness of flood management measures on peak discharges in the Rhine catchment. Using a combination of a hydrological model (HBV) and a 1D hydraulic model (SOBEK) the study tests the impact of reforestation, restored polders, channel bypasses and river restoration on the water depths from low probability flood events. From a historic as opposed to future land use change, Zope et al. (2016) combine HEC-HMS and a 1D HEC-RAS model to assess the impact of land cover change over time on the inundation extent in a small Indian catchment.

It is apparent that there is a sizeable amount of research done using a coupled hydrological and hydraulic modelling approach within flood modelling. However, there are few studies using a coupled approach to investigate the potential impact on the inundation patterns of catchment-scale flood management measures. From the literature review it is apparent that a coupled hydrological and hydraulic modelling approach is a suitable method to quantify the effectiveness of a catchment-scale scenario on localised inundation patterns.

1.5.6 Uncertainty throughout hydrological modelling

Uncertainty analysis of a model output is a means of representing the certainty in which the model results represent the reality of the modelled subject (Singh, 1997; Pechlivanidis et al., 2011). As noted by Beven (1989), with regards to catchment modelling, it is not feasible to collect observed data or set up experiments at a suitable spatial or temporal resolution to properly represent a catchment. Uncertainty can be split into two types: aleatory and epistemic (Boelee et al., 2017). Aleatory uncertainty is a result of natural variability and randomness whilst epistemic uncertainty is considered to be down to a lack of knowledge (Boelee et al., 2017). Pechlivanidis et al. (2011) outlines for sources of uncertainty within hydrological modelling that need identifying and quantifying during uncertainty analysis:

1. Natural uncertainty – this describes the uncertainty produced from random natural effects. Stated in Melching et al. (1990), this type of uncertainty includes the spatial and temporal fluctuations in the physical processes underpinning runoff generation. The quality and availability of relevant data can impact how natural uncertainty is described.

Pechlivanidis et al. (2011) provide the example of a denser rainfall gauge network improving the representation of the spatial randomness of precipitation. However, Beven (2009) argues that additional relevant data will not necessarily provide a better representation of a hydrological system with the increased complexity from the extra data requiring additional model parameters to be defined. This can lead to overparameterisation within the model when trying to represent the system (Beven, 2009; Ampadu et al., 2013).

2. Data uncertainty – this describes the uncertainty within the data, commonly rainfall or river flow data in hydrological modelling, that could be attributed to factors such as poor-quality assurance and control or data collection methods (McMillan et al., 2010; McMillan et al., 2011). McMillan et al. (2011) illustrate the data uncertainty within rainfall data that can derive from either sampling error or measurement error. Sampling error is caused by inadequacies in the spatial representation of the catchment through the use of only a few gauges and by the assumptions used to interpolate the rain rates between the gauges (McMillan et al., 2011). Measurement errors occur within the gauges themselves; the commonly used tipping bucket gauges are prone to wind effects, evaporation losses and mechanical limitations (McMillan et al., 2011).
3. Model parameter uncertainty – this describes the uncertainty in the model parameter values attained from the model calibration process undertaken using limited and uncertain data (McIntyre et al., 2002; Freer et al., 2004). Beven and Freer (2001) detail that over-parameterised models, regardless of data and model structure, will have parameter equifinality. Equifinality is where different model parameter sets and model structures can produce equally acceptable results (Pechlivanidis et al., 2011). Using uncertainty frameworks, such as the GLUE method (Beven and Binley, 1992; Beven, 2006; Beven and Binley, 2014), the sources of parameter uncertainty can be represented.
4. Model structure uncertainty – this describes the mathematical representations of the hydrological processes within a catchment with many unobserved hydrological processes often ignored. Hydrological model structure uncertainties are usually identified through model behaviour to runoff (Pechlivanidis et al., 2011). These behaviours include time to peak, runoff volume, and peak discharge (Butts et al., 2004).

These sources of uncertainty are cascaded through a coupled modelling approach; this is conceptualised using a flood forecasting example from Pappenberger et al. (2005) in Figure 1.10. McMillan and Brasington (2008) note that when applying an uncertainty framework, such as the GLUE

method, to coupled models the results relating to each parameter set in the initial model must be propagated through the model chain individually.

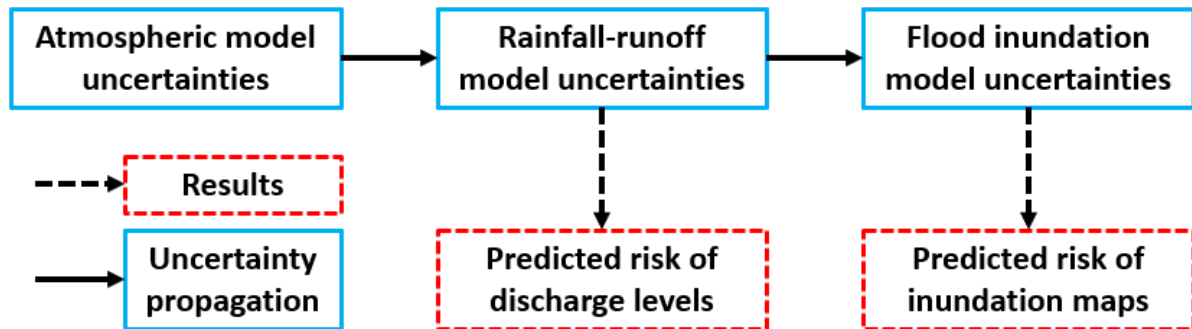


Figure 1.10: A conceptual overview of the uncertainty cascade through a coupled modelling approach looking at medium range flood forecasting (modified from Pappenberger et al., 2005 [pp. 383]).

In Pappenberger et al. (2005), this uncertainty cascade starts with 52 available medium range rainfall forecasts. Each rainfall forecast provides a different behaviour in the runoff generation in the rainfall-runoff model (LISFLOOD-FF) which in turn has uncertainty through the model parameter sets. Functional similarity, a similar approach to the GLUE methodology, was used to reduce the computational demand and produced 6 parameter sets for the rainfall-runoff model. A further 10 parameter sets were used to represent the uncertainty in the hydraulic flood inundation model (LISFLOOD-FP). In total 312 (52*6) model runs were used to produce the inflow hydrographs to the flood inundation models with 3120 (52*6*10) different inundation extents produced for each medium range flood forecast; predictive percentiles are then used to better understand the output of the flood inundation models. This approach used for flood forecasting is also undertaken in He et al. (2009) for the River Severn in the UK using LISFLOOD-RR (a rainfall-runoff model) and LISFLOOD-FP. The research uses 6 parameter sets and 216 rainfall forecast members to produce 1296 forecast discharges per timestep; forecasted discharges that met the observed data were modelled using the hydraulic model at the end of the cascade to provide inundation depth and extent (He et al., 2009).

It is apparent that there are many sources of uncertainty within the hydrological modelling process ranging from uncertainty in the observed data to uncertainty in the model parameters and structure. These sources of uncertainty, and the measures used to combat them, are exacerbated when using a coupled modelling approach. Based on examples found in literature for flood forecasting and flood risk assessments using a model chain there is a need to constrain the approach to representing uncertainty in order to match available computing resources whilst still capturing the uncertainty in the predictions.

1.6 SUMMARY

Flooding in Nepal has been responsible for over 8,500 deaths (1971 to 2013), affecting a further 5.53 million people and causing millions in economic losses (Government of Nepal, 2017; DesInventar, 2019; EM-DAT, 2019). This ranges from significant flood events, such as the 1993 central Nepal floods or the 2017 southern Nepal floods, to smaller events that impact the lowland parts of the country on an annual basis (Merz et al., 2006; Government of Nepal, 2010; Government of Nepal, 2017). The nature of the flooding is driven by distribution of rainfall with between 70% and 90% of the annual rainfall total and, consequently, 80% of the total annual flow and 88% of the categorised flood events happening in the monsoon period (Gautum and Acharya, 2011, Andermann et al., 2012a; EM-DAT, 2019). The most common flood type, rainfall-generated fluvial flooding in rain-fed catchments flowing into the Terai region, occurs when high volume, long duration, and medium intensity rainfall events cause saturation excess overland flow in the latter part of the monsoon season (Gilmour et al., 1987; Merz et al., 2006; WECS, 2011).

The existing method for fluvial flood management in Nepal involves reactively placed, localised interventions in affected areas (Dhakal, 2013). This reactive approach largely fails to consider the catchment as a connect system, notably the relationship between the flood sources and impacted areas, and contrasts with this catchment-based approach being implemented in many other countries (Nisbet et al., 2011; Dhakal, 2013; Nepal et al., 2014; POST, 2014; Lane, 2017). The application of a catchment-scale approach to flood management is especially important with many Nepali catchments facing changes to the hydrological regime from land use changes such as the abandonment of upland terraced agriculture, deforestation and urban expansion (Ives and Messerli 1989; Nepal, 2012; Paudel et al., 2014; Chaudary et al., 2016; Rimal et al., 2019). Whilst there is literature promoting a shift towards the implementation of an integrated catchment approach (e.g. Dhakal, 2013; Singh, 2013; Nepal et al., 2014; Government of Nepal, 2017) and available guidance on the flood risk reduction approaches (e.g. Shrestha et al., 2012) there is minimal research that attempts to quantify the effectiveness of a catchment-scale approach to flood management.

This thesis fills a void in the existing research through the development of a process to determine the impact of spatially targeted catchment-scale flood management measures in a Nepali catchment context. The developed, three stage, end-to-end approach combines to create a catchment-scale flood management toolkit that functions at a range of spatial scales. The approach identifies flood source areas and impact areas at the catchment-scale, quantifies the impact of the flood management measures and land use change on the flow regime and local inundation pattern. The end-to-end approach is applied to the East Rapti catchment in southern central Nepal; a medium-sized catchment that was heavily impacted in the 2017 flood event.

2 THE EAST RAPTI CATCHMENT

2.1 INTRODUCTION

The topography of the East Rapti catchment is representative of a medium-sized Nepali catchment with the monsoonal flood waters originating in the hill areas of the Mahabharat Range and flowing out and impacting the relatively densely populated Terai plains. The representative land use within the catchment is a mixture of warm temperate, subtropical hardwood and coniferous forest, including the Chitwan National Park, and traditional irrigated lowland and terraced upland agriculture (Bruns et al., 2002). The variation in land use allows for the analysis of potential changes to the hydrological regime due to land cover change. With regards to flood history, there was severe flooding in the East Rapti catchment in 1954, 1971, 1975, 1993 and 2017 in addition to annual monsoon generated riverine flooding (Singh, 2013; Government of Nepal, 2017). These characteristics mean that the East Rapti catchment is a suitable case study location to test the end-to-end approach for assessing the spatial targeting of flood management measures.

This chapter provides an overview of the East Rapti catchment through introducing the catchment location (Section 2.2) within Nepal and the wider Himalayan region, catchment characteristics (Section 2.3), climate (Section 2.4), hydrological regime of the catchment (Section 2.5) and detailing a critique on the available gauged data for the catchment used in this research (Section 2.6).

2.2 LOCATION

The East Rapti basin is a 3,084 km² sub-catchment of the Nayarani River that is located 25 km to the south west of Kathmandu in the Bagmati Pradesh province in southern central Nepal (see inset of Figure 2.1). The catchment has several major tributaries with the majority originating the hilly region in the northern part of the catchment (Figure 2.1). The Lothar Khola, Manahari Khola, Budhi Khola and Rapti River drain the northern part of the catchment. The Reu Khola drains the southern area of the catchment and joins the main East Rapti channel immediately before the confluence with the Narayani River.

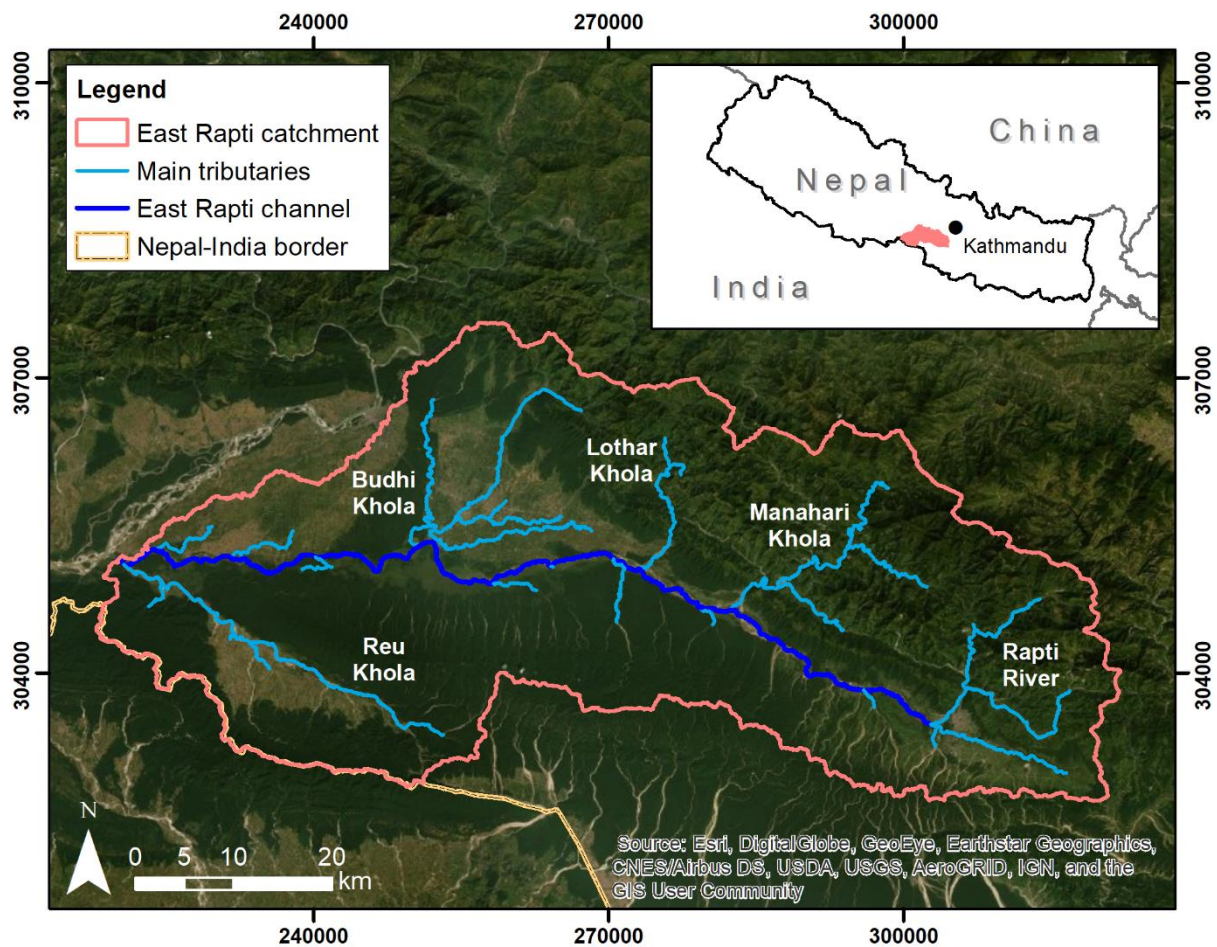


Figure 2.1: The main channel network in the East Rapti catchment (main window) and the catchment location within Nepal (red polygon in the inset). Note: presented national boundary in inset does not account for updates made in June 2020.

2.3 CATCHMENT CHARACTERISTICS

The hydrological behaviour of the East Rapti catchment is significantly influenced by the geology (Section 2.3.1), topography (Section 2.3.2), soil characteristics (Section 2.3.3) and land cover (Section 2.3.4).

2.3.1 Geology

The geology of the East Rapti catchment comprises of three groups that can be related to the catchment geomorphic zones (Section 2.3.2). Shown in Figure 2.2, the boundaries between the geomorphic zones roughly coincide with major thrust faults with the Main Frontal Thrust at the southern edge of the Siwalik Range and the Main Boundary Thrust at the southern edge of the Mahabharat Range (Lavé and Avouac, 2001).

The Siwalik Range, which includes the southern part of the East Rapti catchment, is predominantly comprised of metasedimentary rocks and is bounded by the Main Boundary Thrust to the north and the Main Frontal Thrust to the south (Upreti, 1999). The geological composition of the Siwalik Range

includes layers of fine-grained sedimentary (sandstone, mudstone, siltstone, clays and shale), coarse sandstone and coarse-grained conglomerates that originate from the Neogene (Upreti, 1999; Department of Agriculture, 2000; Lavé and Avouac, 2001; Bhatt, 2013). The Siwalik Range has a steep, immature topography with rugged terrain dissected with gullies with uplift rates of up to 15 mm yr⁻¹; with a fragile lithology the hills deliver large volumes of sediment into the channel network during the monsoon season (Hurtrez et al., 1999; Upreti, 1999). Hurtrez et al. (1999) establish that a dynamic equilibrium between uplift and sedimentation is reached at the basin scale in the Siwalik Range.

The Mahabharat Range in the northern part of the East Rapti catchment belongs to the Lesser Himalayan Zone and contains a mixture of sedimentary and metasedimentary rocks (limestone, dolomite, slate and phyllite) that predominantly formed in the Pre-Cambrian and Palaeozoic (Upreti, 1999; Singh, 2013). Within the East Rapti catchment there is an igneous intrusion (granite) in the north-eastern part of the catchment. The geology of the Mahabharat Range disrupts the river drainage patterns in the Himalayas with southward flowing rivers from the High Himalayas altering to an easterly or westerly direction to get around the range before flowing south again into the Gangetic Plain (Sakai et al, 2006).

The Chitwan (Dun) Valley in the centre of the East Rapti catchment comprises a tectonic depression filled with thick alluvial deposits from the Quaternary to present (Upreti, 1999; Bruns et al., 2002). The Dun Valley deposits are predominantly (>80%) comprised of sand and boulders with gravel and clay layers present (Neupane and Shrestha, 2009). The Dun Valleys are the only regions across Nepal in which the rivers are not cutting down into bedrock with fluvial incision happening across the Mahabharat Range to compensate for active thrusting and folding (Lavé and Avouac, 2001).

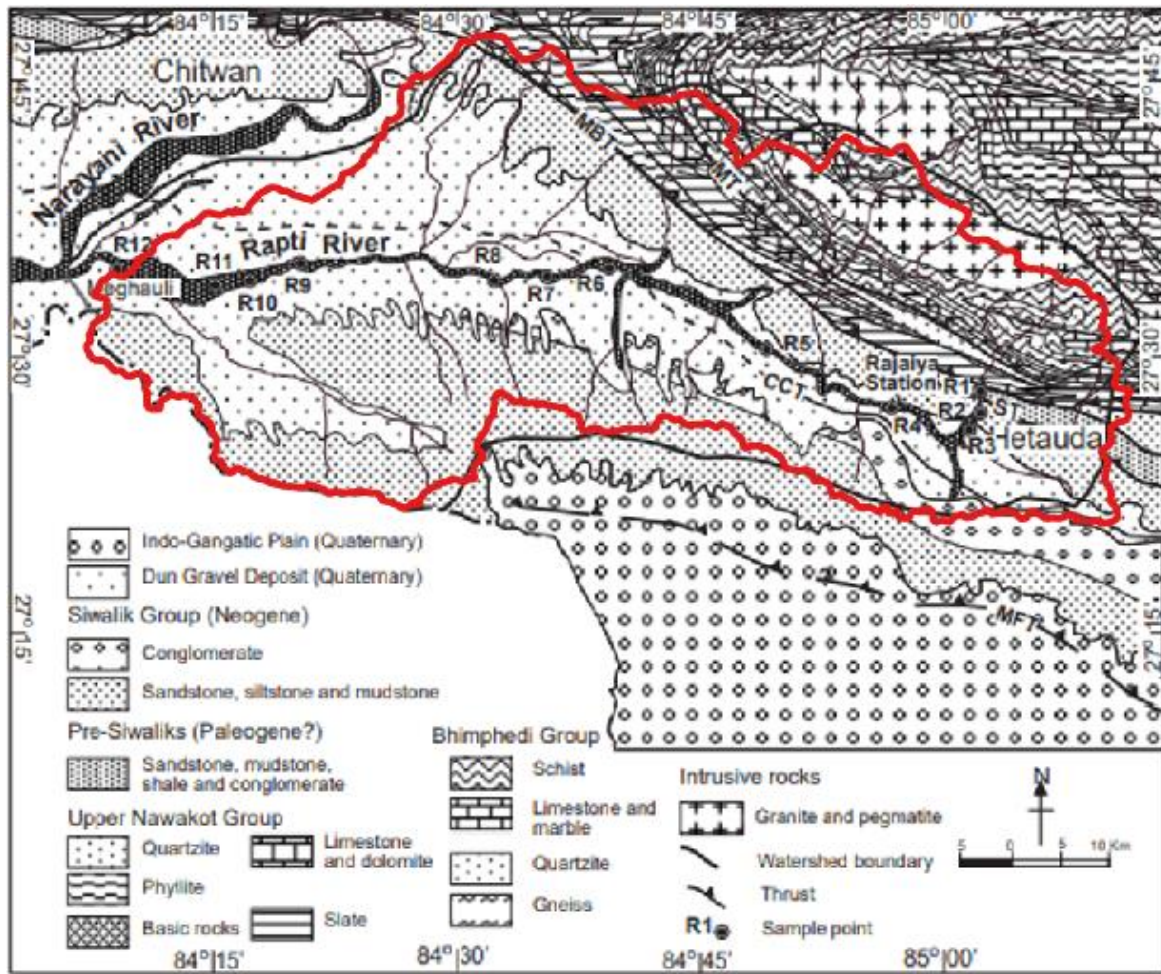


Figure 2.2: The geology of the East Rapti catchment (red outline) as modified from Tamrakar et al. (2008 [pp. 25]). Note the dominant surficial geology is located as Quaternary deposits in the central part of the catchment.

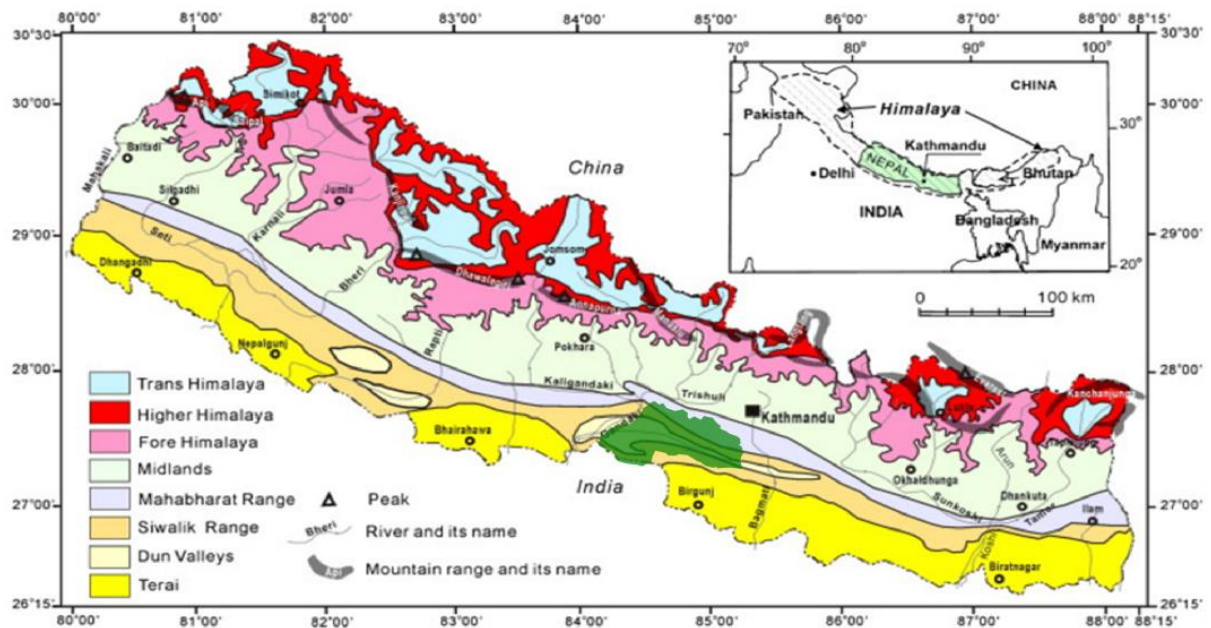


Figure 2.3: A regional geomorphic map of Nepal with the East Rapti catchment (dark green polygon) extent highlighted (modified from Dahal and Hasegawa, 2008 [pp. 431]).

2.3.2 Topography

The topography of Nepal varies from lowland plains (Terai) in the south of Nepal to mountainous peaks with elevations of up to 8,848 mASL in the High Himalayas to the north (Samir, 2013; Panthi et al., 2015). Dahal and Hasegawa (2008) classify eight defined geomorphological zones within Nepal with each zone having distinct slope and relief characteristics, altitudinal variation, and climate. Illustrated in Figure 2.3, the East Rapti catchment comprises of four of these geomorphic zones. Starting at the Indian border to the south and progressing in a northerly direction the four geomorphic zones are the Terai, Siwalik Range, Dun Valleys, and the Mahabharat Range. The Terai zone is on the northern edge of the Indo-Gangetic Plain and has a varying width of between 10 and 50 km along the southern edge of the Nepal-India border. The elevation ranges between 100 and 200 mASL. The Siwalik Range is the southernmost hill range associated with the Himalayas and has an elevation range of between 200 and 1,300 mASL. The geomorphic zone is marked by an abrupt rise in elevation and relief from the Terai and runs the length of Nepal with a width of between 10 and 50 km. The Dun Valleys are wide, alluvium filled, valleys between the divided Siwalik hill ranges running in an east-west direction. The valleys have an elevation range of between 200 and 300 mASL and a width of between 5 and 30 km. Finally, within the context of the East Rapti catchment, the most northerly geomorphic zone is the Mahabharat Range, a mountainous range extending the length of Nepal that is breached only by the larger rivers (Kosi, Nayarani, Karnali and Mahakali) from the north of the country (Upreti, 1999). The elevations across the Mahabharat Range are between 1,000 and 3,000 mASL with the range spanning, in an east-west direction, the length of Nepal with a width of between 10 and 35 km. The range forms the first effective barrier to the monsoonal clouds and, as such, has a large influence on the rainfall distribution across Nepal (Upreti, 1999). It should be noted that, whilst reading this chapter, Nepali academic literature often attempts to categorise geomorphological zones and features. This approach often uses classifications that could be considered arbitrary and are not necessarily transferable.

The East Rapti has an elevation range of 2,454 m with a maximum elevation of 2,599 mASL in the northern part of the catchment and a minimum elevation of 145 mASL in the western part of the catchment at the confluence with the Narayani River (Figure 2.4). As evident in Figure 2.5, the highest slope gradients, of between 20° and 74°, are concentrated in the more mountainous northern part of the catchment. There are large areas of slopes <10° in the western, downstream part of the catchment; it is in this flat region in which the flood waters are not confined to the channel during high flow events.

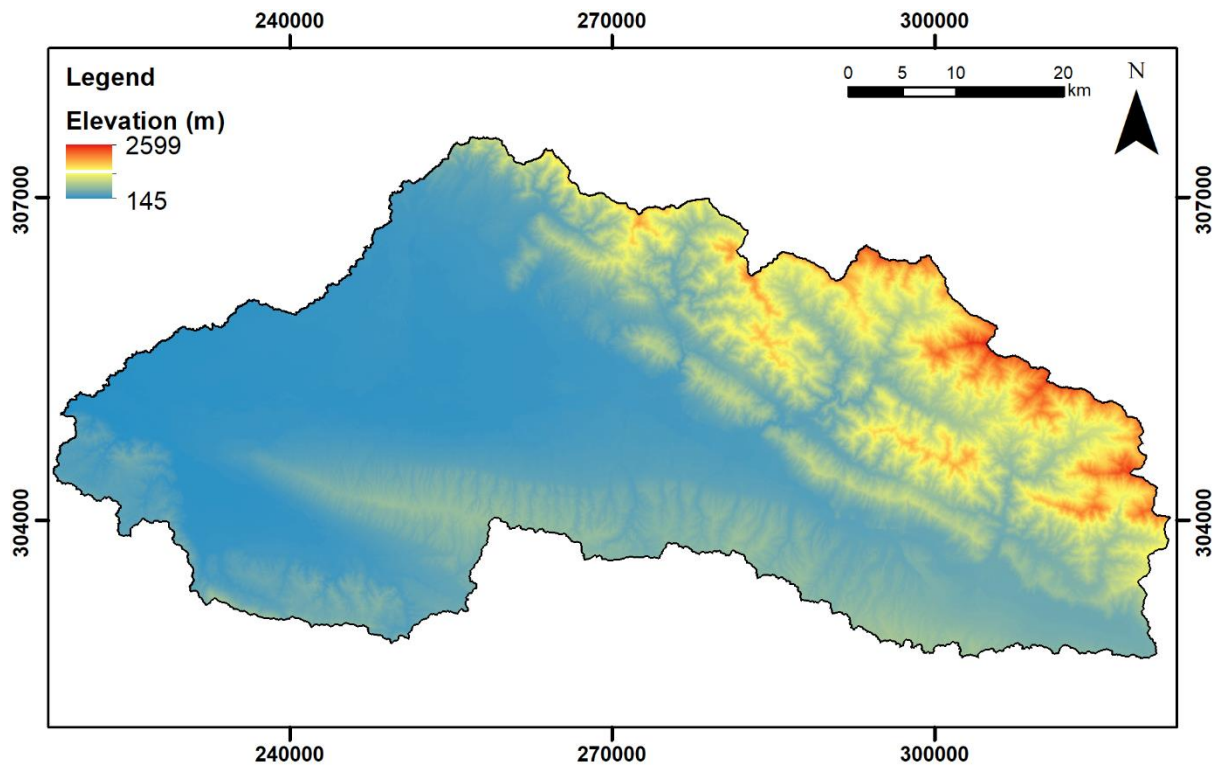


Figure 2.4: A DEM showing the elevation variation throughout the East Rapti catchment based on the ALOS Global Digital Surface Model (AW3D30) 30 m dataset.

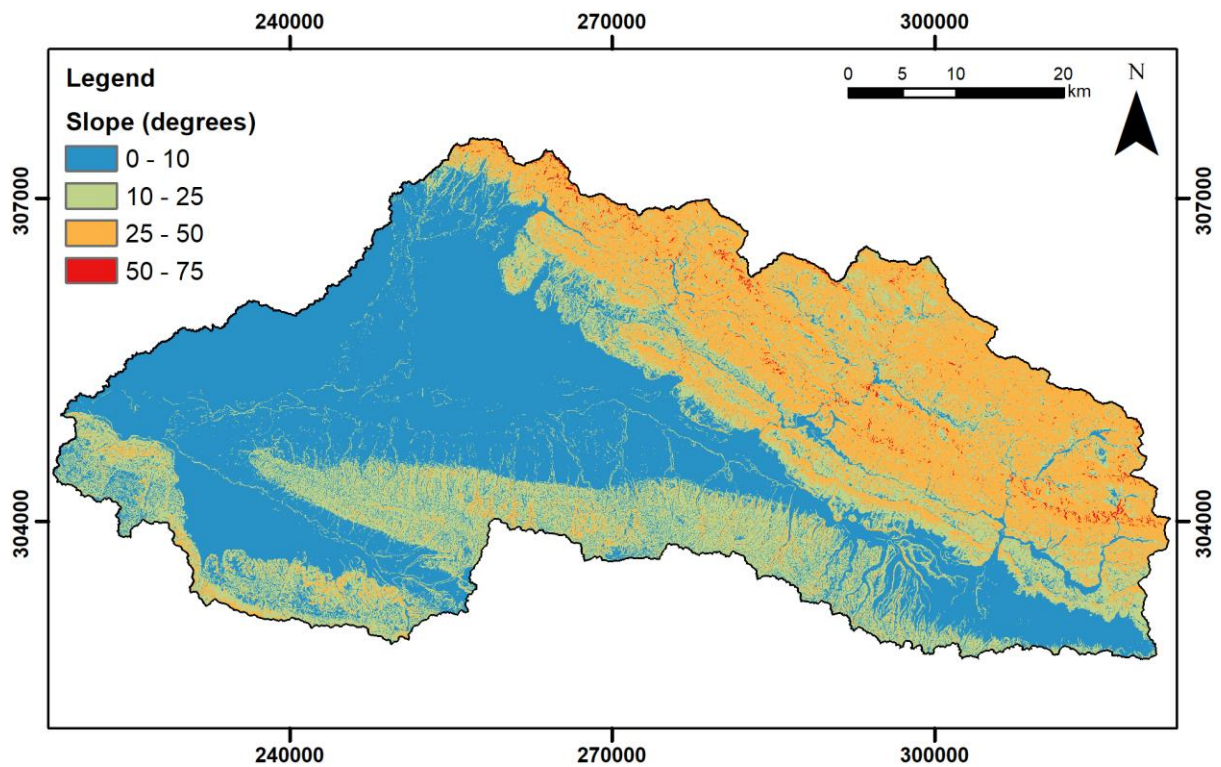


Figure 2.5: A slope map of the East Rapti catchment based on the ALOS Global Digital Surface Model (AW3D30) 30 m dataset.

2.3.3 Soils

The dominant soil textures within the East Rapti catchment are sandy loam and loam with sporadic patches of sandy clay loam (Khatri-Chhetri et al., 2003). The soils in the steep mountainous terrain of the Siwalik and Mahabharat Ranges are predominantly Eutric Cambisols that are shallow, very coarse, and generally drain rapidly (Department of Agriculture, 2000; Dijkshoorn and Huting, 2009). Bruns et al. (2002) note that the soil drainage in the Siwalik Range is more variable than that in the Mahabharat Range. Despite a similar rainfall regime, the Siwalik Range is more likely to have erosion driven landforms (gullies and rills for example) than the Mahabharat Range with an increased rate of soil erosion and sediment mobilisation (Ghimire et al., 2013). Ghimire et al. (2013) note that, for a catchment in the Siwalik Range, there was a mean erosion rate of between 3 and 5 mm yr⁻¹; this is noticeably higher when compared to between 1.2 and 1.6 mm yr⁻¹ in the Middle Mountain region and 0.1 to 2 mm yr⁻¹ in the High Himalayas. The soils in the alluvial deposits in the southern and western parts of the catchment are a combination of Gleyic Cambisols, Haplic Phaeozems and Dystric Regosols that are deep, fertile, and well drained loamy soils (Department of Agriculture, 2000; Dijkshoorn and Huting, 2009). Throughout the catchment the soil depth to the water table ranges from 2 m to > 15 m depending on the season (Bruns et al., 2002).

2.3.4 Land cover

The catchment land cover, based on a supervised classification of Landsat 8 imagery from 2016 (see Section 3.2.2.4 for details on this approach), for the East Rapti is shown in Figure 2.6 with the percentage coverage outlined in Table 2.1. The dominant land cover throughout the catchment is a mixture of warm temperate, subtropical hardwood and coniferous forest, with 58% of the catchment covered in trees. This forest is predominantly Sal (*Shorea robusta*), a native tree of the Indian sub-continent, which makes up over 70% of the forest coverage in a southern East Rapti sub-catchment (Shrestha et al., 2008). Much of the forested area includes the Chitwan National Park which extends along the southern bank of the main East Rapti channel. Examples of the different land covers within the catchment are shown in Figure 2.7.

A further 32% of the catchment is made up of rainfed (18%) and irrigated (10%) agriculture in addition to associated settlements (4%). The largest of the settlements are Hetauda in the south east of the catchment and a section of Bharatpur in the north west of the catchment. As noted in Singh (2013), the majority of the population within the East Rapti catchment live on the Terai plain with fertile, flat land that promotes agricultural productivity but is flood prone. The dominant crops grown in the catchment are rice, wheat, maize, and potatoes (Department of Agriculture, 2000).

Singh (2013) states that there has been a significant reduction in forest cover within the East Rapti catchment since the 1970s. The research found that, through analysis of satellite imagery, within 13 Village Development Committees in the Eastern Chitwan watershed there was a loss of 60 km² of forest coverage between 1976 and 1992 and a further loss of 109 km² between 1992 and 2010 (Singh, 2013). This deforestation is predominantly due to the creation of new land for agriculture. Land use change throughout Nepal and the wider Himalayan region, notably deforestation and the abandonment of agricultural terraces, is discussed in detail in Section 1.5.2.

Table 2.1: Percentage coverage of the main land covers in the East Rapti catchment in 2016 based on supervised classification of Landsat 8 imagery

Land Cover	% coverage
Rainfed Agriculture	18%
Irrigated Agriculture	10%
Shrubland	6%
Forest	58%
Built-Up Areas	4%
Bare Ground	2%
Water	1%

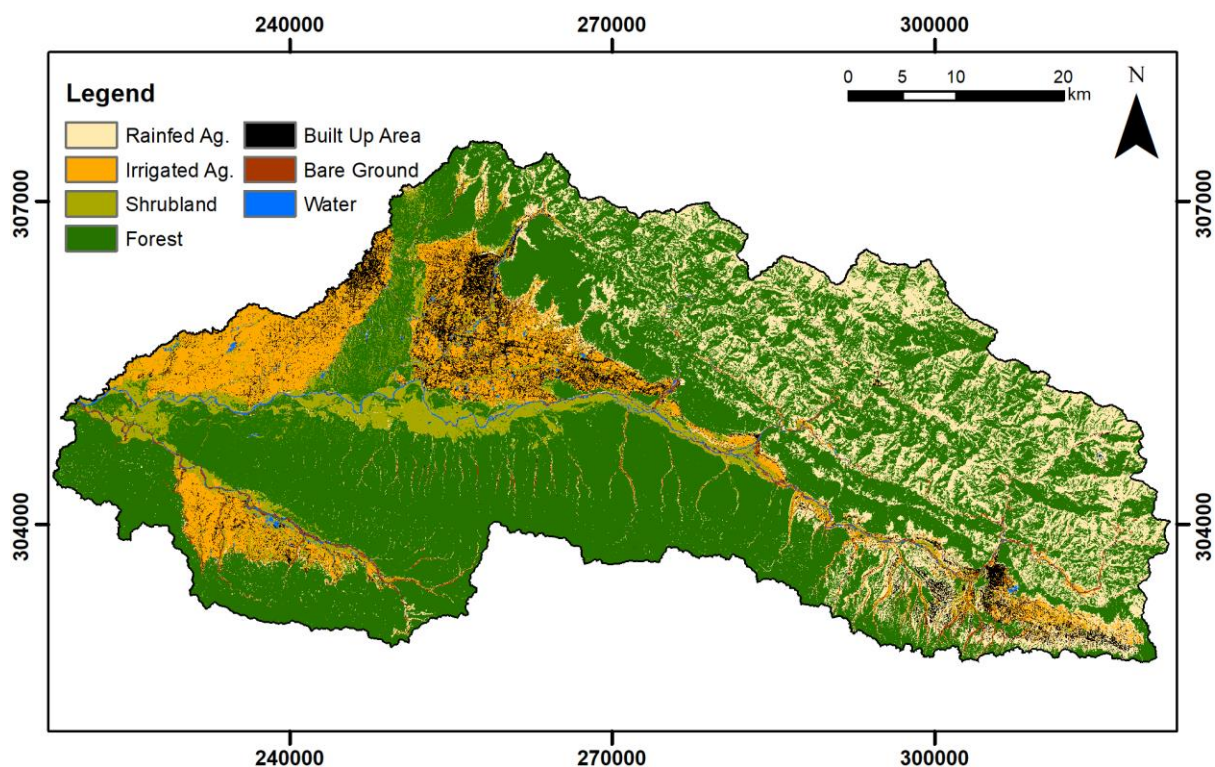


Figure 2.6: A map of the main land cover categories in the East Rapti catchment based on supervised classification of Landsat 8 imagery taken in 2016. The land cover data creation process is detailed in Section 3.2.2.4.



Figure 2.7: A selection of photos taken by the author of the different land covers within the East Rapti catchment. (a) upland rainfed terraced agriculture around a small tributary channel, (b) and (c) upland rainfed agriculture and forest, (d) irrigated agriculture in the downstream part of the catchment, (e) shrubland in the downstream part of the catchment, (f) and (g) a combination of built-up area and irrigated agriculture in the low-relief downstream parts of the catchment.

2.4 CLIMATE

The climate differs across the geomorphic zones within the East Rapti catchment. The Terai region in the south of Nepal has a subtropical climate, whilst the Siwalik Range, Mahabharat Range and Midland region have an elevation dependant climate that ranges from partially subtropical to temperate (see Figure 2.3) (Andermann, 2011). There are four climatic seasons in Nepal; the dry pre-monsoon period (March to May), the wet monsoon period (June to September), the dry post-monsoon period (October

to November) and the winter period (December to February) (Petley et al., 2007; Gautam and Acharya, 2011). During the wet monsoon period 78% of the annual precipitation occurs, with 14% falling in the pre-monsoon period and 8% in the post-monsoon winter period (Merz et al., 2006). This temporal distribution of rainfall has a significant impact on the hydrology of the country and the generation and timing of flood hazards (Merz et al., 2006).

The East Rapti catchment has an average annual rainfall of 2,008 mm based on the Government of Nepal's Department of Hydrology and Meteorology (DHM) rainfall gauges within the catchment (Shilpakar et al., 2011). The location of the meteorological gauges within, and in close proximity to, the East Rapti catchment are shown in Figure 2.8 with station information, including completeness of the data record, in Table 2.2 at the end of this chapter. The average annual rainfall total, however, differs throughout the catchment with variation across the available gauge network. For the period 1998 to 2016 in the eastern part of the catchment at the Rampur gauge (DHM Station Number – 902) was 2,011 mm, in the central part of the catchment at the Beluwa gauge (DHM Station Number – 920) was 1,816 mm and in the western part of the catchment at the Hetauda N.F.I (National Forest Inventory) gauge (DHM Station Number – 906) was 2,494 mm; an overview of the data acquired is in Section 2.6.1. In addition to difference across the catchment, there is variability in the annual totals recorded at each of the gauges across the time period. This variation is evident between monsoon seasons with rainfall totals depending upon a range of global and regional climatic factors (Shrestha et al., 2000). The variation in strength of monsoon can be attributed to atmospheric circulation differences, most notably the wind field (Li and Zeng, 2002; Li and Zeng, 2003). Within the East Rapti catchment at the Hetauda N.F.I. gauge the lowest annual rainfall total of 1,626 mm was in 2012, while the highest annual rainfall total of 3,323 mm was recorded in 2002. Another example of the interannual variability at a gauge is evident at Rampur with the lowest annual rainfall total of 1,184 mm (2011) and the highest annual rainfall total of 2,743 mm (2007).

The monthly rainfall total pattern follows the typical monsoonal pattern outlined above. Illustrated in Figure 2.9, the highest monthly rainfall totals throughout the catchment fall between June and September with the lowest totals between November and January. The highest monthly total recorded between 1998 and 2016 within the East Rapti catchment was 1,765 mm at the Makwanpur Gadhi gauge (DHM Station Number – 919) in July 2002. The highest recorded monthly total at the Rampur gauge was 930 mm (July 2003), at the Beluwa gauge was 1,230 mm (July 2002) and the Hetauda N.F.I. gauge was 1,599 mm (July 2002). Shilpakar (2003) established that there was no clear relationship between elevation and rainfall totals within the catchment with an R^2 of 0.13 between gauged annual rainfall totals and elevation; this relationship is determined using only one gauge

(Daman at 2314 mASL [DHM Station Number – 905]) representing the higher elevations with the majority of the rainfall gauges within the East Rapti below 500 mASL.

The highest daily rainfall recorded within the catchment was 516.2 mm which was recorded at the Hetauda N.F.I. gauge on 13/08/2017; this is associated with the August 2017 flood event. In the western and central parts of the catchment the highest recorded daily rainfall totals were both recorded on the 31/07/2003 with the Rampur gauge total of 296.3 mm and the Beluwa gauge total of 304.2 mm respectively.

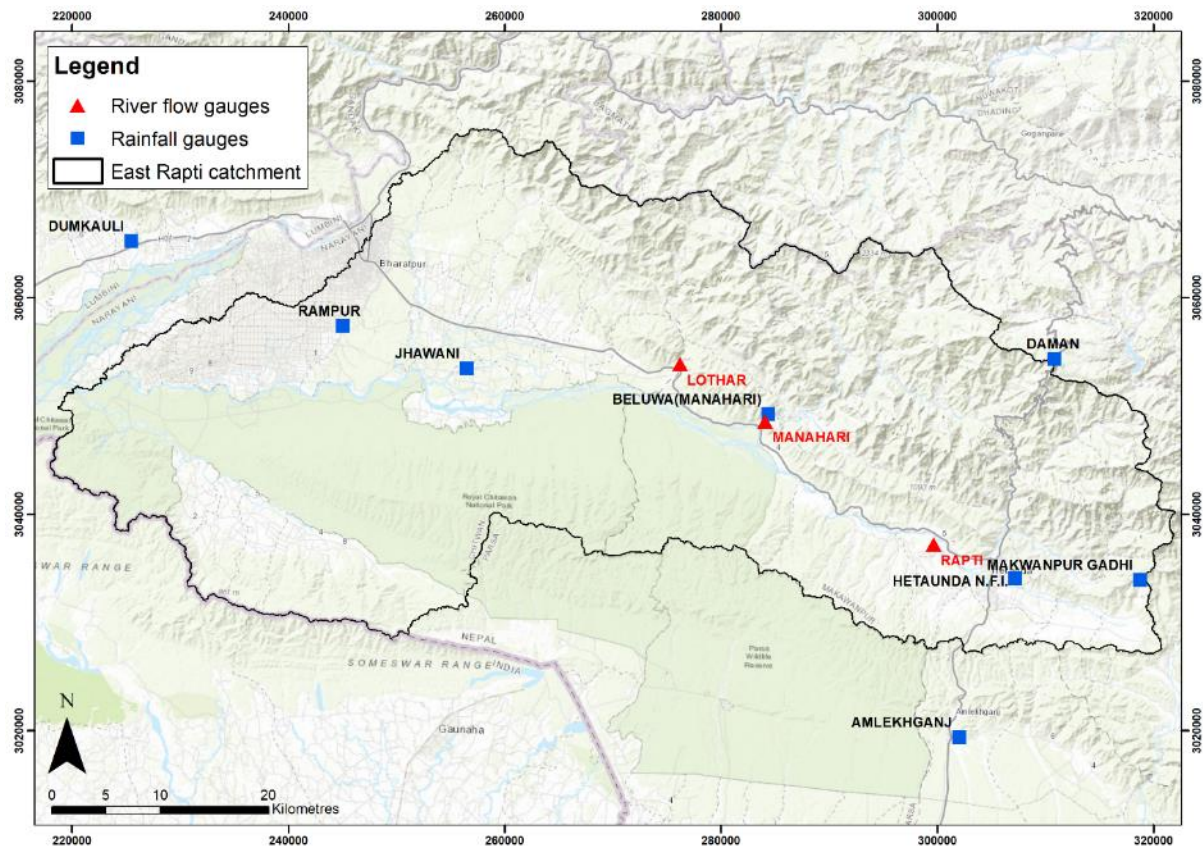


Figure 2.8: The location of the DHM rainfall and river flow gauges within, or in close proximity to, the East Rapti catchment. Temperature data was also attained from the Hetauda N.F.I. meteorological station.

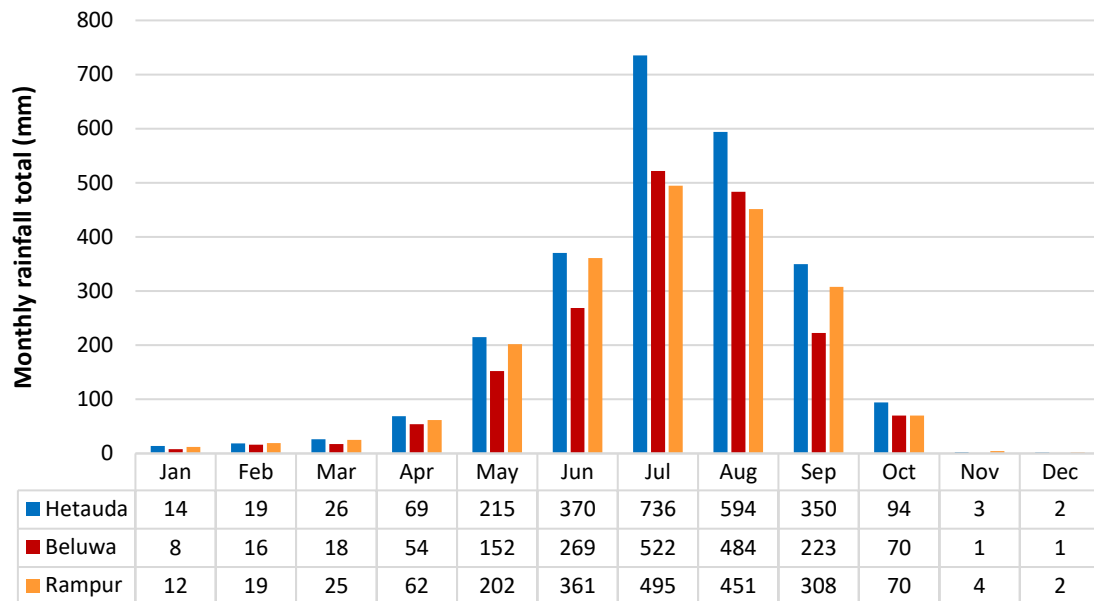


Figure 2.9: Average monthly rainfall totals in mm (1998-2016) for three DHM rain gauges distributed across the East Rapti catchment

The warmest month in the East Rapti catchment is June with an average daily temperature of between 30°C at the Rampur meteorological station (181 mASL) and 18°C at the Daman meteorological station (2,380 mASL). The coldest month is January with an average daily temperature of 15°C at Rampur and 7°C at Daman (Shilpakar et al., 2011). From DHM temperature data at the Hetauda N.F.I. meteorological station, the highest recorded temperature between 1998 and 2016 was 40.8°C (11/05/2014) and the lowest recorded temperature was 0.2°C (26/12/2003).

Using the Surface Energy Balance Algorithm for Land (SEBAL), Shilpakar et al. (2011) found that there was a spatially variable evapotranspiration pattern across the East Rapti catchment linked to land cover characteristics. The highest evapotranspiration rates occur in the forested areas of Chitwan National Park (a maximum annual rate of 1,478 mm), lower rates in the populated central area of the catchment (between 900 and 1,100 mm annually), and the lowest evapotranspiration rates in the hilly areas in the north of the catchment (between 300 and 500 mm annually).

2.5 CATCHMENT HYDROLOGY

2.5.1 Hydrological regime

The monthly flows of Nepali rivers generally peak during July and August and record the lowest flows during February and March with 80% of the total annual flow occurring during the monsoon period (Shrestha et al., 2000; WECS, 2011; Andermann et al., 2012a). This is true for the rainfall-dominated flow in East Rapti and corresponds with the rainfall pattern outlined in Section 2.4. Evaporation has a limited impact (<10%) on the hydrological budget in higher elevation mountainous catchments in

Nepal and the wider Himalayan Region; Bookhagen and Burbank (2010) state evaporation plays increased role on the hydrological budget (~30%) at lower elevations in areas such as the Terai. There is little known about the physical properties of the deep groundwater aquifer storage in Nepal and the contribution to the hydrological budget has been excluded in previous studies (Bookhagen and Burbank, 2010; Bricker et al., 2014). In the larger Nepali catchments (e.g. Kosi, Nayarani and Karnali) fractured basement aquifers could have a contribution to the hydrological regime (Andermann et al., 2012b). However, as noted in other catchment studies, the groundwater contribution to the hydrological regime in a Nepali catchment context predominantly occurs as baseflow outside of the monsoon period and, as such, is not a key factor when modelling of monsoonal flood flows (Shilpakar et al., 2011; Nepal, 2012).

Established in research by Shilpakar et al. (2011), there is a strong correlation between rainfall and river flow in the East Rapti catchment. This relationship is evident in Figure 2.10 with the highest average daily flows from the flow gauges within the East Rapti catchment occurring during the monsoon season, and specifically in August at all three flow gauge locations. The available flow data is discussed in Section 2.6.3 with the location of the three gauges shown in Figure 2.8 and further station information and completeness of records summarised in Table 2.3. The lowest average daily flows occur in March and April with a long period of minimal rainfall and water abstraction for agriculture throughout the catchment. The highest average daily flow total from the acquired gauged flow (1998 to 2016) for the Rapti River at Rajaiya gauge (DHM Station Number – 460; catchment area – 471 km²) was 1,260 m³ s⁻¹ (24/08/2010), for the Lothar Khola at Lothar gauge (DHM Station Number – 470; catchment area – 169 km²) was 530 m³ s⁻¹ (27/07/1999) and the Manahari Khola at Manahari gauge (DHM Station Number – 465; catchment area – 427 km²) was 913 m³ s⁻¹ (14/08/2015). It must be noted that there are apparent issues with some of the gauged data within the catchment (see Section 2.6.3.1).

In addition to rainfall, water is imported into the East Rapti catchment from the Bagmati catchment as part of the Kulekhani hydropower scheme. This interbasin transfer operates throughout the year with a minimum average monthly discharge of 1.0 m³ s⁻¹ and a maximum average monthly discharge of 4.8 m³ s⁻¹ (Shilpakar, 2003). Water balance research for the East Rapti catchment undertaken by Shilpakar et al. (2011) indicates that this water transfer accounts for less than 2.5% of the water budget in the catchment.

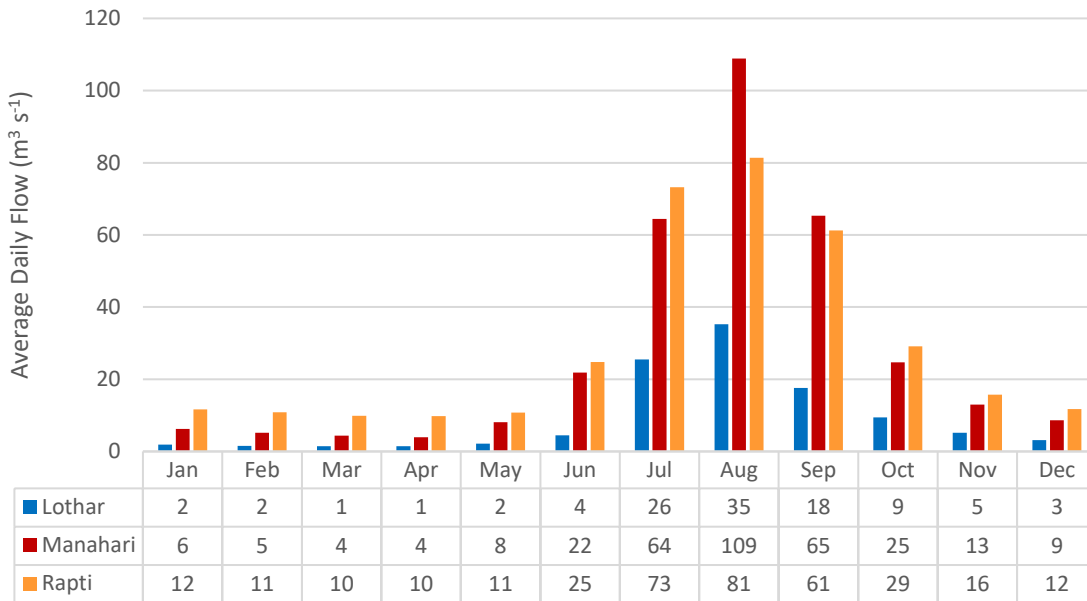


Figure 2.10: Average daily flows in $m^3 s^{-1}$ at the DHM river flow gauges in the East Rapti catchment (1998 to 2016).

2.5.2 Flood events in the East Rapti catchment

There have been several major flood events in the East Rapti catchment since the 1950s, with the most recent in August 2017. Singh (2013) highlights other notable flood events in 1954, 1971, 1975 and 1993 whilst the Asian Development Bank (2016) report that there have been 143 flood incidents between 1993 and 2015 in the catchment. The 1993 flood event, occurring due to an embankment breach, was the most damaging with 24 deaths and 5,300 households affected within the catchment (Singh, 2013). The August 2017 flood was a result of continuous monsoonal rainfall, with several districts on the Terai recording the highest rainfall in 60 years (Government of Nepal, 2017). Within the Chitwan and Makwanpur districts that make up the East Rapti catchment, flooding in 2017 was responsible for 12 deaths (Government of Nepal, 2017). In addition to the extreme flood events that result in extensive damage and the loss of life, many of the communities in the East Rapti catchment experience annual flooding. The Gardi Village Development Committee (the former second lowest government administrative unit prior to federalisation) in Chitwan, for example, floods every monsoon which results in the loss of land and property (UNDP Nepal, 2009).

The flood hazard within the East Rapti catchment occurs from both long duration rainfall overtopping the banks along the main East Rapti channel network and flash flooding in small tributaries originating in the Siwalik Range (Asian Development Bank, 2016; Government of Nepal, 2017). Singh (2013) notes that previous, continuous rainfall driven, floods along the main East Rapti channel have both risen and receded gradually with a low velocity. Several factors are responsible for increasing the flood risk occurring in the East Rapti catchment, and similar catchments that drain the Mahabharat Range across

Nepal. As the population in the more productive plains area the catchment increases so does the flood risk with dense, often poorly planned and unsafely built, urban settlements along the course of the river that encroach into current, or historic, floodplain areas (WWF Nepal, 2013). Additionally, in many Terai catchments structural flood defence measures are often poorly designed and maintained; the 1993 flood in the East Rapti catchment was caused by the breaching of a dyke for example (Singh, 2013; Government of Nepal, 2017). The removal of vegetation along the riverbanks, and the increased role of sedimentation is changing and reducing channel capacity is also cited as a flood risk increasing factor in the larger tributaries such as the Lothar Khola (Singh, 2013).

2.6 EVALUATION OF THE GAUGED CLIMATE AND RIVER FLOW DATA FOR THE EAST RAPTI CATCHMENT

A detailed assessment of the climate and river flow data within the East Rapti catchment has been undertaken on the gauged data acquired from the DHM for between 1998 and 2016. This evaluation was undertaken to establish if there were any issues with the acquired data, with some concerns arising during the initial modelling phase, and to determine the necessary steps to incorporate the data into the research. Discussed in Section 2.6.3.1, the results of the evaluation highlight apparent issues within the river flow data. The 1998 to 2016 period was selected to coincide with available satellite rainfall data from the TRMM (Tropical Rainfall Measuring Mission) project (see Section 3.2.2.3) with the data after this period not available at the time that this research was undertaken.

The location of the meteorological and river gauges within, and in close proximity to, the East Rapti catchment are shown in Figure 2.8. The temperature records were analysed for the Hetauda N.F.I. gauge for the same time period. Section 2.6.1 outlines the gauged rainfall data, Section 2.6.2 details the temperature data and Section 2.6.3 investigates the river flow data and critiques some of the potential issues that the data contains. Section 2.6.4 discusses the selected time period used in the CRUM3 hydrological modelling in Chapter 4.

2.6.1 Rainfall data

Daily rainfall data was analysed for eight rainfall gauges within, or in close proximity to, the East Rapti catchment. Table 2.2 provides an overview of the gauge information and the incomplete months at each gauge for the period 1998 to 2016. There is notable variation between the gauges with regards to completeness of the rainfall data record. Dumkauli, Hetauda N.F.I. and Rampur stations have a complete, or near complete (> 99%) dataset whilst other stations, such as Daman and Makwanpur Gadhi, have extended periods of rainfall data missing. It should be noted that there is a further rainfall station located in the East Rapti at Bharatpur (DHM Station Number – 927). This station was excluded

due to a reduced period of data availability (2001 to 2016), extensive periods of missing data (79% data completion) and close proximity to the Rampur meteorological station (5.7 km).

A full time series of the rainfall data for each of the eight rainfall gauges for the 1998 to 2016 period is shown in Appendix 7.1 (Amlekgunj and Beluwa), Appendix 7.2 (Daman and Dunkauli), Appendix 7.3 (Hetauda [1998 to 2017] and Jhawani) and Appendix 7.4 (Makwanpur Gadhi and Rampur).

2.6.2 Temperature data

Minimum and maximum daily temperature data for the period 1998 to 2016 was obtained from DHM for the Hetauda N.F.I. meteorological station; details of the station are reported in Table 2.2. This was the only meteorological station in the East Rapti catchment that had temperature data. The data record was complete for the acquired time period other than the month of December 2015.

2.6.3 River flow data

Gauged river flow data from DHM was evaluated for the three available locations in the East Rapti catchment: Lothar Khola at Lothar, Manahari Khola at Manahari and Rapti River at Raijaya (see Figure 2.11). Daily average flow data was acquired for the three gauges for the period 1998 to 2015 from the Department of Hydrology and Meteorology. There was no data available for 2016 onwards at the time of the research being undertaken. Unfortunately, there is not a gauging location towards the downstream end of the main East Rapti channel near the confluence with the Nayarani River.

A full time series of the river flow data for the 1998 to 2016 period and also for the modelled 2009 to 2011 period for each of the three gauges is shown in Appendix 7.6 (Lothar), Appendix 7.7 (Manahari) and Appendix 7.8 (Rapti).

A combination of the river flow time series and rainfall hyetographs at the Lothar/Beluwa and Rapti/Hetauda gauges for the 2009 and 2010 monsoon seasons are shown in Appendix 7.8 to Appendix 7.11. This allows for a comparison of rainfall patterns within the wet part of the year and the resultant discharges across the catchment.



Figure 2.11: The Rapti River at Rajaiya gauge (taken on 23/05/2018). Note that it was not evident that there were additional gauges implemented across the bridge.

2.6.3.1 Issues with gauged daily flow data

Following preliminary analysis during model setup using the period 2009 to 2011 several issues became apparent within the DHM daily flow data. These issues include anomalous annual hydrograph patterns, probable missing decimal points within the acquired data and extended periods of high flow followed by an unexpected instantaneous reduction to low flow or vice versa. The issues are discussed below in the context of the 2009 to 2011 period, but similar issues are apparent across the entire 1998 to 2015 period. This section will explore these issues with the three DHM gauges (Lothar Khola at Lothar, Manahari Khola at Manahari and Rapti River at Rajaiya) for the period and the actions taken in response. However, with the overall end-to-end catchment flood management assessment process used in this research designed to work in areas of poor data coverage, both spatially and temporally, the DHM flow data was still utilised in the research approach.

Two checks were undertaken to explore the reasons behind the differences seen in the gauged river flow data and preliminary modelled river flow output based on a combined input of DHM gauged rainfall and satellite rainfall data. Firstly, the annual average daily flow hydrographs for each year between 1998 and 2015 were compared to gain an understanding of the annual hydrograph shape.

One of the key issues that was apparent from this check was the possibility of mis-placed decimal points within sections of the data that would result in gauged flows being an order of magnitude higher than predicted. The second check used water balance in the respective gauge catchments to assess to what extent approximate rainfall into the catchment was comparable to the flow out of the gauged catchment. This was achieved using the total annual flow at the respective DHM gauge, the total rainfall at the closest DHM rainfall gauge (see Figure 2.8) and the catchment area.

Lothar Khola at Lothar

As shown in Figure 2.12, plotting hydrographs as individual time series' highlights that the latter part of 2011 is a notable anomaly as compared to the annual hydrograph pattern. The mean average daily flow for the period 20th July to 31st December for the other years with a complete time series ranges between $2.7 \text{ m}^3 \text{ s}^{-1}$ in 2005 to $20.5 \text{ m}^3 \text{ s}^{-1}$ in 1999 with an average of $10.5 \text{ m}^3 \text{ s}^{-1}$. For comparison, the mean average daily flow for 2011 in the same period is $94.1 \text{ m}^3 \text{ s}^{-1}$. This is probably attributable to a series of missing decimal points within the acquired data. Other examples of potential decimal point errors in the Lothar flow data occur in 1999 and 2004.

Additionally, a check on water balance in the Lothar sub-catchment, the area contributing to the flow at the gauge, was undertaken. This was achieved using the total annual flow at the Lothar river gauge and the total rainfall at the Beluwa rain gauge (see Figure 2.8); whilst not in the Lothar catchment it is the closest gauge to the catchment and therefore the best representation of the total annual rainfall in this area. The total annual flow for 2011 based on the gauge was calculated as 1.373 km^3 . The total annual rainfall at the Beluwa gauge was found to be 0.288 km^3 across the Lothar catchment and thus results in the Lothar gauge recording a water excess of 1.085 km^3 . This excess could perhaps be attributed to a physical change to the gauged area as a result of high flows, a calibration issue, or a data recording issue. The rainfall water input deficit, albeit at lower values, is also evident for 1999 (0.017 km^3), 2008 (0.0005 km^3) and 2012 (0.006 km^3) at the Lothar gauge.

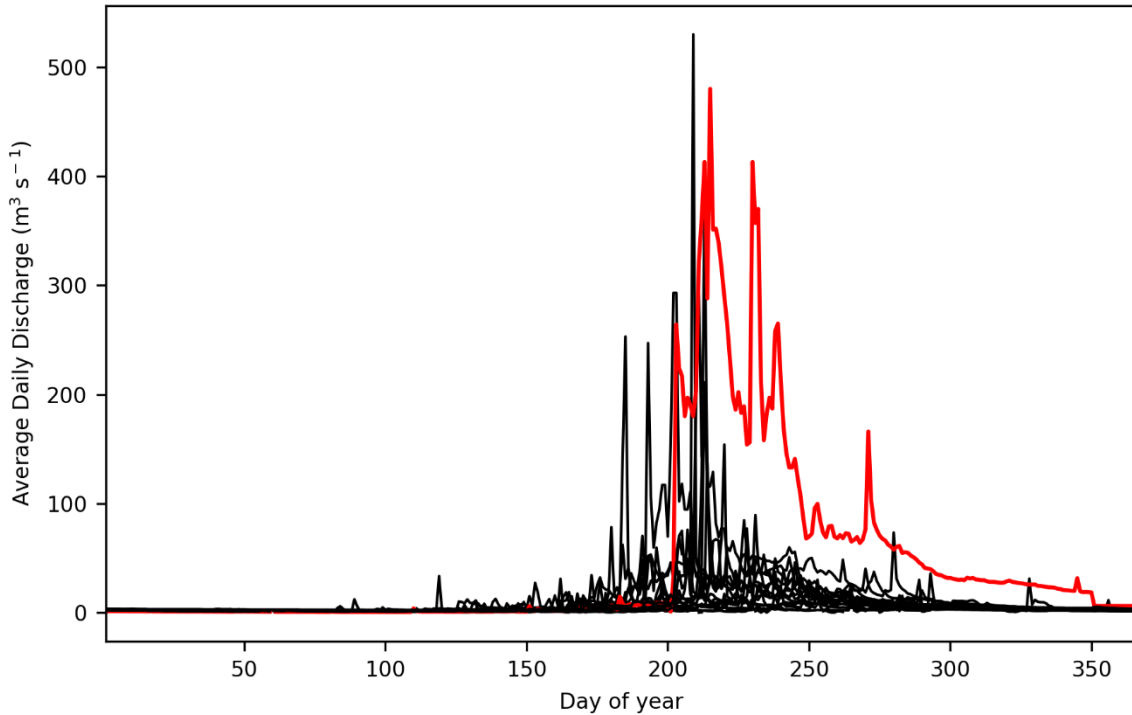


Figure 2.12: The Lothar Khola at Lothar average daily flow data for each year between 1998 and 2015. The 2011 average daily flow series is shown as a red line with the remaining years represented with a black line.

Manahari Khola at Manahari

The Manahari flow gauge records extended periods of high flow followed by an unexpected instantaneous reduction to low flow. For example, the 2009 average daily flow suddenly falls from a 25-day period with an average daily flow of $295 \text{ m}^3 \text{ s}^{-1}$ and a high flow of $441 \text{ m}^3 \text{ s}^{-1}$ to $36.7 \text{ m}^3 \text{ s}^{-1}$ over a one day period; this is shown in Figure 2.13. This recurrent pattern is also evident in 2002, 2003 and 2013.

As with the Lothar catchment, a check on water balance in the Manahari catchment was undertaken, using the total annual flow at the Manahari flow gauge and the total rainfall at the Beluwa rain gauge (see Figure 2.8). The Beluwa rain gauge is at the southern edge of the Manahari Khola catchment and is the best representation of the total annual rainfall in the catchment available. The total annual flow for 2009 based on the gauge was calculated as 1.061 km^3 . The total annual rainfall at the Beluwa gauge for 2009 was 0.772 km^3 across the Manahari catchment and results in the Manahari gauge recording a water excess of 0.290 km^3 . As with the Lothar gauge this excess could perhaps be attributed to a physical change to the gauged area as a result of high flows, a calibration issue, or a data recording issue. It should be noted that the rainfall between 1st January and 13th January 2009 at the Beluwa gauge was not available but as this was outside of the monsoon season the likelihood of extreme rainfall is small and therefore the rainfall input deficit likely remains. The rainfall water input deficit is

also evident for 2002 (1.149 km³), 2003 (1.233 km³), 2012 (0.164 km³) and 2014 (0.265 km³) in the Manahari data. It must be stated that both 2002 and 2003 do not contain a complete annual record but are notably not missing months associated with the monsoon period.

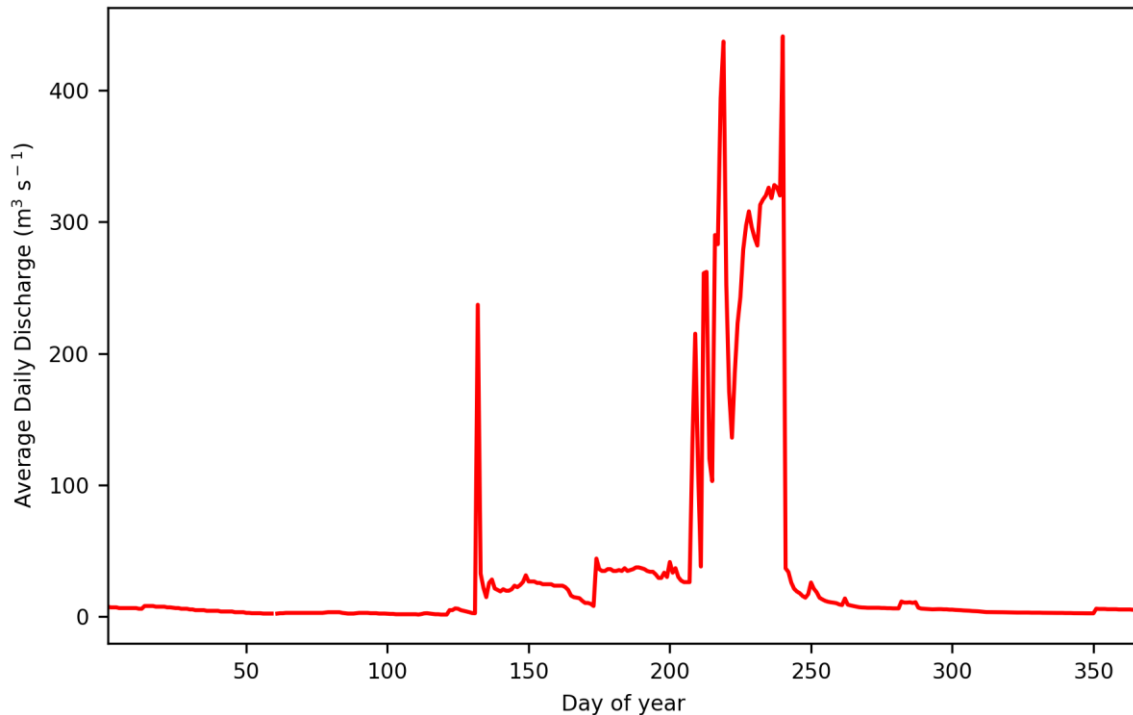


Figure 2.13: The Manahari Khola at Manahari average daily flow data for the year 2009. Note the significant drop in average daily flow at day 240.

Rapti River at Rajaiya

Based on visual analysis of the annual hydrographs there are potential errors related to individual values that likely relate to missing decimal points throughout the Rapti dataset. For example, as shown in Figure 2.14, in 2004 a high flow of 1150 m³ s⁻¹ is preceded and succeeded by 10 days of flow values between 90 m³ s⁻¹ and 117 m³ s⁻¹; so it is likely that the gauged value should be 115 m³ s⁻¹. These issues are also apparent to values in 2011 and 2012 within the Rapti data.

As with the Lothar and Manahari gauges, a check on the water balance was undertaken for the Rapti catchment. This was achieved using the total annual flow at the Rapti flow gauge and the total rainfall at the Hetauda N.F.I. rainfall gauge (see Figure 2.8). The Hetauda N.F.I. gauge is at the southern edge of the Rapti River catchment and is the best representation of the total annual rainfall in the catchment available. A rainfall water input deficit is evident for 2004 (0.241 km³) and 2012 (0.117 km³) in the Rapti data.

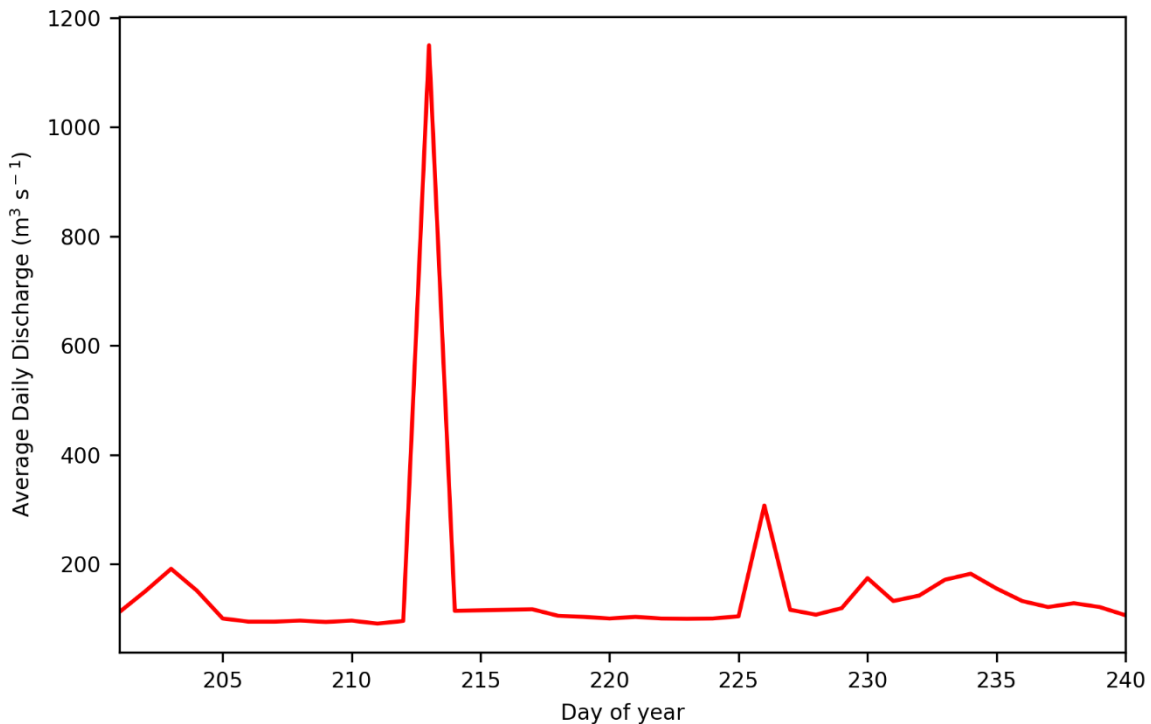


Figure 2.14: The Rapti River at Rajiaya average daily flow data for the year 2004. Note the significant increase in average daily flow at day 213 that is likely due to a missing decimal point.

2.6.4 Justification of gauged data used in the CRUM3 hydrological modelling

The gauged data used in Chapter 4 in the CRUM3 hydrological model set up was taken for the period 2009 to 2010. This period was selected for having the most continuous period of precipitation and temperature, key climatic drivers of the CRUM3 hydrological model, in the available DHM data for the East Rapti catchment. With no identified issues with the rainfall and temperature data there was no climate data excluded in the model set up.

For the hydrological model calibration, a flow record was necessary to assess the model performance. Many of the issues noticed in the river flow data appear to have occurred due to calibration or data recording issues; one possibility is missing decimal places in the acquired data. However, determining exactly where to stop re-adding decimal places to correct the data is a difficult proposition and therefore data that likely required correcting to become usable in the model calibration process was excluded. It was apparent from the investigation that the Manahari flow gauge data for 2009 and 2010 was not suitable for model calibration purposes within the simulated time period and, as such, was excluded from the model assessment process. The Manahari gauged data for 2009 and 2010 had sudden reductions in flow between days, annual low flows occurring for individual days in the monsoon period and annual water balance issues. In contrast to the Manahari gauge, the Lothar Khola at Lothar and Rapti River at Rajiaya gauges exhibited no obvious issues throughout the 2009 to 2010 period and the gauged data at both sites is used in the model assessment and calibration process.

Table 2.2: DHM rainfall gauge information that shows the data period available for the rainfall gauges around the East Rapti catchment. Grey indicates a complete record. Light red indicates an incomplete data record with the months missing numbered (1 = January, 2 = February etc.).

Station Name	Amlekhganj	Beluwa (Manahari)	Daman	Dumkauli	Hetaunda N.F.I.	Jhawani	Makwanpur Gadhi	Rampur
DHM Station No.	907	920	905	706	906	903	919	902
Elevation (m)	396	274	2314	154	474	270	1030	256
Data Period	1998 - 2016	1998 - 2016	1998 - 2016	1998 - 2016	1998 - 2017	1998 - 2016	1998 - 2016	1998 - 2016
Completion (%)	91.2	95.6	64.5	100	100	98.2	91.7	99.6
1998								
1999								
2000								
2001							11-12	
2002	4-12						1-4, 9-10	
2003			5-6					
2004			2-4, 10-12					
2005			1-3					
2006							11-12	
2007			6-7, 9-12					
2008			1-6					
2009		1						
2010			5-7					
2011			10-12			5-6		
2012			1-12					
2013			1-12					
2014		11-12	1-12					
2015	1-2, 4-12	1, 10-12	1-12				5-9, 11-12	
2016		10-12	9-12			11-12	11-12	12

Table 2.3: DHM river flow gauge information that shows the data period available for the gauges within the East Rapti catchment Grey indicates a complete record. Light red indicates an incomplete data record with the months missing numbered (1 = January, 2 = February etc.).

Station Name	Lothar Khola at Lothar	Manahari Khola at Manahari	Rapti River at Rajaiya
DHM Station No.	470	465	460
Station Type	Cable Way	Cable Way	Cable Way
Data Period	1998 - 2015	1998 - 2015	1998 - 2015
Station Area (km²)	169	427	471
Completion (%)	96	98	91
1998		9-10	
1999			1-12
2000			1-10
2001	4-6		
2002	7-9	3-4,10	
2003		11-12	
2004	8-12	11-12	7
2005		1	
2006			
2007			
2008			
2009			
2010			
2011			
2012			
2013			
2014			
2015			
2016			

2.7 EAST RAPTI CATCHMENT SUMMARY

The East Rapti catchment was selected as an appropriate case study location as it has the topographical and land cover characteristics of a typical medium-sized Nepali catchment, covering in this case the geomorphological zones of the Terai, Dun Valley, Siwalik and Mahabharat Ranges. The East Rapti has a recent flood history with severe flooding in 1954, 1971, 1975, 1993 and 2017 in addition to annual monsoonal flood waters originating in the upland areas of the catchment and impacting on the more densely populated Terai downstream.

The East Rapti, as with most Nepali catchments, experiences the majority of its annual precipitation in the monsoon period (June to September) with the remaining rainfall in the pre-monsoon period (March to May) and in the post-monsoon winter period (October to November). Based on available gauged data, the catchment has an average annual rainfall of 2,008 mm with spatial variation in recorded totals throughout the catchment. For the period 1998 to 2016 in the eastern part of the catchment at the Rampur gauge was 2,011 mm, in the central part of the catchment at the Beluwa gauge was 1,816 mm and in the western part of the catchment at the Hetauda gauge was 2,494 mm. The highest daily rainfall recorded within the catchment was 516.2 mm which was recorded at the Hetauda gauge on 13/08/2017.

The distribution of annual rainfall controls the distribution of flood flows in the East Rapti catchment, with monthly flows of Nepali rivers generally peaking during July and August and recording the lowest flows during February and March. From the three available river gauges within the catchment, the highest average daily total flow from the monitored period (1998 to 2015) for the Rapti River at Rajaiya gauge was $1,260 \text{ m}^3 \text{ s}^{-1}$ (24/08/2010), for the Lothar Khola at Lothar was $530 \text{ m}^3 \text{ s}^{-1}$ (27/07/1999) and the Manahari Khola at Manahari was $913 \text{ m}^3 \text{ s}^{-1}$ (14/08/2015).

As outlined in Section 2.6.3.1, there are apparent issues with some of the gauged river flow data within the catchment. Two checks, a comparison of annual hydrographs and a water balance assessment, were undertaken to explore the reasons behind the differences seen in the gauged river flow data and preliminary model river flow output. These issues include anomalous annual hydrograph patterns, probable missing decimal points within the acquired data and extended periods of either high or low flow followed by an unexpected, rapid change. However, with the overall end-to-end approach used in this research designed to work in areas of poor data coverage, both spatially and temporally, the available river flow data was still used. It was apparent from the investigation that the Manahari gauged data for 2009 and 2010 was not suitable for model calibration purposes within the simulated

period. The Lothar and Rapti gauges, conversely, exhibited no apparent issues throughout the period and the gauged data at both sites is used in the model assessment and calibration process

3 IDENTIFYING FLOOD WATER SOURCE AREAS FOR THE SPATIAL TARGETING OF FLOOD MANAGEMENT MEASURES AT THE CATCHMENT-SCALE

3.1 INTRODUCTION

The management of flooding is moving away from mitigation solely at the point of the impact, and towards an integrated catchment management approach which considers source areas, flow pathways of flood waters and the impacted communities and infrastructure (Evans et al., 2002, Calder and Aylward, 2006; Werrity, 2006; Merz et al., 2010; Nisbet et al., 2011; Lane, 2017). The parts of the catchment generating flood waters that impact communities can be targeted through the identification of critical source areas (Heathwaite et al., 2005). Originally developed to aid diffuse pollution management (Heathwaite et al., 2005), critical source areas are hillslope areas that produce rapid overland runoff and are well connected to the channel network (Thomas et al., 2016; Metcalfe, 2017; Roberts et al., 2017). Measures that attempt to disconnect areas of high hydrological connectivity or increase storage in areas generating overland flow can impact on the flood regime in the catchment (Metcalfe, 2017). Further catchment measures can utilise floodplain storage (Acreman and Holden, 2013; Quinn et al., 2013) and alter river conveyance to slow the flow of water through the channel network (Nisbet and Thomas, 2008; Odoni and Lane, 2010; Dixon et al., 2016) and hence reduce flood peaks.

Catchment-scale flood management considers the impact of localised measures across the catchment-scale and thus there is a need to balance and optimise the peak flow at key locations (Nisbet and Thomas, 2008; Lane, 2017). A flood management measure must be assessed for its impact across the catchment, with the magnitude of the downstream flow a combination of tributary inputs that increase the flow and attenuation processes that reduce it; changes in attenuation have the potential to cause a negative impact on the peak flow downstream (Turner-Gillespie et al., 2003; Hooijer et al., 2004; Lane, 2017). It is therefore essential to consider flood wave propagation throughout the catchment when selecting a location for a flood management measure (Pattison et al., 2014; Dixon et al., 2016).

Spatial targeting using geospatial data and GIS analysis has become recognised as an essential tool in environmental policy design and planning with measures such as water quality, flood risk reduction and carbon sequestration targeted within a catchment or landscape (e.g. Juracek, 2000; O'Connell et al., 2007; van der Horst, 2007; Reaney et al., 2011; da Silva et al., 2012; Jackson et al., 2013; Naden,

2013). From a flood management perspective, there is a significant amount of research on the rapid assessment and mapping of flood hazard areas using weighted multi-criteria decision analysis with a GIS platform (e.g. Diakakis, 2010; Kourgialas and Karatzas, 2011; Kazakis et al., 2015; Abdelkareem, 2017; Xiao et al., 2017; Mahmoud and Gan, 2018; Patrikaki et al., 2018; Tang et al., 2018). With regards to the implementation of flood management measures at the catchment-scale, there are few tools that provide an assessment, especially rapidly, of areas within that a catchment that generate flood water and would benefit from having flood management measures implemented. Through assessment of geomorphic unit hydrographs (e.g. Saghafian and Khosroshani, 2005; Roughani et al., 2007; Saghafian et al., 2010; Sulaiman et al., 2010; Saghafian et al., 2013), there is research looking at prioritising and targeting sub-catchments for flood management purposes but much of the research does not consider the combination of the spatial and temporal variability in patterns of rainfall, land cover, and hydrological connectivity across a catchment. Other studies have used geospatial data-driven frameworks to look at critical runoff source areas in catchments (Juracek, 2000; Hlaing et al., 2008; Leh and Chaubey, 2009; da Silva et al., 2012; Ameri et al., 2018) from the perspective of land, but not flood, management. Previous research has also mapped suitable locations for the implementation of natural flood management approaches, such as runoff attenuation features and woodland planting, using specific spatial criteria for certain interventions; the locations identified do not necessarily target the source areas of flood water but determine areas that the intervention could be placed (Benavidez et al., 2016; Hankin et al., 2017).

To identify areas within the East Rapti catchment that are most suitable for the implementation of flood management measures, through targeting the flood water source areas, the SCIMAP-Flood decision support framework has been used (Section 3.2.1) (Reaney, *in prep.*). SCIMAP-Flood uses a combination of spatial rainfall patterns and land cover, the incorporation of transmission times across a catchment, and modelling of hydrological connectivity to map flood water generating areas. Applied to the East Rapti catchment, the SCIMAP-Flood output identifies locations where flood management measures would be most suitable to have a positive effect for multiple flood impacted zones across the catchment. If these practices are adopted, the catchment-scale flood management approaches implemented may reduce the dependency upon hard engineering solutions as protection from flooding. This chapter presents the development of the SCIMAP-Flood Fitted approach that uses an inverse modelling approach to determine the land use risk weightings for the East Rapti catchment. An inverse modelling approach has previously only been used within the diffuse pollution SCIMAP framework (Reaney et al., 2011; Milledge et al., 2012). Chapter 3 also outlines the first application of SCIMAP-Flood in a data sparse context with a view to developing a system suitable for usage in other catchments, similar to the East Rapti catchment, with poorer data availability.

3.2 METHODS

Figure 3.1 conceptualises the approach taken in this chapter. SCIMAP-Flood was the model framework chosen to identify the source areas of flooding in the East Rapti catchment and allow for the spatial targeting of flood management measures at the catchment-scale (Reaney, *in prep.*). SCIMAP-Flood is a variant of SCIMAP, a decision support framework that uses risk-based analysis on a catchment-scale with minimal input data (Reaney et al., 2011). SCIMAP-Flood can be utilised to help locate areas within the catchment that were responsible for generating flood waters to areas impacted by flooding. Catchment-scale flood management scenarios created from the SCIMAP-Flood output can then be tested using a distributed hydrological model. Additionally, SCIMAP-Flood requires minimal input data to operate and can be run using global datasets; thus, the framework can be applied to catchments with limited or no available local data. This ability to function with global datasets makes SCIMAP-Flood a suitable tool for applying to the relatively data poor East Rapti catchment which has a sparse, relative to many comparably sized European catchments, climate monitoring network and no freely available high-resolution (< 5 m) elevation data. Differing from previous research using SCIMAP-Flood, an extension of SCIMAP-Flood called SCIMAP-Flood Fitted has been used to determine the land cover weightings.

Within the methods, Section 3.2.1 explores the SCIMAP-Flood decision support framework. Section 3.2.2 outlines the data used to run SCIMAP-Flood approach for the East Rapti catchment and illustrates the process used to convert the initial data in a format suitable for running in SCIMAP-Flood. Section 3.2.3 details the SCIMAP-Flood Fitted extension for deriving the land cover weightings and the data used to run this extension is shown in Section 3.2.4.

3.2.1 SCIMAP-Flood

SCIMAP-Flood has been developed to gain understanding into the runoff regime at a catchment-scale using the same principles of hydrological connectivity associated with diffuse pollution modelling in the original SCIMAP fine sediment risk mapping tool (Reaney et al., 2011; Reaney and Pearson, 2016; Reaney, *in prep.*). SCIMAP-Flood identifies critical source areas for flood waters using a combination of mapping flood water generation areas, transmission times across the catchment and hydrological connectivity (Reaney and Pearson, 2016; Reaney, *in prep.*). Critical source areas are defined where there is both a source area and a connection to the river or lake (Heathwaite et al., 2005). As shown in Figure 3.2, the sources of flood waters are determined by the local land cover, rapid runoff generation potential, the rainfall pattern and travel times.

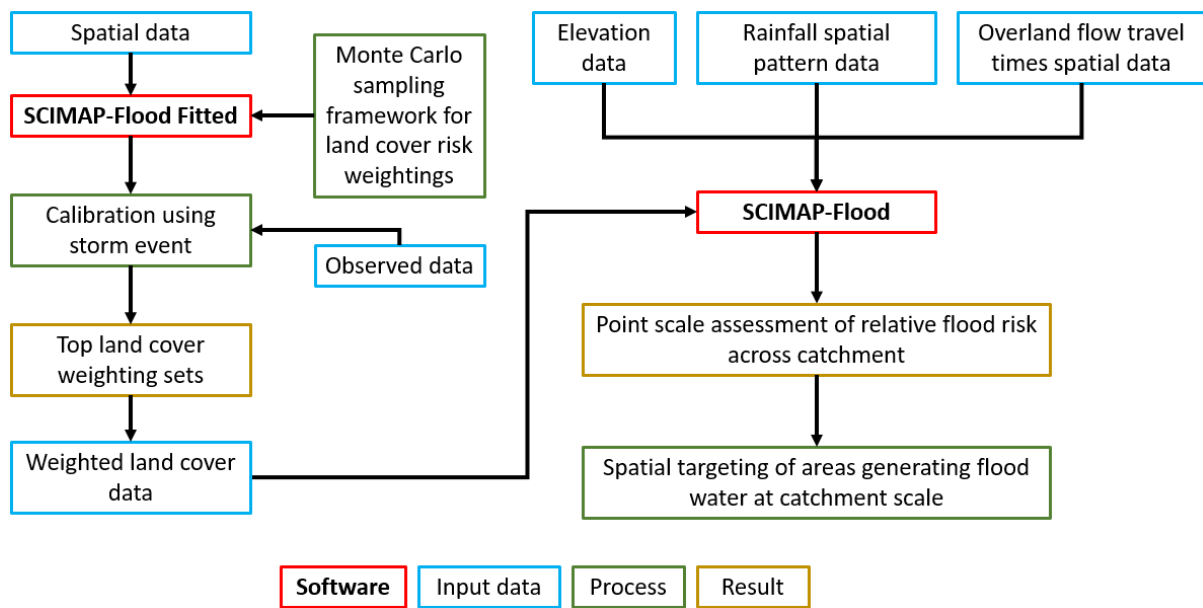


Figure 3.1: A diagram outlining the SCIMAP-Flood and SCIMAP-Flood Fitted approaches used in this chapter.

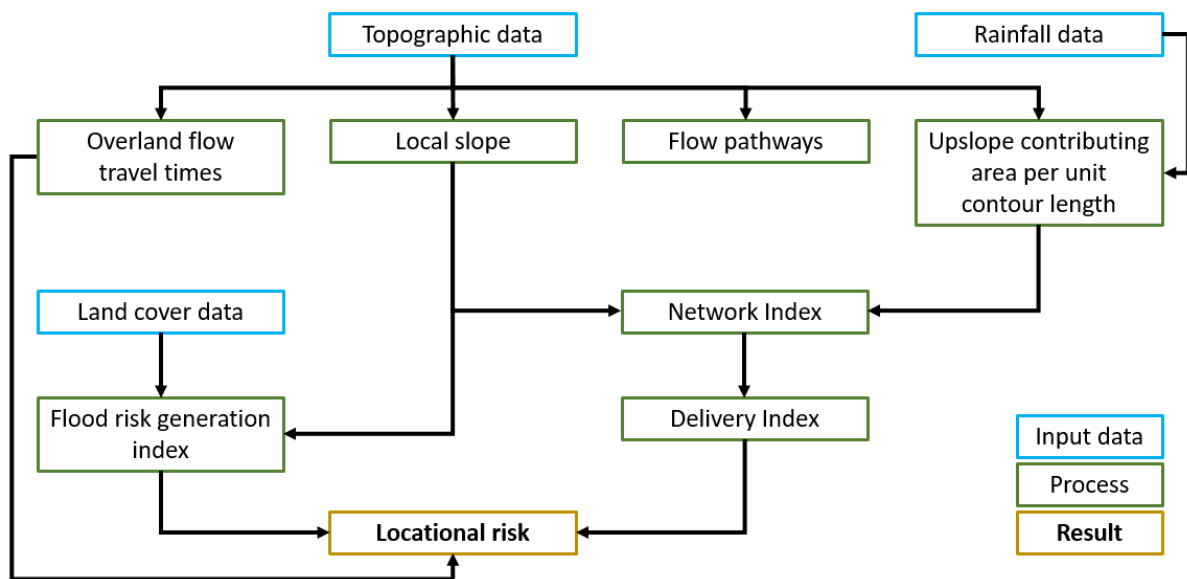


Figure 3.2: A diagram illustrating the processes used in SCIMAP-Flood to calculate relative flood risk at a catchment-scale (modified from Pearson, 2016 [pp. 53]).

Local runoff generation potential is based on a combination of land cover, land management, soil properties and slope gradient; the potential runoff increases with slope gradient (Kirkby et al., 2002; Bracken and Croke, 2007; El Kateb et al., 2013; Reaney et al., 2014). With the minimal information requirement approach used in SCIMAP-Flood, these combined factors are simplified with land cover taken as the dominant factor and scaled with slope gradient. A flood risk generation weighting of between zero and one is assigned to the catchment land covers based on either logical values, in-field infiltration measurements, or fitted to the observed pattern of flood magnitude.

Travel times are considered within SCIMAP-Flood in order to determine the magnitude of a flood event due to synchronisation of sub-catchments. Travel times are represented using a simplified geomorphic unit hydrograph approach, as described in Rigon et al. (2016). The average travel distance to a specific location is given the highest weighting (0 to 1) with the other travel times rescaled linearly based on the comparative distance to the average travel distance.

Hydrological connectivity is calculated from the elevation data and is determined using the Network Index (Lane et al., 2004). The Network Index shows the relative ease with which each location can contribute flood water through firstly calculating the runoff generation of each point in the catchment using the Topographic Wetness Index; this index is a function of upslope contributing areas and local slope gradient with the equation shown as (Beven and Kirby, 1979):

$$TWI = \ln \left(\frac{a}{\tan \beta} \right)$$

Equation 3.1

where a is the local upslope area draining through a given point per unit contour length and $\tan \beta$ is the local slope (Beven and Kirkby, 1979; Sorensen et al., 2006).

The second calculation step of the Network Index uses a flow tracing algorithm to identify the landscape scale wetness required for each point within the catchment to generate runoff. This is undertaken by analysing the runoff transmission characteristics of the points on the downslope path to the river or lake (Lane et al., 2004).

SCIMAP-Flood attributes a risk weighting of between 0 and 1 to each of the flood hazard driving factors and then amalgamates the values to provide a point scale assessment of the potential value of implementing a flood management measure to reduce flood risk at a given location (Reaney and Pearson, 2016). The overall flood risk (F) for each location is determined using:

$$F = \sum_{n=x}^{rf} \sum_{n=y}^{tt} L * R * C * T$$

Equation 3.2

where rf is the rainfall map, x is the number of rainfall maps analysed, tt is the travel time map, y is the number of travel time maps used, L is the land cover flood water generation risk factor, R is the rainfall pattern factor, C is the hydrological connectivity factor and T is the travel time factor.

3.2.2 East Rapti catchment data for SCIMAP-Flood

The SCIMAP-Flood framework requires four main data sources to operate: elevation data (Section 3.2.2.1), overland flow travel time data (Section 3.2.2.2), rainfall data (Section 3.2.2.3) and land cover data (Section 3.2.2.4).

3.2.2.1 *Elevation data*

With no free catchment-scale high-resolution elevation data available for the East Rapti catchment the elevation data used in SCIMAP-Flood was sourced from the Japanese Aerospace Exploration Agency (JAXA) ALOS (Advanced Land Observing Satellite) dataset. The digital elevation model used for the East Rapti catchment is shown in Figure 2.4 in Chapter 2.

The ALOS Global Digital Surface Model (AW3D30) is a free global digital surface model (DSM) that is gridded on a 30 m mesh. The 30 m mesh is based on the average and median elevation values of a 5 m version (Tadono et al., 2014; Takaku et al., 2014). The ALOS 30 m elevation data was selected as it has an absolute and relative height accuracy of under 5 m, which is an improvement on earlier free 30 m resolution global elevation datasets (Takaku et al., 2016). The Shuttle Radar Topography Mission (SRTM) has an absolute height accuracy of 9 m and relative height accuracy of 10 m (Rodriguez et al., 2006) and the Advanced Spaceborne Thermal Emission and Reflectance Radiometer (ASTER) has a height accuracy of 13 m (Tachikawa et al., 2011).

3.2.2.2 *Overland flow travel time data to selected flood impact points*

The consideration of travel times and synchronisation in generating flood waters is a key factor in determining the flood peak. Using a simplified version geomorphic unit hydrograph (e.g. Rigon et al., 2016) approach and calculated using 'Overland Flow Distance to Channel' tool in SAGA GIS, SCIMAP-Flood requires the relative flow distance from different parts of the catchment to the specific flood impact point.

This approach has been used for six flood impact locations within the East Rapti catchment (see Figure 3.3), with an example of the overland flow travel time data to Sauraha shown in Figure 3.4. The sites were selected as they were either populated locations that were impacted in the August 2017 flood event (Sauraha [catchment area – 2209 km²]), large population centres along the main channel network and key tributaries (Hetauda [432 km²], Lothar [174 km²] and Manahari 436 km²), key pieces of infrastructures that connect parts of the catchment (Madi Bridge [348 km²]) or locations with a vulnerable population close to the main channel in the East Rapti catchment (Andrauli [2555 km²]). These six key locations were chosen for the implementation of SCIMAP-Flood, but further consideration could be given to smaller settlements or those at risk of flooding from smaller tributaries within the catchment.

As part of the sensitivity analysis of the SCIMAP-Flood inputs the effect of splitting the flood impact points close to confluences into multiple sub-catchments was tested. The approach considers the flood water generation potential from each sub-catchment individually, taken upstream of the confluence, rather the combined potential from both, taken downstream of the confluence. This split

was undertaken for the flood impact points at both Sauraha and Hetauda; the locations of the split flood impact points are shown in red in Figure 3.3. For Hetauda this involved having an impact point for the Rapti channel and the Karra River tributary from the east; this impact on the contributing overland flow areas having split the flood impact points is illustrated in Figure 3.5. For Sauraha this resulted in the consideration of the main East Rapti channel and the Budhi Khola and tributary from the north.

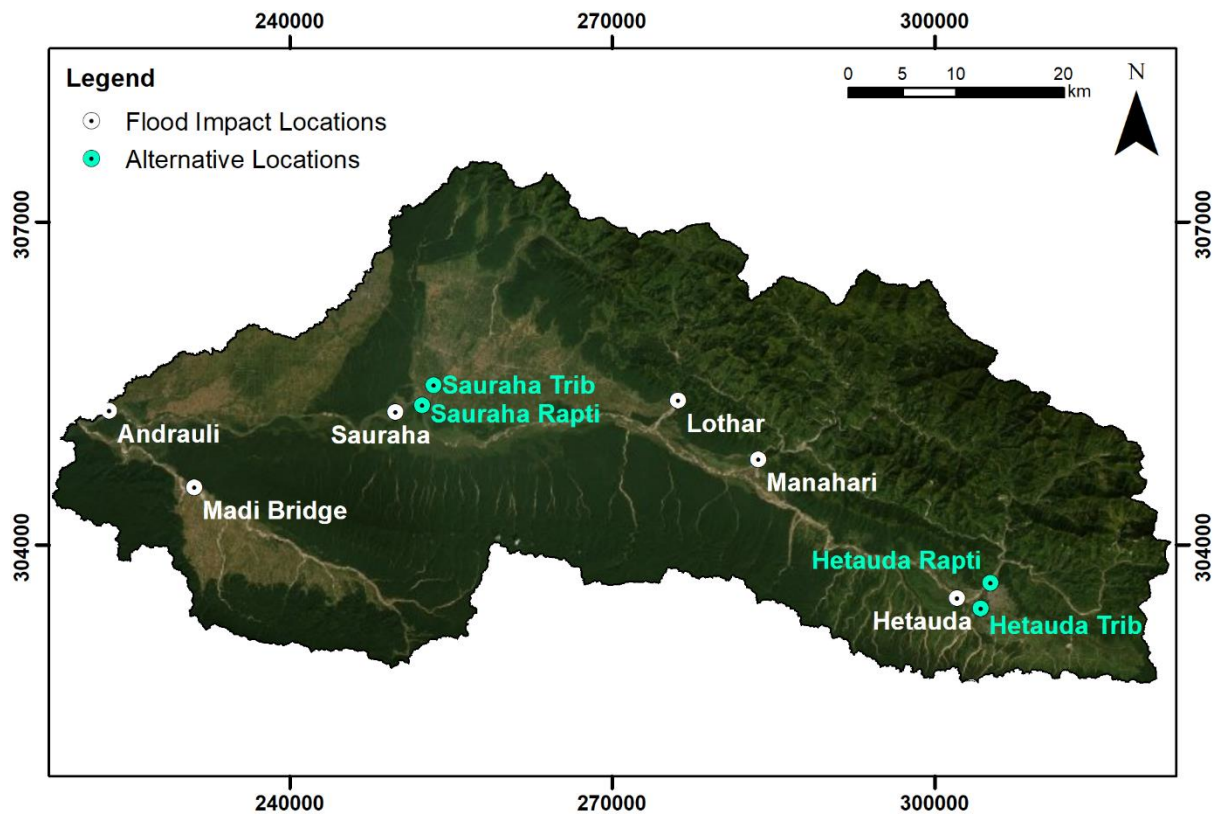


Figure 3.3: The location of selected flood impact points in the East Rapti catchment. The final chosen impact points used in SCIMAP-Flood are denoted with white circles. The effects of splitting impact points where two channels combine was tested using locations denoted by light blue circles.

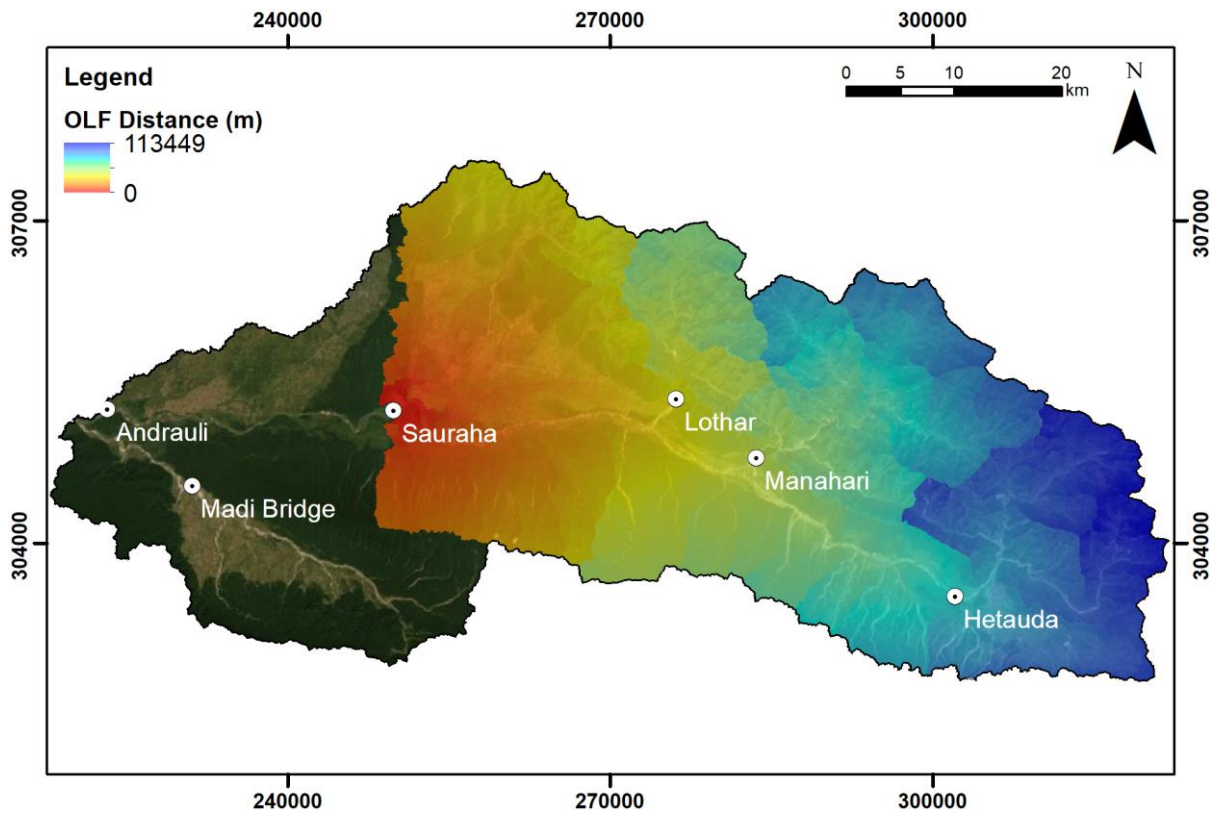


Figure 3.4: An example of the overland flow travel time spatial data to the Sauraha flood impact point.

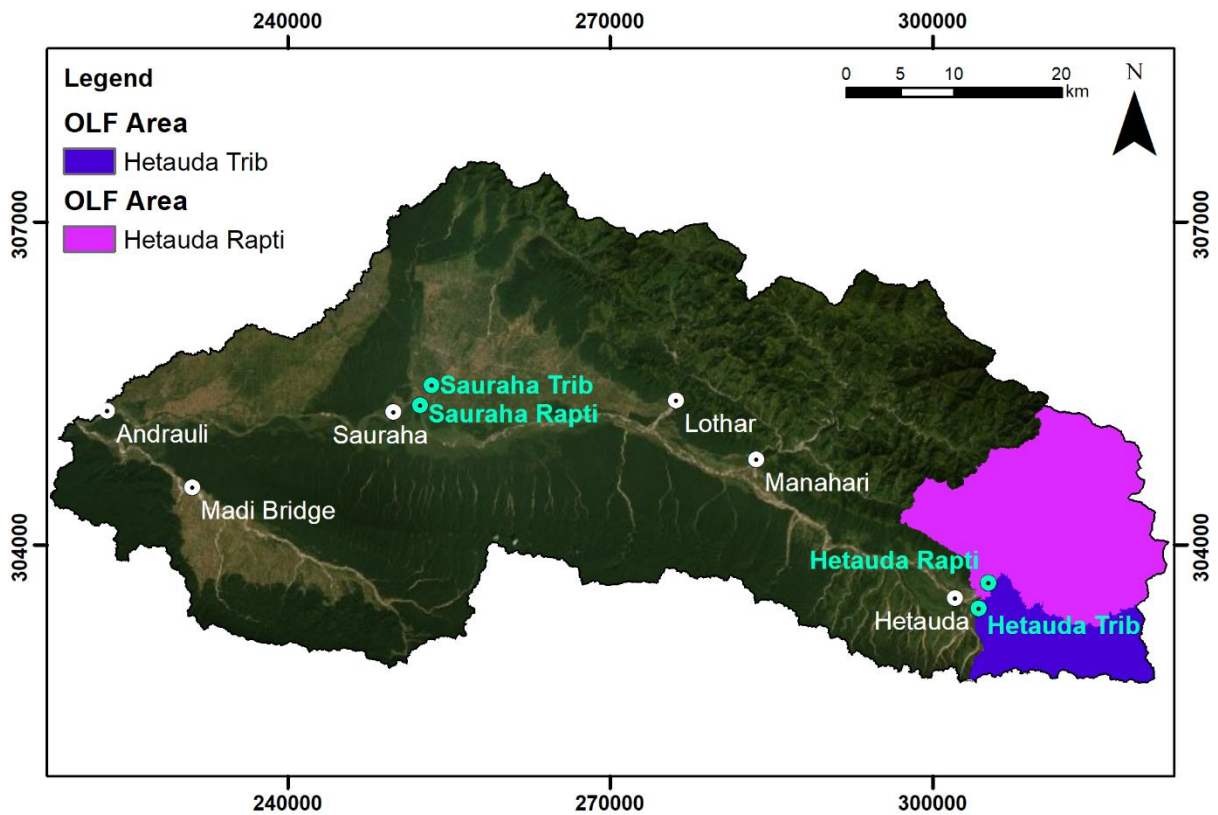


Figure 3.5: The overland flow contributing area for the split Hetauda flood impact points shown in Figure 3.3. The combined Hetauda contributing area is a combination of both the pink and purple regions.

3.2.2.3 *Spatial rainfall pattern data*

A combination of gauged rainfall data from the Nepalese Government's Department of Hydrology and Meteorology (DHM) and satellite rainfall estimates from NASA's Tropical Rainfall Measuring Mission 3B42 (TRMM_3B42_Daily) precipitation data (Huffman et al., 2007) was used in SCIMAP-Flood. The relationship between the two sources of rainfall data and the process used to combine the gauges and bias-corrected satellite rainfall sources to create a gridded rainfall product suitable for SCIMAP-Flood is discussed within this section. The final part of this section explores the rainfall storm event selection for SCIMAP-Flood output generation.

A combination of gauged rainfall estimates and bias-corrected satellite rainfall estimates was deemed necessary to compensate for areas of catchment poorly represented by the spatial distribution of the DHM gauge network. This combined approach has been successfully implemented in previous research undertaking hydrological modelling in data-sparse catchments (Arias-Hidalgo et al., 2013; Liu et al., 2017) and allows for SCIMAP-Flood to be implemented with a denser rainfall network than purely relying on the gauged data network coverage.

In addition to combined gauged and satellite rainfall grids for the East Rapti catchment, other rainfall scenarios and products were utilised to assess the effectiveness of a more detailed approach for using rainfall data within SCIMAP-Flood. Other rainfall data sources assessed; 1) the use of only the TRMM 3B42 satellite rainfall data for the identical storm event selection, and 2) TRMM 3B42 satellite rainfall data only for the monsoon seasons (May to September inclusive) for each year between 1998 and 2016.

Gauged rainfall data

Daily rainfall data was acquired for eight rainfall gauges within, or in close proximity to, the East Rapti catchment from the Government of Nepal's Department of Hydrology and Meteorology (DHM). To coincide with the available satellite rainfall estimates, the DHM gauged data was obtained for the period 1998 to 2016 (2017 data for all but one station was not available at the time this research was undertaken). In the previous chapter, Table 2.2 outlines the information for each of the gauges and Figure 2.8 illustrates where the gauges are in relation to the East Rapti catchment.

In addition to general gauge information, Table 2.2 shows the incomplete months at each gauge for the period 1998 to 2016. There is significant variation between the gauges with regards to completeness of the rainfall data record. Three of the stations (Dumkauli, Hetauda and Rampur) have a complete or near complete dataset, whilst other stations, such as Daman and Makwanpur Gadhi, have extended periods of missing data. A further station, Bharatpur, was excluded due to a reduced

period of data availability (2001 to 2016), extensive periods of missing data and its proximity to the Rampur meteorological station (5.7 km).

Tropical Rainfall Measuring Mission satellite rainfall data

Tropical Rainfall Measuring Mission (TRMM) is a joint space mission between NASA and JAXA designed to monitor tropical and sub-tropical precipitation. TRMM rainfall data offers high spatial and temporal resolution precipitation estimates and is useful for investigating distribution, frequency and intensity of rainfall and thus has been selected as the rainfall source for the SCIMAP-Flood analysis. TRMM rainfall data has been successfully used in previous research on Nepal and other regions with a monsoonal climate (Bookhagen and Burbank, 2010; Shrestha and Barros, 2010; Shrestha et al., 2012; Zhang et al., 2016). There is TRMM rainfall data available for the period 1998 to the present day. Global Precipitation Measurement (GPM), the successor to the TRMM project, and Asian Precipitation Highly Resolved Observational Data Integration Towards Evaluation of Water Resources (APHRODITE), a distance-weighted, interpolated dataset from rainfall gauging stations, were also considered as sources of rainfall data; however the projects did not have a comparable length of record or had ceased to be operational at the time this research was undertaken (Andermann et al., 2011).

TRMM 3B42 daily data was acquired for the period 1st January 1998 to 31st December 2017. TRMM 3B42 (Version 7) is research-grade daily gridded precipitation data available between 1998 and 2017 and at a resolution of 0.25° (approximately 25 km grids in Nepal). TRMM 3B42 data is calibrated, in part using the TRMM orbital data with the algorithm producing TRMM-adjusted merged-infrared precipitation and root-mean-square precipitation-error estimates (Fensterseifer et al., 2016). After pre-processing, 3-hourly multi-satellite fields are summed for the month and combined with the monthly accumulated GPCC (Global Precipitation Climatology Centre) rain gauge analysis; the GPCC dataset has gauge-based gridded monthly precipitation data for the global land surface (Nicholson et al., 2003). Rain gauge data is used to apply a large-scale bias-adjustment to the multi-satellite estimates - almost exclusively over land - with the monthly gauge-adjusted merged satellite estimate then combined with the rain gauge estimates using inverse error variance weighting (Huffman et al., 2007).

A comparison of the TRMM data to the DHM gauged rainfall data established that the coefficient of determination between the data sources was similar to other research (e.g. Su et al., 2007; Ward et al., 2011; Arias-Hidalgo et al., 2013; Meng et al., 2014; Liu et al., 2017); the TRMM data had a good correlation with the gauged data at a monthly resolution and a low correlation at a daily and sub-daily resolution. Table 3.1 shows the R^2 values between the DHM gauged rainfall data and the TRMM satellite data. As with findings in previous studies (e.g. Arias-Hidalgo et al., 2013; Liu et al., 2017) there

was a better correlation between the monthly data than the daily data. In the East Rapti catchment, there was a monthly resolution maximum R^2 value of 0.90 at Dumkauli and Hetauda and a minimum of 0.76 at Daman. There were lower R^2 values at a daily resolution with a maximum of 0.45 at Hetauda and a minimum of 0.26 at Amlekgunj, Daman and Makwanpur Gadhi.

Table 3.1: A comparison of the monthly and daily R^2 values comparing the DHM gauged rainfall and the TRMM satellite rainfall totals at the gauges within, or in close proximity, to the East Rapti catchment

DHM Gauge	Monthly R^2	Daily R^2
Amlekgunj	0.83	0.26
Beluwa	0.86	0.31
Daman	0.76	0.26
Dumkauli	0.90	0.35
Hetauda	0.90	0.45
Jhawani	0.90	0.36
Makwanpur Gadhi	0.84	0.26
Rampur	0.88	0.40

SCIMAP-Flood rainfall grid creation

To create the combined rainfall grid using gauged data and TRMM satellite data a monthly bias-correction approach using TRMM rainfall data has been adopted. This temporal resolution has previously been used in similar research using the TRMM 3B42 satellite data (Hughes, 2006; Rollenbeck and Bendix, 2011; Arias-Hidalgo et al., 2013; Liu et al., 2017). The totals for each month, in addition to the average monthly totals in the acquired rainfall data period (1998 to 2016), were calculated for each rain gauge and compared against the corresponding TRMM tile monthly total. As in Arias-Hidalgo et al. (2013) the relationship between the rain gauge and uncorrected TRMM monthly values at a given location is expressed as:

$$TP = TRMM * K$$

Equation 3.3

where TP is the total rainfall at the gauge, $TRMM$ is the uncorrected monthly rainfall total from satellite data and K is the bias-adjustment factor at the rain gauge location.

This process produces a bias-adjustment factor for each individual month in the data period and an average monthly bias-adjustment factor for the whole time period that can be applied to account for months with missing daily data. The bias-adjustment factors, both individual and average monthly, were dependent on the season with larger adjustment factors needed in the drier periods (October – April) where the difference between small rainfall totals exaggerated the adjustment factor. For example, at the Jhawani gauge in November 2001, a rainfall total of 5.6 mm was recorded whilst the TRMM rainfall total was 11.5 mm; this creates an adjustment factor of 0.49. In contrast to August

2001, during the heavy rains of the monsoon period, in which the gauge recorded a monthly total of 686 mm and the TRMM total was 657 mm; the corresponding adjustment factor for the month is 1.04. To spatially distribute the bias-adjustment factor across the catchment a Thiessen polygon method for the DHM rain gauge locations was used. To establish a virtual rainfall network that covered the catchment, covering areas not represented by DHM gauge data, TRMM rainfall data at select locations was adjusted at a monthly resolution based on the closest DHM rainfall gauge. Similar to Arias-Hidalgo et al. (2013), the spatially distributed bias-adjustment coefficient can be represented as:

$$TRMM_{adj,m} = TRMM_m * K_{local,m} \quad \text{Equation 3.4}$$

where $TRMM_{adj,m}$ is the bias-adjusted monthly total at a given TRMM centre point, $TRMM_m$ is the TRMM monthly total from the 3B42 satellite data and $K_{local,m}$ is the monthly scaling factor for a given month within period 1998 to 2016 established from the closest DHM rain gauge within the East Rapti catchment.

If the individual monthly rainfall data for $K_{local,m}$ is unavailable then the average monthly bias-adjustment factor for the period is used. To best represent the catchment, four TRMM data points were added to the DHM rain gauge network. The location of these selected TRMM points, two to the north and two along the southern edge of the East Rapti catchment, are shown in Figure 3.6.

With the rainfall data input for SCIMAP-Flood occurring at a sub-monthly resolution, looking at the rainfall associated with the top 10 flow events within the East Rapti catchment, the rainfall grids needed to be created at a daily resolution. The distribution of bias-adjusted TRMM daily rainfall was undertaken by attaining the percentage of total monthly rainfall for a given day in that month from the uncorrected TRMM data and applying this percentage to the bias-adjusted monthly rainfall totals. The process completes the spatial pattern of rainfall within the catchment, using the satellite data to fill areas not represented by the DHM gauge network. This daily rainfall distribution is represented as:

$$TRMM_{adj,d} = \left(\frac{TRMM_d}{TRMM_m} \right) * TRMM_{adj,m} \quad \text{Equation 3.5}$$

where $TRMM_{adj,d}$ is the bias-adjusted daily total for the TRMM points added to the gauge network, $TRMM_d$ is the daily total from the TRMM 3B42 satellite data, $TRMM_m$ is the monthly total from the TRMM 3B42 satellite data and $TRMM_{adj,m}$ is the bias-adjusted monthly total at a given TRMM centre point.

The final rainfall product, produced at a daily resolution, is a gridded combination of the daily DHM rain gauge data and the bias-adjusted TRMM satellite data; covering the East Rapti catchment an example output is shown in Figure 3.6. The gridded product was created using an Inverse Distance

Weighted (IDW) function, as in Liu et al. (2017), using the daily totals to create an interpolated grid over the catchment. The interpolated grid had a resolution of 30 m to match the ALOS elevation data grid resolution.

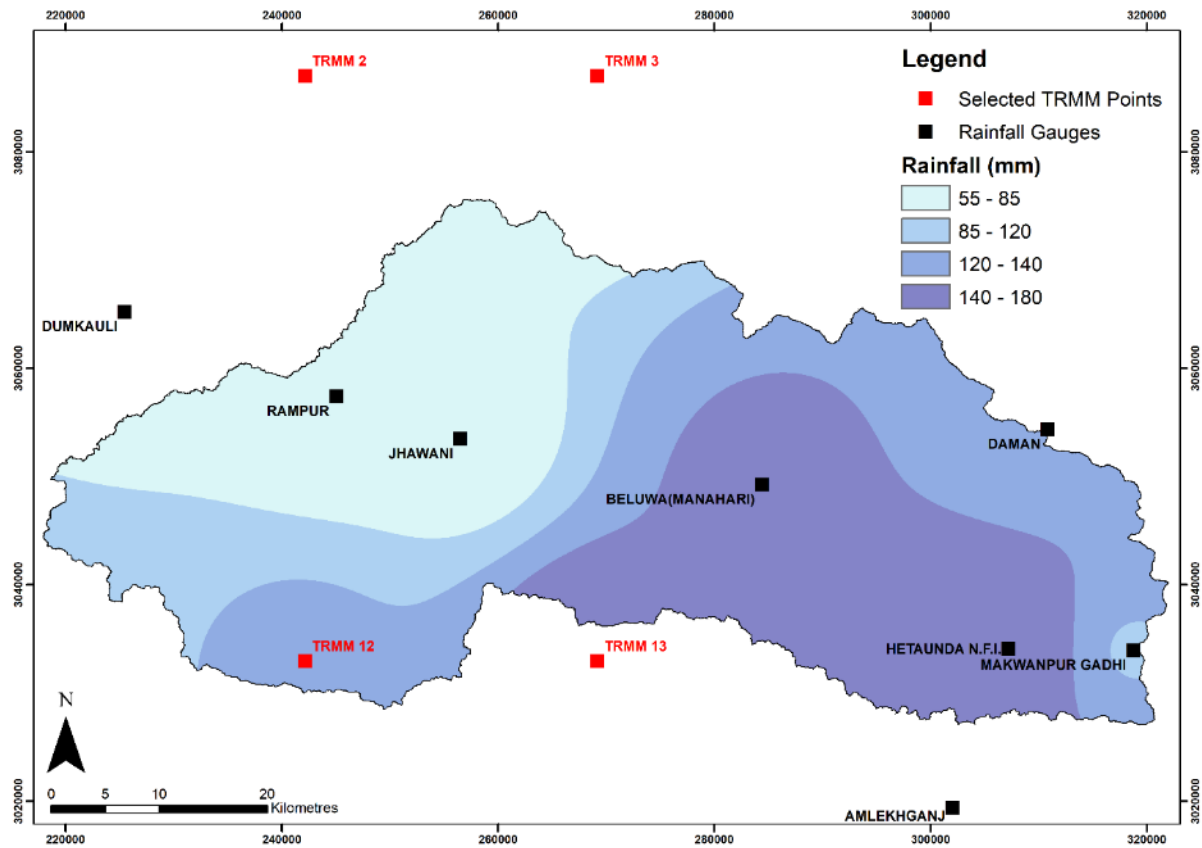


Figure 3.6: An example of the gridded daily rainfall output for the East Rapti catchment with the final combination of DHM rain gauges and TRMM satellite points used to obtain the daily rainfall grids overlain.

Storm rainfall event selection

To assess where flood waters were likely to be generated in the East Rapti catchment, it was necessary to determine which rainfall events were responsible for the highest river flows across the catchment between 1998 and 2015. The spatial distribution of the rainfall in the build-up and during the high flow events helps determine areas in which catchment-scale management measures could be implemented.

The three DHM river flow gauging sites within the catchment are shown in Figure 2.8. The general hydrological characteristics of the East Rapti catchment and the flow characteristics at the Rapti, Manahari and Lothar gauges were discussed in Section 2.5 and Section 2.6.3 accordingly.

Table 3.2: Periods of rainfall data used that are associated with the top 10 flow events in the East Rapti catchment

Event Ranking	Dates (including 5 preceding days)
1	25/07/2001 – 01/08/2001
2	25/07/2003 – 08/08/2003
3	09/08/2014 – 16/08/2014
4	20/07/1998 – 27/07/1998
5	22/07/2009 – 07/08/2009
6	17/07/2002 – 22/07/2002
7	15/07/2004 – 21/07/2004
8	18/08/2011 – 27/08/2011
9	19/08/2010 – 24/08/2010
10	22/07/2011 – 27/07/2011

The 10 largest peak river flow events in which the data were available for all the gauges within the period of river flow data available are shown in Table 3.2; these are referred to as the top 10 flow events throughout the chapter. To enable the high flow event selection across the river flow gauges with different catchment areas, these events were selected by normalising the daily river flow to between 0 and 1 at each of the three available DHM flow gauges in the East Rapti catchment. The minimum flow in the time period is 0 and the maximum flow is 1, as derived using the following formula:

$$n_i = \frac{x_i - \min(x)}{\max(x) - \min(x)}$$

Equation 3.6

where n is the normalised data and x is the flow time series data.

To create an overall flow score for each day across the catchment the normalised values for each of the three flow gauges were multiplied together. With none of the three gauges influencing the flows at the remaining gauges there is no double counting of water within the catchment. The overall total across the three gauges was then ranked with the total closest to 1 considered the highest flow event in the East Rapti catchment.

The majority of the top 10 flow events spanned across multiple day of high flows and as such an event was deemed over when the daily flow on the subsequent day receded to the flow prior to the event. For example, the second highest scored flow was on 04/08/2003 but, after investigating the days around this day, there were high flows for the entire period between 30/07/2003 and the 08/08/2003 and thus the whole period was included as one high flow event. Finally, to better assess the build-up to the beginning of the high flow event, and to take into consideration catchment-scale travel times, the preceding 5 days of rainfall grids were included as part of the event.

The final product for the SCIMAP-Flood analysis was a cumulative bias-adjusted daily rainfall grid for each of the 10 largest peak flow events in the East Rapti catchment. The spatial pattern for the top two river flow events, 2001 and 2003, in the catchment is shown in Figure 3.7 with the remaining eight rainfall patterns in Appendix 7.12 to 7.19.

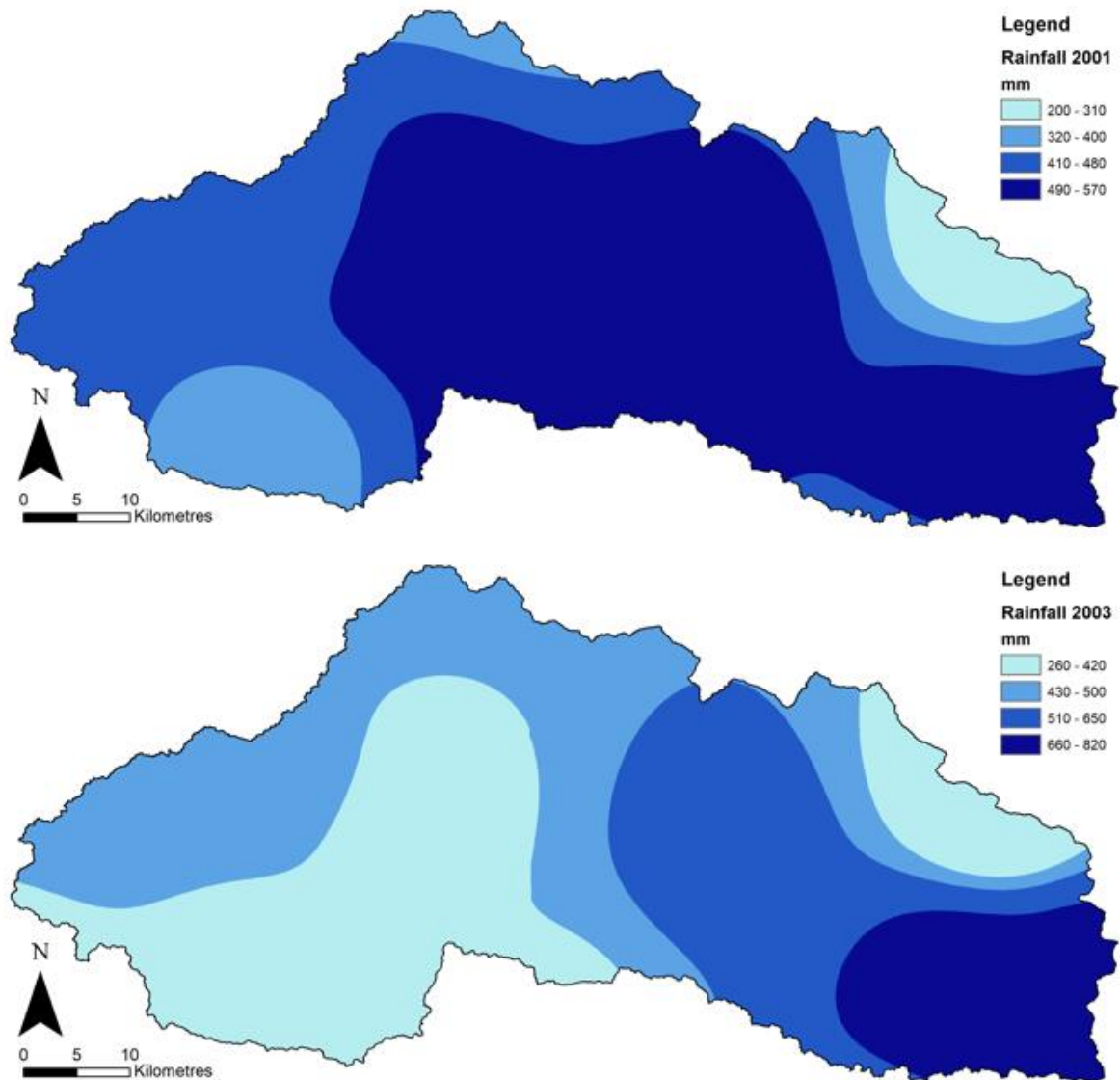


Figure 3.7: The cumulative bias-adjusted rainfall spatial rainfall patterns associated with the 2001 and 2003 high flow events.

3.2.2.4 Spatial land cover data

The East Rapti land cover data used for the SCIMAP-Flood risk mapping was created using supervised classification of a combination of Landsat 8 satellite imagery and slope and aspect data generated from the ALOS 30 m elevation data. The land cover risk weightings for each of the main land covers within the East Rapti catchment were determined using an inverse modelling approach with SCIMAP-

Flood called SCIMAP-Flood Fitted; this approach is detailed in Section 3.2.3 with this section detailing how the spatial land cover data was attained.

Landsat 8 is the most recent instrumentation on the NASA Landsat program. The supervised classification approach was chosen over using a global land cover dataset, for example the European Space Agency Climate Change Initiative (ESA CCI) Land Cover Project, as the Landsat imagery can be classified to a 30 m grid resolution in comparison to the > 300 m grid that current global land cover datasets use (Mora et al., 2014; Tsendbazar, 2016). Additionally, the classification process allows for control over selecting the main land cover classes for a given catchment can therefore be tailored for the East Rapti catchment. With 30 m resolution Landsat 8 satellite imagery was selected over the European Space Agency's higher resolution Sentinel imagery (10 - 20 m resolution) due to the existing cell size limitation of the 30 m DEM from the ALOS elevation data; it should be noted that if a higher resolution DEM was available at the catchment-scale then Sentinel imagery could be considered.

The East Rapti catchment is covered by two Landsat 8 images, 142/41 and 141/41, with the images acquired for 01/11/2016 and 10/11/2016 accordingly. These dates were chosen as they were the most recent images with < 2% cloud coverage at the time of processing. After combining the Landsat bands with slope and aspect data a supervised classification, using the maximum likelihood classification tool (Otukey and Blaschke, 2010), was undertaken using Esri's ArcMap 10.3. The inclusion of ancillary information, such as slope, has been used to improve supervised classification in mountainous landscapes previously (Bahadur, 2009). The maximum likelihood classification algorithm is based on the cells in each sample class being normally distributed and the application of Bayes' theorem of decision making (Otukey and Blaschke, 2010). The training samples were selected using a combination of high-resolution remote sensing images, photographs, and local information. Landsat imagery was classified into seven classes that represented the dominant land coverage within the East Rapti catchment; the classes are summarised in Table 3.3. A total of 150 training samples were created for the 7 classes with a maximum of 33 for the Forest land cover class and a minimum of 12 for the Built-Up Areas land cover class.

Table 3.3: The main land cover categories in the East Rapti catchment that were classified during the creation of the land cover map

Land cover class	Description
Rainfed Agriculture	Terraced agriculture in the steeper, upland areas of the catchment
Irrigated Agriculture	Areas of agriculture in the flat, lowland parts of the catchment
Shrubland	Areas of a mix of non-agricultural vegetation
Forest	Areas consisting of a mosaic of evergreen and deciduous forest
Bare Ground	Areas with no vegetation, including dry river channels and bare rock
Built-Up Area	Residential and commercial areas and the road network
Water	Areas of water bodies and rivers

There are numerous approaches to assessing the accuracy of a classified image; these range from using point samples to assessing areal extents (Stehman and Czaplewski, 1998; Foody, 2002). The accuracy of the classified Landsat images was assessed through a random sampling approach with 200 sample points generated across the catchment. The pixel class under each point was compared against high resolution satellite imagery and photographs. The overall user accuracy of the supervised land cover map using the point comparison was 84% with a confusion matrix of the supervised classification evident in Table 3.4. This is an improvement on available current global land cover datasets with Mora et al. (2014) determining accuracies of between 67% to 81.2%, Tsendbazar (2016) finding accuracies of between 61.3% and 71.4% and Yang et al. (2017) ascertaining accuracies of between 38.46% and 82.39%. The final classified land cover map is shown in Figure 2.6.

Table 3.4: A confusion matrix of the supervised land cover mapping for the East Rapti catchment. The overall accuracy of the supervised land cover map using the point comparison was 84%.

		Reference Data								User Accuracy
		RT	IT	S	F	BG	BUA	W	Count	
Classified Data	RT	18	2	2	4	1	0	0	27	0.67
	IT	0	25	2	1	0	1	1	30	0.83
	S	1	1	8	0	1	1	0	12	0.67
	F	2	0	3	9	0	0	0	14	0.96
	BG	0	0	0	0	4	0	0	4	1.00
	BUA	1	6	0	1	0	4	0	12	0.33
	W	0	1	0	0	0	0	0	1	0.00
	Count	22	35	15	115	6	6	1	200	
	Producer Accuracy	0.82	0.71	0.53	0.95	0.17	0.67	0.00		

*note: RT = Rainfed Terrace, IT = Irrigated Terrace, S = Shrubland, F = Forest, BG = Bare Ground, BUA = Built-Up Area and W = Water

3.2.3 The SCIMAP-Flood Fitted approach used to determine land cover risk weightings

The East Rapti land cover risk weightings within SCIMAP-Flood were attained using an inverse modelling approach using an extension called SCIMAP-Flood Fitted. The risk weightings of between 0 and 1, with 1 having a higher risk of flood water generation, are established for each of the seven land covers in the East Rapti catchment (see Table 3.3) and then spatially distributed with the land cover map outlined in Figure 2.6. The overall approach used to obtain the land cover risk weightings using SCIMAP-Flood Fitted is illustrated in Figure 3.8.

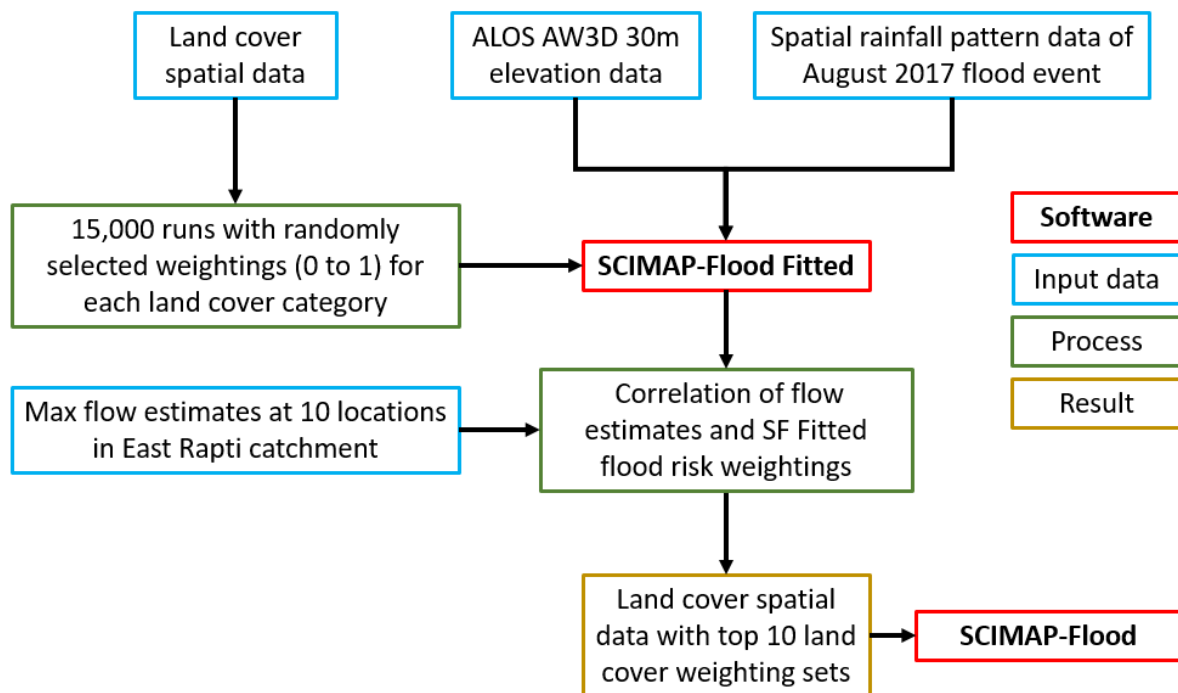


Figure 3.8: An overview of the SCIMAP-Flood Fitted inverse modelling approach to derive the top land cover parameter sets for the East Rapti catchment using the August 2017 storm event.

This inverse modelling approach follows Mosegaard and Tarantola (2002), in which a physical theory is used to connect a set of observations to a set of parameters and has been successfully applied in SCIMAP to make assumptions about the drivers of river water quality patterns (Reaney et al., 2011; Milledge et al., 2012). A detailed description of the inference of land cover risk weighting using a fitted version of SCIMAP and measured instream nutrient concentrations is available in Milledge et al. (2012). The inference of the risk weightings uses a null hypothesis in which there is no systematic variation in model performance between model runs as a function of a given land use weighting. This null hypothesis can then be rejected as it is evident that a particular land use weighting influences the performance of SCIMAP-Flood and thus influences the flow regime in the catchment.

The inverse modelling approach can be used to attain information on the influence of a particular land cover. A risk weighting can define the importance of the land cover with regards flow generation in

the East Rapti catchment. Land covers with below average weightings (less than 0.5) will lower the likelihood of flow generation; this likelihood to generate flow decreases as the value moves towards zero. Land covers with above average weightings (greater than 0.5) will increase the likelihood of flow generation; this likelihood increases as the value moves towards 1.

The approach uses a Monte Carlo sampling framework to deduce the land cover risk weightings with 15,000 model simulations undertaken with randomly selected weightings between 0 and 1 assigned for each land cover category based on a uniform distribution; no *a priori* likelihood is assigned to the weightings. For each simulation an objective function was determined that details the level of association between the estimated risk indicator and the spatially corresponding SCIMAP-Flood risk estimates.

For the East Rapti catchment the objective function used was the Pearson's correlation coefficient. Pearson's correlation coefficient is one of three commonly used correlation coefficients (the others being Spearman's and Kendall's) and is a measure of strength of a linear relationship between two variables (Chok, 2010; Hauke and Kossowski, 2011). Pearson's correlation coefficient was selected as it offers an appropriate solution for continuous nature of the SCIMAP-Flood Fitted output data.

The estimated risk indicators used were the peak flows associated with the August 2017 East Rapti floods. This event was chosen as it was a high magnitude flood event and there was the opportunity to collect post-event data to help ascertain the land cover risk weightings using the SCIMAP-Flood Fitted approach. The Pearson's correlation coefficient is then used to detail the level of association between the August 2017 peak flow estimates and spatially corresponding SCIMAP-Flood risk estimates for each of the 15,000 model simulations. The model simulations with a correlation coefficient closest to 1 are determined to have a land cover weighting set that best represented the runoff generation in the East Rapti catchment. Following the concept of equifinality that underpins the Generalised Likelihood Uncertainty Estimation (GLUE) approach (Beven, 2006; Pechlivanidis et al., 2011), in which more than one combination of parameters can result in the same outcome the land cover values from the best 10 land cover weighting sets are then taken forward to the final SCIMAP-Flood runs to better represent the uncertainty stemming from the land cover parameters.

3.2.4 East Rapti catchment data for SCIMAP-Flood Fitted

As shown in Figure 3.8, SCIMAP-Flood Fitted requires elevation data, land cover spatial distribution and a spatial rainfall pattern for the calibration storm event to run; this spatial data is discussed in Section 3.2.2. Additionally, to get the necessary risk indicators to run the inverse modelling approach, the peak flow estimates associated with the August 2017 flow events were calculated from data collected in the field.

3.2.4.1 Spatial data for SCIMAP-Flood Fitted

The elevation data used to run SCIMAP-Flood Fitted was the ALOS Global Digital Surface Model (AW3D30) 30 m resolution global elevation dataset. The description of this elevation data is available in Section 3.2.2.1. The land cover spatial distribution was that produced in Section 3.2.2.4 from supervised classification of Landsat 8 satellite imagery combined with slope and aspect data generated from the ALOS 30 m elevation data.

3.2.4.2 Estimated peak flows for the August 2017 flood event

The estimation of the August 2017 peak flows was measured at ten locations throughout the East Rapti catchment (see Figure 3.9). This was undertaken using cross-sectional area and channel slope information from the high-resolution elevation model, field-based observations of Manning's n and the flood extent visible in high-resolution (3 to 6 m grid resolution) Planet imagery to help deduce wetted perimeter (Planet Team, 2017). Manning's Equation (Manning, 1891) was then used to obtain the estimated flow. This process allows for the estimation of peak flows at multiple ungauged locations throughout the catchment.

The Manning's Equations to calculate open channel flow using S.I. units is:

$$Q = VA \quad V = \frac{1}{n} \left(\frac{A}{P} \right)^{\frac{2}{3}} \sqrt{S}$$

Equation 3.7

where Q is flow rate ($\text{m}^3 \text{s}^{-1}$), V is flow velocity (m s^{-1}), n is Manning's Roughness Coefficient, A is flow area (m^2), P is the wetted perimeter (m) and S is the channel slope (m/m).

The ALOS 30 m data, due many of the tributaries having a channel width of less than 30 m and thus not being accurately represented, was not preferential for high-resolution cross-sectional area and channel slope data for calculating Manning's n . A secondary, higher-resolution elevation product was used to determine the cross-sectional area of the flood discharge and slope for the SCIMAP-Flood Fitted approach. This was achieved using a photogrammetry approach termed 'Structure-from-Motion' (SfM) (Westoby et al., 2012) using helicopter-based survey taken during a flight in January 2018. The high-resolution elevation products were built using between 18 and 40 images depending on the site. The images were taken from a Canon 5Dsr at a resolution of 51 megapixels and taken from an altitude of approximately 800 m above ground level. These images were processed with Agisoft PhotoScan Pro version 1.4. This survey covered sections of the main East Rapti channel and main tributaries in the eastern part of the catchment. The final elevation product for each of the 10 cross-section locations had a resolution of between 0.4 and 0.6 m. Cross-sections to calculate flow area and channel slope measurements were taken at ten locations in the catchment (see Figure 3.9).

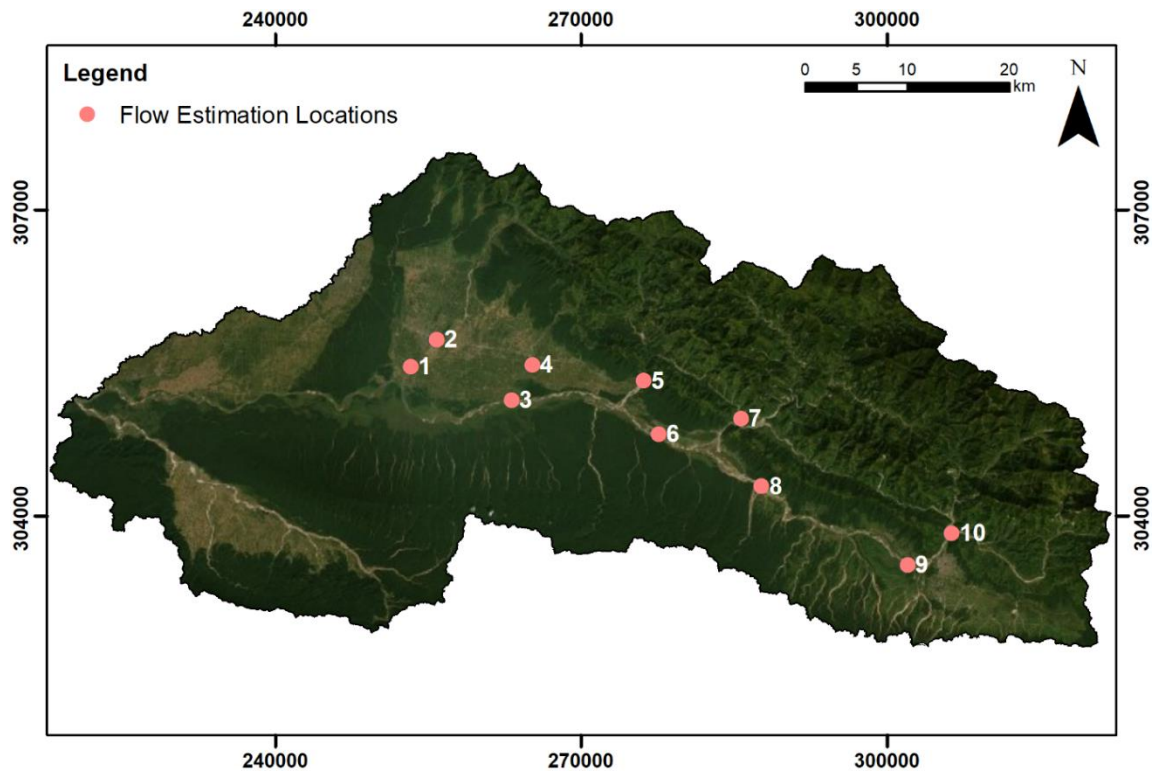


Figure 3.9: The locations within the East Rapti catchment from which the August 2017 peak flows were estimated.

High-resolution Planet (Planet Team, 2017) imagery taken from both before and after the August 2017 flooding was then used, in conjunction with the detailed cross-sections from the high resolution SfM elevation models, to estimate a peak water level from the event. The Planet imagery from before the event was taken on 13/07/2017 and 14/07/2017 with the post-event imagery from 26/08/2017, 29/08/2017 and 30/08/2017; these were the closest available days with cloud-free coverage in which the channel network was visible. An example comparison of the pre- and post-event Planet satellite imagery is shown in Figure 3.10. The sediment deposition from the post-event image indicates the extent at which the flood waters reached during the August 2017 event. With the elevation of the bank flood extent marked on the cross-section then both the flow area and wetted perimeter can be calculated.

A version of the Manning’s Equation (Manning, 1891) was used to obtain the Manning’s n value from the gauged flows:

$$n = \frac{\left(\frac{A}{P}\right)^{\frac{2}{3}} \sqrt{S}}{V}$$

Equation 3.8

where n is Manning’s Roughness Coefficient, A is flow area (m^2), P is the wetted perimeter (m) and S is the channel slope (m/m) and V is flow velocity (m s^{-1}).

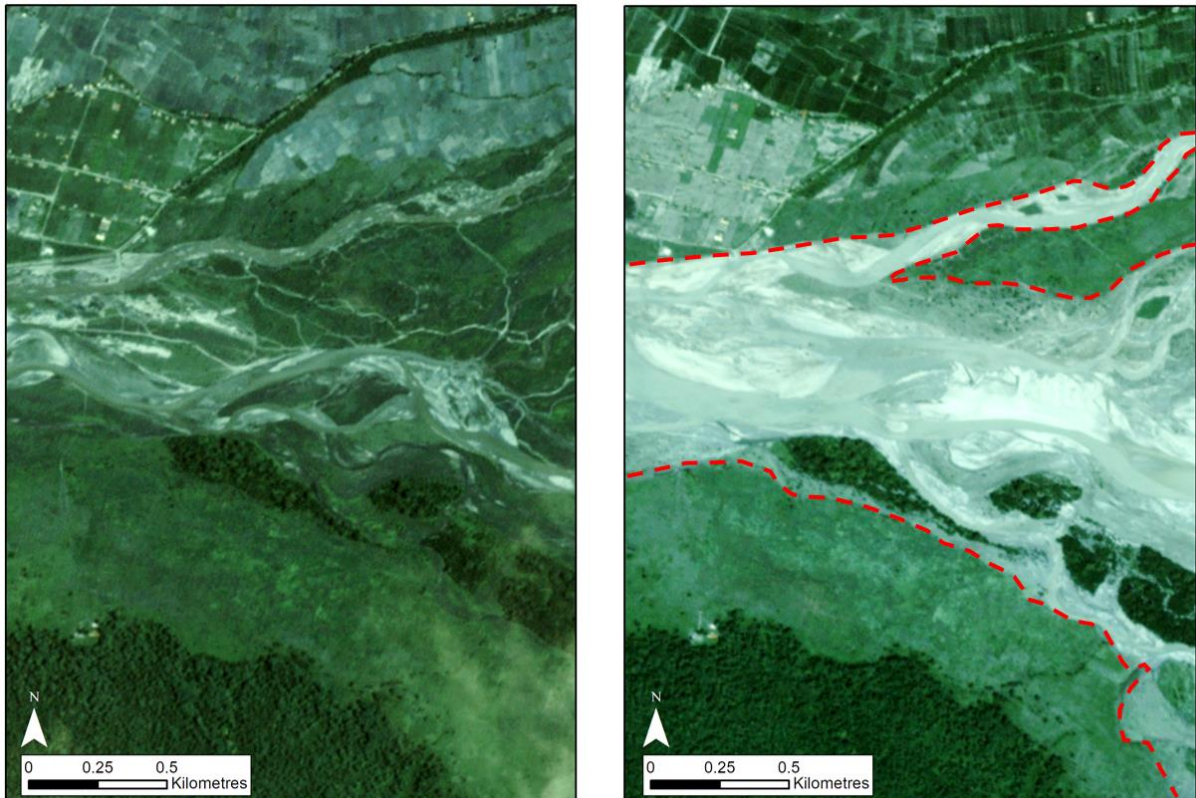


Figure 3.10: A comparison of the pre- (left) and post-event (right) Planet (Planet Team, 2017) satellite imagery for a section of the East Rapti catchment. The sediment deposition used to help estimate flood extent is clear in the image on the right with an indicative inundation extent marked in red.

Manning's n values were established for three classes of channel within the East Rapti catchment which could then be used for the peak flow estimates. A Manning's n value of 0.0422 was used for the flow estimation points on the Terai plains in the downstream part of the catchment, a value of 0.0484 was used for the estimation points on the main East Rapti channel and large tributary channels and a value of 0.0663 was used for the values in the steeper upstream flow estimation locations. These representative Manning's n values were attained from data collection undertaken throughout the East Rapti catchment during fieldwork in May 2018.

Between 16/05/2018 and 23/08/2018, a total of 25 locations throughout the East Rapti catchment were visited to measure the discharge and channel slope used to help drive the Manning's Equation; these locations are shown in Figure 3.11. Of the 25 sites, 6 were not gauged due to either not containing water with the ephemeral nature of some of the smaller tributaries in the catchment or were not safe to survey. At these locations field-based estimates of Manning's n had to be made. An example of one of these dry sites is shown in Figure 3.12.

Flow gauging was undertaken at the remaining 19 sites and was achieved using either a remote-controlled boat (Seafloor HyDrone RCV) (Figure 3.13) with an attached Acoustic Doppler Current Profiler (ADCP) or manually with instream measurements taken using a handheld flow meter (Valeport

Model 801 Electromagnetic Flow Meter) (Figure 3.14). The remote-controlled boat with ADCP attachment was used for the wider and deeper channels, such as the main East Rapti channel, and recorded the flow velocity and bathymetry across the channel. Using the software WinRiverII, the data taken by the ADCP boat was converted into a discharge measurement for each site. In the manual measurements, water depth and flow velocity reading were taken at regular intervals across the cross-section. Both methods provided cross-sectional area, wetted perimeter, and flow velocity to be used to calculate Manning's n (see Equation 3.8). The channel slope was originally measured in the field using a dGPS at each of the sites but a combination of the low water slope gradient at several of the sites and technical difficulties with the surveying equipment, the collected data did not result in a usable dataset. As a result, at each of the 19 sites the channel slope was measured from the ALOS 30 m elevation data, using the average slope of the channel for 1 km either side of cross-section location; this approach kept the method employed consistent between sites.

With the necessary data to input into the Manning's Equation, the peak August 2017 flows could be calculated for the 10 locations within the East Rapti catchment. The flows and selected Manning's n values for each flow estimation location are shown in Table 3.5. The flow estimates were converted from $\text{m}^3 \text{s}^{-1}$ to mm prior to becoming the risk indicator in SCIMAP-Flood Fitted to factor in the size of the contributing catchment.

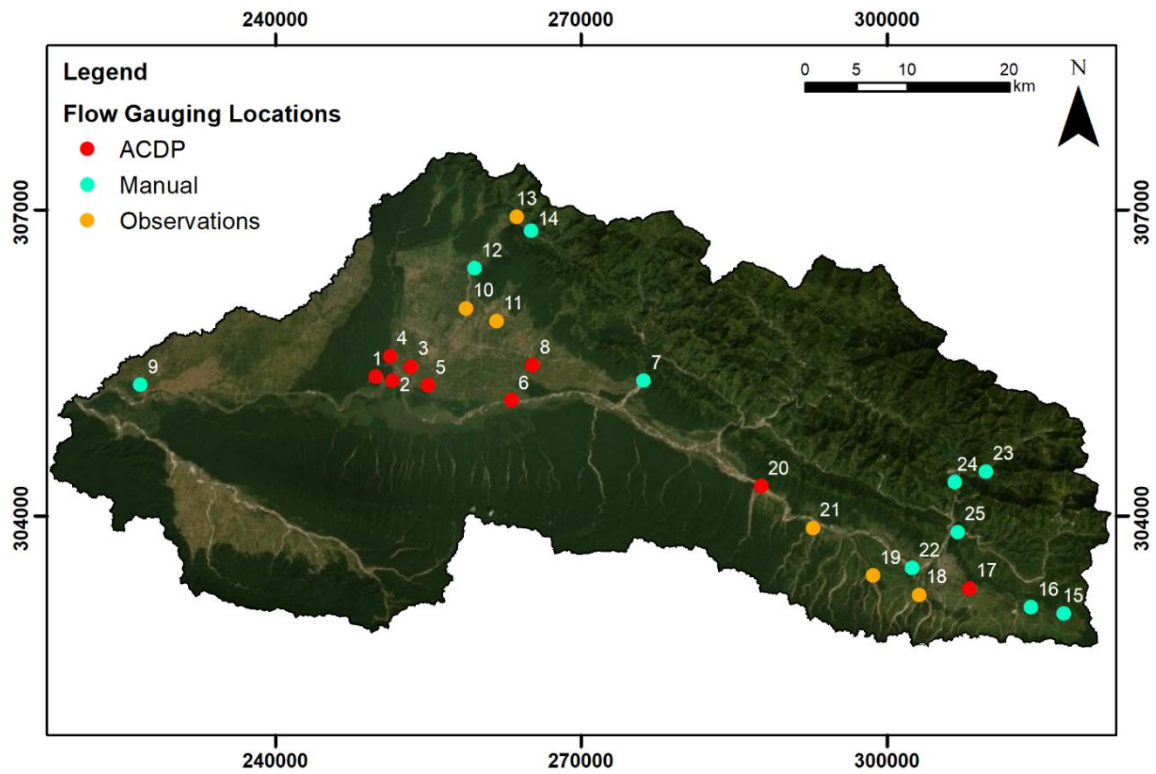


Figure 3.11: The location of the 25 flow gauging locations broken down by the method used at each location.

Table 3.5: Peak flow estimates and corresponding data used to obtain the estimated risk indicators for SCIMAP-Flood Fitted. The ID number in the first column relates to the locations shown in Figure 3.9.

ID	Channel Area (m ²)	Manning's n	Estimated Discharge (m ³ s ⁻¹)	Catchment area (km ²)	Discharge (mm)
1	154	0.0422	223	223	87
2	62	0.0422	85	92	79
3	1803	0.0484	3476	1518	198
4	15	0.0422	13	49	23
5	202	0.0484	579	169	295
6	1391	0.0484	2519	1156	188
7	362	0.0663	1303	425	265
8	569	0.0484	1223	605	175
9	374	0.0484	739	426	150
10	212	0.0663	551	292	163



Figure 3.12: An example of one of the dry tributaries (site 19 in Figure 3.11) in which field-based observations were made (taken on 22/05/2018).



Figure 3.13: The Seafloor HyDrone RCV with attached ADCP for gauging wider and deeper channels (taken on 16/05/2018).



Figure 3.14: Measuring the flow across a cross-section using the handheld flow meter (taken on 17/05/2018 at site 7 in Figure 3.11).

3.2.5 SCIMAP-Flood methods summary

The SCIMAP-Flood approach outlined in Figure 3.1 is a multi-part process to produce a point scale assessment that helps identify critical source areas for flood waters in a catchment. It is this point scale assessment that can be used a decision support framework for the spatial targeting of flood management measures at the catchment-scale.

For the East Rapti catchment the spatial data used in SCIMAP-Flood was taken from a variety of sources. The elevation data used to calculate slope and hydrological connectivity was from the ALOS 30 m resolution global elevation dataset. The overland flow travel time data, made using a simplified geomorphic unit hydrograph, was developed for six locations within the catchment that either flooded in the August 2017 flood event, or are adjacent to the main channel network. The spatial rainfall pattern data for the 10 largest peak river flow events between 1998 and 2016 was made using a scaled combination of DHM rainfall gauge data and TRMM satellite rainfall data. The events were selected using DHM flow gauge information used to work out the top 10 flow events in the East Rapti catchment. Finally, the land cover spatial distribution was undertaken through supervised classification of Landsat 8 satellite imagery and slope and aspect data generated from the ALOS 30 m elevation data. The land cover risk weightings, representing local runoff generation potential for each category, were derived using an inverse modelling approach with SCIMAP-Flood Fitted (Figure 3.8)

with the top 10 land cover weighting sets used in the final SCIMAP-Flood run for the East Rapti catchment.

3.3 RESULTS

This section presents the results attained from SCIMAP-Flood for the East Rapti catchment and shows areas that are identified as generating peak flood waters during high flow events. Section 3.3.1 illustrates the results of the inverse modelling approach undertaken in SCIMAP-Flood Fitted. Section 3.3.2 outlines the results from the SCIMAP-Flood decision support framework for the East Rapti catchment and considers the sensitivity of the inputs. The final SCIMAP-Flood output for the East Rapti catchment is shown in Section 3.3.2.1. Section 3.3.2.2 looks at the possibility of using other rainfall data sources within the SCIMAP-Flood framework and the potential impact this has the location of the identified areas of higher flood water generation. Section 3.3.2.3 considers the influence of the selection of impact points and the potential impact that this has on the location of the identified areas of higher flood water generation. Both comparisons are done through analysing the change in areas of higher relative risk in the East Rapti catchment with different sets of travel times to impact points.

3.3.1 SCIMAP-Flood Fitted results to determine the land cover weightings

An inverse modelling approach, discussed in Section 2.2.3, was undertaken using SCIMAP-Flood Fitted to derive the best land cover weighting sets for the East Rapti catchment. The highest Pearson's correlation coefficient between the peak flow estimates from the August 2017 storm event and the spatially corresponding SCIMAP-Flood risk estimates was 0.776; this illustrates a strong positive correlation between the risk indicator and SCIMAP-Flood risk estimates. The lowest Pearson's correlation coefficient value was -0.865 with an average value of 0.685 across the 15,000 model simulations. Pearson's correlation coefficient has a value of between 1 and -1 with a value of 1 having a positive linear relationship, a value of 0 having no linear correlation and -1 having a negative linear relationship (Chok, 2010).

The left-hand side of Figure 3.15 is a series of dot plots (Wagener and Kollat, 2007) that compare the Pearson's correlation coefficient with the SCIMAP-Flood land cover weighting for each of the seven land covers in the East Rapti catchment from the 15,000 model simulations; these dot plots can be used to assess the influence of a given land cover on the flood regime in the catchment. From the dot plots the *Irrigated Agriculture* and *Built-Up Area* land cover weighting values show the most obvious influence on the correlation coefficient value. The *Irrigated Agriculture* land cover weightings show an improving correlation as the weighting value is over 0.2 with the range of correlation coefficient values smaller as the *Irrigated Agriculture* weighting is closest to 1. The *Built-Up Area* land cover weighting value has the highest correlation coefficient between 0.2 and 0.6. Based on the entire 15,000 model simulations the other five land covers in the East Rapti catchment show no discernible

trend between land cover weighting value and correlation coefficient with weighting values across the entire 0 to 1 range having correlation coefficient values > 0.75 .

On the right-hand side of Figure 3.15 is a series of dot plots that shows the top five percent, 750 simulations, of the correlation coefficients attained from the model simulations and sheds a clearer insight into land cover weighting value trends. The *Irrigated Agriculture* land cover weightings show an improving correlation with the risk weighting value between 0.75 and 0.9. The *Built-Up Area* land cover weighting value has the highest correlation coefficient between 0.2 and 0.4. The correlation coefficients increased for *Shrubland*, *Water* and *Forest* as the risk weighting value is closer to 0; this trend is most obvious for the *Shrubland* category. Both *Rainfed Agriculture* and *Bare Ground* show no discernible trend between land cover weighting value and correlation coefficient with weighting values across the entire 0 to 1 range having correlation coefficient in the top five percent.

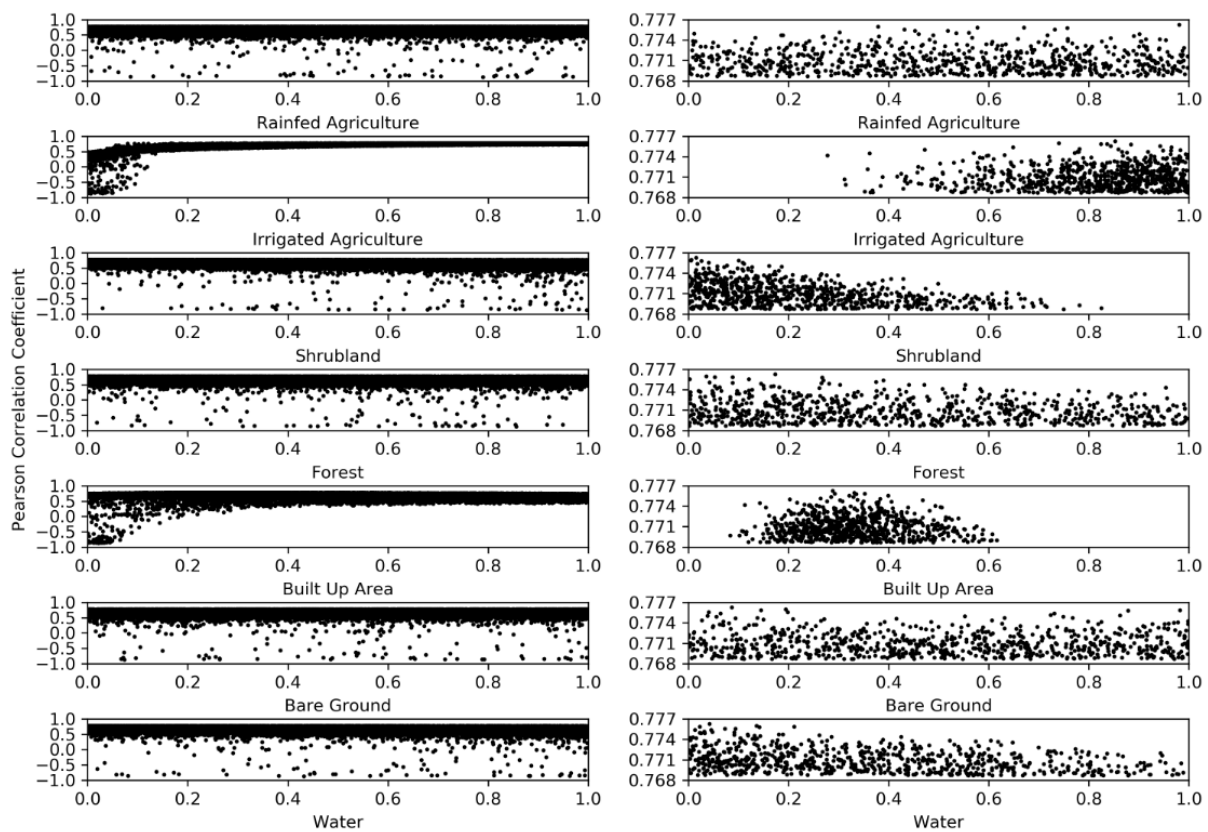


Figure 3.15: Dotty plots from all 15,000 (left) and the top 750 (5%) (right) of the SCIMAP-Flood Fitted model simulations showing the Pearson correlation coefficient compared to the SCIMAP-Flood land cover weighting value for each of the seven land cover classes in the East Rapti catchment. The highest Pearson correlation coefficient values indicate that the land cover flood water generation weightings in that simulation provided the strongest relationship between the peak flow estimates from the August 2017 storm event and the spatially corresponding SCIMAP-Flood risk estimates.

Using the concept of equifinality (Beven, 2006) in which more than one combination of parameters can result in the same outcome, the top 10 land cover weighting sets, those with the Pearson’s correlation coefficient closest to 1, are then taken forward to the final SCIMAP-Flood runs. All the top 10 land cover weighting sets had a Pearson’s correlation coefficient of between 0.776 and 0.775. The SCIMAP-Flood weightings for each of the seven land covers in the East Rapti catchment from the top 10 land cover weighting sets are shown in Table 3.6 with the spread illustrated in Figure 3.16.

Table 3.6: The SCIMAP-Flood land cover weighting values for each land cover in the top 10 weighting sets, based on the Pearson’s correlation coefficient and the SCIMAP-Flood Fitted inverse modelling approach. These are the simulated land cover weighting sets that provided the strongest relationship between the peak flow estimates from the August 2017 storm event and the spatially corresponding SCIMAP-Flood risk estimates.

Rainfed Agriculture	Irrigated Agriculture	Shrubland	Forest	Built-Up Area	Bare Ground	Water
0.98	0.85	0.02	0.17	0.29	0.09	0.04
0.38	0.74	0.01	0.04	0.33	0.19	0.14
0.67	0.82	0.10	0.05	0.35	0.98	0.02
0.58	0.84	0.00	0.09	0.29	0.15	0.21
0.76	0.88	0.03	0.27	0.33	0.88	0.14
0.43	0.84	0.04	0.00	0.40	0.04	0.09
0.73	0.94	0.11	0.12	0.32	0.20	0.07
0.52	0.96	0.11	0.27	0.33	0.06	0.05
0.45	0.65	0.02	0.39	0.29	0.73	0.01
0.30	0.78	0.08	0.37	0.26	0.72	0.03

In SCIMAP-Flood, land covers with a risk weighting closest to 0 will lower the risk of flow generation whilst land covers greater than 0.5 will increase the risk of flow generation; the risk increases as the value moves towards 1. Of the top 10 weighting sets shown in Table 3.6, the *Irrigated Agriculture* (0.65 to 0.96), *Shrubland* (0.00 to 0.11), *Forest* (0.00 to 0.39), *Built-Up Area* (0.26 to 0.40) and *Water* (0.01 to 0.21) values are all fairly constrained. The *Irrigated Agriculture* SCIMAP-Flood weightings are increasing the likelihood of flow generation with all the values > 0.5 whilst *Shrubland*, *Forest* and *Water* have the lowest risk weightings with the lowest potential for flow generation. The weighting for the *Built-Up Area* land cover also has a less than average risk of flow generation. The values from the top 10 land cover weightings sets from the SCIMAP-Flood Fitted approach for *Rainfed Agriculture* and *Bare Ground* are far less constrained with values of between 0.30 and 0.98 for *Rainfed Agriculture* and 0.04 and 0.98 for *Bare Ground*. With the SCIMAP-Flood risk weighting for these two land covers being uncertain, with values signify both a low and high risk of flow generation, using the top 10 weighting values rather than one weighting value allows this range to be accounted for.

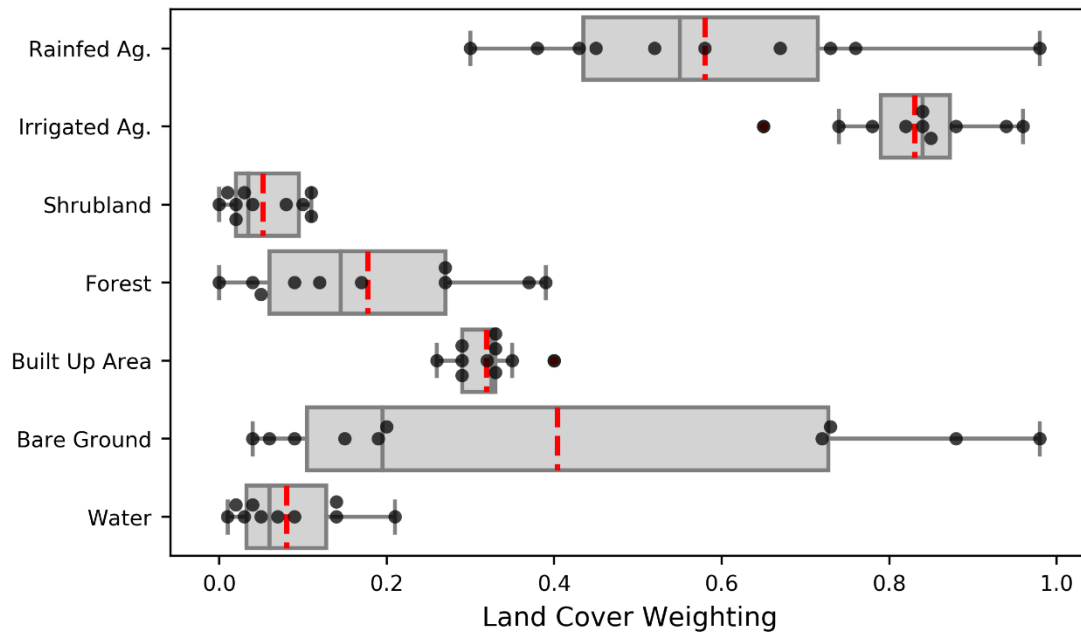


Figure 3.16: A boxplot showing the SCIMAP-Flood land cover weightings for the top 10 weightings sets based on the Pearson's correlation coefficient and the SCIMAP-Flood Fitted inverse modelling approach. The red line represents the mean with the spread of the individual data value across the top 10 weightings shown as a swarm plot (black dots).

3.3.2 SCIMAP-Flood results

3.3.2.1 SCIMAP-Flood for the East Rapti catchment

SCIMAP-Flood was used to identify areas within the East Rapti catchment that, on a relative scale, are more likely to generate flood water during a high flow event. The resultant output for the East Rapti catchment can be seen in Figure 3.17 with Figure 3.18 illustrating in more detail the key area with the highest flood risk generation potential around Hetauda. Using the rainfall patterns associated with the top 10 flow events, the top 10 land cover weighting sets and 6 flood impact points, it is evident that the eastern part of the East Rapti catchment near Hetauda is most likely to be the source of flood water to the respective impact points with the highest flood risk score values. There are also areas along the main East Rapti channel and in the Lothar and Manahari sub-catchments with a higher relative potential to generate flood waters to the points of impact.

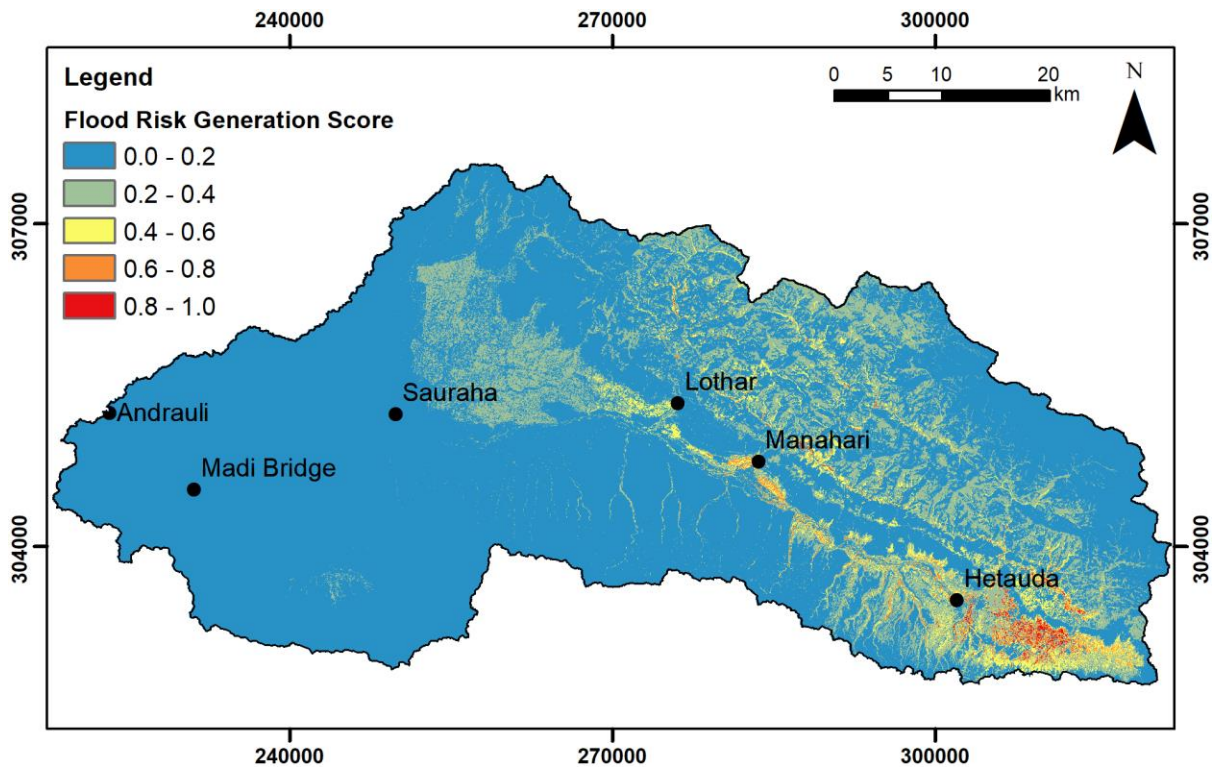


Figure 3.17: SCIMAP-Flood output for the East Rapti catchment created using the rainfall patterns associated with the top 10 flow events, the top 10 land cover weighting sets and 6 flood impact points. Red represents areas with the greatest relative flood risk generation values during a high flow event with blue representing areas of low flood risk generation.

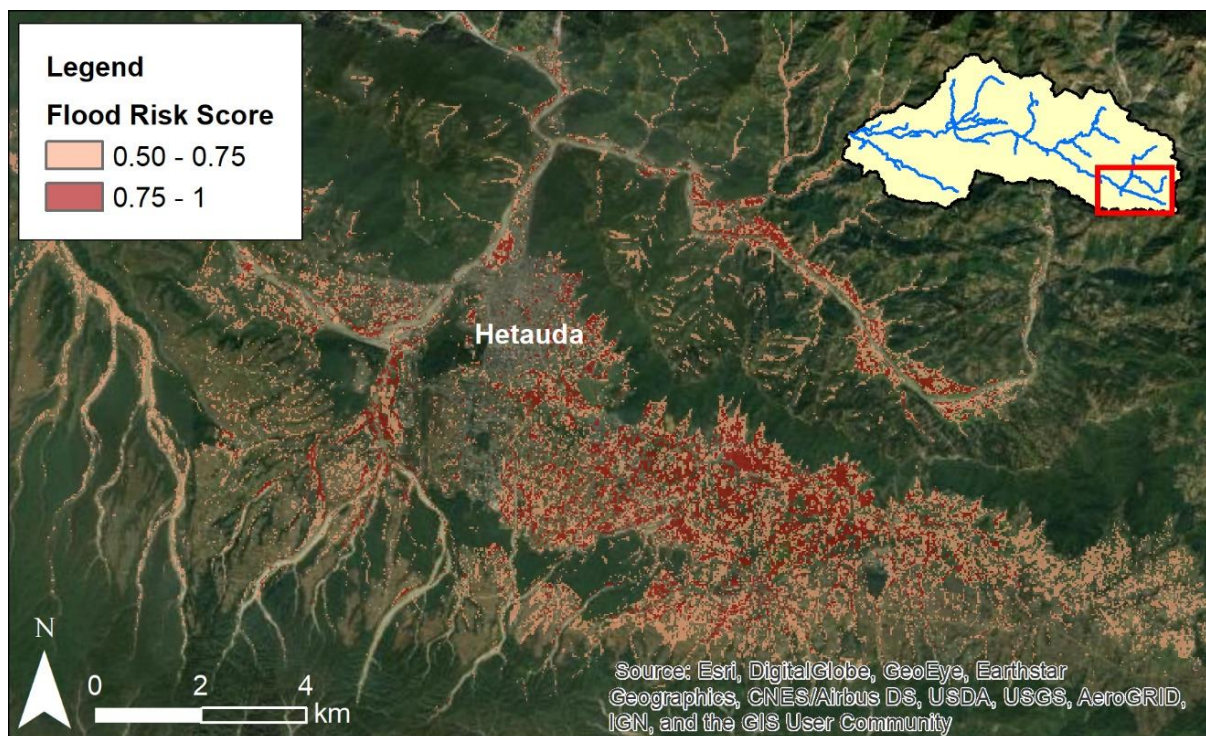


Figure 3.18: A focused view on one of the key areas with the highest potential to generate flood waters within the East Rapti catchment taken from Figure 3.17. This location is in the eastern part of the catchment (see extent within catchment in inset) around Hetauda.

3.3.2.2 SCIMAP-Flood rainfall input sensitivity analysis

Spatial rainfall patterns from using only satellite rainfall data

The final SCIMAP-Flood output shown in Figure 3.17 for the East Rapti catchment uses a time intensive process of scaling and combining rainfall from DHM gauged rainfall data and TRMM satellite data to get the spatial rainfall patterns for the top 10 flow events. To assess the difference in areas identified as likely to generate flood water during a high flow event using a simpler approach, SCIMAP-Flood was run using only TRMM satellite rainfall data. This was undertaken using the rainfall totals, and thus spatial patterns, associated with the top 10 flow events in the catchment. The other parameters were kept identical to those displayed in Figure 3.17 with the top 10 land cover weighting sets and 6 selected flood impact points.

The SCIMAP-Flood output for the simplified TRMM satellite rainfall data is shown in Figure 3.19. It is evident that, as with the more complex scaled rainfall, the eastern part of the East Rapti is most likely to be the source of flood water to the respective impact zones.

A comparison of the distribution of the SCIMAP-Flood flood water generation scores between the base scaled rainfall output and the TRMM-only rainfall output is shown in Figure 3.20. There is a change in the distribution of the SCIMAP-Flood scores with a marked decrease in values > 0.75 (areas with the highest relative potential to generate flood waters) attained from using the TRMM-only rainfall patterns. There is also a reduction in values > 0.50 (areas with a higher relative potential to generate flood waters). Conversely, there is a noticeable increase in areas with a lower relative potential to generate flood waters (< 0.50) until the 0 to 0.05 bin. As with the highest potential areas there is also a large reduction in the areas with the lowest potential (0 to 0.05) to generate flood waters.

An incremental comparison to assess the spatial distribution of the change through the use of point density analysis between the SCIMAP-Flood output from the scaled rainfall data and the TRMM satellite data associated with the top 10 flow events is shown in Figure 3.21. Through comparing the distribution of the areas that SCIMAP-Flood weights as more likely to generate flood waters in the East Rapti, the influence and need for more complicated rainfall inputs can be assessed. The figure shows that the areas with a flood risk score of > 0.5 (pink areas in Figure 3.21) are broadly similar and cover the eastern and central northern parts of the East Rapti catchment. There are fewer areas with a high potential to generate flood waters (> 0.75) identified by SCIMAP-Flood using the TRMM-only rainfall patterns. The scaled rainfall and TRMM-only rainfall patterns also identify different areas with the scaled rainfall areas predominantly in the south east of the catchment and the TRMM-only areas along the main East Rapti channel towards the middle of the catchment.

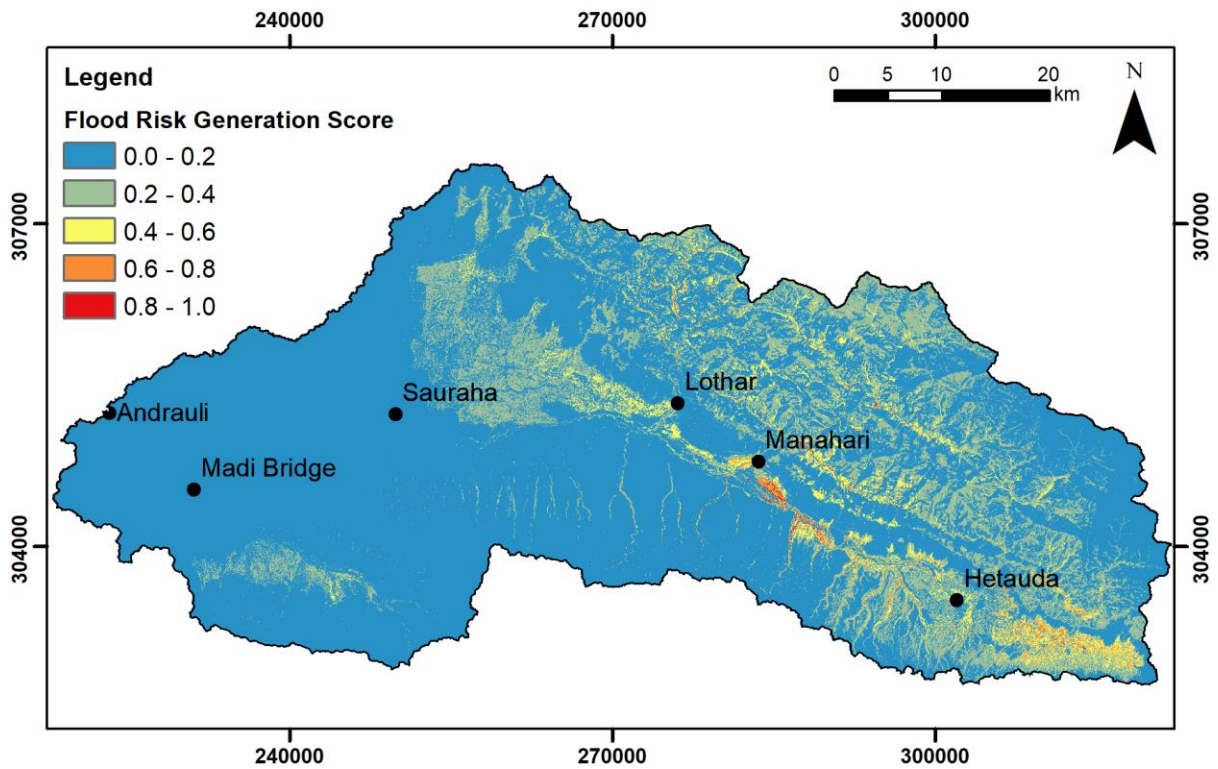


Figure 3.19: SCIMAP-Flood output for the East Rapti catchment created using TRMM satellite-only rainfall patterns associated with the top 10 flow events, the top 10 land cover weighting sets and 6 flood impact points. Red represents areas that exhibit the greatest relative flood risk generation values during a high flow event, with blue represents areas of lower flood risk generation.

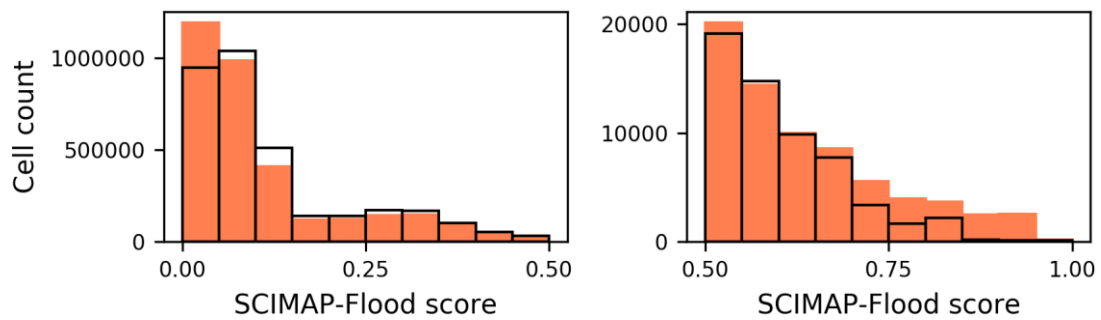


Figure 3.20: A comparison of the distribution of SCIMAP-Flood flood risk generation scores across the SCIMAP-Flood output created using the scaled rainfall patterns (red) (Figure 3.17) and the TRMM satellite-only rainfall patterns (black outline) (Figure 3.19). The distribution is split into lower potential flood water generating areas with a score of < 0.50 (left) and higher potential flood water generating areas with a score of > 0.50 (right).

Legend

Flood Risk Score > 0.75



Flood Risk Score > 0.50

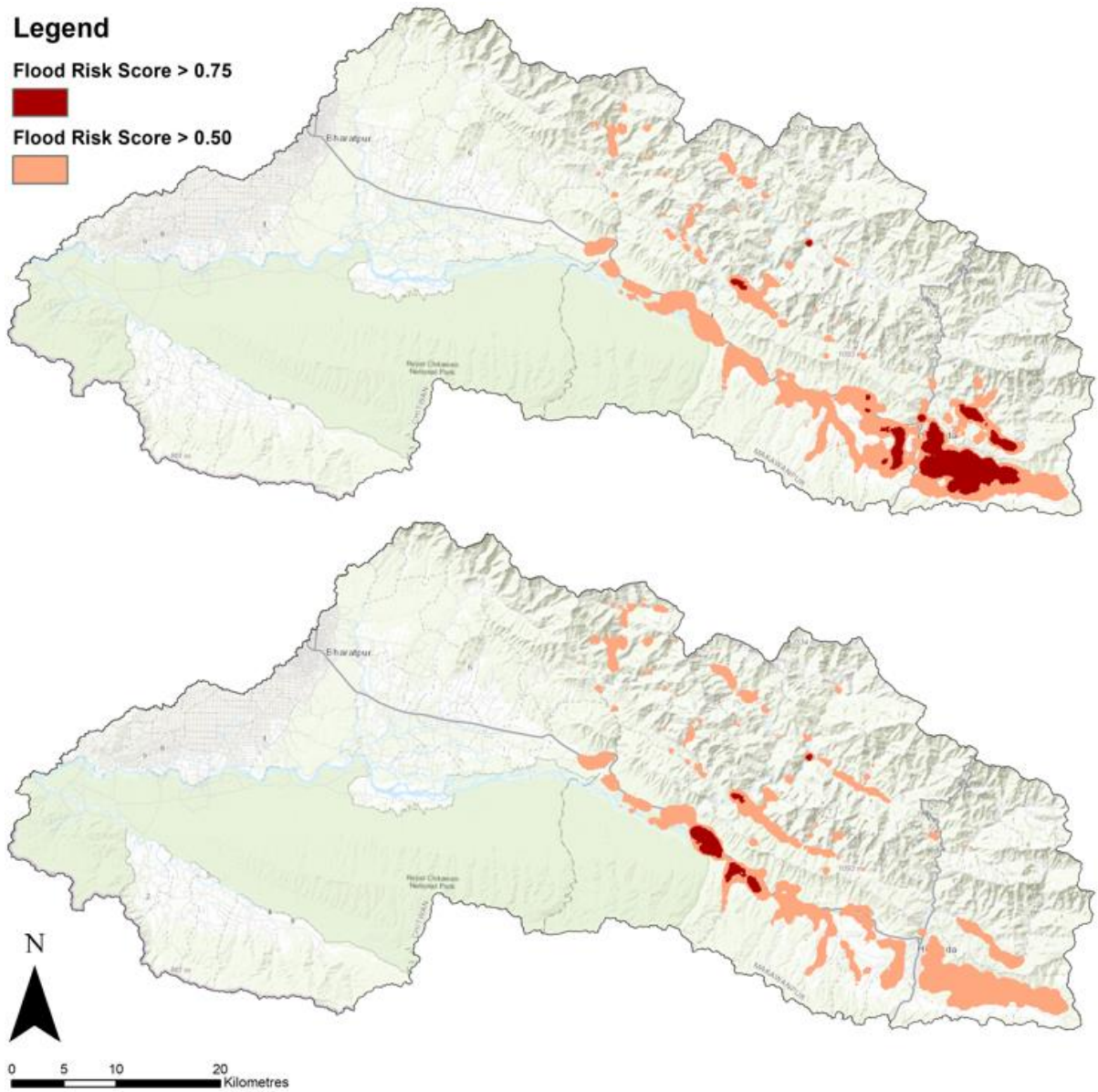


Figure 3.21: Point density analysis of SCIMAP-Flood output using the scaled rainfall data (top) and TRMM-only rainfall data (bottom) showing the areas of with the highest flood water generation weighting. The areas with a flood risk score of > 0.50 are pink and > 0.75 are dark red.

Temporal variation from using only satellite rainfall data

It is necessary to investigate the potential differences in SCIMAP-Flood output due to variation in the temporal resolution of rainfall. This analysis was undertaken through running SCIMAP-Flood for the East Rapti using TRMM satellite rainfall totals, and spatial pattern, for each monsoon period (May to September) between 1998 and 2016.

The SCIMAP-Flood output for the simplified TRMM satellite rainfall data is shown in Figure 3.22 with red representing areas that exhibit the greatest relative flood risk generation values during a high flow event with blue representing the areas of lower flood risk generation. It is evident that, as with the more complex scaled rainfall and the TRMM-only top 10 flow event rainfall, the eastern part of the East Rapti is most likely to be the source of flood water to the respective impact zones.

A comparison of the distribution of the SCIMAP-Flood flood water generation scores between the TRMM storm event rainfall patterns output and the TRMM monsoonal rainfall patterns output is shown in Figure 3.23. There is a change in the distribution of the SCIMAP-Flood scores with a large decrease in values > 0.50 (areas with a higher relative potential to generate flood waters) attained from using the TRMM monsoonal rainfall patterns. There is also a reduction in values > 0.75 (areas with the highest relative potential to generate flood waters) from using the monsoonal patterns to the extent that there is minimal coverage within the catchment of these high potential areas. On the other hand, there is a large increase in areas with the lowest relative potential to generate flood waters (< 0.25) outside of the 0.10 to 0.15 bin.

A comparison using point density analysis for the higher potential flood water generating areas between SCIMAP-Flood output from TRMM satellite data associated with the top 10 flow events and the TRMM satellite data with a monsoonal resolution is illustrated in Figure 3.24. This figure compares data from the same source and thus the impact of temporal resolution and storm selection rather than the spatial resolution comparison in Section Figure 3.21. From Figure 3.24 it is apparent that, whilst covering similar areas along the main East Rapti channel and in eastern parts of the catchment near Hetauda, using the monsoon rainfall patterns reduces the extent of the areas more likely to generate flood waters. Additionally, there are no areas with a flood risk score of > 0.75 produced using the monsoonal rainfall patterns.

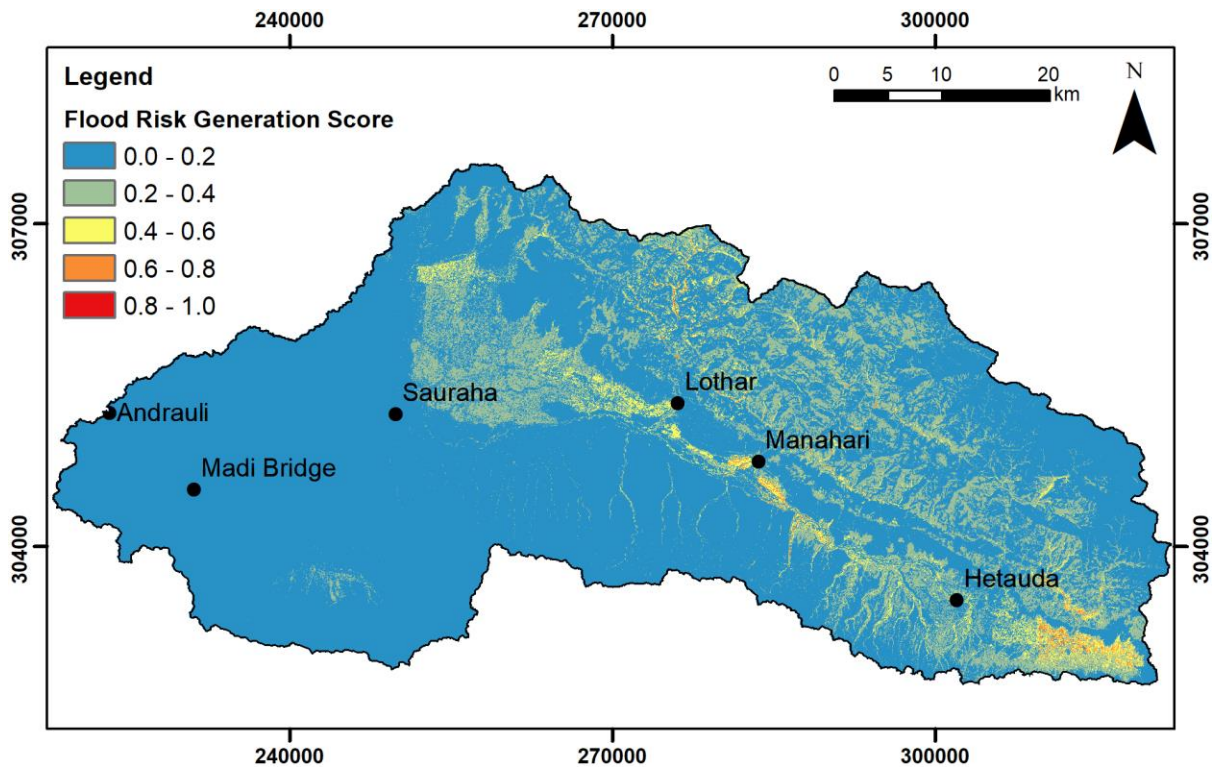


Figure 3.22: SCIMAP-Flood output for the East Rapti catchment created using TRMM satellite only rainfall patterns for each monsoon period (May to September) between 1998 and 2016, the top 10 land cover weighting sets and 6 flood impact points. Red represents areas that exhibit the greatest relative flood risk generation values during a high flow event, with blue represents areas of lower flood risk generation.

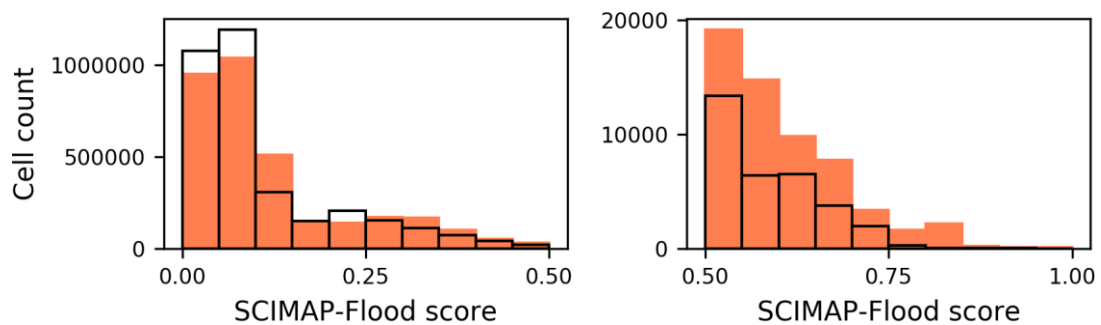


Figure 3.23: A comparison of the distribution of SCIMAP-Flood flood risk generation scores across the SCIMAP-Flood output created using the TRMM storm even rainfall patterns (red) (Figure 3.19) and the TRMM monsoonal rainfall patterns (black outline) (Figure 3.22). The distribution is split into lower potential flood water generating areas with a score of < 0.50 (left) and higher potential flood water generating areas with a score of > 0.50 (right).

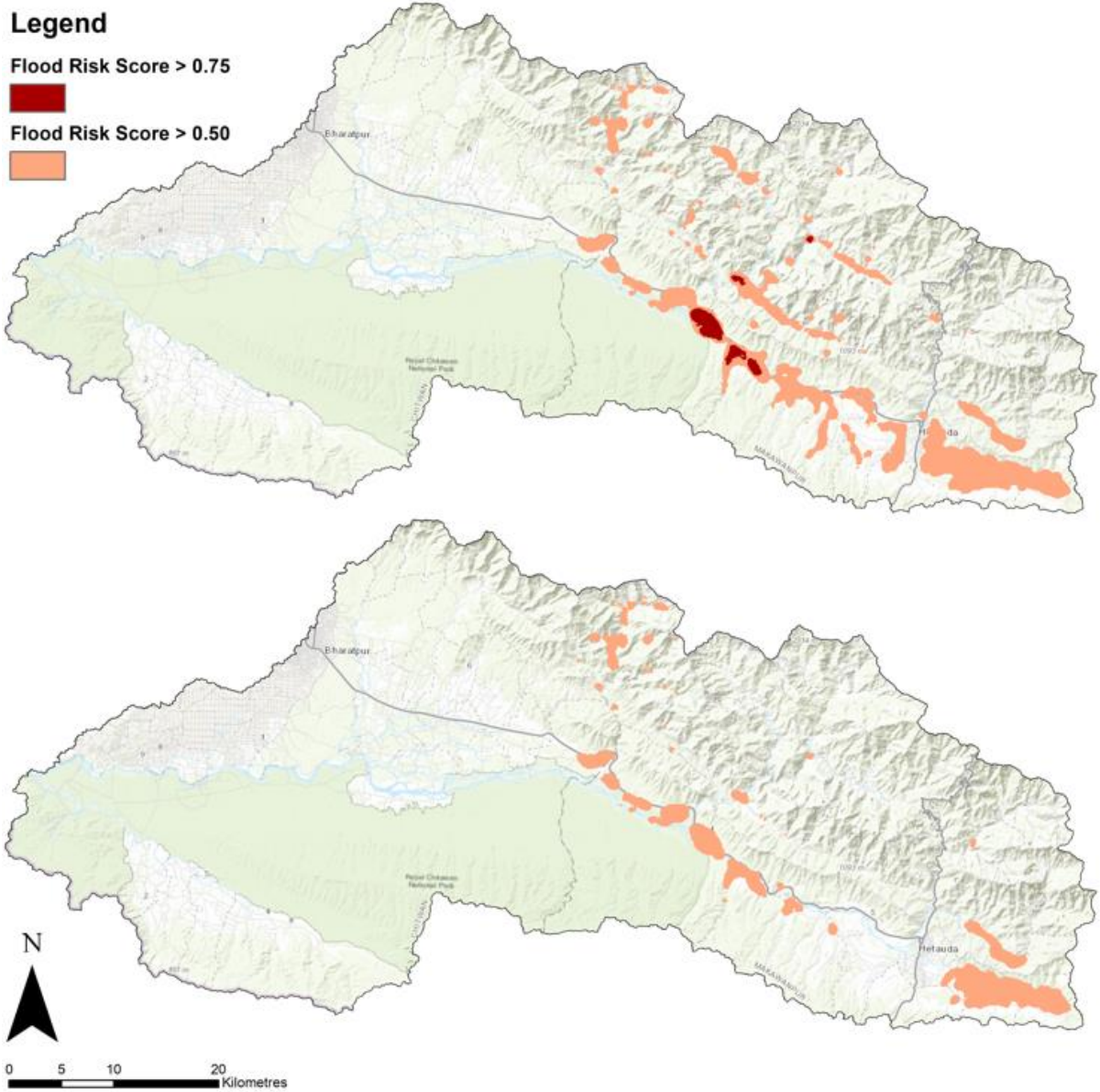


Figure 3.24: Point density analysis of SCIMAP-Flood output using TRMM-only rainfall data for the top 10 storm events (top) and the TRMM-only rainfall data for the monsoon periods between 1998 and 2016 (bottom) showing the areas of with the highest flood water generation weighting. The areas with a flood risk score of > 0.50 are pink and > 0.75 are dark red.

Storm rainfall pattern selection

The final output for SCIMAP-Flood was achieved using the top 10 storm rainfall patterns from the top 10 flow events in the East Rapti catchment. It is necessary to consider the impact on the identification of flood water generating areas if the number of selected storm patterns changes. To assess the potential impact of storm selection SCIMAP-Flood was run using the top 5 storm rainfall patterns from the top 5 flow events in the catchment with the 6 selected flood impact points and top 10 land cover weighting sets were kept the same. The SCIMAP-Flood output from the top 5 spatial rainfall patterns is shown in Figure 3.25 with red representing areas that exhibit the greatest relative flood risk generation values and blue representing the areas of low flood risk generation during a high flow event.

A comparison of the distribution of the SCIMAP-Flood flood water generation scores between the top 10 storm event rainfall patterns output and the top 5 storm event rainfall patterns output is shown in Figure 3.26. There is a change in the distribution of the SCIMAP-Flood scores with a slight decrease in values > 0.50 (areas with a higher relative potential to generate flood waters) attained from using the only the top 5 storm event rainfall patterns. There is also a reduction in values > 0.75 (areas with the highest relative potential to generate flood waters) from using the top 5 storm events with almost the complete removal of the highest potential areas > 0.85 . Alternatively, there is a slight increase in areas with the lowest relative potential to generate flood waters (< 0.25) outside of the 0.10 to 0.15 bin and no clear change in the lower relative potential flood water generating areas between 0.25 and 0.50.

A comparison using point density analysis for areas with a higher potential to generate flood waters between the SCIMAP-Flood output using the rainfall spatial patterns from the top 10 flow events and the rainfall spatial patterns from the top 5 flow events is illustrated in Figure 3.27. Varying the number of selected storm events from the top 10 to top 5 events produces only minor changes in the areas identified as having a high flood water generation potential. As seen in Figure 3.27 the analysis of both SCIMAP-Flood outputs highlights the eastern parts of catchment as areas with a flood risk score > 0.75 with the top 5 event output showing smaller areal coverage. The distribution of areas with a flood risk score > 0.50 is similar between both runs.

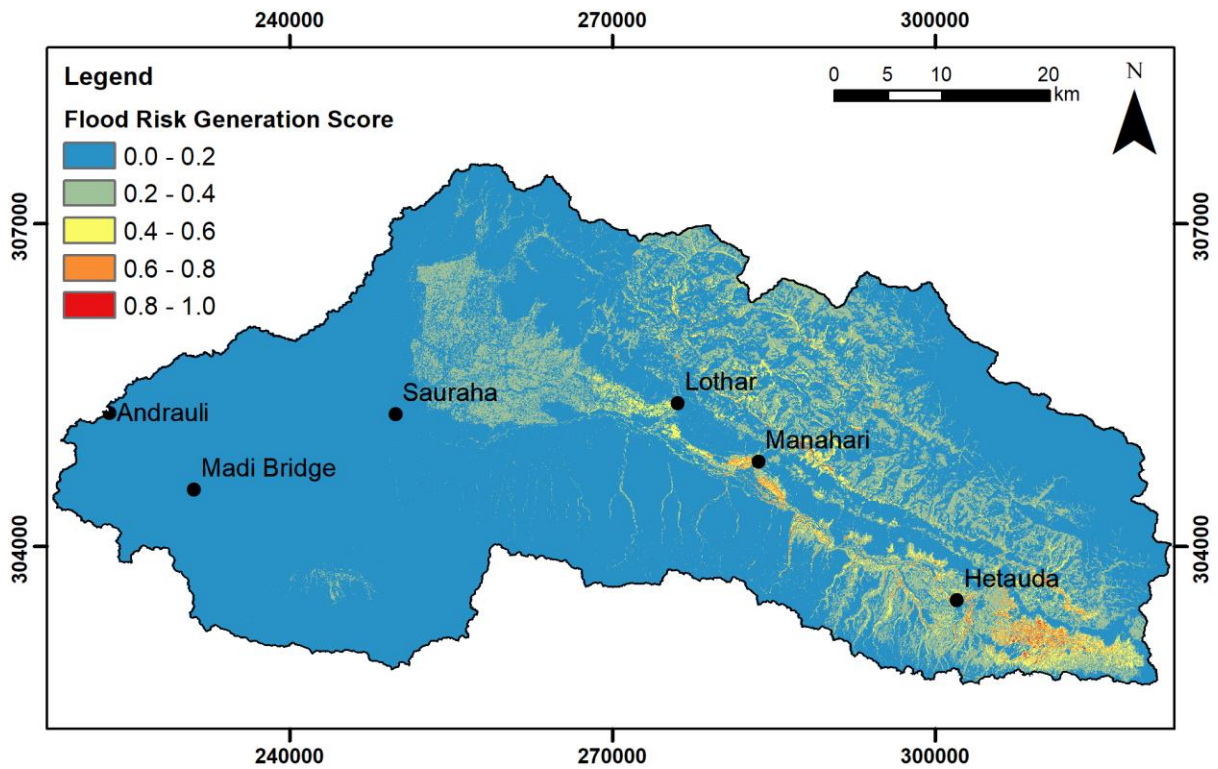


Figure 3.25: SCIMAP-Flood output for the East Rapti catchment created using the rainfall patterns associated with the top 5 flow events, the top 10 land cover weighting sets and 6 flood impact points. Red represents areas that exhibit the greatest relative flood risk generation values during a high flow event, with blue represents areas of lower flood risk generation.

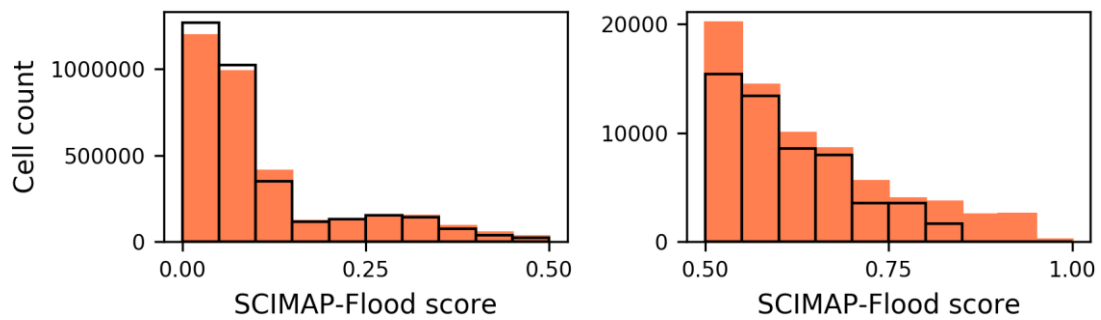


Figure 3.26: A comparison of the distribution of SCIMAP-Flood flood risk generation scores across the SCIMAP-Flood output created using the top 10 storm event rainfall patterns (red) (Figure 3.17) and the top 5 storm event rainfall patterns (black outline) (Figure 3.25). The distribution is split into lower potential flood water generating areas with a score of < 0.50 (left) and higher potential flood water generating areas with a score of > 0.50 (right).

Legend

Flood Risk Score > 0.75



Flood Risk Score > 0.50

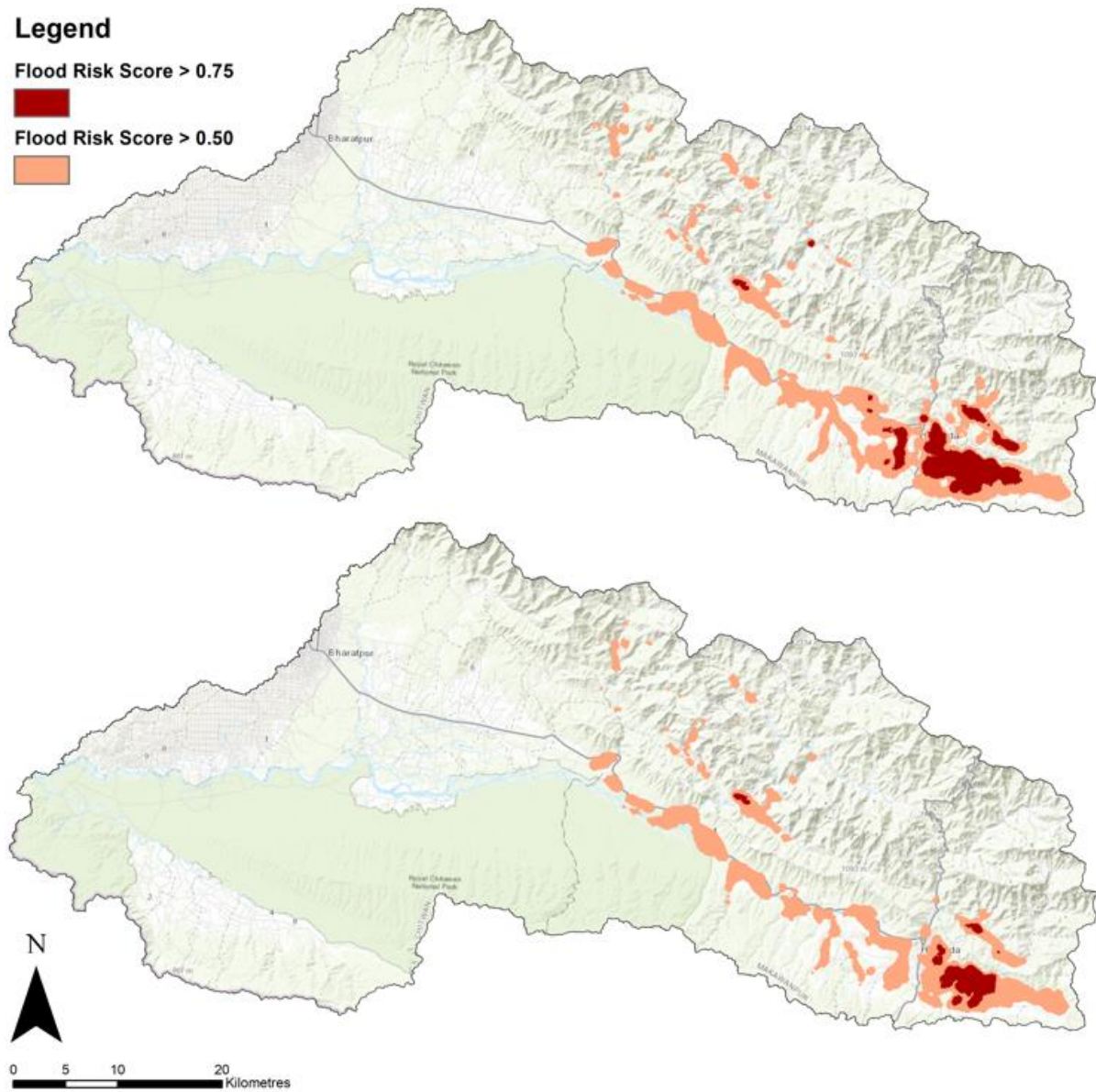


Figure 3.27: Point density analysis of SCIMAP-Flood output using the rainfall spatial patterns from the top 10 flow events (top) and the rainfall spatial patterns from the top 5 flow events (bottom) showing the areas of with the highest flood water generation weighting. The areas with a flood risk score of > 0.50 are pink and > 0.75 are dark red.

3.3.2.3 SCIMAP-Flood overland flow travel time sensitivity analysis

Selection of flood impact points

In addition to testing the sensitivity of the SCIMAP-Flood framework for the East Rapti catchment by varying the spatial rainfall inputs it is also necessary to consider the possible impact of varying the selection of the chosen flood impact points, the corresponding overland flow travel time data and the impact that the selection, or lack thereof, of a group of flood impact points can have on the SCIMAP-Flood output. With the selection of the final grouping flood impact points dependent on the user it is necessary to assess the change in flood water generating areas as determined by a point in a specific location. This analysis was done by removing each of the six flood impact points shown in Figure 3.3 individually and running SCIMAP-Flood with the remaining five flood impact points, the top 10 storm event rainfall patterns, and top 10 land cover weighting sets.

A comparison of the higher potential flood water generating areas using point density analysis between SCIMAP-Flood output using all 6 flood impact points and each of the scenarios with a removed flood impact point is shown in Figure 3.28. The removal of the Andrauli flood impact point concentrates the flood water generating areas within the East Rapti catchment to the far east with many of the areas with a flood risk score > 0.50 in the centre of the catchment removed or diminished. The removal of the Hetauda flood impact point results in large areas to the east of Hetauda no longer identified as having a very high (> 0.75) flood water generation potential. The identified flood water generation potential extent along the main East Rapti channel and in the northern sub-catchments remains the same. The removal of the Lothar flood impact does not significantly change the spatial extent of the identified flood water generation areas with small areas of > 0.50 in the Lothar sub-catchment no longer highlighted. As with the Lothar flood impact point, the removal of the Manahari flood impact does not significantly change the spatial extent of the identified flood water generation areas with small areas of greater than 0.50 and 0.75 in the Manahari sub-catchment removed. The removal of the Madi Bridge flood impact point does not change the extent of the identified flood water generating areas in the central and eastern parts of the catchment. The removal of the Sauraha flood impact point results in large areas extent along the main East Rapti channel and in the northern sub-catchments no longer identified as having a high (> 0.50) flood water generation potential. The identified flood water generation potential extent to the east of Hetauda remains the same.

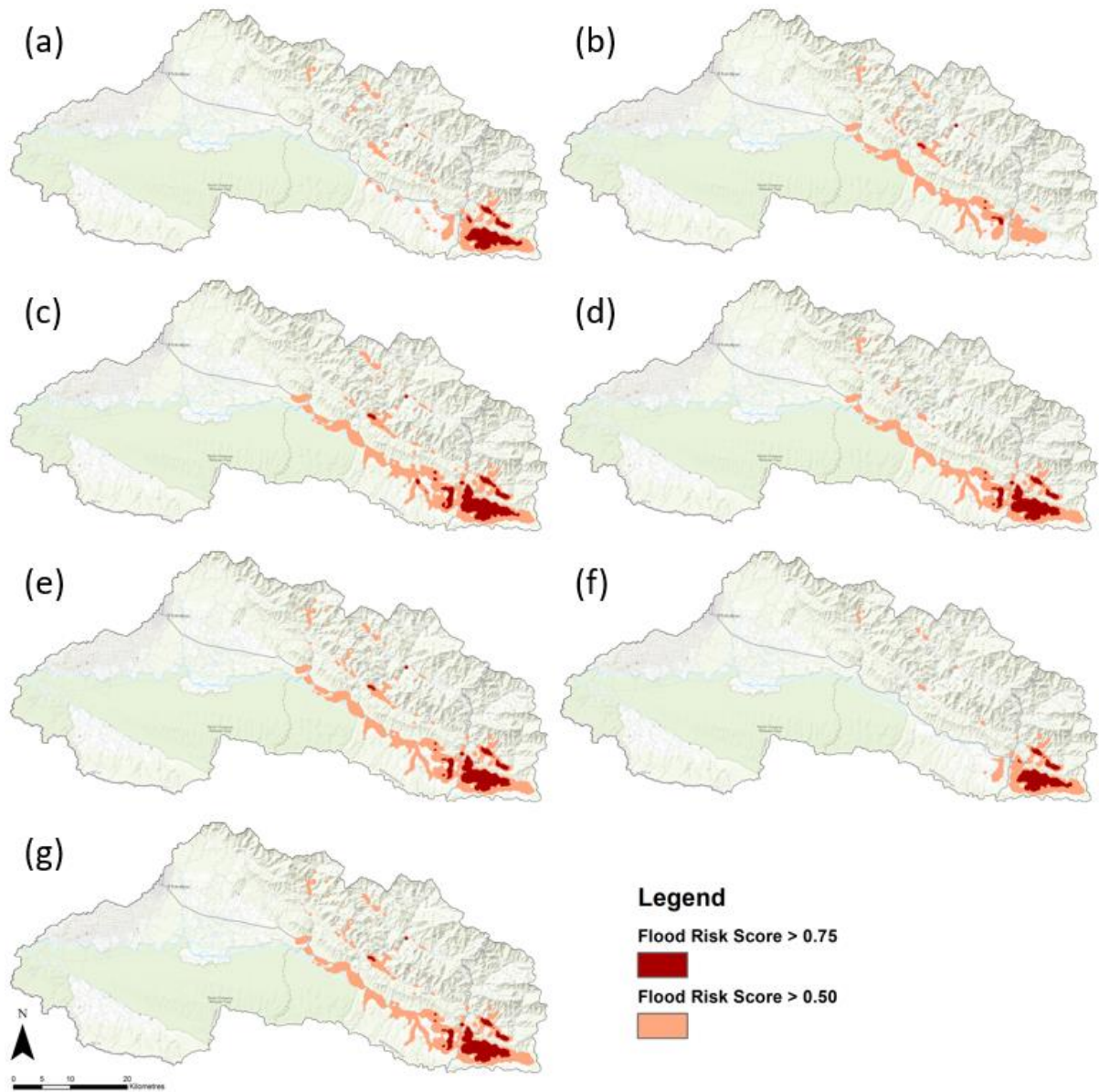


Figure 3.28: Point density analysis of SCIMAP-Flood output comparing the removal of the Andrauli flood impact point (a), the removal of the Hetauda flood impact point (b), the removal of the Lothar flood impact point (c), the removal of the Manahari flood impact point (d), the removal of the Madi Bridge flood impact point (e), the removal of the Sauraha flood impact point (f) and the use of all 6 flood impact points (g).

Placement of flood impact points

The sensitivity of the location of the flood impact point at a given location is also a factor to be investigated with regards to SCIMAP-Flood output. To assess the potential effect of this the location Sauraha and Hetauda flood impact points were removed and replaced with two flood impact points that covered both rivers (the main East Rapti channel and a tributary) that flow towards the impacted location. This alternative approach considers both the risk from the main East Rapti channel and tributary through separate overland flow travel time data, in comparison to the original approach used in Section 3.3.2.1 which takes overland flow travel time data for the entire contributing catchment to each settlement. The locations of the alternative points are shown in Figure 3.3. The Sauraha flood impact point was split to have a point on the main East Rapti channel and a point on the Budhi Khola tributary to the north of the settlement. The Hetauda flood impact point was split to have a point on the Rapti channel to the north and a point on the Karra River tributary to the east. The other inputs into SCIMAP-Flood remained the same with the top 10 storm event spatial rainfall patterns, remaining 4 flood impact points and top 10 land cover weighting sets used. The SCIMAP-Flood output from the alternative placement of flood impact point approach is shown in Figure 3.29 with red representing areas that exhibit the greatest relative flood risk generation values and blue representing the areas of low flood risk generation during a high flow event.

A comparison of the distribution of the SCIMAP-Flood flood water generation scores between the original flood impact locations output and the split flood impact locations output is shown in Figure 3.30. There is a change in the distribution of the SCIMAP-Flood scores with a decrease in both values > 0.50 (areas with a higher relative potential to generate flood waters) and values > 0.75 (areas with the highest relative potential to generate flood waters) reached from using the only the split flood impact locations. However, there is an increase in areas with the lowest relative potential to generate flood waters (< 0.25) outside of the 0.10 to 0.15 bin.

A comparison using point density analysis between SCIMAP-Flood output using the original flood impact point placement and the split flood impact point placement is illustrated in Figure 3.31. Splitting the flood impact points around Sauraha and Hetauda reduces the extent of the flood water generating areas with a flood risk score of greater than 0.50 in the central parts of the catchment. The main areas of high flood risk generation potential, those with a flood risk score of > 0.75 , remain in the eastern parts of the catchment near Hetauda.

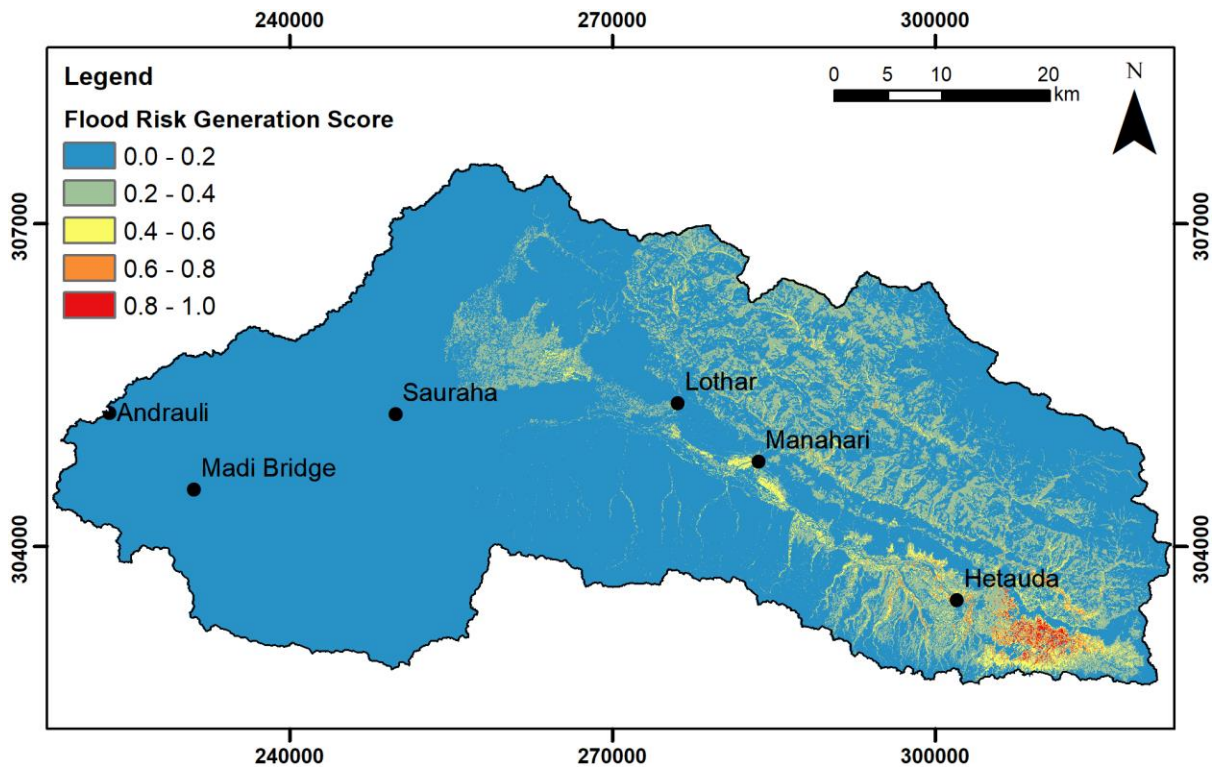


Figure 3.29: SCIMAP-Flood output for the East Rapti catchment created using the rainfall patterns associated with the top 10 flow events, the top 10 land cover weighting sets and split flood impact points at Sauraha and Hetauda with the 4 other flood impact points also used in Figure 3.17. Red represents areas that exhibit the greatest relative flood risk generation values during a high flow event, with blue represents areas of lower flood risk generation.

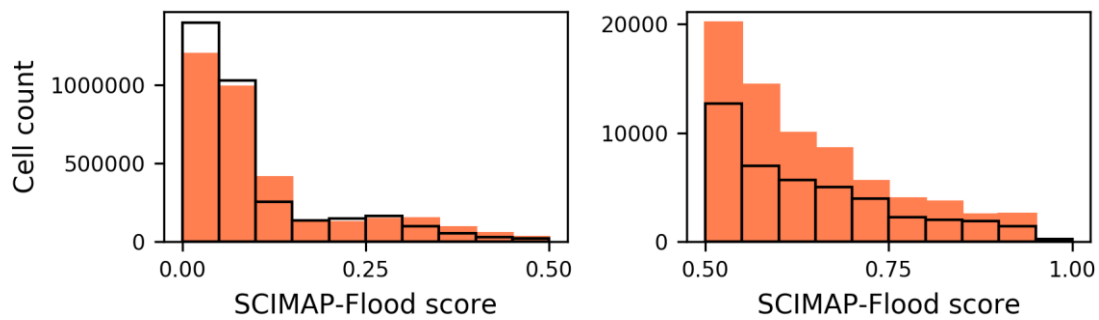


Figure 3.30: A comparison of the distribution of SCIMAP-Flood flood risk generation scores across the SCIMAP-Flood output created using the original flood impact point placement (red) (Figure 3.17) and the split flood impact point placement (black outline) (Figure 3.29). The distribution is split into lower potential flood water generating areas with a score of < 0.50 (left) and higher potential flood water generating areas with a score of > 0.50 (right).

Legend

Flood Risk Score > 0.75



Flood Risk Score > 0.50

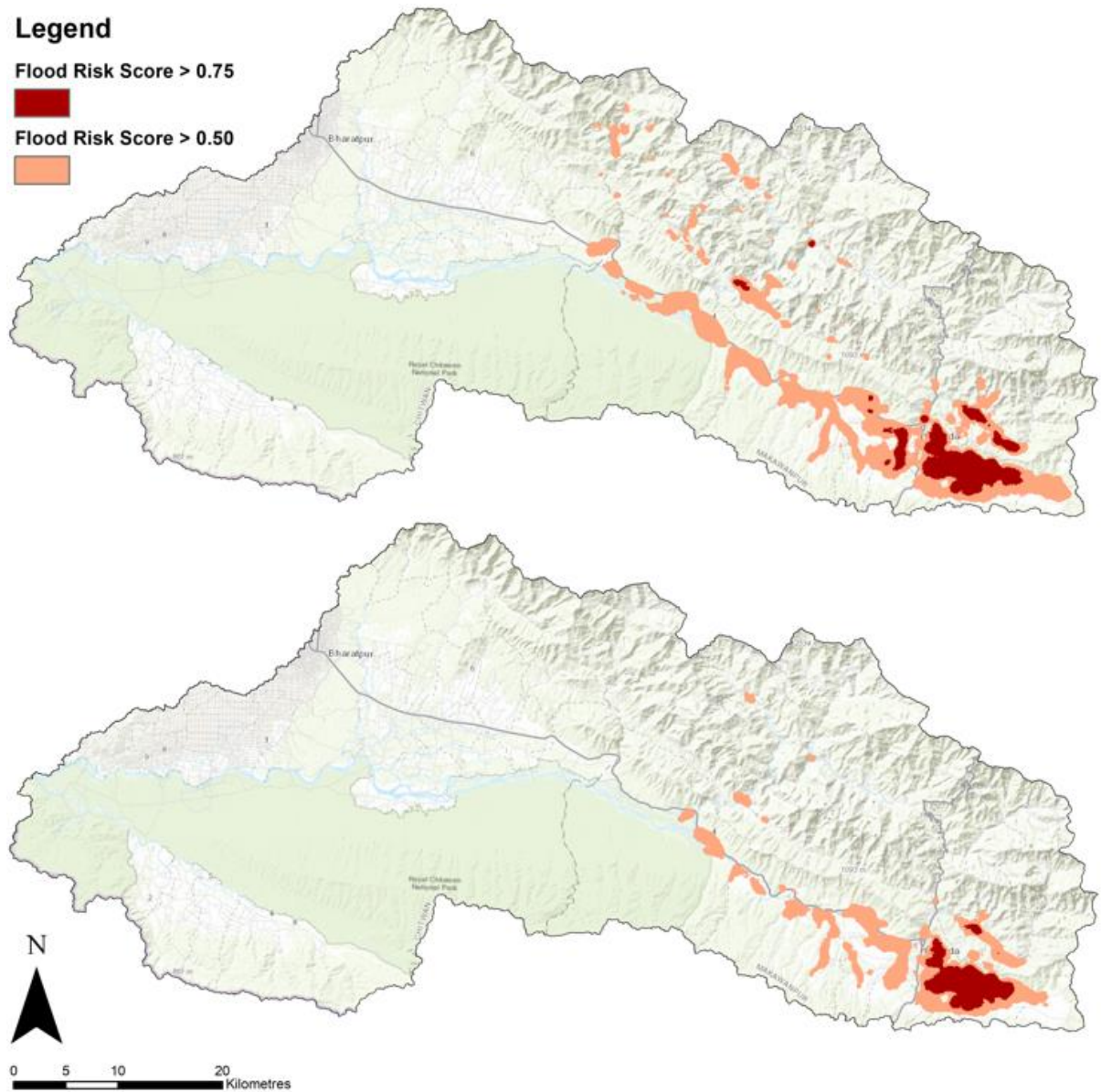


Figure 3.31: Point density analysis of SCIMAP-Flood output using the 6 selected flood impact points (top) and alternative flood impact points (bottom) showing the areas of with the highest flood water generation weighting. The areas with a flood risk score of > 0.50 are pink and > 0.75 are dark red.

3.3.2.4 Overall SCIMAP-Flood sensitivity analysis

Having shown that the SCIMAP-Flood output can vary depending on the rainfall data used and the location of the selected flood impact points, an overall sensitivity analysis was undertaken using an ensemble with all the sensitivity scenarios. This allows for the identification of areas that are present in all the sensitivity runs and those that are reliant on more specific SCIMAP-Flood input sets. To establish the likelihood of a location within the catchment being identified as flood water generating by SCIMAP-Flood, regardless of the input data, the coverage of areas > 0.50 and > 0.75 across the different SCIMAP-Flood runs was analysed. The sensitivity of areas having a flood risk score > 0.50 and > 0.75 are shown in Figure 3.32 and is calculated using the number of times an area appears across all the different sensitivity runs outlined in Section 3.3.2.2 and Section 3.3.2.3.

Figure 3.32 illustrates that the majority of areas with a flood risk score of > 0.50 are insensitive to either the spatial or temporal resolution of the rainfall or the selection of flood impact points. The areas to the east of Hetauda, along the main East Rapti channel and in the northern part of the Lothar sub-catchment that appear in $> 75\%$ of the runs undertaken for sensitivity analysis. There are areas within the northern part of the Manahari sub-catchment that are more sensitive to the input. The areas with a flood risk score of > 0.75 are more sensitive to the SCIMAP-Flood inputs. These are the areas that are most likely to generate flood waters to the flood impact locations within the catchment. The least sensitive > 0.75 area is to the east of Hetauda which features in $> 50\%$ of sensitivity analysis runs undertaken. The identified parts of the catchment along the main East Rapti channel are highly sensitive to the SCIMAP-Flood inputs. It must be noted however that these areas are still featured in the > 0.50 data and are still identified as flood water generating.

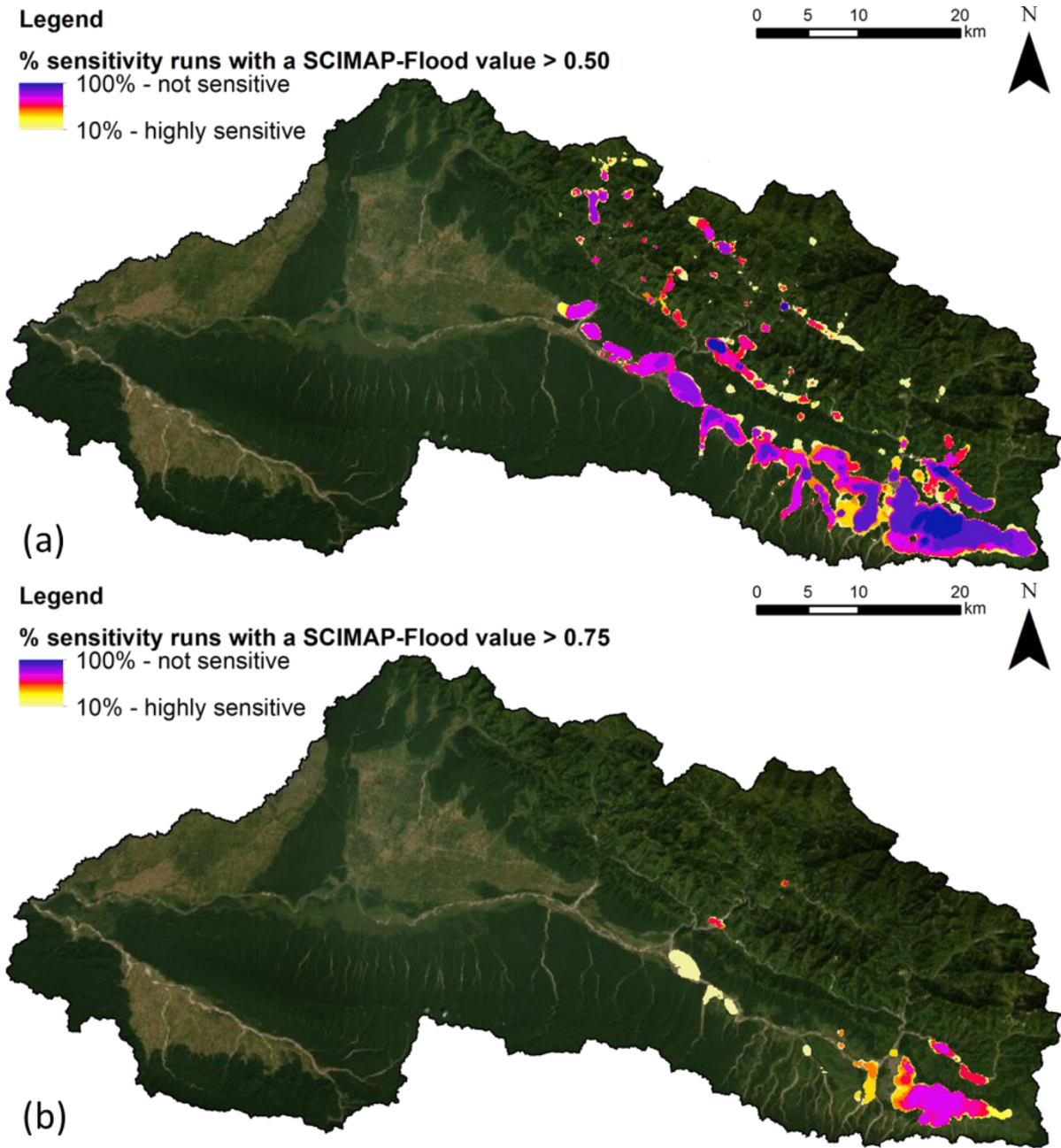


Figure 3.32: The overall sensitivity of areas having a flood risk score of (a) > 0.50 and (b) > 0.75. Based on the point density analysis of SCIMAP-Flood output and the percentage appearance of an area across the sensitivity scenarios. The areas in dark blue have a low sensitivity to the data input and the light-yellow areas have a high sensitivity to the data input.

3.4 DISCUSSION

3.4.1 Determining flood source areas in the East Rapti catchment using SCIMAP-Flood

The SCIMAP-Flood results demonstrated that the eastern part of the East Rapti catchment near Hetuada had the greatest potential to generate flood waters to the six flood impact locations. This is illustrated in Figure 3.17. There were additional areas along the main East Rapti channel and in the upland areas of the Lothar, Manahari and Rapti sub-catchments that were also identified as having a higher flood water generation potential. Using zonal statistics with the East Rapti land cover spatial data and the other SCIMAP-Flood spatial data inputs, the impact of the drivers of flood water generation can be assessed at the catchment-scale. The make-up of these flood water generating drivers is catchment specific, but is a function of catchment topography, geometry, soil conditions and the spatial distribution of rainfall (O'Connell et al., 2007). The influence of catchment topography, channel network and rainfall as flood water generation drivers are discussed below. The impact of land cover, which includes the representation of soil conditions, on the flood regime is discussed separately in Section 3.4.3.

The average slope across the land covers within the catchment produced two distinct groups. Evident in Figure 3.33, a breakdown of the distribution of the slope values across each land cover class, and Table 3.7 there was a large relative difference between the groups. With SCIMAP-Flood using the relative difference across the catchment, the large contrast between the areas of steep slopes and flat areas is reflected in the amalgamated output and therefore slope can be considered a key driving factor in the flood water generation based on the SCIMAP-Flood Fitted approach. The average slope of the areas in the catchment covered in *Rainfed Agriculture* and *Forest* was noticeably higher than the average slope of the other land covers in the East Rapti catchment. These areas of land cover with steeper slope values cover a significant proportion (76%) of the catchment. The average slope in areas of *Rainfed Agriculture* was 21.7° and in areas of *Forest* was 18.4° in contrast to a maximum average of 6.5° for *Bare Ground* and $< 1.5^\circ$ for the remaining land covers. It must be noted, however, that the location and extent of the certain land covers is arguably defined by slope, with rainfed agricultural terraces and forest coverage in the East Rapti concentrated in the upland parts of the catchment. The lower gradient parts of the catchment contain the irrigated agriculture and more densely populated areas due, in part, to having a high agricultural productivity potential (Singh, 2013).

Table 3.7: The percentage coverage of the land covers within the East Rapti catchment and respective average and standard deviation (SD) of the slope gradient and Network Index values. Network Index represents hydrological connectivity with 0 being poorly connected and 1 being well connected.

Land cover	% of catchment area	Average slope (degrees)	SD slope (degrees)	Average Network Index	SD Network Index
<i>Rainfed Agriculture</i>	18.0	21.7	13.1	0.24	0.24
<i>Irrigated Agriculture</i>	10.5	1.0	1.0	0.60	0.21
<i>Shrubland</i>	6.4	1.3	1.2	0.60	0.23
<i>Forest</i>	58.3	18.4	13.1	0.24	0.21
<i>Built-Up Areas</i>	4.4	1.5	1.2	0.55	0.21
<i>Bare Ground</i>	1.6	6.5	6.8	0.56	0.30
<i>Water</i>	0.9	1.3	1.5	0.66	0.24

As outlined in Section 3.2.1, the slope is one of the inputs to calculate the Topographic Wetness Index, and thus the Network Index (Lane et al., 2004), which represents the hydrological connectivity of the catchment. The large difference between the slope values across the different land covers is reflected in the average Network Index value (see Table 3.7). The distribution of the Network Index values across the different land cover classes is shown in Figure 3.33. The areas of lower slope, predominantly located in the downstream parts of the East Rapti catchment but also immediately to the south east of Hetauda, are better connected with a greater upslope contributing area and transfer water into the drainage network more easily. With a higher Topographic Wetness Index these areas are also more likely to generate overland flow (Juracek, 2000). Regardless of the land cover risk weightings, the impact of the contrasting relative slopes across throughout the East Rapti, and the large percentage coverage of areas of higher slope values, is a key factor in driving the generation of flood waters to the flood impact points.

The spatial distribution of rainfall was a dominant factor with regards to identifying areas that generated flood water during high flows in the East Rapti catchment. The dominance of rainfall pattern was also apparent in a previous SCIMAP-Flood study by Reaney and Pearson (2016). The necessity to factor in spatial rainfall pattern, rather than use a uniform rainfall across the catchment, is noted in Saghafian et al. (2013) who identify differing flood source producing sub-catchments once storm patterns are variable. As evident in the spatial rainfall patterns developed using the DHM gauged data and scaled TRMM satellite rainfall data (see Figure 3.7 and Appendix 7.12 to 7.19) the highest rainfall totals associated with the top 10 high flow events were recorded principally in the south eastern corner of the catchment around Hetauda. Though varied, the rainfall patterns predominantly had the lowest totals in the western parts of the catchment.

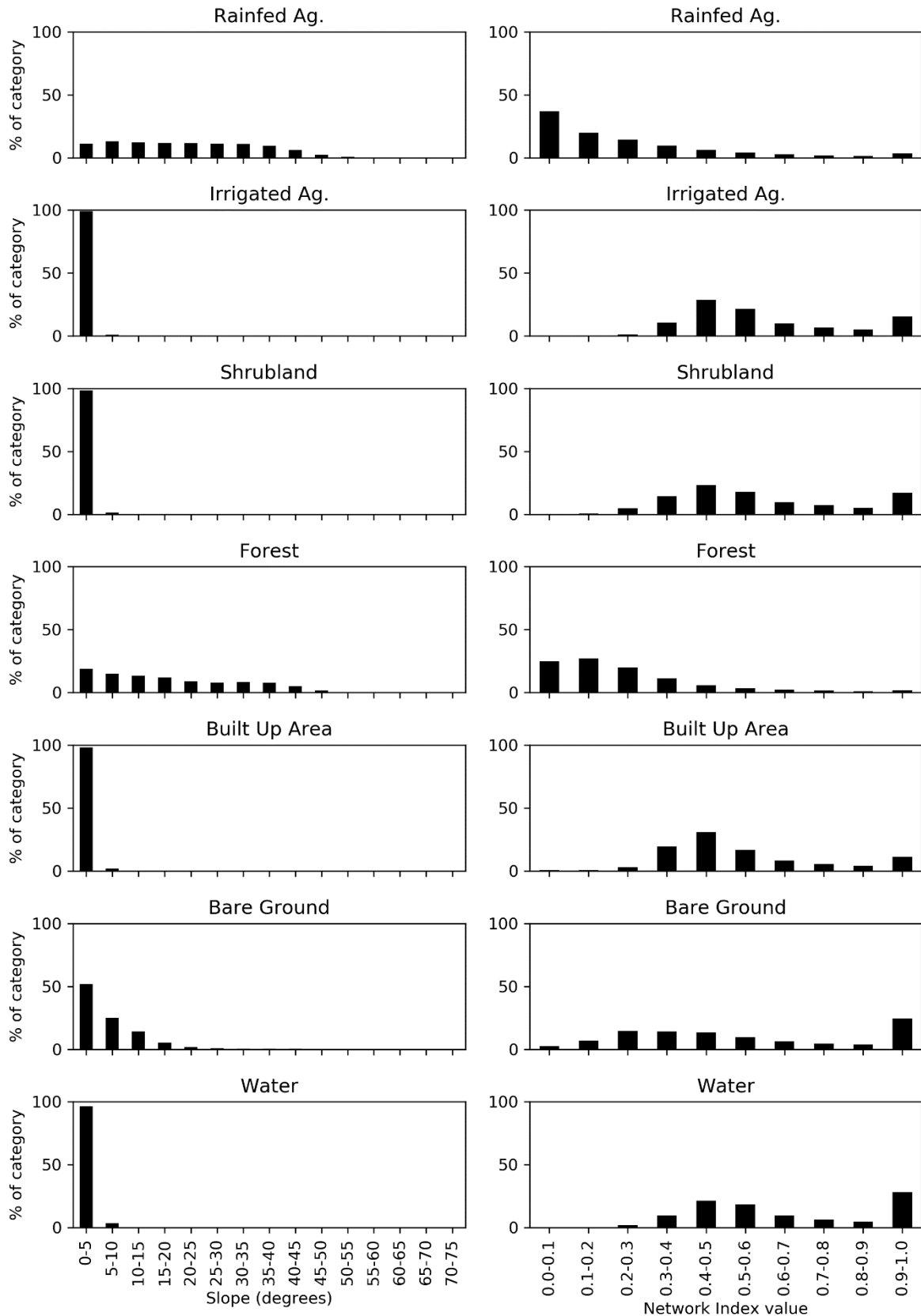


Figure 3.33: The percentage distribution of slope (left) and Network Index (right) values throughout each of the land cover categories in the East Rapti.

The identified high potential flood water generating areas around Hetuada in the east of the catchment, whilst not having the steep terrain of the hills to the north, are dominated by *Irrigated Agriculture*. The localised dominance of land coverage with a high relative flood water generation weighting will increase the likelihood of flood water being generated from the area. This area is also very well connected, having a high relative connectivity value with the water able to enter the channel system through a dense network of pathways. The determined *Built-Up Area* land cover weightings represented a below average risk of flow generation which signifies a positive impact on the flood regime for the settlement of Hetauda. However, with a small (4% of the catchment) areal coverage and a notably wide spread between 0 and 1 across the top 750 model simulations (Figure 3.15), the final risk weightings given to *Built-Up Area* could have been due to the limited impact of the land cover in the inverse modelling approach.

The areas in the north eastern part of the East Rapti, within the Rapti and Manahari sub-catchments, that are highlighted as flood water generating are predominantly in the upper parts of the catchment where the steep terrain, despite not having a high level of connectivity, conveys water to the channel quickly. Additionally, in contrast to the heavily forested southern and central northern parts of the catchment, there are large areas of *Rainfed Agriculture*. Whilst the terraced agricultural land cover does not convey water to channel network at the same rate as the *Irrigated Agriculture*, for example, it does have a higher relative risk weighting to the *Forest* land cover; this is discussed in Section 3.4.2.

These highlighted flood water generating locations are in the upstream parts of the catchment network and feature within the contributing areas to many of the selected flood impact points. With the combined approach to all six flood impact points considered, these areas have a higher frequency of appearing as a contributing, and thus a potential flood source, area in the amalgamated SCIMAP-Flood results; this pattern due to contributing frequency is also evident in the only other SCIMAP-Flood research using multiple impact points (Reaney and Pearson, 2016). The areas upstream of the Hetauda flood impact point, for example, have the potential to be a flood source area to the Hetauda, Sauraha and Andrauli flood impact points.

It is apparent that, using the methods and data outlined in this chapter, SCIMAP-Flood can identify flood source areas in a catchment through a combination of flood water generation factors. Within the East Rapti catchment it is evident that the rainfall patterns associated with high flow events was a key factor and, as a result, both the hilly north eastern part of catchment and the highly connected agricultural and Built-Up area in the south eastern part of the catchment have a high relative potential to generate flood water. The frequency of contribution to the selected flood impact point for a given area within the catchment is also a key criterion for the identification as a higher potential for flood

water generation. With the East Rapti exhibiting catchment characteristics typical to those of catchments across the southern edge of Nepal the rainfall pattern dominance in SCIMAP-Flood is likely to be prevalent in similar catchments.

3.4.2 Identifying locations for catchment-scale flood management measures in the East Rapti catchment using SCIMAP-Flood

The implementation of flood management measures at the catchment-scale should target source areas of flooding throughout the catchment whilst minimising the risk of increasing the risk of flooding at the flood impact areas within the catchment (Turner-Gillespie et al., 2003; Hooijer et al., 2004; Lane, 2017; Metcalfe, 2017). With varying hydrological connectivity and land cover throughout the catchment producing variation in overland flow travel times and spatially diverse rainfall patterns associated with flooding events, there needs to be an approach that considers how flood water generating factors interact at the catchment-scale. SCIMAP-Flood is an approach that achieves this using limited data and low levels of computational requirement. With the SCIMAP-Flood output giving a relative likelihood of an area to generate flood water during a rainfall event whilst considering travel times to ensure that synchronisation of flows from sub-catchments does not increase flood risk at an impact zone in the catchment. By identifying areas that have a high likelihood of generating flood waters then it is possible to develop catchment-scale flood management measures through targeted implementation in these areas.

The spatial targeting of flood management measures can be achieved by reconsidering the initial SCIMAP-Flood output. Through reinterpreting the output presented in Figure 3.17 for the East Rapti catchment it is possible to consider the benefit of placing an intervention in a particular part of the catchment. This reinterpretation is illustrated in Figure 3.34 where areas in the catchment that are more likely to generate flood water to the flood impacted areas are considered areas in which a flood management measure could have a high impact on the flooding regime. Coloured red and orange in Figure 3.34, we can establish the areas within the East Rapti catchment in which flood management measures would best be implemented. Flood management measures, such as targeted afforestation or check dams, placed in the areas of blue, green, and yellow would also be expected to reduce flooding to the points of impact but to a lesser degree.

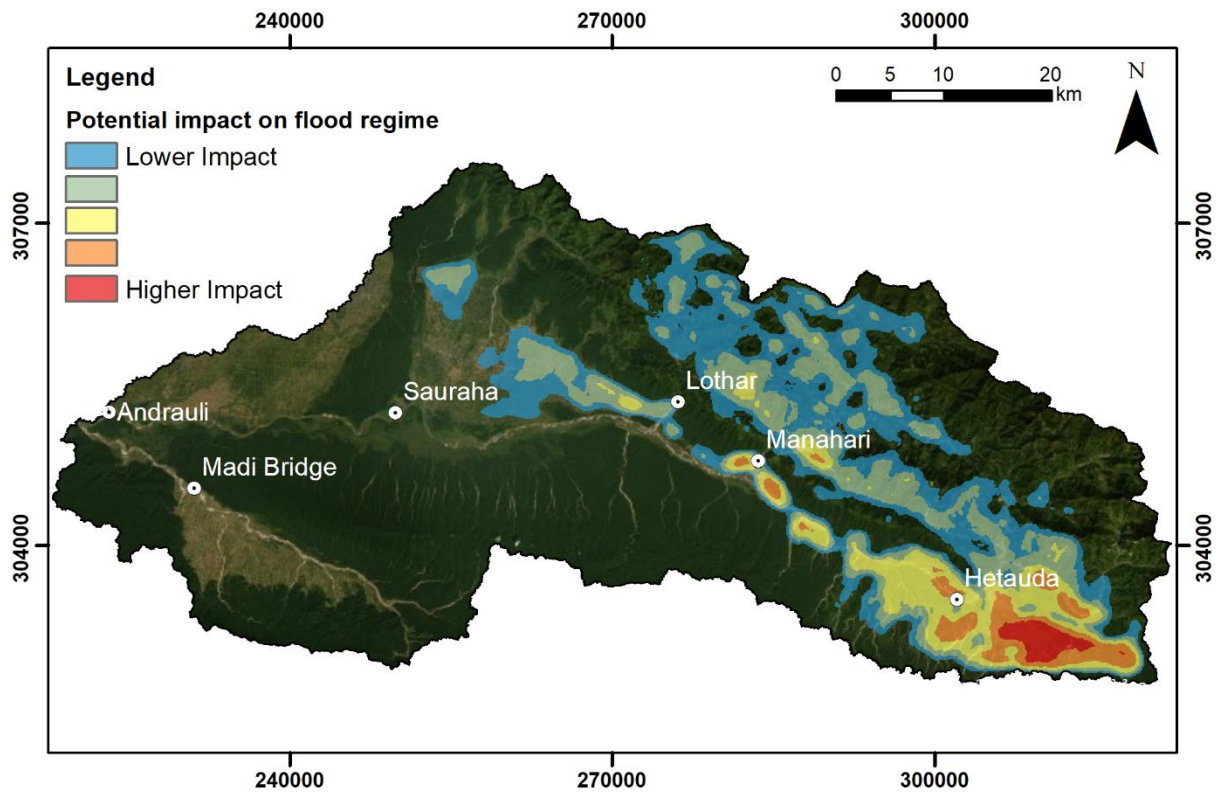


Figure 3.34: SCIMAP-Flood output for the East Rapti catchment (as presented in Figure 3.17) reinterpreted to help with the spatial targeting of flood management measures. Areas in red would have the highest impact on the flooding regime to the areas impacted by flooding and therefore would be the best locations for flood management measures.

The SCIMAP-Flood results demonstrated that the eastern part of the East Rapti catchment near Hetuada had the greatest potential to generate flood waters to the six flood impact locations and, as a result, this is the area most appropriate to implement flood management measures. There were additional areas along the main East Rapti channel and in the upland areas of the Lothar, Manahari and Rapti sub-catchments that were also identified as having a higher flood water generation potential and are key areas for the spatial targeting of flood management measures.

Equally, the identification of areas suitable for positive impacts on the flood regime in the East Rapti catchment also locates the areas in which changes would have the largest negative impact to the flood impact points. With regards to the East Rapti catchment, and other catchments in Nepal and the wider Himalayan region, land use changes such as terrace abandonment and deforestation have a detrimental impact by increasing the runoff generation potential (Ives and Messerli 1989; Nepal, 2012; Paudel et al., 2014; Chaudary et al., 2016; Rimal et al., 2019). Ensuring that such land use change does not occur at the key areas identified at the catchment-scale can reduce the likelihood of increased flooding at the flood impact points.

The pattern of the SCIMAP-Flood output for the spatial targeting of flood management measures in the East Rapti are comparable to the only previous study undertaken using the framework with

multiple storm events and multiple points of flood impact; the 2,300 km² River Eden catchment in Cumbria, UK (Reaney and Pearson, 2016). As in the East Rapti case study, the areas in the River Eden study identified as flood water generating, and as such suitable for the targeting of flood management measures, were contributing areas to all three of the flood impact points and located in the upper parts of the channel network. The dominant coverage of the high flood water generation potential areas is also in part of the catchment with higher relative rainfall totals and encompasses areas of well-connected, high land cover risk weighting agricultural grassland. An alternative study using the 69 km² Roe Beck, also in Cumbria, UK, only used one flood impact point and a uniform rainfall total; this study identified key flood water generating areas as those with a high land cover weighting (agricultural grassland) and higher relative slope but not constrained in the same manner as the East Rapti results to the upper reaches of the catchment (Pearson, 2016).

The SCIMAP-Flood approach can be used to determine which flood management interventions could be most suitable for the chosen catchment but is not designed to quantify how effective a given flood management scenario would be. By looking at the identified flood source areas, establishing if they are strong connectivity or flood water generation driven the dominant flood drivers can be understood. The pattern of dominance across the flood drivers can inform the type of mitigation measure that could be implemented. The provided output can be used to engage with stakeholders, as in Pearson (2016), and catchment specific flood management scenarios can be created. Further modelling to assess to effectiveness of a given scenario can then be undertaken to investigate the impact on peak flow and flood extent reduction at impact points.

3.4.3 Assessing the impact of land cover on the flood regime in the East Rapti catchment using SCIMAP-Flood Fitted

From the results of the inverse modelling approach undertaken using SCIMAP-Flood Fitted to deduce the risk weightings for the seven main land covers in the East Rapti catchment it is apparent that the weighting values of certain land cover values produced a higher Pearson's correlation coefficient if within a specific range whilst other land covers did not show such a trend. This trend, or lack thereof, can be used to ascertain if land cover weightings have a quantifiable impact on driving the flood regime in the East Rapti catchment. From the top SCIMAP-Flood land cover risk weightings of a certain land cover based on the inverse modelling approach results an assessment of the local runoff generation potential can be made. This runoff generation potential reflects a combination of land cover, land management, soil properties and slope gradient (Kirkby et al., 2002; Bracken and Croke, 2007; El Kateb et al., 2013; Reaney et al., 2014).

As evident in the dot plots in Figure 3.15, with the top five percent of the 15,000 model simulations the *Irrigated Agriculture* land cover categories exhibited a higher Pearson's correlation coefficient as the weighting value is close to 1. This would suggest that land cover weighting has a significant impact on increasing the flood water generation potential within the East Rapti catchment. The *Built-Up Area* land cover weighting value has the highest correlation coefficient between 0.2 and 0.4. Based on the inverse modelling results the *Built-Up Area* land cover weightings indicate that areas with this land cover have a slightly lower than average flood water generation potential but is not a key contributor to generating flood waters in the East Rapti catchment. The risk weightings of the *Shrubland*, *Forest* and *Water* land covers, as shown in Figure 3.15, show an improved correlation coefficient close to 0. This suggests that the three land covers have a low relative potential for generating flood waters in the East Rapti catchment.

Evident in Figure 3.15, the *Rainfed Agriculture* and *Bare Ground* land cover classes in the catchment do not show a clear trend with regards to SCIMAP-Flood risk weighting and Pearson's correlation coefficient across the top five percent of the 15,000 model runs. The contribution of these land covers towards generating flood waters in the East Rapti catchment, from the SCIMAP-Flood Fitted results, is unknown with weighting values indicating both high and low potential runoff generation in relation to the rest of the catchment. Using equifinality to represent the spectrum of top SCIMAP-Flood Fitted results for these values offers a solution however, plot scale research undertaken in Nepal (Gardner and Gerrard, 2002; Merz et al., 2006; Zokaib and Nasser; 2011), indicates a positive relation between ground cover and localised runoff generation and would suggest that *Bare Ground* should have a SCIMAP-Flood risk weighting > 0.50 ; contributing to flood regime in the East Rapti catchment. Further work investigating upland terrace agriculture (*Rainfed Agriculture* in SCIMAP-Flood) identifies that runoff on 'bari' terraces is highly variable and largely dependent on the rainfall (Gardner and Gerrard, 2003). Although Merz et al. (2006), also using plot-scale runoff measurements in central Nepal, established that terraced management of agricultural land is beneficial to reducing flood water generation downstream with agricultural land less prone to runoff generation and yielding lower runoff rates when compared to bare ground.

This pattern in flood water generating potential can be seen in disparity between runoff coefficients for certain land covers within the catchment and can be evidenced with research around terrace abandonment and deforestation; key points of research in many Nepalese catchments (Ives and Messerli, 1989; Metz, 1991; Gerrard and Gardner, 2002; Neupane et al., 2015; Chaudary et al., 2016). Gardner and Gerrard (2003) establish that the monsoon runoff coefficients, expressing estimated total runoff as a percentage of total rainfall, for a site in the Middle Hills of Nepal was 1% for good secondary

forest cover whilst land converted to terraced agriculture had a runoff coefficient of between 5% and 26% (Gardner and Gerrard, 2003). This runoff coefficient change has an impact on the flow regime with Sastry and Dhruva Narayana (1986) finding that the cumulative impact on runoff in a catchment experiencing deforestation converted to agriculture resulted in the volume of runoff increasing by 15% with a 72% increase in peak runoff; this indicates the relative flood water generating potential of both land covers. Further evidence is seen in modelling undertaken by Rai and Sharma (1998) that supports this increase in flood water generation potential between land covers with land use change in a catchment from forestry and agro-forestry to open agriculture increasing streamflow by 11%. Notably, the agricultural runoff coefficients used in SCIMAP-Flood do not consider vegetation type variation within the land cover type which have a significant impact on the runoff coefficient of agricultural terraces; with a variation in runoff coefficient of between 5% and 50% in a monsoonal climate (Gardner and Gerrard, 2003; van Dijk et al., 2005; Seeger and Ries, 2008; Arnaez et al., 2011).

An assessment of the importance of the land cover weightings as a driver of the flood regime in the East Rapti catchment requires consideration of the spatial coverage of each land cover within the catchment. The spatial distribution of the land cover in the East Rapti is shown in Figure 2.6 with the percentage coverage of each of the seven classes in Table 3.7. The land cover with the highest relative flood water generation potential, *Irrigated Agriculture*, accounts for 10.5% of the East Rapti catchment. Notably, the distribution of much of the *Irrigated Agriculture* is in the western, downstream, part of the East Rapti catchment. Situated on the flat Terai plains, in close proximity to many of the flood impact locations, *Irrigated Agriculture* is not located in the upland source areas of the East Rapti and despite the high local runoff generation potential, is unlikely to be in areas identified as generating flood waters. Using high risk weightings for the poorly correlated land covers, *Rainfed Agriculture* and *Bare Ground*, then a maximum of 30.1% of the catchment would be likely to increase the potential of flood water generation when considering the impact of land cover on the flood regime. With the remainder (between 69.9% and 89.5% depending on the values of the *Rainfed Agriculture* and *Bare Ground*) of the catchment having land cover risk weighting values of below 0.50, lower than the relative average, the majority of the land cover in the East Rapti catchment is not increasing the risk of flooding to the flood impact locations.

With the East Rapti being a representative, medium-sized Nepalese catchment it is likely that, across Nepal and the wider Himalayan region, the land cover weightings established through using the SCIMAP-Flood Fitted approach could be used as donor values to regional catchments with a similar catchment characteristics. The ascertained land cover weighting values could be applied to other catchments, such as the West Rapti, Babai and Kamala, which exhibit similar land cover, climatic

conditions, and geomorphology to the East Rapti. At present, this would exclude the larger meltwater affected catchments, such as the Koshi, Karnali and Nayarani, in which the influence of snow/ice cover would need to be considered. Finally, it must be noted that if future work using SCIMAP-Flood was attempting to use a single weighting set for the region, thereby moving away from the equifinality-based approach used in this research, work would need to be done to constrain the land cover weightings of *Rainfed Agriculture* and *Bare Ground*.

3.4.4 The influence of the spatial data inputs on the SCIMAP-Flood output

As there are currently no guidelines on the required input data for the implementation of SCIMAP-Flood for a given catchment, it is necessary to consider the impacts of varying the rainfall spatial pattern data and overland flow travel times to flood impact locations data input files. Undertaking a sensitivity analysis on the possible areal extent changes to the identification of areas with a higher flood risk generation potential allows a comparison to be made.

With rainfall as the dominant factor within the East Rapti, it is necessary to establish what effect the selection of rainfall data can have on the flood water generating areas identified by SCIMAP-Flood. To assess whether a complex approach to create accurate rainfall data at a daily timescale must be used or whether the spatial pattern from satellite rainfall at a daily temporal resolution can be used was explored in Section 3.3.2.2. Further assessments in Section 3.3.2.2 were made to determine whether a monsoonal temporal resolution could be used instead of using cumulative rainfall patterns associated with high flow events and also the impact of the number of storm events selected, with a comparison using the top 10 and top 5 spatial rainfall patterns from the top high flow events.

Maintaining the use of selecting storm events, despite a variation in number selected or resolution of data, produced similar extents identifying areas of higher flood risk generation potential. This has implications with regards to the use of SCIMAP-Flood in catchments that have sparse rainfall data as, in the absence of gauged data, then the spatial patterns derived from a satellite rainfall product, such as TRMM 3B42, can be used to establish relative rainfall weightings. Additionally, fewer top storm events could be used with the same higher relative flood water generating areas being identified using 5 storm events as with 10 events. However, the use of fewer storm events could lead to a bias-in the spatial rainfall pattern with more events used creating a better representation of the rainfall associated with the average high flow event in the catchment.

The use of the TRMM monsoonal rainfall patterns highlighted fewer areas with a higher-than-average flood water generation potential. However, the areas identified were the same as those attained from using the TRMM-only storm events and the higher resolution combined rainfall data. In a monsoonal dominated catchment such as the East Rapti that has 80% of rainfall falling within the summer period

(Bookhagen and Burbank, 2010), a coarser temporal resolution could be used if there were time constraints on data processing.

The impact of varying the selection of the chosen flood impact points and corresponding overland flow travel time data was also investigated; the results are shown in Section 3.3.2.3. Whilst the extent of the areas identified by SCIMAP-Flood as having a higher relative potential to generate flood water was impacted to the selection of the impact points were broadly similar the output was sensitive to the removal of specific impact points. The removal of the Hetauda flood impact location, for example, had the clearest impact on the identified extent with large area with a flood risk score > 0.75 to the east of the city no longer having as high a relative flood water generation potential. If using to this as the output from which to spatially target flood management measures in the East Rapti catchment the initial locations for measures would be concentrated in the Manahari sub-catchment and to the west of Hetauda along the main East Rapti channel and not in the area to the east of Hetauda identified using all 6 flood impact points. This sensitivity to the removal of impact points is also seen when removing the Andrauli and Sauraha flood impact points. The removal of both locations concentrated the identified higher relative flood water generating areas to predominantly the area to the east of Hetauda and not along the main East Rapti channel and in the Lothar and Manahari sub-catchments. As noted with the removal of the Hetauda point, a potential catchment management plan would differ based on the differing SCIMAP-Flood inputs.

The removal of one of the overland flow travel time datasets from certain areas within the East Rapti catchment noticeably altered the SCIMAP-Flood output. This can be attributed to reduction in frequency that a particular high relative flood water generating area or sub-catchment appeared in the amalgamated SCIMAP-Flood results. It is therefore necessary to consider the possible effects of the selection, both in number and location, of the flood impact points prior to running the decision support framework. Whilst more computationally expensive, the selection of more flood impact points, in addition to considering the benefits of flood management measures to more settlements, reduces the likelihood that the SCIMAP-Flood output will be impacted by the exclusion of one location.

With no 'perfect' version of SCIMAP-Flood for a given catchment an alternative approach could be to consider the overall sensitivity of the catchment to the range of SCIMAP-Flood inputs through an ensemble approach. The outcome of this approach is illustrated in Section 3.2.2.4 and explores how sensitive areas identified as flood water generating are to the inputs. This approach, however, begins to diminish the rapid, minimal input data criteria which underpins the usefulness of SCIMAP-Flood in providing an initial, simple, risk-based analysis on a catchment-scale. The application of the ensemble approach would begin to encroach on the ground in which a more detailed assessment, perhaps using

a fully distributed catchment-scale model such as CRUM3 (see Chapter 4), would be more sensible to understand the flooding regime in a given catchment.

3.4.5 The application of the SCIMAP-Flood approach in data sparse catchments

There will be differing levels of data available when undertaking the application of SCIMAP-Flood in other catchments, both within a Nepal context and elsewhere around the globe. With SCIMAP-Flood designed to create a quick approach to assessing areas in which to place catchment-scale flood management measures there ideally needs to be simple, easy to access data for any catchment on a global scale.

Whilst the SCIMAP-Flood output created in Section 3.3.2.1 used rainfall data from the Nepalese Governments Department for Hydrology and Meteorology, it has been shown in subsequent Section 3.3.2.2 that there is significant overlap in areas with a higher relative potential to generate flood risk using only TRMM satellite rainfall data. With satellite rainfall data available at a global scale this approach could be applied to catchments that do not have a suitable rain gauge network. TRMM satellite data was used in this research due to length of record and use in prior studies, but as advancements are made then satellite rainfall data with more accurate daily rainfall total estimates and a finer spatial resolution, such as NASAs Global Precipitation Measurement (GPM) rainfall data, can be used.

In addition to the use of a global dataset for rainfall, then both the land cover and elevation data can be attained from global datasets to run SCIMAP-Flood for a given catchment in the absence of regional data. This research, for example, uses ALOS Global Digital Surface Model (AW3D30) elevation data which provides an accurate, freely available DEM. However, as with the rainfall data, there will be improvements made in the accuracy and spatial resolution of satellite-based elevation data in future research. With regards to land cover there are available global land cover datasets in existence, such as the ESA CCI project, that can be applied in SCIMAP-Flood with relative land cover risk weightings attained from literature or developed for a given catchment. Additionally, as used in this project, freely available satellite imagery, such as the Landsat data, can be reclassified to create a land cover dataset designed for a specific catchment.

The use of SCIMAP-Flood Fitted to ascertain the land cover weightings requires risk indicators to run the inverse modelling approach. This was achieved using peak flow estimates throughout the East Rapti catchment, but the approach does require either data collection or available peak flow data throughout the catchment. In order to implement SCIMAP-Flood without the capacity to collect risk indicators to drive the SCIMAP-Flood Fitted inverse modelling approach the land cover weightings would have to be derived from literature or from previous research in different catchments.

There are existing databases, such as HydroATLAS (Linke et al., 2019), that have collated much of the required information, albeit at a coarse (~500 m) resolution, but different catchments, regions and countries will access to specific data and as such implementation of the SCIMAP-Flood framework should be considered on a catchment-by-catchment elevation basis. In the United Kingdom, for instance, freely available high-resolution (1 m) elevation data, nation specific land cover data and a denser rainfall and river flow gauge network would render the creation of the scaled rainfall grids, classified land cover spatial distribution unnecessary and SCIMAP-Flood able to run at a finer resolution.

As shown in Chapter 3, SCIMAP-Flood has been successfully applied to a catchment with limited and, outside of the DHM rainfall gauged data, freely available spatial data. There is available spatial data to run SCIMAP-Flood using available global, rainfall and land cover datasets for catchments with sparsely available regional and local data in a similar approach to that used for the East Rapti catchment. However, to get land cover weightings for a catchment in which there are no available risk indicators to run the SCIMAP-Flood Fitted approach then values will have to be estimated either literature or from donor catchments with similar characteristics.

3.5 CONCLUSIONS

The research presented in this chapter displays the development and implementation of the SCIMAP-Flood Fitted approach within the SCIMAP-Flood framework; using an inverse modelling approach to determine the land use risk weightings for the East Rapti catchment. **The research also showcases the first application of SCIMAP-Flood in a data sparse catchment context and outlines a process suitable for usage in other catchments, comparable to the East Rapti catchment, with poorer data availability.**

SCIMAP-Flood is effective as a decision support framework that can identify the areas within the East Rapti catchment responsible for generating flood waters to the flood impacted communities. The SCIMAP-Flood approach enables the user to determine which flood management interventions could be most suitable for the catchment but is not designed to quantify how effective a given flood management scenario would be. As presented in Chapter 4, further modelling can then be used to assess to effectiveness of a given catchment-scale flood management scenario.

The spatial targeting of flood management measures can be achieved by reconsidering the initial SCIMAP-Flood output. **The SCIMAP-Flood results demonstrated that the eastern part of the East Rapti catchment near Hetuada had the greatest potential to generate flood waters to the six flood impact locations.** There were additional areas along the main East Rapti channel and in the upland areas of the Lothar, Manahari and Rapti sub-catchments that were also identified as having a higher flood water generation potential in relation to the rest of the catchment. **It is in these parts of the catchment that flood management measures would have the greatest positive impact on the flooding regime at the points of flood impact within the catchment.**

Within the East Rapti catchment it is evident that the rainfall patterns associated with assessed high flow events was a key factor in the generation of flood waters and, as a result, both the mountainous north eastern part of catchment and the highly connected agricultural and Built-Up area in the south eastern part of the catchment have a high relative potential to generate flood water.

Designed to run using a minimal data approach, SCIMAP-Flood can be used in both data sparse and data rich catchments. **As illustrated in the East Rapti case study, there is available data to run SCIMAP-Flood using freely available global elevation, rainfall, and land cover datasets for catchments with sparsely available regional and local data.**

The potential influence of varying the SCIMAP-Flood input data needs to be considered when running SCIMAP-Flood. The selection of the spatial resolution of the rainfall data had less of an impact on the identification of flood water generating areas within the East Rapti catchment than selection

of the temporal resolution of the rainfall data. The selection of more flood impact points, in addition to considering the benefits of flood management measures to more settlements, reduces the likelihood that the SCIMAP-Flood output will be impacted by the exclusion of one location.

4 ASSESSING THE CHANGE TO THE HIGH FLOW REGIME UNDER CATCHMENT-SCALE FLOOD MANAGEMENT SCENARIOS USING SIMULATION MODELLING

4.1 INTRODUCTION

There has been a paradigm shift within flood management towards an integrated catchment management approach which implements localised measures whilst considering the impact across the catchment-scale (Evans et al., 2002, Calder and Aylward, 2006; Werrity, 2006; Nisbet and Thomas, 2008; Merz et al., 2010; Nisbet et al., 2011; Lane, 2017). Conversely, Dhakal (2013) notes that the present dominant approach to flood management in Nepal often uses a reactive approach through placing physical flood control measures at points of flood impact. There is a movement, presented in Shrestha et al. (2012), Nepal et al. (2014) and by the Government of Nepal (2017), towards an integrated land and water management approach, undertaken at the catchment-scale that would bring the flood management process in Nepal in line with the global trend and help mitigate some of the flood-related issues that many Nepalese catchments experience.

ICIMOD provide a guide on applicable interventions that combine to form an approach for flood risk management in a Himalayan catchment that involves both soft- and hard-engineering (Shrestha et al., 2012). As in Lane (2017), the addition of soft-engineering at the catchment-scale can improve the effectiveness of hard-engineered flood management measures. Localised hard-engineering interventions applicable to Himalayan catchments include levees and embankments, terracing for slope gradient control and check dams for sediment and discharge control (Shrestha et al., 2012; Shrestha, 2014). Soft-engineering interventions include the use of vegetation for slope stability and retaining soil to maintain or increase the infiltration capacity (Shrestha et al., 2012). Additionally, Dhawan (1993) and Nepal et al. (2014) highlight that with deforestation being a potential cause of increased flood risk in the Himalayas, that afforestation could reduce the risk of flooding.

Land use change and degradation, including the abandonment of agricultural terraces, deforestation, and over-grazing, are key factors with a potential detrimental impact on the hydrological regime in many Nepalese catchments. In parts of the Nepali Himalayan area, up to 30% of the previously cultivated land, predominantly labour intensive, low production, upland terraced agriculture, has been abandoned (Khanal and Watanabe, 2006; Paudel et al., 2014; Jaquet et al., 2015; Ojha et al., 2017). Abandoned terraced agriculture, often in a poor condition, causes significant changes to the hydrological dynamics of hillslopes with a broken terrace walls and risers concentrating runoff,

creating faster overland flows, and thus resulting in an increased catchment peak discharge (Arnaez et al., 2015). Deforestation throughout Nepal has occurred largely due to growing population requiring more fuelwood, more timber for construction and more agricultural land for grazing (Ives and Messerli, 1989; Metz, 1991; Gerrard and Gardner, 2002; Neupane et al., 2015; Chaudary et al., 2016). The annual rate of deforestation in Nepal during the 1980s and 1990s was 1.7% but it has slowed to between 0.06% and 0.18% between the 1990s and 2010 with the implementation of preventative measures (Chaudary et al., 2016). Notably, research indicates that deforestation will continue towards the 2030s as a result of urban expansion (Rimal et al., 2019). Deforestation disrupts the existing hydrological regime through a reduced infiltration capacity increasing overland flow entering the river system, reduced evapotranspiration and additional sedimentation from deforested areas reducing the storage capacity of the channel network (Ives, 1989; Ives and Messerli, 1989; Singh, 2013; Nepal et al., 2014). The hydrological impact of deforestation in the Himalayan region, at the micro-scale, can be seen in a range of research across Nepal and the wider Himalaya region. For example, Gardner and Gerrard (2003) found that the monsoon runoff coefficients (estimated total runoff as a percentage of total rainfall) was 33% for 'degraded forest cover' and only 1% for 'good secondary forest cover'. Sastry et al. (1986) found that the cumulative impact on runoff in a Himalayan catchment experiencing deforestation converted to agriculture resulted in the volume of runoff increasing by 15%, and a 72% increase in peak runoff. However, the role of deforestation on the flood regime in Nepalese catchments is contested with some research indicating that deforestation would have only a minor, localised, role in monsoonal flooding (Gilmour et al., 1987; Hamilton and Pearce, 1987; Metz, 1991; Beschta, 1998; Thomson et al., 2006; van Dijk et al., 2009; Nepal, 2012).

In Chapter 4, the potential impact of a variety of catchment management scenarios for the East Rapti catchment is assessed using CRUM3, a fully distributed hydrological model which operates at a landscape scale (Lane et al., 2009). Research applications of distributed modelling in mountainous watersheds have been undertaken at a range of spatial scales and modelled outputs include the impact of climate change on the hydrological regime (e.g. Mauser and Bach, 2009; Rahman et al., 2012), the impact of snow and glacial melt on the hydrological budget (e.g. Marks et al., 1999; Luo et al., 2012; Pelliccioti et al., 2012), hydrological processes in a mountainous catchment (e.g. Lehning et al., 2006; Li et al., 2012; Nepal et al., 2014; Neupane et al., 2015) and flash flooding (e.g. Zocatelli et al., 2010; Nikolopoulos et al., 2011). With regards to modelling flood management techniques and interventions at the catchment-scale, spatially distributed models have predominantly been used to investigate the impact of catchment-scale afforestation and land use change (e.g. De Roo et al., 2001; Fohrer et al., 2001; Calder et al., 2003; Bronstert et al., 2007; Nepal, 2012; Salazar et al., 2012; Nepal et al., 2015; Dixon et al., 2016).

The CRUM3 output allows for the comparison of hydrographs at multiple locations to test catchment-scale flood management scenarios at all the flood impact points throughout the catchment. The modelling of catchment-scale measures, such as targeted afforestation or check dams in key sub-catchments, can provide quantitative evidence that their implementation would positively impact on the flow regime in the East Rapti catchment. Conversely, scenarios that would have a negative impact on the flood regime within the catchment are also modelled to determine the possible effects of continued deforestation or land degradation.

The research presented in this chapter covers, to my knowledge, the first detailed catchment-scale flood management study using a distributed hydrological model in a Nepalese catchment and provides evidence of an approach that can be used to consider the effect of a mitigation scenario across multiple points of flood impact. The spatially explicit scenarios, in which individual catchment cells can be altered, provides a more accurate picture of the hydrological impact of catchment-scale land use change and possible flow magnitude reduction scenarios than a lumped or semi-distributed model. Additionally, the approach used is the first study using CRUM3 to have spatially distributed rainfall with a scaled rainfall grid providing individual daily rainfall totals for each cell in the catchment.

Notably, this chapter focuses on impact of change on the hydrological regime, predominantly high flow magnitude, from the catchment management scenarios. The impact that a given scenario has on the flood inundation patterns is investigated in Chapter 5. The work undertaken in this chapter builds on the output from the SCIMAP-Flood research (Figure 3.34) with the areas identified as more likely to generate flood waters to the points of flood impact within the East Rapti catchment spatially targeted in the modelled CRUM3 catchment management scenarios. The impact of these scenarios are assessed at the 6 points of flood impact (Figure 3.3) presented throughout the SCIMAP-Flood research; Andrauli, Hetauda, Madi Bridge, Manahari, Lothar and Sauraha.

4.2 METHODS

Figure 4.1 illustrates the approach undertaken in the research presented in this chapter. CRUM3 has previously been used for a variety of academic research relevant to the intended outcome of this project. This research includes assessing the impact of rural land management on flood risk in a large UK catchment (Pattison, 2010), the impact of rural land management on low flows in a small UK catchment (Smith, 2012) and the effectiveness of implementation of catchment-scale natural flood management measures in a small UK catchment (Pearson, 2016; Fraser 2018).

Section 4.2.1 describes the structure of the CRUM3 hydrological model. Section 4.2.2 details the data used to setup CRUM3 for the East Rapti catchment. Section 4.2.3 presents the sensitivity analysis undertaken on the main CRUM3 parameters. Section 4.2.4 critiques the East Rapti dataset used to calibrate CRUM3 for the catchment. Section 4.2.5 describes the implementation of the GLUE approach for uncertainty estimation for the East Rapti catchment using CRUM3. Section 4.2.6 outlines the approach used to spatially represent each of the land cover categories in the East Rapti catchment. The approach used in the creation of the East Rapti catchment scenarios assessed using CRUM3 is shown in Section 4.2.7.

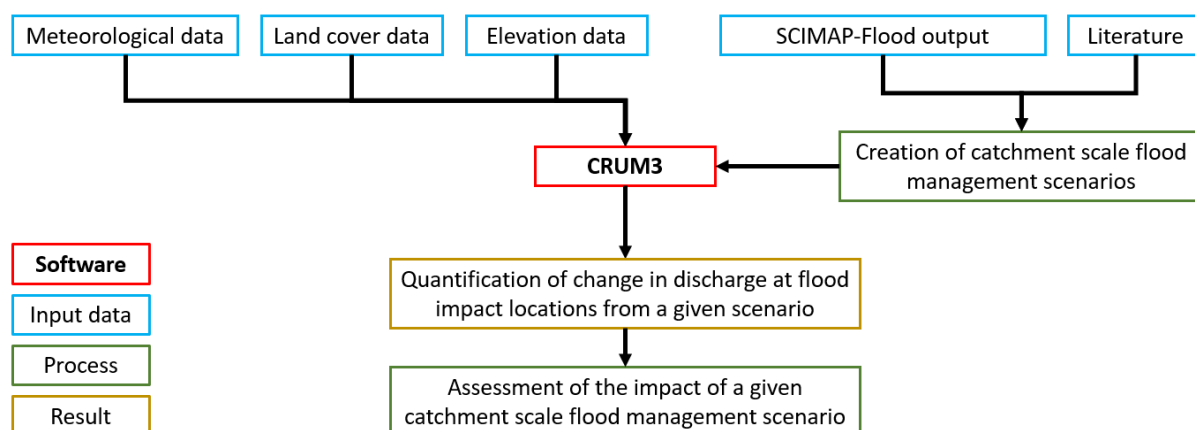


Figure 4.1: A diagram outlining the CRUM3 simulation modelling approach taken in this chapter.

4.2.1 CRUM3

CRUM3 (Connectivity of Runoff Model, v.3) is a fully distributed, object orientated, physically-based hydrological model which operates at a landscape-scale in surface water dominated catchments (Lane et al., 2009). With the flow regime, in particular the high flow regime, dominated by surface runoff generated from monsoon rainfall CRUM3 is a suitable model for the East Rapti catchment (Shilpakar et al., 2011). It was designed to address questions related to the impact on flow extremes from projected climate change and land management techniques whilst using a minimal parameter set derived from accessible national datasets (Lane et al., 2009).

CRUM3 represents the key hydrological processes in a catchment but is reliant on less required data than similar fully distributed models (Lane et al., 2009). These processes comprise of evapotranspiration, canopy interception, infiltration, overland flow, throughflow and river flow. Additionally, the stochastic nature of the weather generator in CRUM3 allows for natural variability during a storm event to be simulated with rainfall generated at the per-second level and then integrated into a computationally efficient variable time step. The river flow predictions are then output on a 15-minute time step. With the high-performance computer cluster available at Durham University, the large computational demands of running the model at a 150 m spatial resolution for the period 2009 to 2011, enabled both a sensitivity analysis and a GLUE approach (Beven and Binley, 1992) to be utilised for the entire East Rapti catchment.

4.2.1.1 CRUM3 model structure

CRUM3 is comprised of four key sections: a weather module, a hydrological processes module, a landscape module, and a river channel network module (Lane et al., 2009). The CRUM3 structure is shown in Figure 4.2 with the details of each of the modules outlined below.

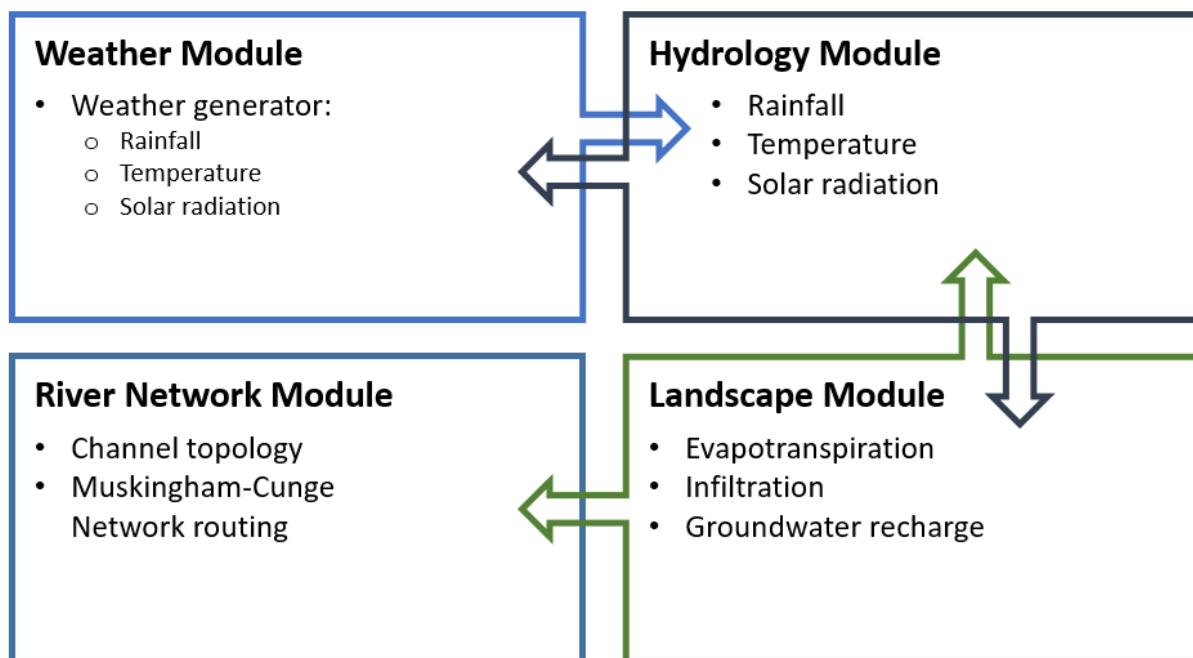


Figure 4.2: A conceptual representation of the CRUM3 model structure (modified from Pearson, 2016 [pp. 34]).

Weather module

Rainfall data is the dominant hydrological input into the modelled catchment with hydrological processes related to rapid overland flow generation, and the corresponding transmission of catchment runoff, calculated at a per-minute timescale. The construction of a per-minute rainfall time series within CRUM3 is done using a stochastic rainfall generator based on the approach used by

Mulligan (1996) and detailed in Lane et al. (2009). The rainfall generator uses data from a tipping bucket rain gauges to characterise the storm events and daily rainfall totals to produce the time series. A Monte Carlo approach was used to create stochastic storm events throughout a day and then generate the per-minute rainfall intensities. The weather module In CRUM3 integrates time-dependent and spatially distributed rainfall, temperature, and solar radiation data. Both the temperature and solar radiation information are used in the calculation of evapotranspiration rate and to define the timing of vegetation growth. Solar radiation was calculated throughout the year based on solar geometry using the day of the year and the latitude of the catchment. The module uses daily maximum and minimum air temperature from observed records with the corresponding values interpolated into per-second temperature values using:

$$T_{a(s)} = \frac{\sin\left(d_s + td + \frac{(12 * 60 * 60)}{4 * 60 * 60}\right) + 1}{2} * (t_{max} - t_{min}) + t_{min} \quad \text{Equation 4.1}$$

where $T_{a(s)}$ is the air temperature at the current second, d_s is the current second of the day, td is the time between midday and the maximum daily temperature, t_{max} is the daily maximum temperature, t_{min} is the daily minimum temperature.

Hydrological processes module

The structure of the hydrological process module in CRUM3 is shown in Figure 4.3. The module simulates interception of precipitation by vegetation, the infiltration of water into soil, the recharge of the aquifer from the soil, the storage of water on the soil surface and the generation of throughflow and surface runoff (Lane et al., 2009; Smith, 2012).

Within CRUM3 the canopy is a non-leaking store throughout the process of rainfall interception. To represent this, the rainfall is split into throughfall and intercepted water in the canopy store. The latter is dependent on canopy gap fraction value and will retain precipitation until the canopy store is full and overflows. Water leaves the canopy store as evaporation. The vegetation type with the catchment and amount of biomass dictates the volume of the canopy storage and percentage of rainfall intercepted.

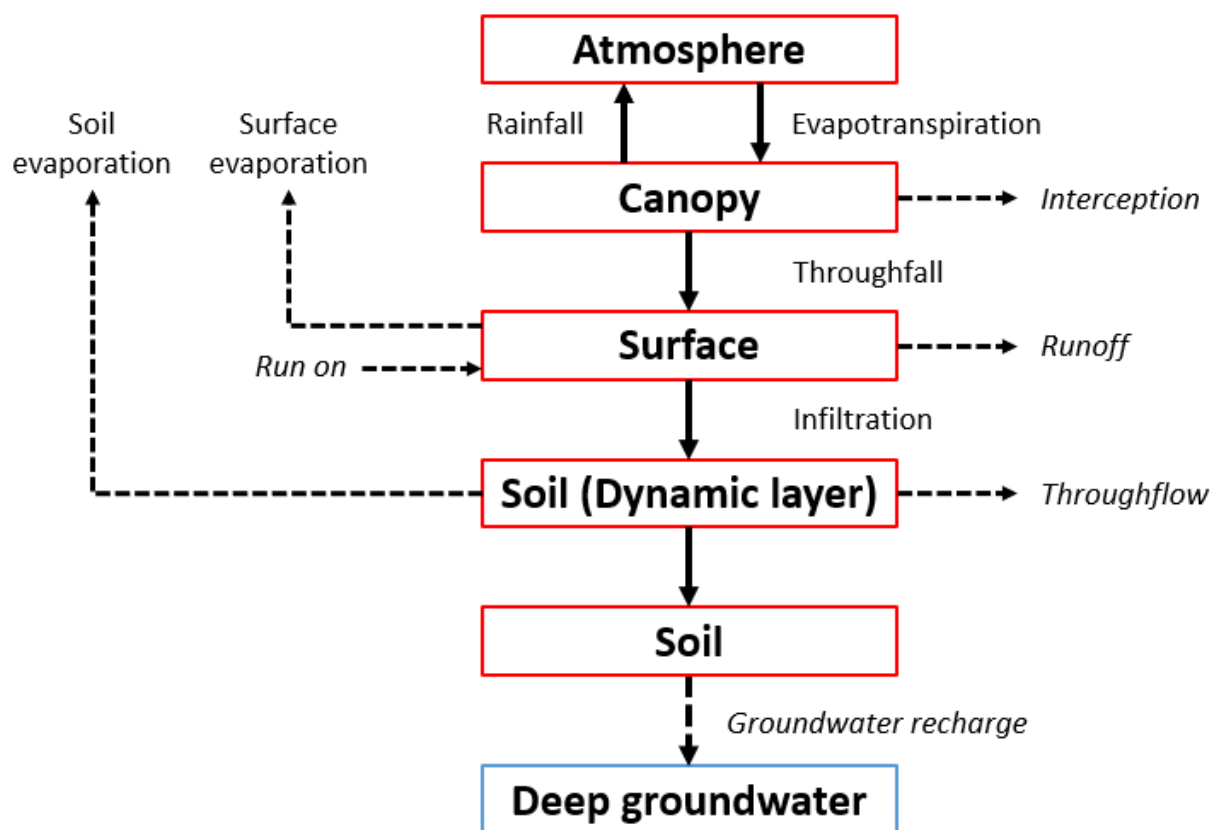


Figure 4.3: A conceptual diagram of the hydrological processes in CRUM3 (modified from Smith, 2012 [pp. 42]). Red boxes are layers represented within CRUM3. Water leaves the soil layer in the CRUM3 model via groundwater recharge.

Evapotranspiration within CRUM3 is calculated using either the Priestley-Taylor (Priestley and Taylor, 1972) or Penman-Monteith equations (Penman, 1948; Monteith, 1965). The Penman-Monteith equation is the more detailed of the two but requires time series data on temperature, solar radiation, wind speed, relative humidity, and vegetation information (Dingman, 1994). Not all this data was available for the East Rapti catchment, and thus the Priestley-Taylor equation (Equation 4.2) was selected as the best compromise between process representation and data requirements. The Priestly-Taylor equation is as follows:

$$PET_{PT} = \frac{a_{PT}\Delta(R_n - G)}{\Delta y} \quad \text{Equation 4.2}$$

where PET_{PT} is the potential daily evapotranspiration, R_n is the net radiation, G is the soil heat flux, Δ is the slope of the saturation vapour pressure temperature relationship, y is the psychrometric constant; and a_{PT} is the Priestley-Taylor constant location parameter, which under normal conditions is 1.26.

The amount of solar radiation at the surface is derived from the energy at the top of the atmosphere, the transmission of the energy through the atmosphere and the reflection of energy by the surface cover. The equations used to determine the amount of energy arriving at the top of the atmosphere

are documented in Dingman (1994). Variations in the amount of energy reaching the surface due to scattering is dependent on atmospheric depth and localised weather conditions with cloud coverage being the dominant factor. In CRUM3, the reduction in energy through a cloud free atmosphere is determined by:

$$R_{ES} = R_{TA} * 0.54.3 \quad \text{Equation 4.3}$$

where R_{ES} is the amount of solar radiation reaching the surface and R_{TA} is the amount of solar radiation at the top of the atmosphere.

Within CRUM3, days that are deemed to have cloud cover have a 50% reduction in solar radiation. This includes all days with rain and additional non-rain days determined using a Monte Carlo model parametrised from observed data. Solar radiation can be either emitted as long wave radiation or directly reflected upon reaching the surface. Albedo determines the amount of radiation that is reflected off the surface and is given as:

$$r_{sw} = R_{ES} * a \quad \text{Equation 4.4}$$

where r_{sw} is reflected short wave radiation and a is the surface albedo. The amount of solar energy reflected as long wave radiation is attributed to both temperature and surface emissivity and is determined by:

$$r_{lw} = e_{ms} * (5.6696 * 10^{-8}) * (T_a + 273.15)^4 \quad \text{Equation 4.5}$$

where r_{lw} is reflected long wave radiation, e_{ms} is surface emissivity and T_a is the air temperature (°C). Once the reflected solar radiation has been subtracted the remainder impacts on the evapotranspiration process.

The actual evaporation of water from the soil surface and vegetation canopy occurs at the calculated potential evaporation rate derived from the Priestly-Taylor equation (Equation 4.2). The potential transpiration is related to the leaf area index of the vegetation and is represented as (Scott, 2000):

$$t_p = PET_{PT} * (-0.21 + 0.7^{LAI}) \quad \text{Equation 4.6}$$

where t_p is potential transpiration, PET_{PT} is potential daily evapotranspiration according to the Priestley-Taylor equation and LAI is the leaf area index. The actual transpiration amount is linked to the availability of water in the dynamic layer, main soil store and the vegetation root depth.

The water retention characteristics of the soil affect the amount of evaporation achieved from water travelling through the soil matrix with a linear relationship that accounts for increased tension at low soil moisture levels:

$$e_{\theta} = PET_{PT}\theta \quad \text{Equation 4.7}$$

where e_{θ} is the soil moisture evaporation rate, PET_{PT} is potential daily evapotranspiration according to the Priestley-Taylor equation and θ is the soil moisture ($\text{m}^3 \text{ water}/\text{m}^3 \text{ pore space}$).

Surface gradient and roughness determine the depth of the surface depression and detention stores. The depression store is the water held within the surface troughs due to roughness and the detention store is water detained above the depression store and, as such, can move as overland flow. From Kirkby et al. (2002) the surface depression store depth is calculated as:

$$\frac{dp}{a} = 0.11 \exp\left(-\frac{0.02B}{a}\right) \quad \text{Equation 4.8}$$

where dp is the surface depression storage capacity (mm), a is the surface roughness and B is the slope gradient.

CRUM3 generates overland flow in three ways: saturated overland flow; return overland flow; and infiltration excess overland flow. With saturated soil conditions, precipitation is no longer able to infiltrate into the soil and is therefore converted to saturated overland flow. Return overland flow occurs when the storage capacity of a cell is exceeded by throughflow entering the cell from upslope and as a result water overflows out of the top of the cell. Infiltration excess overland flow occurs when the rainfall rate is $>$ the soil infiltration capacity and where rainfall will infiltrate at a maximum rate and excess water will develop into overland flow. Infiltration is defined through a simplification of the Green and Ampt (1911) equation developed by Kirkby (1985):

$$i = a + \frac{b}{\theta} \quad \text{Equation 4.9}$$

where i is the infiltration rate, a and b are coefficients and θ is soil moisture.

Soil depth applies notable control on the hydrological processes whilst working at a point-scale. As noted in Huggett and Cheesman (2002), there is a clear relationship between soil depth and geomorphological form and therefore, to represent the differences the soil properties related to surface topography, CRUM3 classifies the landscape into ridges, slopes, channels and plain areas and assigns consistent soil properties to each landscape category.

Within CRUM3 the deep groundwater recharge rate is attained from the minimum hydraulic conductivity at the soil profile base and the hydraulic conductivity of the underlying bedrock. Variation of the CRUM3 bedrock conductivity parameter alters the amount of water that has the potential to leave the surface water catchment into the deep groundwater layer. Deep groundwater flows are not represented within CRUM3 with water leaving the model domain as a separate flux to the surface

water catchment outflows. Water leaving the soil layer to deep groundwater is assumed to leave the surface water catchment to recharge the deep groundwater layer.

The groundwater contribution to the hydrological regime in a southern Nepalese catchment predominantly occurs as baseflow after the monsoon period (e.g. Shilpakar et al., 2011; Nepal, 2012). Notably, with water entering the deep groundwater in CRUM3 not returning to the surface water catchment this limits the model representation of baseflow contribution. However, with the model results not being used for year-round water balance management and instead concentrating on the high flow regime during the monsoon period (where the groundwater layer is being recharged with water from the surface water catchment) CRUM3 is considered to provide a suitable, if simplistic, representation of the groundwater relationship during flood water generation.

Landscape scale processes module

Using a raster grid structure to represent spatial data, each cell in CRUM3 generates and receives water laterally through overland flow and throughflow. Overland flow is represented using the Darcy-Weisbach equation and can occur under laminar, transitional, and turbulent conditions (Abrahams et al., 1992; Baird, 1997):

$$v = \sqrt{\frac{8gRs}{ff}} \quad \text{Equation 4.10}$$

where v is the velocity of overland flow ($\text{m}^3 \text{s}^{-1}$), g is the gravity constant, s is the slope (degrees) and ff is the friction factor.

Through flow volume is determined by Darcy's Law in the saturated zone:

$$tf_v = wt * y * K_d * \frac{dh}{dx} \quad \text{Equation 4.11}$$

where tf_v is the throughflow volume per second ($\text{m}^3 \text{s}^{-1}$), wt is the height of the water table above the bedrock (m), y is the width of the routing facet (m), K_d is the soil hydraulic conductivity at the water table depth (m s^{-1}), h is the hydraulic head (m) and x is the horizontal distance between model cells (m).

The soil hydraulic conductivity is represented through:

$$K_d = K_{sat} \exp\left(\frac{-d}{dc}\right) \quad \text{Equation 4.12}$$

where K_d is the soil conductivity at the water table depth (m s^{-1}), K_{sat} is the soil saturated conductivity, d is the depth of the water table and dc is the decay factor for change in hydraulic conductivity with depth.

The FD8 algorithm is used for the routing of overland flow within CRUM3 (Quinn et al., 1991). Unlike a single flow routing method, such as D8 (O’Callaghan and Mark, 1984), FD8 allows for water to flow from one cell to multiple others which helps the representation of flow dispersion and concentration. The amount of flow allocated to each cell in FD8 is achieved on a slope-weighted basis (Quinn et al., 1991; Freeman, 1991):

$$F_i = \frac{\beta_i^v}{\sum_{i=1}^8 \beta_i^v} \quad \text{Equation 4.13}$$

where β_i is the slope from the central node to a neighbour (i) and v is a positive constant. The v constant is a flow concentration factor. An increased value of v results in an increased concentration of flow, with Holmgren (1994) suggesting a value of between 4 and 6 for distributed modelling.

At each model iteration, the flow directions and hydraulic gradients are updated for both the surface and sub-surface flows. This allows for the surface depressions to fill and overflow, thus providing greater realism.

River channel network module

The Muskingham-Cunge method (Cunge, 1969; Ponce and Lugo, 2001) is used to represent the movement of water in the channel network. The channel network topology is calculated through DEM analysis for flow directions, slope gradients and the upslope contributing area. Each river reach within the channel network is associated with a landscape cell and receives water from both overland flow and throughflow, in addition to receiving water from the upstream river reach. The discharge from a river channel cell is determined by:

$$Q = (C_0 * U) + (C_1 * U_1) + (C_2 * Q_1) \quad \text{Equation 4.14}$$

where Q is existing discharge ($\text{m}^3 \text{s}^{-1}$), Q_1 is the discharge from the previous time step, U is the inflow from the upstream reach, U_1 is the inflow from the upstream reach from the existing time step and C_0 , C_1 and C_2 are routing coefficients. Routing coefficients are explored in detail in Lane et al. (2009).

4.2.2 East Rapti catchment data for CRUM3 model setup

4.2.2.1 Elevation data

As used within the SCIMAP-Flood approach in the previous chapter, Section 3.2.2.1, the ALOS 30 m (AW3D30) product was used for the CRUM3 model for the East Rapti catchment (Tadono et al., 2014; Takaku et al., 2014). To reduce CRUM3 model run times the 30 m grid was resampled to a 150 m grid; the resampling process was undertaken using the ‘Bilinear Interpolation’ option within the ArcMap ‘Resample’ tool. This grid size was chosen to bring the model run times down to minimise the

computational usage whilst maintaining a detailed representation of the East Rapti catchment topography and channel network.

4.2.2.2 Land cover data

The process to create the land cover map used supervised classification of a combination of Landsat 8 satellite imagery and slope and aspect data generated from the ALOS elevation data; this creation process is explained in detail in Section 3.2.2.4. The base land cover data used in CRUM3 for the East Rapti catchment was a resampled version of this land cover map. As with the topographic data, the initial land cover data was resampled from 30 m to 150 m; the resampling process was undertaken using the 'Majority' option within the ArcMap 'Resample' tool.

4.2.2.3 Climate data

To drive CRUM3, a daily time series of minimum and maximum temperature and precipitation is required. A two-year period was selected for the East Rapti CRUM3 model runs: 1st January 2009 to 31st December 2011. This period, as evident in Table 2.2, was selected for having the most complete precipitation record closest to the present day in the DHM data for the East Rapti catchment.

Rainfall data

A gridded rainfall created from a combination of gauged rainfall data from the DHM and satellite rainfall data from the joint NASA and JAXA Tropical Rainfall Measuring Mission was used to represent the spatial variation of daily rainfall across the catchment (Section 3.2.2.3). This product was also used in the SCIMAP-Flood framework for the rainfall data input and the process undertaken to create a gridded rainfall product is described in latter part of Section 3.2.2.3. This combination of gauged rainfall estimates and bias corrected satellite rainfall estimates was used to compensate for areas of the catchment poorly represented by the spatial distribution of the DHM gauge network.

To enter the spatially distributed rainfall into CRUM3, a time series containing the mean rainfall value across all the grid cells that represent the catchment is required. In addition to a time series of the grid-wide daily mean rainfall, a grid of the scaling factor between the grid-wide mean daily rainfall value and the daily rainfall total for each individual cell is necessary. This scaling factor in each cell is then multiplied by the daily mean rainfall within the CRUM3 model to get the total daily rainfall for an individual cell. This approach is used to keep the stochastic weather generator generating uniform storms over the catchment and not operating independently on adjacent cells.

Temperature data

A time series of both minimum and maximum daily temperature for the period 2009 to 2011 was obtained from DHM for the Hetauda meteorological station. This was the only gauge in the East Rapti

catchment that temperature data was available for, and so the temperature from the Hetauda gauge was applied across the whole catchment in CRUM3; the temperature change due to elevation is accounted for within the model. The location of the gauge is shown in Figure 2.8 and has an elevation of 424 mASL.

4.2.3 CRUM3 parameter sensitivity analysis

4.2.3.1 *Single parameter sensitivity analysis*

Sensitivity analysis evaluates the impact of changes of model parameters and inputs on the desired model output (Sorooshian and Gupta, 1995). As a distributed model, CRUM3 has many model parameters and sensitivity analysis can be undertaken to help determine which processes have the greatest impact on the hydrological regime in the catchment (Pechlivanidis et al., 2011). Preliminary assessment eases model calibration through differentiating parameters that greatly impact on the intended output from those that have a negligible influence (Crosetto et al., 2000). This preliminary assessment is done through single parameter sensitivity analysis to determine the most sensitive CRUM3 parameters. The selected sensitive parameters are then advanced to a multiple parameter sensitivity assessment undertaken using the Generalised Likelihood Uncertainty Estimation (GLUE) approach; this stage of the sensitivity analysis is shown in Section 4.2.5.

Each parameter in CRUM3 is assigned an upper and lower bound determined from a review of the literature. The bounds are then used to bracket evenly distributed samples whilst all other parameters are kept at a base value. The impact of each parameter is then assessed by quantifying change in the hydrograph against the base values. For CRUM3 the sensitivity analysis was undertaken using different percentiles from the flow duration curve to understand the response to altering a parameter across a range of flow conditions.

Following previous research using CRUM3 (Pattison, 2010; Baugh, 2010; Smith, 2012; Pearson, 2016) each parameter was altered methodically from the existing base values to encompass a range between the lower and upper values. Each parameter was tested independently with the other soil, land cover and channel parameters kept at base values, with five evenly spaced values between a central base value and both the lower and upper limit. For example, the *Hydraulic Geometry k* parameter would have sensitivity analysis values of: 0.1, 0.28, 0.46, 0.64, 0.82, 1.0, 1.2, 1.4, 1.6, 1.8 and 2.0. The CRUM3 parameter values tested are described in Table 4.1.

Table 4.1: Parameter values for sensitivity analysis (Clapp and Hornberger, 1978; Dingman, 1994; Reaney et al., 2005; Baugh, 2010; Pattison, 2010).

Parameter	Lower Limit	Base Value	Upper Limit
Soil Parameters			
Saturated Conductivity (K_{SAT}) ($m s^{-1}$)	1×10^{-8}	2×10^{-4}	1×10^{-3}
K_{decay} with depth	-9	-3	-1
Soil Porosity (ϕ) (decimal %)	0.01	0.451	0.7
Soil Depth Channels (m)	0.1	1.0	2.0
Soil Depth Slopes (m)	0.05	0.16	1.2
Soil Depth Ridges (m)	0.2	0.5	1.5
Soil Depth Plains (m)	0.2	0.5	1.5
Dynamic Layer Depth (m)	1×10^{-5}	0.05	0.5
Dynamic Layer K_{SAT} ($m s^{-1}$)	2×10^{-5}	9×10^{-3}	2×10^{-2}
Dynamic Layer b parameter	0	4.05	16
Bedrock Conductivity ($m s^{-1}$)	1×10^{-11}	2.5×10^{-10}	1×10^{-7}
Green and Ampt a parameter ($mm hr^{-1}$)	0	10	100
Green and Ampt b parameter ($mm hr^{-1}$)	0	5	100
Land Cover Parameters			
Canopy Gap Fraction (decimal %)	0	0.2	1.0
Maximum Vegetation Height (m)	0	1.0	15
Canopy Interception Depth (m)	0	0.002	0.01
Albedo (decimal %)	0.05	0.1897	0.5
Darcy-Weisbach Friction Factor	1	75	500
Per cent of cell with overland flow (decimal %)	0.1	0.3	1.0
Vegetation Growth Rate ($g s^{-1} m^2$)	0	0.02	1
Vegetation Growth Threshold ($^{\circ}C$)	0	5	10
Channel Routing Parameters			
Hydraulic Geometry k	0.1	1.0	2.0
Hydraulic Geometry m	0.1	0.32	0.5
Discharge per unit width ($m^2 s^{-1}$)	0.1	5.0	10.0

The sensitivity of the parameters in Table 4.1 was assessed using the flow duration curve (FDC) for the modelled period where the percentage of time a specified flow is equalled or exceeded can be quantified. Using the FDC was preferred over just selecting the maximum flow to ensure that sensitivity of a parameter to low flows was also accounted for. Despite this study concentrating on high flows the combined approach ensures that the model could be setup for catchment management issues centred on low flows without rerunning the sensitivity analysis. For this research, the sensitivity analysis was undertaken using data from the entire year of 2009 in the East Rapti catchment.

Both low and high flows were considered during sensitivity analysis with the average change in maximum discharge, Q01, Q05, Q50, Q95 and Q99 between the model run with the altered parameter and the model run with the existing base value parameter figures being used. Q01 refers to the

discharge being equalled or exceeded one percent of the time and Q99 refers to the discharge equalled or exceeded ninety-nine percent of the time. This quantification was achieved using:

$$Cd_i = \frac{A_v - B_v}{B_v} * 100 \quad \text{Equation 4.15}$$

where Cd_i is the change in discharge for i (maximum discharge, Q01, Q05, Q50, Q95 and Q99), A_v is the altered discharge value and B_v is the base value discharge value. And then followed by:

$$F_{cd} = \frac{\sum_{i=1}^n Cd_i}{n} \quad \text{Equation 4.16}$$

where F_{cd} is the final change in discharge, Cd_i is the change in maximum discharge, Q01, Q05, Q50, Q95 and Q99 percentiles and n is the number of variables.

4.2.3.2 Single parameter sensitivity analysis results

The average percentage change for the CRUM3 parameters across the five chosen percentiles and maximum discharge is shown in Figure 4.4. It is evident that some CRUM3 parameters such as the *Soil Depth Channel* (average % change in discharge of 0.39%) and *Maximum Vegetation Height* (0.35%) parameters were unresponsive to change, and thus the change from the existing base value has a minimal influence on the hydrological regime in the East Rapti catchment model. Other parameters, including the *Bedrock Conductivity* (30.90%), *Soil Porosity* (22.81%) and *KSAT* (15.86%) parameters, exhibited a significant hydrological response to parameter change across both high and low flows.

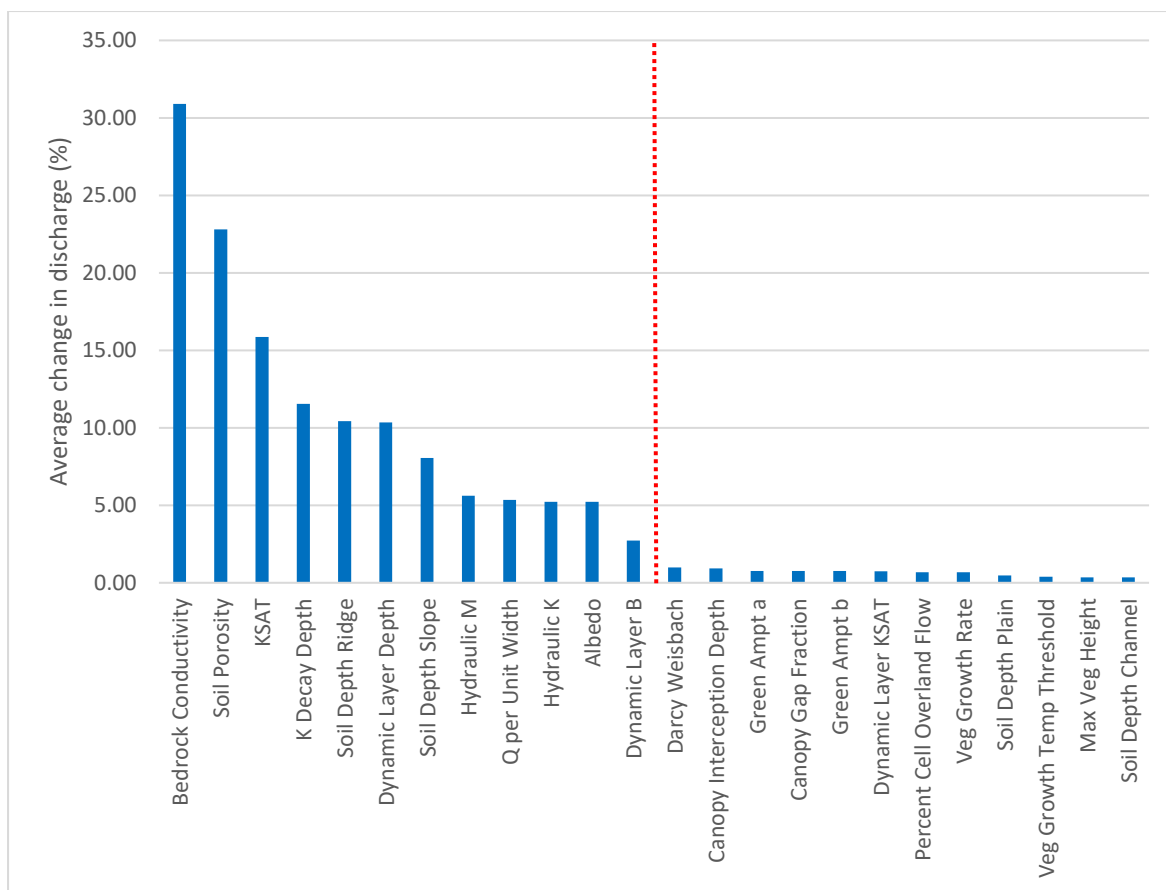


Figure 4.4: Average percentage change in discharge for Q01, Q05, Q95 and Q99 for each CRUM3 model parameter. Parameters to the left of the red line were used in the GLUE experiment.

Whilst this study is concentrated on flood risk reduction and high flows there is also a need to consider low flows and ensure that the model represents these conditions effectively. Therefore, the twelve most sensitive parameters averaged from discharge change for maximum discharge, Q01, Q05, Q50, Q95 and Q99 were taken forward to be varied in the GLUE approach (Section 4.2.5). The selected parameters had an average change in discharge of > 2.5% with the other parameters have a change of < 1%. These parameters are *Bedrock Conductivity, Soil Porosity, KSAT (Saturated Conductivity), K_{decay} with depth, Soil Depth Ridge, Dynamic Layer Depth, Soil Depth Slope, Hydraulic Geometry m, Q per unit width, Hydraulic Geometry k, Albedo and Dynamic Layer B*.

4.2.4 East Rapti data for CRUM3 model assessment and calibration

4.2.4.1 River flow data

In order to assess and calibrate a model such as CRUM3, a performance measure was required to assess each run's performance at predicting the observed river flow values from the selected time period. Gauged river flow data from the DHM was attained for the three gauging locations within the East Rapti catchment. The locations of these gauges are shown in Figure 2.8 and a summary of the hydrology of the catchment, including information on the flow data, is given in Section 2.5 with a data

critique in Section 2.6.3. It is notable that there was not a gauging location towards the downstream end of the main East Rapti channel.

4.2.4.2 Selected river flow data for model assessment and calibration

Discussed in more detail in Section 4.2.5 below, the GLUE model runs are assigned a performance measure that is required to assess the ability of each model run at predicting the observed values from the selected period. The observed values for the East Rapti model set up and calibration are taken from the DHM daily flow data for the period 2009 to 2010. This period was selected for having the most continuous period of precipitation and temperature – key climatic drivers of the CRUM3 model – in the available DHM data for the East Rapti catchment.

After a pilot investigation following preliminary CRUM3 model runs (Section 2.6.3), several issues became apparent within the DHM daily flow data for the modelled period. These issues include anomalous annual hydrograph patterns, probable missing decimal points within the acquired data and extended periods of either high or low flow followed by an unexpected, rapid change. It was deemed from the investigation that the Manahari gauged data for 2009 and 2010 was not suitable for model calibration purposes as was excluded from the model evaluation process; there was no evident global solution to correcting the flow data to a usable format. In contrast, the Lothar and Rapti gauges exhibited no obvious issues throughout the 2009 to 2010 period and the gauged data at both sites is therefore used in the model assessment and calibration process.

4.2.5 CRUM3 GLUE approach

4.2.5.1 East Rapti GLUE approach

Equifinality is the concept whereby more than one combination of parameters can result in the same outcome and thus have the same model performance strength (Pechlivanidis et al., 2011). Therefore, we cannot think of there being one preferred model parameter set, but instead a group of equally suitable parameter sets (Beven, 2006; Pechlivanidis et al., 2011). With a move towards more robust uncertainty frameworks in hydrological modelling, the GLUE approach (Beven and Binley, 1992) uses Bayesian estimators to evaluate the likelihood that different combinations of parameter sets are suitable predictors of hydrological behaviour (Wainwright and Mulligan, 2004). GLUE utilises a Monte Carlo simulation and a likelihood measure, such as Nash-Sutcliffe efficiency, to determine the degree of acceptability of a model (Pechlivanidis et al., 2011). The approach aims to avoid over-conditioning to obtain a single parameter set and allows subsequent model runs to use an ensemble of parameter sets to give predictions (Pechlivanidis et al., 2011).

The main limitation of using the GLUE approach is the dependency of a cut-off threshold value to define acceptable (behavioural) and unacceptable (non-behavioural) simulations (Pechlivanidis et al.,

2011). Additionally, with the number of model runs required to complete the GLUE analysis, there is a high associated computational cost, especially with fully spatially distributed models. The result of the GLUE analysis enables a full assessment of model predictive uncertainty within the final output and thus gives a clearer indication into predicted changes in flood flows.

GLUE parameter choices

The GLUE approach uses groups of parameters to develop an ensemble of potential model outputs. Consequently, different parameter sets could perform equally well at predicting the observed flow (Stedinger et al., 2008; Pechlivanidis et al., 2011). The parameter sets selected for GLUE analysis are the most responsive parameters from the single parameter sensitivity analysis. The twelve most sensitive parameters selected for the GLUE approach are *Bedrock Conductivity*, *Soil Porosity*, *KSAT (Saturated Conductivity)*, *K_{decay} with depth*, *Soil Depth Ridge*, *Dynamic Layer Depth*, *Soil Depth Slope*, *Hydraulic Geometry m* , *Q per unit width*, *Hydraulic Geometry k* , *Albedo* and *Dynamic Layer B* .

Latin Hypercube sampling

Whilst the Monte Carlo simulation method is widely used for uncertainty problems in hydrological modelling it depends on random number generation to sample parameter space and requires a great number of model runs to represent all probable results (Beven, 2009; Pechlivanidis et al., 2011, Milledge et al., 2012). Based on Binley et al. (1991) and Beven and Binley (2014), it is ascertained that 1×10^{12} model runs would be required to adequately cover the parameter space using the Monte Carlo method, taking an estimated 9.13×10^8 years of CPU time (based on the 8 hour simulation length using the 150 m grid and simulating the entire 2009 to 2010 period) and thus a more effective method is necessary. This increase in efficiency can be achieved using less informed approaches in which segments of probability distributions are split or stratified (Jackson, 2007). The Latin Hypercube sampling technique is such an alternative solution which divides the range of values for each parameter into ordered segments of equal probability and combines individual samples to produce parameter ensembles (Helton and Davis, 2003).

The Latin Hypercube sampling approach was developed using the *lhsdesign* function in MATLAB (MathWorks, 2018). Through $X = lhsdesign(n,p)$ a n -by- p matrix (X) is returned; this contains a Latin Hypercube sample of n values on each of p variables (MathWorks, 2018). For each column of X , the n values are randomly distributed with one from each interval $(0,1/n)$, $(1/n,2/n)$, ..., $(1-1/n,1)$, and are randomly arranged (MathWorks, 2018). The *lhsdesign* function generates Latin Hypercube samples to find the most suitable distribution across the parameter bounds according to the criteria of '*maximin*' which maximises the minimum distance between points and '*correlation*' which reduces correlation. As in previous research using CRUM3, for this investigation the criterion was set to

'*maximin*'; 100 iterations were used and a sample size for of 5,000 was deemed appropriate for 12 variables (Smith, 2012; Pearson, 2016). Additionally, the upper and lower parameter values used for the sensitivity analysis were run three times, the mean parameter values run three times, and the base values five times. The use of the Latin Hypercube sampling design ensures that each model simulation adds the greatest amount of information on the behaviour of the model since it removes redundancy of multiple model simulations with similar parameterisation. This experimental design culminated in 5,014 model runs, taking an estimated 4.01×10^4 years of CPU time in comparison, which were completed on a High-Performance Computing cluster at Durham University.

4.2.5.2 *East Rapti GLUE model evaluation*

On completion of the 5,014 GLUE model runs, a performance measure was required to assess each run's performance at predicting the observed values from the selected time period. There are numerous model performance indicators and methods with comparisons of the indicators discussed in depth in an array of literature (e.g. Legates and McCabe, 1999; Krause et al., 2005; Moriasi et al., 2007; Bennett et al., 2013). The choice of method to assess the measure of agreement between modelled and observed data is an important factor in any modelling study with the degree of confidence in a prediction and the replication of the observed data (Westerberg et al., 2011). A combination of the several model performance indicators, often covering different aspects of the hydrograph, can provide the most rounded approach to selecting the best representation of the catchment (Gupta et al., 1998; Freer et al., 2003; Westerberg et al., 2011).

Traditionally, model evaluations are undertaken using formal statistical procedures (Coffey et al., 2004; Westerberg et al., 2011). The formal statistical approaches can be divided into three categories: standard regression, dimensionless and error index (Legates and McCabe, 1999; Moriasi et al., 2007). The standard regression statistics, such as Pearson's correlation coefficient (r) and the coefficient of determination (R^2), provide information on the linear relationship between the modelled and observed data. The dimensionless statistics, such as the index of agreement (Willmott, 1981) and Nash-Sutcliffe efficiency (NSE) (Nash and Sutcliffe, 1970), produce a relative model evaluation. The error indices, such as mean absolute error (MAE), root mean square error (RMSE) and percent bias (PBIAS), determine the deviation between the modelled and observed data. Of the formal statistical approaches, Moriasi et al. (2007) recommend using NSE and PBIAS for model evaluation whilst Legates and McCabe (1999) suggesting that NSE is the most appropriate measure available in conjunction with MAE or RMSE. Both papers agree that, and further supported in Willmott (1981), error indices should be used in addition to a dimensionless statistic such as NSE during model evaluation.

Other approaches to model evaluations use informal evaluation measures (Westerberg et al., 2011). These measures often employ hydrological signals to reflect the behaviour of the modelled catchment that the simulations should be able to reproduce (Wagener et al., 2007; Winsemius et al., 2009; Carrilo et al., 2011; McMillan et al., 2012; Shafii and Tolson, 2015 for example). Examples of hydrological signatures that have been successfully used for model evaluation include flow duration curves (Yadav et al., 2007; Yilmaz et al., 2008; Westerberg et al., 2011), rising limb density (Shamir et al., 2005; Yadav et al., 2007; Shafii and Tolson; 2015), peak distribution (Sawicz et al., 2011; Shafii and Tolson, 2015), base flow index (Arnold and Allen, 1999; Vrugt and Sadegh, 2013) and the spectral density of runoff (Winsemius et al., 2009).

Assessing the GLUE model performance

Following a review of model performance measures, and taking into consideration the CRUM3 model structure and the quality control issues with the available gauged river flow data, a combination of methods were used to select the CRUM3 model parameters that best represent the East Rapti catchment. The first approach uses the formal statistical methods to establish the best performing model runs with the second approach utilising an informal hydrological signatures method. The combined approach used to assess model performance helps assess uncertainty within the available flow data and creates the capacity for presenting the uncertainty in the modelled flood management scenarios.

Of the 5,014 model runs undertaken within the GLUE approach, the best performing 8 model runs for both the Lothar and Rapti catchments were selected under both the traditional formal statistical approach and the hydrological signatures method. This selection provides the top 32 model runs, and the corresponding parameter sets, which were taken forward into the catchment-scale flood management scenarios in Section 4.2.7.

Formal statistical model evaluation approach

The formal statistical approach used for model evaluation used a combination of NSE and MAE. NSE was selected as one of the methods for the CRUM3 model evaluation as it is the most common technique for model performance analysis within the field of hydrology (Schaeffli and Gupta, 2007). The Nash-Sutcliffe efficiency is calculated as:

$$NSE = 1 - \frac{\sum_{i=1}^n (O_i - P_i)^2}{\sum_{i=1}^n (O_i - \bar{O})^2} \quad \text{Equation 4.17}$$

where O_i is the observed discharge at time (i), P_i is the modelled discharge at time (i) and \bar{O} is the average observed discharge. NSE is a normalised measure with a range of between 1, for a perfect fit between the modelled and observed data, and $-\infty$. An NSE value of 0 indicates that the model is performing on a par with only the use of the mean observed value as a prediction. In a review on reported NSE values, Moriasi et al. (2007) found that NSE values deemed satisfactory ranged from > 0.36 to > 0.80 depending on the model used and available data.

MAE is an error index that is commonly used in model evaluation (Moriasi et al., 2007). Along with RMSE and mean square error (MSE), MAE indicates error between two variables in the units of interest ($\text{m}^3 \text{s}^{-1}$ in this instance) and is attained using:

$$MAE = \frac{\sum_{i=1}^n |O_i - P_i|}{n} \quad \text{Equation 4.18}$$

where O_i is the observed discharge at time (i), P_i is the modelled discharge at time (i) and n is the number of data points in the time series. A MAE value of 0 indicates a perfect fit between the observed and modelled flow data. As noted in Singh et al. (2004), MAE values of $<$ half the standard deviation of the observed data can be considered suitable for model evaluation.

The formal statistical approach to the CRUM3 model evaluation used NSE values of the daily flow data from 2009 as a calibration dataset and from 2010 as a validation dataset for both the Lothar and Rapti gauges. To account for the stochastic weather generator in CRUM3, the NSE values were obtained using a 3-day moving average of the daily flow data through the time series. This approach was necessary as daily rainfall totals are distributed stochastically through the creation of a per-minute rainfall time series and thus high magnitude rainfall events and the corresponding high flow events could occur later in the day or on the following day rather than in the observed gauge data.

Of the 5,014 model runs, only those with a NSE value of > 0.6 for both the calibration data and validation data remained. The model runs that met these criteria were then ranked by MAE and the eight runs with the lowest MAE value for both the Lothar and Rapti gauges selected for the catchment-scale flood management scenario modelling.

Hydrological signatures model evaluation approach

The informal approach used for model evaluation used a combination of hydrological signatures. The hydrological signatures used were peak distribution (PD), rising limb density (RLD), autocorrelation (AC), s and the standard deviation (SD), mean and median of the flow data in the time series (Shamir et al., 2005; Yadav et al., 2007; Sawicz et al., 2011; Euser et al., 2013; Shafii and Tolson, 2015). Additionally, the NSE of the Flow Duration Curves (FDC) between the observed and modelled

hydrographs was factored into the model evaluation as a representation of the overall behaviour of the catchment (Yadav et al., 2007; Yilmaz et al., 2008; Blazkova and Beven, 2009; Westerberg et al., 2011; Euser et al., 2013). A commonly used hydrological signature, comparison of FDCs using NSE, allows for the evaluation of the magnitude of the flows and without focusing on timing problems and missed or unrepresented events due to rainfall patterns (Euser et al., 2013).

Peak distribution (PD) is a measure of showing the differences in the height of peak discharges throughout the time series defined as when both the previous and subsequent daily flows are lower than the present time step. Using the PD hydrological signature, factoring in the high peak flows, gives an indication of relative peak heights within the hydrograph whilst accounting for measurement errors (Sawicz et al., 2011; Euser et al., 2013) and the flow timings due to the stochastic weather generation in the CRUM3 model structure. A flow duration curve is constructed from all the peaks in the time series and the slope between the 10th percentile and 50th percentile calculated. Following Euser et al. (2013), PD is calculated as:

$$PD = \frac{Q_{10} - Q_{50}}{0.9 - 0.5} \quad \text{Equation 4.19}$$

where Q_{10} is the peak flow exceeded 10 percent of the time and Q_{50} is the peak flow exceeded 50% of the time.

Rising limb density (RLD) is a measure of that indicates the smoothness of the hydrograph. Independent of flow volume, RLD is calculated by dividing the number of peaks in the time series by the total time the hydrograph is rising (Shamir et al., 2005; Yadav et al., 2007; Euser et al., 2013). RLD is, therefore, the inverse of the mean time-to-peak and is calculated as (Shamir et al., (2005):

$$RLD = \frac{N_{peaks}}{T_{rising}} \quad \text{Equation 4.20}$$

where N_{peaks} is the number of peaks and T_{rising} is the time (days) where the hydrograph is rising.

As with RLD, autocorrelation (AC) is a measure of the smoothness of the hydrograph with a high AC value indicating a small difference between two respective points (Euser et al., 2013). AC is used as a hydrological signature to represent the timing of the peaks (Euser et al., 2013). As in Winsemius et al. (2009), Euser et al. (2013) and Shafii and Tolson (2015), a lag of 1-day was used in the derivation of AC. This entails a data point within the hydrograph being compared to the previous days data point. AC is calculated as (Shafii and Tolson, 2015):

$$AC = \frac{\sum_{i=1}^{n-1} (Q_i - \bar{Q})(Q_{i+1} - \bar{Q})}{\sum_{i=1}^n (Q_i - \bar{Q})^2} \quad \text{Equation 4.21}$$

where Q_i is the flow at a given time step and \bar{Q} is the average flow from the time series.

A final hydrological signature of an NSE value of each FDC, both from the modelled runs and the observed data, was also calculated from the entire data period. The FDC for each time series was sampled, as per Westerberg et al. (2011), at 19 intervals. This was done with even intervals between the 95th percentile and the 5th percentile (e.g. 5th, 10th, 15th...to...85th, 90th, 95th percentiles) and the NSE was then calculated between each of the 5,014 modelled runs and the observed data for both the Lothar and Rapti gauges. The NSE of the FDCs was calculated using (Nash and Sutcliffe, 1970):

$$NSE_{FDC} = 1 - \frac{\sum_{i=1}^n (O_{FDC} - P_{FDC})^2}{\sum_{i=1}^n (O_{FDC} - \overline{O_{FDC}})^2} \quad \text{Equation 4.22}$$

where O_{FDC} is the observed FDC at time (i), P_{FDC} is the modelled FDC at time (i) and $\overline{O_{FDC}}$ is the average observed FDC. As with the NSE, the FDC comparison using NSE is a normalised measure with a range of between 1, for a perfect fit between the modelled and observed data, and $-\infty$.

In addition to PD, RLD, AC and NSE of the FDC of each time series, the standard deviation, mean and median of the flow values in the entire hydrograph were calculated. These hydrological signatures are used, amongst others, in Shafii and Tolson (2015).

For each of the model runs in the GLUE approach, the hydrological signatures of the modelled time series were compared to the observed hydrological signatures. An absolute hydrological signature ratio (*absHS*) was created for each of the signatures above; excluding the FDC comparison which is already comparing the modelled and observed data. The *absHS* ratio was calculated using:

$$absHS = 1 - ABS \left[\frac{O_{hs} - P_{hs}}{O_{hs}} \right] \quad \text{Equation 4.23}$$

where O_{hs} is the observed hydrological signature value, P_{hs} is the modelled hydrological signature value and *ABS* making the ratio an absolute value. The *absHS* works so that a value of 1 would mean that the modelled hydrological signature value is the same as the observed hydrological signature value.

Each of the *absHS* values and the FDC NSE value were then normalised between 0 and 1; 1 representing the highest and 0 the lowest value of the model runs. The normalised values were then averaged for each model run with the top 8 (those with the highest average value) for both the Lothar and Rapti gauges selected for the catchment-scale flood management scenario modelling.

4.2.6 Spatial representation of land cover in CRUM3

The variation in the areal coverage and type of land cover has the potential to have a significant impact on the hydrological regime of the catchment. With the selected top 32 GLUE model runs having

utilised a homogenous catchment land cover and soil properties, it is necessary to apply weighted land cover and corresponding soil categories to the model to improve the representation of the East Rapti catchment. The weighting and distribution of the land covers within the East Rapti catchment allows for the assessment of catchment-based land management techniques and interventions through the alteration of vegetation and soil properties as part of the simulated catchment-scale flood management scenarios.

The land cover data, based on the supervised classification approach discussed in Section 3.2.2.4 and shown in Figure 2.6, was used to represent the spatial land cover distribution in the East Rapti catchment. This classification was done to make 7 land cover categories that cover the catchment: *Rainfed Agriculture, Irrigated Agriculture, Shrubland, Forest, Built-Up Area, Bare Ground* and *Water*. The classified land cover produced in Section 3.2.2.4 was resampled from 30 m to 150 m to use in CRUM3 using the ‘Majority’ setting on the ArcMap ‘Resample’ tool with the resampled land cover data evident in Figure 4.5.

Legend

Base

-  Rainfed Ag.
-  Irrigated Ag.
-  Shrubland
-  Forest
-  Built Up Area
-  Bare Ground
-  Water

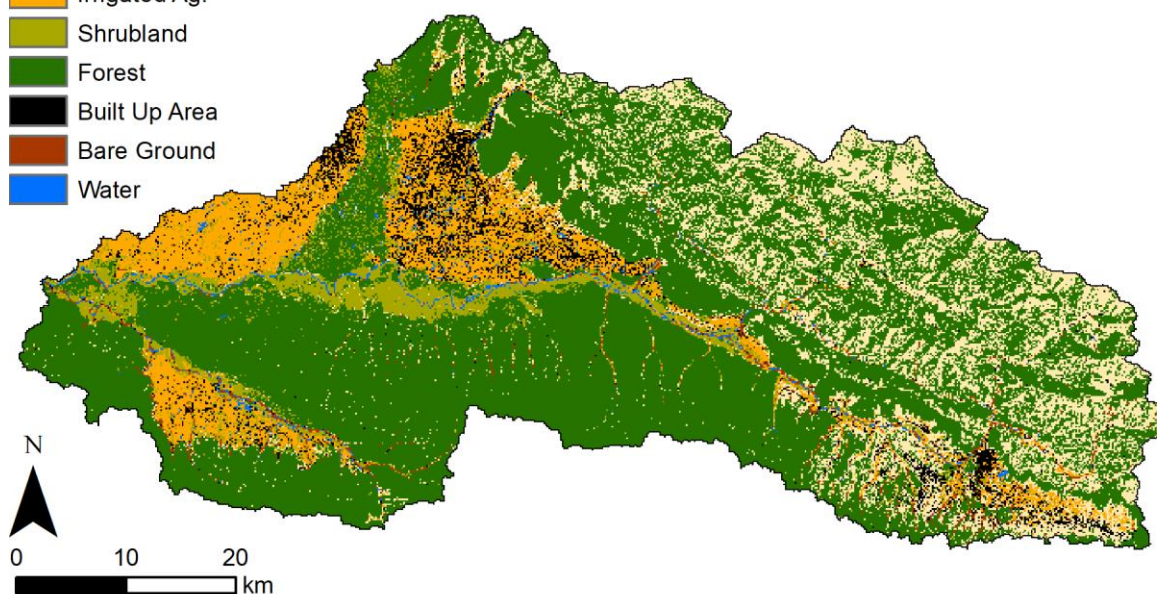


Figure 4.5: The 150 m base land cover spatial pattern resampled from the supervised classification land cover data

Soil and land cover parameter values, for parameters in the CRUM3 model, were acquired from literature for the seven land cover categories. For the distribution of the land cover and soil parameters, the *Water* category was included with the *Bare Ground* category. These values are used to describe the relationship between the land cover categories for each CRUM3 parameter. The attained values for the land cover parameters used in CRUM3 are illustrated in Appendix 7.20 and

7.21 with the soil parameters in Appendix 7.22. As in Smith (2012) and Pearson (2016), figures established from literature given as zero were represented as 1^{E-9} as the division of zero gives infinite solution.

The CRUM3 parameter values from literature highlight the disparity between the different land covers. It is essential to represent the variation between the land cover parameters from the GLUE results. The existing area of each land cover in the East Rapti catchment was considered during the proportional rescaling of the parameters for the top 32 ranked GLUE runs. With 58% coverage of the East Rapti catchment, *Forest* was the dominant land cover category for use in the rescaling process which was used in Pearson (2016). The rescaling process is achieved through:

$$A = \frac{LITvalue}{Forest\ LITvalue}$$

$$B = A * GLUEvalue$$

$$C = A * B$$

$$D = LCOVarea * C$$

$$E = (Rainfed\ Ag.\ D + Irrigated\ Ag.\ D + Shrubland\ D + Forest\ D + Built\ Up\ Area\ D + Bare\ Ground\ D)$$

$$Scaled\ CRUM3\ Parameter\ Value = C * \left(\frac{GLUEvalue}{E} \right)$$

Equation 4.24

where *LITvalue* is the parameter value as derived from literature, *GLUEvalue* is the corresponding parameter value from one of the top 32 GLUE model runs, *LCOVarea* is the area of the relevant land cover and the six catchment land covers used in the scaling process are represented with *Rainfed Ag.*, *Irrigated Ag.*, *Shrubland*, *Forest*, *Built Up Area*, *Bare Ground*.

This proportional rescaling creates individual parameter values for each land cover in the top 32 ranked GLUE runs whilst maintaining the original representation of the East Rapti catchment discharge. An example of the rescaled parameters is shown in Table 4.2. The rescaled parameters are used for the creation of soil and land cover parameter sets for each of the six land covers. The spatial distribution of the parameter sets is represented through a land cover map in CRUM3 and the spatial data can be manipulated to simulate land cover change.

Table 4.2: An example of a rescaled parameters across the different land covers for one of the top GLUE model runs.

CRUM3 Parameter	Original value	<i>Rainfed Agriculture</i>	<i>Irrigated Agriculture</i>	<i>Shrubland</i>	<i>Forest</i>	<i>Built-Up Area</i>	<i>Bare Ground</i>
Albedo	0.4305	0.4858	0.6073	0.3644	0.3887	0.5344	0.3401

4.2.7 The development of catchment-scale scenarios using CRUM3

Following sensitivity and GLUE analysis to establish the top 32 parameter sets for the East Rapti catchment, CRUM3 was then used to simulate a variety of catchment-based land management scenarios to assess the potential impact of implementation on the flood regime across the catchment. The scenarios are assessed though comparing the flow hydrographs at the points of flood impact with the flow hydrographs from the existing base land cover scenario (see Figure 4.5). This impact assessment is made at each of the six flood impact points originally discussed in the SCIMAP-Flood research; Andrauli, Hetauda, Madi Bridge, Manahari, Lothar and Sauraha (see Figure 3.3).

This section outlines the creation process used to simulate the catchment scenarios for the East Rapti catchment. The created scenarios are hypothetical but informed from a combination of existing literature, stakeholder consultation and previous experience creating spatially targeted catchment-scale scenarios for CRUM3 (Pattison, 2010; Smith, 2012; Pearson, 2016). Section 4.2.7.1 discusses the initial bounding scenarios made using complete coverage of the catchment with each of the six main land cover categories. The main catchment scenarios were then split into potential flow magnitude increasing scenarios (Section 4.2.7.2) that simulate future land use change, such as deforestation, and potential flow magnitude reducing scenarios (Section 4.2.7.3) that simulate flood management practices, such as spatially targeted afforestation. A third set of combined scenarios (Section 4.2.7.4) that test the potential impact of flood management practices at offsetting future negative land use change within the East Rapti catchment. Section 4.2.7.5 provides an overview of the scenarios that were run on CRUM3, including Table 4.3 which contains the scenario IDs that each scenario is referred as within the results and discussion.

4.2.7.1 *Blanket catchment coverage*

An initial land cover change scenario was made with complete coverage of the East Rapti catchment with each of the six main land cover categories. Though unrealistic in their implementation, these scenarios gave an indication of the greatest predicted impact that potential land use change could have on flows within the catchment (Smith, 2012; Pearson, 2016). The scenarios were created through reclassifying, using the 'Reclassify' tool on ArcMap, all the land cover data to represent a single land cover category. An example output using blanket coverage of forest can be seen in Figure 4.6.

Legend

Blanket (to Forest)

-  Rainfed Ag.
-  Irrigated Ag.
-  Shrubland
-  Forest
-  Built Up Area
-  Bare Ground
-  Water



Figure 4.6: The blanket coverage of the catchment using the Forest land cover class.

4.2.7.2 Flow magnitude increase through land use change and degradation scenarios

Deforestation around the populated fringes within the catchment

A potential scenario exhibiting deforestation around the populated areas of East Rapti catchment was created to test future land use change experienced in many Nepalese catchments. With a key driver of deforestation in Nepal being an increased population depending on expanded agricultural output and fuelwood, the perimeter of the populated part of the East Rapti catchment was digitised (Nepal, 2012; Neupane et al., 2015; Chaudary et al., 2016). From this a shapefile of a buffer was created using the 'Buffer' tool on ArcMap. A buffer width of 500 m was used to replicate continued deforestation of the accessible parts of the forested areas in the East Rapti catchment. The deforestation scenarios model a loss of 5.1% of the existing *Forest* cover which is equivalent to approximately 25 years of future tree-felling in accordance with the higher annual rate of deforestation from Chaudary et al. (2016). The areas within the shapefile buffer were altered to represent land use change to *Irrigated Agriculture*, testing agricultural expansion of the Terai region in the catchment, and *Shrubland*, testing vegetation growth on deforested land from increased grazing and overharvested fuelwood. The *Forest* to *Shrubland* scenario is proposed in modelled land cover scenarios by Nepal (2012) as a realistic conversion; an example of the change in Figure 4.7. The deforestation scenarios offer a different, more spatially realistic, perspective to scenarios modelled by Neupane et al. (2015) who used slope and

elevation characteristics to determine percentage change of forest coverage in different hydrologic response units in the SWAT semi-distributed model.

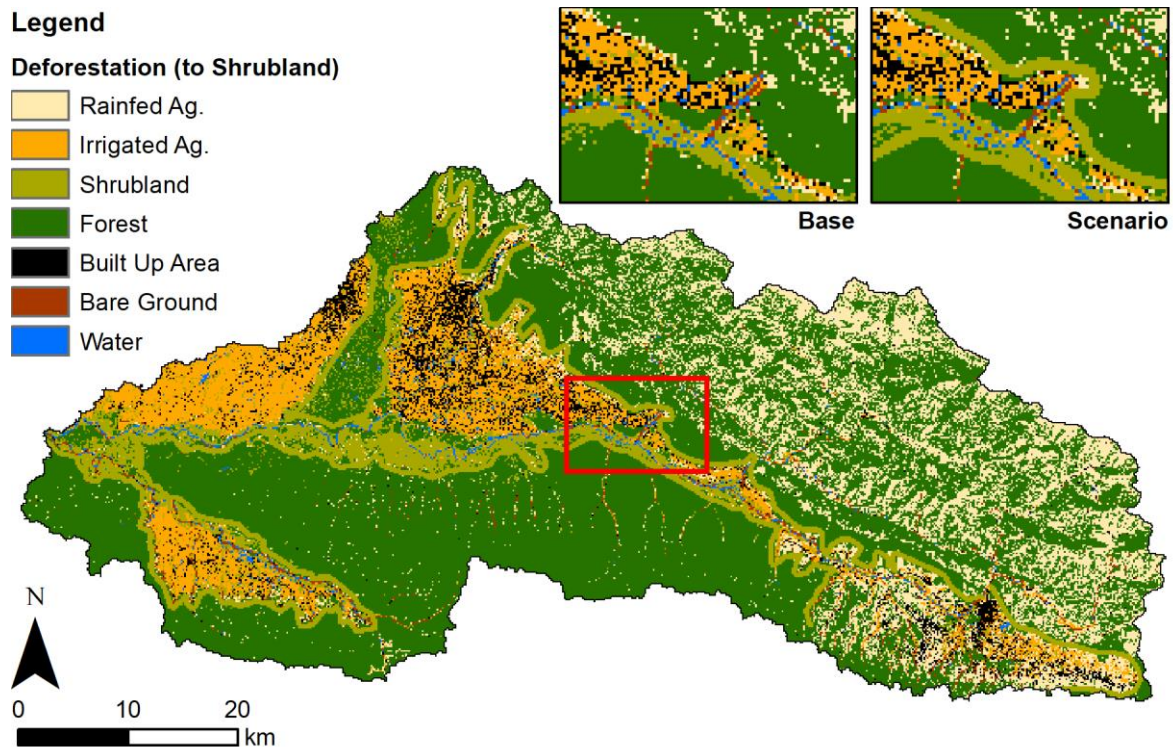


Figure 4.7: The deforestation land use change scenario with areas of Forest around the populated part of the catchment replaced with Shrubland. See inset for a comparison between the scenario and base land cover for the extent within the red box.

Urban expansion

With Nepal one of the most rapidly urbanising populations in South Asia a land cover change scenario assessing the impact of increased urbanisation, and the corresponding changes to the hydrological regime, through the expansion of the larger settlements within the East Rapti catchment was created (Nepal et al., 2014; Rimal et al., 2019). The existing boundary of the cities Hetauda in the east and Bharatpur in the west, in addition to the larger towns of Ratnanagar and Khairahani in the central part of the catchment, were digitised and a buffer of 1 km was made, using the ‘Buffer’ tool on ArcMap, to represent a larger area housing the increased urban population. The land cover within the buffered area is altered to represent the *Built-Up Area* land cover with an example of the change seen in Figure 4.8. The enlargement of only the larger settlements along the main transport route within the catchment in the urbanisation scenario was informed by an assessment of historic land use change by Rimal et al. (2019) in a Terai catchment. The CRUM3 urban expansion scenario increased the percentage coverage of *Built-Up Area* in the East Rapti catchment from 4.3% to 6.1%; this areal increase of 42% is comparable to the 38.51% increase in urban area between 2016 and 2026 modelled by Rimal et al. (2019).

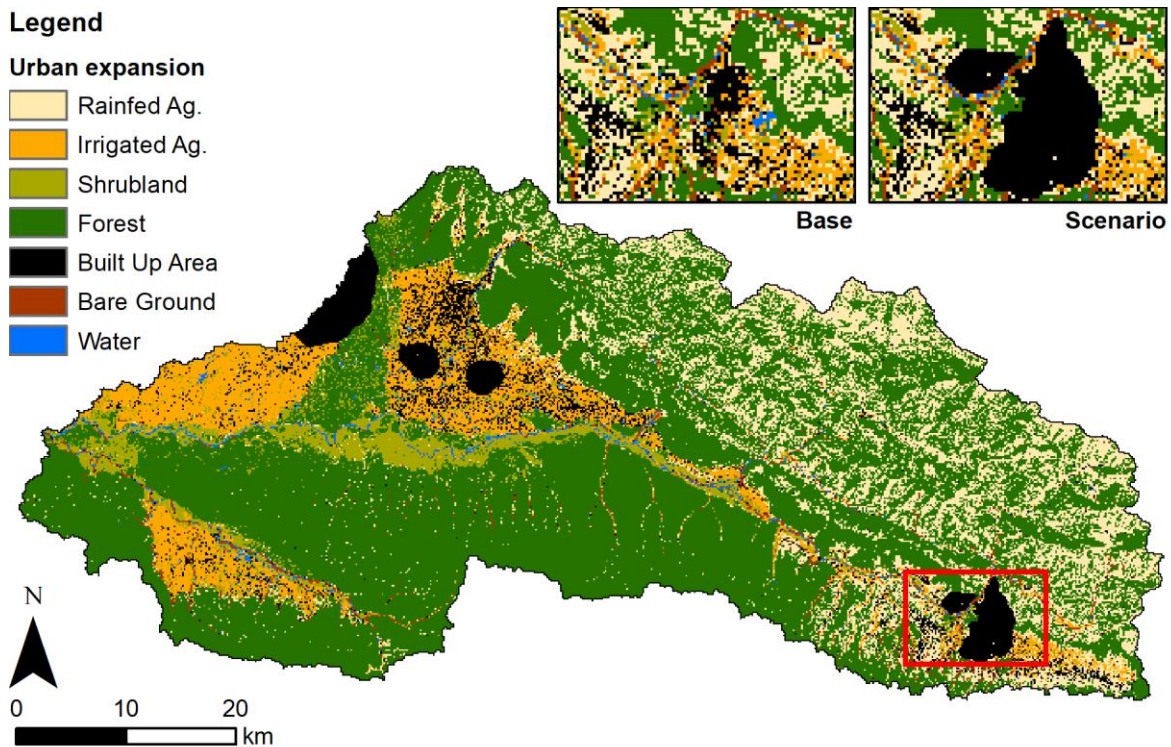


Figure 4.8: The urban expansion scenario with Built-Up Area increased around four settlements using a 1 km buffer. See inset for a comparison between the scenario and base land cover for the extent within the red box.

Land degradation due to terrace abandonment

Since the 1990s, an accelerating proportion of the upland, rainfed agriculture in Nepal has become underutilised or permanently abandoned (Paudel et al., 2014; Jaquet et al., 2015; Ojha et al., 2017). Paudel et al. (2014) notes that in the lower hills, encompassing the East Rapti catchment, 33% of agricultural land is being abandoned. Terrace abandonment in areas of *Rainfed Agriculture* is characterised through a change in the land cover to *Bare Ground* to represent the bare soil conditions and *Shrubland* to represent vegetation growth on abandoned terraces; the conversion of *Rainfed Agriculture* to *Shrubland* is the dominant transition (Jaquet et al., 2015). With no information on the spatial pattern of terrace abandonment in the East Rapti catchment the scenarios created converted 50% of randomly selected *Rainfed Agriculture* cells. The 50% conversion reduces the catchment coverage of *Rainfed Agriculture* from 18.0% to 9.0% and represents an extreme future scenario simulating the upwardly increasing trend of agricultural land abandonment (Paudel et al., 2014). The random selection of *Rainfed Agriculture* cells throughout the catchment was done using the ‘Random Selection’ tool in QGIS after converting the base land cover raster to points to differentiate between the land cover class values. An illustration of the 50% terrace abandonment scenario to *Shrubland* is shown in Figure 4.9.

Legend

Terrace abandonment (to Shrubland)

-  Rainfed Ag.
-  Irrigated Ag.
-  Shrubland
-  Forest
-  Built Up Area
-  Bare Ground
-  Water

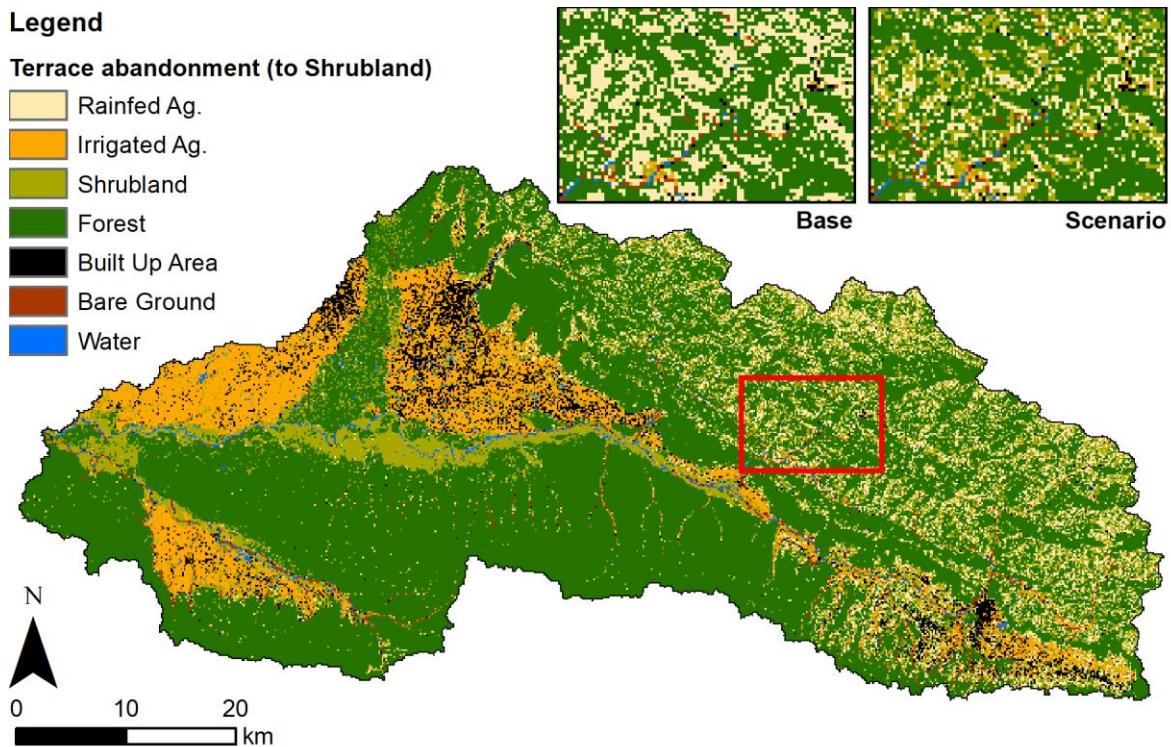


Figure 4.9: The terrace abandonment land use change scenario with 50% of the Rainfed Agriculture in the catchment converted to Shrubland. See inset for a comparison between the scenario and base land cover for the extent within the red box.

Combined land use change

A combined land use change scenario was created to simulate urban expansion, deforestation, and terrace abandonment within the East Rapti catchment. Notably, the individual scenarios are not mutually exclusive with an urbanising population increasing localised deforestation and abandoning rural upland agricultural practices (Jaquet et al., 2015; Chaudary et al., 2016; Ojha et al., 2017; Rimal et al., 2019). This scenario, shown in Figure 4.10, combines the land use changes that many Nepalese catchments are facing to test the cumulative impact on the hydrological regime. The areas of deforestation and terrace abandonment are converted to *Shrubland* to represent unmanaged vegetation growth.

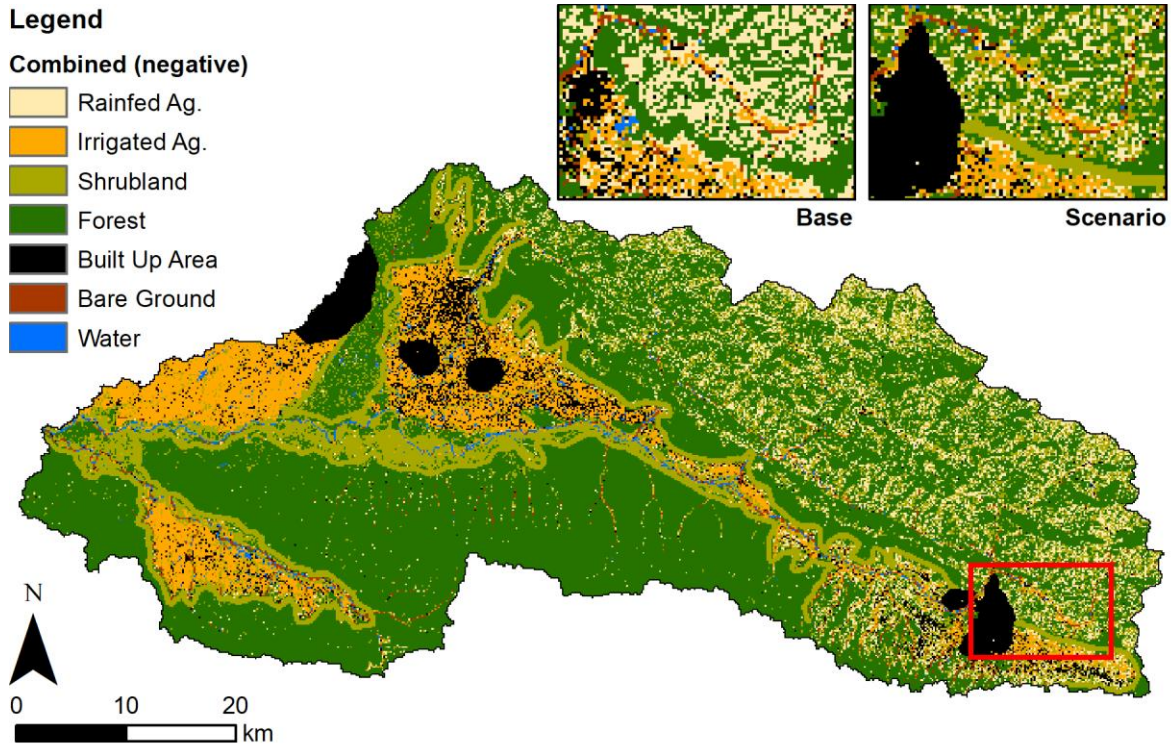


Figure 4.10: The combined urban expansion, deforestation and terrace abandonment scenario within the East Rapti catchment. Both the deforested and abandoned areas are converted to Shrubland. See inset for a comparison between the scenario and base land cover for the extent within the red box.

4.2.7.3 Flow magnitude reduction using spatially targeted flood management measures scenarios

Spatial targeting afforestation using the SCIMAP-Flood output

The SCIMAP-Flood output (see Section 3.3.2.1) for the East Rapti catchment identified areas within the catchment that are more likely to generate flood waters to the points of flood impact. These flood water generating areas can be targeted with positive land use change, such as afforestation, to provide the greatest positive impact on the flooding regime (Salazar et al., 2012; Shrestha et al., 2012; Iacob et al., 2017). Targeted afforestation scenarios, often in areas meeting particular slope or land cover criteria, have been used in previous modelling studies (for example Salazar et al., 2012; Iacob et al., 2017). A SCIMAP-Flood informed spatial targeting approach used for a small UK catchment in Pearson (2016) and a larger UK catchment in Reaney and Pearson (2016); the Pearson (2016) research used the SCIMAP-Flood output to afforest specific fields and field boundaries that were identified as key flood water generating parts of the catchment.

The SCIMAP-Flood output for the East Rapti catchment has been used to create catchment management scenarios using this spatial targeting. Areas that the SCIMAP-Flood output identified as 'more likely' to be flood water generating (SCIMAP-Flood value > 0.50) and 'very likely' to be flood water generating (SCIMAP-Flood value > 0.75) have land cover changes applied to test the applicability

of spatial targeting within the East Rapti catchment. Testing a proposed positive impact to the flood regime these flood water generating areas have been reclassified as *Forest*.

In addition to using the original SCIMAP-Flood output, a similar series of scenarios have been created using the SCIMAP-Flood output reinterpreted using point density analysis. This approach establishes simplified regions of higher flood water generation potential through selecting areas within the East Rapti catchment that have a high density of flood water generating cells. An example of both spatially targeted scenarios with a SCIMAP-Flood value of > 0.50 is shown in Figure 4.11 and Figure 4.12.

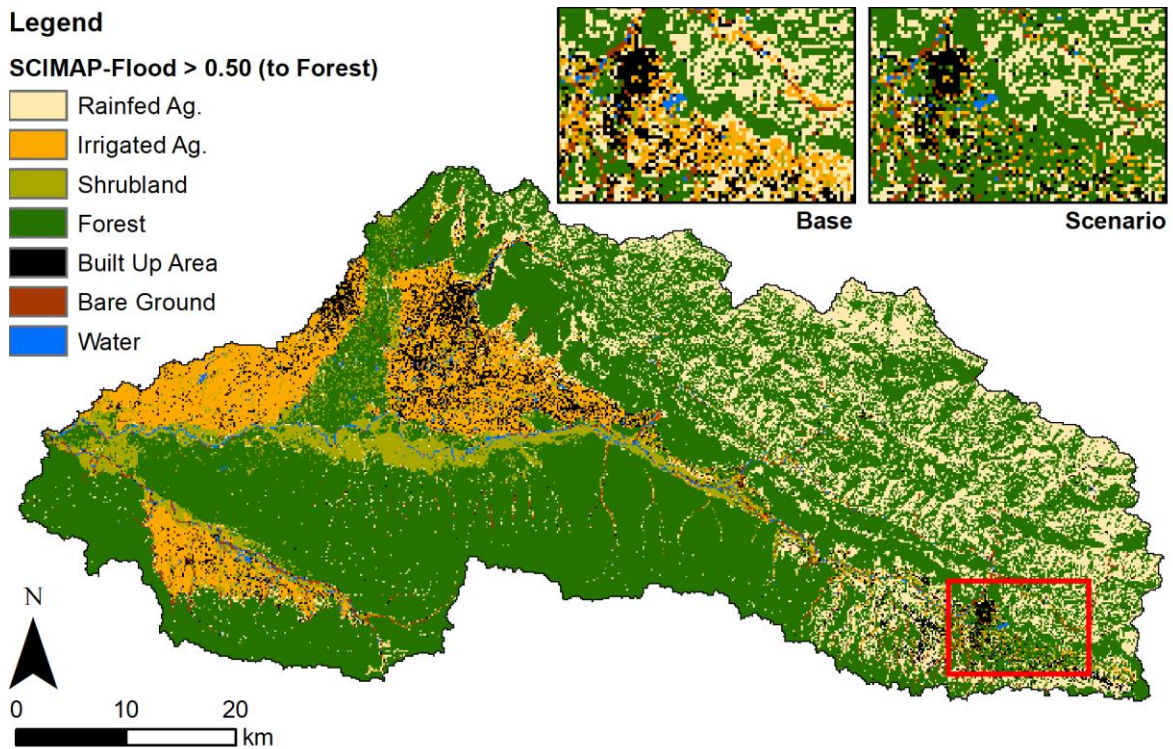


Figure 4.11: The targeted afforestation scenario areas of the catchment with a SCIMAP-Flood value > 0.50 . See inset for a comparison between the scenario and base land cover for the extent within the red box.

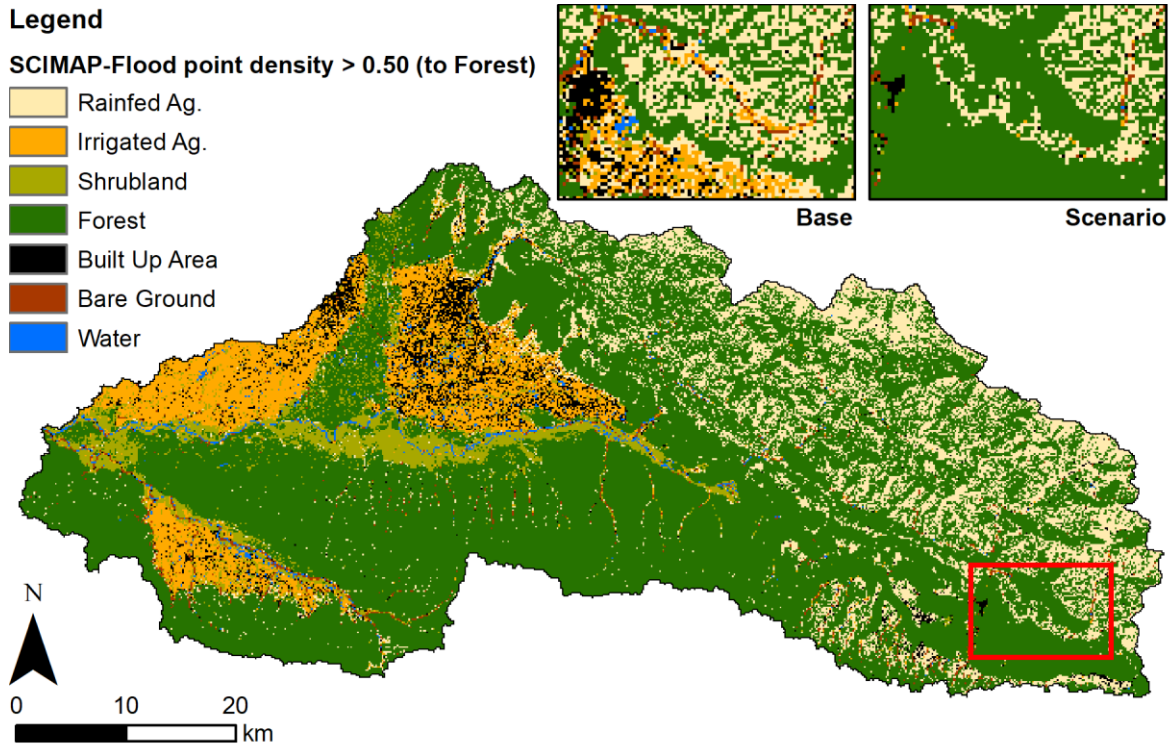


Figure 4.12: The targeted afforestation scenario areas of the catchment with a SCIMAP-Flood value > 0.50 derived from point density analysis. See inset for a comparison between the scenario and base land cover for the extent within the red box.

Spatially targeting the implementation of check dams using the SCIMAP-Flood output

Check dams are small, low drop structures constructed of a wide range of materials, including concrete and wood, that are built across the channel to help decrease the velocity of flow and the channel slope gradient; see Figure 4.13 (ICIMOD, 2012; Abbasi et al., 2019). Placed at intervals in the higher gradient, upper reaches of the catchment, the structures help reduce high flows through retaining water and sediment (ICIMOD, 2012; Xu et al., 2013; Abbasi et al., 2019). Check dams can be split into open-check dam and closed-dam categories with the former having a slit or grid opening to help flush sediment through and the latter requiring deposited sediment to be periodically removed. Open-check dams are more appropriate for a sediment rich channel system such as in Nepal (Shrestha, 2014).



Figure 4.13: Examples of four different check dams (from Abbasi et al., 2019 [pp. 689]).

Check dams are difficult to represent in a model at a catchment-scale due to the complex hydraulic processes involved at the local scale. They have been represented using CRUM3 through the ability to restrict flow to a set value for specific selectable channel reaches in the channel network. Each of the chosen channel reach restriction points, see Figure 4.14, are at the downstream end of sub-catchments in the upper parts of the East Rapti catchment. The flow will be restricted at these locations to simulate the impact of a chain of check dams being implemented along the channel network upstream of the restriction point. Based on detailed hydraulic modelling of open-check dams in an upland Nepalese sub-catchment by Shrestha (2014) a high flow reduction of 10% at the chosen flow restriction points is used to model check dam implementation throughout the sub-catchment. The conservative 10% flow reduction also represents the smallest check dam size modelled by Shrestha (2014) and is more conservative than the lowest rainy season peak flow reduction (14.7%) from check dams modelled in Xu et al. (2013). As such, a 10% flow reduction will be applied to the 99.9th percentile flow to each selected sub-catchment.

The sub-catchments in which the assessment of check dam implementation is made were chosen based on the SCIMAP-Flood output and Strahler stream order. The Strahler stream order was calculated using the channel network with only smaller sub-catchments (those with a Strahler value of 1 to 2) considered for check dams. Two check dam scenarios are modelling using CRUM3 within

sub-catchments in areas with a SCIMAP-Flood score > 0.50 and > 0.75 , chosen respectively. In both scenarios the existing baseline land cover spatial distribution (Figure 4.5) is used.

Legend

- > 0.75 Check Dams
- > 0.50 Check Dams
- Channel Network
- SCIMAP-Flood > 0.75
- SCIMAP-Flood > 0.50

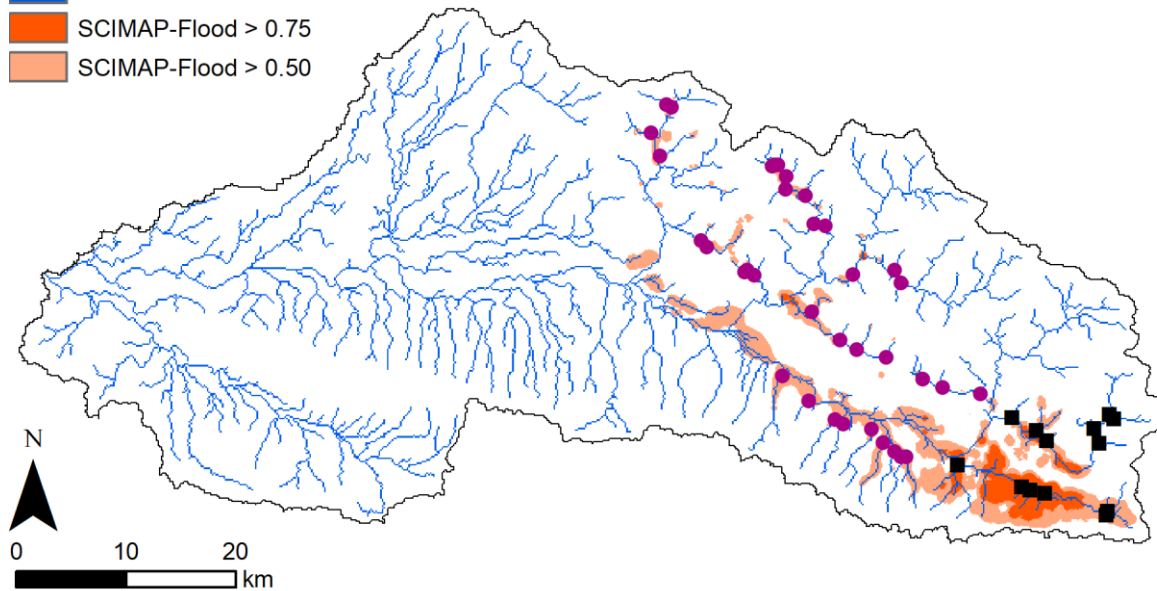


Figure 4.14: The distribution of sub-catchments with check dams implemented in based on the point density analysis of the SCIMAP-Flood output.

Afforestation of abandoned terraces

With unmanaged terrace abandonment (Section 4.2.7.2) represented through converting areas of *Rainfed Agriculture* to *Bare Ground* and *Shrubland*, the representation of managed terrace abandonment is undertaken through converting areas of *Rainfed Agriculture* to *Forest*. This scenario represents a proactive approach to reducing the impact of terrace abandonment on the flooding regime with the afforestation occurring on abandoned or underutilised land rather than spatially targeted areas as in the SCIMAP-Flood informed scenarios. With an increasing proportion of the upland, rainfed agriculture in Nepal being abandoned (Paudel et al., 2014; Jacquet et al., 2015) there is a potential opportunity to afforest on available land for flood risk reduction benefits (Shrestha et al., 2012; Nepal et al., 2014). As with the unmanaged scenarios, a scenario was created that converted 50% of randomly selected *Rainfed Agriculture* cells to *Forest*. The selection of *Rainfed Agriculture* cells to be altered are the same randomly selected cells as those converted to *Bare Ground* or *Shrubland* in the unmanaged terrace abandonment scenarios.

Combined spatially targeted flood management

Two scenarios were created that combined the spatially targeted afforestation from the SCIMAP-Flood point density analysis output and the targeted check dam implementation in highlighted sub-catchment. A scenario was created for the spatial targeting for areas with a SCIMAP-Flood value of > 0.50 and > 0.75 ; the > 0.50 combined flood management scenario is shown in Figure 4.15.

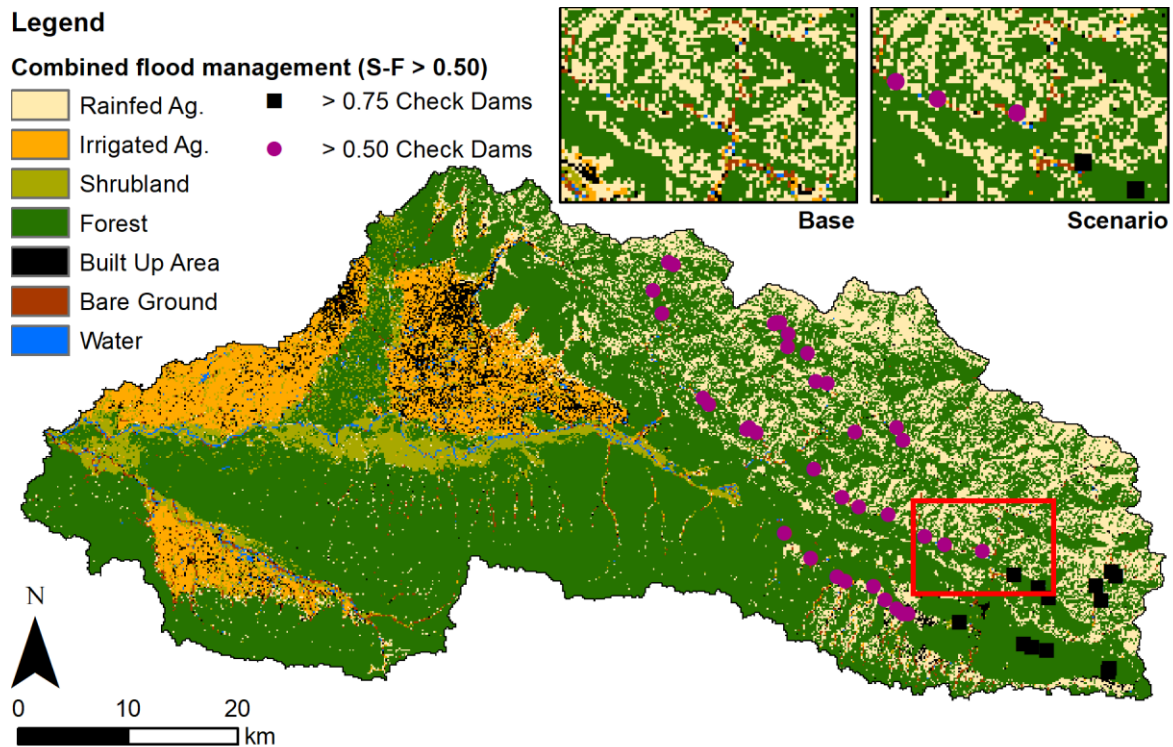


Figure 4.15: The combined spatially targeted afforestation and check dam flood management scenario using point density analysis of the SCIMAP-Flood output (SCIMAP-Flood values > 0.50). See inset for a comparison between the scenario and base land cover for the extent within the red box.

4.2.7.4 Offsetting flow magnitude increasing land use change with spatially targeted flood management measures scenarios

A final set of scenarios were created that merged the combined land use change scenario, shown in Figure 4.16, with the spatially targeted flood management approaches from Section 4.2.7.3 to quantify the impact of offsetting the impact of future land use change on the flood regime in the catchment. The combined land use change scenario was merged with both spatially targeted afforestation from the SCIMAP-Flood point density analysis, spatially targeted check dams and a combination of both spatially targeted afforestation and check dams. These scenarios were created for spatial targeting in areas with a SCIMAP-Flood value of > 0.50 and > 0.75 . Figure 4.16 shows the combined land use change scenario with spatially targeted afforestation in areas with a SCIMAP-Flood value > 0.75 .

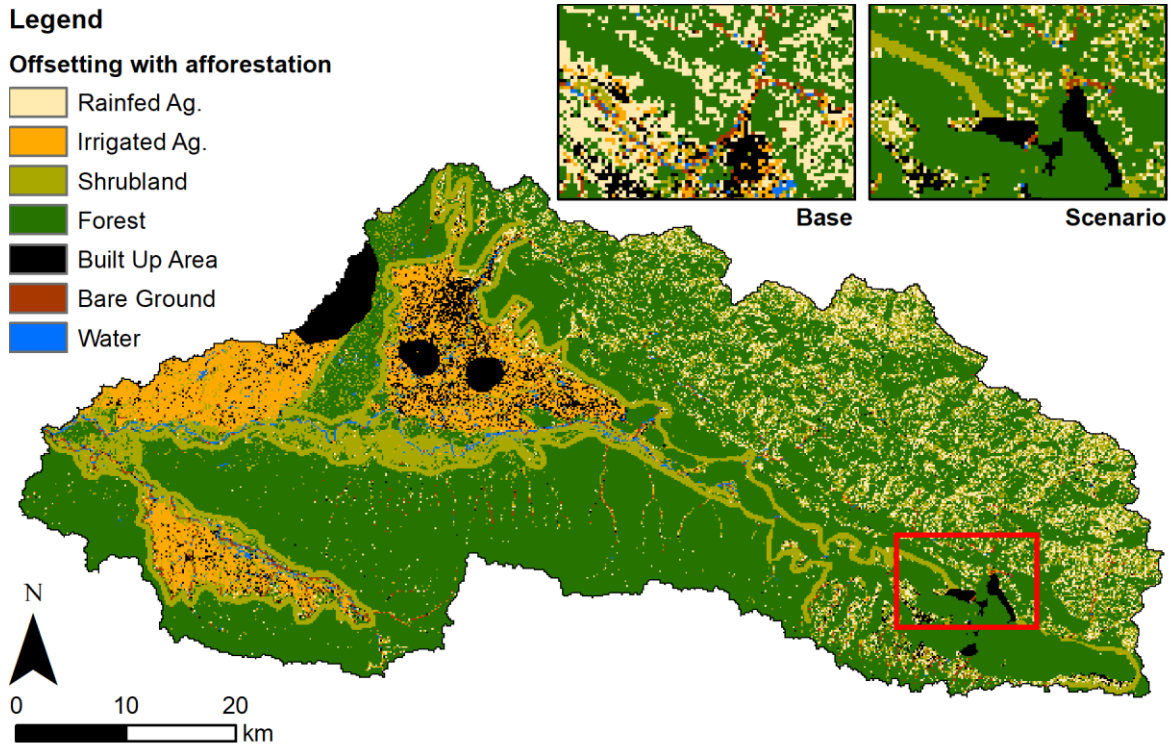


Figure 4.16: *Offsetting the combined land use change (urban expansion, deforestation and terrace abandonment) through the use of targeted afforestation from point density analysis of the SCIMAP-Flood output (SCIMAP-Flood value > 0.50). See inset for a comparison between the scenario and base land cover for the extent within the red box.*

4.2.7.5 East Rapti catchment-scale scenarios overview

The complete list of modelled scenarios and the corresponding scenario ID for each given scenario is presented in Table 4.3. A total of 27 catchment-scale scenarios were modelled using the 32 run model ensemble. These runs include 6 blanket coverage scenarios to help find the upper and lower bounds of the impact on flow magnitude due to land cover change, 6 flow magnitude increasing land use change scenarios, 9 flood management through flow magnitude reduction scenarios and a further 6 scenarios that investigate offsetting future negative land use change with a catchment-scale flood management approach.

Table 4.3: A description of each catchment-scale scenario for the East Rapti catchment and the corresponding scenario ID.

BOUNDING RUNS	SCENARIO ID
Blanket coverage (Bare Ground)	<i>BLA_BG</i>
Blanket coverage (Built-Up Area)	<i>BLA_BUA</i>
Blanket coverage (Forest)	<i>BLA_F</i>
Blanket coverage (Irrigated Ag.)	<i>BLA_IA</i>
Blanket coverage (Rainfed Ag.)	<i>BLA_RA</i>
Blanket coverage (Shrubland)	<i>BLA_S</i>
FLOW MAGNITUDE INCREASING SCENARIOS	
Deforestation (to Irrigated Ag.)	<i>DEF_IA</i>
Deforestation (to Shrubland)	<i>DEF_S</i>
Increased urbanisation	<i>URB_BUA</i>
Terrace abandonment (to Bare Ground)	<i>TER_BG</i>
Terrace abandonment (to Shrubland)	<i>TER_S</i>
Combined negative land use change (to Shrubland)	<i>NEG_S</i>
FLOW MAGNITUDE DECREASING SCENARIOS	
SCIMAP-Flood afforestation (> 0.50)	<i>AFF50_F</i>
SCIMAP-Flood afforestation (> 0.75)	<i>AFF75_F</i>
SCIMAP-Flood afforestation (point density analysis > 0.50)	<i>AFF50_PDA_F</i>
SCIMAP-Flood afforestation (point density analysis > 0.75)	<i>AFF75_PDA_F</i>
SCIMAP-Flood check dam implementation (sub-catchments > 0.50)	<i>DAM50</i>
SCIMAP-Flood check dam implementation (sub-catchments > 0.75)	<i>DAM75</i>
Terrace abandonment (to Forest)	<i>TER_F</i>
Combined flood management approach (SCIMAP-Flood > 0.50)	<i>POS50</i>
Combined flood management approach (SCIMAP-Flood > 0.75)	<i>POS75</i>
OFFSETTING SCENARIOS	
SCIMAP-Flood afforestation (point density analysis > 0.50) vs negative land use change	<i>AFF50_PDA_F_NEG_S</i>
SCIMAP-Flood afforestation (point density analysis > 0.75) vs negative land use change	<i>AFF75_PDA_F_NEG_S</i>
SCIMAP-Flood check dam implementation (sub-catchments > 0.50) vs negative land use change	<i>DAM50_NEG_S</i>
SCIMAP-Flood check dam implementation (sub-catchments > 0.75) vs negative land use change	<i>DAM75_NEG_S</i>
Combined flood management approach (SCIMAP-Flood > 0.50) vs negative land use change	<i>POS50_NEG_S</i>
Combined flood management approach (SCIMAP-Flood > 0.75) vs negative land use change	<i>POS75_NEG_S</i>

4.2.8 CRUM3 methods summary

The CRUM3 approach outlined in Figure 4.1 is the second stage of the end-to-end catchment-scale scenario assessment process. The CRUM3 hydrological model is designed to assess the impact on flow extremes from projected climate change and land management techniques whilst using a minimal parameter set derived from accessible national datasets. Therefore, it is a suitable choice for assessing land use change scenarios – both flow magnitude increasing and decreasing – for the East Rapti catchment. The complete list of the modelled scenarios is provided in Table 4.3. The assessment on the hydrological regime for the scenarios is made at each of the six flood impact points carried on from the SCIMAP-Flood research.

For the East Rapti catchment case study the spatial data used in CRUM3 was taken from a variety of sources. The elevation data was from the ALOS Global Digital Surface Model (AW3D30) 30 m resolution global elevation dataset and the land cover spatial distribution was undertaken through supervised classification of Landsat 8 satellite imagery and slope and aspect data generated from the ALOS elevation data. The climate data (rainfall and temperature) used to drive the model and the river flow data used to evaluate the model parameter sets were attained from the DHM.

Under the concept of equifinality the GLUE approach was used to establish the top performing 32 model parameter sets for the East Rapti catchment from an original 5014 model runs. The model parameter sets were evaluated with a combination of both formal statistical measures and hydrological signatures. These top 32 model runs created a model ensemble from which the catchment-scale flow magnitude increasing and decreasing scenarios were assessed.

4.3 RESULTS

This section presents the results of the CRUM3 catchment scenario modelling for the East Rapti catchment. Section 4.3.1 outlines the results of the GLUE approach used to ascertain the top performing model parameter sets based on both the combined model evaluation methods used. This section concludes with the identification of the top 32 model parameter sets that comprise the model ensemble used in the scenario modelling. Section 4.3.2 illustrates the results of the East Rapti catchment-scale scenario modelling and provides an assessment of the impact of the array of catchment scenarios created in Section 4.2.7. The breakdown of results within this section is presented at the beginning of the section.

4.3.1 East Rapti GLUE results

Of the 5,014 model runs completed under the GLUE approach, the top 32 model runs were taken forward to model the catchment management scenarios. Throughout the results section these top 32 model runs are referred to as the model ensemble. These were selected using the top eight model runs for both the Lothar and Rapti catchments were selected under both the traditional formal statistical approach and the hydrological signatures method; this model evaluation approach is discussed in detail in Section 4.2.5. A total of 32 runs in the model ensemble, and the corresponding eight per model evaluation approach, was selected to provide a large enough coverage of variation in model parameter sets and to maintain an optimum computational run time configuration on the high-performance computing resources.

The model evaluation values of top eight model runs selected using the statistical combination of NSE and MAE with the Lothar and Rapti gauge data are shown in Tables 4.4 and 4.5 respectively. The corresponding CRUM3 model parameter ensembles for the selected model runs are shown in Appendix 7.23 and Appendix 7.24.

From the 5,014 GLUE model runs, the maximum NSE for the 2009 Lothar data was 0.88 with a maximum of 0.77 for the 2010 Lothar data. The model evaluation using the Lothar gauged data produced 24 model runs that had an NSE value of > 0.6 for both the 2009 calibration data and 2010 validation data and met the assessment criteria outlined in Section 4.2.5.2. The MAE of these 24 runs ranged between 2.03 and 2.69; all 24 models had a MAE of below half of the standard deviation value (SD - 8.39) and therefore are deemed suitable based on Singh et al. (2004). Ranking the models by MAE produced the top eight model runs evident in Table 4.4.

Table 4.4: The top 8 model runs based on a formal statistical approach to model evaluation and using the Lothar gauge, ranked by MAE.

Model Run	NSE 2009	NSE 2010	MAE
3086	0.65	0.69	2.03
2165	0.73	0.65	2.04
545	0.65	0.72	2.08
3997	0.65	0.74	2.10
3590	0.74	0.63	2.16
3253	0.70	0.76	2.17
2754	0.74	0.60	2.21
2342	0.69	0.69	2.26

From the 5014 GLUE model runs, the maximum NSE for the 2009 Rapti data was 0.73 with a maximum of 0.62 for the 2010 Rapti data. The model evaluation using the Rapti gauged data produced 10 model runs that had an NSE value of > 0.6 for both the 2009 calibration data and 2010 validation data and met the assessment criteria. The MAE of these 10 runs ranged between 15.46 and 20.14; all 10 models had a MAE of below half of the standard deviation value (SD – 62.49) and therefore are deemed suitable based on Singh et al. (2004). Ranking the models by MAE produced the top 8 model runs evident in Table 4.5.

Table 4.5: The top 8 model runs based on a formal statistical approach to model evaluation and using the Rapti gauge, ranked by MAE.

Model Run	NSE 2009	NSE 2010	MAE
5009	0.70	0.60	15.46
1993	0.72	0.60	17.01
462	0.72	0.61	17.23
241	0.65	0.60	17.30
2377	0.66	0.62	17.47
3108	0.72	0.61	17.73
881	0.61	0.61	17.85
1432	0.66	0.61	18.53

The model evaluation values of top 8 model runs selected using the hydrological signatures approach based on the Lothar and Rapti gauge data are shown in Tables 4.6 and 4.7 respectively. The corresponding CRUM3 model parameter ensembles for the selected model runs are shown in Appendix 7.25 and Appendix 7.26. The top 8 were selected from the average normalised values of the *absHS* from the hydrological signatures used; the hydrological signatures used were PD, RLD, AC, SD, mean, median and NSE of the FDC.

For the Lothar gauge data, the maximum average of the hydrological signature normalised values was 0.91 with all top 8 having a value of ≥ 0.87 . With a maximum *absHS* value of 1 indicating that the modelled hydrological signature value is identical to the observed hydrological signature value across the 5014 modelled runs, the high average *absHS* values at the Lothar gauge show that particular parameter sets performed well across each signature. NSE values comparing the FDCs of the observed and modelled data at the Lothar gauge across the top eight model runs all scored > 0.99 .

For the Rapti gauge data the maximum average of the hydrological signature normalised values was 0.79 with all top 8 having a value of ≥ 0.76 . This result is notably lower than the average *absHS* values from the Lothar gauge and is a result of the model runs not scoring consistently across the hydrological signatures, performing well in particular signatures and poorly in others. The SD, mean and median hydrological signature values from the observed Rapti gauged data were significantly larger than the maximum from the top model runs. The PD, RLD and FDC hydrological signatures, that represent hydrograph shape rather than specific values derived from the gauged data, were comparable between the observed and modelled data.

An average daily flow hydrograph showing the top 32 model runs and using the base catchment land cover (see Figure 4.5) for the period 2009 to 2010 is shown at the Lothar gauge in Figure 4.17 and the Rapti gauge in Figure 4.18. Evident in Figure 4.17, the model runs calibrated from the Lothar gauged data, both using the formal statistical approach and the informal hydrological signatures approach, provide a closer fit to the observed Lothar hydrograph. The CRUM3 parameter ensembles from model runs calibrated from the Rapti observed data tend to overestimate the peak average daily flows in the Lothar catchment, most notably in 2010 (see the top of Figure 4.17). The CRUM3 parameter ensembles from model runs calibrated from the Lothar observed data also tend to slightly overestimate the peak average daily flows in the Lothar catchment. The pattern of model runs calibrated from the Rapti having higher peak flows than those calibrated from the Lothar catchment is reflected in the Rapti data in Figure 4.18. Notably within Figure 4.18 however, all four model assessment groups underpredict the average daily flow for the latter half of the monsoon period in 2009.

Table 4.6: The top 8 model runs based on an informal approach using hydrological signatures for model evaluation and using the Lothar gauge. Norm is short for normalised.

Model Run	PD	PD norm	RLD	RLD norm	AC	AC norm	SD	SD norm	Mean	Mean norm	Median	Median norm	FDC	FDC norm	Normalised Average
Observed	44.75		1.32		0.67		8.40		4.60		1.61				
1724	44.50	1.00	1.49	0.85	0.78	0.66	7.79	0.92	4.52	0.98	1.72	0.93	1.00	1.00	0.91
72	62.95	0.82	1.02	0.74	0.73	0.82	9.24	0.89	4.60	1.00	1.65	0.98	1.00	1.00	0.89
2431	66.58	0.78	1.13	0.84	0.69	0.93	9.16	0.90	4.91	0.91	1.86	0.85	1.00	1.00	0.89
4883	64.05	0.81	1.24	0.93	0.78	0.65	8.46	0.99	4.63	0.99	1.34	0.84	1.00	1.00	0.89
3887	46.40	0.98	1.01	0.73	0.78	0.66	7.93	0.94	4.36	0.94	1.54	0.96	1.00	0.99	0.89
4501	47.75	0.97	0.99	0.72	0.76	0.71	7.11	0.83	4.36	0.93	1.61	1.00	1.00	1.00	0.88
635	47.45	0.97	1.31	0.99	0.82	0.53	9.00	0.92	4.94	0.91	1.29	0.81	0.99	0.99	0.87
4551	48.83	0.96	1.27	0.96	0.84	0.46	7.00	0.82	4.56	0.99	1.78	0.90	1.00	1.00	0.87

Table 4.7: The top 8 model runs based on an informal approach using hydrological signatures for model evaluation and using the Rapti gauge. Norm is short for normalised.

Model Run	PD	PD norm	RLD	RLD norm	AC	AC norm	SD	SD norm	Mean	Mean norm	Median	Median norm	FDC	FDC norm	Normalised Average
Observed	186.10		1.45		0.48		62.49		28.89		13.45				
37	176.45	0.95	1.41	0.97	0.73	0.49	39.65	0.91	19.60	0.97	2.36	0.30	0.85	0.94	0.79
54	196.12	0.95	1.34	0.90	0.70	0.55	37.38	0.84	19.08	0.94	2.79	0.36	0.80	0.90	0.78
83	211.75	0.86	1.45	1.00	0.69	0.56	37.46	0.85	18.55	0.91	2.05	0.26	0.83	0.93	0.77
461	187.77	0.99	1.51	0.94	0.66	0.64	35.84	0.80	17.13	0.83	1.97	0.25	0.82	0.91	0.77
196	217.10	0.83	1.39	0.94	0.63	0.70	38.05	0.86	18.05	0.88	2.50	0.32	0.73	0.81	0.77
39	198.18	0.93	1.27	0.83	0.71	0.52	37.20	0.84	18.65	0.91	3.41	0.44	0.78	0.87	0.76
383	222.12	0.81	1.43	0.99	0.64	0.66	36.69	0.82	17.09	0.83	2.13	0.27	0.84	0.94	0.76
15	211.15	0.86	1.20	0.76	0.64	0.68	43.03	1.00	19.72	0.97	1.35	0.17	0.78	0.87	0.76

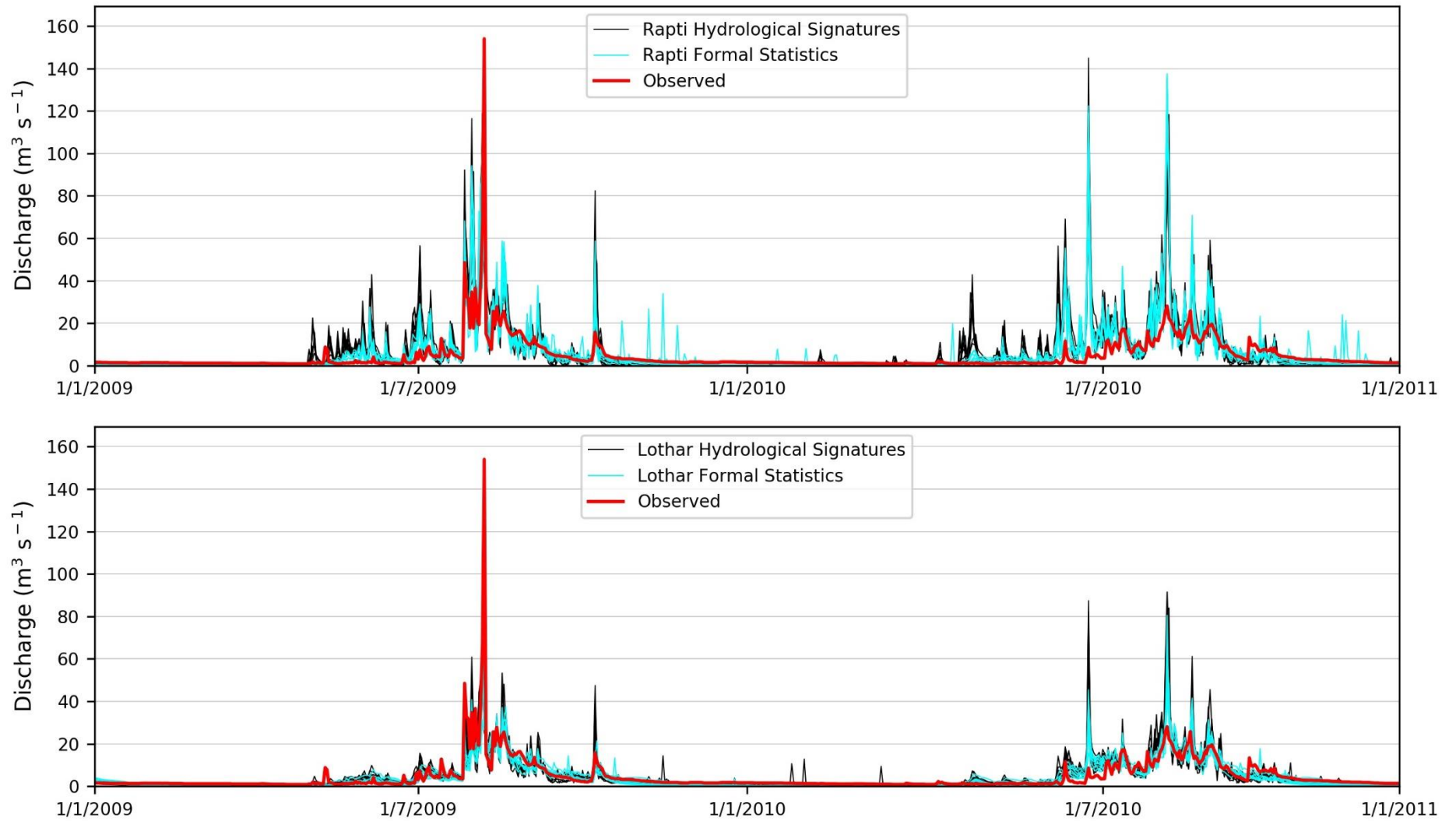


Figure 4.17: Simulated and observed average daily flow hydrographs at the Lothar gauge based on the calibration using the Rapti gauged data (top) and Lothar gauged data (bottom).

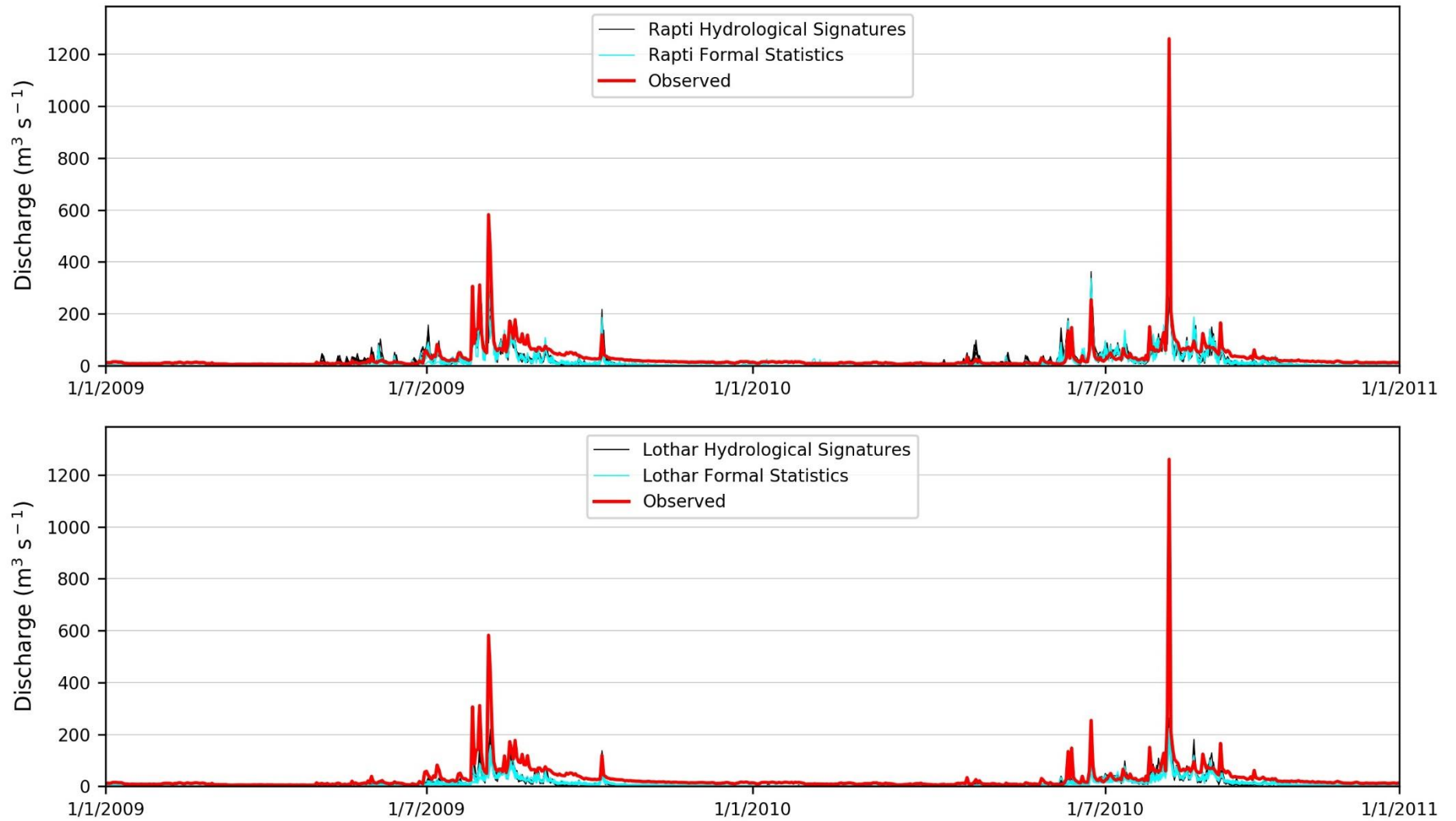


Figure 4.18: Simulated and observed average daily flow hydrographs at the Rapti gauge based on the calibration using the Rapti gauged data (top) and Lothar gauged data (bottom).

4.3.2 East Rapti catchment-scale scenario results

The assessment of changes to the flood regime across the East Rapti catchment under different catchment scenarios was analysed with the percentage change in the 99.9th percentile discharge (Q99.9) between the base scenario and the scenario for the behavioural model ensemble. The change in Q99.9 was calculated at the locations of the six flood impact points (Figure 3.3) to understand how a given scenario impacts the high flow regime. Flow hydrographs and time-to-peak comparisons for the largest flow event in 2010 are also used to determine the impact the various scenarios on the hydrological regime. Within the results section the scenarios are predominantly referred to by their individual scenario ID; the ID for each scenario is outlined in Table 4.3 in Section 4.2.7.5.

The median ($\widetilde{Q99.9}$) and mean ($\overline{Q99.9}$) change in Q99.9 across the 32 run model ensemble for all the modelled scenarios are shown at the beginning of this section in the results overview (Section 4.3.2.1). The remaining sections go into more detail for each of the individual scenarios with Section 4.3.2.2 outlining the results of the blanket catchment land cover change scenarios used to bound the potential change in the catchment. Section 4.3.2.3 illustrates the results of the flow magnitude increase through land degradation and land cover change scenarios with Section 4.3.2.4 showing the results of the flow magnitude reduction scenarios. Finally, Section 4.3.2.5 explores the results of the offsetting scenarios in which a combination of flow magnitude reduction measures are modelled to assess the ability to mitigate against future land use change.

Combined boxplot and swarmplot information

For each of the six flood impact points the percentage change in Q99.9 across the model ensemble for each catchment-scale scenario is displayed as a combined boxplot and swarmplot (Matplotlib, 2020; Seaborn, 2020). Within the boxplot the central grey line represents the $\widetilde{Q99.9}$ change, and the red line represents the $\overline{Q99.9}$ change across the model ensemble. The coloured box constrains the 25th to 75th percentiles across the model ensemble. The whiskers either side of the coloured box extend to the first data point greater than the 75th percentile plus, or less than the 25th percentile minus, the interquartile range (the 75th percentile minus the 25th percentile); data points beyond this range are considered outliers (Matplotlib, 2020). The swarmplot represent the spread of Q99.9 across the model ensemble with a black dot for each of the 32 model results; the points are adjusted (along the categorical axis) so that they do not overlap (Seaborn, 2020).

4.3.2.1 East Rapti catchment-scale scenarios results overview

The tables below present the median ($\widetilde{Q99.9}$) (Table 4.8) and mean ($\overline{Q99.9}$) (Table 4.9) percentage change in Q99.9 across the 32 run model ensemble at each of the six flood impact points within the East Rapti catchment.

The greatest reduction across the 27 modelled scenarios in both average $\overline{Q_{99.9}}$ and $\overline{Q_{99.9}}$ was from scenario *BLA_F* ($\overline{Q_{99.9}}$: -9.3%, $\overline{Q_{99.9}}$: -10.0%), with the greatest increase in both average $\overline{Q_{99.9}}$ and $\overline{Q_{99.9}}$ from scenario *BLA_IA* ($\overline{Q_{99.9}}$: +50.8%, $\overline{Q_{99.9}}$: +48.2%). Both the *BLA_F* and *BLA_IA* scenarios had the greatest decrease and increase at an individual flood impact point accordingly. At Hetauda, under the *BLA_F* scenario, there was a modelled $\overline{Q_{99.9}}$ decrease of 12.4% and $\overline{Q_{99.9}}$ decrease of 12.1%. The Lothar flood impact point produced the greatest increase in both $\overline{Q_{99.9}}$ (+75.1%) and $\overline{Q_{99.9}}$ (+69.9%) under the *BLA_IA* scenario.

The greatest increase across the flow magnitude increasing scenarios in both average $\overline{Q_{99.9}}$ and $\overline{Q_{99.9}}$ was jointly between *TER_BG* and *NEG_S* ($\overline{Q_{99.9}}$: +3.4%, $\overline{Q_{99.9}}$: +3.5%). From the flow magnitude increasing scenarios, the Lothar flood impact point produced the greatest increase in both $\overline{Q_{99.9}}$ (+5.8%) and $\overline{Q_{99.9}}$ (+5.7%) under the *TER_BG* scenario.

The *POS50* scenario ($\overline{Q_{99.9}}$: -5.3%, $\overline{Q_{99.9}}$: -5.6%) produced the greatest average $\overline{Q_{99.9}}$ and $\overline{Q_{99.9}}$ reduction from the flow magnitude decreasing scenarios. The Hetauda flood impact point produced the greatest reduction in both $\overline{Q_{99.9}}$ (-10.3%) and $\overline{Q_{99.9}}$ (-10.9%) under the *POS50* scenario from the range of flow magnitude reduction scenarios.

The greatest reduction across the offsetting scenarios in both average $\overline{Q_{99.9}}$ and $\overline{Q_{99.9}}$ was from scenario *POS50_NEG_S* ($\overline{Q_{99.9}}$: -2.8%, $\overline{Q_{99.9}}$: -2.8%), with the greatest $\overline{Q_{99.9}}$ increase from scenario *AFF50_PDA_F_NEG_S* (+1.3%) and the greatest $\overline{Q_{99.9}}$ increase from scenario *AFF75_PDA_F_NEG_S* (+3.0%).

Table 4.8: Median percentage change in Q99.9 for the catchment scenarios across all six flood impact points. The Scenario ID corresponds to those in Table 4.3 (Section 4.2.7.5).

SCENARIO ID	Andrauli	Hetauda	Lothar	Madi Bridge	Manahari	Sauraha	Average
BLANKET COVERAGE SCENARIOS							
<i>BLA_BG</i>	38.2	38.7	59.0	34.0	49.2	39.8	43.1
<i>BLA_BUA</i>	38.2	41.1	63.0	35.2	55.3	40.9	45.6
<i>BLA_F</i>	-7.9	-12.4	-6.7	-8.8	-10.9	-9.2	-9.3
<i>BLA_IA</i>	42.4	41.6	75.1	37.2	63.4	44.9	50.8
<i>BLA_RA</i>	11.6	7.8	20.3	11.5	13.7	12.0	12.8
<i>BLA_S</i>	29.6	23.5	45.1	25.7	33.8	30.4	31.4
FLOW MAGNITUDE INCREASE SCENARIOS							
<i>DEF_IA</i>	2.1	1.2	0.0	5.3	0.0	2.1	1.8
<i>DEF_S</i>	1.8	0.6	0.1	4.1	-0.2	1.7	1.3
<i>URB_BUA</i>	0.2	0.7	0.2	0.0	0.0	0.0	0.2
<i>TER_BG</i>	2.2	4.5	5.8	0.6	4.8	2.3	3.4
<i>TER_S</i>	1.3	3.1	2.8	0.2	2.9	1.5	2.0
<i>NEG_S</i>	3.0	4.2	3.0	3.9	3.0	3.1	3.4
FLOW MAGNITUDE DECREASE SCENARIOS							
<i>AFF50_F</i>	-0.5	-1.8	-0.3	0.1	-0.2	-0.4	-0.5
<i>AFF75_F</i>	-0.2	-0.4	0.1	0.0	-0.1	-0.1	-0.1
<i>AFF50_PDA_F</i>	-1.7	-3.7	-1.1	0.0	-0.8	-2.0	-1.6
<i>AFF75_PDA_F</i>	-0.5	-2.0	0.3	0.3	0.0	-0.6	-0.4
<i>DAM50</i>	-3.0	-5.9	-5.9	0.1	-3.6	-3.2	-3.6
<i>DAM75</i>	-1.0	-5.2	0.1	0.1	-0.1	-1.0	-1.2
<i>TER_F</i>	-2.1	-4.2	-3.0	-0.3	-5.6	-2.0	-2.9
<i>POS50</i>	-5.0	-10.3	-7.0	0.0	-4.5	-5.2	-5.3
<i>POS75</i>	-1.2	-7.3	-0.1	0.2	0.0	-1.3	-1.6
OFFSETTING SCENARIOS							
<i>AFF50_PDA_F_NEG_S</i>	0.7	-1.3	1.9	3.9	1.9	0.5	1.3
<i>AFF75_PDA_F_NEG_S</i>	0.5	-2.3	2.1	4.0	2.0	0.3	1.1
<i>DAM50_NEG_S</i>	-0.6	-3.1	-4.2	4.5	-1.0	-0.9	-0.9
<i>DAM75_NEG_S</i>	1.7	-2.5	2.5	4.3	2.8	2.3	1.9
<i>POS50_NEG_S</i>	-2.4	-7.1	-5.1	4.1	-1.7	-3.1	-2.5
<i>POS75_NEG_S</i>	1.5	-4.0	2.7	4.4	2.9	1.5	1.5

Table 4.9: Mean percentage change in Q99.9 for the catchment scenarios across all six flood impact points. The Scenario ID corresponds to those in Table 4.3 (Section 4.2.7.5).

SCENARIO ID	Andrauli	Hetauda	Lothar	Madi Bridge	Manahari	Sauraha	Average
BLANKET COVERAGE SCENARIOS							
<i>BLA_BG</i>	34.1	36.7	59.1	31.8	53.1	35.9	41.8
<i>BLA_BUA</i>	35.2	38.7	63	32.5	56.5	37.6	43.9
<i>BLA_F</i>	-9.9	-12.1	-7.9	-10.8	-9.6	-9.7	-10.0
<i>BLA_IA</i>	39.4	41.5	69.9	34.3	62.2	41.6	48.2
<i>BLA_RA</i>	13.1	9.5	21.2	11.7	17.8	13.4	14.4
<i>BLA_S</i>	26.3	25.3	46.7	22.9	40.6	27.8	31.6
FLOW MAGNITUDE INCREASE SCENARIOS							
<i>DEF_IA</i>	2.4	1.4	0.2	5.1	0.0	2.4	1.9
<i>DEF_S</i>	1.9	0.9	0.3	3.7	-0.3	1.9	1.4
<i>URB_BUA</i>	0.1	0.6	0.2	0.1	-0.3	0.1	0.1
<i>TER_BG</i>	2.4	4.9	5.7	0.5	5.2	2.4	3.5
<i>TER_S</i>	1.5	3.1	3.5	0.3	3.1	1.5	2.2
<i>NEG_S</i>	3.3	4.3	3.2	4.0	3.2	3.3	3.5
FLOW MAGNITUDE DECREASE SCENARIOS							
<i>AFF50_F</i>	-0.8	-2.4	-0.4	-0.1	-0.6	-0.8	-0.8
<i>AFF75_F</i>	-0.2	-0.5	0.2	0.0	-0.2	-0.1	-0.1
<i>AFF50_PDA_F</i>	-2.4	-5.3	-1.2	0.1	-1.1	-2.7	-2.1
<i>AFF75_PDA_F</i>	-0.5	-2.7	0.4	0.5	-0.3	-0.8	-0.6
<i>DAM50</i>	-2.9	-6.0	-5.6	0.1	-3.3	-3.5	-3.6
<i>DAM75</i>	-1.0	-5.4	0.3	0.2	-0.4	-1.2	-1.3
<i>TER_F</i>	-1.9	-4.3	-3.1	-0.2	-4.6	-2.5	-2.8
<i>POS50</i>	-5.3	-10.9	-6.7	0.0	-4.7	-5.9	-5.6
<i>POS75</i>	-1.3	-7.7	-0.2	0.3	-0.1	-1.6	-1.8
OFFSETTING SCENARIOS							
<i>AFF50_PDA_F_NEG_S</i>	2.7	2.0	2.7	3.9	2.9	2.6	2.8
<i>AFF75_PDA_F_NEG_S</i>	2.8	1.4	3.6	4.0	3.1	2.7	3.0
<i>DAM50_NEG_S</i>	0.0	-2.8	-3.4	3.9	-0.6	-0.5	-0.6
<i>DAM75_NEG_S</i>	2.3	-1.9	3.4	3.9	3.1	2.1	2.2
<i>POS50_NEG_S</i>	-2.6	-8.2	-4.6	3.9	-1.8	-3.3	-2.8
<i>POS75_NEG_S</i>	1.8	-4.6	3.3	4.0	3.0	1.6	1.5

4.3.2.2 East Rapti blanket catchment coverage results

The impact on Q99.9 across the model ensemble from the blanket coverage scenarios is presented in Figure 4.19. Figure 4.20, and Figure 4.21 shows a comparison between the modelled base hydrograph and modelled scenario hydrograph for both *BLA_F* and *BLA_IA* respectively.

The *BLA_F* scenario produced the greatest average reduction (average $\overline{Q99.9}$: -9.3%, average $\overline{Q99.9}$: -10.0%) across the six flood impact locations. The greatest reduction in Q99.9 from *BLA_F* across the six flood impact points was at Hetuada ($\overline{Q99.9}$: -12.4%, $\overline{Q99.9}$: -12.1%) with the smallest reduction in Q99.9 at Lothar ($\overline{Q99.9}$: -6.7%; $\overline{Q99.9}$: -7.9%). The greatest average increase in $\overline{Q99.9}$ and $\overline{Q99.9}$ across the six impact points was from *BLA_IA* (average $\overline{Q99.9}$: +50.8%, average $\overline{Q99.9}$: +48.2%). This increase in Q99.9 was largest at the Lothar ($\overline{Q99.9}$: +75.1%, $\overline{Q99.9}$: +69.9%) and Manahari ($\overline{Q99.9}$: +63.4%, $\overline{Q99.9}$: +62.2%) flood impact points and smallest at the Madi Bridge flood impact point ($\overline{Q99.9}$: +37.2%, $\overline{Q99.9}$: +34.3%). The pattern of the Lothar and Manahari flood impact points having the greatest increase in Q99.9 due to blanket catchment coverage upstream is replicated in the *BLA_BG*, *BLA_BUA* and *BLA_S* scenarios.

The hydrograph impact is shown for both *BLA_F*, as the blanket scenario with the greatest reduction in Q99.9, in Figure 4.20 and *BLA_IA*, as the blanket scenario with the greatest increase in Q99.9, in Figure 4.21. The overall shape of the hydrographs is very similar to the base scenario with *BLA_F* reducing the peaks and the *BLA_IA* increasing the peaks. A comparison of time-to-peak across the high flow event shows that there is minimal impact on the timing of the peak discharge. The median change in time-to-peak throughout the catchment across the model ensemble was 0.0 hours for *BLA_F* and 0.1 hours earlier for the *BLA_IA*. The mean time-to-peak change throughout the catchment across the top model runs was 0.2 hours later for *BLA_F* and 0.0 hours for *BLA_IA*.

Using blanket land cover change to assess the potential change to the flood regime through land management has identified the relative effectiveness of the six land cover categories. The *BLA_F* scenario, whilst not a realistic option for implementation, gives an indication of the maximum reduction (average $\overline{Q99.9}$: -9.3%, average $\overline{Q99.9}$: -10.0%) to the flow magnitude available through land cover change in the East Rapti. The assessment of blanket land use change to *Irrigated Agriculture* (*BLA_IA*) (average $\overline{Q99.9}$: +50.8%, average $\overline{Q99.9}$: +48.2%), widespread land degradation to *Bare Ground* (*BLA_BG*) (average $\overline{Q99.9}$: +43.1%, average $\overline{Q99.9}$: +41.8%) or extensive urbanisation to *Built-Up Area* (*BLA_BUA*) (average $\overline{Q99.9}$: +45.6%, average $\overline{Q99.9}$: +43.9%) provides an indication of the maximum increase in flow magnitude that could be expected.

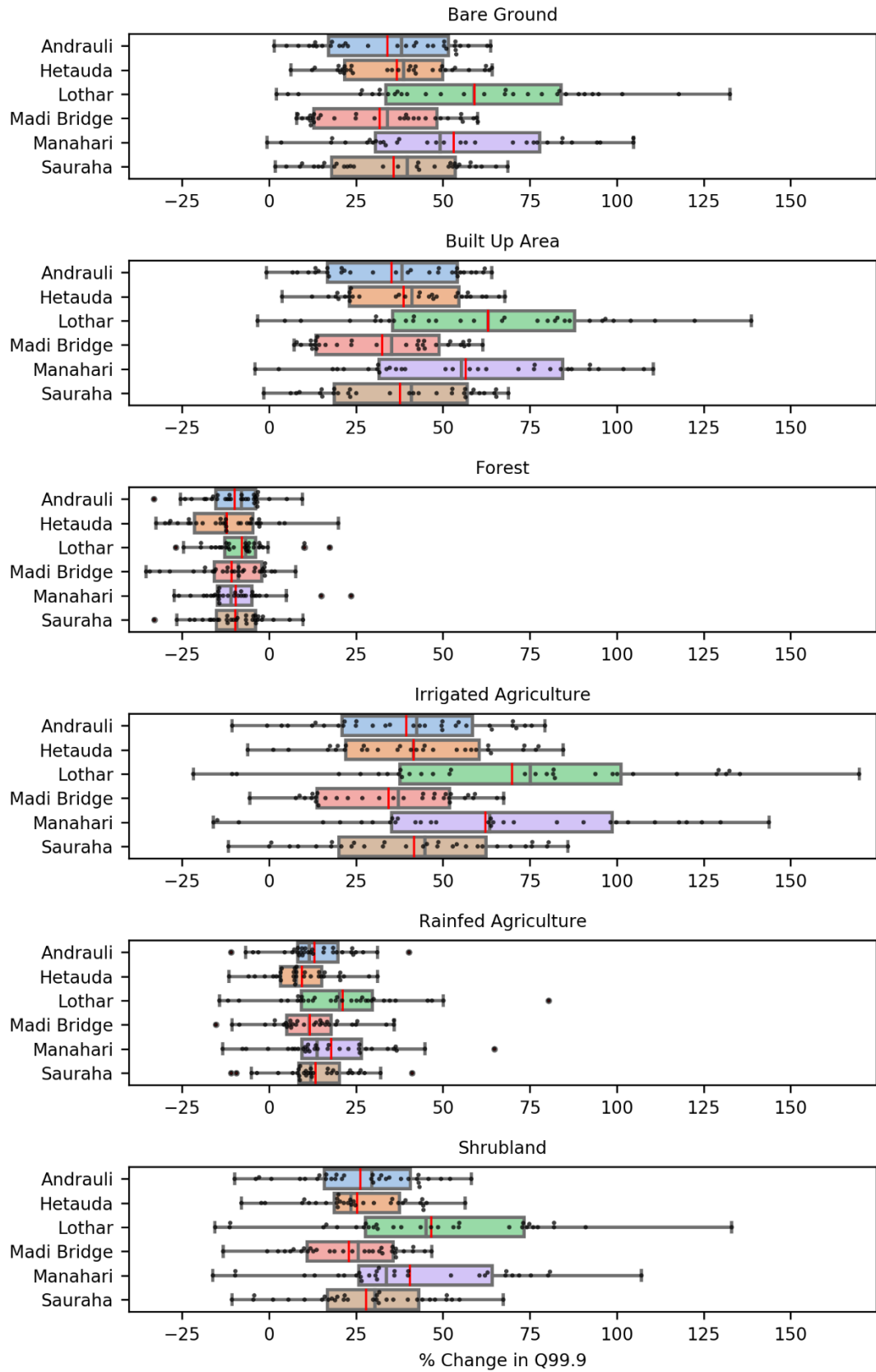


Figure 4.19: A combined boxplot and swarmplot showing the blanket land cover change scenarios and the corresponding percentage change in Q99.9 at the six flood impact points. See the beginning of Section 4.3.2 for general plot information.

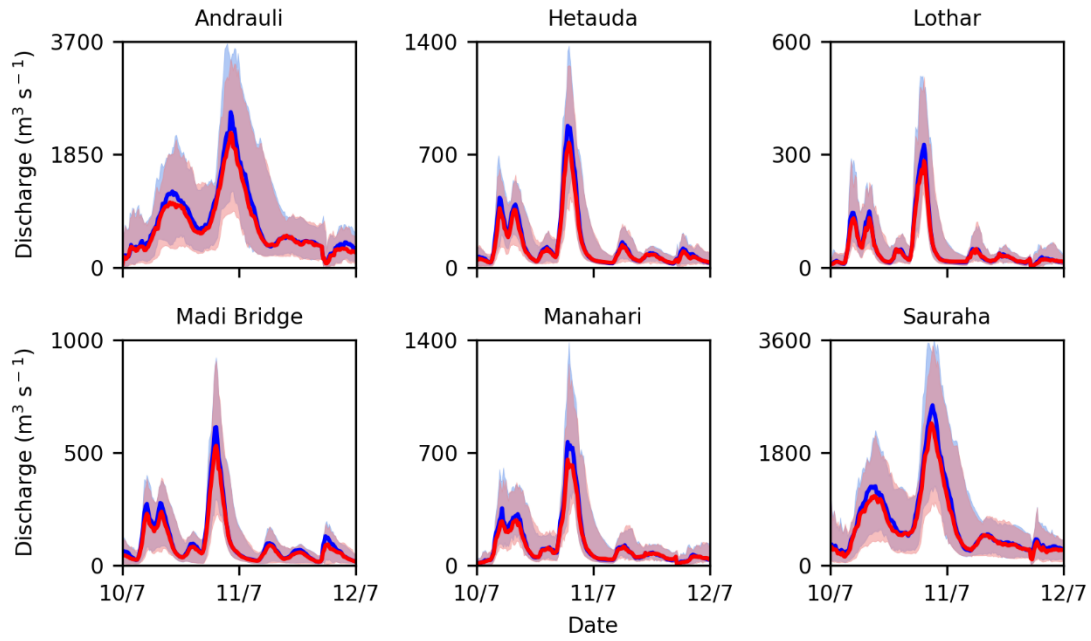


Figure 4.20: A comparison of median flow for the six flood impact points for the base (blue) and BLA_F (red) scenarios. The shaded areas represent the 10th and 90th percentile flows across the top 32 model runs. Note different y-axis scales.

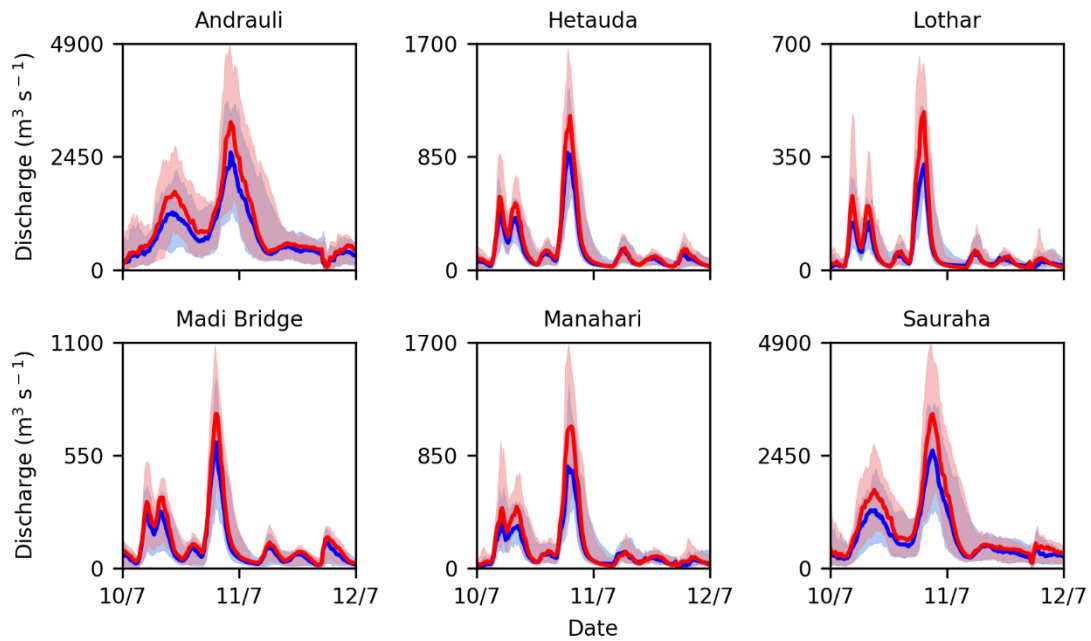


Figure 4.21: A comparison of median flow for the six flood impact points for the base (blue) and BLA_IA (red) scenarios. The shaded areas represent the 10th and 90th percentile flows across the top 32 model runs. Note the different y-axis scales.

4.3.2.3 East Rapti catchment flow magnitude increase through land degradation and land cover change scenario results

Deforestation around the populated fringes within the catchment

The change in Q99.9 from two scenarios exhibiting future deforestation throughout the catchment is shown in Figure 4.22 with a hydrograph comparison of the 2010 high flow event in Figure 4.23. The deforestation scenarios produced the larger increase in flow when converted to *Irrigated Agriculture* (*DEF_IA*) (average $\overline{Q99.9}$: +1.8%, average $\overline{Q99.9}$: +1.9%) compared to *Shrubland* (*DEF_S*) (average $\overline{Q99.9}$: +1.3%, average $\overline{Q99.9}$: +1.4%). The greatest increase in Q99.9 for both deforestation scenarios across the six flood impact points was at Madi Bridge (to *Shrubland* - $\overline{Q99.9}$: +4.1%, $\overline{Q99.9}$: +3.7%; to *Irrigated Agriculture* - $\overline{Q99.9}$: +5.3%, $\overline{Q99.9}$: +5.1%). There was a slight reduction in Q99.9 at Manahari from *DEF_S* ($\overline{Q99.9}$: -0.2%, $\overline{Q99.9}$: -0.3%) and no change from the base scenario from *DEF_IA* ($\overline{Q99.9}$: +0.0%, $\overline{Q99.9}$: +0.0%).

The overall shape of the *DEF_S* hydrographs in Figure 4.23 are nearly identical to the base scenario across the six flood impact locations with only a minor increase in the peak flow from the base scenario. A comparison of time-to-peak across the 2010 high flow event determines that there is a negligible impact on altering the timing of the peak discharge under the deforestation scenario, with a median and mean change in time-to-peak across the 32 model runs of 0.0 hours.

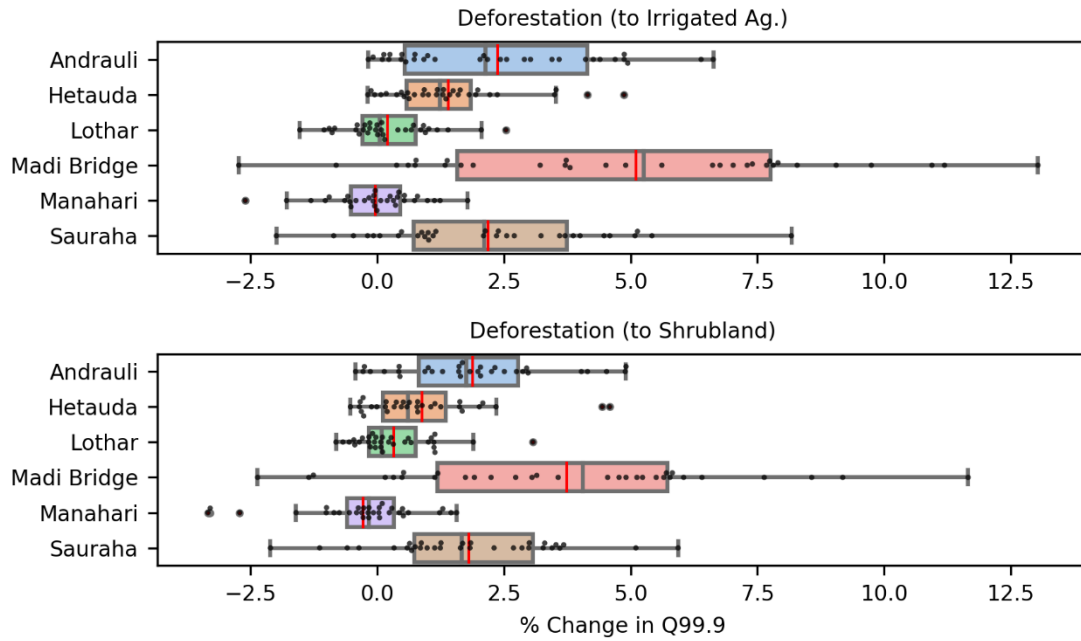


Figure 4.22: A combined boxplot and swarmplot showing the DEF_IA and DEF_S scenarios and the corresponding percentage change in Q99.9 at the six flood impact points. See the beginning of Section 4.3.2 for general plot information.

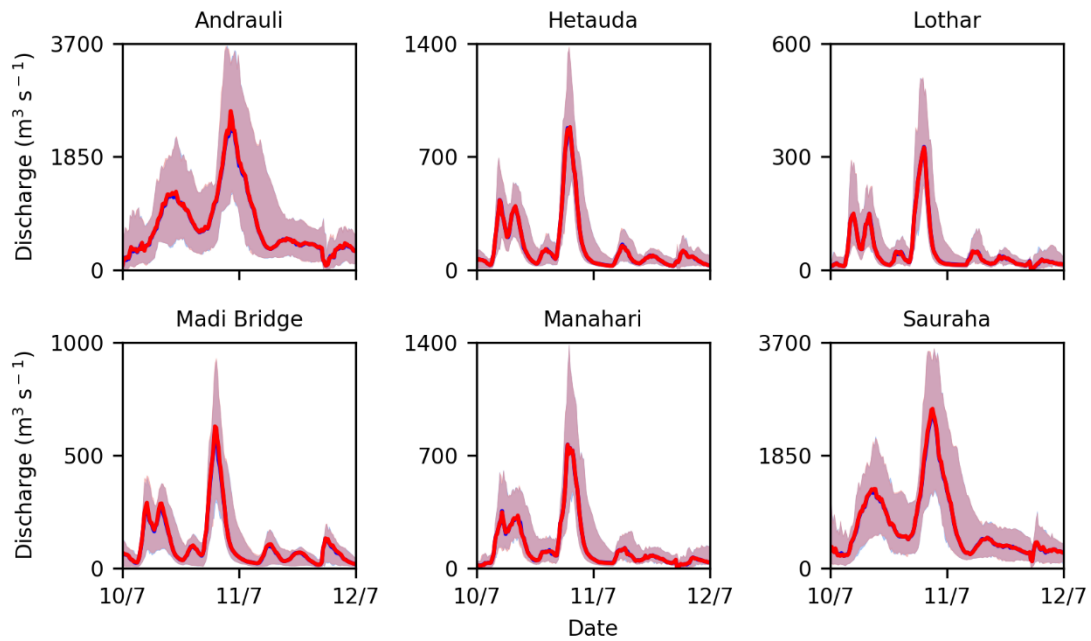


Figure 4.23: A comparison of median flow for the six flood impact points for the base (blue) and DEF_S (red) scenarios. The shaded areas represent the 10th and 90th percentile flows across the top 32 model runs. Note the different y-axis scales.

Urban expansion

The modelled change in Q99.9 from a scenario exhibiting future urban expansion in the East Rapti catchment is shown in Figure 4.24 with a hydrograph comparison of the 2010 high flow event in Figure 4.25. The *URB_BUA* scenario produced only a minor increase in peak flows (average $\overline{Q99.9}$: +0.2%, average $\overline{Q99.9}$: +0.1%) across the six flood impact locations. The greatest increase in Q99.9 from *URB_BUA* across the six flood impact points was at Hetauda ($\overline{Q99.9}$: +0.7%, $\overline{Q99.9}$: +0.6%) with a median change of +0.0% from the base scenario predicted at Madi Bridge, Manahari and Sauraha.

The overall shape of the *URB_BUA* hydrographs in Figure 4.25 are nearly identical to the base scenario across the six flood impact locations. A comparison of time-to-peak across the 2010 high flow event determines that there is a negligible impact on altering the timing of the peak discharge from *URB_BUA* with a median and mean change in time-to-peak across the model ensemble of 0.0 hours.

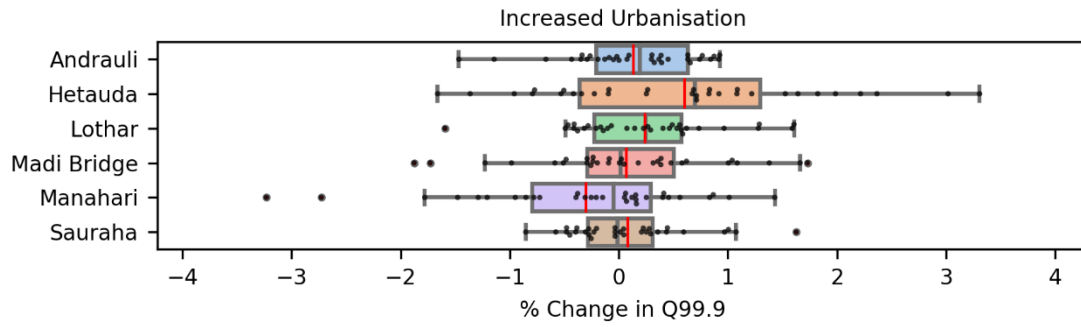


Figure 4.24: A combined boxplot and swarmplot showing the URB_BUA and the corresponding percentage change in Q99.9 at the six flood impact points. See the beginning of Section 4.3.2 for general plot information.

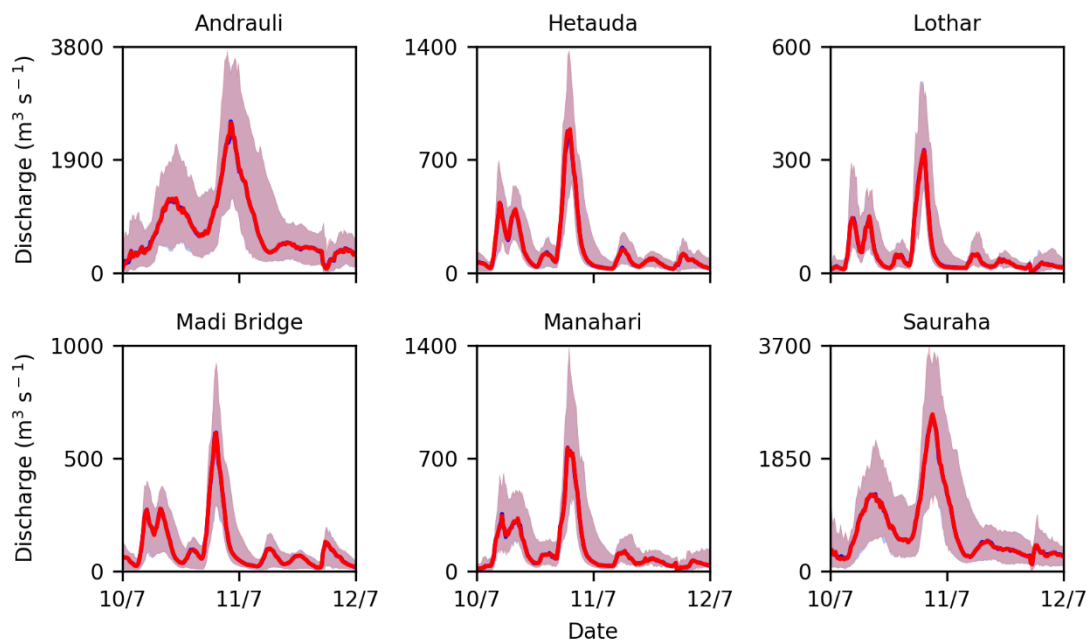


Figure 4.25: A comparison of median flow for the six flood impact points for the base (blue) and URB_BUA (red) scenarios. The shaded areas represent the 10th and 90th percentile flows across the top 32 model runs. Note the different y-axis scales.

Land degradation due to terrace abandonment

The modelled change in Q99.9 from two scenarios exhibiting future terrace abandonment (*TER_BG* and *TER_S*) in the upland parts of the catchment is shown in Figure 4.26 with a hydrograph comparison of the 2010 high flow event in Figure 4.27.

TER_BG produced the greatest increase in Q99.9 (average $\overline{Q99.9}$: +3.4%, average $\overline{Q99.9}$: +3.5%) when compared to *TER_S* (average $\overline{Q99.9}$: +2.2%, average $\overline{Q99.9}$: +2.0%). The greatest increase in Q99.9 for the *TER_BG* scenario across the six flood impact points was at Lothar ($\overline{Q99.9}$: +5.8%, $\overline{Q99.9}$: +5.7%). Under the *TER_S* scenario the greatest increase in Q99.9 across the six flood impact points was at Hetauda ($\overline{Q99.9}$: +3.1%, $\overline{Q99.9}$: +3.1%) although the change at Manahari and Lothar was also close to +3%. The smallest change in Q99.9 under both terrace abandonment scenarios was at Madi Bridge (to *Bare Ground* - $\overline{Q99.9}$: +0.6%, $\overline{Q99.9}$: +0.5%; to *Shrubland* - $\overline{Q99.9}$: +0.2%, $\overline{Q99.9}$: +0.3%).

The hydrographs showing the flow throughout the 2010 high flow event for the *TER_S* scenario (see Figure 4.27) are nearly identical to the base scenario across the six flood impact locations only a minor increase in the peak flow from the base scenario. A comparison of time-to-peak across the 2010 high flow event determines that there is a negligible impact on altering the timing of the peak discharge under both the terrace abandonment scenarios with a median and mean change in time-to-peak across the 32 model runs of 0.0 hours.

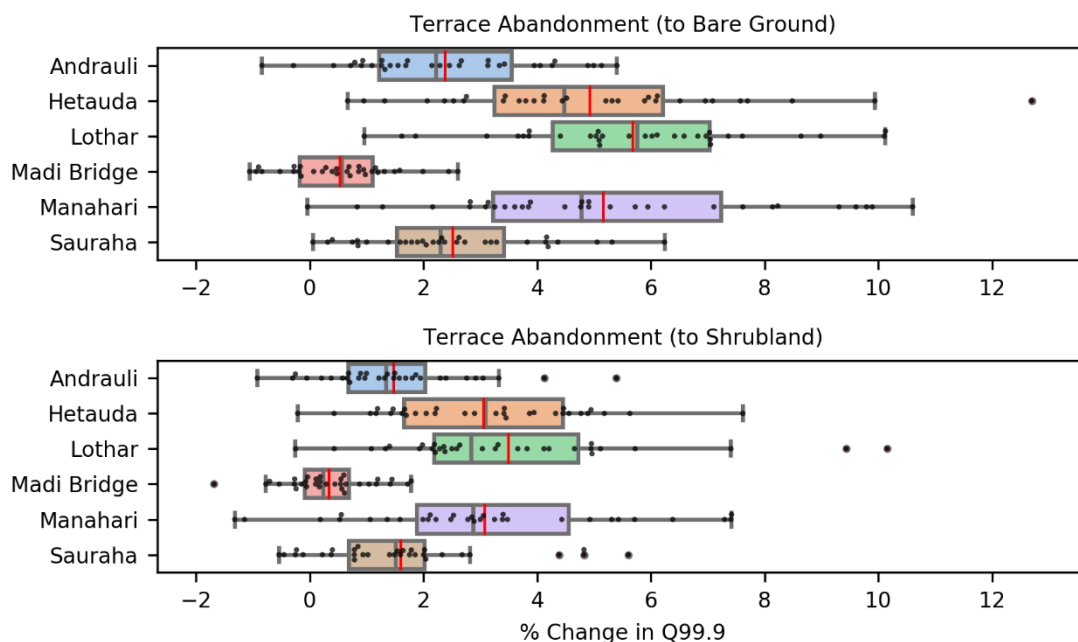


Figure 4.26: A combined boxplot and swarmplot showing the *TER_BG* and *TER_S* scenarios and the corresponding percentage change in Q99.9 at the six flood impact points. See the beginning of Section 4.3.2 for general plot information.

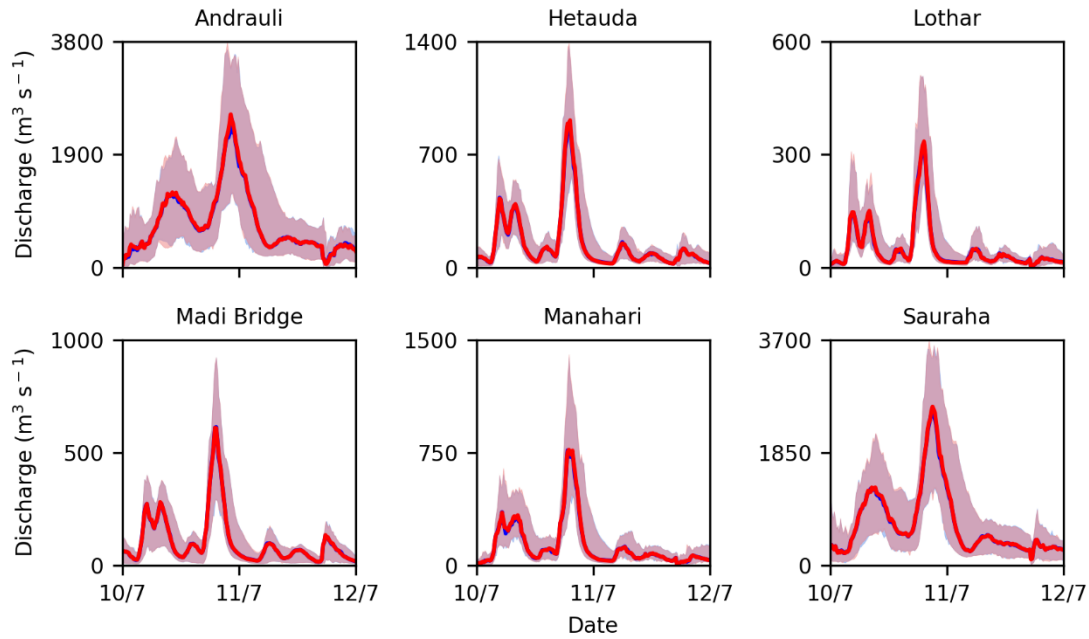


Figure 4.27: A comparison of median flow for the six flood impact points for the base (blue) and TER_S (red) scenarios. The shaded areas represent the 10th and 90th percentile flows across the top 32 model runs. Note the different y-axis scales.

Combined land use change

The *NEG_S* scenario modelled to the impact of a combination of urban expansion (*URB_BUA*), deforestation (*DEF_S*), and terrace abandonment (*TER_S*). The modelled change in $\overline{Q99.9}$ from *NEG_S* is shown in Figure 4.28, and a hydrograph comparison of the 2010 high flow event in Figure 4.29.

The *NEG_S* scenario produced an average $\overline{Q99.9}$ increase of 3.4% and an average $\overline{Q99.9}$ increase of 3.5% across the six flood impact locations. The greatest increase in $\overline{Q99.9}$ from the combined effect of urban expansion, deforestation and terrace abandonment across the six flood impact points was at Hetauda ($\overline{Q99.9}$: +4.2%, $\overline{Q99.9}$: +4.3%) but there was an increase of > 3.0%, both of median and mean, at all the other impact points.

As with the individual land use change scenarios in Section 4.3.2.2, the overall shape of the *NEG_S* scenario hydrographs in Figure 4.29 are nearly identical to the base scenario across the six flood impact locations with a minimal increase to the peak flow when compared to the base hydrograph. A comparison of time-to-peak across the 2010 high flow event determines that there is a negligible impact on altering the timing of the peak discharge under the *NEG_S* scenario with a median and mean change in time-to-peak across the model ensemble of 0.0 hours.

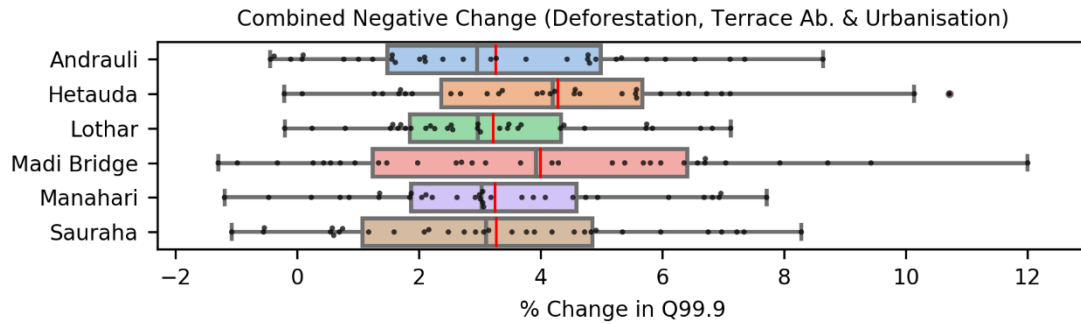


Figure 4.28: A combined boxplot and swarmplot showing the NEG_S scenario and the corresponding percentage change in Q99.9 at the six flood impact points. See the beginning of Section 4.3.2 for general plot information.

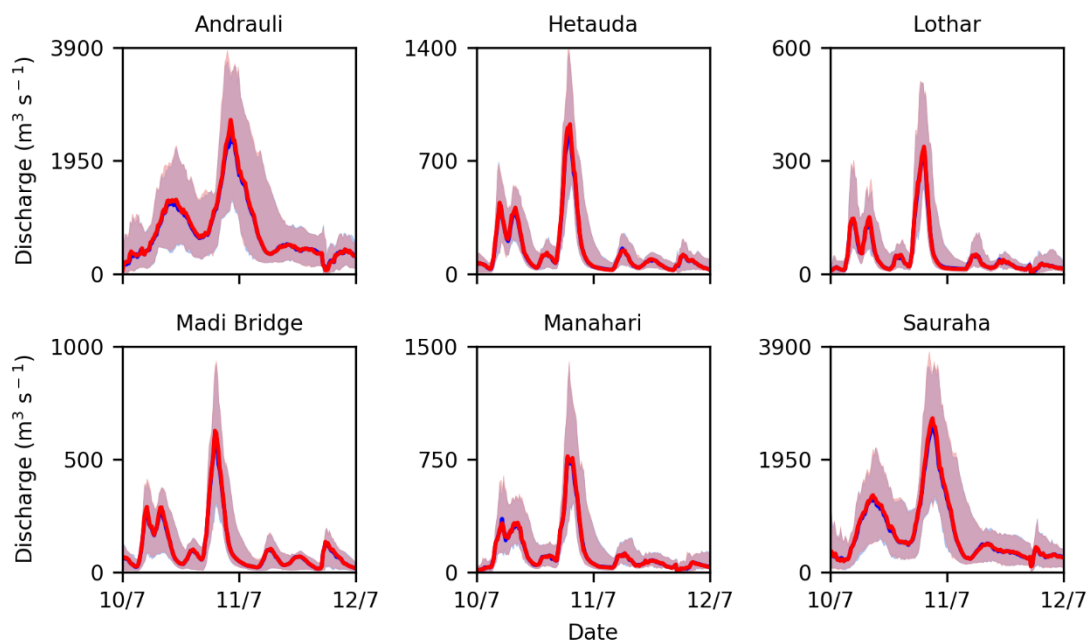


Figure 4.29: A comparison of median flow for the six flood impact points for the base (blue) and NEG_S (red) scenarios. The shaded areas represent the 10th and 90th percentile flows across the top 32 model runs. Note the different y-axis scales.

4.3.2.4 East Rapti catchment flow magnitude reduction scenario results

Spatial targeting of afforestation using the SCIMAP-Flood output

The modelled change in Q99.9 from scenarios using the SCIMAP-Flood output (Chapter 3) to determine where in the catchment the spatial targeted afforestation could be implemented is illustrated in Figure 4.30. This approach shows the impact of targeting areas that the SCIMAP-Flood output using scenarios *AFF50_F* and *AFF75_F*. Figure 4.31 shows the modelled change in Q99.9 scenarios *AFF50_PDA_F* and *AFF75_PDA_F*. Figures 4.32 and 4.33 show the respective hydrograph comparisons of the 2010 high flow event from both *AFF50_F* and *AFF50_PDA_F* and the base scenario.

With a larger forested area, the *AFF50_F* scenario produced a greater reduction in Q99.9 (average $\overline{Q99.9}$: -0.5%, average $\overline{Q99.9}$: -0.8%) than the *AFF75_F* scenario (average $\overline{Q99.9}$: -0.1%, average $\overline{Q99.9}$: -0.1%) across the six flood impact locations. The greatest reduction in Q99.9 for both spatial targeted afforestation scenarios across the six flood impact points was at Hetauda (> 0.50 - $\overline{Q99.9}$: -1.8%, $\overline{Q99.9}$: -2.4%; > 0.75 - $\overline{Q99.9}$: -0.4%, $\overline{Q99.9}$: -0.5%). The point density analysis created scenario produced a similar pattern to the original SCIMAP-Flood spatial targeting scenario with the *AFF50_PDA_F* scenario producing a greater reduction in Q99.9 (average $\overline{Q99.9}$: -1.6%, average $\overline{Q99.9}$: -2.1%) than the *AFF75_PDA_F* scenario (average $\overline{Q99.9}$: -0.4%, average $\overline{Q99.9}$: -0.6%) across the six flood impact locations. As with the *AFF50_F* and *AFF75_F* scenarios, the greatest reduction in Q99.9 point density analysis scenarios across the six flood impact points was at Hetauda (> 0.50 - $\overline{Q99.9}$: -3.7%, $\overline{Q99.9}$: -5.3%; > 0.75 - $\overline{Q99.9}$: -2.0%, $\overline{Q99.9}$: -2.7%).

The hydrographs presented in Figure 4.32 and Figure 4.33 are near identical to the base scenario across the six flood impact locations. The *AFF50_PDA_F* scenario in Figure 4.33 resulted in largest reduction in peak flows and are noticeably lower than the base scenario at the Andruali, Hetauda and Sauraha impact points. However, the overall scenario hydrograph shape in both figures are similar to the base scenario. A comparison of time-to-peak across the 2010 high flow event determines that there is a negligible impact on altering the timing of the peak discharge under the spatially targeted afforestation scenarios with a median and mean change in time-to-peak across the model ensemble of 0.0 hours for all scenarios.

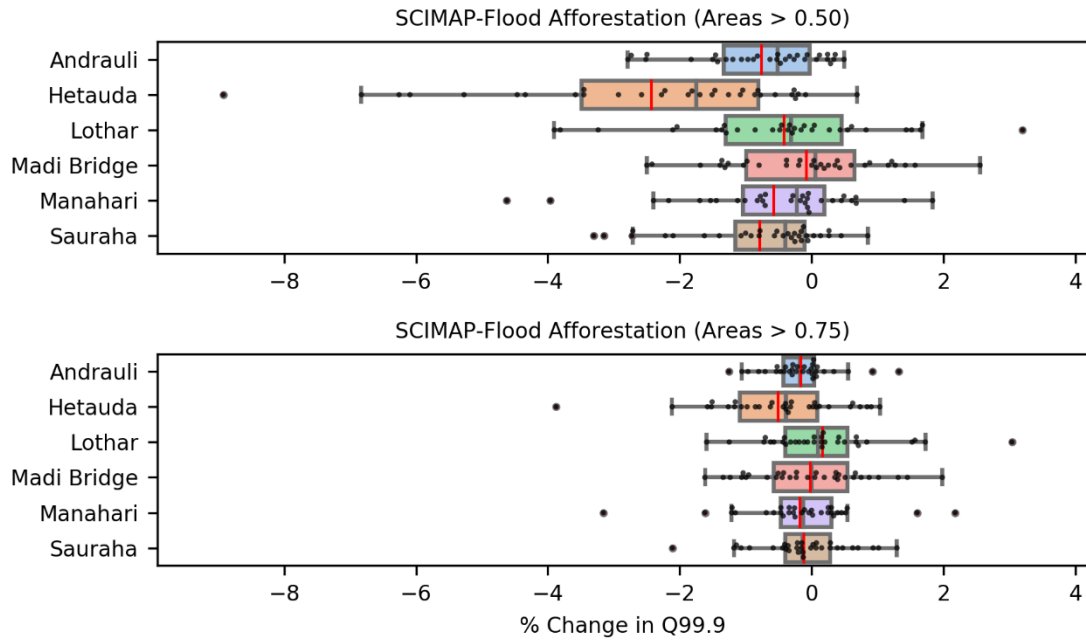


Figure 4.30: A combined boxplot and swarmplot showing the AFF50_F and AFF75_F scenarios and the corresponding percentage change in Q99.9 at the six flood impact points. See the beginning of Section 4.3.2 for general plot information.

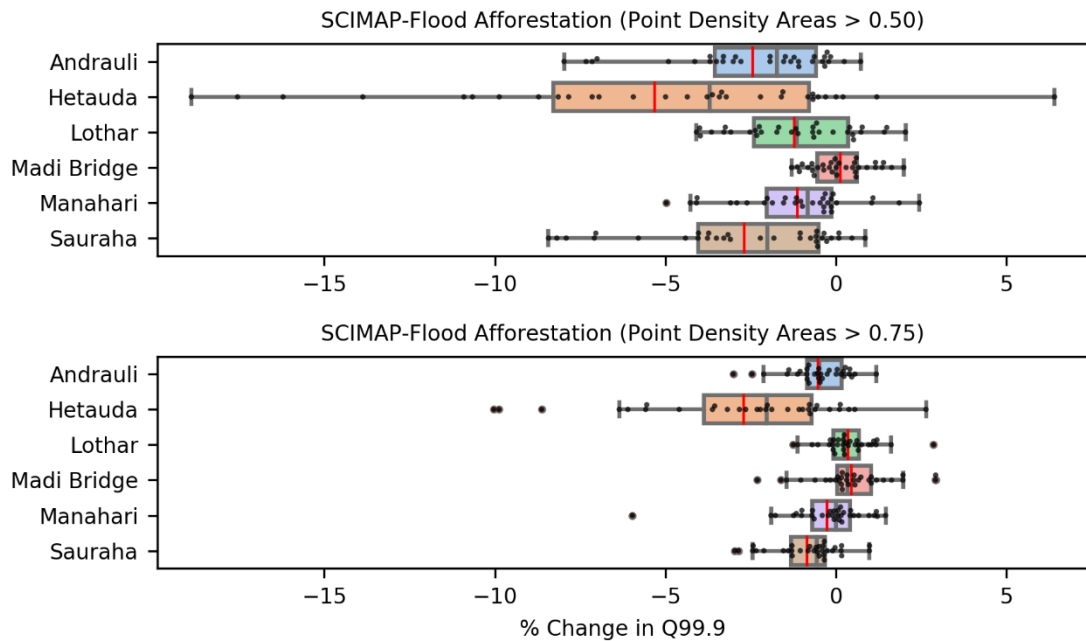


Figure 4.31: A combined boxplot and swarmplot showing the AFF50_PDA_F and AFF75_PDA_F scenarios and the corresponding percentage change in Q99.9 at the six flood impact points. See the beginning of Section 4.3.2 for general plot information.

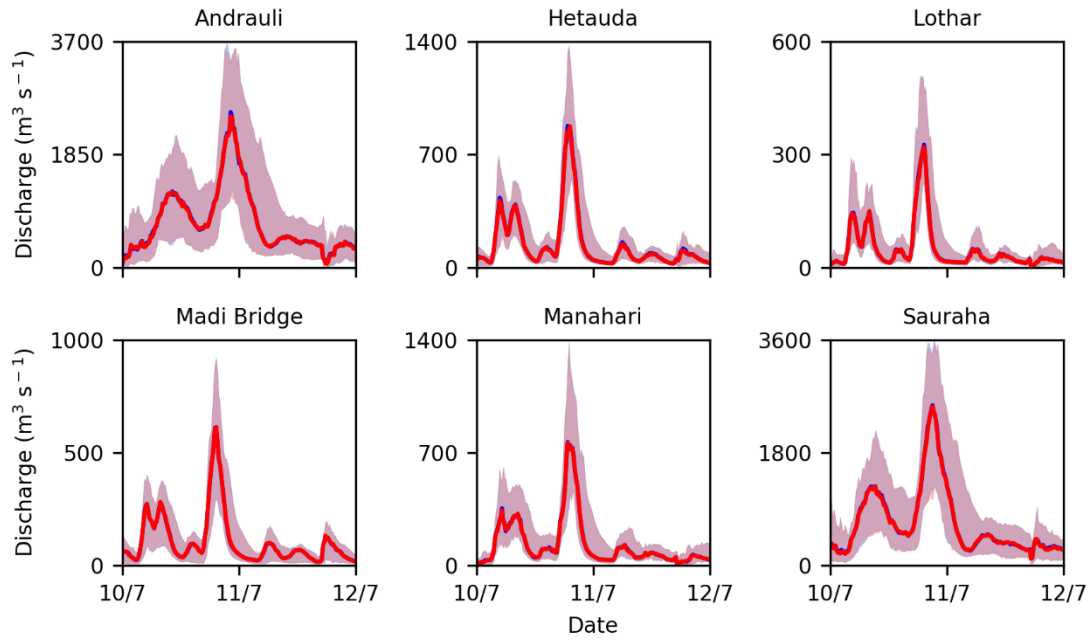


Figure 4.32: A comparison of median flow for the six flood impact points for the base (blue) and AFF50_F (red) scenarios. The shaded areas represent the 10th and 90th percentile flows across the top 32 model runs. Note the different y-axis scales.

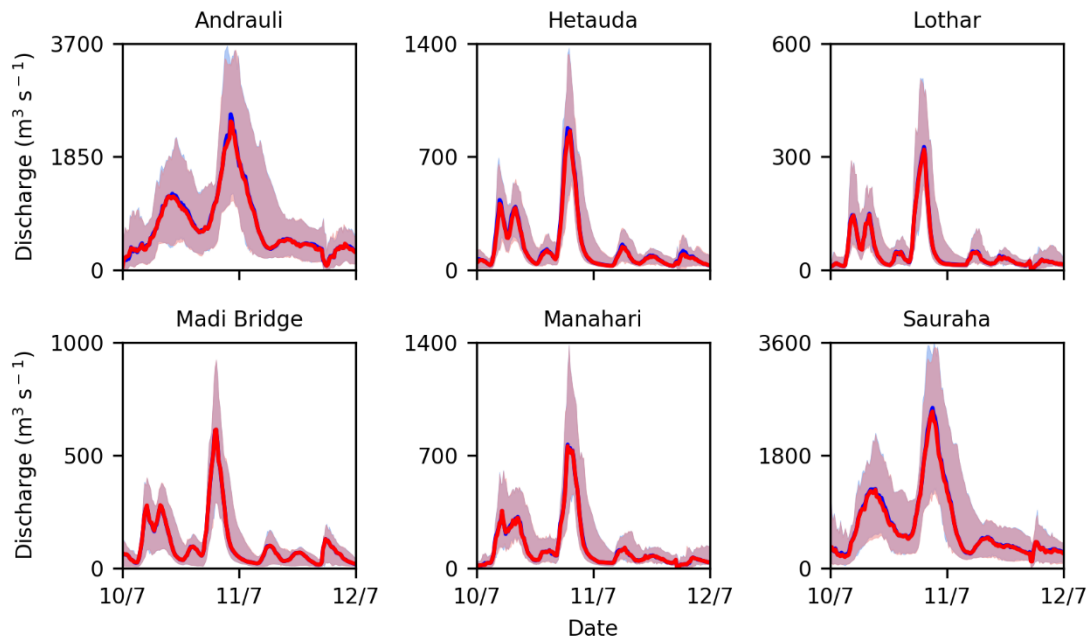


Figure 4.33: A comparison of median flow for the six flood impact points for the base (blue) and the AFF50_PDA_F (red) scenarios. The shaded areas represent the 10th and 90th percentile flows across the top 32 model runs. Note the different y-axis scales.

Spatial targeting of check dams using the SCIMAP-Flood output

The modelled change in Q99.9 from *DAM50* and *DAM75* shown in Figure 4.34. The check dam implementation was undertaken for sub-catchments in areas with a SCIMAP-Flood value of > 0.50 and > 0.75 accordingly. A hydrograph comparison of the 2010 high flow event for the *DAM50* scenario is shown in Figure 4.35.

With more sub-catchments affected, the *DAM50* scenario produced a greater Q99.9 reduction (average $\overline{Q99.9}$: -3.6%, average $\overline{Q99.9}$: -3.6%) across the six flood impact locations than the *DAM75* scenario (average $\overline{Q99.9}$: -1.2%, average $\overline{Q99.9}$: -1.3%). The greatest reduction in Q99.9 for both spatial targeting scenarios across the six flood impact points was at Hetauda (> 0.50 - $\overline{Q99.9}$: -5.9%, $\overline{Q99.9}$: -6.0%; > 0.75 - $\overline{Q99.9}$: -5.2%, $\overline{Q99.9}$: -5.4%). Neither check dam implementation scenario produced a change in Q99.9 at Madi Bridge.

The overall shape of the flood management through check dam implementation scenario hydrographs in Figure 4.35 are nearly identical to the base scenario across the six flood impact locations. There is, however, a reduction in the discharge peaks throughout the high flow event at every flood impact point other than Madi Bridge. A comparison of time-to-peak across the 2010 high flow event determines that there is limited impact on altering the timing of the peak discharge under the check dam flood management scenarios with a median change in time-to-peak across the 32 model runs of 0.0 hours and a mean change of -0.1 hours.

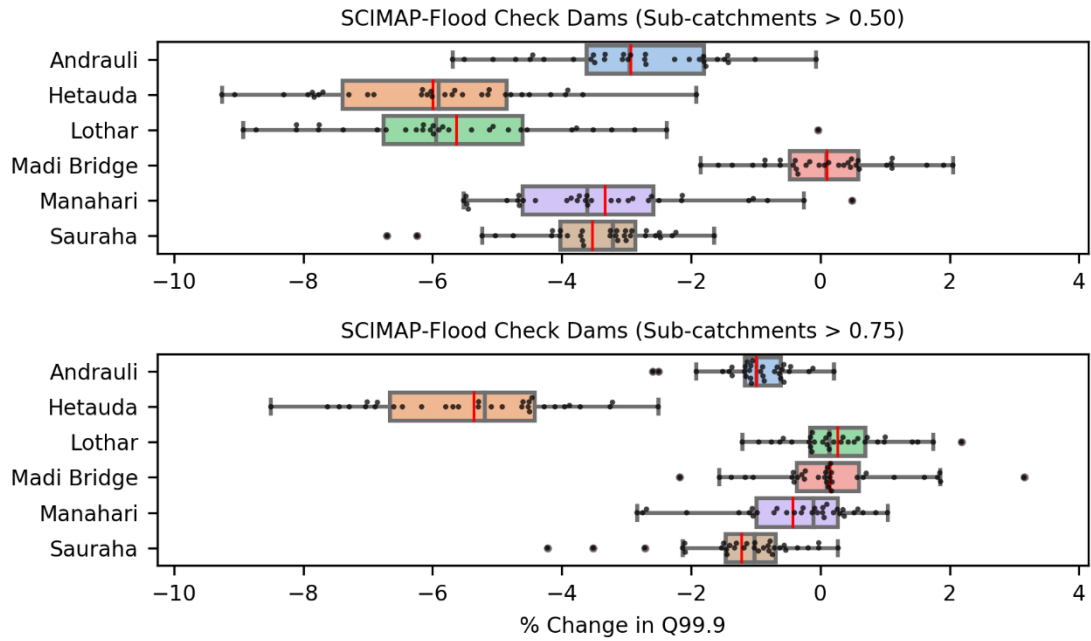


Figure 4.34: A combined boxplot and swarmplot showing the DAM50 and DAM75 scenarios and the corresponding percentage change in Q99.9 at the six flood impact points. See the beginning of Section 4.3.2 for general plot information.

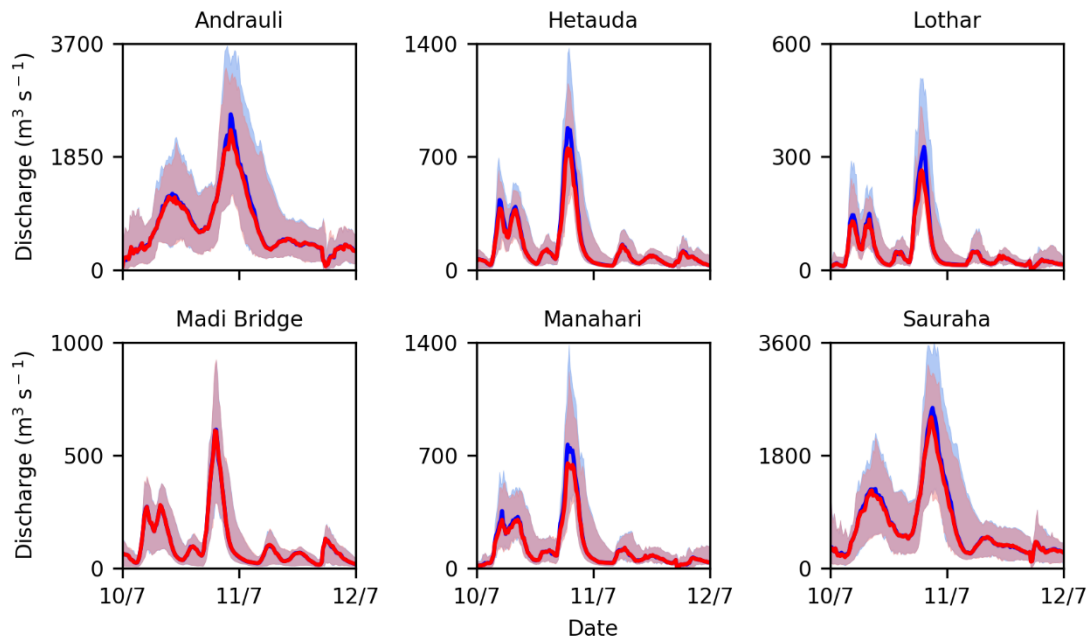


Figure 4.35: A comparison of median flow for the six flood impact points for the base (blue) and the DAM50 scenario (red) scenarios. The shaded areas represent the 10th and 90th percentile flows across the top 32 model runs. Note the different y-axis scales.

Afforestation of abandoned terraces

The modelled change in Q99.9 from the *TER_F* scenario is shown in Figure 4.36 with a hydrograph comparison of the 2010 high flow event in Figure 4.37.

The *TER_F* scenario produced an average $\widetilde{Q99.9}$ decrease of 2.9% and an average $\overline{Q99.9}$ decrease of 2.8% across the six flood impact locations. The greatest decrease in Q99.9 from the *TER_F* scenario across the six flood impact points was at Manahari ($\widetilde{Q99.9}$: -5.6%, $\overline{Q99.9}$: -4.6%) with the smallest reduction seen at Madi Bridge ($\widetilde{Q99.9}$: -0.3%, $\overline{Q99.9}$: -0.2%).

The overall shape of the *TER_F* hydrographs in Figure 4.37 are nearly identical to the base scenario across the six flood impact locations but there are slightly reduced high flow peaks as a result of the afforestation. A comparison of time-to-peak across the 2010 high flow event determines that there is a negligible impact on altering the timing of the peak discharge under the afforestation scenario with a median and mean change in time-to-peak across the 32 model runs of 0.0 hours.

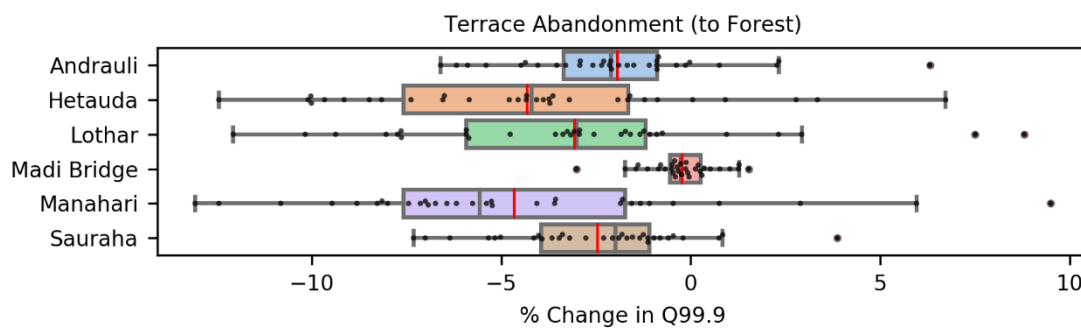


Figure 4.36: A combined boxplot and swarmplot showing the *TER_F* scenario and the corresponding percentage change in Q99.9 at the six flood impact points. See the beginning of Section 4.3.2 for general plot information.

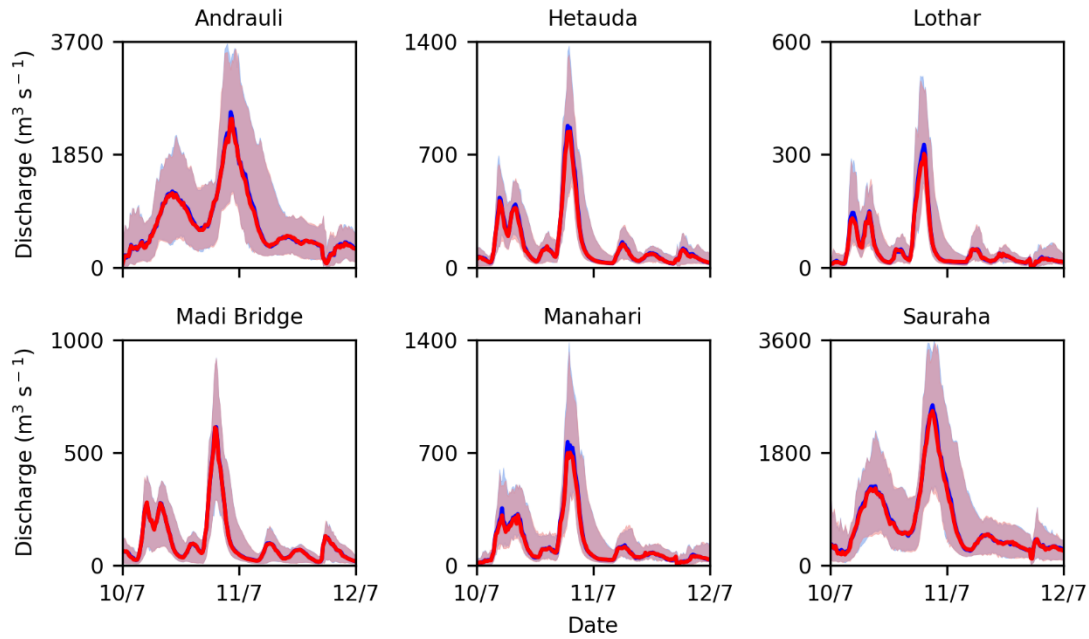


Figure 4.37: A comparison of median flow for the six flood impact points for the base (blue) and the TER_F (red) scenarios. The shaded areas represent the 10th and 90th percentile flows across the top 32 model runs. Note the different y-axis scales.

Combined spatially targeted flood management

Two combined flood management scenarios (*POS50* and *POS75*) tested the impact of spatially targeted afforestation from the SCIMAP-Flood point density analysis output and the targeted check dam implementation in highlighted sub-catchments. The modelled change in Q99.9 from the *POS50* and *POS75* scenarios is shown in Figure 4.38 with a hydrograph comparison of the 2010 high flow event for the *POS50* scenario in Figure 4.39.

With more areas afforested and more sub-catchments with spatially targeted check dam implementation, the *POS50* scenario produced a greater Q99.9 reduction (average $\overline{Q99.9}$: -5.3%, average $\overline{Q99.9}$: -5.6%) across the six flood impact locations than the corresponding *POS75* scenario (average $\overline{Q99.9}$: -1.6%, average $\overline{Q99.9}$: -1.8%). The greatest reduction in Q99.9 for both spatial targeting scenarios across the six flood impact points was at Hetauda (> 0.50 - $\overline{Q99.9}$: -10.3%, $\overline{Q99.9}$: -10.9%; > 0.75 - $\overline{Q99.9}$: -7.3%, $\overline{Q99.9}$: -7.7%). Neither scenario produced a predicted change in Q99.9 at Madi Bridge.

As with the individual flood management approach scenarios in through Section 4.3.2.3, the overall shape of the *POS50* hydrographs in Figure 4.39 are nearly identical to the base scenario across the six flood impact locations. There is, however, a notable reduction in the peaks throughout the high flow event at every flood impact point apart from Madi Bridge. A comparison of time-to-peak across the 2010 high flow event determines that there is limited impact on altering the timing of the peak

discharge under the POS50 scenario with a median change in time-to-peak across the 32 model run ensemble of 0.0 hours and a mean change of -0.1 hours.

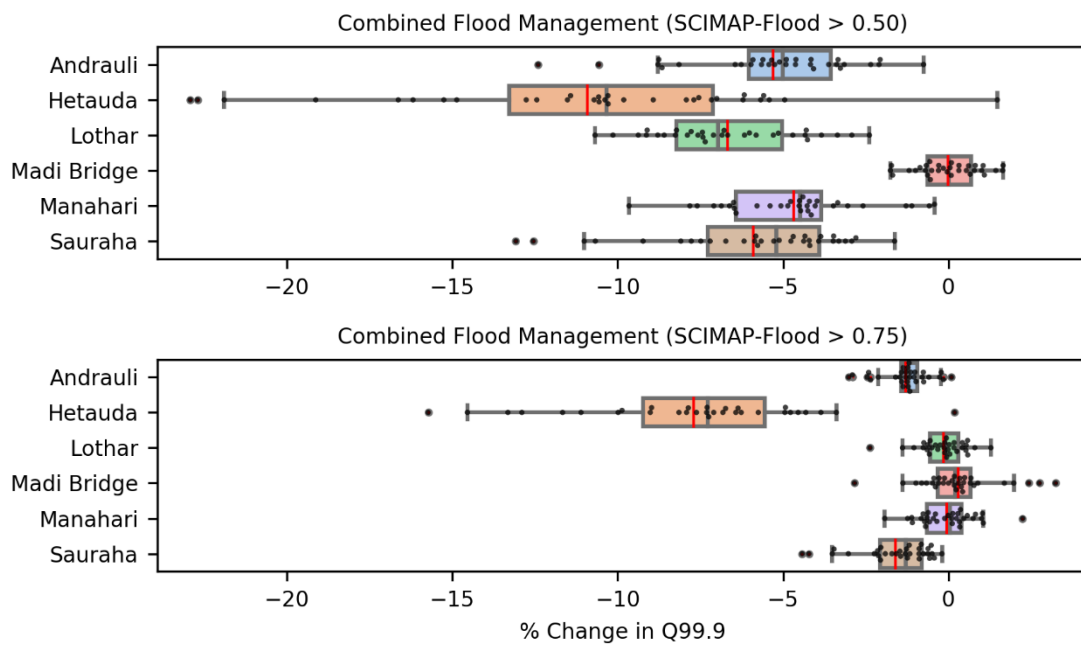


Figure 4.38: A combined boxplot and swarmplot showing the POS50 and POS75 scenarios, and the corresponding percentage change in Q99.9 at the six flood impact points. See the beginning of Section 4.3.2 for general plot information.

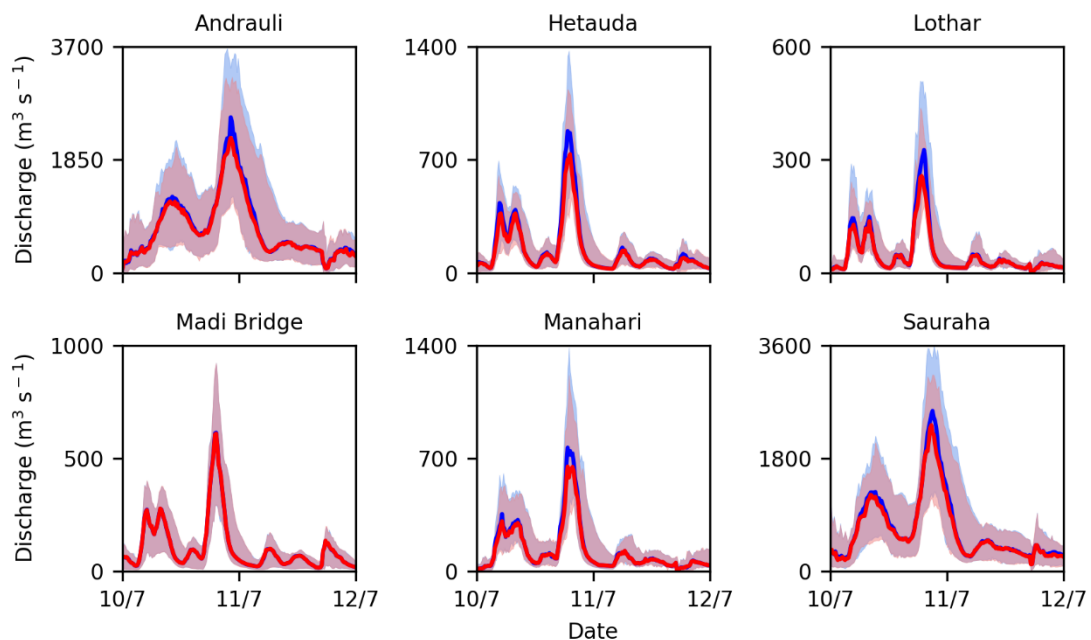


Figure 4.39: A comparison of median flow for the six flood impact points for the base (blue) and the POS50 (red) scenarios. The shaded areas represent the 10th and 90th percentile flows across the top 32 model runs. Note the different y-axis scales.

4.3.2.5 *Offsetting the impact of negative land use change with catchment-scale flow magnitude reduction interventions scenarios results*

Offsetting negative land use change with spatially targeted afforestation

Two combined flood management scenarios tested the impact of spatially targeted afforestation from the SCIMAP-Flood point density analysis and the potential to mitigate the possible flow magnitude increasing land use change. This was undertaken using scenarios *AFF50_PDA_F_NEG_S* and *AFF75_PDA_F_NEG_S*. The modelled change in Q99.9 from the offsetting afforestation scenarios are shown in Figure 4.40 with a hydrograph comparison of the 2010 high flow event for the *AFF50_PDA_F_NEG_S* scenario in Figure 4.41.

The *AFF50_PDA_F_NEG_S* scenario produced an average $\overline{Q99.9}$ increase of 1.3% and an average $\overline{Q99.9}$ increase of 2.8% across the six flood impact locations. The *AFF75_PDA_F_NEG_S* scenario modelled an average $\overline{Q99.9}$ increase of 1.1% and an average $\overline{Q99.9}$ increase of 3.0%. The only reduction in Q99.9 for both spatially targeted afforestation scenarios across the six flood impact points was the $\overline{Q99.9}$ change at Hetauda ($> 0.50 - \overline{Q99.9}$: -1.3%, $> 0.75 - \overline{Q99.9}$: -2.3%). The $\overline{Q99.9}$ change at Hetauda showed an increase ($> 0.50 - \overline{Q99.9}$: +2.0%, $> 0.75 - \overline{Q99.9}$: +1.4%). The impact of targeted afforestation to offset land use change did not result in a decrease in Q99.9 at the other flood impact points for either scenario.

The overall shape of the *AFF50_PDA_F_NEG_S* scenario hydrographs in Figure 4.41 are nearly identical to the base scenario across the six flood impact locations, with a slight reduction in peak flows at Hetauda from the flood management approach. A comparison of time-to-peak across the 2010 high flow event determines that there is limited impact on altering the timing of the peak discharge under the afforestation flood management scenarios with a median and mean change in time-to-peak across the 32 model run ensemble of 0.0 hours.

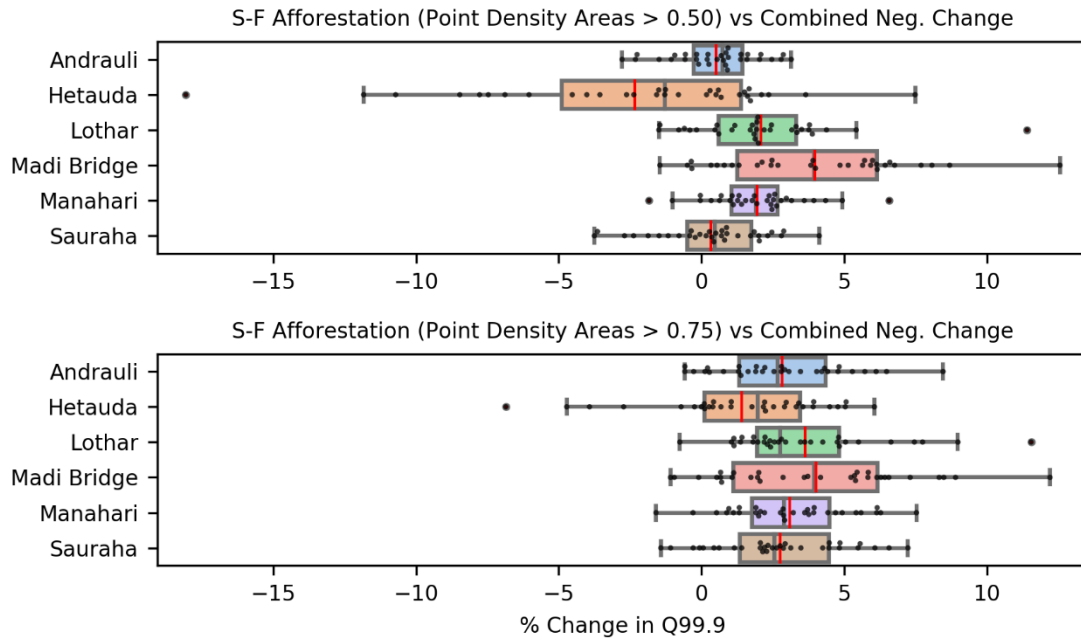


Figure 4.40: A combined boxplot and swarmplot showing the *AFF75_PDA_F_NEG_S* and *AFF50_PDA_F_NEG_S* scenarios and the corresponding percentage change in Q99.9 at the six flood impact points. See the beginning of Section 4.3.2 for general plot information.

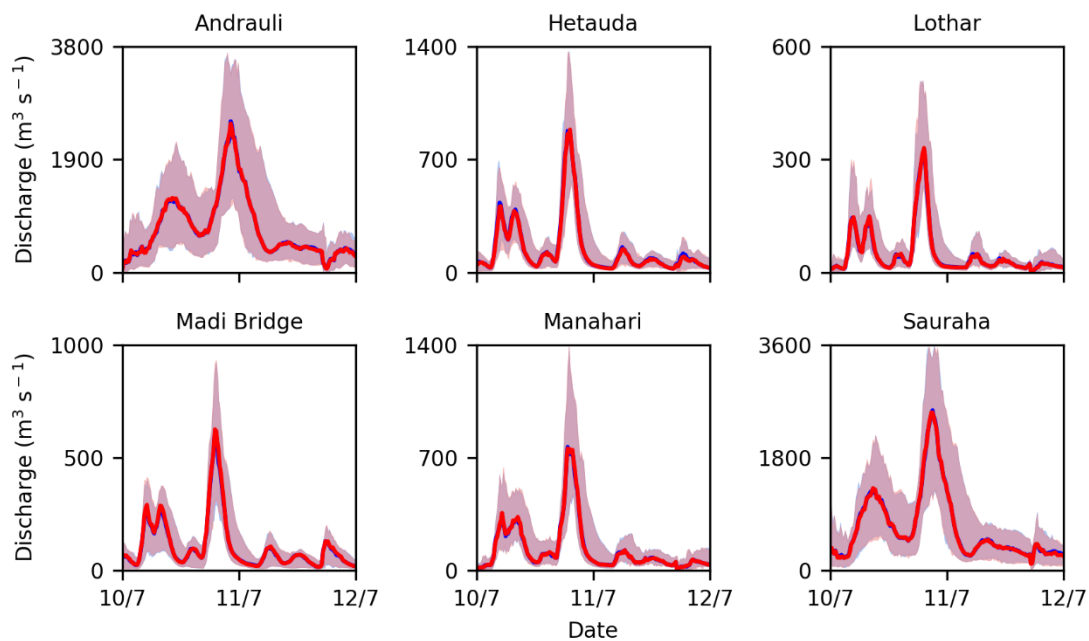


Figure 4.41: A comparison of median flow for the six flood impact points for the base (blue) and the *AFF50_PDA_F_NEG_S* (red) scenarios. The shaded areas represent the 10th and 90th percentile flows across the top 32 model runs. Note the different y-axis scales.

Offsetting negative land use change with spatially targeted check dam implementation

Two combined flood management scenarios assessed the impact of spatially targeted check dam implementation at mitigating the potential flow magnitude increasing future land use change: scenarios *DAM50_NEG_S* and *DAM75_NEG_S*. The modelled change in Q99.9 from the *DAM50_NEG_S* and *DAM75_NEG_S* scenarios are shown in Figure 4.42 with a hydrograph comparison of the 2010 high flow event for the *DAM50_NEG_S* scenario in Figure 4.43.

The *DAM50_NEG_S* scenario produced average $\overline{Q99.9}$ reduction of 0.9% and an average $\overline{Q99.9}$ reduction of 0.6% across the six flood impact locations with the *DAM75_NEG_S* scenario resulting in an average $\overline{Q99.9}$ increase of 1.9% and an average $\overline{Q99.9}$ increase of 2.2%. The greatest reduction in Q99.9 for the *DAM50_NEG_S* scenario across the six flood impact points was at Manahari ($\overline{Q99.9}$: -4.2%, $\overline{Q99.9}$: -3.4%). Madi Bridge was the only flood impact point to have a predicted increase in Q99.9 under the check dam implementation in the *DAM50_NEG_S* scenario. The only reduction in Q99.9 for the *DA750_NEG_S* scenario across the six flood impact points was at Hetauda ($\overline{Q99.9}$: -2.5%, $\overline{Q99.9}$: -1.9%).

The overall shape of the *DAM50_NEG_S* scenario hydrographs in Figure 4.43 are nearly identical to the base scenario across the six flood impact locations with a slight reduction in peak flows at all flood impact points outside of Madi Bridge. A comparison of time-to-peak across the 2010 high flow event determines that there is limited impact on altering the timing of the peak discharge under the check dam flood management scenarios with a median change in time-to-peak across the 32 model runs of 0.0 hours and a mean change of -0.1 hours.

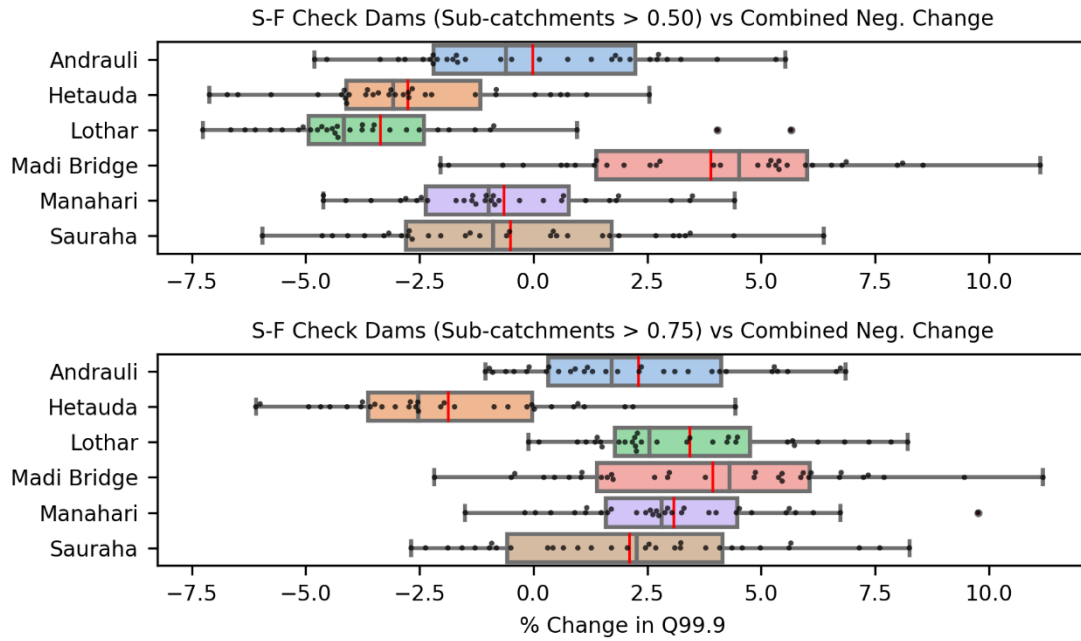


Figure 4.42: A combined boxplot and swarmplot showing the DAM50_NEG_S and DAM75_NEG_S scenarios and the corresponding percentage change in Q99.9 at the six flood impact points. See the beginning of Section 4.3.2 for general plot information.

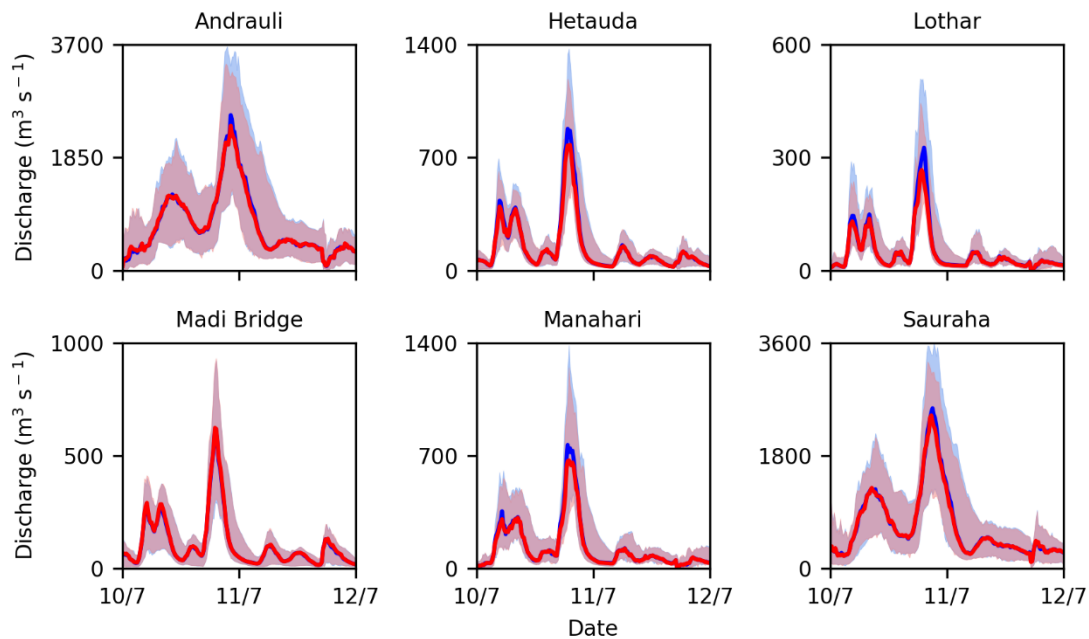


Figure 4.43: A comparison of median flow for the six flood impact points for the base (blue) and the DAM50_NEG_S (red) scenarios. The shaded areas represent the 10th and 90th percentile flows across the top 32 model runs. Note the different y-axis scales.

Offsetting negative land use change with a combined flood management approach

Both scenario *POS50_NEG_S* and *POS75_NEG_S* tested the impact of spatially targeted afforestation and check dam implementation at mitigating the potential flow magnitude increasing future land use change. The modelled changes in Q99.9 for both scenarios are shown in Figure 4.44 with a hydrograph comparison of the 2010 high flow event for the *POS50_NEG_S* scenario in Figure 4.45.

The *POS50_NEG_S* scenario produced average $\overline{Q99.9}$ reduction of 2.5% and an average $\overline{Q99.9}$ reduction of 2.8% across the six flood impact locations. The *POS75_NEG_S* scenario had an average $\overline{Q99.9}$ increase of 1.5% and an average $\overline{Q99.9}$ increase of 1.5%. The greatest flood impact point reduction in Q99.9 for the *POS50_NEG_S* was at Hetauda ($\overline{Q99.9}$: -7.1%, $\overline{Q99.9}$: -8.2%). Madi Bridge was the only flood impact point to have a predicted increase in Q99.9 under the *POS50_NEG_S* scenario. The only reduction in Q99.9 for the *POS75_NEG_S* scenario across the six flood impact points was at Hetauda ($\overline{Q99.9}$: -4.0%, $\overline{Q99.9}$: -4.6%).

The overall shape of the *POS50_NEG_S* scenario hydrographs in Figure 4.45 are nearly identical to the base scenario across the six flood impact locations with a slight reduction in peak flows at all flood impact points outside of Madi Bridge. A comparison of time-to-peak across the 2010 high flow event determines that there is limited impact on altering the timing of the peak discharge under a combined flood management scenario to offset future land use change with a median change in time-to-peak across the 32 model runs of 0.0 hours and a mean change of -0.1 hours.

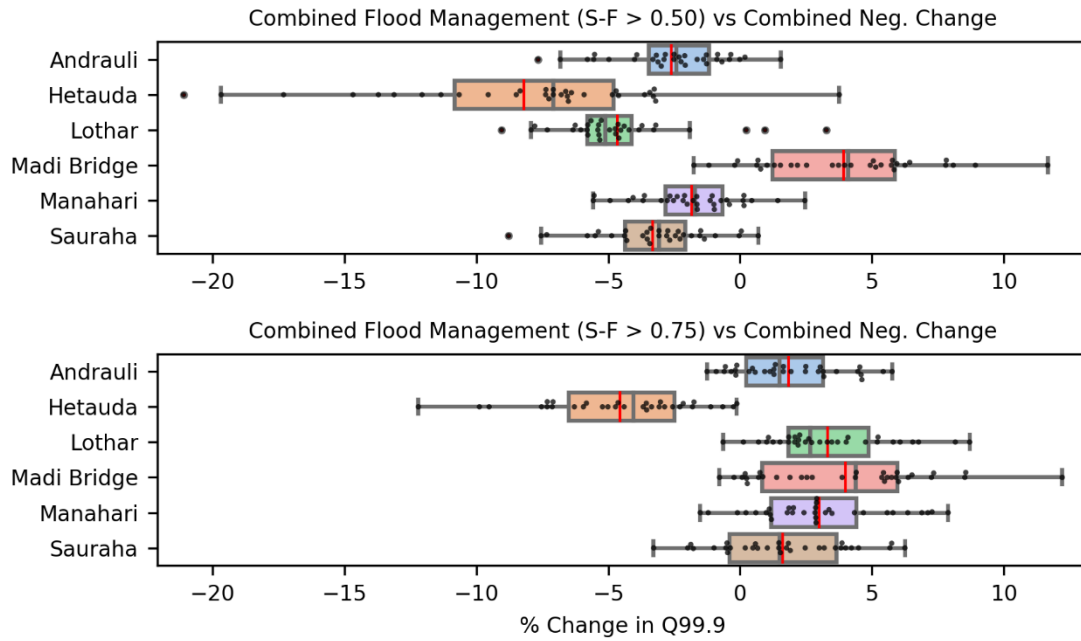


Figure 4.44: A combined boxplot and swarmplot showing the POS50_NEG_S and POS75_NEG_S scenarios, and the corresponding percentage change in Q99.9 at the six flood impact points. See the beginning of Section 4.3.2 for general plot information.

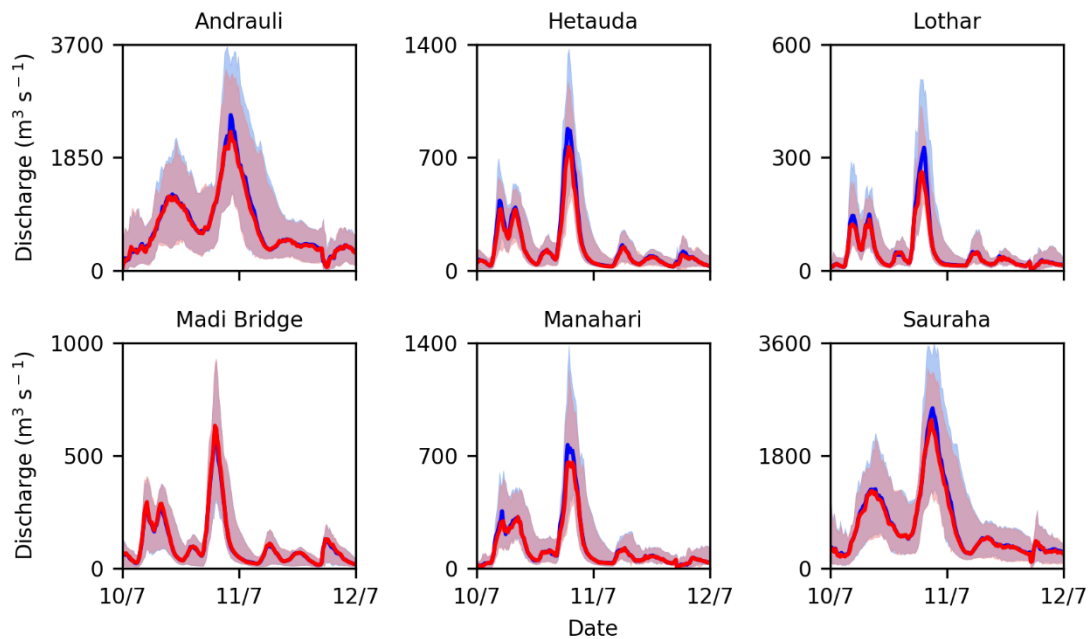


Figure 4.45: A comparison of median flow for the six flood impact points for the base (blue) and POS50_NEG_S (red) scenarios. The shaded areas represent the 10th and 90th percentile flows across the top 32 model runs. Note the different y-axis scales.

4.4 DISCUSSION

4.4.1 The potential impacts of future land use change and degradation on the flood regime in the East Rapti catchment

Land use change and degradation, including the abandonment of agricultural terraces, deforestation and urbanisation, are key factors with a potential detrimental impact on the hydrological regime in many Nepalese, and more generally Himalayan, catchments (e.g. Gerrard and Gardner, 2002; Neupane et al., 2015; Chaudary et al., 2016; Rimal et al., 2019). Through a combination of the simulation of the impacts of blanket coverage (Section 4.3.2.1) and the flow magnitude increase through land use change scenarios (Section 4.3.2.2), it is evident from the CRUM3 model results that future land use change in the East Rapti catchment can potentially have a large ($\overline{Q99.9}$ increase of up to 75.1%) impact on flood regime at a given flood impact point.

Although unrealistic in their implementation, the blanket coverage scenarios provide an indication of the bounds of the flow magnitude alteration impact of each land cover within the catchment. The results of the blanket coverage scenarios of the main land covers indicate that only the blanket Forest coverage (*BLA_F*) (average Q99.9 change - $\overline{Q99.9}$: -9.3%, $\overline{Q99.9}$: -10.0%) has a positive impact on the reduction of high flows across the flood impact points. The results suggest that any land within the East Rapti catchment that is changed from *Forest* will contribute to increasing the flow magnitude and any land changed to *Forest* will help decrease the flow magnitude; the impact of this on flood inundation patterns is shown in Chapter 5.

With 58% of the East Rapti catchment presently covered with forest, then future land use change scenarios based on deforestation and the loss of *Forest* coverage to flow magnitude increasing land covers should increase the flow magnitude to the points of flood impact. The loss of the entire *Forest* coverage in the other blanket coverage scenarios shows the significance of the cumulative impact from the localised, model cell-scale, hydrological impact of forestry. The model results agree with previous research on this issue through simulating the altered soil condition produced by deforestation; this includes the impacts of reduced canopy interception (Haigh et al., 1990) and increased runoff coefficients from a lower infiltration capacity (Pathak et al., 1985; Gardner and Gerrard, 2002). As a result of extensive deforestation in the other blanket coverage scenarios, a large increase in Q99.9 is predicted throughout the catchment. With erosion and sediment dynamics not represented in CRUM3, any additional flow change from a reduced channel capacity due to deforestation-produced sediment aggradation is not considered (Singh, 2013). The results of the blanket change to either Rainfed (*BLA_RA*) or Irrigated Agriculture (*BLA_IA*) adheres with the increased flow trend of prior studies in Himalayan catchments, such as Sastry et al. (1986) and Rai and

Sharma (1998), who predict catchment runoff volumes increasing by between 11% and 15% with a shift from forest coverage to agriculture and a peak runoff increase of up to 72%.

However, the potential of forest coverage within a Himalayan context to reduce flow magnitude is contested with some research concluding that deforestation would have only a minor role in monsoonal flooding (Gilmour et al., 1987; Hamilton and Pearce, 1987; Thomson et al., 2006; Nepal, 2012). Metz (1991) and Beschta (1998), amongst others, determine that there would be a localised, sub-catchment-scale impact of deforestation. This reduced and localised impact is certainly apparent in the more realistic deforestation scenarios modelled on CRUM3 that represented land use change (to either *Shrubland* or *Irrigated Agriculture*) in the accessible areas around the populated fringes of the flat agriculturally productive parts of the East Rapti catchment. The scenarios model a loss of 5.1% of the existing *Forest* cover which, based on the higher annual rate of deforestation outlined in Chaudary et al. (2016), is equivalent to approximately 25 years of future tree-felling. The results of both fringe deforestation scenarios (*DEF_IA* and *DEF_S*) show a slight increase in average Q99.9 across the six flood impact locations of between 1.3% and 1.9%. The changes in high flows are comparable to a modelled deforestation scenario in the Dudh Kosi River catchment by Nepal (2012) who saw an increase in flow of 1%. The impact of this is localised with a minimal (< 0.3%) increase in Q99.9 at the Lothar and Manahari flood impact points and a larger increase (up to 5.1%) at the Madi Bridge point. The variation in change can be attributed to the spatial distribution of the deforestation in the scenarios with both the Lothar and Manahari sub-catchments having little upstream areas of fringe deforestation. In contrast the Madi Bridge flood impact point has large areas of deforestation around the populated plains region in relation to sub-catchment area, and thus more area is converted to a higher flow magnitude producing land cover.

From the initial blanket coverage scenario results, an additional land use change within the East Rapti catchment that will exacerbate the increase in flow magnitude is the alteration from *Rainfed Agriculture* to any of the other land cover classes apart from *Forest*. The *Rainfed Agriculture* blanket scenario (*BLA_RA*) had the lowest average increase in Q99.9 ($\overline{Q99.9}$: +12.8%, $\overline{Q99.9}$: +14.4%) of the remaining five blanket coverage scenarios, and thus the abandonment of upland terraced agriculture has the possibility to be altered to a land use change with a higher flow magnitude increasing potential. The construction of terraces reduces the slope and alters the soil characteristics through increasing the infiltration rates (Arnaez et al., 2015). Within CRUM3, the *Rainfed Agriculture* is represented through the soil and land cover characteristics. The potential issues of catchment-scale modelling and the corresponding localised topographic representation of the terrace agriculture discussed in Section 4.4.3.

The abandonment of the upland terraced agriculture is an issue impacting many Nepalese catchments with over 30% of the previously cultivated land across the country having been abandoned (Khanal and Watanabe, 2006; Paudel et al., 2014). This abandonment can be attributed to outmigration as foreign labour and an urbanising population shifting away from subsistence farming towards alternative income sources (Paudel et al., 2014; Jaquet et al., 2015; Ojha et al., 2017). From a flooding perspective, the abandoned terraces, often left in a poorly maintained or degrading condition, cause significant changes to the hydrological dynamics of hillslopes (Arnaez et al., 2015). This change in the hydrological regime can be seen from the CRUM3 model results for the abandoned terrace scenarios where the change to *Shrubland* (TER_S) or *Bare Ground* (TER_BG) of 50% of the *Rainfed Agriculture* area results in an increase in Q99.9 of up to 5.8%. The increase in Q99.9 can be attributed to a greater area of the East Rapti catchment with the altered, unmanaged land cover and therefore a lower infiltration rate and an increased runoff generation potential.

Conversely, a land cover change from abandoned terrace to *Forest* (TER_F), a scenario that could be managed afforestation or long term forest development from *Shrubland*, results in a decrease in Q99.9 with a greater coverage of the catchment having the capacity to store more water in the soil. As with the deforestation scenario, there are localised differences across the flood impact points from the effects of upstream terrace abandonment. The land cover in the Hetauda, Lothar and Manahari sub-catchments is predominantly a mixture of *Forest* and *Rainfed Agriculture* and thus the alteration of terraced agriculture in the upper parts of the catchment to either a flow magnitude increasing (*Bare Ground* or *Shrubland*) or decreasing (*Forest*) land cover has an impact on the Q99.9 flow. The Madi Bridge sub-catchment has limited *Rainfed Agriculture* upstream and therefore only a slight change in Q99.9 is predicted. The resultant increase in Q99.9 at the furthest downstream flood impact point (Andrauli) between the DEF_S ($\overline{Q99.9}$: +1.8%, $\overline{Q99.9}$: +1.9%) and abandoned TER_S ($\overline{Q99.9}$: +1.3%, $\overline{Q99.9}$: +1.5%) scenarios are comparable albeit with the latter scenario altering 9% (in contrast to 5.1%) of the catchment area.

With Nepal one of the most rapidly developing countries in Asia, there have been large increases in the percentage of the population in urban areas; the urban population has risen from 2.9% in the 1950s, 9.2% in 1991, 17.1% in 2011 and more than 50% in 2017 (Rimal et al., 2019). Urban extent expansion modelling undertaken by Rimal et al. (2019) in several districts in the Terai region indicates that the spatial coverage of urban areas is set to expand by a further 38.51% by 2026 and 55.77% by 2036 compared to 2016 based on the current urbanisation trends. The model results of an urban expansion scenario in the East Rapti catchment indicate that this urban expansion alone, through the increased *Built-Up Area* (URB_BUA), would have a minimal impact on the high flow regime at the

points of flood impact. Despite the *BLA_BUA* scenario increasing the average Q99.9 flow by around 45%, the *URB_BUA* scenario had a $\overline{Q99.9}$ increase of 0.2% and a $\overline{Q99.9}$ increase of 0.1%. With 2% of the catchment area being converted to *Built-Up Area* it would suggest that there was not enough of a land cover change to significantly disrupt the hydrological regime within the East Rapti catchment given the currently low *Built-Up Area* coverage. Additionally, this change in land cover predominantly occurred in the downstream, lower gradient central part of the catchment where less of the flood waters are generated.

However, the progressively expanding urban population within many Nepalese catchments does help exacerbate the terrace abandonment and deforestation issues that, based on the CRUM3 model results, do have a larger impact on the flooding regime. A combined scenario (*NEG_S*), modelling a potential mixture of terrace abandonment, deforestation and urban expansion, predicted an increase of > 3% in the Q99.9 flow across all the six flood impact points and the effects witnessed throughout the East Rapti catchment. The catchment-scale scenarios that investigate the potential for future land use change to increase the flow magnitude illustrate that there is the possibility for increased high flows due to land use change and degradation. There will need to be an effort to manage against the detrimental changes at the catchment-scale and preventative measures, such as the Community Forest Program (Chaudary et al., 2016), are vital in the effort to mitigate against the impact of future land use change on the flow regime.

4.4.2 The potential for flood risk reduction through catchment-scale flood management in the East Rapti catchment

The implementation of flood management schemes in Nepal has generally been reactive to individual flood events with localised implementation at the point of flood impact (Government of Nepal, 2017). This reactive implementation fails to consider the hydrological connectivity across the whole catchment and the implementation of possible flood risk reduction solutions on a wider scale (Dhakal, 2013; Government of Nepal, 2017). As such, research from Nepal et al. (2014) and the Government of Nepal (2017) highlights that an integrated land and water management approach undertaken at the catchment-scale, is necessary to ensure sustainable development and reduced detrimental impacts. The CRUM3 model results (Section 4.3.2.3), which support the proposed shift towards the catchment-scale approach, predict that the flow magnitude in the East Rapti catchment can be reduced. However, with a combined approach of large scale spatially targeted afforestation and check dam implementation (*AFF50_PDA_F_NEG_S*) reducing the Q99.9 flow by < 6% ($\overline{Q99.9}$: -5.3%, $\overline{Q99.9}$ -5.6%), the use of solely catchment-scale flood management approaches to combat flood risk might not be effective. Additionally, none of the flood management scenarios had a significant impact on the timing

or shape of the flood peaks with no significant alterations to the modelled flood hydrograph between the existing base scenario and the catchment-scale scenarios.

Soft-engineering techniques and interventions include the use of vegetation for slope control and soil retention to maintain or increase the infiltration capacity, with afforestation a key tool in providing this benefit across the catchment (Shrestha et al., 2012; Singh, 2013). The blanket coverage *Forest* scenario (*BLA_F*) provided the maximum available Q99.9 decrease (average Q99.9 change - $\overline{Q99.9}$: -9.3%, $\overline{Q99.9}$: -10.0%). This scenario involved the remaining 42% of the catchment being converted to the *Forest* class. Through using the SCIMAP-Flood results to help spatially target key flood water generating areas within the East Rapti catchment, the afforestation scenarios (*AFF50_F* and *AFF75_F*) did not convert enough land to a flow magnitude decreasing land cover to provide a substantial Q99.9 reduction across the catchment (maximum average Q99.9 change - $\overline{Q99.9}$: -1.6%, $\overline{Q99.9}$: -2.1%).

Additionally, it must be noted that a proportion of land identified for the spatially targeted afforestation, particularly from the point density analysis approach, is in close proximity to the city of Hetauda. Proactive land use change in these areas would potentially be difficult to enact due to the pressures of urban expansion. The original SCIMAP-Flood output targeted areas altered 1.8% and 0.3% of the catchment to *Forest* for the *AFF50_F* and *AFF75_F* scenarios respectively. Whilst the *AFF50_PDA_F* and *AFF75_PDA_F* scenarios, using point density analysis, altered 5.4% and 1.3% of the catchment to *Forest*. The results of the spatial targeted scenarios do, however, indicate that afforestation in key flood water generating areas does provide a better Q99.9 reduction per the amount of land cover changed. The *AFF50_PDA_F* scenario provided a greater Q99.9 reduction at the downstream flood impact points of Andrauli and Sauraha than the afforestation on abandoned terraces (*TER_F*) scenario whilst altering less of the catchment; 5.4% as opposed to 9.0% accordingly.

The limited impact of a more realistic implementation of catchment-scale afforestation for flood management purposes, as seen in the East Rapti model results, has been present in other modelling studies (e.g. Beschta et al., 2000; Lane et al., 2005; Bathurst et al., 2011; Salazar et al., 2012). Calder and Aylward (2006 [pp.89-90]) highlight that “although land use change effects on floods may be detectable on small catchments the “signal” is likely to be weaker on large catchments”. Iacob et al. (2017), working on a 100% catchment coverage scenario for a small (72 km²) Scottish catchment, predicted high flow reductions (from a peak flow of 12.5 m³s⁻¹) of 39% for a 10-year return period event and 30% for a 100-year return period event with the flood reducing capacity for new woodland diminished in extreme events. Even in a smaller catchment, the Iacob et al. (2017) study shows that relatively large, often unrealistic, increases in areal coverage of forest are needed to provide a worthwhile high flow reduction and to induce a delayed flood peak. In three larger European

catchments (catchment areas: 184 km² - 954 km²) a peak flow reduction in smaller flood events of up to one third is predicted due to an increased area of forestry (from 1% to 28%, 14% to 23% and 32% to 65% forest coverage) but Salazar et al. (2012) determined no change in peak flows during the largest flood events. The reduced impact of afforestation (up to 97% forest coverage) in larger flood events is also seen in a study by Bathurst et al. (2011) on three Chilean catchments (catchment area – 94 km² to 1,545 km²) where peak discharges are higher for the pre-afforestation conditions but the difference decreases as the size of the rainfall event and the peak discharge increase. Notably, within the East Rapti afforestation results, only the full blanket coverage scenario had any impact on the time-to-peak of the 2010 high flow event. The weaker “signal” also identified by Calder and Aylward (2006), and seen in other studies on larger catchments, from the impact of afforestation on the flow regime is evident in East Rapti scenario modelling.

Check dams are a hard-engineering approach implemented in the upper parts of catchments for discharge control but due to rapid sediment deposition can often have a limited lifespan in a Himalayan catchment context (Shrestha et al., 2012; Dhakal, 2013; Shrestha, 2014). The implementation of check dams (*DAM50* and *DAM75*) in key flood water generating sub-catchments provided a greater Q99.9 reduction than the spatially targeted afforestation. This high flow reduction (up to -5.9%) was largely localised with the sub-catchments with check dams in (Manahari, Lothar and Hetauda) producing the largest change in Q99.9. However, a positive impact was also simulated in the downstream flood impact points along the main East Rapti channel at Andrauli and Sauraha. With the SCIMAP-Flood results (Section 3.3.2.1) not predicting any key flood water generating areas in the Reu Khola sub-catchment, which contains the Madi Bridge flood impact location, no check dams were implemented and thus no change in Q99.9 was predicted.

As a comparison to the East Rapti results, a study looking at the impact of check dams on the flood regime in the 2,210 km² Fuping catchment in China found that catchment wide check dam implementation reduced flood peaks by between 0.6% and 24.6% (Chen et al., 2018). The reduction in peak flow due to check dam implementation was reduced when events with greater return period (Chen et al., 2018). With the check dams represented in the CRUM3 model in a simplified way there could be potential for further peak flow reductions at the localised sub-catchment level, if not at the larger catchment level, with optimised check dam design and layout. Based on an approach such as that used by Yazdi et al. (2018), who investigate the optimal design for check dams in a mountainous watershed, detailed modelling of the check dam network in the SCIMAP-Flood identified, flood water generating sub-catchments for the East Rapti catchment could result in an increased localised flow reduction of up to 54% for 10-year return period events. Notably, the cumulative impact of each

optimally designed sub-catchment network would need to be considered, taking into consideration flow synchronisation at the catchment-scale.

Using debris dams in a UK catchment a potential approach to assess the suitability of river reaches for interventions with regards to the impact on peak flows was undertaken by Odoni and Lane (2010). The research established, within individual sub-catchments, some locations have the potential to produce either a neutral (little impact on peak flows) or negative (increase in peak flows) impact on the flow regime. With the check dams represented in CRUM3 through a simplistic flow limit, a more detailed approach, such as the OVERFLOW modelling in the Odoni and Lane (2010), would be advisable for the identified sub-catchments in the East Rapti catchment to help pinpoint the locations of check dams within the channel system.

A final set of scenarios looked at the possibility of catchment-scale flood management approaches being used to offset the flow magnitude increases resulting from future land use change (deforestation, urbanisation, and terrace abandonment) within the East Rapti catchment. Without any flood mitigation interventions, the *NEG_S* scenario predicted a Q99.9 increase of 3.5%. All the flood mitigation scenarios that concentrated solely on the highest potential flood water generating areas (*AFF75_PDA_F_NEG_S*, *DAM75_NEG_S* and *POS75_NEG_S*) reduced the impacts of future land use change to an average $\widetilde{Q99.9}$ increase of < 2%. The *DAM50_NEG_S* and *POS50_NEG_S* scenarios, targeting areas with a SCIMAP-Flood value of > 0.75, were predicted to offset the impact of future land use change and slightly reduce the Q99.9 value. With the interventions placed along the sub-catchments that feed into the main East Rapti channel (Manahari, Lothar and upstream of Hetauda) the greatest impact was at these locations. The Madi Bridge flood impact point had no mitigation from future land use change from the spatially targeted catchment scenarios with no interventions in the upper part of the Reu Khola. Though part of the East Rapti catchment, with the Reu Khola and main East Rapti channel confluence only 2 km upstream of the East Rapti and Nayarani confluence, a separate catchment management plan would be best suited for reducing flood risk to the Madi Bridge impact point.

From the perspective of altering the high flow regime across the East Rapti catchment and with a view to reducing the risk of flooding at several points of the flood impact, the CRUM3 model results indicate that there were not significant reductions in the flood flows that can be achieved through catchment-scale land use change for flood management. Across all the modelled scenarios the impact was localised with greatest reduction in Q99.9 was at the flood impact points in the upstream parts of the East Rapti catchment. These locations (Manahari, Lothar and Hetauda) were immediately downstream of the implemented flood management interventions and, as such, observed the largest benefit. The

afforestation scenarios, even accounting for the spatial targeting of flood water generating areas, required excessive spatial coverage of land cover change to result in large positive impacts on the flow regime. The use of spatial targeting to determine where to implement a flood management measure had a drawback in a catchment with the channel network layout like the East Rapti. The entry of the Reu Khola at the very downstream end of the main East Rapti channel, almost immediately prior to the confluence with the Nayarani River, resulted in a lack of impact a flood management measures placed in the sub-catchment. Any flood management measures within the Reu Khola sub-catchment would have no effect on the other flood impact points and therefore the area was not highlighted as one of the most beneficial in the spatial targeting approach. This resulted in scenarios not placing flood management measures in the sub-catchment and the Madi Bridge flood impact point unaided when combating future change.

4.4.3 The representation of the East Rapti catchment in the CRUM3 hydrological model

The CRUM3 model was designed to represent landscape-scale hydrological processes to help answer questions related to flow extremes and the potential impact of land management techniques (Lane et al., 2009). As with many distributed modelling studies, to represent the East Rapti catchment in a suitable manner for assessing the impact of flood management scenarios, several assumptions have been made and balances sought. For example, when using a distributed model to assess the impact of land use change, there is an assumption of model parameters with the spatiotemporal variations, particularly of soil and vegetation properties, constrained to between land cover categories and not within each land cover category (Iacob et al., 2017). The CRUM3 model uses different land cover parameters for the six main catchment land covers within the East Rapti. There are, however, no variations beyond water balance within individual cells for each land cover category and therefore no accounting for differences across each land cover category, such as vegetation species throughout the *Forest* class or crop type in the *Irrigated Agriculture* class. There is variation within crop types grown across Terai regions of Nepal, such as that in densely populated part of the East Rapti, with a mixture of rice, lentils, wheat, vegetables and maize in the irrigated areas and maize, millet and potatoes in the upland terrace areas (Shilpakar, 2003). The different crops will have different properties and thus could require varied model parameters to have their impact on the hydrological regime represented. A potential solution within the CRUM3 set up to help factor in this variation within each land cover would be to distribute the soil and vegetation parameters from an acceptable range for each land cover using a Monte Carlo approach. This process would greatly increase the number of simulations required to determine the most effective model parameter sets.

The research has been constrained by the amount of computing time on the high-performance computing cluster at Durham University. To find a balance between landscape representation and computing time in the cell size used in the East Rapti catchment model was set at 150 m. Compared to the original ALOS World 3D-30m (AW3D30) product, the use of a coarser resolution 150 m grid may lose some of the landscape features vital for hydrological response (Quinn et al., 1991). Several distributed modelling studies (e.g. Zhang and Montgomery, 1994; Wolock and Price, 1994; Yang et al., 2001; Sulis et al., 2011) have determined that, due to changes in topographic characteristics (local slope, plan curvature and drainage area) and wetness index, that predicted peak discharge increased and lows flow decreased as the cell size increased. It must be noted, however, that a wetness index is not used within CRUM3. Zhang and Montgomery (1994), note that the impact of cell size will be reduced in larger catchments, such as the East Rapti, with the runoff hydrograph dominated by channel routing. With the East Rapti, as with many Nepalese catchments, having a complex topography with areas of high slope in the upland upstream parts of the catchment and flatter plain regions in the downstream parts of the catchment there is the potential for an impact on the modelled flows due to the CRUM3 cell size. The coarser cell size will reduce the localised impact of upland topographic features such as terraced agriculture and gullies, which can delay and accelerate the ability of the landscape to transfer runoff into the channel network respectively. On the flatter plains with the East Rapti the coarser cell size will remove smaller features such as irrigation channels that can impact the conveyance and flow direction of water across the catchment. Nonetheless, the representation of the topographic features is the same across both the present day and future catchment management scenarios and does not impact the comparison.

CRUM3 has been developed for surface water driven catchments and thus, despite a groundwater recharge rate and representation of the water table within model structure, there is only a simplified capacity within the model for deep groundwater aquifer recharge. There is little known about the physical properties of the deep groundwater aquifer storage in Nepal and the contribution to the hydrological budget has been excluded in previous studies (Bookhagen and Burbank, 2010; Bricker et al., 2014). As noted in previous catchment-scale modelling studies (e.g. Shilpakar et al., 2011; Nepal, 2012), the groundwater contribution to the hydrological regime in a Nepalese catchment context predominantly occurs as baseflow outside of the monsoon period. With the CRUM3 model results not being used for year-round water balance management, and this study concentrating on the high flow regime in the monsoon period, the simplified representation of the deep groundwater aquifer is not considered to be a significant factor in the comparison between catchment-scale flood management approaches.

The flow routing within the river channel network within CRUM3 uses the Muskingham-Cunge method (Cunge, 1969; Ponce and Lugo, 2001) to represent the flood wave propagation through the catchment. This simplified flow method is prominent in many distributed catchment-scale models due to the ability calculate the flow rates at all stream-network nodes at a single time-step and the ability to apply this approach in data deficient situations (Perumal and Sahoo, 2008; Takeuchi et al., 2009). A limitation of the Muskingham-Cunge method is that it assumes a rectangular channel section and therefore does not consider the impacts of reach scale channel morphology throughout the catchment. It must also be considered that, with a dynamic sediment system in the East Rapti catchment (Shrestha et al., 2008), the use of a high-resolution representation of the local channel morphology, such as surveyed cross sections, would potentially be incorrect after the subsequent flow event capable of sediment transport. With the successful application of the Muskingham-Cunge method in prior research using distributed catchment modelling (e.g. Orlandini and Rosso, 1998; Takeuchi et al., 2009; Li et al., 2014) the simplified approach to flow routing is a limitation to consider but the use of the method not invalidate the investigation into the impact of flood management scenarios in the East Rapti catchment.

These limitations in the CRUM3 modelling approach, as with any modelling study, do require consideration when interpreting the actual magnitude of hydrological change produced from the catchment-scale flood management scenarios simulated in the East Rapti catchment. Nonetheless, the CRUM3 results clearly indicate that there is a far greater potential for land use change in increase the flow magnitude in the East Rapti catchment with scenarios such as deforestation increasing the percentage of the catchment covered in a flow magnitude increasing land cover.

4.5 CONCLUSIONS

Through a case study based on the East Rapti catchment, the research presented in this chapter describes one of the first attempts at identifying the potential changes from catchment-scale flood management and land use change scenarios on flow regime within Nepal. With a proposed shift towards a catchment-scale approach to mitigating and managing flood risk in Nepal, the use of the fully distributed, physically-based CRUM3 hydrological model allows for the impact of spatially targeted land use change scenarios to be tested. The potential impact the same scenarios have on altering the localised flood extent at the points of flood impact is investigated in Chapter 5.

The most significant outcome from the catchment-scale modelling work was that the CRUM3 results illustrate a far greater potential for land use change to increase flow magnitudes in the East Rapti catchment. Across all the land use change scenarios there was a negligible impact on the timings of the peak flows; this was most likely due to catchment alterations. **The blanket coverage scenario results suggest that any land within the East Rapti catchment that is changed from *Forest* will contribute to increasing the flow magnitude and any land changed to *Forest* will help decrease the flow magnitude.** With many Nepalese catchments facing potential future land use change through the abandonment of agricultural terraces, deforestation, and urbanisation there is predicted to be an increase in high flow magnitude as a consequence. There is currently *Forest* coverage of 58% in the East Rapti catchment and, as such, future land use change scenarios involving loss of *Forest* coverage to a flow magnitude increasing land cover will result in increased flow magnitudes at the points of flood impact. To help manage against the detrimental changes at the catchment-scale preventative measures, such as the Community Forest Program (Chaudary et al., 2016), are vital in the effort to combat negative change to the high flow regime.

Building on the research presented in the Chapter 3, the flood management scenarios were created using a spatial targeting approach, targeting the identified flood water generating areas to the six points of flood impact in the SCIMAP-Flood process. **However, even using a combined approach of large scale spatially targeted afforestation and check dam implementation, the resulting reduction in the Q99.9 flow indicates that the use of solely catchment based flood management approaches to combat flood risk in the East Rapti would appear not to have the required impact on the high flow regime to reduce flood hazard; the impact of scenarios on flood hazard is presented in Chapter 5.** The flow reduction through afforestation scenarios, excluding the full catchment afforestation scenario, required too great change of land cover to have useful positive impact on the flow regime. With no land cover change required, the spatially targeted check dam implementation in flood water generating catchments appears to be the most suitable individual flood management intervention for

the East Rapti catchment. **However, the use of check dams, in combination with proactive land use change in the form of targeted afforestation, would be the best solution to mitigate the impact of future detrimental land use change across the catchment.**

5 DETERMINING THE IMPACT OF CATCHMENT-SCALE LAND USE CHANGE ON LOCAL-SCALE INUNDATION PATTERNS

5.1 INTRODUCTION

The use of a coupled hydrological and hydraulic modelling approach allows for the representation of complex channel morphology and complex hydrodynamic interactions between the channel and floodplain (Hankin et al., 2019). The catchment-scale hydrological model, CRUM3 in Chapter 4, uses a simplified Muskingham-Cunge flow routing method (Cunge, 1969; Ponce and Lugo, 2001) that does not use channel cross section information. As such, there is a need to increase the understanding of the impacts of reach scale channel morphology at the key flood-impacted parts of the catchment. The impact that catchment-scale upstream interventions, such as targeted afforestation or check dams in key sub-catchments, could have on flow magnitude and the corresponding change to inundation extent and depth due to a change in flows can be addressed with the additional inundation modelling (Metcalfe et al., 2017).

The process of model coupling involves the outputs of one model being fed into another model as boundary conditions or input parameters. An example would be the hydrograph from a hydrological model becoming inflows into a hydraulic model as input boundary conditions (e.g. Grimaldi et al., 2013; Mateo et al., 2014; Nguyen et al., 2016; Zope et al., 2016; Felder et al., 2017). From a flood management perspective, Felder et al. (2017) note that a coupled hydrological model is often used to determine the conversion of rainfall to runoff. The corresponding modelled flood event hydrograph is then used as the inflow condition in a hydraulic flood inundation model. Examples of this coupled hydrological/hydraulic modelling approach to investigate flood extent change as the final step of a model cascade include Biacamaria et al. (2009), Bonnifait et al. (2009), Rodriguez-Rincon et al. (2015), Nguyen et al. (2016) and Felder et al. (2017). In a comparable approach to that used in this research, McMillan and Brasington (2008) developed an end-to-end flood risk assessment approach through a coupled model chain comprising of a stochastic rainfall model, rainfall-runoff model, and a floodplain inundation model. While many studies use a coupled modelling approach for flood inundation mapping, there is limited research using the approach to test the impact of catchment-scale flood management measures. Looking at historic rather than future land use change, Zope et al. (2016) use a combination of HEC-HMS (hydrological) and a 1D HEC-RAS (hydraulic) model to assess the impact of different land covers across a 25 km² Indian catchment on inundation extent. Hankin et al. (2019) integrate a hillslope runoff model (Dynamic Topmodel) with a 2D hydrological model (both JFlow and HEC-RAS were used) to model the impact of runoff attenuation features. At a large-scale, Linde et al.

(2011) model the effectiveness of flood management measures on peak discharges in the Rhine catchment. Using a combination of a hydrological model (HBV) and a 1D hydraulic model (SOBEK) the study tests the impact of reforestation, restored polders, channel bypasses and river restoration on the water depths from low probability flood events (Linde et al., 2011).

There has been previous inundation modelling undertaken within the East Rapti catchment using different modelling approaches. The Asian Development Bank (2016) used a steady-state 1D HEC-RAS (Brunner, 1995) to undertake return period analysis and a climate change impact assessment on a 96 km stretch of the main East Rapti channel. The model was established using a combination of surveyed cross-sections and satellite-derived elevation data. Notably, the Asian Development Bank (2016) report determines that the existing embankments along the main East Rapti channel are often overtopped and are therefore excluded from the modelling. Singh (2013) also used HEC-RAS to look at the impact of integrated catchment solutions on the low gradient downstream parts of the catchment. The study established that river training works (e.g. dykes, check dams and embankments) implemented in the sub-catchments north of Sauraha could help alleviate flooding on the Terai plains. However, Singh (2013) notes that the many existing embankments are vulnerable to overtopping and outflanking in higher return period events.

The final stage of the end-to-end approach in this research assesses the localised impact of the flow magnitude changing catchment-scale scenarios (see Section 4.2.7). This is achieved using a LISFLOOD-FP hydraulic model (Bates and De Roo, 2000) that has been set up for Hetauda and Sauraha; two of the six flood impact areas within the East Rapti catchment. LISFLOOD-FP is a raster-based hydraulic model that allows for the comparison of inundation extents produced by different catchment-scale scenarios. The results of the hydraulic modelling help determine if the flow magnitude and hydrograph shape changes produced as the result of a catchment-scale management intervention provide a significant change in the inundation extent at key flood impacted areas. The effectiveness of a scenario can then be assessed by the change in inundation patterns produced. Within this research the effectiveness of a catchment-scale flood management scenario is investigated using a combination of inundation extent reduction across the model area and the change in inundation depths over the *Built-Up Area* land cover. The *Built-Up Area* land cover represents settlements and infrastructure within the catchment and assessing the pattern of inundation over the land cover is vital when considering whether a scenario can be determined as effective.

The research presented in Chapter 5 is the final stage of the catchment management analysis and quantifies the impact on inundation extent of a range of flow magnitude alteration scenarios. The work undertaken in this chapter builds on the output from the CRUM3 research (see Chapter 4) with

hydrographs produced throughout the catchment from the hydrological modelling used as LISFLOOD-FP model inflows. The outputs of this chapter provide evidence for the effectiveness or otherwise of upstream catchment interventions and so has implications for the planning process in flood-impacted areas.

5.2 METHODS

Figure 5.1 provides an overview of the methodological approach used. LISFLOOD-FP (Bates and De Roo, 2000) hydraulic model was selected to undertake the detailed flood inundation modelling (detailed in Section 5.2.1). LISFLOOD-FP has been used in a range of research looking at both urban and rural flood inundation extents across the globe (e.g. Horritt and Bates, 2002; Pappenberger et al., 2005; Wilson et al., 2007; Wright et al., 2008; Neal et al., 2012; Komi et al., 2017). A key advantage of the LISFLOOD-FP model is that it can work with both low- and high-resolution elevation data and can therefore be applied data-sparse catchments relying on globally available lower resolution elevation data (Gobeyn et al., 2017). The flexibility within the data requirements for the LISFLOOD-FP model and the ability to mass produce, through code, model run files make it a suitable inundation model for the final stage of the end-to-end approach when consideration application to other catchments.

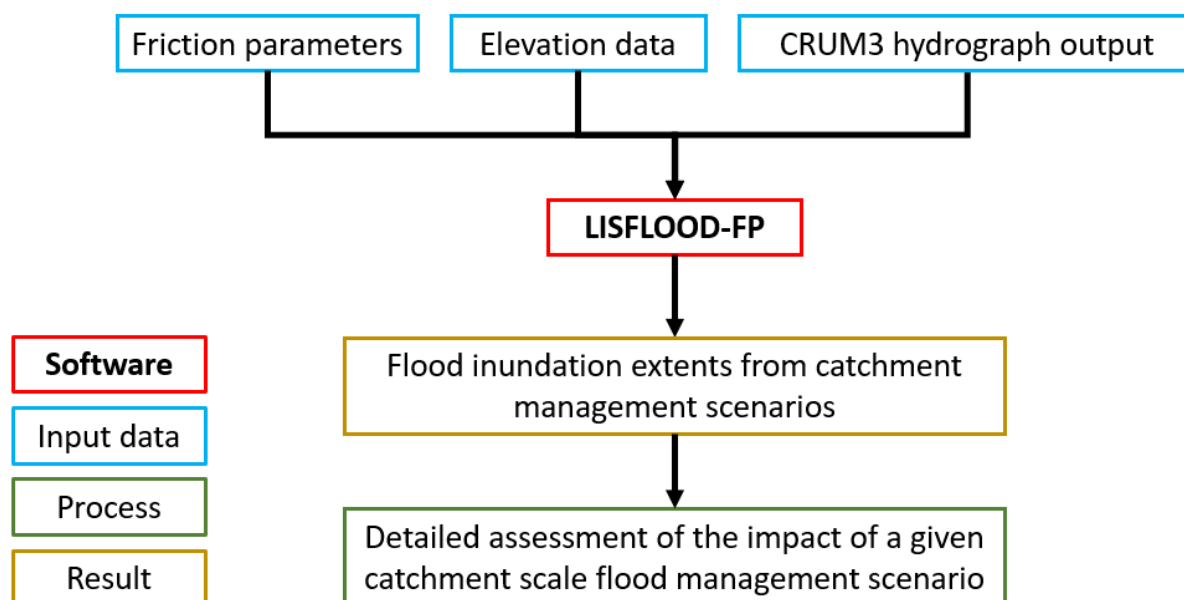


Figure 5.1: Outline of the process used in this chapter to provide a detailed assessment of the impacts of a given catchment management scenario

Due to the lack of detailed observed flows and flood inundation data (from SAR or cloud free optical imagery), model results use a relative comparison approach between scenarios and existing baseline conditions within the East Rapti catchment. A lack of information to validate flood risk models is an issue which occurs in many studies in data sparse areas (e.g. Apel et al., 2009; Vojtek and Vojtekova, 2016; Dottori et al., 2013; Winter et al., 2018). As in previous research using unvalidated models (e.g. Winter et al., 2018), a description of the sensitivity within the modelling approach will be presented to communicate the potential uncertainty in the modelling process. As noted by Leow et al. (2011), model results should not be used for design purposes as results indicate relative, not exact, potential change in flood extent and depths from different catchment scenarios. Importantly, the hydraulic flood inundation model uses representative model parameters derived from a mixture of field-based

observations from the catchment together with appropriate model parameter estimation techniques as used in previous research, for example, Domeneghetti et al. (2013), Falter et al. (2016) and Vojtek and Vojtekova (2016). Therefore, whilst the baseline model parameters perhaps do not produce the optimal model performance, they are representative of the modelled area.

When applying an uncertainty framework to a coupled modelling approach, such as the GLUE method used in Chapter 4, the results relating to each parameter set in the initial model must be propagated through the model chain individually (McMillan and Brassington, 2008). As such, and in keeping with the equifinality approach undertaken in the catchment-scale hydrological modelling, the catchment-scale scenario hydrographs produced for a model ensemble containing the top 32 CRUM3 parameter sets are used in the inundation modelling. The ensemble of inflow hydrographs results in the prediction of inundation area as a probability (e.g. Romanowicz and Beven, 1996; Aronica et al., 2002; Pappenberger et al., 2005; Di Baldassarre et al., 2010), enabling an improved representation of the uncertainty in the modelling predictions (Di Baldassarre et al., 2010; Domeneghetti et al., 2013; Beven et al., 2015).

Section 5.2.1 provides a brief overview of the LISFLOOD-FP hydraulic model. Section 5.2.2 describes the data used to set up LISFLOOD-FP for the Sauraha and Hetauda models within the East Rapti catchment. Section 5.2.3 investigates the sensitivity analysis approach to assess variation in the main inputs. Section 5.2.4 outlines the catchment-scale scenarios brought forward from the CRUM3 modelling in Chapter 4 that are modelled using LISFLOOD-FP.

5.2.1 LISFLOOD-FP

LISFLOOD-FP is a raster-based hydraulic model developed at the University of Bristol to simulate the dynamics of a floodplain using high resolution topographic data (Bates and De Roo, 2000; Horritt and Bates, 2002; Hunter et al., 2005; Bates et al., 2010; Neal et al., 2011; Neal et al., 2012; Savage et al., 2016). LISFLOOD-FP is an explicit finite difference model and solves the inertial approximation of shallow water equations where advection is neglected (Savage et al., 2016). The version of LISFLOOD-FP outlined in Neal et al. (2012) uses a sub-grid channel in which the channel is defined separately from the floodplain; this version allows for channel widths to be defined independently from the floodplain raster spatial resolution (e.g. Komi et al. 2017). This version is used for this research on Nepal with channel widths defined using measurements from Google Earth satellite imagery (Google Earth, 2019). A similar approach is used by Komi et al. (2017) and O'Loughlin et al. (2019) amongst others. A full overview of the LISFLOOD-FP model, including information on the floodplain and channel flow solvers and the detailed data requirements, is available in Bates et al. (2013) with mathematic

descriptions of the LISFLOOD-FP model and sub-grid version in Bates et al. (2010) and Neal et al. (2012).

The principal data requirements for the LISFLOOD-FP model are topography data, inflow and outflow conditions and friction parameters. Topography is represented through a raster elevation grid. The inflow conditions are a time series of stage or discharge inflows at the upstream end of the modelled extent. The outflow conditions are a downstream boundary that is either a free flow boundary or derived from gauged river levels. The model friction parameters are a raster grid representing Manning's n values for different categories of land cover classes in the modelled extent.

5.2.2 LISFLOOD-FP model setup

The LISFLOOD-FP model has been set up for two flood impacted locations: 1) the village of Sauraha in the central part of the catchment along the main East Rapti channel and 2) the city of Hetauda in the upstream part of the catchment. These two locations cover a range of localised morphology with the Sauraha model exemplifying the lower gradient downstream part of the catchment and the Hetauda model representing a more constrained upstream part of the catchment. The model extent and location with the East Rapti catchment of the two locations are shown in Figure 5.2 (Sauraha) and 5.3 (Hetauda) accordingly. The Sauraha model covers an area of 34.6 km² and the Hetauda model covers an area of 45.6 km². Sauraha is the tourism centre for visitors to Chitwan National Park and was heavily impacted in the 2017 flood event. Hetauda is located in close proximity to the SCIMAP-Flood identified flood water generating areas and is the location in which the CRUM3 model results predicted that many of the catchment-scale flood management scenarios would have the greatest impact (in terms of percentage change) on the high-flow regime. With this chapter looking at the change in flood extent due to flow magnitude change Hetauda is therefore an ideal flood impact point to assess. Both settlements are one of the chosen flood impact points from SCIMAP-Flood chapter (Section 3.2.2.2) and, as such, were selected for the detailed flood inundation modelling to assess the impact of the catchment management scenarios.

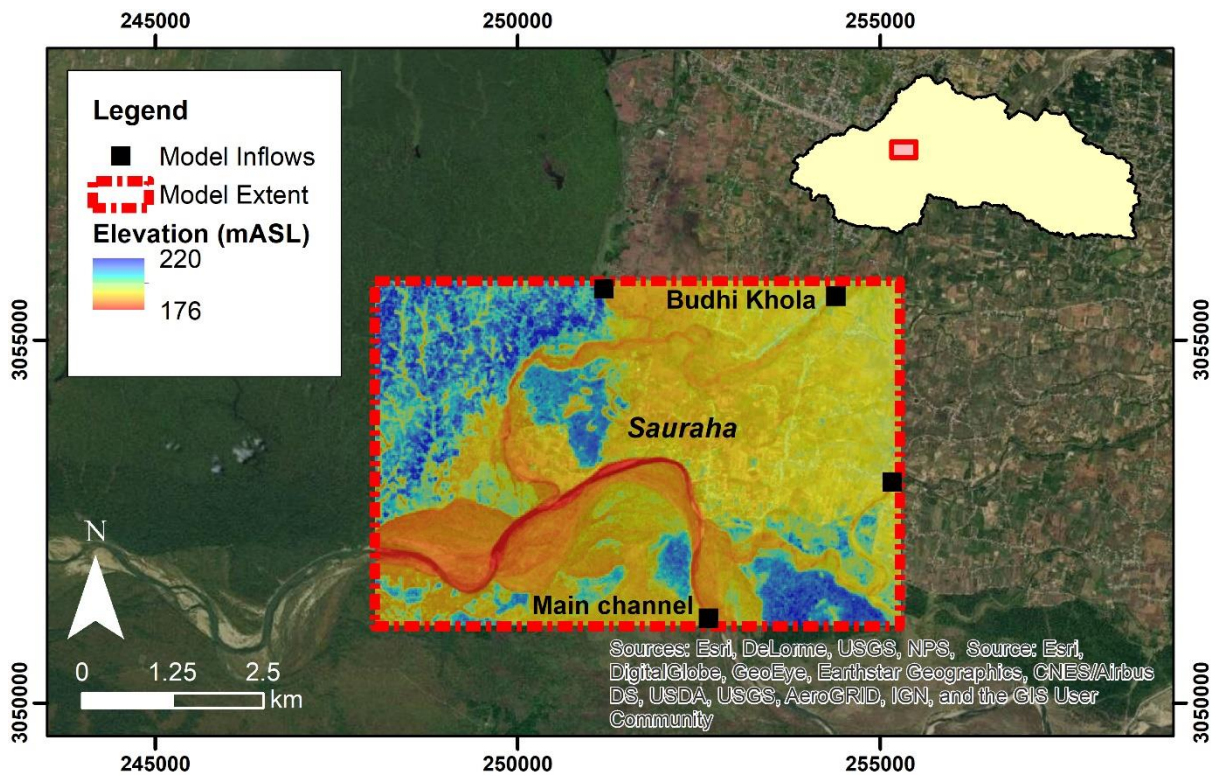


Figure 5.2: The LISFLOOD-FP model extent and inflow locations for Sauraha. The ALOS elevation data is shown within the model extent. The inset (top right) shows the location of the modelled area within the East Rapti catchment.

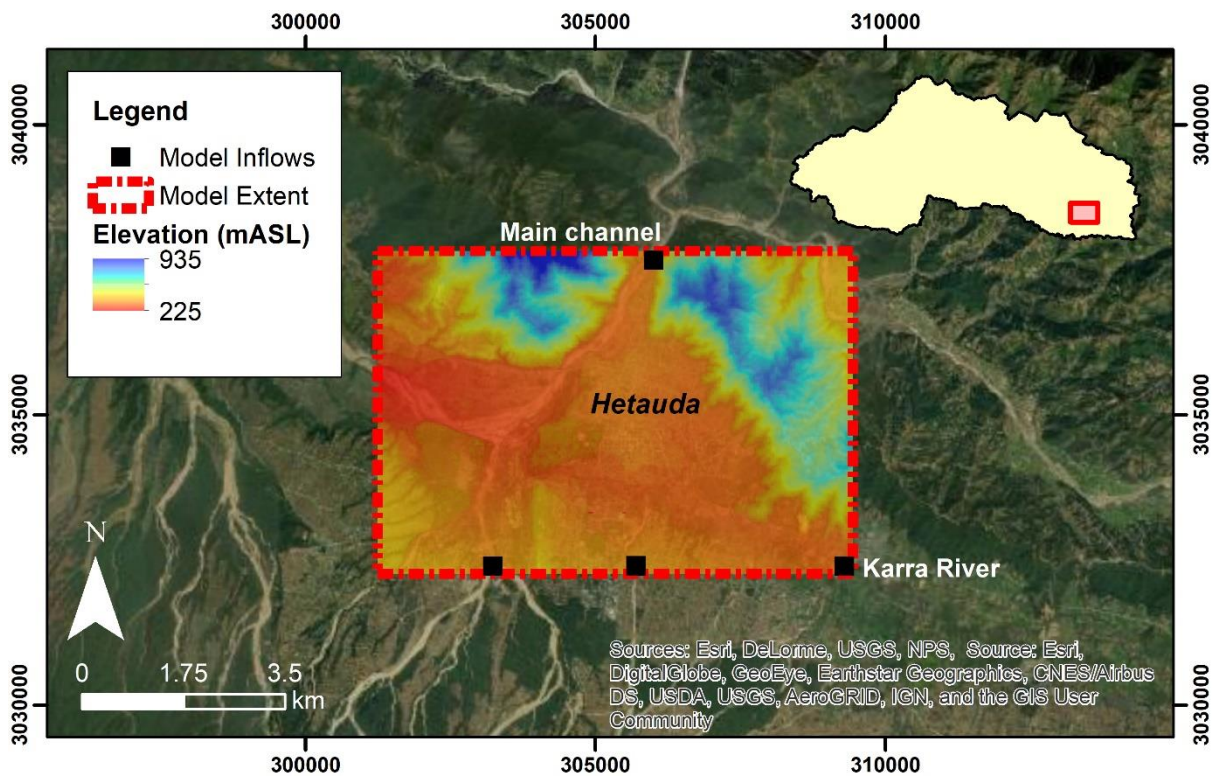


Figure 5.3: The LISFLOOD-FP model extent and inflow locations for Hetauda. The ALOS elevation data is shown within the model extent. The inset (top right) shows the location of the modelled area within the East Rapti catchment.

5.2.2.1 *Elevation data*

The ALOS World 3D (AW3D) digital surface model data was attained for parts of the East Rapti catchment that include the modelled areas around Sauraha and Hetauda. The ALOS AW3D is a commercially available global elevation dataset with a 5 m grid resolution and a vertical and horizontal accuracy of 5 m (Tadono et al., 2014; Takaku et al., 2014). The ALOS AW3D elevation data forms the basis of the free ALOS AW3D30 global digital surface model used in the SCIMAP-Flood and CRUM3 chapters (Chapter 3 and Chapter 4 respectively).

The Sauraha and Hetauda LISFLOOD-FP models use a 20 m spatial resolution to balance detailed inundation extents with computational processing time. The sensitivity of the inundation extent due to the use of alternative grid sizes was investigated as part of the model sensitivity analysis (Section 5.3.2). As in other flood inundation studies (e.g. Di Baldassarre et al., 2010; Rollason et al., 2018), the 20 m grid was created through resampling the 5 m resolution AW3D elevation data using an averaging technique ('Aggregate' in ArcGIS 10.3). Prior to resampling, the major bridges represented in the AW3D data were removed to allow the channel to flow continuously. No other alterations were made to the elevation data and as such the flood extent produced is, in part, a product of the accuracy of the DEM. This grid resolution is deemed suitable for rural flood models with LISFLOOD-FP performing acceptably at matching observed flood extents at up to 50 m resolution (e.g. Horritt and Bates, 2001; Aronica et al., 2002; Neal et al., 2011; Savage et al., 2016; Rollason et al., 2018). For larger scale reaches LISFLOOD-FP can be run at far coarser spatial resolutions (e.g. 905 m in Neal et al. (2012) and 60 m, 120 m, 240 m, 480 m, and 960 m in Komi et al. (2017)).

5.2.2.2 *Inflow and outflow model boundary conditions*

Inflow conditions are acquired from the CRUM3 catchment-scale model results. An ensemble approach, using 32 inflow hydrographs for each scenario, has been used to represent the variability of the predicted flow regime from the catchment-scale hydrological modelling. CRUM3 was configured to produce hydrographs with a 15-minute temporal resolution for any point within the modelled channel network, meeting the temporal resolution suggested for LISFLOOD-FP of at least hourly data (Bates et al., 2013). For both sites, four inflow hydrographs were used to represent the main East Rapti channel and three main tributaries in the modelled extent, as shown in Figure 5.2 and Figure 5.3.

Two flow events were chosen, one from 2009 and one from 2010, shown in Figure 5.4. Based on prior modelling and discharge analysis undertaken by the Asian Development Bank (2016) in the East Rapti catchment, the 2009 event approximately equates to a 2-year (50% AEP) return period flood and the 2010 event would have a return period of 5 years (20% AEP) for the Sauraha discharges. The discharge

analysis was not extended upstream to include the Hetauda model extent, but it is assumed that the associated storm events had a similar return period.

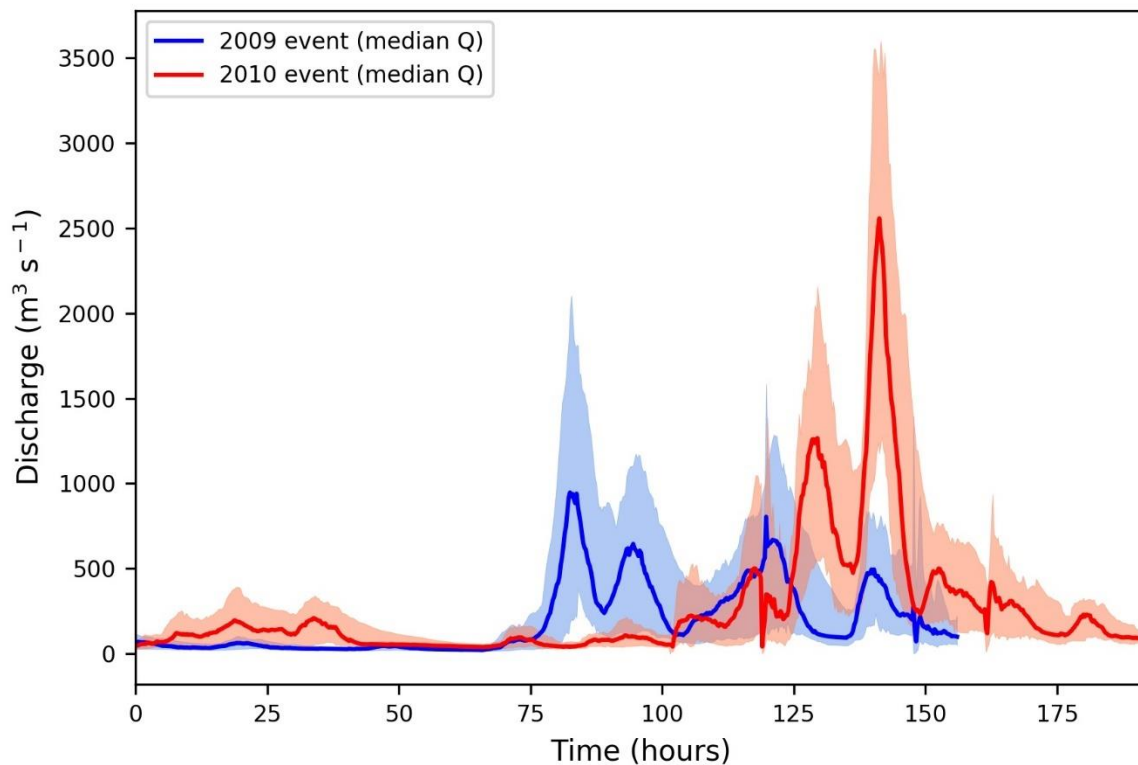


Figure 5.4: The CRUM3 modelled hydrographs from the downstream end of the Sauraha LISFLOOD-FP model for the chosen 2009 (blue) and 2010 (red) high-flow events. The coloured line represents the median flow across the 32 run model ensemble with the lighter coloured areas representing between the 10th and 90th percentile flows.

The outflow boundary condition used for the models was a ‘free’ flow boundary based on the slope of the channel at the downstream end of the modelled extent, measured from the AW3D elevation data (Sauraha: 0.006, Hetauda: 0.007). The results of the sensitivity analysis on the downstream boundary values for both models are shown in Section 5.3.2.

5.2.2.3 Friction parameters

The friction parameter used in LISFLOOD-FP is Manning’s n roughness coefficient. The coefficient is, in theory, a spatio-temporally-distributed parameter with the roughness varying over time (e.g. seasonal changes in floodplain vegetation) and space (e.g. bed channel versus vegetated floodplain) (Gobeyn et al., 2017). However, within flood inundation modelling, Manning’s roughness coefficients are predominantly only distinguished between the main channel and the floodplain and are assumed as temporally and spatially constant (e.g. Horritt and Bates, 2001; Pappenberger et al., 2006; Gobeyn et al., 2017; Rollason et al., 2018; O’Loughlin et al., 2019). As noted in several studies using LISFLOOD-FP (e.g. Horritt, 2006; Di Baldassarre et al., 2009; Komi et al., 2017) the sensitivity of the floodplain friction parameter is often negligible or noticeably lower than the model sensitivity to the channel

friction parameter. The sensitivity of the Sauraha and Hetauda models to changes in both the channel and floodplain friction parameter values are assessed in Section 5.3.2.

Channel Manning's n values were measured in the field (discussed in detail in Section 3.2.4.2), and values were established for three classes of channel within the catchment (main channel: 0.0484, lower gradient tributaries: 0.0422, and steeper gradient tributaries: 0.0663). For the Sauraha LISFLOOD-FP model the Manning's n values were 0.0422 for the Budhi Khola and two smaller tributaries and 0.0484 for the main East Rapti channel. For the Hetauda LISFLOOD-FP model the Manning's n values were 0.0422 for the Karra River, 0.0663 for the other two tributaries and 0.0484 for the main East Rapti channel. The selected channel Manning's n values are comparable to the values attained by the highest model performance ratings in other LISFLOOD-FP studies (e.g. Yan et al., 2014; Komi et al., 2017; Rollason, 2018).

The Manning's n value for the floodplain was calculated based on the standard roughness coefficient value, (Chow, 1959), for the land cover around the channel network from satellite imagery and field visits (e.g. Vojtek and Vojtekova, 2016; Gobeyn et al., 2017; Papaioannou et al., 2018). The floodplain friction value estimated from Chow (1959) assumes light brush and trees and Manning's n is therefore set as 0.0600.

5.2.2.4 Sub-grid channel geometry parameter

In addition to Manning's friction coefficients for both the channel network and the floodplain, the sub-grid channel solver in LISFLOOD-FP uses a range of parameters to represent the hydraulic geometry of the channel. The hydraulic geometry coefficients are estimated from the relationship proposed in Leopold and Maddock (1953) and determine the area and hydraulic radius of the channel bank full cross-section (Neal et al., 2012). More information on the parameters used in the sub-grid channel solver within LISFLOOD-FP is available in Neal et al. (2012) and Bates et al., (2013).

The r parameter, detailing the average relationship between the width and depth of the channel, was calculated using available channel geometry data. This was from a combination of cross-section information measured in the field and from the high-resolution (between 0.4 and 0.6 m) elevation product made from the helicopter surge (see peak flow estimation in Section 3.2.4.2). The calculated r parameter value for the channel network in both the Sauraha and Hetauda LISFLOOD-FP models was 0.03. This value is comparable to the effective model values used in Komi et al. (2017) who used initial model parameters obtained from Leopold and Maddock (1953).

5.2.2.5 Baseline LISFLOOD-FP parameters

The baseline LISFLOOD-FP model parameters used for the final Sauraha and Hetauda models are shown in Table 5.1 and Table 5.2 accordingly. Predominantly attained from field-based data, it is this

set of model parameters that will be used for the comparison of flood extents under different catchment flood management scenarios.

Table 5.1: The baseline parameters used for the Sauraha LISFLOOD-FP model.

LISFLOOD-FP parameter	DEM grid res. (m)	Manning's n main channel	Manning's n all tributaries	Manning's n floodplain	DS boundary slope	Sub-grid channel r
Baseline parameters	20	0.0484	0.0422	0.0600	0.006	0.03

Table 5.2: The baseline parameters used for the Hetauda LISFLOOD-FP model.

LISFLOOD-FP parameter	DEM grid res. (m)	Manning's n main channel	Manning's n Karra River	Manning's n southern tributaries	Manning's n floodplain	DS boundary slope	Sub-grid channel r
Baseline parameters	20	0.0484	0.0422	0.0663	0.0600	0.007	0.03

5.2.3 Sensitivity analysis of the LISFLOOD-FP model parameters

A sensitivity analysis of the main LISFLOOD-FP parameters was undertaken to highlight the potential variability in flood extent and depths due to changes in the model parameters. A comparison between the model results from the baseline parameter set and each of the sensitivity analysis model run parameter sets provides an indication as to potential changes in flood extent, should a different model parameter be subsequently used. The model sensitivity to changes in floodplain friction and channel friction values, downstream boundary slope, sub-grid channel r geometry parameter value and model DEM grid resolution were assessed based on the inflow hydrograph from the 2010 high-flow event. The model inputs are comparable to that used in Savage et al. (2016). The experimental design for the Sauraha model sensitivity is shown in Table 5.3 and for Hetauda model in Table 5.4. The results of the sensitivity analysis are shown in Section 5.3.2, with the comparison between the baseline and altered model runs illustrated through assessing changes in median flood extent across the model ensemble above a range of depth thresholds.

Table 5.3: The model runs used to undertake a sensitivity analysis of the main LISFLOOD-FP parameters for the Sauraha model. The values in bold are those changed from the baseline value for a given sensitivity model run.

Sensitivity analysis model scenario	DEM grid resolution (m)	Manning's <i>n</i> main channel	Manning's <i>n</i> other channels	Manning's <i>n</i> floodplain	Downstream boundary slope	Sub-grid channel <i>r</i>
Baseline parameters	20	0.0484	0.0422	0.0600	0.006	0.03
Floodplain friction parameter sensitivity						
Channel friction -20%	20	0.0387	0.0338	0.0600	0.006	0.03
Channel friction -10%	20	0.0436	0.0380	0.0600	0.006	0.03
Channel friction +10%	20	0.0532	0.0464	0.0600	0.006	0.03
Channel friction +20%	20	0.0581	0.0506	0.0600	0.006	0.03
Channel friction parameter sensitivity						
Floodplain friction -20%	20	0.0484	0.0422	0.0480	0.006	0.03
Floodplain friction -10%	20	0.0484	0.0422	0.0540	0.006	0.03
Floodplain friction +10%	20	0.0484	0.0422	0.0660	0.006	0.03
Floodplain friction +20%	20	0.0484	0.0422	0.0720	0.006	0.03
Downstream boundary slope sensitivity						
Downstream slope ($\div 100$)	20	0.0484	0.0422	0.0600	0.00006	0.03
Downstream slope ($\div 10$)	20	0.0484	0.0422	0.0600	0.0006	0.03
Downstream slope (x10)	20	0.0484	0.0422	0.0600	0.06	0.03
Downstream slope (x100)	20	0.0484	0.0422	0.0600	0.6	0.03
Sub-grid channel <i>r</i> parameter sensitivity						
Sub-grid <i>r</i> 0	20	0.0484	0.0422	0.0600	0.006	0
Sub-grid <i>r</i> 0.05	20	0.0484	0.0422	0.0600	0.006	0.05
Sub-grid <i>r</i> 0.1	20	0.0484	0.0422	0.0600	0.006	0.1
Sub-grid <i>r</i> 0.15	20	0.0484	0.0422	0.0600	0.006	0.15
Sub-grid <i>r</i> 0.2	20	0.0484	0.0422	0.0600	0.006	0.2
DEM grid resolution sensitivity						
Grid resolution 10m	10	0.0484	0.0422	0.0600	0.006	0.03
Grid resolution 50m	50	0.0484	0.0422	0.0600	0.006	0.03

Table 5.4: The model runs used to undertake a sensitivity analysis of the main LISFLOOD-FP parameters for the Hetuuda model. The values in bold are those changed from the baseline value for a given sensitivity model run.

Sensitivity analysis model scenario	DEM grid resolution (m)	Manning's <i>n</i> main channel	Manning's <i>n</i> Karra River	Manning's <i>n</i> southern tribs.	Manning's <i>n</i> floodplain	Downstream boundary slope	Sub-grid channel <i>r</i>
Baseline parameters	20	0.0484	0.0422	0.0663	0.0600	0.007	0.03
Floodplain friction parameter sensitivity							
Channel friction -20%	20	0.0387	0.0338	0.0530	0.0600	0.007	0.03
Channel friction -10%	20	0.0436	0.0380	0.0597	0.0600	0.007	0.03
Channel friction +10%	20	0.0532	0.0464	0.0729	0.0600	0.007	0.03
Channel friction +20%	20	0.0581	0.0506	0.0796	0.0600	0.007	0.03
Channel friction parameter sensitivity							
Floodplain friction -20%	20	0.0484	0.0422	0.0663	0.0480	0.007	0.03
Floodplain friction -10%	20	0.0484	0.0422	0.0663	0.0540	0.007	0.03
Floodplain friction +10%	20	0.0484	0.0422	0.0663	0.0660	0.007	0.03
Floodplain friction +20%	20	0.0484	0.0422	0.0663	0.0720	0.007	0.03
Downstream boundary slope sensitivity							
Downstream slope (÷100)	20	0.0484	0.0422	0.0663	0.0600	0.00007	0.03
Downstream slope (÷10)	20	0.0484	0.0422	0.0663	0.0600	0.0007	0.03
Downstream slope (x10)	20	0.0484	0.0422	0.0663	0.0600	0.07	0.03
Downstream slope (x100)	20	0.0484	0.0422	0.0663	0.0600	0.7	0.03
Sub-grid channel <i>r</i> parameter sensitivity							
Sub-grid <i>r</i> 0	20	0.0484	0.0422	0.0663	0.0600	0.007	0
Sub-grid <i>r</i> 0.05	20	0.0484	0.0422	0.0663	0.0600	0.007	0.05
Sub-grid <i>r</i> 0.1	20	0.0484	0.0422	0.0663	0.0600	0.007	0.1
Sub-grid <i>r</i> 0.15	20	0.0484	0.0422	0.0663	0.0600	0.007	0.15
Sub-grid <i>r</i> 0.2	20	0.0484	0.0422	0.0663	0.0600	0.007	0.2
DEM grid resolution sensitivity							
Grid resolution 10m	10	0.0484	0.0422	0.0663	0.0600	0.007	0.03
Grid resolution 50m	50	0.0484	0.0422	0.0663	0.0600	0.007	0.03

5.2.4 Modelled catchment-scale flood management scenarios

A collection of hydrographs produced from the CRUM3 catchment-scale management scenarios (see Chapter 4), for the 2009 and 2010 high-flow events, have been modelled using LISFLOOD-FP. Scenarios selected for flood extent modelling are shown in Table 5.5. These were selected to provide a range of flow magnitude changes at both the Sauraha and Hetuuda flood impact points. The selected flow magnitude increase scenarios, showing the potential change in the flow regime from future land use change, cover a range Q99.9 (99.9th percentile flow) change from 0.6% at Hetuuda in the deforestation (to *Shrubland – DEF_S*) scenario through to an increase of 44.9% at Sauraha in the blanket coverage

scenario of *Irrigated Agriculture (BLA_IA)*. The selected flow magnitude reduction scenarios, illustrating the potential change in the flood regime due to catchment-scale flood management approaches, encompass a range in Q99.9 change from 0.4% in Sauraha due to SCIMAP-Flood informed targeted afforestation (*AFF50_F*) through to -12.4% at Hetauda from the blanket coverage scenario of *Forest class (BLA_F)*. Through the use of an ensemble approach with the inflow hydrographs from all 32 CRUM3 model runs for each scenario, the modelling process will allow for an assessment as to whether a change in flow magnitude has a meaningful change in inundation extent and depth for a given scenario.

Table 5.5: The median percentage change in flow magnitude (Q99.9) for the catchment scenarios modelled using CRUM3 (see Chapter 4) at Hetauda and Sauraha. The final column has the average change across at six flood impact points for each scenario. These are the scenarios being modelled using LISFLOOD-FP to assess the change in flood extent.

FLOW MAGNITUDE INCREASE SCENARIOS	SCENARIO ID	Hetauda	Sauraha	Average
Deforestation (to Shrubland)	DEF_S	+0.6	+1.7	+1.3
Terrace abandonment (to Shrubland)	TER_S	+3.1	+1.5	+2.0
Combined negative land use change (to Shrubland)	NEG_S	+4.2	+3.1	+3.4
Blanket coverage (Rainfed Ag.)	BLA_RA	+7.8	+12.0	+12.8
Blanket coverage (Irrigated Ag.)	BLA_IA	+41.6	+44.9	+50.8
FLOW MAGNITUDE DECREASE SCENARIOS				
FLOW MAGNITUDE DECREASE SCENARIOS	SCENARIO ID	Hetauda	Sauraha	Average
SCIMAP-Flood afforestation (> 0.50)	AFF50_F	-1.8	-0.4	-0.5
SCIMAP-Flood afforestation (point density analysis > 0.50)	AFF50_PDA_F	-3.7	-2.0	-1.6
SCIMAP-Flood check dam implementation (sub-catchments > 0.50)	DAM50	-5.9	-3.2	-3.6
Combined flood management approach (SCIMAP-Flood > 0.50)	POS50	-10.3	-5.2	-5.3
Blanket coverage (Forest)	BLA_F	-12.4	-9.2	-9.3

5.2.5 LISFLOOD-FP methods summary

The LISFLOOD-FP approach conceptualised in Figure 5.1 is the final part of the end-to-end catchment-scale scenario assessment process. This final part of the overall approach investigates the change in inundation patterns at key flood impacted areas under different catchment-scale scenarios. The inflow conditions that drive the LISFLOOD-FP model are acquired from the CRUM3 catchment-scale scenario modelling results (Chapter 4). A total of 10 scenarios, 5 simulating flow magnitude increasing and 5 flow magnitude decreasing, were selected from the 27 scenarios modelled in Chapter 4 for the inundation pattern change assessment.

Within the East Rapti case study, the selected flood impact areas were Sauraha and Hetauda; these two locations cover a range of localised morphology with the Sauraha model exemplifying the lower gradient downstream part of the catchment and the Hetauda model representing a more constrained upstream part of the catchment. An uncalibrated modelling approach was used and as such the changes in inundation patterns occurring from a given scenario are relative. This is due to a lack of available calibration and validation data for the 2009 and 2010 flood events. The requirements to set up the LISFLOOD-FP inundation model were met with a combination of a commercially available elevation dataset and representative model parameters derived from a mixture of field-based observations from within the East Rapti catchment and appropriate model parameter estimation techniques as used in existing research. It must be noted that the baseline model parameters are representative of the modelled area around both Sauraha and Hetauda but possibly do not produce the best model performance.

5.3 RESULTS

The section presents the results from the inundation modelling using LISFLOOD-FP for two of the flood impacted areas within the East Rapti catchment; Sauraha and Hetauda. Section 5.3.1 shows the results of the present day baseline condition inundation extent from using both the 2009 and 2010 high-flow events. Section 5.3.2 presents the results of the sensitivity analysis undertaken for both the Sauraha and Hetauda models through varying the key LISFLOOD-FP model parameters and inputs. Finally, Section 5.3.3 displays the results of the catchment management scenario inundation modelling, for both the flow magnitude increasing and decreasing scenarios, and offers a comparison to the baseline conditions presented in Section 5.3.1.

5.3.1 Baseline inundation extents for the 2009 and 2010 high-flow events

5.3.1.1 2009 event

Figure 5.5 indicates the probability of inundation at Sauraha based on the present day conditions scenario modelled in CRUM3 for the top 32 model parameter sets (Section 4.3.1) and baseline LISFLOOD-FP parameters (Table 5.1) using the 2009 high-flow event hydrograph. The model results exhibit flooding throughout the settlement with > 75% of the model runs predicting flooding. The majority of this flooding is occurring from the overtopping of the banks from the tributaries from the north and east of Sauraha rather than from the main East Rapti channel. There is greater variation in modelled flood extent in close proximity to the main East Rapti channel with < 50% of the models predicting extensive inundation across the floodplain towards to the downstream end of the model.

Figure 5.6 illustrates the inundation probability around Hetauda based on the present day conditions catchment scenario modelled in CRUM3, baseline LISFLOOD-FP parameters (Table 5.2) and using the 2009 high-flow event hydrograph. More than 75% of the model runs indicate that there will be flooding from the Karra River that flows from the eastern edge of the model through Hetauda. The western tributary that flows from the southern edge of the model is predicted to remain within the channel. Less than 25% of the models predict that the eastern tributary along the southern edge will exceed the channel capacity. Extensive flooding is not predicted for the main East Rapti channel, with the majority of the flow remaining in the channel. There is, however, an area to the north of the main East Rapti channel predicted to be inundated by < 25% of the models. Flooding in this area indicates that the flood embankment on the right-hand bank of the main East Rapti channel has been overtopped, or that the full height of the structure is not properly represented in the elevation data.

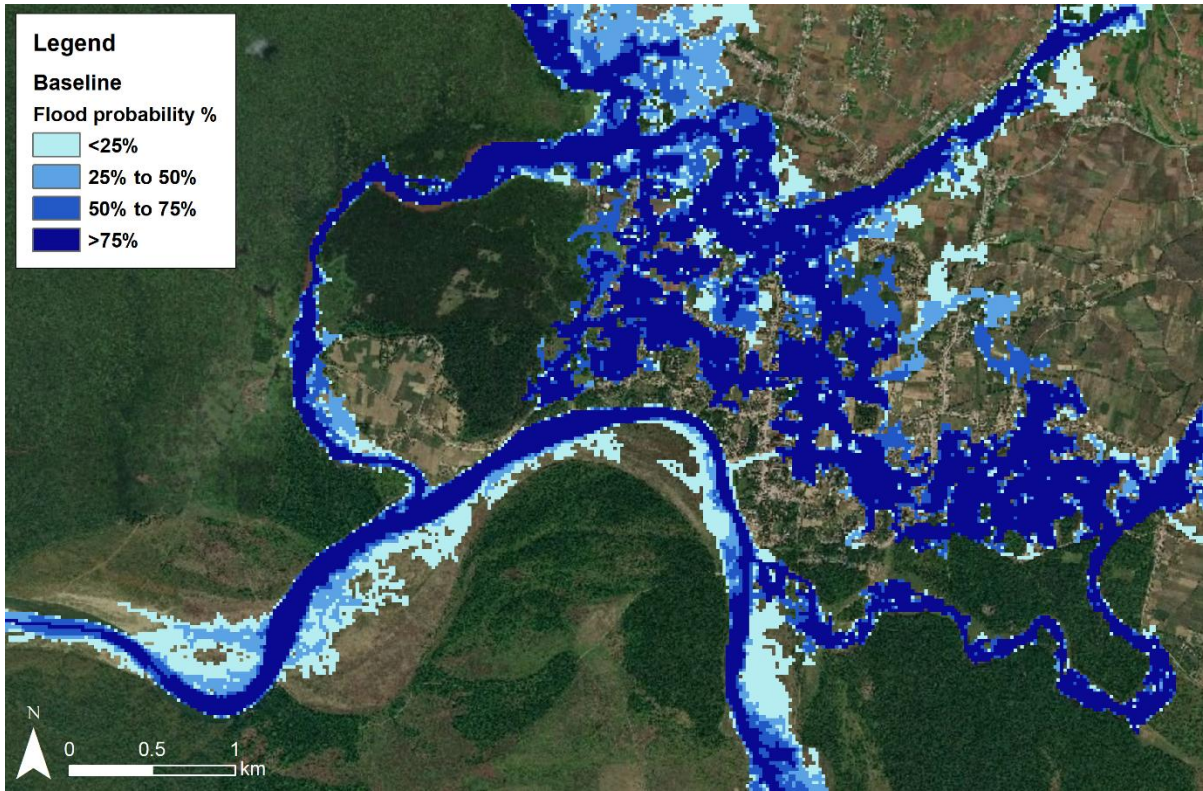


Figure 5.5: A flood probability map for Sauraha using the baseline parameters and 2009 event hydrograph. The flood probability refers to the percentage of the ensemble of the 32 model runs that predict flooding at a specific location.

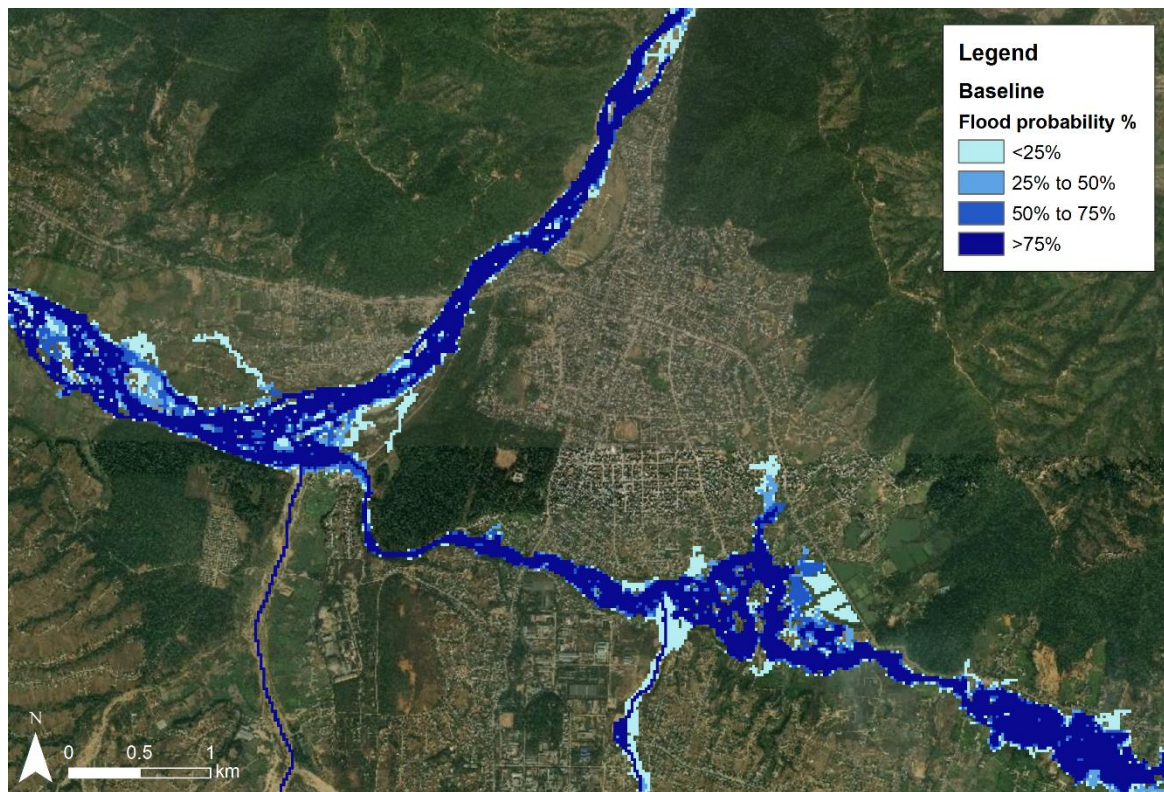


Figure 5.6: A flood probability map for Hetauda using the baseline parameters and 2009 event hydrograph. The flood probability refers to the percentage of the ensemble of the 32 model runs that predict flooding at a specific location.

5.3.1.2 2010 event

Figure 5.7 illustrates the probability of inundation at Sauraha based on the present day conditions scenario modelled in CRUM3 for the top 32 model parameter sets and baseline LISFLOOD-FP parameters using the 2010 high-flow event hydrograph. As evident on the inundation map there is extensive flooding throughout the settlement with > 75% of the model runs predicting flooding. As for the 2009 event, the majority of this flooding is occurring from the overtopping of the banks from the tributaries from the north and east of Sauraha and not from the main East Rapti channel itself. There is greater variation in modelled flood extent in close proximity to the main East Rapti channel with < 50% of the models predicting extensive inundation across the floodplain towards to the downstream end of the model.

Figure 5.8 shows the inundation probability around Hetauda as a result of the 32 model hydrographs from the 2010 high-flow event. Over 75% of the model runs indicate that there will be flooding from the Karra River that flows from the eastern edge of the model through Hetauda. The two tributaries that flow from the southern edge of the model are predicted to remain within the channel. There is not extensive flooding predicted for the main East Rapti channel, with the majority of the flow remaining in the channel. There is, however, an area to the north of the main East Rapti channel predicted to be inundated by < 75% of the models. Additionally, < 25% of the models predicted flooding in a small area to the west of Hetauda. Flooding in both these areas would suggest that the flood embankment on the right-hand bank of the main East Rapti channel has been overtopped or that the full height of the structure is not accurately represented in the elevation data.

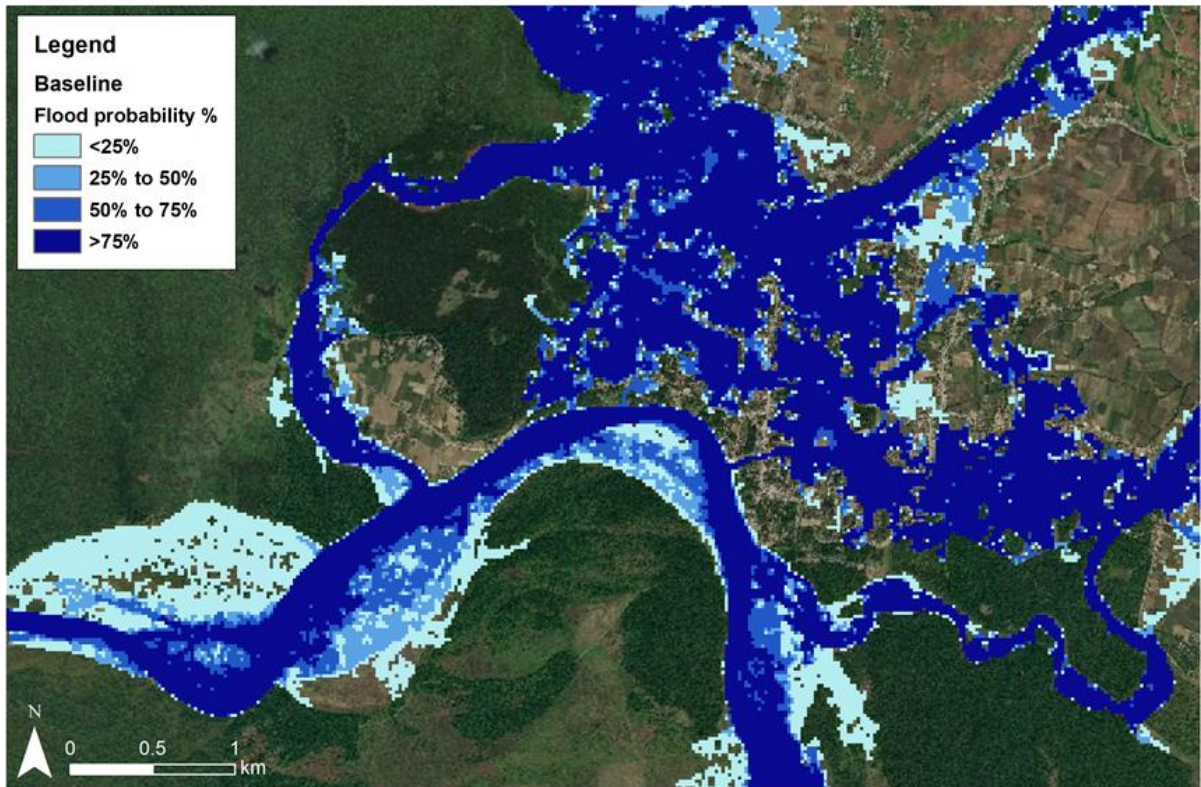


Figure 5.7: A flood probability map for Sauraha using the baseline parameters and 2010 event hydrograph. The flood probability refers to the percentage of the ensemble of the 32 model runs that predict flooding at a specific location.

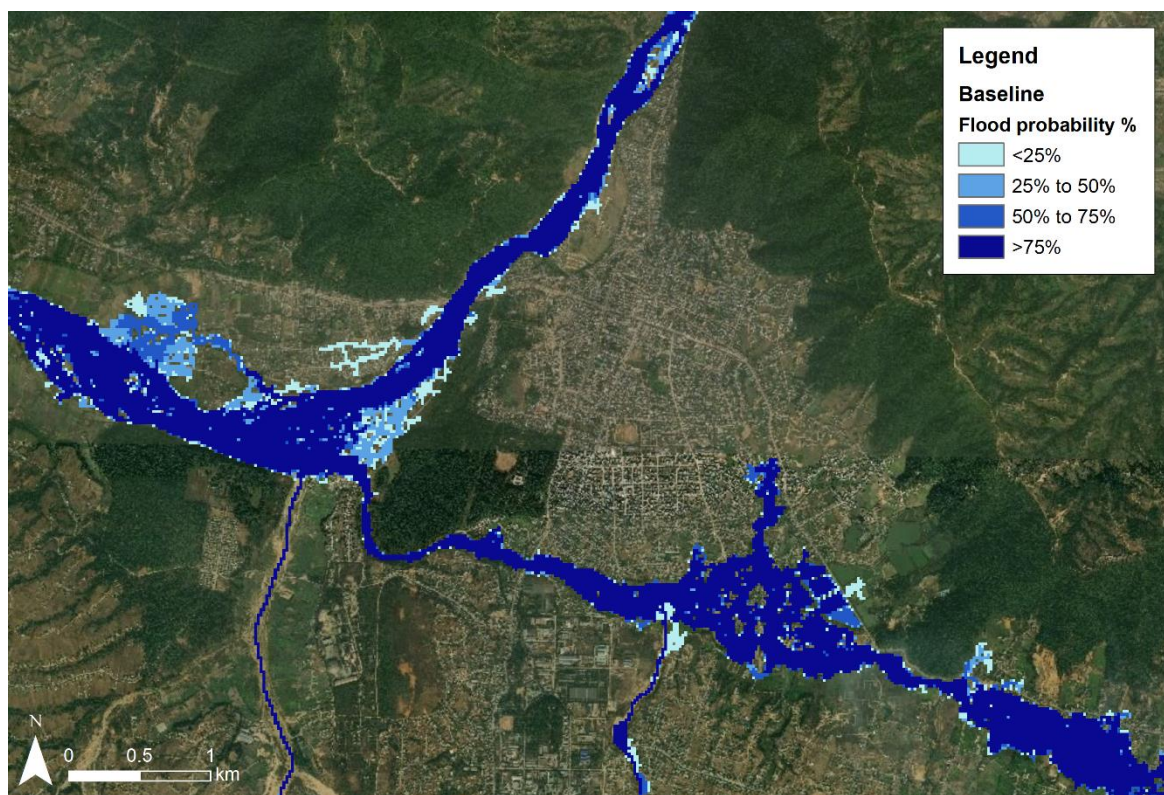


Figure 5.8: A flood probability map for Hetauda using the baseline parameters and 2010 event hydrograph. The flood probability refers to the percentage of the ensemble of the 32 model runs that predict flooding at a specific location.

5.3.2 LISFLOOD-FP sensitivity analysis results

This section illustrates the results of the LISFLOOD-FP parameter sensitivity analysis, using the 2010 high-flow event, for both the Sauraha and Hetauda model extents. The justification and creation process of the sensitivity analysis is discussed in Section 5.2.3. Section 5.3.2.1 outlines the results of the Sauraha model, with Section 5.3.2.2 outlining the results for the Hetauda model.

5.3.2.1 Sauraha LISFLOOD-FP sensitivity analysis results

An overview of the percentage and areal (km²) change in inundation area throughout the Sauraha between the 2010 event baseline model (Figure 5.7) run and sensitivity analysis runs is provided in Table 5.6. The sensitivity analysis of the Sauraha LISFLOOD-FP model showed that the inundation extent produced was most variable using different sub-grid channel geometry r parameter values and coarser model DEM grid resolutions. A spatial comparison between the sensitivity runs and the baseline extent is available across Appendix 7.27 to 7.31 for different model parameters.

It is evident from the sensitivity analysis that the variation in the channel friction values used has an impact on inundation extent with a 20% change in channel friction value increasing or decreasing the wetted cell area by between 7.1% (50th percentile extent -0.62 km² and 90th percentile extent -0.73 km²) to 8.5% (10th percentile extent -0.51 km²) accordingly. This inundation extent variation predominantly occurred along the main East Rapti channel towards the downstream end of the modelled extent (Appendix 7.27).

The variation in the floodplain friction values used had a small (between -1.6% and +1.3%) impact on inundation extent with a maximum wetted cell area increase of +1.3% (+0.08 km²) from the 10th percentile extent. The produced inundation extent is similar across all the sensitivity runs with minor variation to the north of Sauraha from overtopping of the Budhi Khola (Appendix 7.28).

The variation in the downstream boundary slope values had the largest impact on inundation extent when decreased. Lower slope values result in a shallower gradient at the downstream end of the model. The alteration of the downstream boundary slope to 0.0006 resulting in a +21.4% (+1.87 km²) increase in the 50th percentile inundation extent. The other sensitivity runs had a limited impact on the change in flood extent from the measured downstream slope boundary value. As expected, the inundation extent variation occurred at the downstream end of the model with no change in inundation extent towards the upstream end of the modelled extent (Appendix .7.29).

Table 5.6: A comparison of inundation extent percentage and areal change in comparison to the baseline extent under different LISFLOOD-FP model sensitivity analysis scenarios for the Sauraha model

Sensitivity analysis model scenario	% inundated area change (10 th percentile)	Inundated area change (km ²) (10 th percentile)	% inundated area change (50 th percentile)	Inundated area change (km ²) (50 th percentile)	% inundated area change (90 th percentile)	Inundated area change (km ²) (90 th percentile)
Floodplain friction parameter sensitivity						
Channel friction -20%	-8.5	-0.51	-7.1	-0.62	-7.1	-0.73
Channel friction -10%	-3.6	-0.22	-3.1	-0.27	-3.6	-0.37
Channel friction +10%	+4.4	+0.27	+3.7	+0.33	+3.5	+0.36
Channel friction +20%	+8.2	+0.48	+7.0	+0.61	+7.0	+0.72
Channel friction parameter sensitivity						
Floodplain friction -20%	+0.9	+0.05	-1.0	-0.09	-1.6	-0.17
Floodplain friction -10%	+1.3	+0.08	+0.2	+0.02	-0.1	-0.01
Floodplain friction +10%	-0.1	-0.00	+0.3	+0.03	+0.6	+0.06
Floodplain friction +20%	-0.6	-0.03	+0.8	+0.07	+1.2	+0.13
Downstream boundary slope sensitivity						
Downstream slope (÷100)	+21.1	+1.26	+21.4	+1.87	+22.5	+2.30
Downstream slope (÷10)	+1.8	+0.11	+3.3	+0.29	+4.3	+0.47
Downstream slope (x10)	-0.1	-0.01	-0.2	-0.02	-0.3	-0.03
Downstream slope (x100)	-0.1	-0.01	-0.2	-0.02	-0.4	-0.04
Sub-grid channel <i>r</i> parameter sensitivity						
Sub-grid <i>r</i> 0	+38.9	+2.32	+21.9	+1.91	+19.7	+ 2.01
Sub-grid <i>r</i> 0.05	-34.8	-2.07	-16.4	-1.43	-14.6	-1.49
Sub-grid <i>r</i> 0.1	-77.2	-4.60	-55.9	-4.87	-43.8	-4.47
Sub-grid <i>r</i> 0.15	-88.4	-5.27	-82.8	-7.22	-74.2	-7.56
Sub-grid <i>r</i> 0.2	-89.9	-5.36	-91.8	-8.00	-89.3	-9.10
DEM grid resolution sensitivity						
Grid resolution 10m	-6.4	-0.38	-3.9	-0.34	-2.8	-0.28
Grid resolution 50m	+42.2	+2.52	+30.2	+2.64	+25.9	+2.65

The variation in the sub-grid channel geometry *r* parameter values had a sizeable impact on inundation extent. The *r* parameter controls the capacity of the sub-grid to keep water within the channel network and any increase in the value increases the channel capacity and reduces water entering the floodplain. Therefore, the model is highly sensitive to the *r* parameter value. The inundated area only includes the settlement of Sauraha with an *r* value of 0.1 or less (Appendix 7.30). An *r* value of 0.15 or 0.2 keeps the majority of the water in the channel network and results in an inundation extent reduction of > 80% (> +5.2 km²) across the 10th and 50th percentile extents.

It is apparent that increasing the grid resolution to 10 m has a small impact on the modelled flood extent with a reduction in wetted cell area of between 2.8% (90th percentile extent -0.29 km²) and 6.4% (10th percentile extent -0.38 km²). Modelling with a coarser grid resolution results in a large increase in inundated area with an increase of between 25.9% (90th percentile extent +2.65 km²) and 42.2% (10th percentile extent +2.52 km²) using a 50 m grid. The increase in inundation extent occurs predominantly in the north eastern part of the model (Appendix 7.31) where the averaging approach used to coarsen the elevation data has removed some of the subtle topographical features, or noise in the elevation data, that controls the water flow out of the channel network.

5.3.2.2 Hetauda LISFLOOD-FP sensitivity analysis results

An overview of the percentage change and areal change (km²) in inundation area within the Hetauda model resulting from varying the LISFLOOD-FP model parameters from those used to create the 2010 event baseline (Figure 5.8), is provided in Table 5.7. The sensitivity analysis of the Hetauda LISFLOOD-FP model showed that the inundation extent produced was most variable when using different sub-grid channel geometry *r* parameter values. A spatial comparison between the sensitivity runs and the baseline extent is available across Appendix 7.32 to 7.36 for different model parameters.

The variation in the channel friction values used has an impact on inundation extent with a 20% change in channel friction value increasing or decreasing the wetted cell area by between -6.5% (50th percentile extent -0.25 km²) to +5.5% (50th percentile extent +0.21 km²) accordingly. The inundation extent variation predominantly occurred along the main East Rapti channel towards the downstream end of the model (Appendix 7.32). The inundation extent did not change due to altered channel friction values in the other parts of the Hetauda model.

The variation in the floodplain friction values used had a minimal impact on inundation extent with a maximum wetted cell area change of -1.6% (50th percentile extent -0.06 km²). The inundation extent produced by changing the floodplain friction value is similar across all the sensitivity runs (Appendix 7.33).

Altering the downstream boundary slope values had a limited, localised, impact on the flood extent at the downstream end of the model (Appendix 7.34). The alteration of the downstream boundary slope to 0.0007 resulting in a +1.1% (10th percentile extent -0.03 km² and 90th percentile extent -0.05 km²) increase in the inundation extent. The other sensitivity runs had a limited impact on the change in flood extent from the downstream slope boundary value.

Table 5.7: A comparison of inundation extent percentage and areal change in comparison to the baseline extent under different LISFLOOD-FP model sensitivity analysis scenarios for the Hetauda model.

Sensitivity analysis model scenario	% inundated area change (10 th percentile)	Inundated area change (km ²) (10 th percentile)	% inundated area change (50 th percentile)	Inundated area change (km ²) (50 th percentile)	% inundated area change (90 th percentile)	Inundated area change (km ²) (90 th percentile)
Floodplain friction parameter sensitivity						
Channel friction -20%	-3.5	-0.11	-6.5	-0.25	-3.7	-0.16
Channel friction -10%	-1.7	-0.05	-4.1	-0.16	-1.8	-0.08
Channel friction +10%	+2.1	+0.06	+3.1	+0.12	+1.4	+0.06
Channel friction +20%	+4.4	+0.13	+5.5	+0.21	+3.6	+0.16
Channel friction parameter sensitivity						
Floodplain friction -20%	-0.5	-0.02	-0.6	-0.02	-1.0	-0.04
Floodplain friction -10%	-0.1	-0.00	-0.2	-0.01	-0.5	-0.02
Floodplain friction +10%	+0.2	+0.01	-0.9	-0.03	+0.5	+0.02
Floodplain friction +20%	+0.4	+0.01	-1.6	-0.06	+0.8	+0.04
Downstream boundary slope sensitivity						
Downstream slope ($\div 100$)	+1.1	+0.03	+0.8	+0.03	+1.1	+0.05
Downstream slope ($\div 10$)	+0.4	+0.01	+0.2	+0.01	+0.0	+0.00
Downstream slope ($\times 10$)	-0.0	-0.00	-0.1	-0.00	-0.0	-0.00
Downstream slope ($\times 100$)	-0.0	-0.00	-0.1	-0.00	-0.1	-0.00
Sub-grid channel r parameter sensitivity						
Sub-grid r 0	+46.1	+1.38	+31.8	+1.22	+27.8	+1.19
Sub-grid r 0.05	-21.8	-0.65	-15.0	-0.58	-13.5	-0.58
Sub-grid r 0.1	-61.6	-1.84	-55.1	-2.12	-51.8	-2.22
Sub-grid r 0.15	-79.3	-2.37	-77.3	-2.98	-76.0	-3.26
Sub-grid r 0.2	-83.6	-2.45	-86.0	-3.30	-86.4	-3.71
DEM grid resolution sensitivity						
Grid resolution 10m	-2.0	-0.06	-4.8	-0.18	-1.2	-0.05
Grid resolution 50m	+21.0	+0.63	+11.6	+0.45	+12.9	+0.56

The variation in the sub-grid channel geometry r parameter values had the greatest impact on the modelled inundation extent. A greater r parameter value will lower the volume of water exceeding the channel capacity and entering the floodplain. Therefore, as in the Sauraha model, the Hetauda LISFLOOD-FP model is extremely sensitive to the r parameter value. The Karra River in the east of the model only overtops its banks with an r value of > 0.15 (Appendix 7.35). There is no flooding from overtopping of the main East Rapti channel with an r value of > 0.05 . An r value of 0.15 or 0.2 keeps the majority of the water in the channel network and results in an inundation extent reduction of $> 75\%$ ($> -2.3 \text{ km}^2$).

It is apparent that increasing the grid resolution to 10 m has a small impact on the modelled flood extent with a reduction in wetted cell area of between 1.2% (90th percentile extent -0.05 km²) and 4.8% (50th percentile extent -0.18 km²). Modelling with a coarser 50 m resolution results in a larger change in inundated area with an increase of between 11.6% (50th percentile extent +0.45 km²) and 21.0% (10th percentile extent +0.62 km²). The increase in inundation extent occurs predominantly in the smaller tributaries and around the confluence of the East Rapti River and the Karra River (Appendix 7.36).

5.3.3 LISFLOOD-FP catchment-scale scenario inundation modelling results

This section illustrates the LISFLOOD-FP results for Sauraha and Hetauda under the flow magnitude increasing and decreasing catchment-scale scenarios using both the 2009 and 2010 high-flow events. The scenario ID naming system is carried over from Chapter 4 with Table 5.5 providing an overview of the IDs used within this chapter. Section 5.3.3.1 to Section 5.3.3.4 illustrate the results for the flow magnitude increasing scenarios for both Sauraha and Hetauda. Section 5.3.3.5 to Section 5.3.3.8 showcase the results for the flow magnitude decreasing scenarios.

Each sub-section contains a figure illustrating the differences between the 50th percentile baseline inundation extent and scenario inundation extents, produced from the ensemble model runs of the respective flow magnitude increasing or decreasing catchment-scale scenarios using the relevant high-flow event hydrograph. A table provides a comparison of the areal and percentage change in inundated area across the model ensemble between the baseline and scenario 50th percentile inundation extents. A final comparison displays cumulative histograms of inundation depths in areas of *Built-Up Area* for the 10th, 50th and 90th percentile model ensemble extents. This allows for an assessment of the impact of a catchment-scale scenario with regards to altering inundation patterns in the populated parts of each model extent.

5.3.3.1 Flow magnitude increasing catchment-scale scenarios for the 2009 event in Sauraha

The inundation pattern (Figure 5.9) produced by the flow magnitude increasing scenarios is similar to that modelled from the baseline scenario (Figure 5.5). Only the *BLA_IA* scenario, the scenario which had the largest increase to the high-flow regime from the catchment-scale modelling using CRUM3, predicted inundation in previously unaffected areas with a slightly expanded flood extent along the main East Rapti channel and in the northern parts of the model. As shown in Table 5.8, the model results indicate that the flooded area as a result of large-scale catchment change to the *Irrigated Agriculture* land cover (*BLA_IA*) could increase the inundated area by between 15.1% (50th percentile extent +0.84 km²) and 49.1% (10th percentile extent +1.09 km²). Both the 50th ($\geq +20.9\%$; +0.85 km²) and 90th ($\geq +21.3\%$; +1.27 km²) percentile extents had a larger percentage increase in deeper (> 0.5 m) inundation depths. The *DEF_S*, *TER_S* and *NEG_S* scenarios, representing more realistic future land

use change, predicted a flood extent area increase (inundation depths > 0.0 m) of $\leq 2.3\%$. The three scenarios predicted a greater increase ($\leq 5.4\%$) in areas with water depths > 0.5 m and > 1.0 m across the model ensemble. The distribution of inundation depths in areas of *Built-Up Area* (Figure 5.10) are similar between the baseline and all the flow magnitude increasing scenarios except the *BLA_IA* scenario. The *BLA_IA* scenario had a comparable distribution of lower depths (< 0.5 m) to the baseline inundation but had more *Built-Up Area* cells with deeper inundation depths (> 0.5 m) across the Sauraha model ensemble.

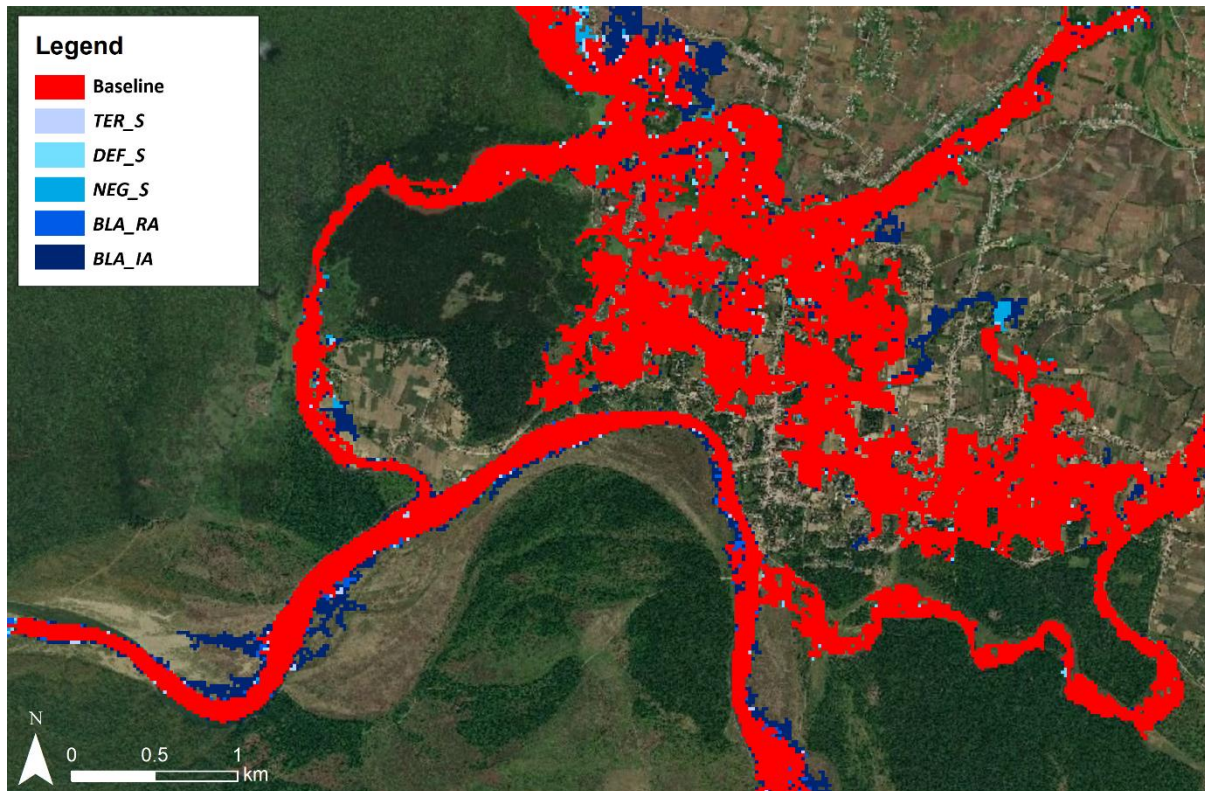


Figure 5.9: The median inundation extents at Sauraha from the model ensemble 2009 event hydrographs for the flow magnitude increasing scenarios and the baseline extent. The scenarios are layered in order of inundation extent with all cells representing an increased inundation extent visible.

Table 5.8: A comparison of inundated area extent change across the model ensemble for flow magnitude increasing catchment-scale scenarios at Sauraha using the 2009 event hydrograph.

Inundation depth (m)	DEF_S inundated area % change	DEF_S inundated area change (km ²)	TER_S inundated area % change	TER_S inundated area change (km ²)	NEG_S inundated area % change	NEG_S inundated area change (km ²)	BLA_RA inundated area % change	BLA_RA inundated area change (km ²)	BLA_IA inundated area % change	BLA_IA inundated area change (km ²)
10th percentile extent										
> 0.0 m	+1.6	+0.04	-0.1	-0.00	+2.3	+0.05	+22.5	+0.50	+49.1	+1.09
> 0.5 m	+3.0	+0.04	+2.1	+0.03	+5.4	+0.08	+23.7	+0.35	+48.8	+0.72
> 1.0 m	+2.5	+0.03	+0.9	+0.01	+4.2	+0.04	+26.6	+0.27	+43.1	+0.44
50th percentile extent										
> 0.0 m	+1.4	+0.08	-0.0	-0.00	+1.9	+0.11	+2.3	+0.13	+15.1	+0.84
> 0.5 m	+2.2	+0.09	+0.2	+0.01	+2.7	+0.11	+4.6	+0.18	+21.9	+0.85
> 1.0 m	+0.9	+0.02	-0.8	-0.02	+1.4	+0.04	+2.3	+0.06	+20.9	+0.54
90th percentile extent										
> 0.0 m	+1.3	+0.10	+0.8	+0.06	+2.0	+0.15	+3.1	+0.24	+16.9	+1.28
> 0.5 m	+1.3	+0.08	+0.6	+0.04	+1.6	+0.10	+3.7	+0.22	+21.3	+1.27
> 1.0 m	+1.8	+0.07	+0.9	+0.03	+2.5	+0.10	+4.8	+0.19	+28.8	+1.14

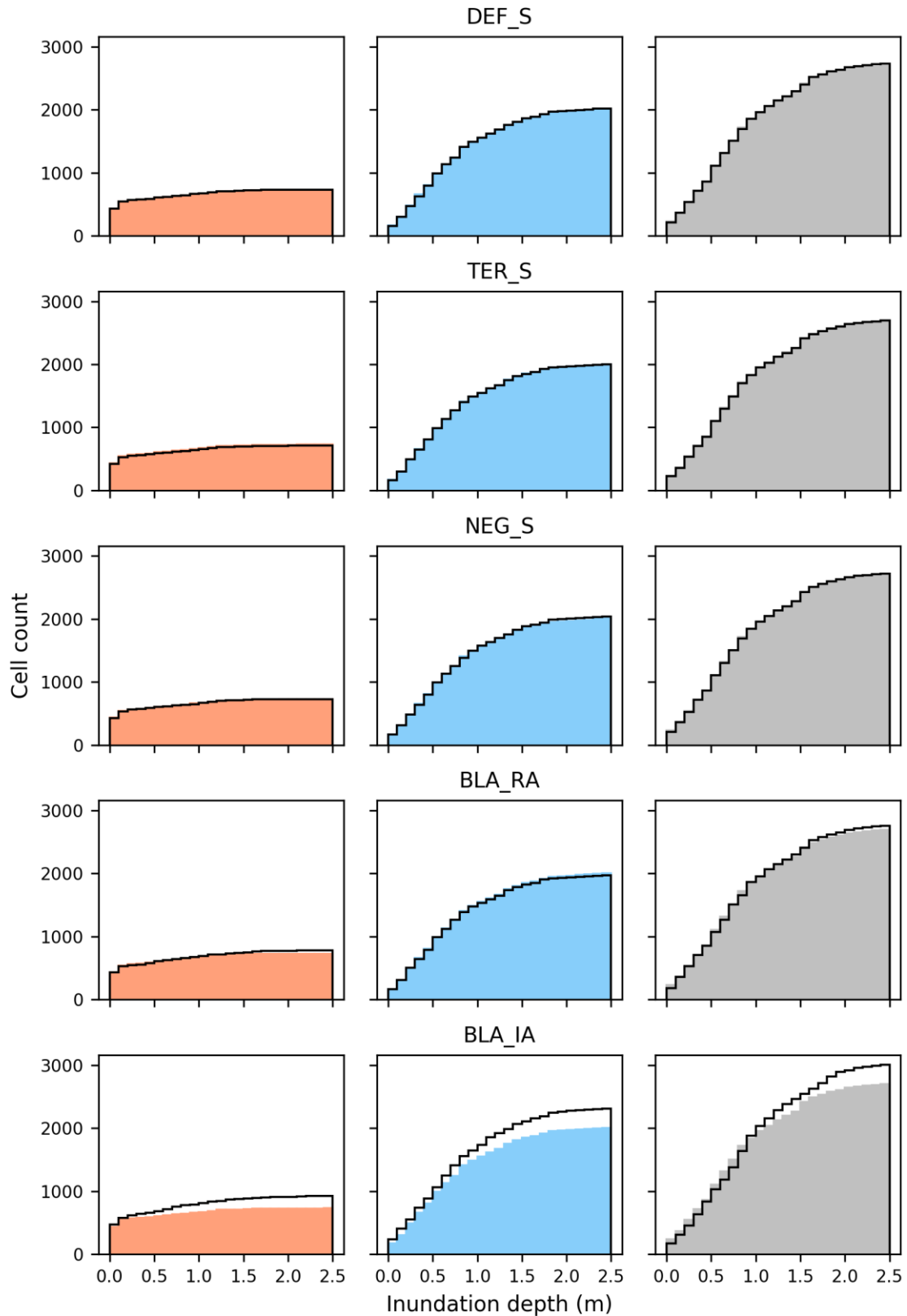


Figure 5.10: A cumulative histogram comparison of the 10th (orange), 50th (blue) and 90th (grey) percentile inundation depths occurring in areas of Built-Up Area throughout the Sauraha model extent using the 2009 event hydrograph. Baseline depths: coloured polygon; flow magnitude increasing scenario depths: black line. A black line above/below the coloured polygon indicates an increase/decrease, up to and including, a given inundation depth from the scenario compared to the baseline.

5.3.3.2 Flow magnitude increasing catchment-scale scenarios for the 2009 event in Hetauda

The inundation pattern (Figure 5.11) produced by the flow magnitude increasing scenarios is similar to that modelled from baseline scenario with the largest increase from the baseline inundation extent occurring around the East Rapti River and Karra River confluence. The *DEF_S*, *TER_S* and *NEG_S* scenarios that represent a more realistic change in the East Rapti catchment predicted a flood extent area change (inundation depths > 0.0 m) of between -3.9% (10th percentile extent -0.06 km²) and +1.9% (90th percentile extent +0.06 km²) (see Table 5.9). The three scenarios predict a change of between -3.1% (10th percentile extent +0.03 km²) and +3.9% (90th percentile extent +0.06 km²) in areas of water depths > 0.5 m and > 1.0 m across the model ensemble. The model results from the *BLA_RA* and *BLA_IA* scenarios produced a slightly expanded inundation extent, when compared to the other scenarios with less land cover change, along the right-hand side of the Karra River channel and downstream of the confluence with the East Rapti. The results indicate that the inundated area, as a result of large-scale catchment change to the *Irrigated Agriculture (BLA_IA)*, is predicted to increase the inundated area by between 7.0% (50th percentile extent +0.20 km²) to 22.4% (10th percentile extent +0.37 km²). There is a larger ($\geq 13.0\%$) increase in deeper (> 0.5 m) inundation depths. The distribution of inundation depths in areas of *Built-Up Area* (Figure 5.12) are similar between the baseline and all the flow magnitude increasing scenarios except the *BLA_IA* scenario. Among the 10th percentile extents there is a slight decrease in inundated *Built-Up Area* cells from the baseline extent across all five scenarios. The *BLA_IA* scenario had a comparable distribution of *Built-Up Area* inundation depths to the baseline inundation across the 10th and 50th percentile extents but had a large increase in inundated *Built-Up Area* cells in the 90th percentile extent. The increase in inundated *Built-Up Area* cells for the 90th percentile extent is evident across the inundation depth range.

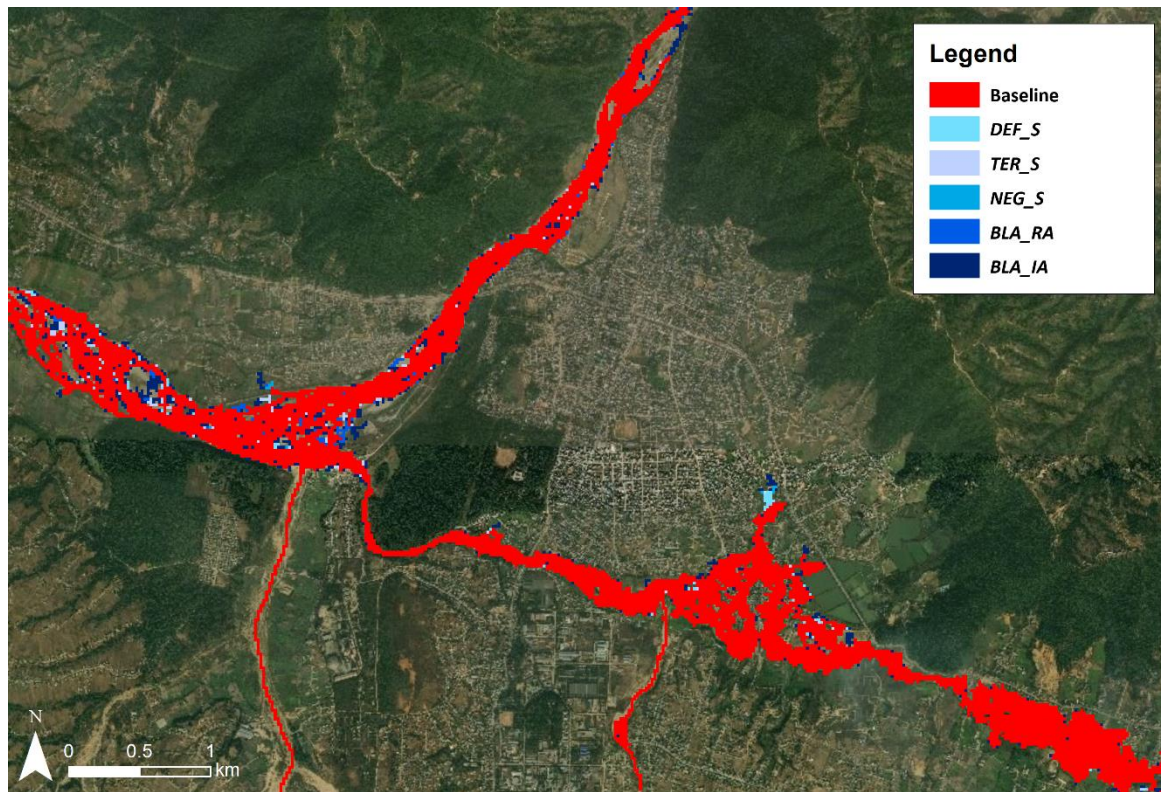


Figure 5.11: The median inundation extents at Hetauda from the model ensemble 2009 event hydrographs for the flow magnitude increasing scenarios and the baseline extent. The scenarios are layered in order of inundation extent with all cells representing an increased inundation extent visible.

Table 5.9: A comparison of inundated area extent change across the model ensemble for flow magnitude increasing catchment-scale scenarios at Hetauda using the 2009 event hydrograph.

Inundation depth (m)	DEF_S inundated area % change	DEF_S inundated area change (km ²)	TER_S inundated area % change	TER_S inundated area change (km ²)	NEG_S inundated area % change	NEG_S inundated area change (km ²)	BLA_RA inundated area % change	BLA_RA inundated area change (km ²)	BLA_IA inundated area % change	BLA_IA inundated area change (km ²)
10th percentile extent										
> 0.0 m	-3.9	-0.06	-2.0	-0.03	-2.9	-0.05	+12.2	+0.20	+22.4	+0.37
> 0.5 m	-2.3	-0.02	-3.1	-0.03	-1.7	-0.01	+17.5	+0.14	+29.9	+0.25
> 1.0 m	-2.5	-0.01	-0.7	-0.00	-1.0	-0.00	+15.3	+0.07	+26.9	+0.13
50th percentile extent										
> 0.0 m	+0.8	+0.02	-1.1	-0.03	-0.4	-0.01	-0.9	-0.03	+7.0	+0.20
> 0.5 m	+1.4	+0.03	-1.7	-0.03	-0.6	-0.01	-1.5	-0.03	+13.0	+0.24
> 1.0 m	+1.5	+0.02	-2.7	-0.03	-0.4	-0.00	-2.3	-0.02	+14.4	+0.15
90th percentile extent										
> 0.0 m	+1.0	+0.04	+1.5	+0.05	+1.9	+0.06	+1.9	+0.07	+16.8	+0.58
> 0.5 m	+1.5	+0.04	+1.9	+0.05	+3.0	+0.07	+3.3	+0.08	+19.2	+0.46
> 1.0 m	+2.0	+0.03	+3.0	+0.05	+3.9	+0.06	+4.2	+0.06	+26.5	+0.40

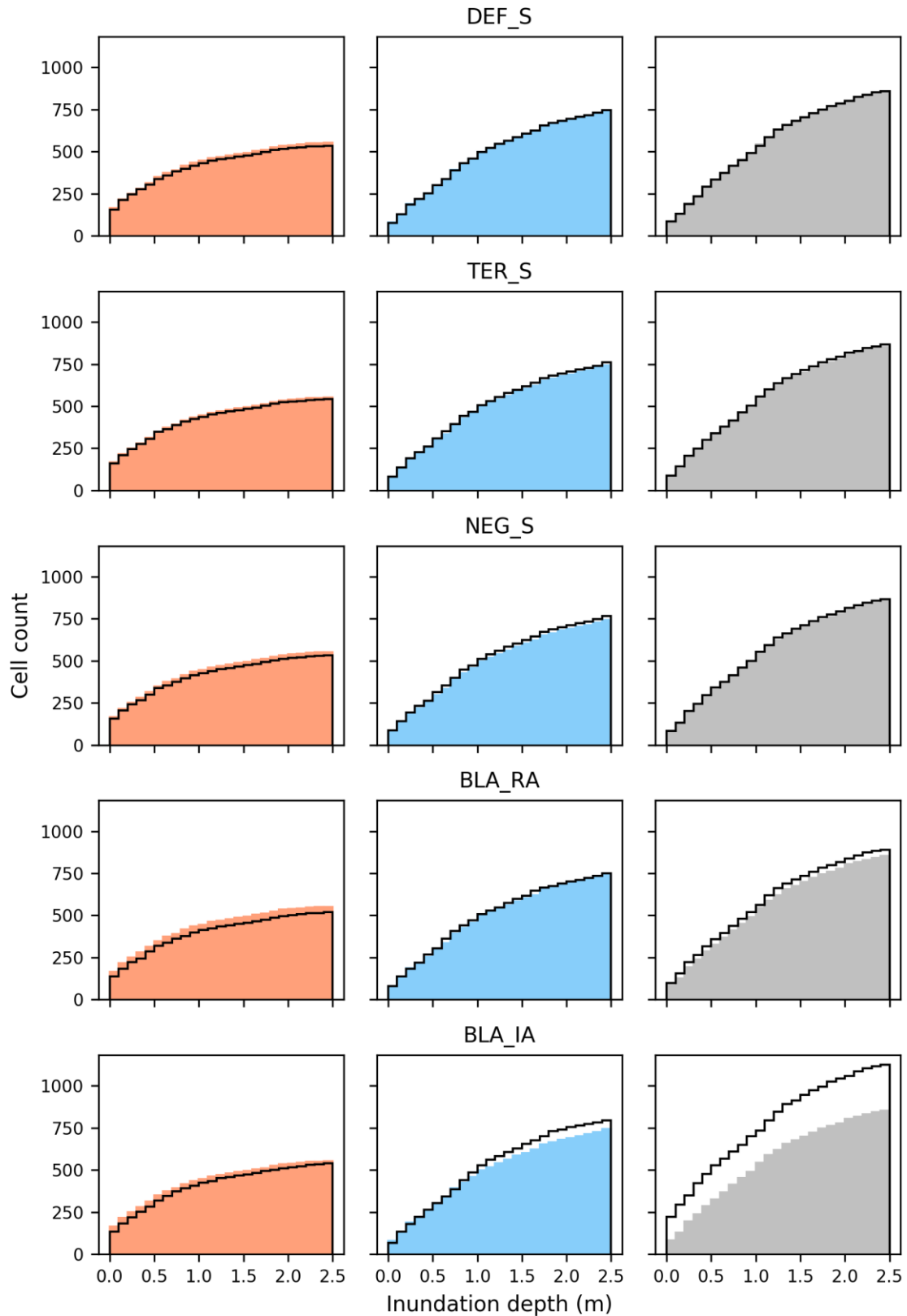


Figure 5.12: A cumulative histogram comparison of the 10th (orange), 50th (blue) and 90th (grey) percentile inundation depths occurring in areas of Built-Up Area throughout the Hetauda model extent using the 2009 event hydrograph. Baseline depths: coloured polygon; flow magnitude increasing scenario depths: black line. A black line above/below the coloured polygon indicates an increase/decrease, up to and including, a given inundation depth from the scenario compared to the baseline.

5.3.3.3 Flow magnitude increasing catchment-scale scenarios for the 2010 event in Sauraha

The inundation pattern (Figure 5.13) produced by the flow magnitude increasing scenarios is similar to that modelled from baseline scenario. The *DEF_S*, *TER_S* and *NEG_S* scenarios predicted a flood extent area increase (inundation depths > 0.0 m) of $\leq 3.6\%$. The three scenarios predict a greater increase ($\leq 7.9\%$) in areas with water depths > 0.5 m and > 1.0 m across the model ensemble results. Shown in Figure 5.13, only the *BLA_IA* scenario predicted inundation in previously unaffected areas with a slightly expanded flood extent in the northern parts of the model extent. The model results, Table 5.10, indicate that the inundation area as a result of the *BLA_IA* scenario could increase the flood extent area by between 12.7% (50th percentile extent +1.11 km²) to 20.5% (10th percentile extent +1.22 km²). There is a larger, $\geq 13.9\%$ (90th percentile extent +1.21 km²) for > 0.5 m and $\geq 18.4\%$ (90th percentile extent +1.24 km²) for > 1.0 m, increase in deeper inundation depths. The distribution of inundation depths in areas of *Built-Up Area* (Figure 5.14) are similar between the baseline and the *DEF_S*, *TER_S* and *NEG_S* scenarios. The 10th percentile extent depths for the *BLA_RA* and *BLA_IA* scenarios show an increase in deeper (> 1.0 m) inundation depths across the *Built-Up Area*. The distribution of the 50th and 90th percentile *BLA_RA scenario* depths are comparable to the baseline scenario. The distribution of the 50th and 90th percentile *BLA_IA scenario* depths are comparable to the baseline scenario below 1.0 m, have a reduced amount of *Built-Up Area* cells with inundation between 1.0 and 1.5 m but an increase in cells with > 2.0 m of inundation.

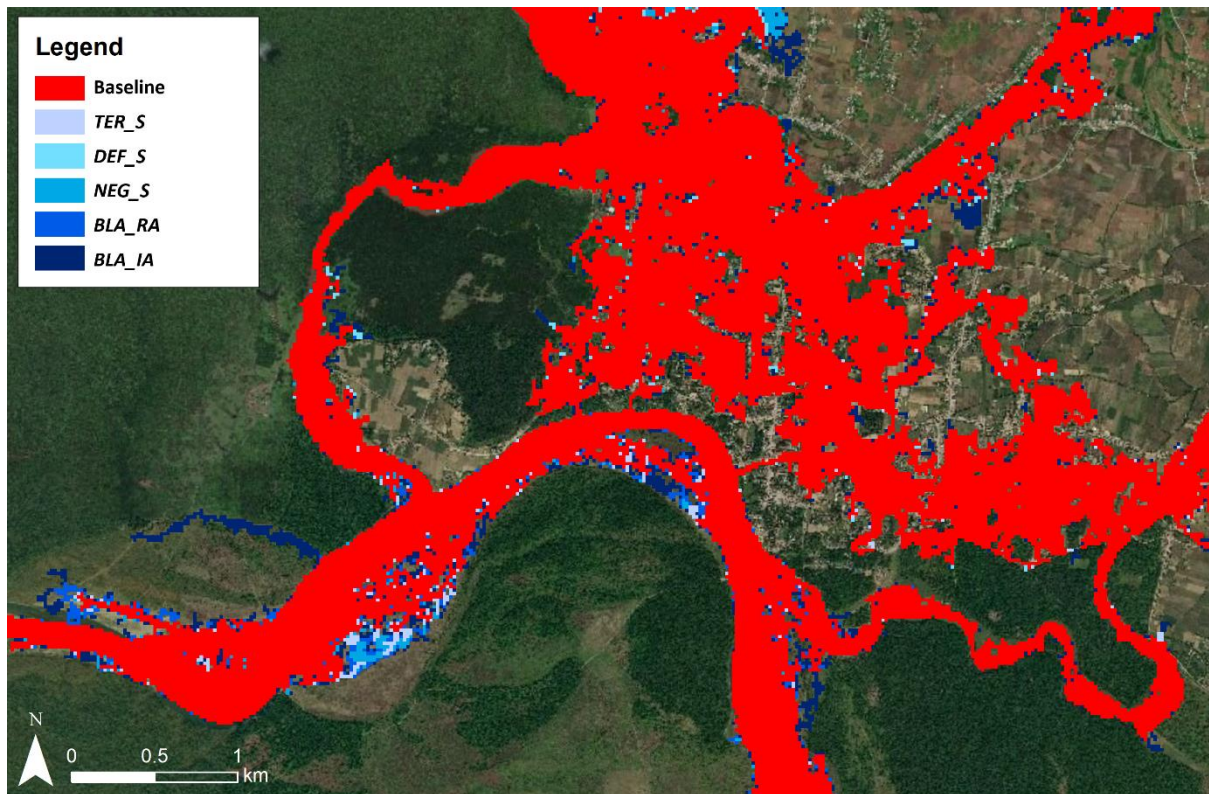


Figure 5.13: The median inundation extents at Sauraha from the model ensemble 2010 event hydrographs for the flow magnitude increasing scenarios and the baseline extent. The scenarios are layered in order of inundation extent with all cells representing an increased inundation extent visible.

Table 5.10: A comparison of inundated area extent change across the model ensemble for flow magnitude increasing catchment-scale scenarios at Sauraha using the 2010 event hydrograph.

Inundation depth (m)	DEF_S inundated area % change	DEF_S inundated area change (km ²)	TER_S inundated area % change	TER_S inundated area change (km ²)	NEG_S inundated area % change	NEG_S inundated area change (km ²)	BLA_RA inundated area % change	BLA_RA inundated area change (km ²)	BLA_IA inundated area % change	BLA_IA inundated area change (km ²)
10th percentile extent										
> 0.0 m	+2.9	+0.17	+0.1	+0.01	+3.6	+0.21	+11.6	+0.69	+20.5	+1.22
> 0.5 m	+2.9	+0.12	+0.3	+0.01	+4.6	+0.19	+14.3	+0.60	+22.8	+0.96
> 1.0 m	+3.0	+0.09	+0.1	+0.00	+4.5	+0.13	+12.9	+0.37	+29.1	+0.84
50th percentile extent										
> 0.0 m	+2.1	+0.19	+1.8	+0.16	+3.3	+0.29	+6.3	+0.55	+12.7	+1.11
> 0.5 m	+2.7	+0.19	+1.8	+0.13	+4.0	+0.29	+7.5	+0.54	+17.4	+1.24
> 1.0 m	+6.3	+0.32	+2.7	+0.14	+7.9	+0.41	+10.5	+0.54	+25.7	+1.32
90th percentile extent										
> 0.0 m	+0.8	+0.08	+0.9	+0.09	+1.8	+0.18	+5.4	+0.55	+12.8	+1.31
> 0.5 m	+0.9	+0.08	+1.0	+0.09	+2.0	+0.18	+6.8	+0.60	+13.9	+1.21
> 1.0 m	+1.0	+0.07	+1.1	+0.07	+2.3	+0.15	+8.3	+0.56	+18.4	+1.24

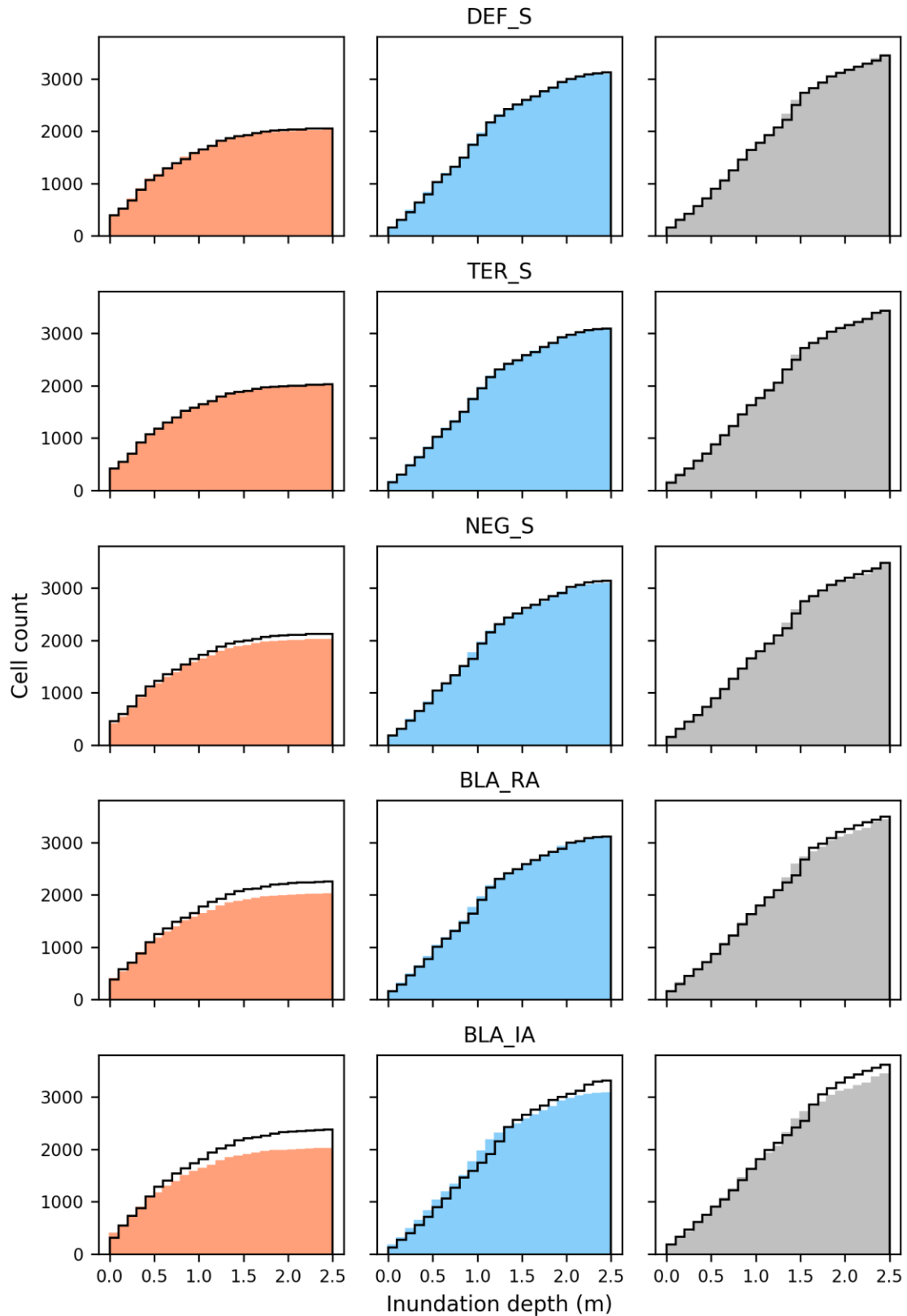


Figure 5.14: A cumulative histogram comparison of the 10th (orange), 50th (blue) and 90th (grey) percentile inundation depths occurring in areas of Built-Up Area throughout the Sauraha model extent using the 2010 event hydrograph. Baseline depths: coloured polygon; flow magnitude increasing scenario depths: black line. A black line above/below the coloured polygon indicates an increase/decrease, up to and including, a given inundation depth from the scenario compared to the baseline.

5.3.3.4 Flow magnitude increasing catchment-scale scenarios for the 2010 event in Hetauda

The inundation pattern (Figure 5.15) produced by the flow magnitude increasing scenarios is similar to that modelled from baseline scenario with the largest increase from the baseline inundation extent occurring around the East Rapti River and Karra River confluence. The *DEF_S*, *TER_S* and *NEG_S* scenarios predicted a flood extent area increase (inundation depths > 0.0 m) of $\leq 2.5\%$ with the scenarios predicting a greater increase ($\leq 4.5\%$) in areas of water depths > 0.5 m and > 1.0 m across the model ensemble (Table 5.11). The model results from the blanket coverage *BLA_RA* and *BLA_IA* scenarios produced a slightly expanded inundation extent, when compared to the more realistic *DEF_S*, *TER_S* and *NEG_S* scenarios, along the right-hand side of the main East Rapti channel. The simulations predict that the flooded area as a result of large-scale catchment change in the *BLA_IA* scenario could increase the inundated area by between 5.1% (90th percentile extent +0.22 km²) and 12.9% (10th percentile extent +0.38 km²) with a larger increase ($\geq 6.0\%$) in deeper (> 0.5 m) inundation depths. The distribution of inundation depths in areas of *Built-Up Area* (Figure 5.16) are similar between the baseline and the *DEF_S*, *TER_S* and *NEG_S* scenarios. The 50th percentile extent depths for the *BLA_RA* scenario illustrates a slight increase across the range of inundation depths in the *Built-Up Area* cells. The distribution of the 10th and 90th percentile *BLA_RA* scenario depths are comparable to the baseline scenario. The depth distribution of all the percentiles in the *BLA_IA* scenario have an increased amount of *Built-Up Area* inundated across both shallow (< 0.5 m) and deeper (> 1.5 m) depths; this increase is most pronounced for the 10th percentile depths.

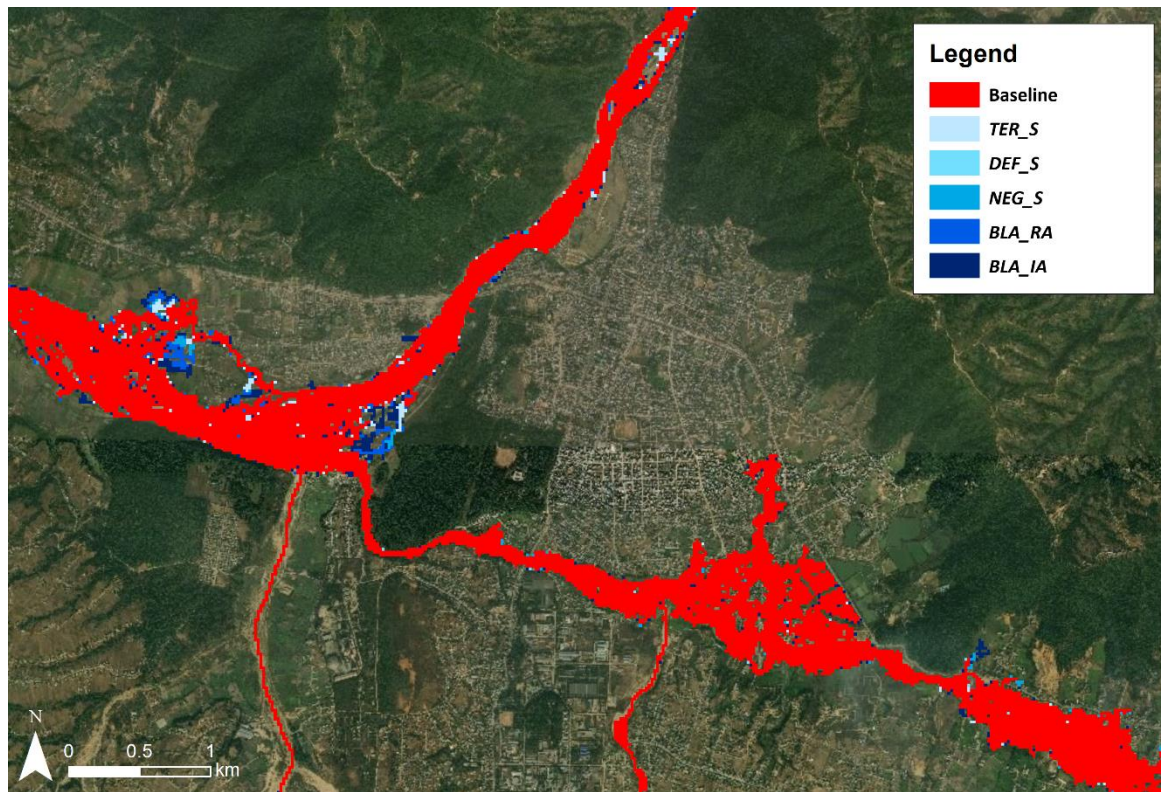


Figure 5.15: The median inundation extents at Hetauda from the model ensemble 2010 event hydrographs for the flow magnitude increasing scenarios and the baseline extent. The scenarios are layered in order of inundation extent with all cells representing an increased inundation extent visible.

Table 5.11: A comparison of inundated area extent change across the model ensemble for flow magnitude increasing catchment-scale scenarios at Hetauda using the 2010 event hydrograph.

Inundation depth (m)	DEF_S inundated area % change	DEF_S inundated area change (km ²)	TER_S inundated area % change	TER_S inundated area change (km ²)	NEG_S inundated area % change	NEG_S inundated area change (km ²)	BLA_RA inundated area % change	BLA_RA inundated area change (km ²)	BLA_IA inundated area % change	BLA_IA inundated area change (km ²)
10th percentile extent										
> 0.0 m	+0.9	+0.03	+0.3	+0.01	+1.7	+0.05	+4.9	+0.14	+12.9	+0.38
> 0.5 m	+1.3	+0.02	+0.6	+0.01	+2.5	+0.05	+8.5	+0.16	+14.0	+0.27
> 1.0 m	+1.2	+0.01	+1.2	+0.01	+3.1	+0.03	+10.0	+0.11	+22.2	+0.25
50th percentile extent										
> 0.0 m	+0.6	+0.02	+1.9	+0.07	+2.5	+0.10	+3.2	+0.12	+8.4	+0.32
> 0.5 m	+0.7	+0.02	+1.5	+0.04	+3.0	+0.08	+1.4	+0.04	+11.4	+0.31
> 1.0 m	+0.7	+0.01	+2.3	+0.04	+4.5	+0.08	+3.3	+0.06	+18.0	+0.32
90th percentile extent										
> 0.0 m	+0.1	+0.00	+0.5	+0.02	+0.5	+0.02	+1.4	+0.06	+5.1	+0.22
> 0.5 m	+0.3	+0.01	+0.9	+0.03	+0.8	+0.03	+2.6	+0.08	+6.0	+0.19
> 1.0 m	+0.4	+0.01	+1.4	+0.03	+1.5	+0.03	+4.3	+0.10	+8.6	+0.19

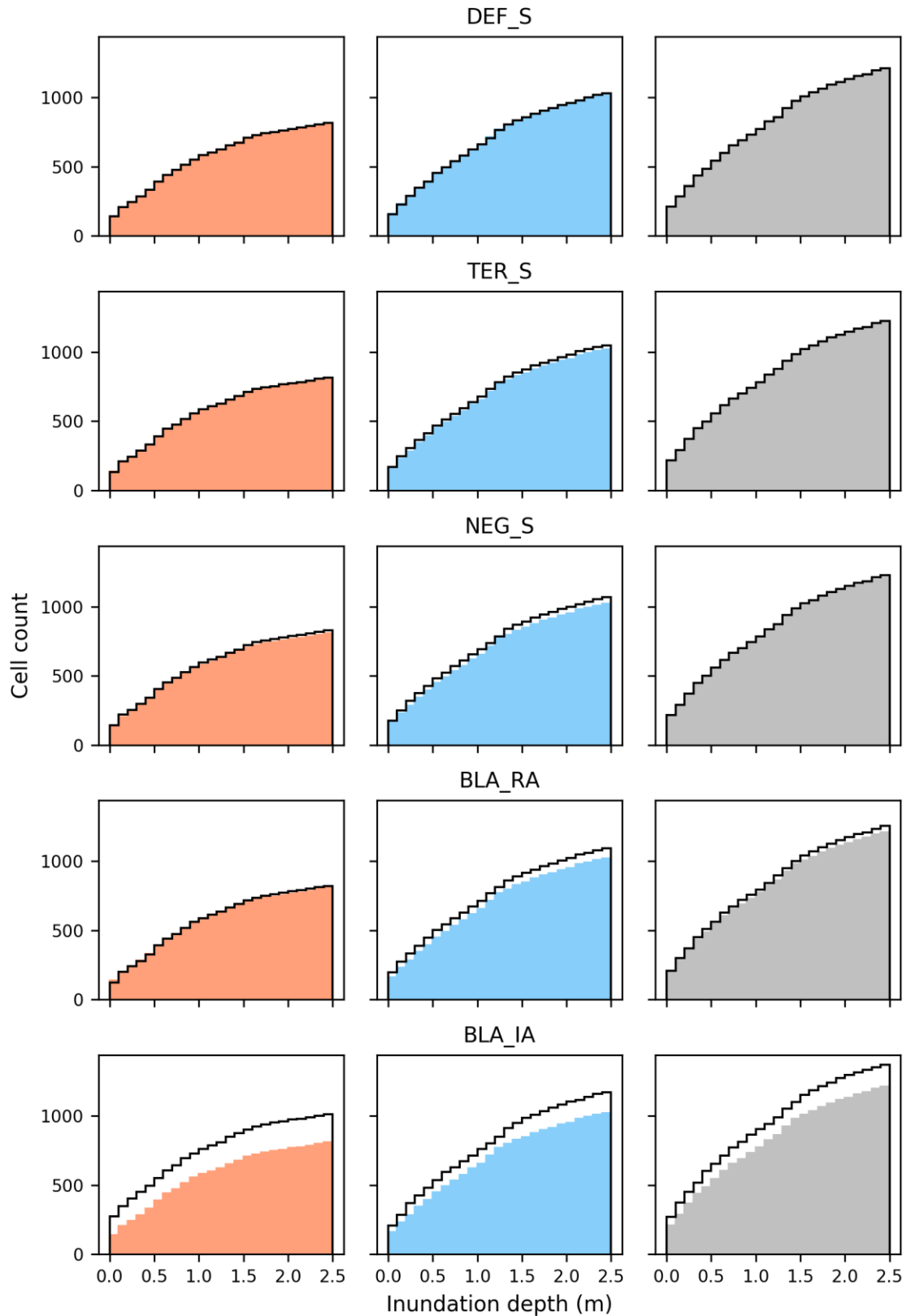


Figure 5.16: A cumulative histogram comparison of the 10th (orange), 50th (blue) and 90th (grey) percentile inundation depths occurring in areas of Built-Up Area throughout the Hetauda model extent using the 2010 event hydrograph. Baseline depths: coloured polygon; flow magnitude increasing scenario depths: black line. A black line above/below the coloured polygon indicates an increase/decrease, up to and including, a given inundation depth from the scenario compared to the baseline.

5.3.3.5 Flow magnitude decreasing catchment-scale scenarios for 2009 in Sauraha

The inundation pattern (Figure 5.17) produced by the flow magnitude increasing scenarios is similar to that modelled from baseline scenario with the majority of small changes in inundation extent predominantly occurring along the main East Rapti channel. Shown in Figure 5.17, only the *BLA_F* scenario, with the largest reduction to the high-flow regime from the catchment-scale modelling using CRUM3, predicted a noticeably smaller inundation extent in the northern part of the model extent from overtopping along the Budhi Khola. Evident in Table 5.12, the model results indicate that the flooded area as a result of the *BLA_F* scenario could decrease the flood extent by between 0.3% (90th percentile extent -0.03 km²) and 23.2% (10th percentile extent -0.51 km²) with a greater (-0.9% to 25.6) increase in inundation depths > 0.5 m. The spatially targeted afforestation scenarios, *AFF50_F* and *AFF50_PDA_F*, predicted an inundated area reduction (inundation depths > 0.0 m) of >= -4.4%. The *DAM50* scenario predicted a lesser reduction when compared to the afforestation scenarios with an inundation extent reduction (inundation depths of > 0.0 m) of <= -1.2%. The *POS50* scenario predicted, excluding the *BLA_F* scenario, the greatest reduction (between -1.3% and -10.5%) in areas with inundation depths of > 0.5 m and > 1.0 m across the model ensemble results. The distribution of inundation depths in areas of *Built-Up Area* (Figure 5.18) are similar between the baseline and all but the 10th and 50th percentile depths from the *BLA_F* scenario. The 10th percentile depths for the *BLA_F* scenario illustrate an inundation reduction across the depth range with a large reduction in inundated *Built-Up Area* cells when compared to the baseline. The 50th percentile depths for the *BLA_F* scenario show a similar amount of *Built-Up Area* cells with shallow (< 0.5 m) inundation but a reduction in cells with deeper (> 0.5 m) inundation depths.

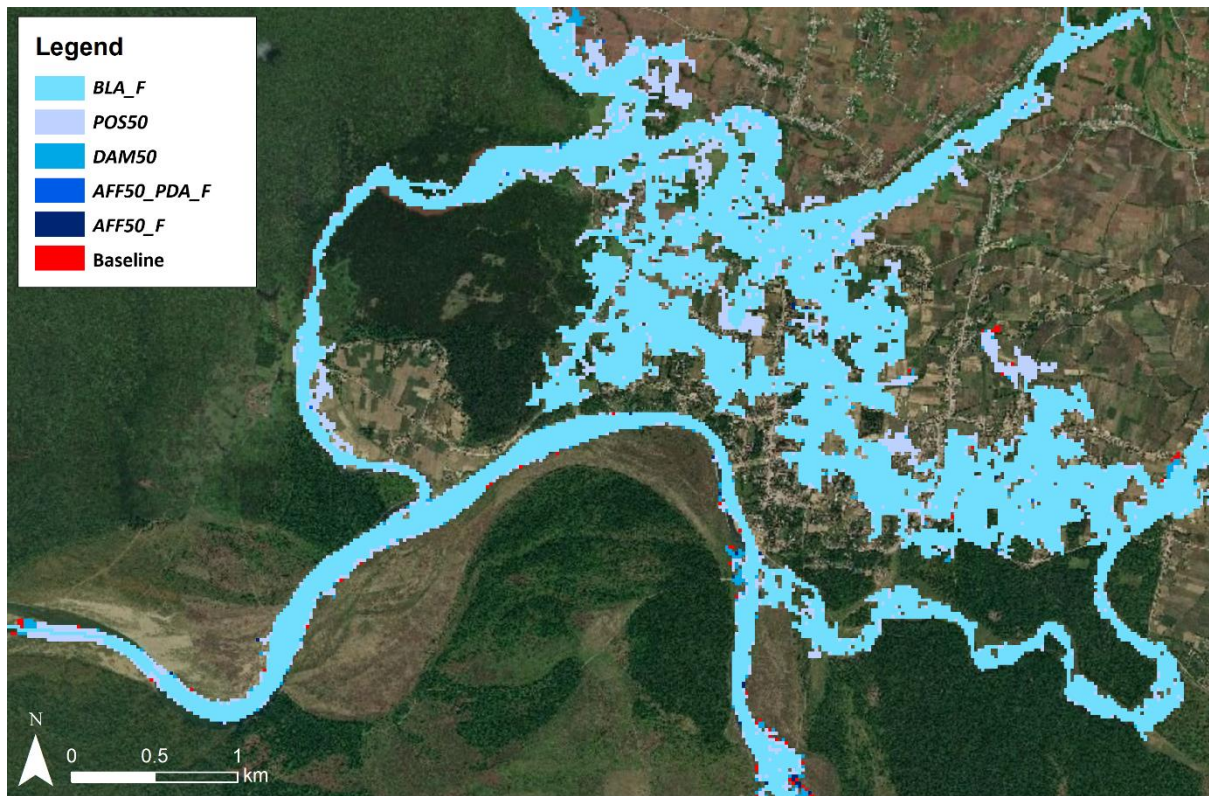


Figure 5.17: The median inundation extents at Sauraha from the model ensemble 2009 event hydrographs for the flow magnitude decreasing scenarios and the baseline extent. The scenarios are layered in order of inundation extent with all cells representing a decreased inundation extent visible.

Table 5.12: A comparison of inundated area extent change across the model ensemble for flow magnitude decreasing catchment-scale scenarios at Sauraha using the 2009 event hydrograph.

Inundation depth (m)	AFF50_F inundated area % change	AFF50_F inundated area change (km ²)	AFF50_PDA_F wet cell area % change	AFF50_PDA_F inundated area change (km ²)	DAM50 inundated area % change	DAM50 inundated area change (km ²)	POSS50 inundated area % change	POSS50 inundated area change (km ²)	BLA_F inundated area % change	BLA_F inundated area change (km ²)
10th percentile extent										
> 0.0 m	-1.7	-0.04	-4.4	-0.10	-1.2	-0.03	-4.3	-0.10	-23.2	-0.51
> 0.5 m	-1.3	-0.02	-4.6	-0.07	-0.6	-0.01	-4.8	-0.07	-25.6	-0.38
> 1.0 m	-2.5	-0.03	-9.5	-0.10	-0.3	-0.00	-10.5	-0.11	-23.1	-0.24
50th percentile extent										
> 0.0 m	-0.2	-0.01	-0.8	-0.05	+0.0	+0.00	-0.9	-0.05	-14.6	-0.82
> 0.5 m	-0.2	-0.01	-1.2	-0.05	-0.1	-0.00	-1.3	-0.05	-21.9	-0.85
> 1.0 m	-0.4	-0.01	-1.7	-0.04	-0.3	-0.01	-1.4	-0.04	-17.4	-0.45
90th percentile extent										
> 0.0 m	+0.0	+0.00	-0.1	-0.01	-0.6	-0.04	-0.8	-0.06	-0.3	-0.03
> 0.5 m	+0.1	+0.01	-0.1	-0.01	-1.4	-0.08	-1.3	-0.08	-2.9	-0.17
> 1.0 m	-0.1	-0.00	-0.3	-0.01	-1.0	-0.04	-1.3	-0.05	-0.9	-0.04

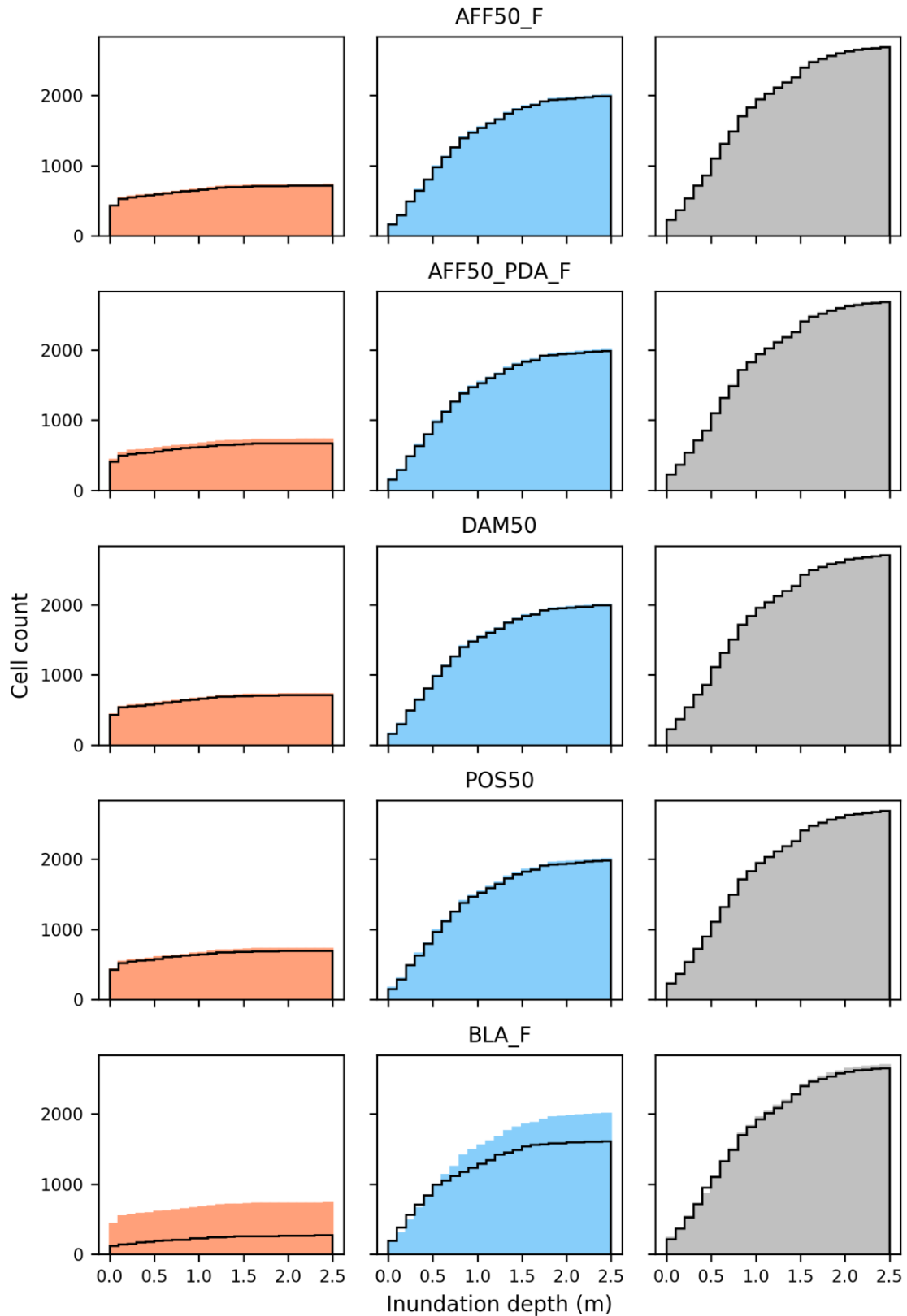


Figure 5.18: A cumulative histogram comparison of the 10th (orange), 50th (blue) and 90th (grey) percentile inundation depths occurring in areas of Built-Up Area throughout the Sauraha model extent using the 2009 event hydrograph. Baseline depths: coloured polygon; flow magnitude decreasing scenario depths: black line. A black line above/below the coloured polygon indicates an increase/decrease, up to and including, a given inundation depth from the scenario compared to the baseline.

5.3.3.6 Flow magnitude decreasing catchment-scale scenarios for 2009 in Hetauda

The inundation pattern (Figure 5.19) produced by the flow magnitude increasing scenarios is similar to that modelled from baseline scenario but with small changes in inundation extent along the Karra River and along the main East Rapti channel downstream of the confluence. Shown in Table 5.13, the spatially targeted afforestation scenarios, *AFF50_F* and *AFF50_PDA_F*, predicted an inundated area reduction (inundation depths > 0.0 m) of $\leq -15.4\%$ (10th percentile extent -0.25 km²). The *DAM50* scenario predicted a lesser reduction when compared to the afforestation scenarios with a flood extent area reduction (inundation depths of > 0.0 m) of $\leq -3.0\%$ (90th percentile extent -0.10 km²). The *POS50* scenario, with both afforestation and check dam implementation, had an inundated area reduction of $\leq -17.7\%$ (10th percentile extent -0.29 km²). The *POS50* scenario also predicted the greater reduction ($\leq -19.0\%$), amongst the realistically implementable scenarios, in areas with inundation depths of > 0.5 m and > 1.0 m across the model ensemble results. The model results indicate that the inundated area as a result of large-scale catchment change to the *Forest* land cover (*BLA_F*) could decrease the extent by between 0.6% (90th percentile extent -0.02 km²) and 40.0% (90th percentile extent -0.66 km²) with a reduction in deeper (> 0.5 m) inundation depths of $\leq -34.3\%$. The distribution of inundation depths in areas of *Built-Up Area* (Figure 5.20) are similar between the baseline and the 50th percentile depths from the *AFF50_F* and *DAM50* scenarios, the baseline and the 10th percentile depths from the *DAM50* scenario, and the baseline and the 90th percentile depths from the *AFF50_F*, *AFF50_PDA_F*, *DAM50* and *BLA_F* scenarios. The four remaining scenarios (*AFF50_F*, *AFF50_PDA_F*, *POS50* and *BLA_F*) 10th percentile inundation depths show a comparable amount of shallower (< 0.5 m) inundation with a reduction in *Built-Up Area* with > 0.5 m inundation. This pattern of reduced areas of deeper inundation is reflected in remaining the 50th and 90th percentile depth comparisons but for inundation depths > 1.5 m.

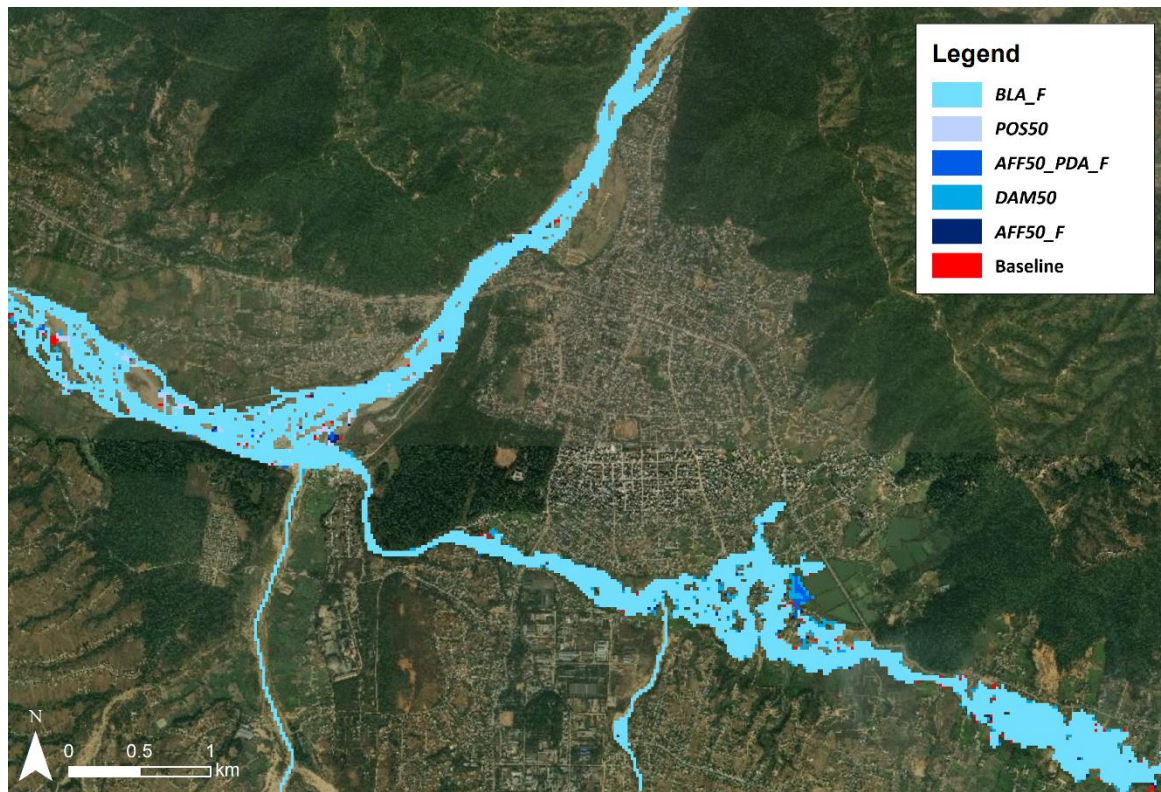


Figure 5.19: The median inundation extents at Hetauda from the model ensemble 2009 event hydrographs for the flow magnitude decreasing scenarios and the baseline extent. The scenarios are layered in order of inundation extent with all cells representing a decreased inundation extent visible.

Table 5.13: A comparison of inundated area extent change across the model ensemble for flow magnitude decreasing catchment-scale scenarios at Hetauda using the 2009 event hydrograph.

Inundation depth (m)	AFF50_F inundated area % change	AFF50_F inundated area change (km ²)	AFF50_PDA_F wet cell area % change	AFF50_PDA_F inundated area change (km ²)	DAM50 inundated area % change	DAM50 inundated area change (km ²)	POSSO inundated area % change	POSSO inundated area change (km ²)	BLA_F inundated area % change	BLA_F inundated area change (km ²)
10th percentile extent										
> 0.0 m	-11.7	-0.19	-15.4	-0.25	-0.8	-0.01	-17.7	-0.29	-40.0	-0.66
> 0.5 m	-9.5	-0.08	-15.5	-0.13	-2.6	-0.02	-19.0	-0.16	-34.3	-0.28
> 1.0 m	-9.4	-0.04	-14.1	-0.07	-1.7	-0.01	-17.0	-0.08	-33.8	-0.16
50th percentile extent										
> 0.0 m	-3.3	-0.10	-7.4	-0.22	-2.8	-0.08	-8.8	-0.26	-11.8	-0.35
> 0.5 m	-4.9	-0.09	-11.4	-0.21	-4.9	-0.09	-14.3	-0.26	-16.9	-0.31
> 1.0 m	-5.5	-0.06	-13.4	-0.14	-6.2	-0.07	-15.9	-0.17	-19.9	-0.21
90th percentile extent										
> 0.0 m	+1.0	+0.04	+0.6	+0.02	-3.0	-0.10	-3.6	-0.13	-0.6	-0.02
> 0.5 m	+1.1	+0.03	+0.2	+0.00	-4.0	-0.10	-4.9	-0.12	-1.1	-0.03
> 1.0 m	+1.5	+0.02	+0.7	+0.01	-4.9	-0.08	-6.2	-0.09	-1.1	-0.02

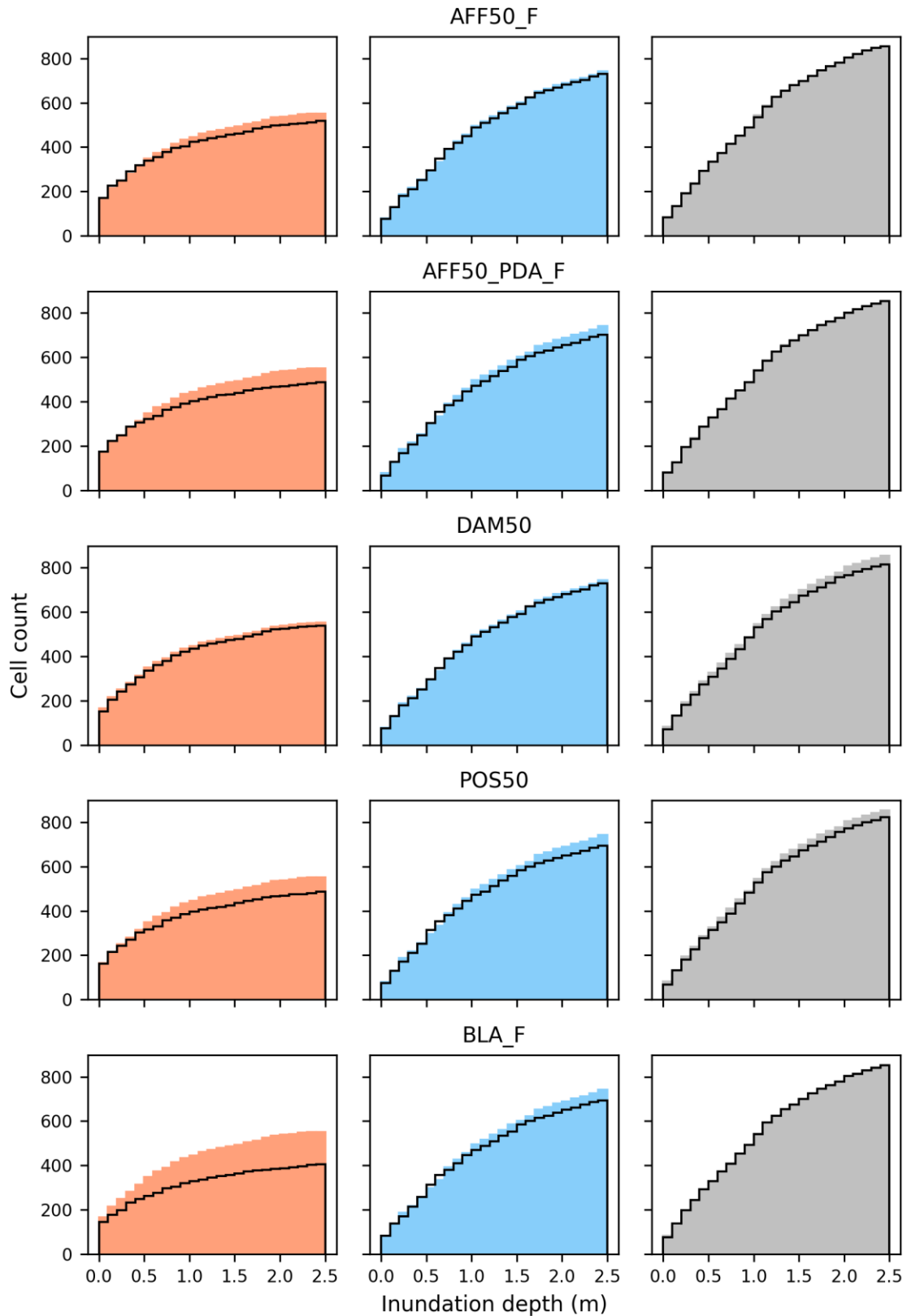


Figure 5.20: A cumulative histogram comparison of the 10th (orange), 50th (blue) and 90th (grey) percentile inundation depths occurring in areas of Built-Up Area throughout the Hetauda model extent using the 2009 event hydrograph. Baseline depths: coloured polygon; flow magnitude decreasing scenario depths: black line. A black line above/below the coloured polygon indicates an increase/decrease, up to and including, a given inundation depth from the scenario compared to the baseline.

5.3.3.7 Flow magnitude decreasing catchment-scale scenarios for 2010 in Sauraha

The inundation pattern (Figure 5.21) produced by the flow magnitude increasing scenarios is similar to that modelled from baseline scenario with the changes in inundation extent predominantly occurring along the main East Rapti channel. The *AFF50_F* and *AFF50_PDA_F* afforestation scenarios predicted a slight inundated area reduction (inundation depths of > 0.0 m) of $\leq -2.3\%$ (see Table 5.14). The *DAM50* and *POS50* scenarios predicted an improved reduction when compared to the afforestation scenarios with an inundated area reduction (inundation depths > 0.0 m) of $\leq -6.4\%$. Both scenarios predicted a greater reduction ($\leq -8.8\%$) in areas with inundation depths of > 0.5 m and > 1.0 m across the model ensemble. Shown in Figure 5.21, only the *BLA_F* scenario predicted a smaller inundation extent in the northern part of the model along the Budhi Khola tributary. The model results indicate that the inundated area as a result of large-scale catchment change to the Forest land cover (*BLA_F*) could decrease the flood extent by between -1.0% (90th percentile extent - 0.10 km²) and -21.9% (90th percentile extent -1.31 km²) with an increase ($\leq 24.3\%$) in the percentage reduction of deeper (> 0.5 m) inundation depths. The distribution of inundation depths in areas of *Built-Up Area* (Figure 5.22) follow the same pattern as the 2009 high-flow event and are similar between the baseline and all but the 10th and 50th percentile depths from the *BLA_F* scenario. The 10th percentile depths for the *BLA_F* scenario illustrate an increase in shallow (< 0.5 m) inundation when compared to the baseline but with a reduction in deeper (> 1.0 m) inundation depths. The 50th percentile depths for the *BLA_F* scenario show a similar amount of *Built-Up Area* cells with shallow (< 0.5 m) inundation but a reduction in cells with deeper (> 1.0 m) inundation depths.

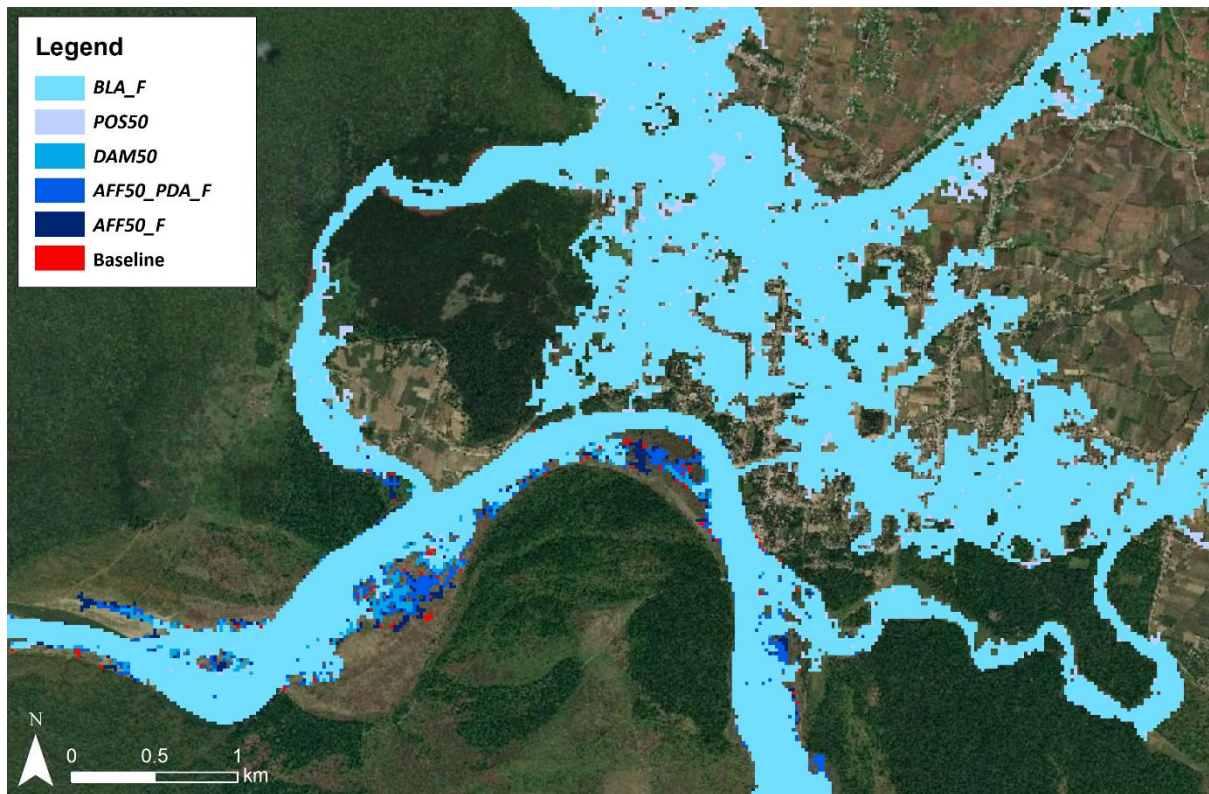


Figure 5.21: The median inundation extents at Sauraha from the model ensemble 2010 event hydrographs for the flow magnitude decreasing scenarios and the baseline extent. The scenarios are layered in order of inundation extent with all cells representing a decreased inundation extent visible.

Table 5.14: A comparison of inundated area extent change across the model ensemble for flow magnitude decreasing catchment-scale scenarios at Sauraha using the 2010 event hydrograph.

Inundation depth (m)	AFF50_F inundated area % change	AFF50_F inundated area change (km ²)	AFF50_PDA_F wet cell area % change	AFF50_PDA_F inundated area change (km ²)	DAM50 inundated area % change	DAM50 inundated area change (km ²)	POSSO inundated area % change	POSSO inundated area change (km ²)	BLA_F inundated area % change	BLA_F inundated area change (km ²)
10th percentile extent										
> 0.0 m	-0.8	-0.05	-2.3	-0.14	-4.1	-0.24	-6.4	-0.38	-21.9	-1.31
> 0.5 m	-1.1	-0.05	-3.5	-0.15	-3.9	-0.16	-8.8	-0.37	-24.1	-1.01
> 1.0 m	-1.1	-0.03	-3.3	-0.10	-5.4	-0.16	-8.3	-0.24	-24.3	-0.70
50th percentile extent										
> 0.0 m	-0.7	-0.06	-1.6	-0.14	-2.8	-0.24	-4.2	-0.37	-7.7	-0.67
> 0.5 m	-0.2	-0.01	-1.9	-0.14	-2.7	-0.20	-4.2	-0.30	-10.1	-0.72
> 1.0 m	-0.1	-0.00	-1.5	-0.08	-3.0	-0.15	-4.0	-0.21	-13.8	-0.71
90th percentile extent										
> 0.0 m	-0.1	-0.01	+0.0	+0.00	-3.2	-0.33	-3.4	-0.35	-1.0	-0.10
> 0.5 m	-0.4	-0.04	-0.0	-0.00	-3.7	-0.32	-3.9	-0.34	-1.4	-0.12
> 1.0 m	-0.3	-0.02	+0.0	+0.00	-4.3	-0.29	-4.6	-0.31	-1.2	-0.08

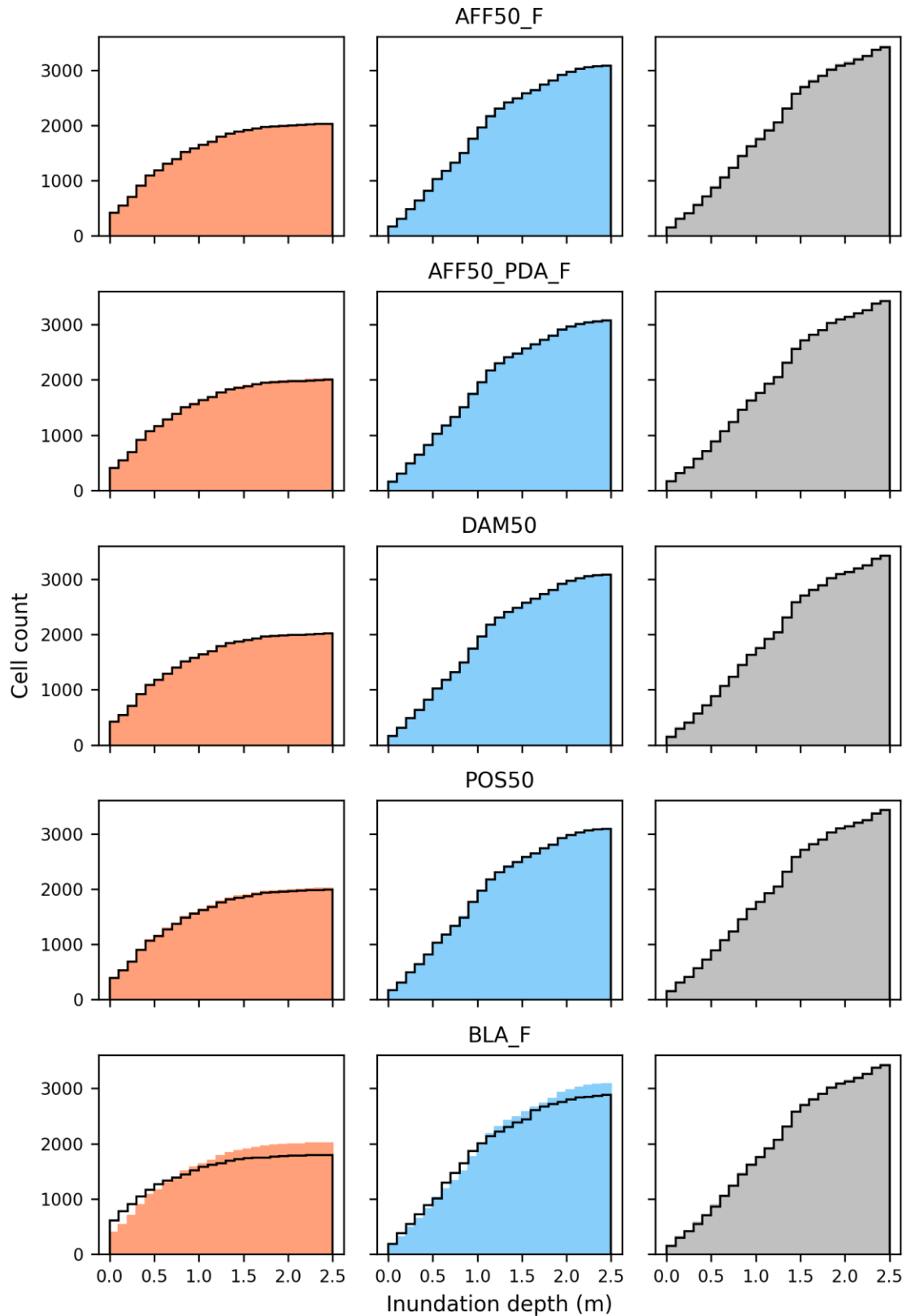


Figure 5.22: A cumulative histogram comparison of the 10th (orange), 50th (blue) and 90th (grey) percentile inundation depths occurring in areas of Built-Up Area throughout the Sauraha model extent using the 2010 event hydrograph. Baseline depths: coloured polygon; flow magnitude decreasing scenario depths: black line. A black line above/below the coloured polygon indicates an increase/decrease, up to and including, a given inundation depth from the scenario compared to the baseline.

1.1.1.1 Flow magnitude decreasing catchment-scale scenarios for 2010 in Hetauda

The inundation pattern (Figure 5.23) produced by the flow magnitude increasing scenarios is comparable to that modelled from the baseline scenario but with small changes in inundation extent along the Karra River and the main East Rapti channel downstream of the confluence. The spatially targeted afforestation scenarios, *AFF50_F* and *AFF50_PDA_F*, predicted an inundated area reduction (inundation depths > 0.0 m) of $\leq -4.5\%$. Both the *DAM50* and *POS50* scenarios predicted an improved reduction when compared to the maximum reduction in the 50th and 90th percentile extents from the afforestation scenarios with an inundated area reduction (inundation depths of > 0.0 m) of $\leq -9.6\%$ and also a greater reduction ($\leq -16.1\%$) in areas with inundation depths of > 0.5 m and > 1.0 m. The *AFF50_PDA_F* scenario had a greater reduction than the *DAM50* scenario across the 10th percentile extents. Displayed in Figure 5.23, the *DAM50* and *POS50* scenarios, along with the *BLA_F* scenario, produced a smaller inundation extent in the area overtopping the right-hand bank of the main East Rapti channel. This overtopping does not occur under the *AFF50_F* and *AFF50_PDA_F* scenarios. The model results indicate that the flooded area as a result of large-scale catchment change to the Forest land cover (*BLA_F*) could decrease the flood extent by between 1.1% (90th percentile extent -0.05 km²) and 8.5% (10th percentile extent -0.25 km²) with a larger ($\leq 18.4\%$) increase in deeper (> 0.5 m) inundation depths. The distribution of inundation depths in areas of *Built-Up Area* (Figure 5.24) are similar between the baseline and the *AFF50_F* and *AFF50_PDA_F* scenarios. The *DAM50*, *POS50* and *BLA_F* scenarios had comparable 10th percentile depth distributions, a noticeable reduction across the range of depths in the 50th percentile distribution and a reduced amount of deeper (> 1.5 m) inundation depths in the 90th percentile distribution when compared to the baseline.

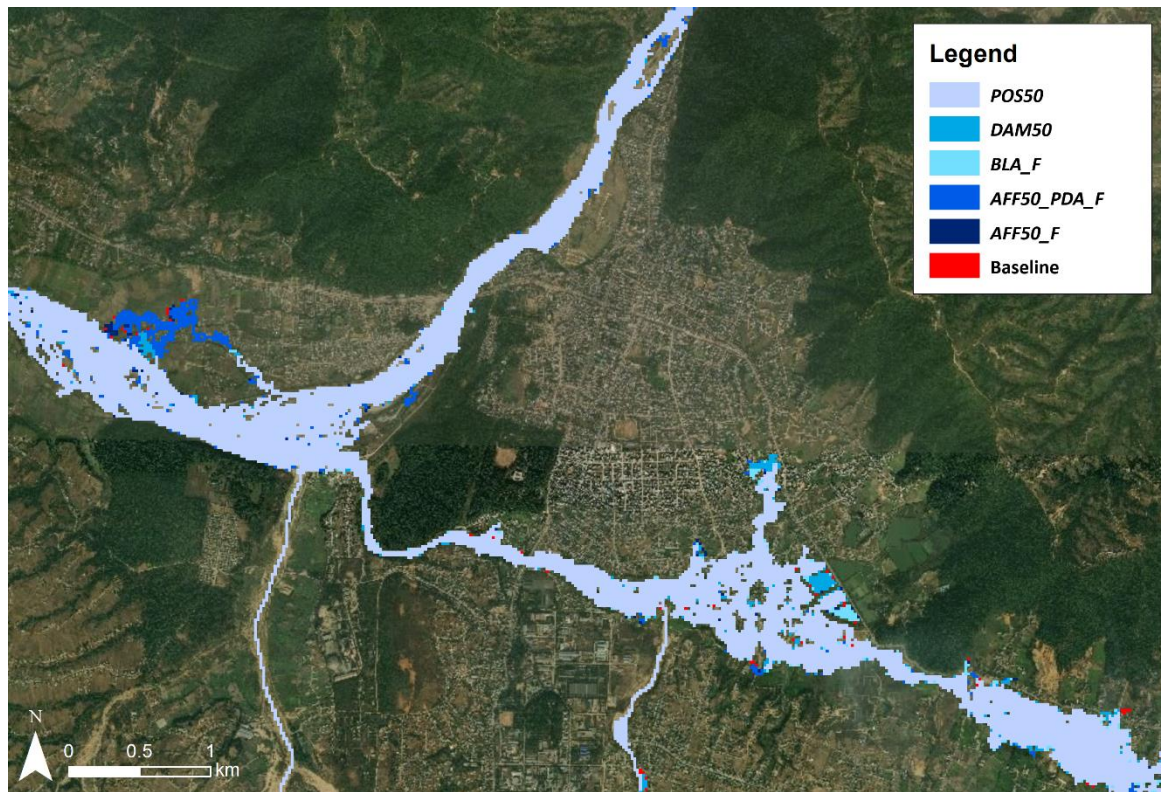


Figure 5.23: The median inundation extents at Hetauda from the model ensemble 2010 event hydrographs for the flow magnitude decreasing scenarios and the baseline extent. The scenarios are layered in order of inundation extent with all cells representing a decreased inundation extent visible.

Table 5.15: A comparison of inundated area extent change across the model ensemble for flow magnitude decreasing catchment-scale scenarios at Hetauda using the 2010 event hydrograph.

Inundation depth (m)	AFF50_F inundated area % change	AFF50_F inundated area change (km ²)	AFF50_PDA_F wet cell area % change	AFF50_PDA_F inundated area change (km ²)	DAM50 inundated area % change	DAM50 inundated area change (km ²)	POS50 inundated area % change	POS50 inundated area change (km ²)	BLA_F inundated area % change	BLA_F inundated area change (km ²)
10th percentile extent										
> 0.0 m	-2.1	-0.06	-4.5	-0.13	-3.4	-0.10	-7.6	-0.23	-8.5	-0.25
> 0.5 m	-6.5	-0.12	-10.1	-0.19	-8.7	-0.17	-16.1	-0.31	-18.4	-0.35
> 1.0 m	-4.4	-0.05	-7.9	-0.09	-7.8	-0.09	-15.6	-0.17	-17.3	-0.19
50th percentile extent										
> 0.0 m	-0.7	-0.03	-2.9	-0.11	-7.6	-0.29	-9.6	-0.37	-7.4	-0.28
> 0.5 m	-2.1	-0.06	-4.5	-0.12	-9.0	-0.24	-11.5	-0.31	-9.1	-0.25
> 1.0 m	-1.7	-0.03	-4.9	-0.09	-10.1	-0.18	-14.1	-0.25	-10.8	-0.19
90th percentile extent										
> 0.0 m	+0.1	+0.01	+0.0	+0.00	-4.0	-0.17	-4.2	-0.18	-1.1	-0.05
> 0.5 m	+0.3	+0.01	+0.2	+0.01	-6.9	-0.22	-7.3	-0.23	-1.4	-0.04
> 1.0 m	+0.1	+0.00	+0.1	+0.00	-10.6	-0.23	-10.7	-0.24	-2.3	-0.05

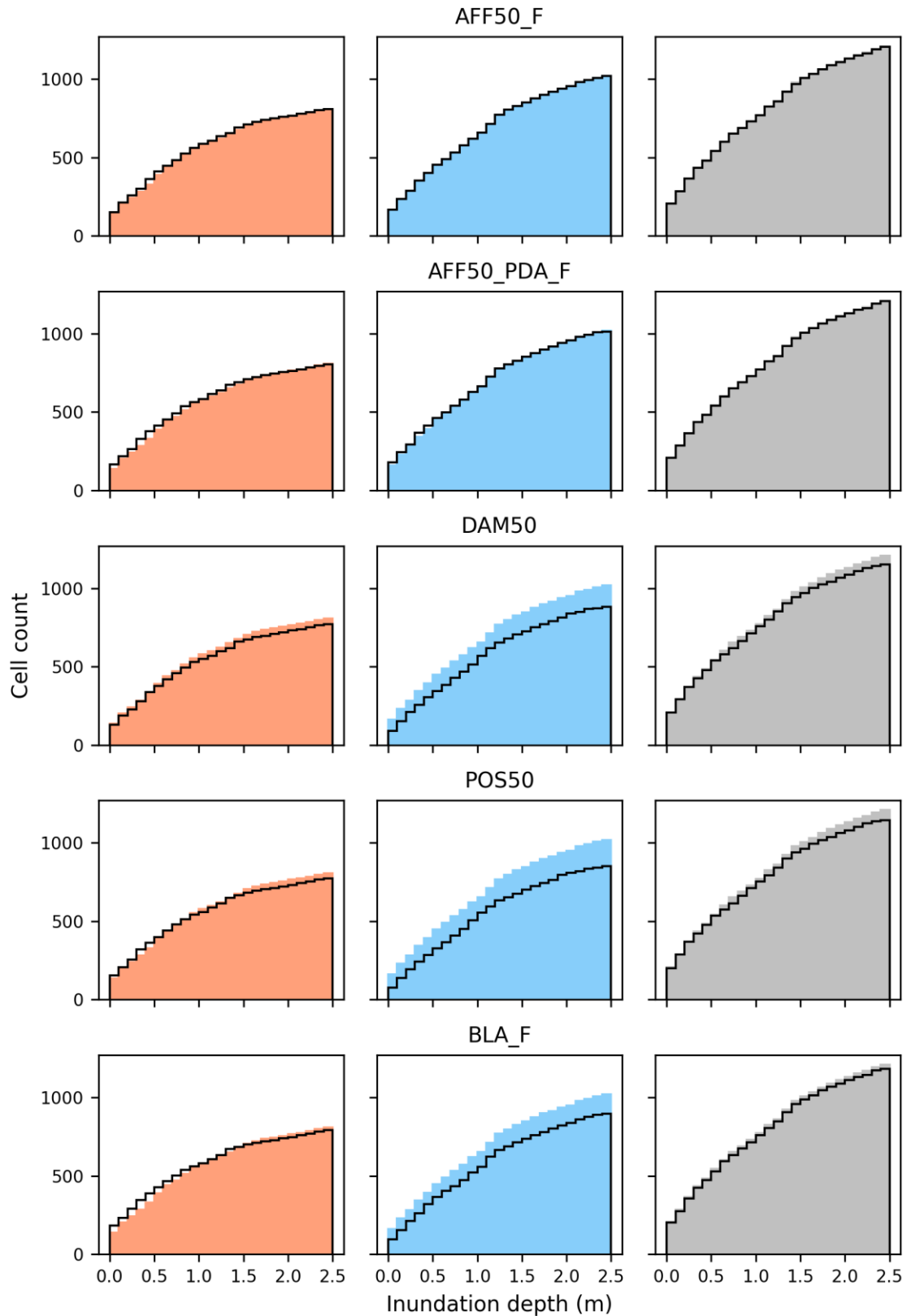


Figure 5.24: A cumulative histogram comparison of the 10th (orange), 50th (blue) and 90th (grey) percentile inundation depths occurring in areas of Built-Up Area throughout the Hetauda model extent using the 2010 event hydrograph. Baseline depths: coloured polygon; flow magnitude decreasing scenario depths: black line. A black line above/below the coloured polygon indicates an increase/decrease, up to and including, a given inundation depth from the scenario compared to the baseline.

5.4 DISCUSSION

5.4.1 The impact of catchment-scale change on the localised inundation characteristics within the East Rapti catchment

For both Sauraha and Hetauda, results of the LISFLOOD-FP inundation modelling indicate that increased flow magnitudes predominantly caused an increased inundation extent and in water depths > 0.5 m and > 1.0 m within the model boundary. This pattern was anticipated as it is also seen in other research on inundation extent and land use change (e.g. Zope et al., 2016). Due to the channel and floodplain morphologies (discussed in Section 5.4.2) this percentage increase in extent from flow magnitude increasing catchment scenarios is largest within the Sauraha model. The LISFLOOD-FP results for realistic future land change scenarios (*DEF_S*, *TER_S* and *NEG_S*) produced limited change to the inundation characteristics from both return period flow events. Investigating the change in inundation depths over the *Built-Up Area* land cover cells reveals that the distribution of depths does not differ noticeably from the baseline scenario under the *DEF_S*, *TER_S* and *NEG_S* scenarios. This pattern of negligible change is prevalent at both Sauraha and Hetauda for both the 2009 and 2010 events.

The largest increase in inundation extent ($\leq 49.1\%$ in the 2009 event 10th percentile extent comparison) occurs within the largest increase in Q99.9 from the CRUM3 catchment modelling under the *BLA_IA* scenario. Within areas of *Built-Up Area*, the *BLA_IA* scenario also saw an increase in inundated areas > 1.5 m for the 50th percentile distribution an increase across the 0.0 m to 2.5 m range in the 90th percentile distribution. However, excluding this single scenario, the change in extent (inundation > 0.0 m) produced through future land use change through the 50th and 90th percentiles of the model ensemble shows a predicted increase percentage of extent area < 6.3% at Sauraha.

With a smaller upstream catchment area, the impacts of future flow magnitude increasing land use change at Hetauda are smaller ($\leq 3.2\%$ for the 50th and 90th percentiles across the two events) with some areas having a slightly reduced inundation extent. The reduced extent is due to the representation of the localised channel network and the areal – rather than point – assessment used in CRUM3. The reduction in flood extent appears to be predominantly along the Karra River that flows through the southern part of the city. The relationship suggests that, at the local scale for Hetauda, there is limited potential change to the inundation pattern from lower return period events due to more realistic land use change scenarios. From the higher return period 2010 event, the model results predicted that Hetauda would experience a small increase in inundation extent around the confluence with the main East Rapti channel. There is additional flooding at the eastern edge of the model that represents overtopping, or poor representation within the elevation data, of the existing flood embankment than runs along the right-hand bank of the main East Rapti channel. The representation

of the channel system and complex nature of the channel and floodplain dynamics within the model are discussed in Section 5.4.3.

All the modelled catchment-scale flow magnitude reduction scenarios produced a reduced flood extent and smaller areas of inundation > 0.5 m and > 1.0 m across both events. However, there was uncertainty across the model ensemble in the predicted inundation extent reductions for each scenario for both the Sauraha and Hetauda models. Additionally, further investigation using cumulative histograms into the change in inundation depths over *Built-Up Area* cells concludes that is a limited change in the depths occurring from the scenarios when compared to the baseline. At shallower depths (< 0.5 m), the distribution produced from the catchment-scale scenarios was similar to the baseline. This indicates that there is a limited beneficial change to the affected population from implementing the scenarios, with limited change in shallow depths found around the perimeter of the inundated area.

Across the model ensemble for the scenarios that used solely land use change for flood mitigation (*AFF50_F*, *AFF50_PDA_F* and *BLA_F*), the reduction in inundation extent and depths was predominantly greatest from the model runs with the lower magnitude hydrographs (10th percentile in the model ensemble) for both events. This is reflected in the inundation depths of *Built-Up Area* which have a reduced cell count of cells with > 0.5 m inundation. Conversely, the lowest change in inundated area and depth across the model extent and within *Built-Up Area* cells was from the model runs with the higher magnitude hydrographs (90th percentile in the model ensemble) for both events. This is seen with the 10th percentile wetted area extents for the lower magnitude 2009 event having the greater reduction in inundation extent when compared to the 10th percentile of the higher magnitude 2010 event for both the Sauraha and Hetauda model.

The flow magnitude reduction scenarios that involved the implementation of check dams (*DAM50* and *POS50*) produced a greater percentage reduction in the higher magnitude events with the 50th and 90th percentile extents having a greater reduction from the baseline conditions. Due to the closer proximity of the Hetauda model to the modelled check dam locations in the upstream parts of the East Rapti catchment there was a greater reduction in inundated area than in the Sauraha model further downstream. The representation of check dams within CRUM3 could impact the difference in extent reduction across the model ensemble as they have been represented within CRUM3 through a flow restriction to a set value (99.9th percentile flow) for selectable channel reaches in the channel network. There will be a greater reduction from the baseline conditions with the higher magnitude events and as such a greater reduction in inundated area.

In addition to the potential range spatial coverage of inundation across the model ensemble, it is important to consider where the change in inundation water depth from a given flood management scenario is occurring. Across all five flow magnitude decreasing scenarios modelled, for both Sauraha and Hetauda, there was a reduction in inundated depths with the area of inundation > 0.0 m, > 0.5 m and > 1.0 m diminished. The catchment-scale flow magnitude analysis CRUM3 results indicate that all the catchment management scenarios had a positive impact at the flood impact points along the main East Rapti channel, Sauraha and Hetauda included. However, it is apparent from the spatial analysis of the LISFLOOD-FP results that, due to where the inundation depth changes are occurring, some catchment management scenarios might not be beneficial to a specific location.

An example of the potential ineffectiveness of a given scenario at reducing inundation depths within the flood impacted area is evident using the differences between the *BLA_F* and *POS50* scenarios at Hetauda (Figure 5.25) and Sauraha (Figure 5.26). Within the Hetauda model both scenarios reduce flood depths across the entire channel network other than a section of the Karra River to the centre of the model. However, due to locations identified using the spatial targeting approach for the placement of flood management measures (afforestation and check dams) being in the upstream parts of the catchment and not in the sub-catchments of the tributaries that join the East Rapti further downstream, the combined flood management scenario does not have as wide an impact for Sauraha. The impact on inundation depths within Sauraha village when compared to the *BLA_F* scenario is clear in Figure 5.26, with reduced water depths only seen along the main East Rapti channel.

The implementation of catchment-scale flow magnitude reduction scenarios in the LISFLOOD-FP modelling produce the expected decrease in inundation extent and depths. Conversely, the flow magnitude increasing scenarios predict an increase in inundation extent and depth. The changes occur both across the entire model extent and, more specifically, within the *Built-Up Area* cells; the representation of the latter at sites of infrastructure and settlement is critical in considering whether a scenario can be properly determined as effective. The spatial nature of this change at a given flood impact point is dependent on the scenario used; evident with the spatial targeting scenario (*POS50*) only reducing inundation along the main East Rapti channel in Sauraha. Discussed further in Section 5.4.4, the spatial nature of the inundation change is also determined by where in the model ensemble the comparison is made (i.e. the 10th percentile compared to the 50th percentile). Within the uncertainty approach used there are a wide range in inundation extents produced through the coupled CRUM3 and LISFLOOD-FP model ensemble.

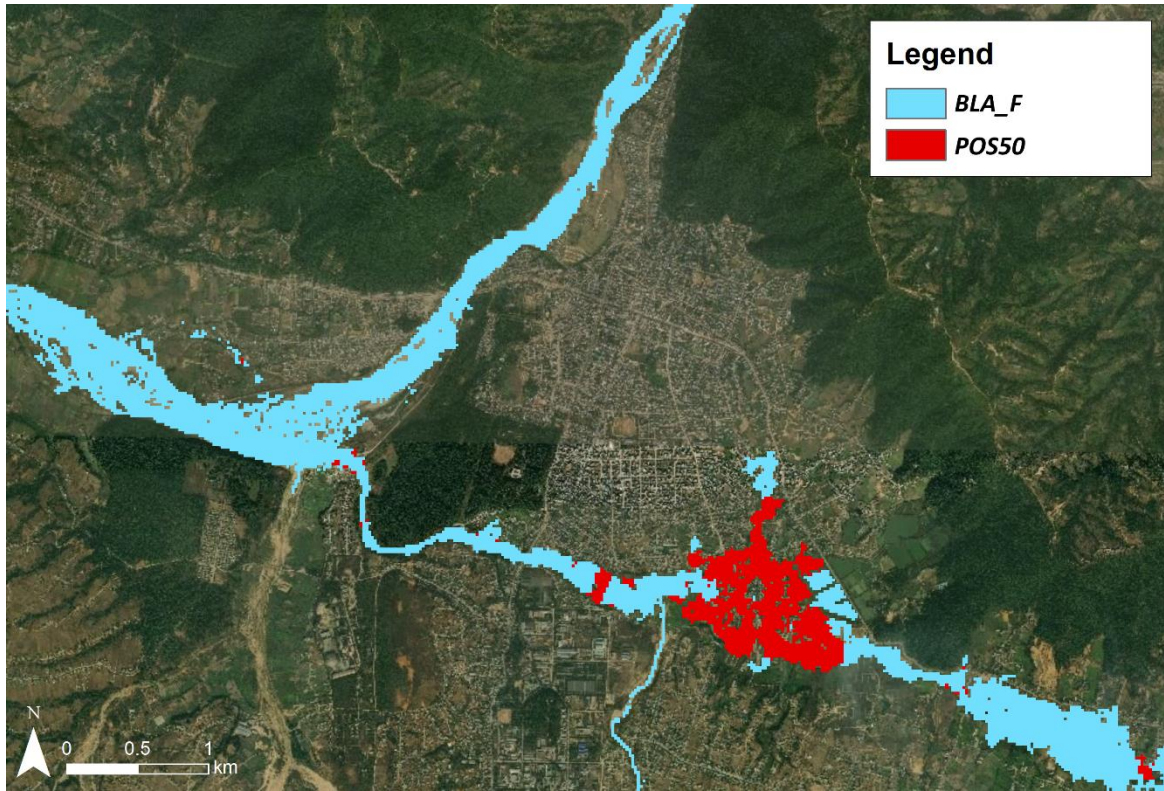


Figure 5.25: A comparison of areas in the Hetauda model in which the inundation depth has been reduced (> 0.05 m) between the BLA_F and POS50 scenarios.

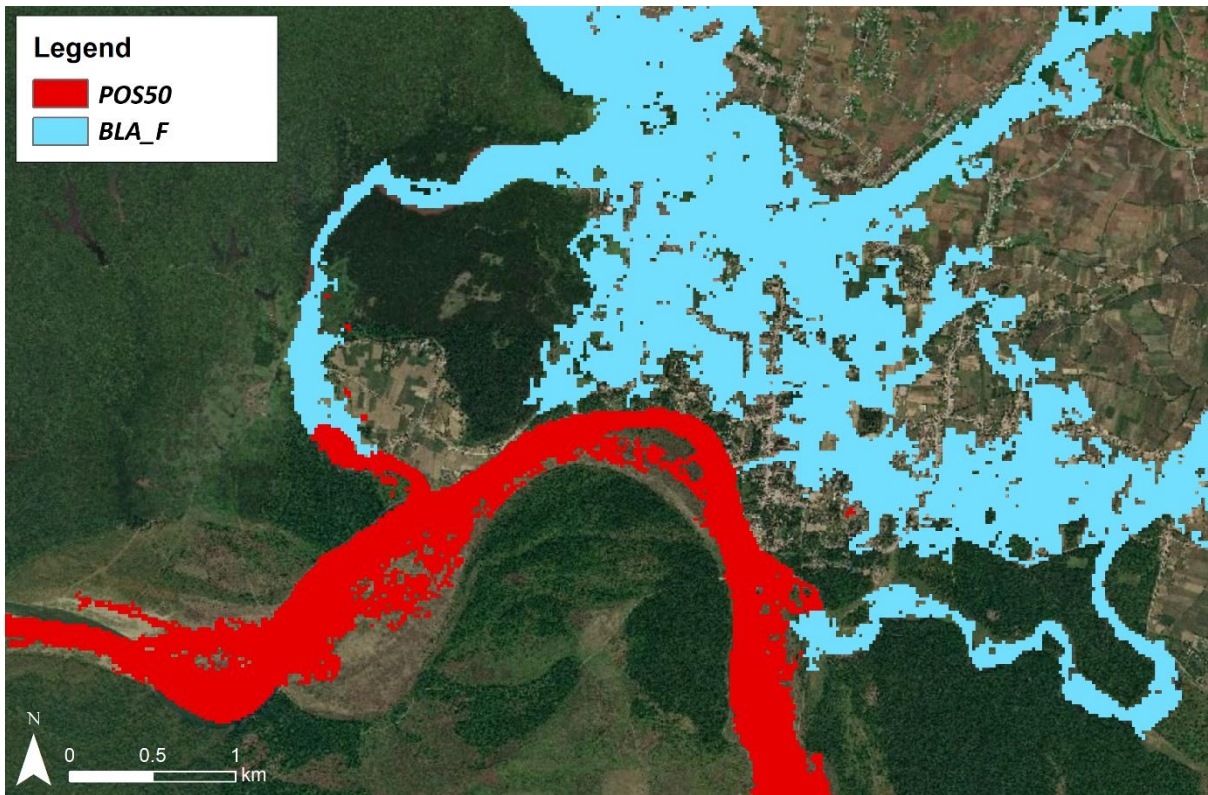


Figure 5.26: A comparison of areas in the Sauraha model in which the inundation depth has been reduced (> 0.05 m) between the BLA_F and POS50 scenarios.

5.4.2 The need for a coupled modelling approach and the use of localised inundation extents in flood impacted areas when developing a catchment management scenario

Due to the additional model set up and computation time required for the inundation modelling in the third stage of the end-to-end process, it is necessary to determine if the value of a catchment management scenario can be assessed using only catchment-scale hydrological modelling. The additional information provided by the inundation mapping allows for the better understanding of the consequences of a high-flow event with advancements in knowledge on possible affected areas for insurance and planning purposes (Felder et al., 2017).

A relationship between inundation extent change and the high-flow change (Q99.9 in the Chapter 4 CRUM3 modelling) could allow for scenarios to be quickly assessed through flow magnitude change with only the hydrograph outputs at the flood impact points from the catchment-scale modelling required. However, a key limitation of solely using a catchment model is the impact on flow routing and flood wave propagation. The CRUM3 model uses a simplified approach – the Muskingham-Cunge method (Cunge, 1969; Ponce and Lugo, 2001) – that does not make assumptions about the channel section and does not consider the impact of reach scale channel morphology throughout the catchment. The use of a coupled approach allows for the representation of both complex channel morphology and the complex hydrodynamic interactions between the channel and floodplain and can thus impact on the hydrograph shape as the flow is routed through the model (Felder et al., 2017; Hankin et al., 2019). Metcalfe et al. (2017) notes that, with concern over the impact that catchment-scale upstream interventions could have on flow synchronisation and the corresponding detrimental impacts due to a change in flows, this additional inundation modelling answers the need to understand the detailed local impacts of these interventions on water depth and extent.

The relationship between the median percentage change values across the ten scenarios in the catchment modelling and the inundation modelling, is shown in Table 5.16. The corresponding data is plotted in Figure 5.27. Despite the differences in topography between the Sauraha and Hetauda models there is a strong correlation between flow magnitude change and inundation extent change for the 2010, higher return period, event (r value - Hetauda: 2010 – 0.86; Sauraha: 2010 – 0.92). This strong relationship is also apparent with the lower return period 2009 event (r value - Hetauda: 2009 – 0.86; Sauraha: 2010 – 0.86). The strong relationship between the results of the flow magnitude change scenarios and corresponding inundation extent change suggests that the catchment model could perhaps be used for a simple catchment management scenario impact assessment. This was most notably for a higher return period 2010 event.

Table 5.16: The relationship (*r* value) between the median percentage change values from the ten scenarios across the 32 run model ensemble, for both the catchment modelling (Chapter 4) and the inundation modelling (Section 5.3)

	2009 event		2010 event	
	Sauraha	Hetauda	Sauraha	Hetauda
<i>r</i> value	0.86	0.86	0.92	0.86
<i>p</i> value	0.0016	0.0014	0.0002	0.0016

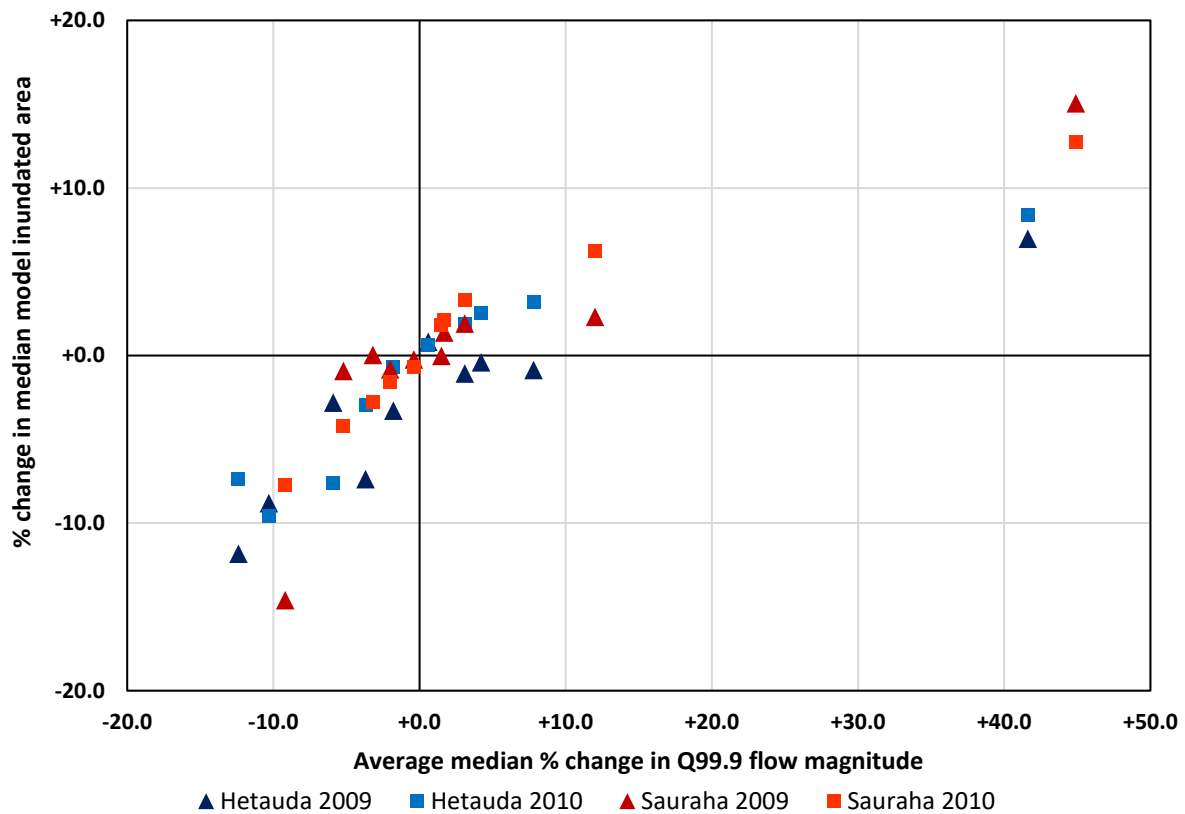


Figure 5.27: The relationship between the percentage change in median LISFLOOD-FP model inundated area and the average median percentage change in $Q_{99.9}$ flow magnitude from the CRUM3 catchment-scale modelling for the ten scenarios.

An assessment using the flow magnitude change and inundation extent change relationship through a meta-modelling (or surrogate modelling) approach could provide a less computationally expensive alternative when assessing catchment-scale scenarios (Ravazzi et al., 2012; Yadzi et al., 2014). Meta-modelling in flood inundation has previously been used to estimate flood inundation from an input hydrograph but struggle to represent the complexity of the processes involved in triggering flood events (e.g. Liu and Pender, 2014; Zischg et al., 2018).

Notably however, the ability to model timings associated with different inflows and the detailed representation of the channel and floodplain hydrodynamics that a detailed inundation model provides can have a significant impact for scenario assessment. This is evident in the different inundation extent and depth patterns presented throughout Section 5.3.2. Within the uncertainty

framework, the impact of the channel and floodplain morphology is an essential factor in determining the positive or detrimental effect of a scenario (McMillan and Brassington, 2008; Di Baldassarre et al., 2010). The variation in inundation extent across the model ensemble results in a range of potential inundation patterns at a specific location. The reliance on a simpler approach to assess a scenario, such as median flow magnitude change from the hydrological modelling, would fail to consider possible changes in inundation extent due to localised morphology; this is explored below using Figure 5.28 and Figure 5.29. Additionally, there are scenarios that produce inundation extents that deviate from the relationship with the CRUM3 scenario flow magnitude change results. At the Hetauda flood impact point, the lower flow magnitude increasing scenarios such as the *TER_S* scenario (average $\overline{Q_{99.9}}$ flow change - +3.1%), produced a slightly reduced median inundation extent (inundation depth > 0.0 m: -0.4 to -1.1%) from the baseline with the 2009 event hydrograph. This could be attributed to the flow distribution across the model ensemble inflows with the land use change influencing the flow regime, and corresponding inundation extent, in the Karra River tributary.

The role of the local morphology in ascertaining the impact of a catchment-scale scenario is critical in a catchment with a diverse topography such as the East Rapti catchment. Large areas of downstream parts of the catchment – the area around Sauraha being an example – have large continuous areas of low slope gradients. Therefore, a small increase or decrease in water levels due to changing flow magnitude can significantly impact the inundation extent. The impacts of floodplain morphology on inundation extent is illustrated in Figure 5.28 and Figure 5.29. The increased flow between the 10th percentile and the 90th percentile extent has a comparatively large increase in inundation extent across the lower gradient Sauraha model than in Hetauda model. The discontinuous nature of the lower gradient parts of the Hetauda model minimises the area in which out-of-channel flow can inundate.

The interaction of land use change within each of the tributaries sub-catchments and subsequent change in inundation extent and depth patterns is not apparent in the CRUM3 flow magnitude study. In part this can be attributed to using only one analysis point at the downstream end of the impacted location in the CRUM3 scenario assessment. The consequence of an absence of spatial assessment for the catchment scenarios is exemplified with Figure 5.25 and Figure 5.26. For the best understanding of the impacts of catchment-scale management approaches, both in terms of future detrimental land use change to the hydrological regime and proposed flood management interventions in flood water generating areas, the coupled modelling approach provides the best evaluation.

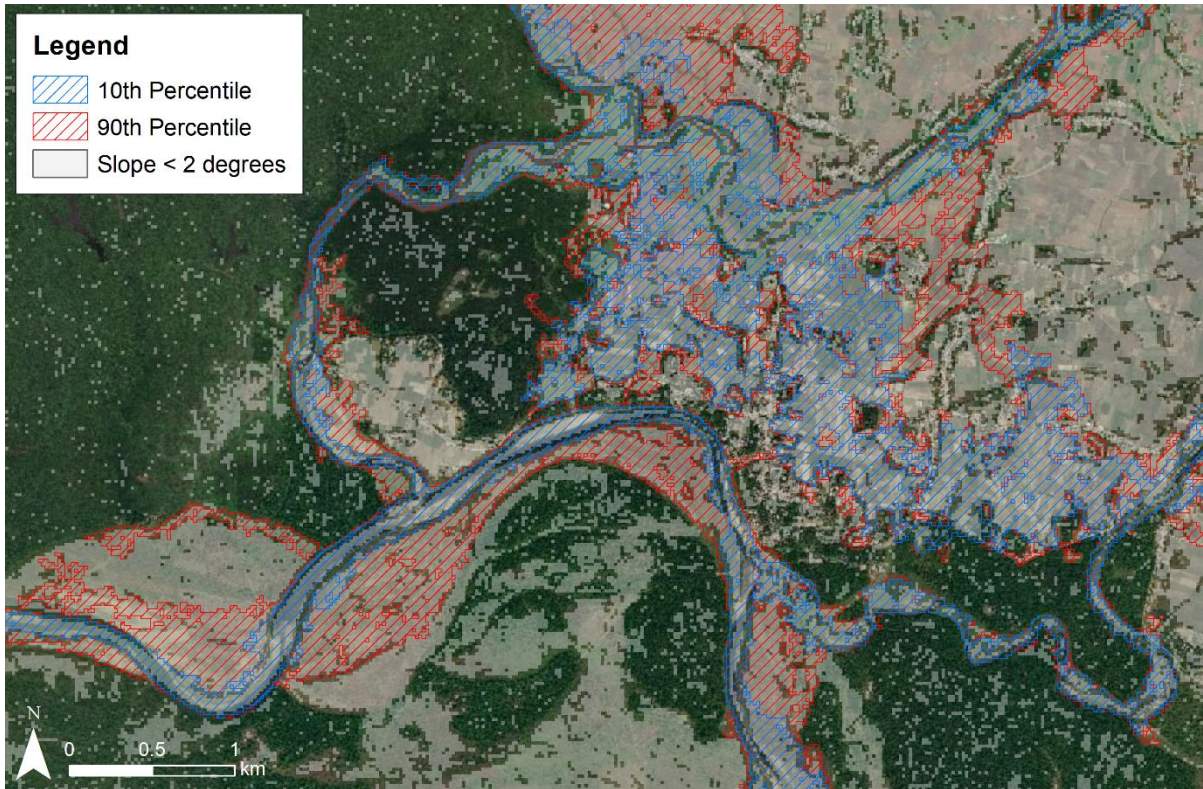


Figure 5.28: The potential impact of the channel and floodplain morphology on the inundation extent. This example uses the 10th and 90th percentile extents at Sauraha from the BLA_F scenario and highlights areas that have a slope < 2 degrees.

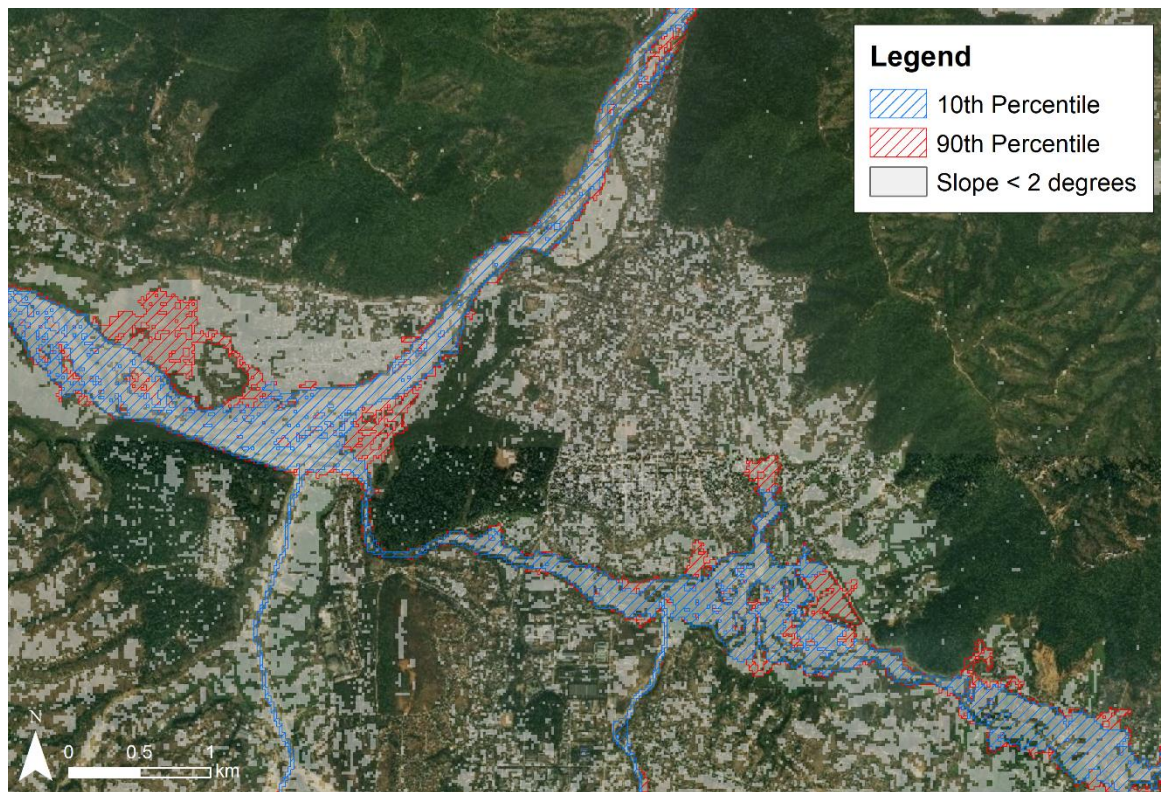


Figure 5.29: The potential impact of the channel and floodplain morphology on the inundation extent. This example uses the 10th and 90th percentile extents at Hetauda from the BLA_F scenario and highlights areas that have a slope < 2 degrees.

5.4.3 The representation of the channel and floodplain at localised flood-impacted areas within the East Rapti catchment

The requirements to set up the uncalibrated LISFLOOD-FP model were met with a combination of a commercially available elevation dataset, results from the first step of the coupled model approach and representative model parameters derived from a mixture of field-based observations from within the East Rapti catchment and appropriate model parameter estimation techniques as used in existing research. This process allowed for a localised representation of the complex channel morphology and the hydrodynamic interactions between the channel and floodplain within the confines of an uncalibrated model approach. The uncertainty within each set of parameters used within the LISFLOOD-FP set up can be seen in the model sensitivity analysis undertaken for both Sauraha and Hetauda. In general, many of the inputs parameters were not overly sensitive, with the impacts of the downstream slope occurring only at the downstream end of the model and the friction parameters influencing inundation extent by < 10% even in the widely-inundated Sauraha model.

The results of the sensitivity analysis, however, highlighted the importance of the sub-grid channel r parameter at representing the channel morphology and corresponding channel capacity. As evident in Appendix 7.30 and Appendix 7.35, a deviation of closer to 0 or 0.05 from the r parameter value of 0.03 used across both models had significant influence on inundation extent. Within the Sauraha model the majority of the inundation extent change, from an r parameter value between 0 and 0.05, occurred along the main East Rapti channel. Within the settlement of Sauraha itself, the median inundation extent witnessed only a slight change with large areas of inundation prevalent. Here it must be noted that, whilst the r value of 0.03 was based on channel morphology measured in the field, cross sections taken elsewhere within the model extents could produce an alternative value. Evidenced by the greatly sensitive nature in inundation extents across the range of r values used in the sensitivity analysis, the use of a global sub-grid parameter r value was noted as a major inaccuracy in a previous LISFLOOD-FP study by Neal et al. (2012). One solution would be the use of localised values throughout the channel network. There are also potential impacts on the inundation extent from continually changing channel capacity due to sediment transport. The channel morphology within many Himalayan catchments is altered during high-flow events with many catchments having a high sedimentation rates and continual scour-and-fill action along the channel bed (Kale and Hire, 2003; Shrestha et al., 2008; Wulf et al., 2010). The role of shifting channel morphology is not implemented in this study but a landscape evolution model such as CAESAR LISFLOOD (Coulthard et al., 2013) or SIBERIA (Hancock et al., 2000; Willgoose, 2005) could help incorporate high-flow sediment dynamics.

The channel and floodplain morphology accuracy in the elevation data is one of the key aspects driving the extent and depths in the inundation model. Outside of altering grid resolution and removing two bridges, no other alterations were made to the elevation data here and, as such, the flood extent produced is in part a product of the accuracy of the DEM. This is evident in the Hetauda model with the inaccurate representation of flood defences within the elevation data having an impact on inundation extent. Through analysis of areas of higher slope gradients of both the original 5 m DEM and the 20 m used in LISFLOOD-FP to assess the extent of the embankment in the elevation data, it is apparent that it does not extend to the same length as the embankment visible in satellite imagery. This mis-represented embankment is illustrated in the original ALOS AW3D 5 m resolution data (Figure 5.30) and occurs in the aggregated 20 m resolution data. Consequently, shown in Figure 5.30, there is inundation occurring at higher magnitude flow events to the north of the main East Rapti channel where the embankment should be in place. A potential solution to this inadequate representation of the flood defences, and to obtain a more accurate channel capacity, is the use of a higher resolution (< 2 m grid resolution) elevation data. With the number of runs required to represent the uncertainty in the model cascade however, there will be constraints due to computational resources. An alternative approach could be to select the maximum value when resampling of the higher resolution original elevation data; the '*maximum*' option in the 'Cell Statistics' tool in ArcGIS 10.3 for example. This approach would better represent any flood defences but would reduce the representation of channel capacity.

The inundation extents, and thus the channel and floodplain morphology and interaction, from LISFLOOD-FP modelling approach used around Sauraha can be compared against other modelling studies undertaken in the East Rapti catchment. The flood extents produced for different return periods from previous work are shown in Figure 5.31 (Singh, 2013) and Figure 5.32 (Asian Development Bank, 2016). It must be noted that the previous modelling studies (Singh, 2013; Asian Development Bank, 2016) used a 1D steady-state approach to get the inundation extent. This approach, undertaken with HEC-RAS in both studies, which uses a static flow and channel cross sections to derive an inundation extent and does not consider the entire topography around the channel and the impact of hydrograph variation and tributary interaction.

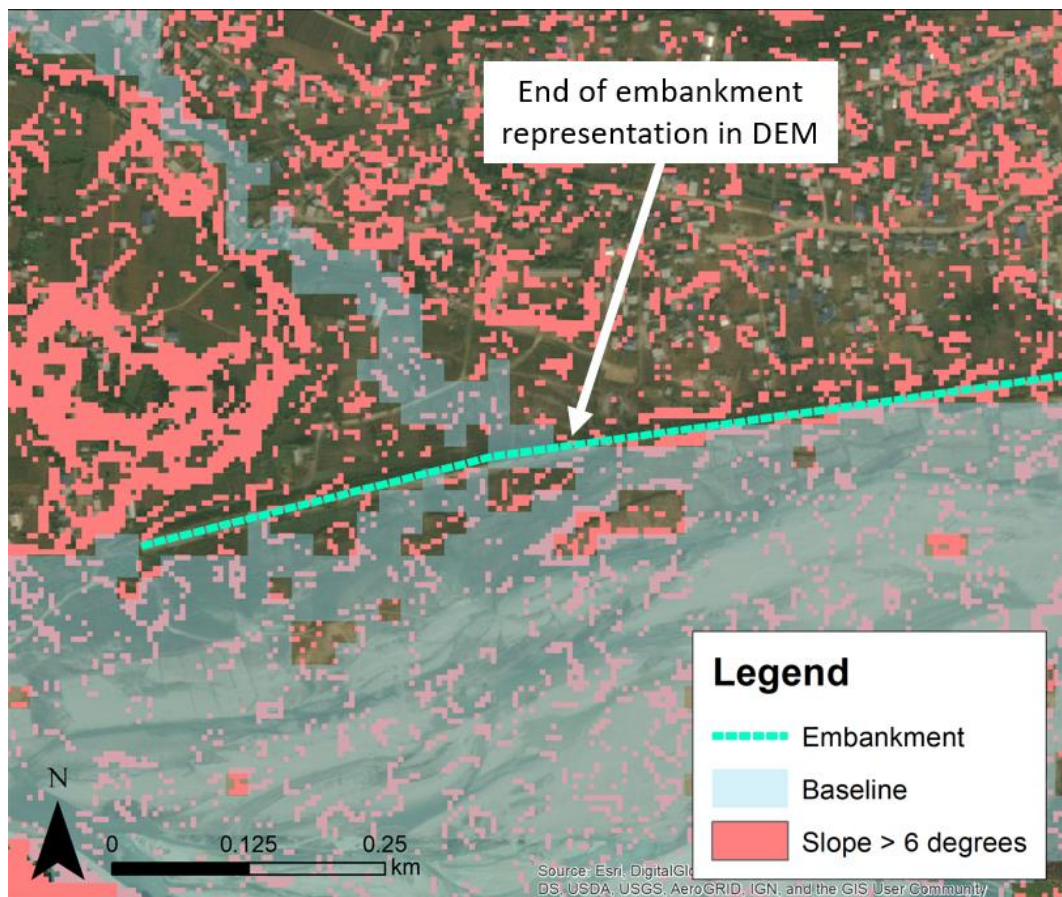


Figure 5.30: Slope analysis of the 5 m ALOS AW3D elevation data highlighting areas of higher slope gradient around the flood defences in Hetauda. This indicates the representation of embankment along the East Rapti channel. The median baseline flood extent from the 2010 flow hydrograph is overlaid to show where it is breached.

The inundation extent from the higher return period events by Singh (2013) considers the tributaries flowing towards Sauraha from the northern parts of the catchment. It shows complete inundation of Sauraha village and illustrates a more extreme version of the lower return period 2009 and 2010 event extents produced in the LISFLOOD-FP modelling approach. The inundation extent produced by the Asian Development Bank study (2016) for Sauraha from the modelling of the main East Rapti channel shows limited inundation from overtopping of the channel from a 5-year return period (20% AEP) event. Without full consideration of the tributaries, such as the Budhi Khola, from the north of Sauraha that overtop in both the LISFLOOD-FP modelling and in the Singh (2013) HEC-RAS modelling and flow into the village it is hard to directly compare the inundation extents. However, the depth change pattern analysis (Figure 5.36) from catchment scenarios that have no change to the northern tributaries indicates that in a 5-year return period (20% AEP) event such as the 2010 event the main East Rapti channel does not have a great impact on the inundation extent in Sauraha village.

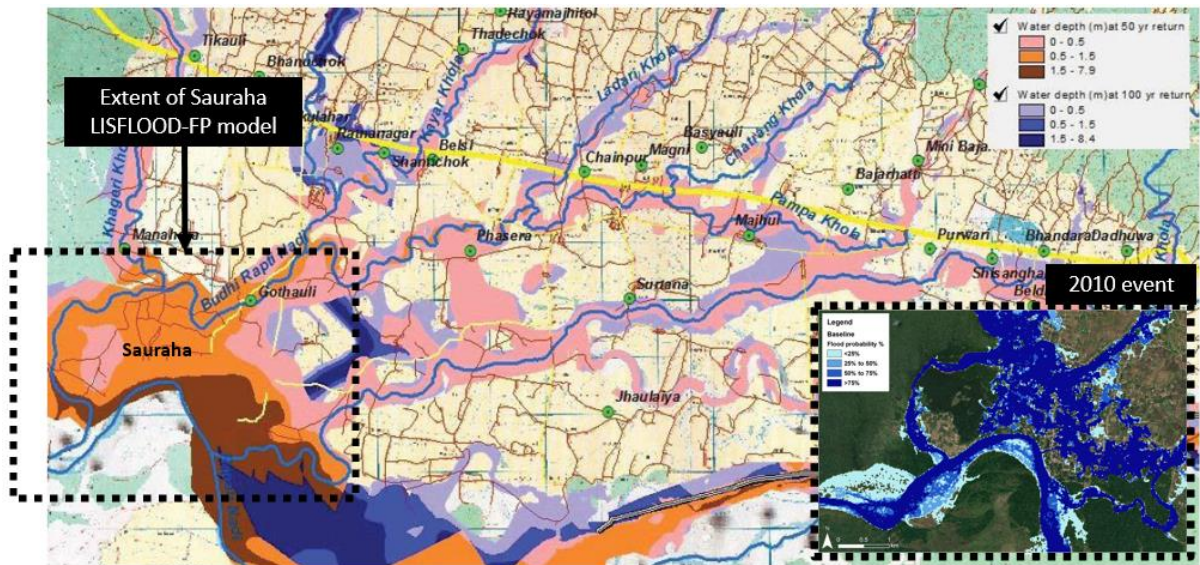


Figure 5.31: The Sauraha LISFLOOD-FP model extent overlaid on the HEC-RAS produced flood extent for a return period of 50 years (2% AEP) (red/orange) and 100 years (1% AEP) (blue) adapted from Singh (2013 [pp. 72]). The LISFLOOD-FP model results for the 2010 event (5-year return period [20% AEP]) are shown in the inset for comparison.

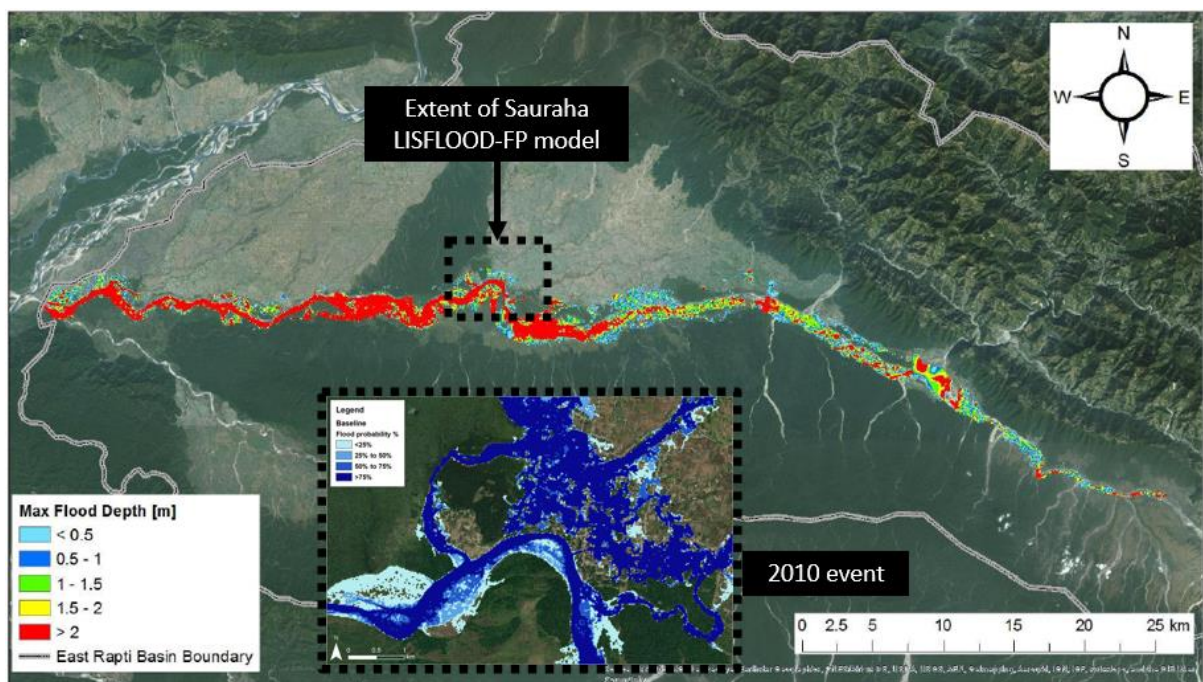


Figure 5.32: The Sauraha LISFLOOD-FP model extent overlaid on the HEC-RAS produced flood extent and depths for a 5-year return period (20% AEP) event for the main East Rapti channel adapted from the Asian Development Bank (2016 [pp. 25]). The LISFLOOD-FP model results for the 2010 event (5-year return period [20% AEP]) are shown in the inset for comparison.

The similarity in inundation patterns from previous studies suggests that the approach used to derive the LISFLOOD-FP model creates plausible model results and provides a fair representation of the channel and floodplain morphology and dynamics. However, the use of the detailed 2D inundation modelling allows for a better depiction of the local topography with the floodplain flow patterns, and corresponding depths in the impacted areas considered in better detail compared to the 1D approach

used in previous studies. Additionally, the use of high-flow event hydrographs, as opposed to a static flow value, accurately represented the relationship in timings between the tributary inflows from each catchment-scale scenario.

5.4.4 Sources and impacts of uncertainty in the LISFLOOD-FP results

There are numerous sources of uncertainty represented in the results of models that have been cascaded through the coupled model approach, with the initial source of uncertainty held within the DHM rainfall and flow data used to drive the coupled model approach (McMillan et al., 2011; Rodriguez-Rincon et al., 2015). Within the coupled modelling approach. Most of the uncertainty is within CRUM3 and this is transmitted to the inundation modelling with range of flows across the model hydrograph ensemble. The potential uncertainty within the LISFLOOD-FP parameters is conveyed within the results of the sensitivity analysis but not considered within the final scenario results. To factor parameter uncertainty into the results would require a significant amount of extra computational time. Pappenberger et al. (2005) use this increased uncertainty approach in the second part of a model cascade in moving from 312 model runs to 3120 model runs. There remain however the standard spatial and temporal uncertainties in the assumptions made in many inundation model setups with aspects such as limited spatial variation in roughness and sub-grid parameters (Beven et al., 2005; Beven et al., 2014).

Within the model cascade, when applying an uncertainty framework such as the GLUE method used in the CRUM3 modelling, the results relating to each parameter set in the initial model must be propagated through the model chain individually (McMillan and Brasington, 2008). As a result, the uncertainty is represented in the LISFLOOD-FP modelling through the continued use of the top 32 model hydrographs generated on from the 32 run CRUM3 model ensemble (McIntyre et al., 2002; Freer et al., 2004). With the model evaluation for CRUM3, a combination of formal statistical approaches and hydrological signatures, there is a diverse range of selected model parameter sets that is reflected in the model hydrographs attained for the LISFLOOD-FP models (see Figure 5.4). This combined model evaluation approach was largely used due to data uncertainty with both the DHM rainfall and flow data used within the model set up and calibration process having apparent issues (see Section 2.6). The uncertainty stemming from the representation of hydrological processes within the CRUM3 model is also captured within the hydrograph model ensemble. Hydrological model structure uncertainties are usually identified through model behaviour to runoff and include time to peak, runoff volume, and peak discharge (Butts et al., 2004; Pechlivanidis et al., 2011). Rodriguez-Rincon et al. (2015) note that improvements in reducing uncertainty are most important in the rainfall to runoff stage of the model cascade (CRUM3 in this research) with the benefits propagating through to the runoff to inundation stage of the process (LISFLOOD-FP in this research).

The presented LISFLOOD-FP inundation modelling results presented throughout Section 5.3.3 offer a comparison of the changes in the 50th percentile inundation extent between the baseline and each of the scenarios. Comparing the 50th percentile flood extents produced from the ensemble hydrographs provides a visual indication of the increase or reduction in predicted flood extent from the model ensemble. However, it does not provide the full picture of the uncertainty associated with each scenario; the presentation of uncertainty in the model ensemble results has therefore implications as to how decision makers interpret and use the information (Beven and Lamb, 2017). Using the Sauraha model, an example of how the uncertainty in the inundation extent across the model ensemble affects the possible value of a catchment scenario is shown using the blanket afforestation scenario in Figure 5.33 for 2009 event and Figure 5.34 for the 2010 event. Illustrated in the figures, the pattern of the inundation extent is fairly constant across the 2010 model predictions and indicates that, covering for the uncertainty throughout the coupled modelling approach, the event would cause widespread flooding. However, the 10th percentile inundation extent in the 2009 model predictions is predominantly constrained within the channel network, with extensive flooding occurring in the 50th and 90th percentile inundation extents. The area difference in inundation extents, factoring in uncertainty in discharge due to the channel and floodplain morphology have significant implications to determining if a catchment-scale scenario is a viable option.

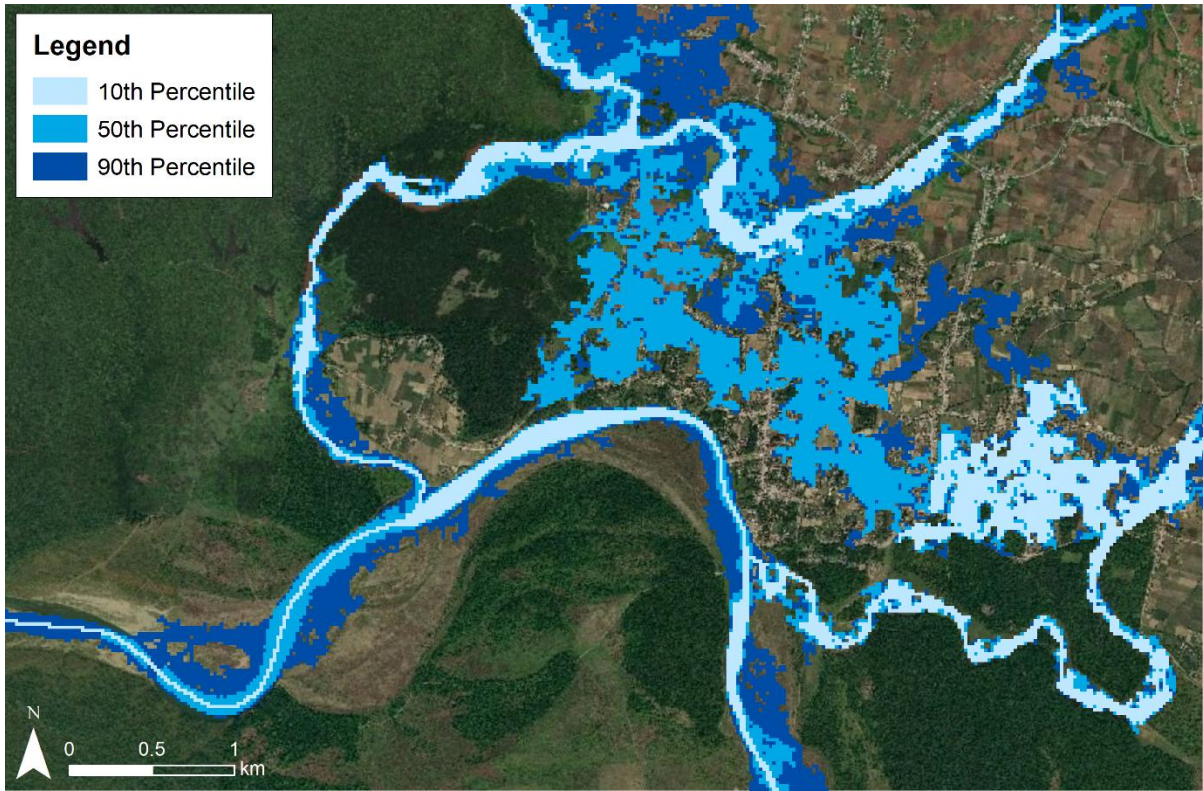


Figure 5.33: A comparison of the 10th, 50th and 90th percentile flood extents for the 2009 high-flow event across the model ensemble from the BLA_F scenario in the Sauraha model.

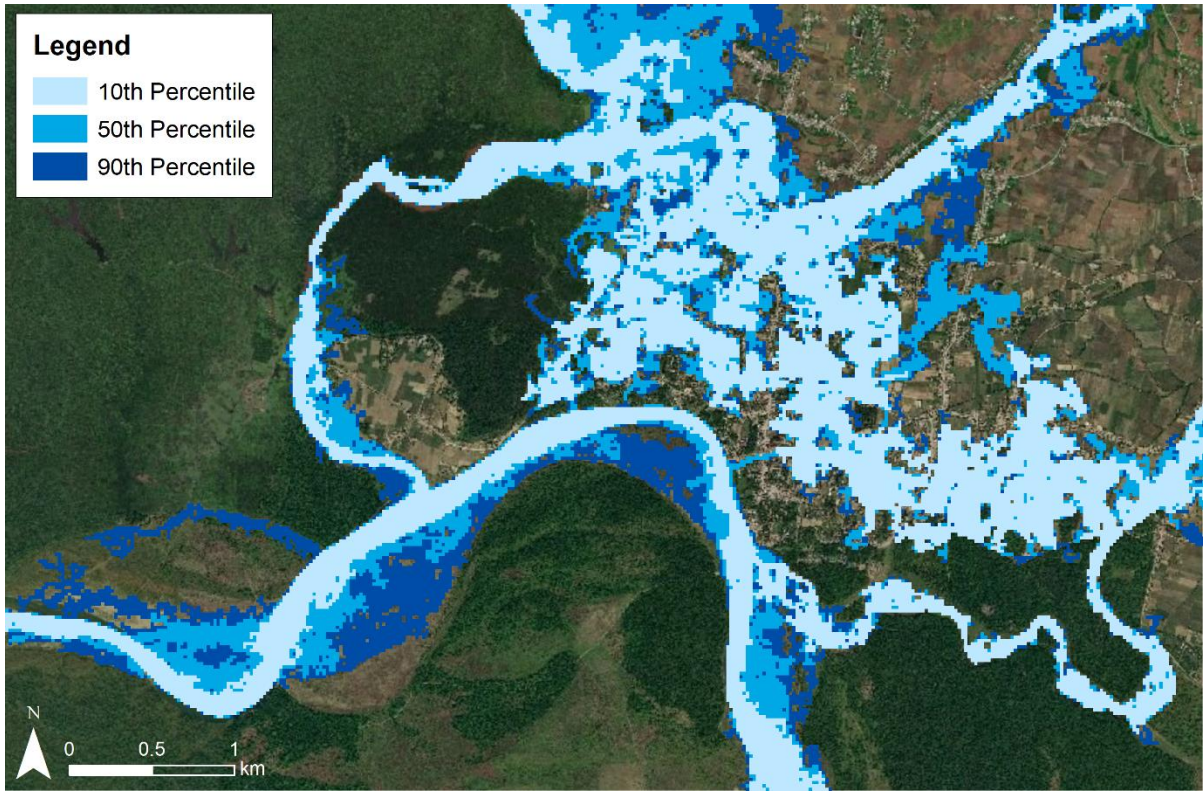


Figure 5.34: A comparison of the 10th, 50th and 90th percentile flood extents for the 2010 high-flow event across the model ensemble from the BLA_F scenario in the Sauraha model.

5.5 CONCLUSIONS

The LISFLOOD-FP inundation modelling presented in this chapter is the final stage of the end-to-end process for creating and assessing the implementation of future catchment-scale flow magnitude increasing and decreasing scenarios for managing flood hazards. **All the modelled catchment-scale flow magnitude reduction scenarios produced a reduced flood extent for both the 2009 and 2010 events.** Conversely, the results of the inundation modelling for the future land use change scenarios indicate that the increased flow magnitudes predominantly caused an increased inundation extent and in water depths across the model ensemble at both Sauraha and Hetauda.

An investigation into the inundation depth distributions across the areas within the model extent with a *Built-Up Area* land cover, representing settlements and infrastructure, determined that in the areas with the shallower inundation depths (< 0.5 m) the depth distribution produced from the catchment-scale scenarios was similar to the baseline scenario. **The *Built-Up Area* inundation pattern assessment indicates that there would be negligible beneficial change experienced by the affected population from implementing the catchment-scale scenarios.** This occurred at both the Hetauda and Sauraha flood impact points from the tested catchment-scale flood management scenarios (*AFF50_F*, *AFF50_PDA_F*, *DAM50* and *POS50*). **Equally, the more realistic flow magnitude increasing future land use change scenarios (*DEF_S*, *TER_S* and *NEG_S*) did not appreciably alter the *Built-Up Area* depth distribution. Consequently, these scenarios are unlikely to worsen the flood impact under future flood events with a similar magnitude to the 2009 and 2010 events.**

From the spatial analysis of the LISFLOOD-FP results assessing where the inundation depth changes are occurring, it is apparent that some catchment management scenarios might not be beneficial for a specific location despite the catchment-scale CRUM3 hydrological modelling predicting a reduced flow magnitude. Within the East Rapti case study this can be attributed to locations identified using the spatial targeting approach for the placement of flood management measures (afforestation and check dams) being in the upstream parts of the catchment and not in the sub-catchments of the tributaries that join the East Rapti further downstream. Within the Sauraha model, results predict reduced water depths only along the main East Rapti channel and not from overtopping tributaries from the north of the village.

Whereas the hydrological catchment model uses a simplified flow routing method, the use of an inundation model in a coupled modelling approach allows for the representation of complex channel morphology and complex hydrodynamic interactions between the channel and floodplain. As seen in the East Rapti catchment case study, this complexity can have a large impact on inundation extent across the model ensemble. There are large areas of around Sauraha that have large

continuous areas characterised by low slope gradients, and therefore a small increase or decrease in water levels due to changing flow magnitude can significantly impact the inundation extent. Meanwhile, the discontinuous nature of the lower gradient parts of the Hetauda model extent was seen to minimise the floodplain area which higher water levels can inundate. **Rather than purely relying on the flow magnitude change results of hydrological catchment modelling, the detailed information provided by the inundation modelling allows for a fuller understanding of the consequences of a high-flow event for key flood impacted areas.**

6 RESEARCH SUMMARY AND CONCLUSIONS

6.1 INTRODUCTION

This chapter returns to the overall aim and research objectives outlined in Chapter 1. The overall aim of this thesis was ***to evaluate the potential for spatially targeted catchment-scale flood management measures in the East Rapti catchment, Nepal***. This aim was addressed through six research objectives that were met across the three stages of the developed end-to-end modelling approach.

Within this chapter, Section 6.2 provides an overview of the original contributions to knowledge arising from the research. Section 6.3 provides a summary for both the complete end-to-end approach and each of the three stages that were developed to meet the overall research aim. Finally, Section 6.4 contains recommendations for future work that can help advance the findings of this research.

6.2 ORIGINAL CONTRIBUTIONS TO KNOWLEDGE

The research presented in this thesis has made the following original contributions to knowledge:

- The overall end-to-end approach developed and applied across Chapter 3, Chapter 4, and Chapter 5 evidenced and significantly improved the understanding of the impacts of implementing a catchment-scale flood management approach in a Nepali catchment context. The research findings indicate that the use of catchment-scale flood management approaches can be most effective as part of a wider flood risk management approach and not as a replacement for the existing hard-engineering approach used in many Nepali catchments. The knowledge gained, and the toolkit created, can help inform and enhance the flood management approaches used in catchments throughout Nepal.
- Chapter 3 presents the development and first usage of the SCIMAP-Flood Fitted approach; an extension of SCIMAP-Flood that uses inverse modelling to determine the land cover risk weightings within the SCIMAP-Flood framework. The SCIMAP-Flood Fitted approach can be used in other studies using the SCIMAP-Flood framework in which the land cover weightings are unknown.
- Chapter 3 illustrates the first application of SCIMAP-Flood in a data sparse context. The developed process for the East Rapti catchment is suitable for application in other catchments with poorer data availability.
- Chapter 4 outlines one of the first detailed catchment-scale flood management studies using a distributed hydrological model in a Nepali catchment. The use of spatially explicit catchment-scale scenarios, such as those applied within the CRUM3 modelling, is not

apparent in previous research. As such, the scenarios further the knowledge of the potential impacts of realistic future change with the case study catchment.

- Chapter 4 contains the first study using the CRUM3 model to have spatially distributed rainfall with a scaled rainfall grid providing individual daily rainfall totals for each cell in the catchment. The development to the CRUM3 model will allow for future users of the model to better distribute rainfall patterns.
- Chapter 4 and Chapter 5 combined present one of the first coupled hydrological/hydraulic modelling approaches undertaken in a Nepali catchment and the first looking at the potential impacts from implementing a catchment-scale flood management approach. The findings provide evidence of an approach that can be used to consider the effect of a mitigation scenario on the flow regime across multiple points of flood impact within other Nepali and Himalayan catchments.

6.3 RESEARCH CONCLUSIONS

This section provides a conclusion for the overall end-to-end approach (Section 6.3.1) and each of the stages (SCIMAP-Flood in Section 6.3.2, CRUM3 in Section 6.3.3 and LISFLOOD-FP in Section 6.3.4) in addition to evidencing which of the research objectives each stage addressed.

6.3.1 The end-to-end approach used to determine the impact of spatially targeted catchment-scale flood management measures

Figure 6.1 provides the conceptual overview for the end-to-end approach developed to address the overall research aim. The final output is an assessment of the inundation patterns produced at key flood impacted areas due to implementing spatially targeted catchment-scale flood management measures within the catchment. Using the East Rapti catchment as a case study, this end-to-end approach has been successfully developed and applied to evaluate the impact of catchment-scale flood management scenarios on key flood impacted areas.

With the flood management approach currently taken in Nepal contrasting to global trend of catchment-based approach to flood management, there is a recommended shift to a more integrated approach that would bring the flood management process in Nepal in line with the global movement (e.g. Singh, 2013; Nepal et al., 2014; Government of Nepal, 2017). The approach used in this thesis allows for the evaluation of the potential for spatially targeted catchment-scale flood management measures a Nepalese catchment context and the application of a catchment-based approach to flood management.

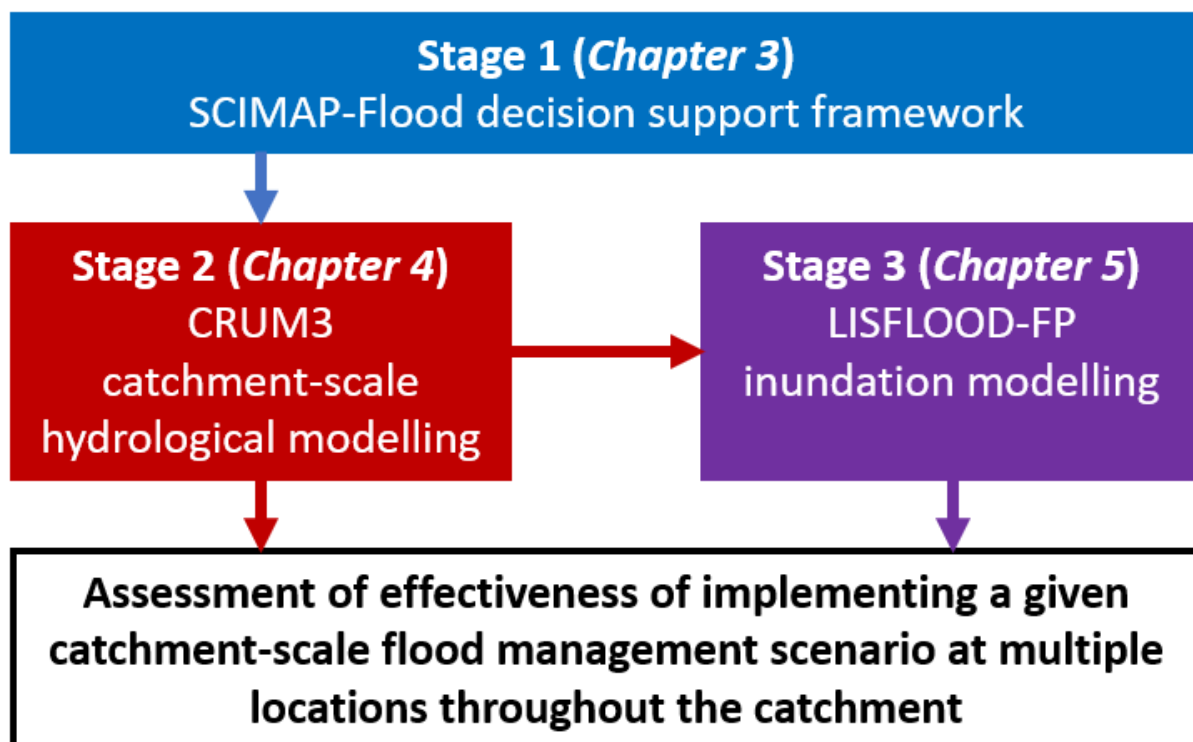


Figure 6.1: An overview of the three stages used in the end-to-end approach for the spatial targeting of flood management measures at the catchment-scale.

The second and third stages of the approach build upon the knowledge attained in the previous stage to reach a final output. SCIMAP-Flood determines the location of where the flood management interventions are most suitable for a given catchment, but this framework is not designed to quantify how effective a given flood management scenario would be. Therefore, further detailed hydrological modelling, such as that undertaken using CRUM3, is necessary to quantify to effectiveness of a given catchment-scale flood management scenario.

The coupled hydrological-hydraulic modelling used in the second and third stage of the approach showed a strong link between flow magnitude change from the CRUM3 hydrological modelling and inundation extent change from LISFLOOD-FP hydraulic modelling. This relationship suggests that solely the catchment model or, alternatively, a meta-modelling approach could perhaps be used for a simple catchment management scenario impact assessment without the extra computational resources and time required for the third stage. It was apparent, however, from the spatial analysis of the LISFLOOD-FP inundation patterns that some catchment management scenarios might not be beneficial to a specific location in the inundated area. An example of the spatial disparity from the East Rapti catchment case study was the spatially targeted check dam scenario which only reduced inundation along the main East Rapti channel in Sauraha. The scenario produced no inundation pattern change from water overtopping of the Budhi Khola tributary from the north of the Sauraha; this was due to the placement of no interventions in the sub-catchment from the spatial targeting approach.

Additionally, the role of the local morphology in ascertaining the impact of a catchment-scale scenario is critical in a catchment with a diverse topography such as the East Rapti catchment. There are large areas of downstream parts of the catchment, the area around Sauraha being an example, that have large continuous areas of low slope gradients. Therefore, a small increase or decrease in water levels due to changing flow magnitude can significantly impact the inundation extent in these areas. The discontinuous nature of the lower gradient parts of the Hetauda model minimise the floodplain area in which higher water levels can inundate. The extra information derived from the inundation modelling is therefore necessary to fully assess the impact of a given catchment-scale scenario in addition to providing the necessary spatial information for the end users of the approach.

Usefully, there is overlap across the data used to drive each of the stages of the approach (Table 6.1). Of the data used in the SCIMAP-Flood framework, the ALOS AW3D30 elevation data, the classified Landsat 8 imagery land cover data and the created combined gauged and satellite rainfall grids were also utilised in the CRUM3 hydrological modelling. Both the SCIMAP-Flood Fitted inverse modelling, used to derive land cover weightings, and the LISFLOOD-FP modelling benefitted from the same field collected data with regards to the Manning’s *n* values. The DHM river flow data was used in both the high flow event identification in the SCIMAP-Flood approach and for model calibration purposes in the CRUM3 modelling. The inundation modelling used a resampled version of higher resolution 5 m AW3D elevation data however could have been run using the 30 m resolution AW3D30 data. Conversely, the SCIMAP-Flood framework and CRUM3 model could have been run using a resampled version of the 5 m AW3D elevation data if were it available at the time of undertaking the research.

Table 6.1: An overview of the shared data (shaded red) across the different stages of the end-to-end approach

Data	Stage 1 SCIMAP-Flood	Stage 2 CRUM3	Stage 3 LISFLOOD-FP
DHM rainfall data			
DHM river flow data			
Classified Landsat 8 land cover data			
ALOS AW3D30 elevation data			
Field collected data (Manning’s <i>n</i>)			

Sources of uncertainty within the end-to-end approach

There are numerous sources of uncertainty represented in the final inundation model ensemble results that have been cascaded through the end-to-end approach. The uncertainty cascade is conceptualised in Figure 6.2. The initial source of uncertainty that underpins the overall approach is held within the DHM rainfall and river flow data. There is uncertainty created from the selection of the SCIMAP-Flood data inputs, most notably in the selection of flood impact points, that determine

the flood water generating areas for spatial targeting. The coupled modelling approach run in the second and final stage uses the concept of equifinality to represent the uncertainty, with the results of the top performing model parameter sets in the catchment-scale CRUM3 modelling used as an inflow hydrograph ensemble in the inundation modelling (Beven, 2009). This approach follows McMillan and Brasington (2008) with the results relating to each parameter set in the initial model propagated through the model chain individually; the rainfall-runoff modelling (CRUM3 in this research) is the key stage to make efforts to improve the uncertainty (Rodriguez-Rincon et al., 2015).

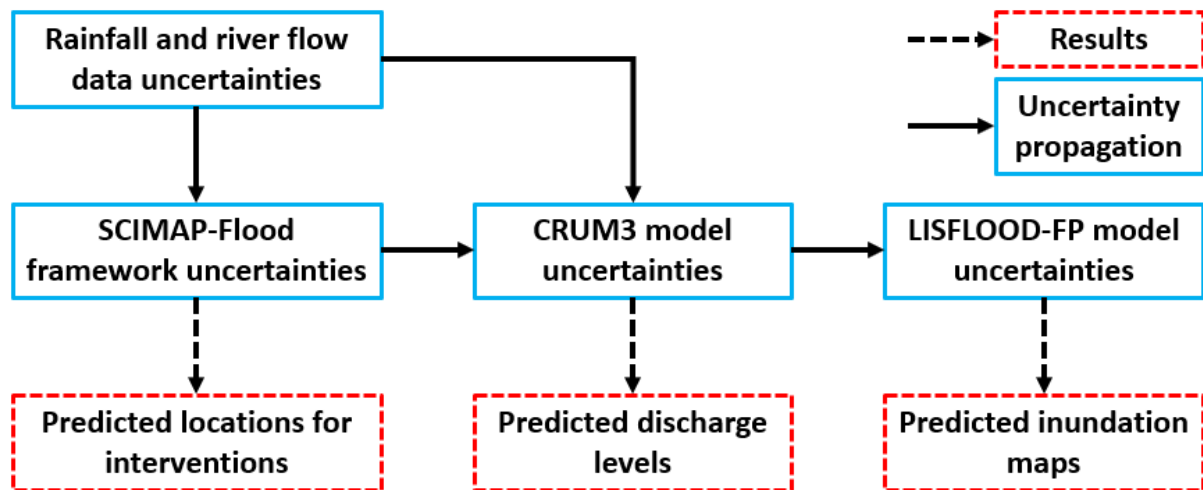


Figure 6.2: A conceptual overview of the uncertainty cascade through the end-to-end approach

6.3.2 Stage 1 – Identifying flood water generating areas using SCIMAP-Flood

The presented SCIMAP-Flood research met the first and second research objectives:

1. **To establish the spatial distribution of source areas that contribute to flooding at the catchment-scale.**
2. **To ascertain where to spatially target flood management measures within a catchment.**

Working at the catchment-scale, the SCIMAP-Flood framework (Reaney, *in prep.*) uses minimal input to determine the flood water source areas to specific flood impacted areas across the catchment. There is available data to run SCIMAP-Flood using global elevation, rainfall, and land cover datasets for catchments with sparsely available regional and local data. Additional data acquired, either from fieldwork or local sources, can be used to enhance the catchment-specific application of the SCIMAP-Flood framework. This was evidenced in this research by the use of globally available data (e.g. the ALOS AW3D30 elevation data) in addition to the catchment-specific implementation of the SCIMAP-Flood Fitted inverse modelling approach based on field data. SCIMAP-Flood Fitted (a variation on an approach used in Reaney et al. (2011) and Milledge et al. (2012)) was used to derive the land cover risk weightings and the creation of a scaled combination of satellite and gauged rainfall data used provide a more detailed spatial rainfall pattern (Arias-Hidalgo et al., 2013; Liu et al., 2017).

The SCIMAP-Flood output is a point scale assessment that helps identify critical source areas (Heathwaite et al., 2005) for flood waters in a catchment by providing the relative likelihood of an area to generate flood water during a rainfall event associated with high flows. By identifying areas that have a high likelihood of generating flood waters then it is possible to develop catchment-scale flood management scenarios through spatially targeted implementation of measures in these areas.

The potential influence of varying the SCIMAP-Flood input data needs to be considered when running the framework. The selection of the spatial resolution of the rainfall data had less of an impact on the identification of flood generating areas than selection of the temporal resolution of the rainfall data. The selection of more flood impact points, in addition to considering the benefits of flood management measures to more settlements, reduces the likelihood that the SCIMAP-Flood output will be impacted by the exclusion of one flood impact location.

The SCIMAP-Flood results for the East Rapti catchment case study demonstrated that the eastern part of the catchment near Hetuada had the greatest potential to generate flood waters to the six selected flood impact locations. There were additional areas along the main East Rapti channel and in the upland areas of the Lothar, Manahari and Rapti sub-catchments that were also identified as having a higher flood water generation potential. These areas within the catchment are those in which the spatially targeted flood management measures could have a high impact on the flooding regime.

With the East Rapti exhibiting catchment characteristics typical to those of catchments across the southern edge of Nepal, the rainfall pattern dominance in SCIMAP-Flood is likely to be prevalent in catchments with a similar physical makeup. The rainfall patterns associated with high flow events were the dominant factor in identifying flood water generating areas (as also found in Reaney and Pearson (2016)) and, as a result, both the high relief north-eastern part of catchment and the highly connected agricultural and urban area in the south eastern part of the catchment have a high relative potential to generate flood water (Figure 3.17).

6.3.3 Stage 2 – Catchment-scale scenario modelling using CRUM3

The presented CRUM3 research met the third and fourth research objectives:

- 3. To quantify the potential impact of spatially targeted flood management measures on the hydrological regime at the catchment-scale.**
- 4. To quantify the potential impact of land use change and degradation on the hydrological regime at the catchment-scale.**

The CRUM3 hydrological model (Lane et al., 2009) was used to quantify the impacts of land use change and flood management scenarios on the flow regime. The CRUM3 output allows for the comparison

of hydrographs at multiple locations to test catchment-scale flood management scenarios at all the flood impact points throughout the catchment.

The model results predict that the high flow magnitude in the East Rapti catchment can be reduced through a wider, catchment-scale approach. However, with a combined approach of spatially targeted afforestation and check dam implementation reducing the 99.9th percentile flow by $\leq 5.6\%$ at the flood impact points, the use of catchment-scale flood management approaches to combat flood risk can be most effective as part of a wider flood risk management approach. In terms of the effectiveness of different flood management approaches, the implementation of check dams (Figure 4.34) in key flood water generating sub-catchments provided a greater high flow reduction than the spatially targeted afforestation scenarios (Figure 4.30 and Figure 4.31). Notably, the cumulative impact of check dams in sub-catchments would need further assessment and designed to ensure no negative impacts with regards to flow synchronisation (Odoni and Lane, 2010, Yadzi et al., 2018).

The most important outcome from the catchment-scale modelling work was that there is a far greater potential for land use change to increase, rather than reduce through mitigation, flow magnitudes in the East Rapti catchment. With many Nepalese catchments facing potential future land use change through the abandonment of agricultural terraces, deforestation, and urbanisation, there is predicted to be an increase in high flow magnitude as a consequence (Ives and Messerli 1989; Nepal, 2012; Paudel et al., 2014; Chaudary et al., 2016; Rimal et al., 2019). Although unrealistic in their implementation, blanket coverage scenarios (Figure 4.19) provided an indication of the bounds of the flow magnitude alteration impact of each land cover within the catchment. Within the East Rapti catchment only blanket forest coverage had a positive impact on the reduction of high flows across the flood impact points. The results suggest that any land within the East Rapti catchment that is altered from existing forest will contribute to increasing the flow magnitude and any land changed to forest will help decrease the flow magnitude at the flood impact points.

More realistic flow magnitude increasing land cover scenarios, modelling deforestation (Figure 4.22), urban expansion (Figure 4.24), and terrace abandonment (Figure 4.26), had a limited impact on the high flow regime. For example, the fringe deforestation scenarios modelling a loss of 5.1% of the existing forest cover (equivalent to approximately 25 years of future tree-felling) resulted in a slight increase in the average 99.9th percentile high flow across the six flood impact locations of 1.9%. The limited impact of a more realistic implementation of catchment-scale afforestation for flood management purposes was present in other modelling studies (e.g. Lane et al., 2005; Bathurst et al., 2011; Salazar et al., 2012; Iacob et al., 2017). Preventative measures, such as the Community Forest

Groups initiative (Chaudary et al., 2016), are vital in ensuring that the impact on the flow regime from future flow magnitude increasing land cover change is limited.

No simulated scenarios, either flow magnitude increasing or decreasing, were observed to have a significant impact on the timing or shape of the flood peaks with no significant alterations to the modelled flood hydrograph between the existing base scenario and the catchment-scale scenarios.

6.3.4 Stage 3 – Inundation modelling at flood impact points using LISFLOOD-FP

The presented LISFLOOD-FP research met the fifth and sixth research objectives:

- 5. To determine the effect of spatially targeted flood management measures on altering the inundation patterns at key flood impact points.**
- 6. To determine the effect of land use change and degradation on altering the inundation patterns at key flood impact points across the catchment.**

A LISFLOOD-FP hydraulic model (Bates and De Roo, 2000) was set up for two of the six flood impact locations (Sauraha and Hetauda) to simulate changes to the inundation pattern from the catchment-scale scenarios and to assess the effectiveness, or ineffectiveness, that upstream catchment interventions have in aiding flood impacted areas for a 2-year and 5-year return period event. The LISFLOOD-FP model was compared against other modelling studies undertaken in the East Rapti catchment (Singh, 2013; Asian Development Bank, 2016).

The catchment-scale hydrological modelling using a simplified Muskingham-Cunge flow routing method (Ponce and Lugo, 2001) that does not use detailed channel cross section information. The use of an additional step and the coupled hydrological and hydraulic modelling (e.g. Nguyen et al., 2016; Zope et al., 2016; Felder et al., 2017) approach allows for the representation of complex channel morphology and complex hydrodynamic interactions between the channel and floodplain (Hankin et al., 2019). With a potential concern over the impact that catchment-scale upstream interventions have on flow synchronisation and the corresponding detrimental impacts due to a change in flows, the inundation modelling evidenced any detailed local impacts that these interventions produced on water depth and extent (Metcalfe et al., 2017).

All the modelled catchment-scale flow magnitude reduction scenarios produced a reduced flood extent (Figure 5.17, Figure 5.19, Figure 5.21, and Figure 5.23). Within the shallower depths (< 0.5 m), the distribution produced from the catchment-scale scenarios was similar to the baseline; this indicates that around the perimeter of the inundated area, representing inundation away from the deeper inundation associated with the main channel network, there is a limited beneficial change to the affected population. Further investigation into inundation depth change over urban areas

concludes that there is a negligible change in the depths occurring from the catchment-scale flood management scenarios when compared to the baseline conditions.

The results of the inundation modelling indicate that the increased flow magnitudes from land use change scenarios predominantly caused an increased inundation extent and depth across both the Sauraha and Hetauda models (Figure 5.9, Figure 5.11, Figure 5.13, and Figure 5.15). This increase in extent is largest in the blanket agriculture land cover scenarios. However, the change in inundation depths over the urban land cover areas reveals that the distribution of depths does not differ noticeably from the baseline scenario under the realistic flow magnitude increasing scenarios. This pattern of negligible change is prevalent at both Sauraha and Hetauda for both return period flow events and, as such, future land use change is unlikely to significantly worsen the flood impact under future events with a similar magnitude.

6.4 RECOMMENDATIONS FOR FUTURE WORK

There are several directions in which future work could further develop the research presented in this thesis:

- A shift away from modelling historic high flow events towards the use of specific design storm events could increase the usefulness of the end-to-end approach from the perspective of the end users. Additionally, the use of design storm events could help futureproof the tested flood management measures by providing an easier pathway to represent future climate change; this could be represented as different spatial rainfall patterns in SCIMAP-Flood or altered climatic data in CRUM3.
- With regards to land cover risk weightings derived using the SCIMAP-Flood Fitted approach, further research into developing a regional set of risk weightings for the main land covers in the Nepal, and across the wider Himalayan region, would significantly speed up the application of the SCIMAP-Flood framework. This work could be achieved with the SCIMAP-Flood Fitted approach being applied for a range of catchments and high flow events to better constrain the values. The SCIMAP-Flood Fitted approach used for the case study was labour-intensive, requiring fieldwork to drive the inverse modelling, and a given set of land cover weightings for each land cover could enable other users to easily run the framework entirely from their desk.
- Within the SCIMAP-Flood research there is no consideration given to the differences between the chosen flood impact points. There is currently an equal weighting assigned to each point with no point considered to have a higher importance than another. This fails to consider variation in factors such as the potential economic damage, number of persons affected, or

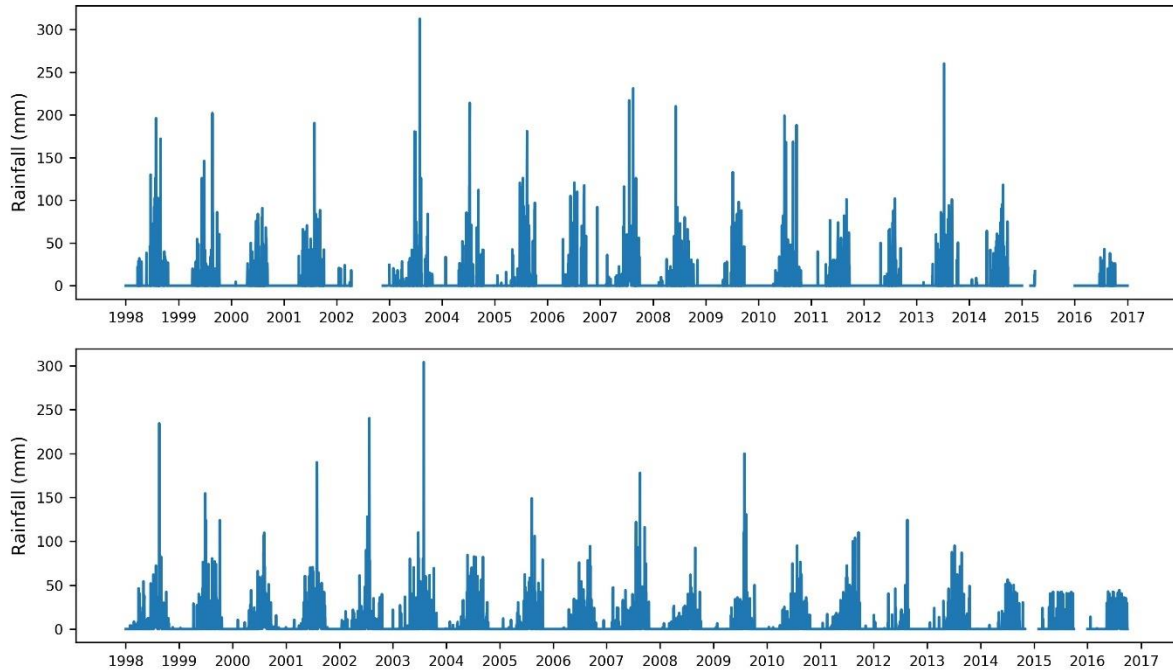
houses destroyed by a flood event. Further research could investigate an approach for determining different weightings for individual flood impact points within a catchment to better locate areas in which flood management measures would have the greatest impact.

- To better represent the soil and land cover parameters in CRUM3, removing the need to rely on available literature to derive the model parameters, a detailed study across Nepalese catchments collecting field measurements specific for enabling the end-to-end approach could enhance the results. This could be developed using an experimental sub-catchment-scale study, such as Chappell et al. (2006) or Owen et al. (2012), with a detailed monitoring network to help determine model parameters. Additionally, with the case study catchment CRUM3 model using a 150 m resolution there is an exclusion of the representation of smaller features. The experimental sub-catchment could allow for the better understanding of impacts on the hydrological regime resulting from smaller features; for example, the soil properties or runoff generation differences produced by either a functioning or abandoned agricultural terrace network.
- The spatial rainfall pattern that drove SCIMAP-Flood and CRUM3 was created using a sparse, eight station, rainfall gauge network with added, low resolution, satellite rainfall information to capture the rainfall distribution across the catchment. A study with a dense monitoring network capable of investigating the rainfall patterns associated with high flow events would be useful to attain better data to drive the catchment hydrological models or to understand how the gauge network in other catchments could be best utilised in the modelling process. This would be undertaken at a larger scale than the proposed experimental sub-catchment with previous research already looking at rainfall amounts and intensities in small Himalayan catchments (e.g. Gardner and Gerrard, 2003; Merz et al., 2006).
- The channel and floodplain morphology accuracy in the elevation data is one of the key aspects driving the extent and depths in an inundation model. The channel morphology within many Himalayan catchments is altered during high-flow events with many catchments having a high sedimentation rate and continual scour-and-fill action along the channel bed. The impact of sediment is not addressed in the study but the use of a landscape evolution model within the end-to-end approach, such as CAESAR LISFLOOD (Coulthard et al., 2013) or SIBERIA (Hancock et al., 2000; Willgoose, 2005), could help take the sediment dynamics during the high-flow event into consideration. A landscape evolution model could replace the use of the inundation model in Stage 3 of the overall process, particularly if applied to a Himalayan catchment, if the impact of localised sediment dynamics are potentially a key contributing factor in the inundation pattern.

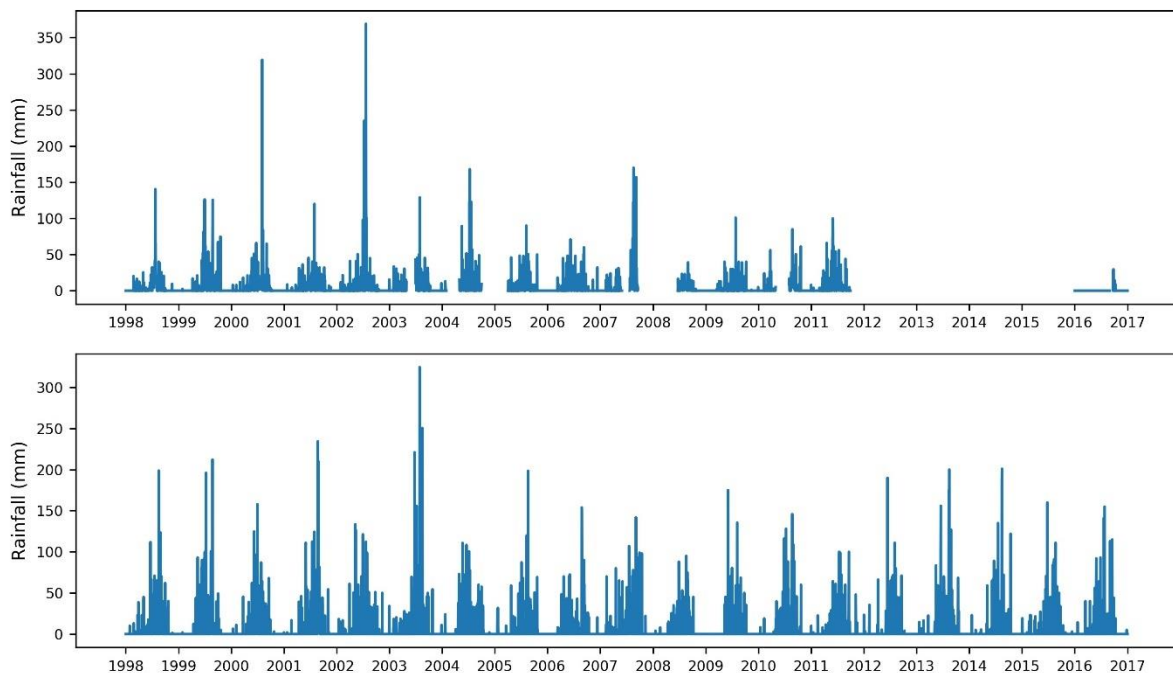
- A secondary improvement with regards to more accurate measurements of the channel morphology could feed into the LISFLOOD-FP input parameters. The sub-grid channel r parameter was determined to be very sensitive with the inundation extent within the model boundary varying depending on the value used (see Section 5.2.3). This research used one r parameter value for the entire channel network however a varied r parameter across the model domain would likely produce a more representative inundation extent. A varied r parameter could be based on more channel geometry measurements taken within the model extent to better capture the variation in channel dimensions.
- Improvements could be made to the gauged data within the East Rapti catchment that was acquired as part of this research; this includes both enhancing the coverage of the monitoring network, bringing the temporal resolution to sub-daily and undertaking more rigorous quality assurance on the measured data. Both the rainfall and river flow gauge network would benefit from more monitoring locations throughout the catchment. The rainfall gauge network would benefit better coverage across the elevation range with only one gauge (Daman) being representative of the higher elevations within the East Rapti catchment. The river flow gauge network could benefit from, at a minimum, a gauge on the main East Rapti channel close to the confluence with the Nayarani River. Finally, the gauged river flow data had numerous issues (discussed in detail in Section 2.6) in which an improved quality assurance proves could begin to rectify.

7 APPENDICES

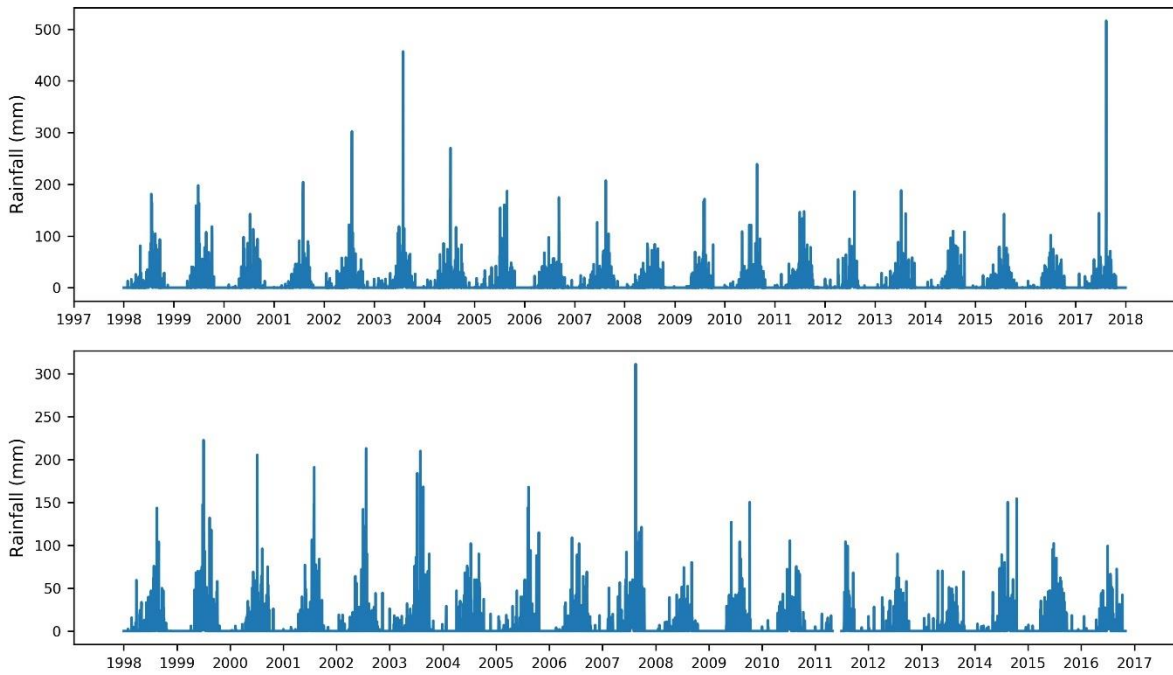
Appendix 7.1: DHM daily rainfall time series for the Amlekgunj (top) and Beluwa (bottom) gauges for 1998 to 2016. Note the different y-axis values.



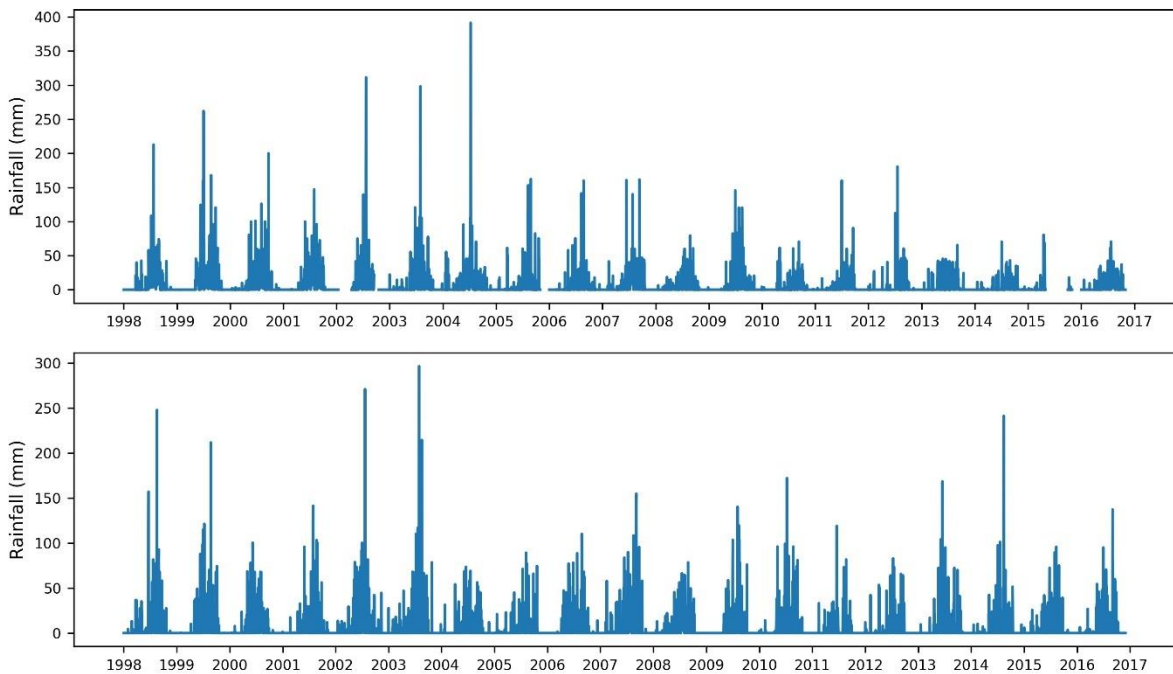
Appendix 7.2: DHM daily rainfall time series for the Daman (top) and Dunkauli (bottom) gauges for 1998 to 2016. Note the different y-axis values.



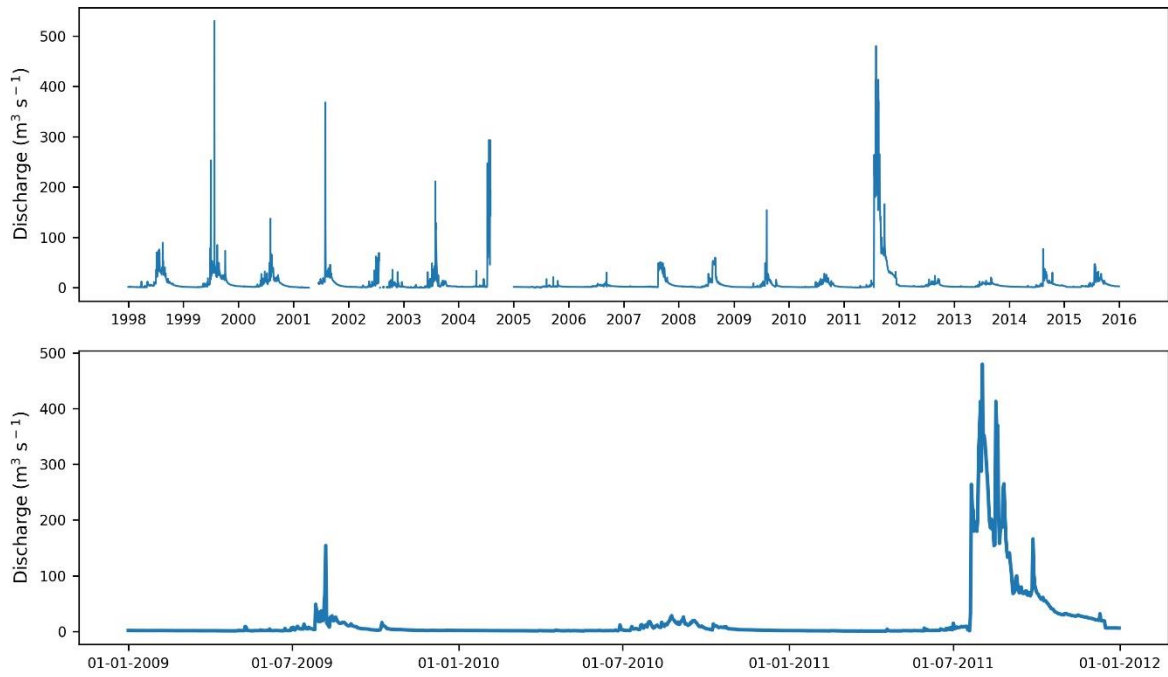
Appendix 7.3: DHM daily rainfall time series for the Hetauda gauge (top) for 1998 to 2017 and Jhawani gauge (bottom) for 1998 to 2016. Note the different y-axis values.



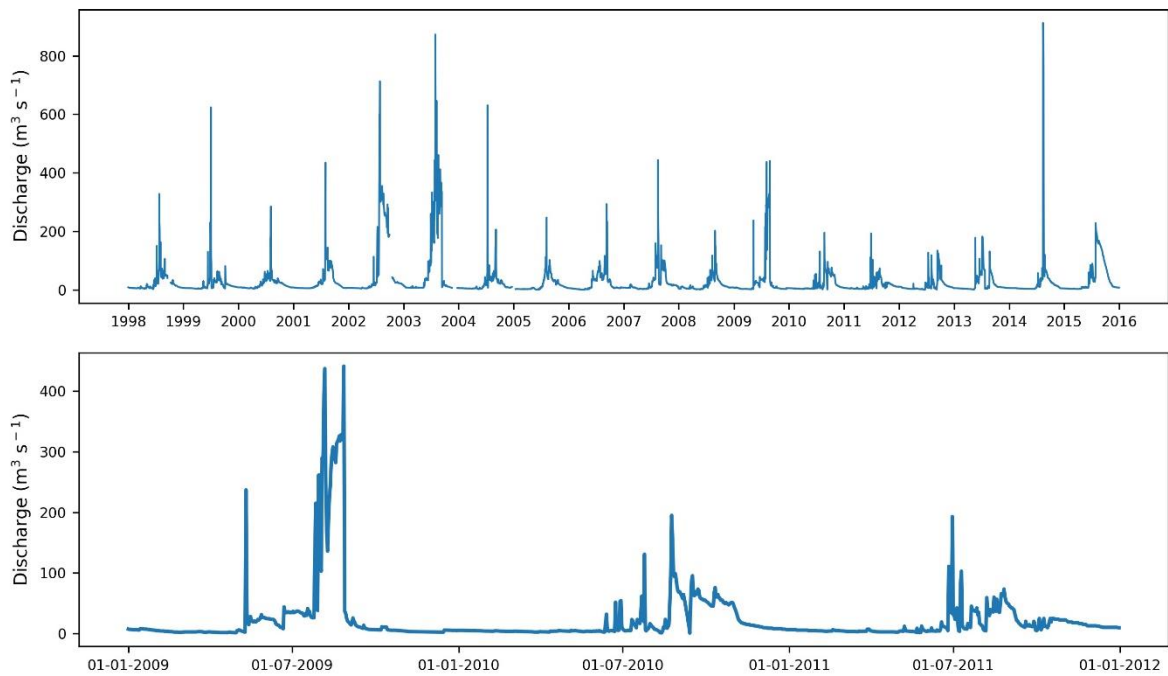
Appendix 7.4: DHM daily rainfall time series for the Makwanpur Gadhi (top) and Rampur gauges (bottom) for 1998 to 2016. Note the different y-axis values.



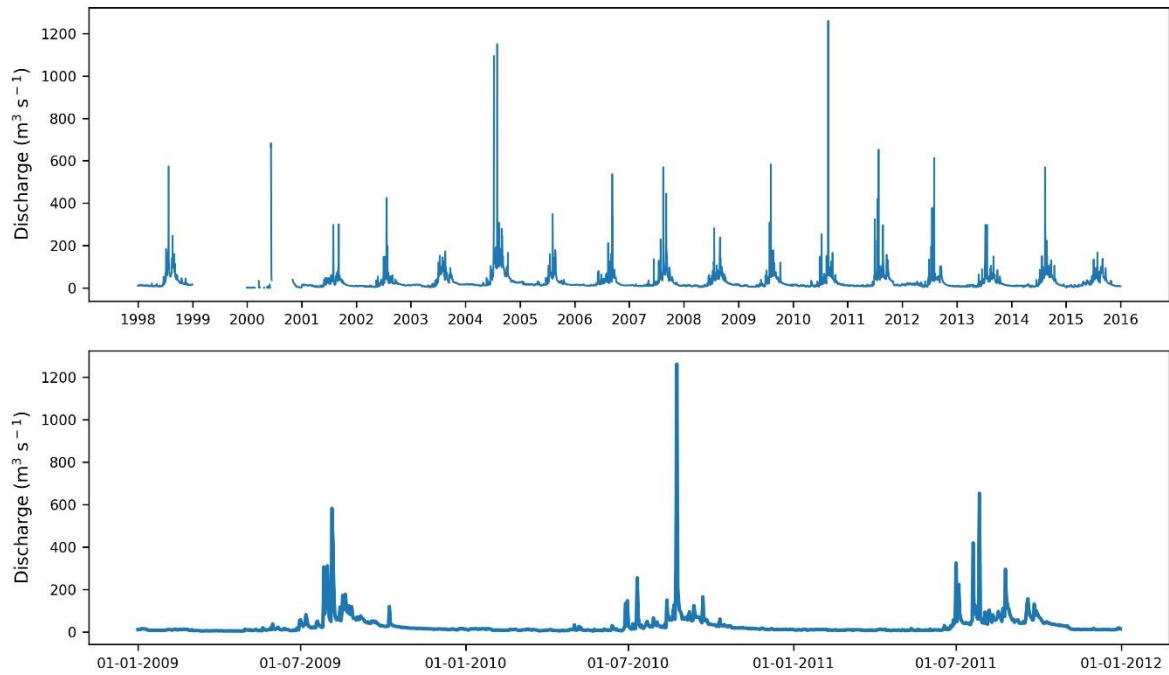
Appendix 7.5: DHM daily average discharge time series for the Lothar gauge for 1998 to 2016 (top) and for 2009 to 2011 (bottom). Note the different y-axis values.



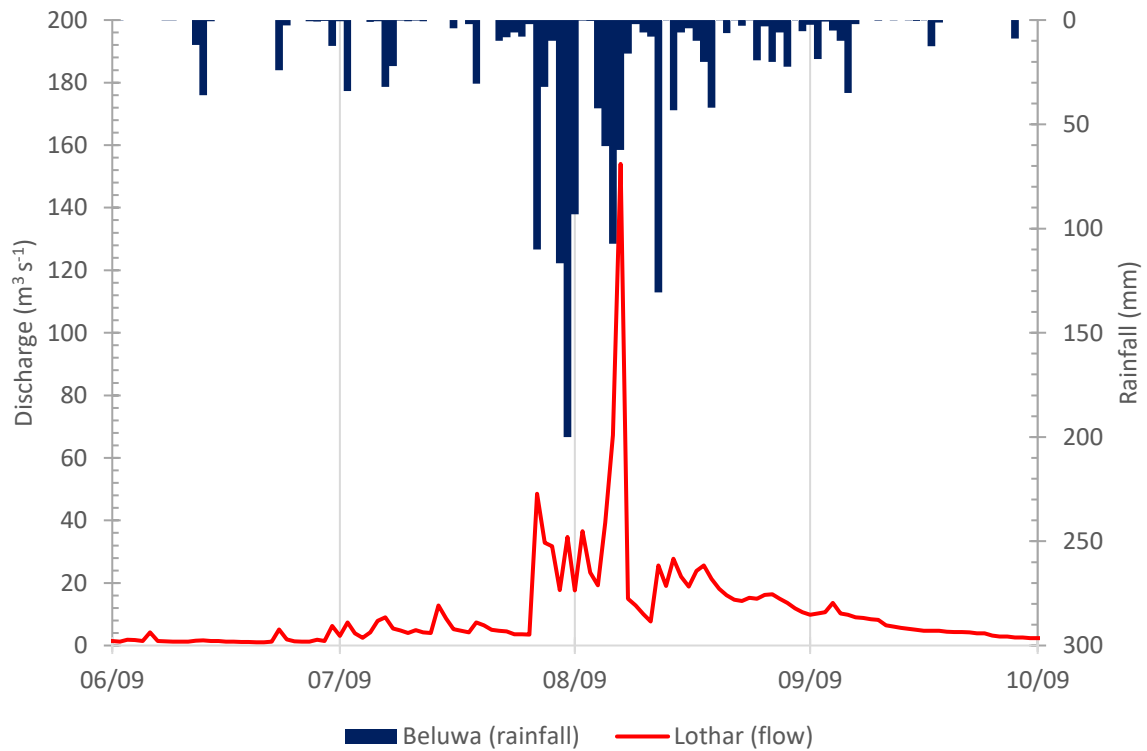
Appendix 7.6: DHM daily average discharge time series for the Manahari gauge for 1998 to 2016 (top) and for 2009 to 2011 (bottom). Note the different y-axis values.



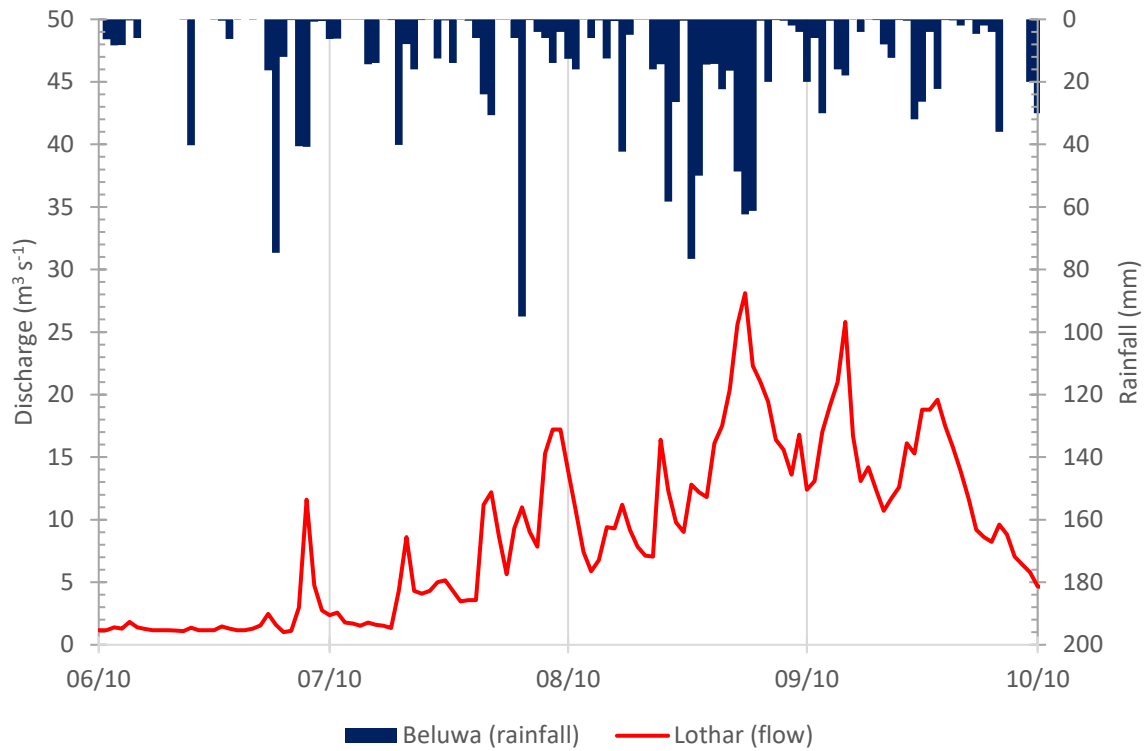
Appendix 7.7: DHM daily average discharge time series for the Rapti gauge for 1998 to 2016 (top) and for 2009 to 2011 (bottom). Note the different y-axis values.



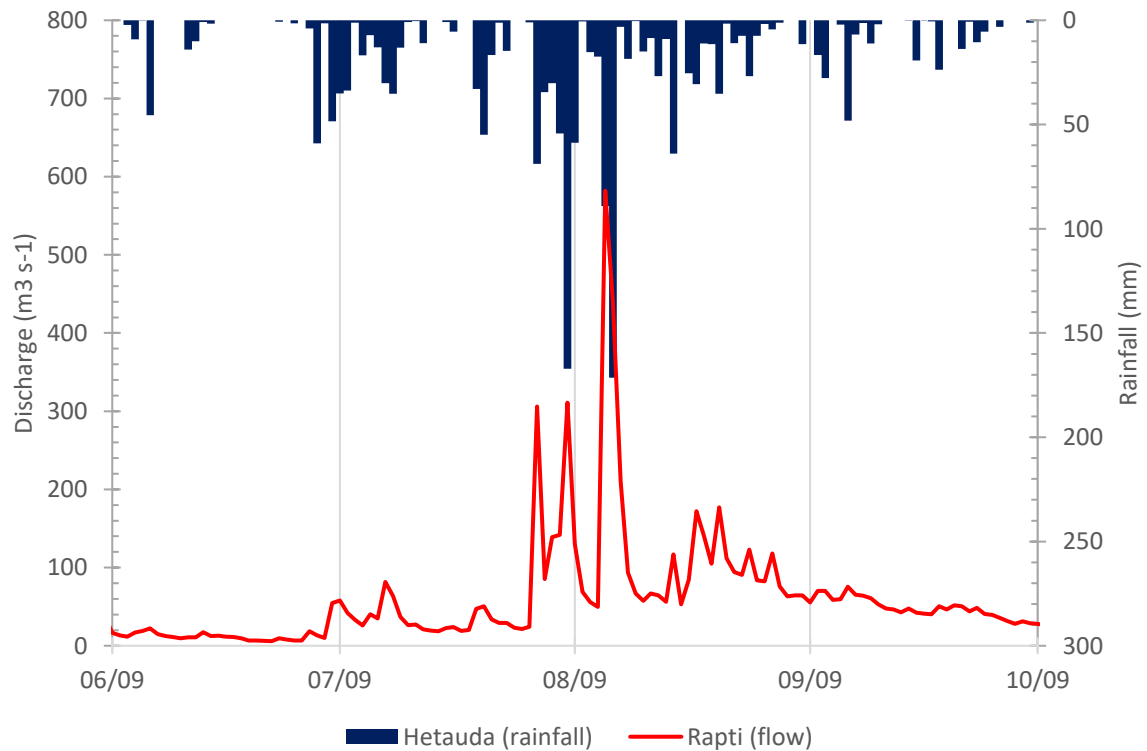
Appendix 7.8: DHM daily rainfall and discharge totals from the 2009 monsoon period (June to September) comparing the Lothar flow gauge and Beluwa rainfall gauged data.



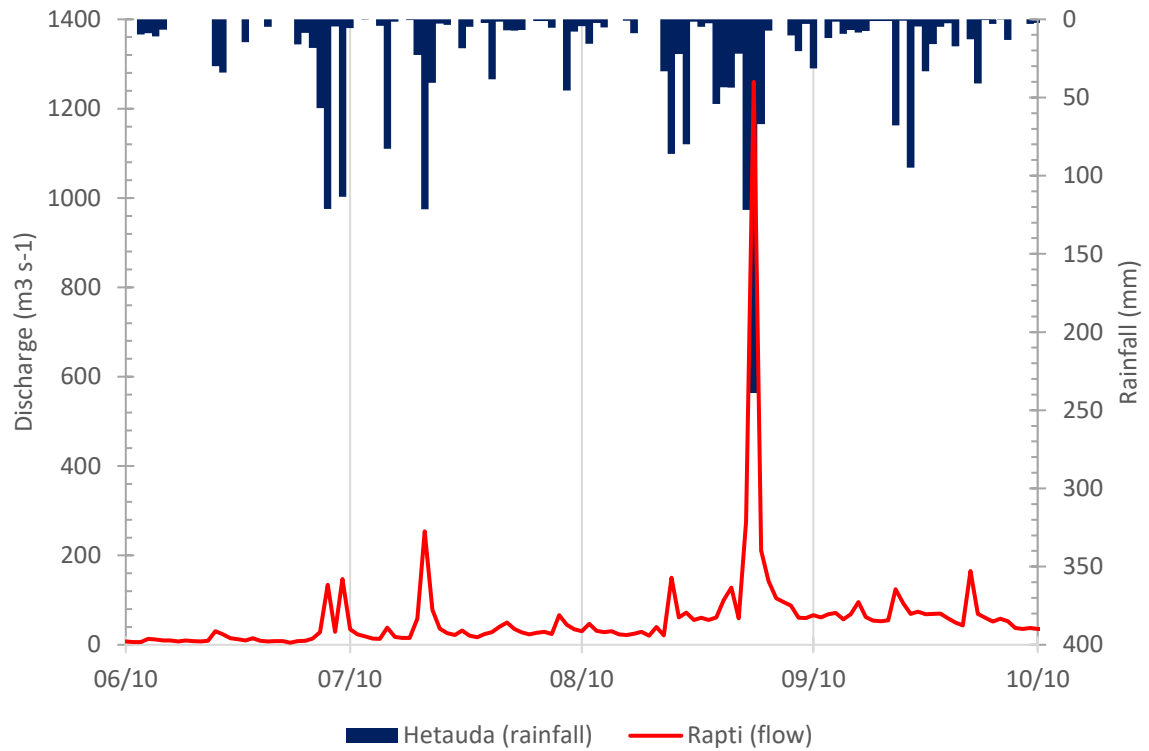
Appendix 7.9: DHM daily rainfall and discharge totals from the 2010 monsoon period (June to September) comparing the Lothar flow gauge and Beluwa rainfall gauged data.



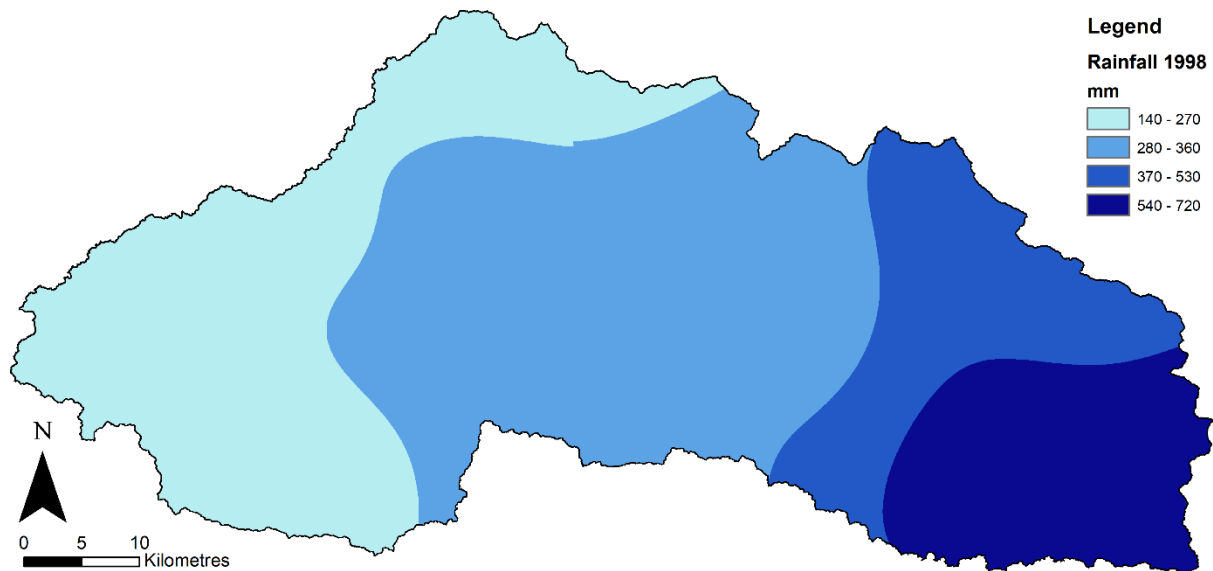
Appendix 7.10: DHM daily rainfall and discharge totals from the 2009 monsoon period (June to September) comparing the Rapti flow gauge and Hetauda rainfall gauged data.



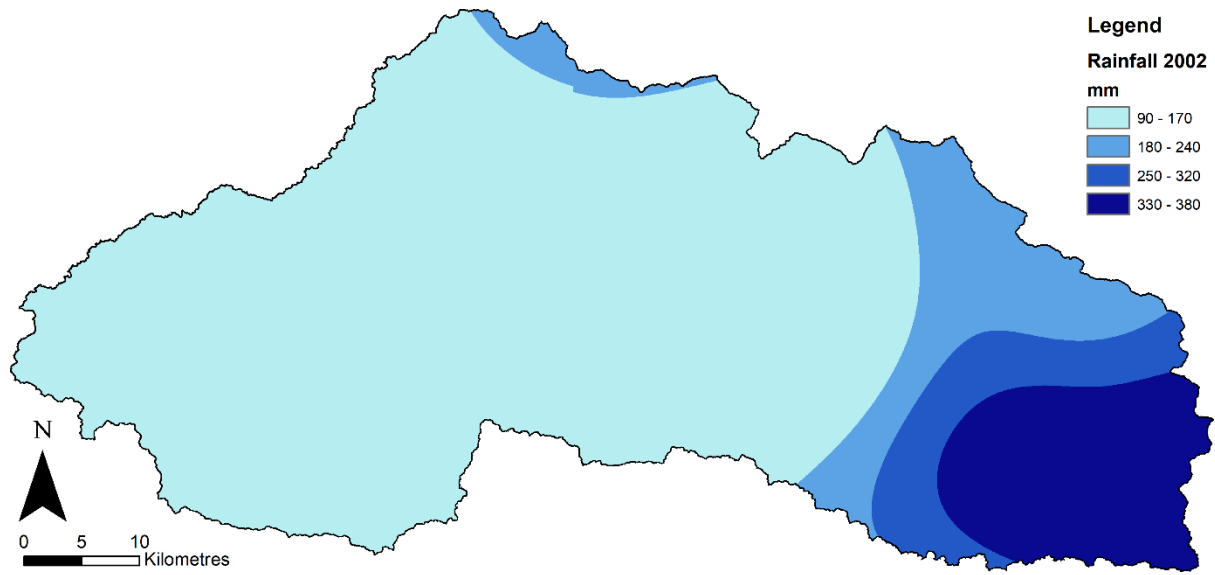
Appendix 7.11: DHM daily rainfall and discharge totals from the 2010 monsoon period (June to September) comparing the Rapti flow gauge and Hetauda rainfall gauged data.



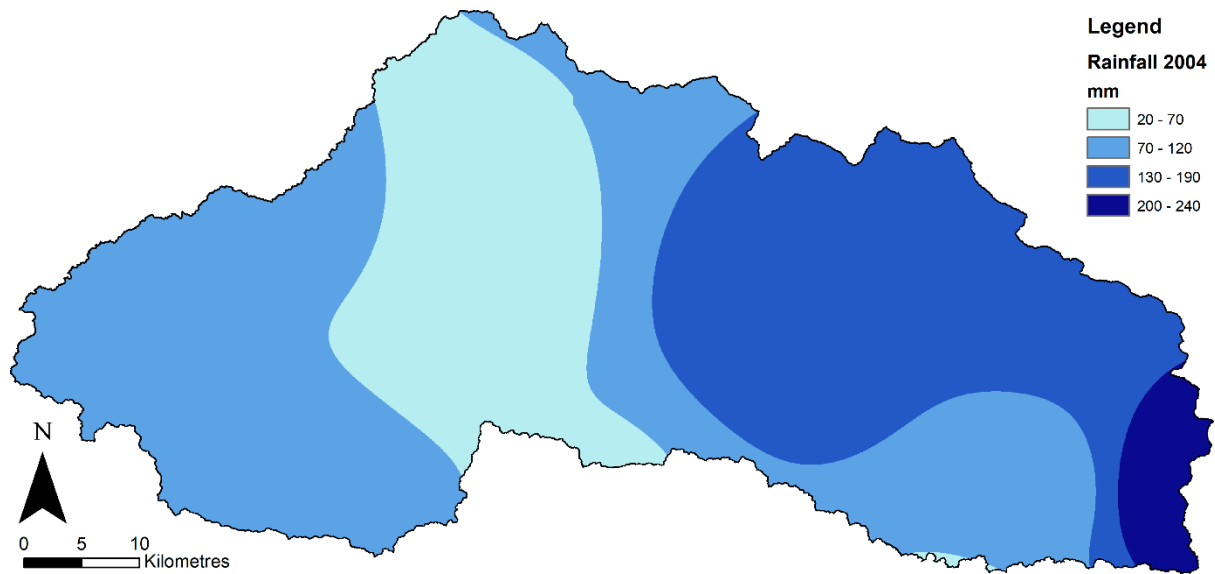
Appendix 7.12: The cumulative bias-adjusted rainfall spatial rainfall pattern associated with the 1998 high flow event.



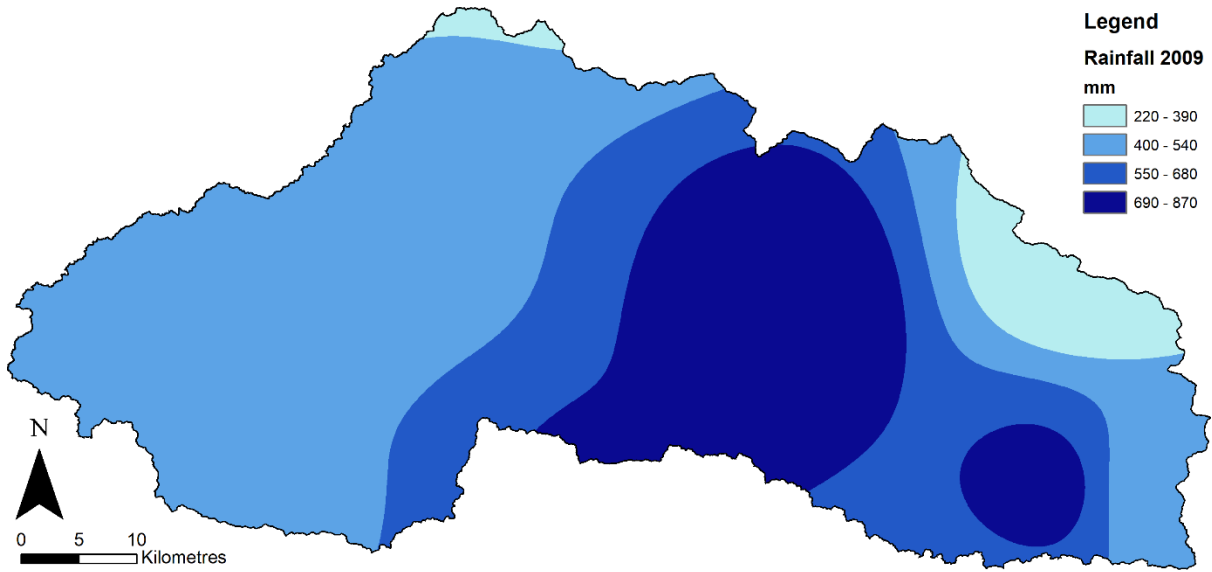
Appendix 7.13: The cumulative bias-adjusted rainfall spatial rainfall pattern associated with the 2002 high flow event.



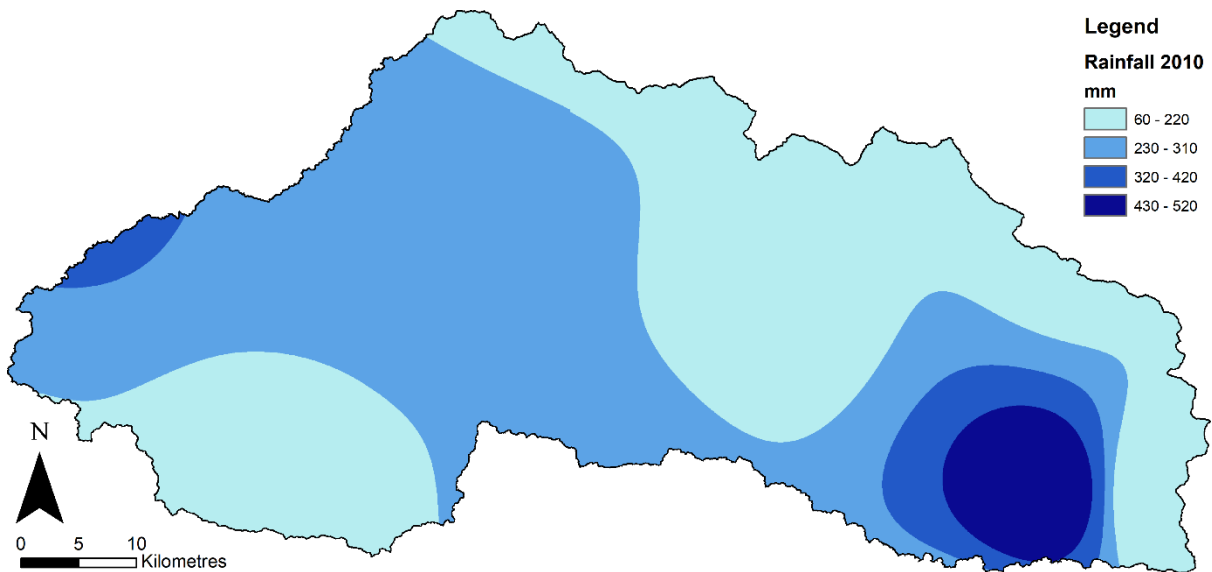
Appendix 7.14: The cumulative bias-adjusted rainfall spatial rainfall pattern associated with the 2004 high flow event.



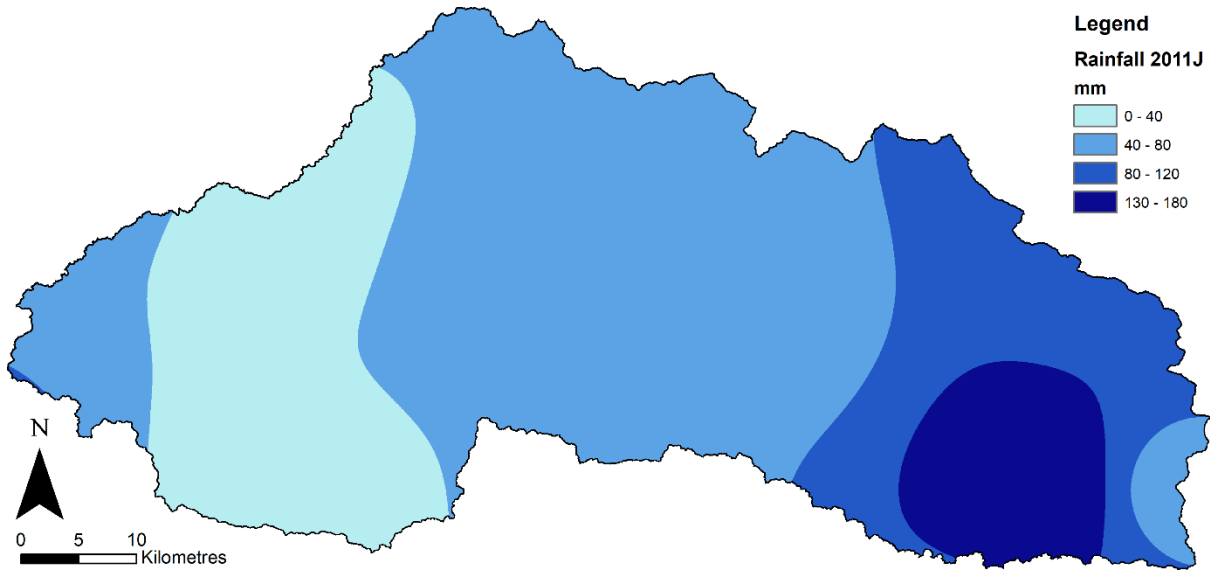
Appendix 7.15: The cumulative bias-adjusted rainfall spatial rainfall pattern associated with the 2009 high flow event.



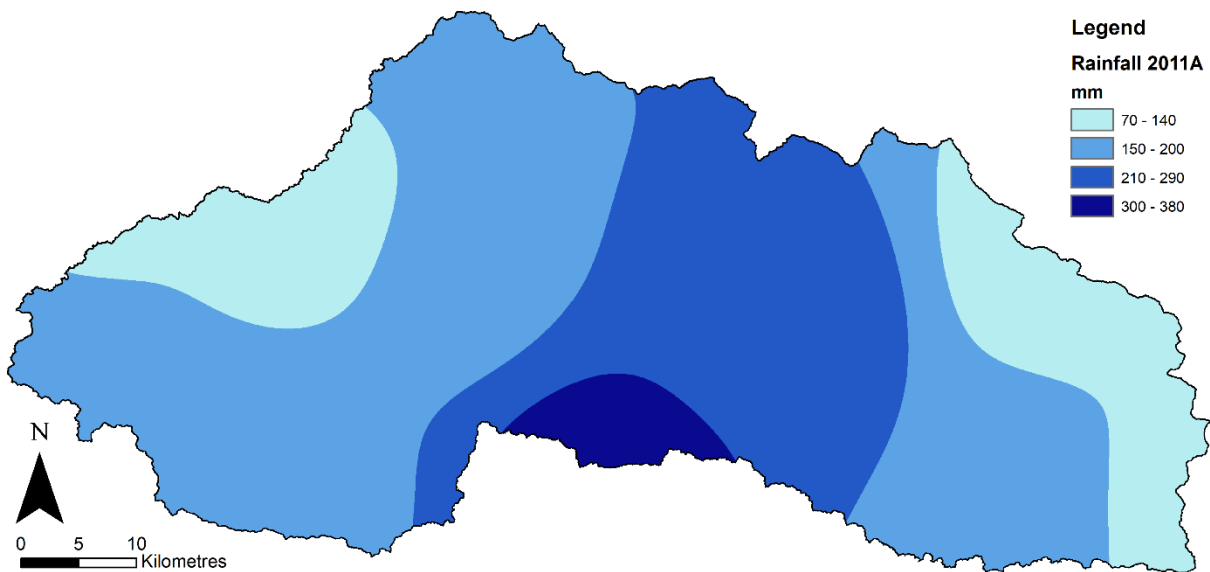
Appendix 7.16: The cumulative bias-adjusted rainfall spatial rainfall pattern associated with the 2010 high flow event.



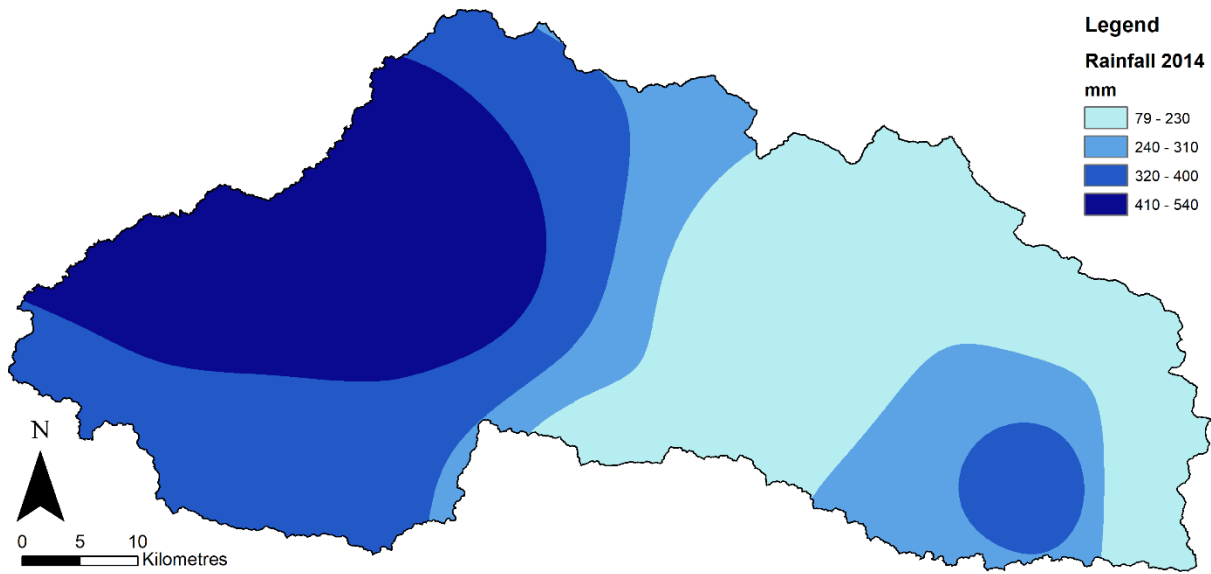
Appendix 7.17: The cumulative bias-adjusted rainfall spatial rainfall pattern associated with the July 2011 high flow event.



Appendix 7.18: The cumulative bias-adjusted rainfall spatial rainfall pattern associated with the August 2011 high flow event.



Appendix 7.19: The cumulative bias-adjusted rainfall spatial rainfall pattern associated with the 2014 high flow event.



Appendix 7.20: Literature values for CRUM3 land cover parameters.

Land cover category	Interception Depth (m)	Canopy Gap Fraction (decimal %)	Albedo (decimal %)	Max Vegetation Height (m)	Darcy-Weisbach FF	Vegetation Growth (g/m ² /sec)	% Cell Overland Flow (decimal %)
<i>Rainfed Agriculture</i>	0.0021	0.4	0.20	1.0	2.17	1.69E-05	0.3
<i>Irrigated Agriculture</i>	0.0021	0.4	0.25	1.5	2.17	1.69E-05	0.3
<i>Shrubland</i>	0.0013	0.5	0.15	2.5	1.91	9.35E-06	0.3
<i>Forest</i>	0.0013	0.3	0.16	16.0	1.50	5.44E-05	0.3
<i>Built-Up Area</i>	0.0021	0.8	0.14	0.5	0.5	1.30E-06	0.3
<i>Bare Ground</i>	0.0021	0.8	0.22	0.5	0.5	1.30E-06	0.3
<i>Water</i>	0.0021	1.0	0.03	1.00E-09	0.5	1.00E-09	0.3
Source	Pattison, 2010	Pattison, 2010	Dingman, 1994; Li et al., 2013; Trlica et al., 2017	Breuer et al., 2003; Pattison, 2010; Ghimire et al., 2014	Emmett, 1970; Gilley et al., 1992; Gilley and Kottowitz, 1994; Abrahams et al., 1995; Musleh and Cruise, 2006; Parsons and Abrahams, 2009; Smith, 2011	Singh et al., 1994; Prince et al., 2013; Zheng et al., 2013; Pearson, 2016	Smith, 2011; Pearson, 2016

Appendix 7.21: Literature values for CRUM3 soil parameters.

Land cover category	Growth Temp (°C)	Channel Soil Depth (m)	Slope Soil Depth (m)	Ridge Soil Depth (m)	Plain Soil Depth (m)	Dynamic Layer K_{SAT} (m s ⁻¹)	K_{SAT} (m s ⁻¹)
<i>Rainfed Agriculture</i>	10	1.0	0.16	0.5	0.5	9.33E-06	3.10E-05
<i>Irrigated Agriculture</i>	10	1.0	0.16	0.5	0.5	1.27E-05	8.42E-06
<i>Shrubland</i>	10	1.0	0.16	0.5	0.5	1.14E-05	1.40E-05
<i>Forest</i>	10	1.5	0.24	0.75	0.75	6.93E-05	1.98E-05
<i>Built-Up Area</i>	10	1.0	0.16	0.5	0.5	2.78E-06	1.14E-05
<i>Bare Ground</i>	10	1.0	0.16	0.5	0.5	5.64E-06	1.28E-05
<i>Water</i>	1.00E-09	1.0	0.16	0.5	0.5	1.00E-09	1.00E-09
Source	Sapkota and Meilby, 2009	Pattison, 2010	Pattison, 2010	Pattison, 2010	Pattison, 2010	Gilmour et al., 1987; Haigh et al., 1990; Gerrard and Gardner, 2000; Ghimire et al., 2013; Shrestha et al., 2013; Saha and Kukal, 2015	Gilmour et al., 1987; Haigh et al., 1990; Gerrard and Gardner, 2000; Ghimire et al., 2013; Shrestha et al., 2013; Saha and Kukal, 2015

Appendix 7.22: Literature values for CRUM3 soil parameters.

Land cover category	Dynamic Layer Depth (m)	Dynamic Layer b Parameter	Green Ampt a Parameter (mm hr ⁻¹)	Green Ampt b Parameter (mm hr ⁻¹)	Porosity (decimal %)	K Decay with depth	Bedrock Conductivity (m s ⁻¹)
<i>Rainfed Agriculture</i>	1.0	4.05	10	5	0.54	-4.37	2.5E-10
<i>Irrigated Agriculture</i>	0.9	4.05	10	5	0.51	-4.37	2.5E-10
<i>Shrubland</i>	0.8	4.05	10	5	0.55	-4.9	2.5E-10
<i>Forest</i>	2.10	4.05	10	5	0.73	-9.8	2.5E-10
<i>Built-Up Area</i>	0.5	4.05	10	5	0.41	-7.8	2.5E-10
<i>Bare Ground</i>	0.75	4.05	10	5	0.41	-7.8	2.5E-10
<i>Water</i>	0.05	4.05	10	5	0.01	-7.8	2.5E-10
Source	Canadell et al., 1996; Breuer et al., 2003; Pattison, 2010;	Smith, 2011; Pearson, 2016	Smith, 2011; Pearson, 2016	Smith, 2011; Pearson, 2016	Bodhinayake and Si, 2004; Meyles et al., 2006; Gonzalez-Sosa et al., 2010; Pattison, 2010; Shrestha et al., 2013	Smith, 2011; Pearson, 2016	Smith, 2011; Pearson, 2016

Appendix 7.23: Parameter ensembles from the top 8 ranked GLUE runs using a formal statistical approach and the Rapti gauged data.

Model Run	Bedrock Conductivity	Soil Porosity	KSAT	K Decay Depth	Soil Depth Ridge	Dynamic Layer Depth	Soil Depth Slope	Hydraulic M	Q per Unit Width	Hydraulic K	Albedo	Dynamic Layer B
241	1.05E-08	0.19	0.00006	-1.50	1.19	0.35	0.25	0.23	2.24	0.85	0.43	7.96
462	7.01E-09	0.13	0.00004	-1.87	0.98	0.25	0.79	0.26	3.43	1.89	0.29	12.59
881	1.76E-08	0.50	0.00003	-1.78	1.03	0.21	0.66	0.21	3.78	1.96	0.44	12.01
1432	3.58E-08	0.14	0.00003	-1.14	0.36	0.32	0.87	0.28	5.82	1.71	0.46	6.36
1993	6.6E-09	0.26	0.00005	-1.80	0.37	0.11	0.69	0.20	7.11	1.72	0.39	7.49
2377	1.4E-08	0.30	0.00008	-1.12	0.57	0.17	0.33	0.47	6.77	1.48	0.42	0.72
3108	2.61E-08	0.13	0.00005	-2.26	0.84	0.45	0.69	0.38	9.64	0.26	0.31	12.81
5009	2.5E-10	0.45	0.00020	-3.00	0.50	0.05	0.16	0.32	5.00	1.00	0.19	4.05

Appendix 7.24: Parameter ensembles from the to 8 ranked GLUE runs using a formal statistical approach and the Lothar gauged data.

Model Run	Bedrock Conductivity	Soil Porosity	KSAT	K Decay Depth	Soil Depth Ridge	Dynamic Layer Depth	Soil Depth Slope	Hydraulic M	Q per Unit Width	Hydraulic K	Albedo	Dynamic Layer B
545	2.29E-08	0.59	0.00029	-1.68	0.66	0.50	0.85	0.35	0.12	0.88	0.12	9.30
2165	1.78E-08	0.64	0.00012	-2.66	0.54	0.30	1.05	0.48	2.05	0.84	0.06	7.69
2342	4.67E-08	0.53	0.00029	-1.83	0.62	0.43	0.80	0.49	4.30	1.09	0.14	2.42
2754	2.29E-08	0.63	0.00028	-1.44	0.74	0.35	0.15	0.34	3.78	1.54	0.42	0.04
3086	1.36E-09	0.59	0.00015	-3.09	0.90	0.45	0.56	0.42	0.72	0.82	0.18	5.57
3253	4.73E-08	0.46	0.00018	-1.38	0.72	0.38	1.00	0.46	5.24	1.50	0.06	1.88
3590	4.7E-08	0.67	0.00018	-1.76	1.15	0.20	0.14	0.18	8.20	1.21	0.20	4.07
3997	5E-08	0.57	0.00021	-1.36	1.12	0.46	0.10	0.31	3.37	0.91	0.41	2.44

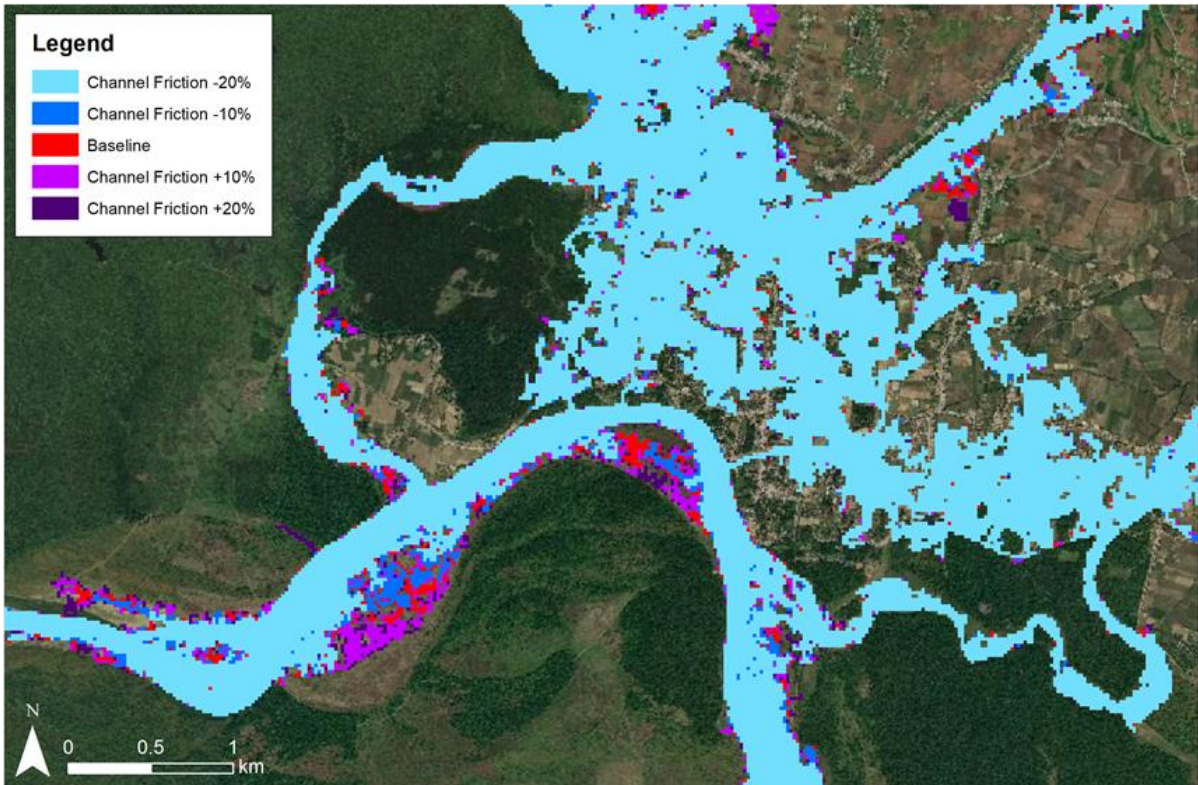
Appendix 7.25: Parameter ensembles from the top 8 ranked GLUE runs using an informal hydrological signatures approach and the Rapti gauged data.

Model Run	Bedrock Conductivity	Soil Porosity	KSAT	K Decay Depth	Soil Depth Ridge	Dynamic Layer Depth	Soil Depth Slope	Hydraulic M	Q per Unit Width	Hydraulic K	Albedo	Dynamic Layer B
15	1.12E-08	0.20	0.00082	-8.61	1.40	0.41	0.52	0.36	1.98	0.80	0.48	9.38
37	6.90E-09	0.12	0.00058	-5.73	0.57	0.16	0.30	0.11	7.66	1.01	0.44	10.46
39	1.05E-08	0.35	0.00051	-4.08	1.31	0.48	0.80	0.25	8.83	0.73	0.08	2.16
54	1.14E-08	0.37	0.00096	-2.24	0.54	0.22	0.23	0.12	6.20	1.54	0.45	10.71
83	3.12E-09	0.25	0.00006	-2.58	0.37	0.47	1.01	0.21	4.86	1.29	0.47	9.96
196	4.54E-08	0.03	0.00067	-1.40	1.35	0.08	0.49	0.19	5.20	1.24	0.17	13.51
383	1.22E-08	0.05	0.00089	-3.15	1.01	0.38	1.15	0.37	8.19	0.43	0.27	3.47
461	5.05E-09	0.22	0.00086	-5.96	0.35	0.50	0.93	0.28	5.81	1.10	0.35	11.39

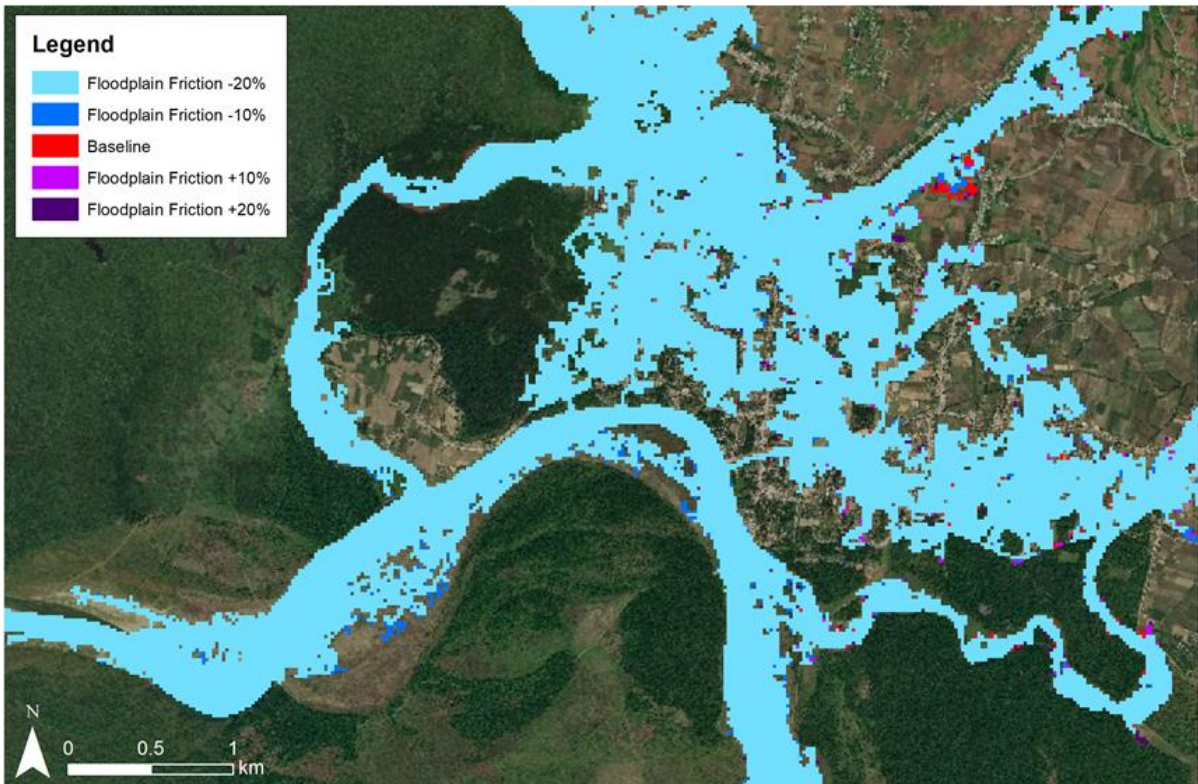
Appendix 7.26: Parameter ensembles from the to 8 ranked GLUE runs using an informal hydrological signatures approach and the Lothar gauged data

Model Run	Bedrock Conductivity	Soil Porosity	KSAT	K Decay Depth	Soil Depth Ridge	Dynamic Layer Depth	Soil Depth Slope	Hydraulic M	Q per Unit Width	Hydraulic K	Albedo	Dynamic Layer B
72	2.25E-08	0.65	0.00003	-3.54	0.97	0.39	0.47	0.38	8.43	0.30	0.25	15.38
635	2.78E-08	0.49	0.00015	-2.42	0.76	0.02	0.80	0.41	6.14	1.92	0.28	5.30
1724	1.33E-08	0.39	0.00010	-2.03	0.97	0.13	0.85	0.41	2.15	0.87	0.08	10.07
2431	1.54E-08	0.51	0.00006	-2.42	0.97	0.39	0.42	0.19	9.99	1.87	0.11	7.36
3887	1.6E-08	0.50	0.00009	-4.42	1.19	0.20	0.31	0.44	0.62	1.04	0.34	4.88
4501	1.67E-08	0.59	0.00003	-4.55	1.12	0.34	0.62	0.48	4.19	1.18	0.10	4.00
4551	2.81E-08	0.68	0.00009	-2.89	0.87	0.09	0.74	0.39	4.07	1.33	0.42	3.78
4883	2.25E-08	0.62	0.00008	-4.25	0.67	0.32	0.56	0.31	8.54	1.49	0.07	12.92

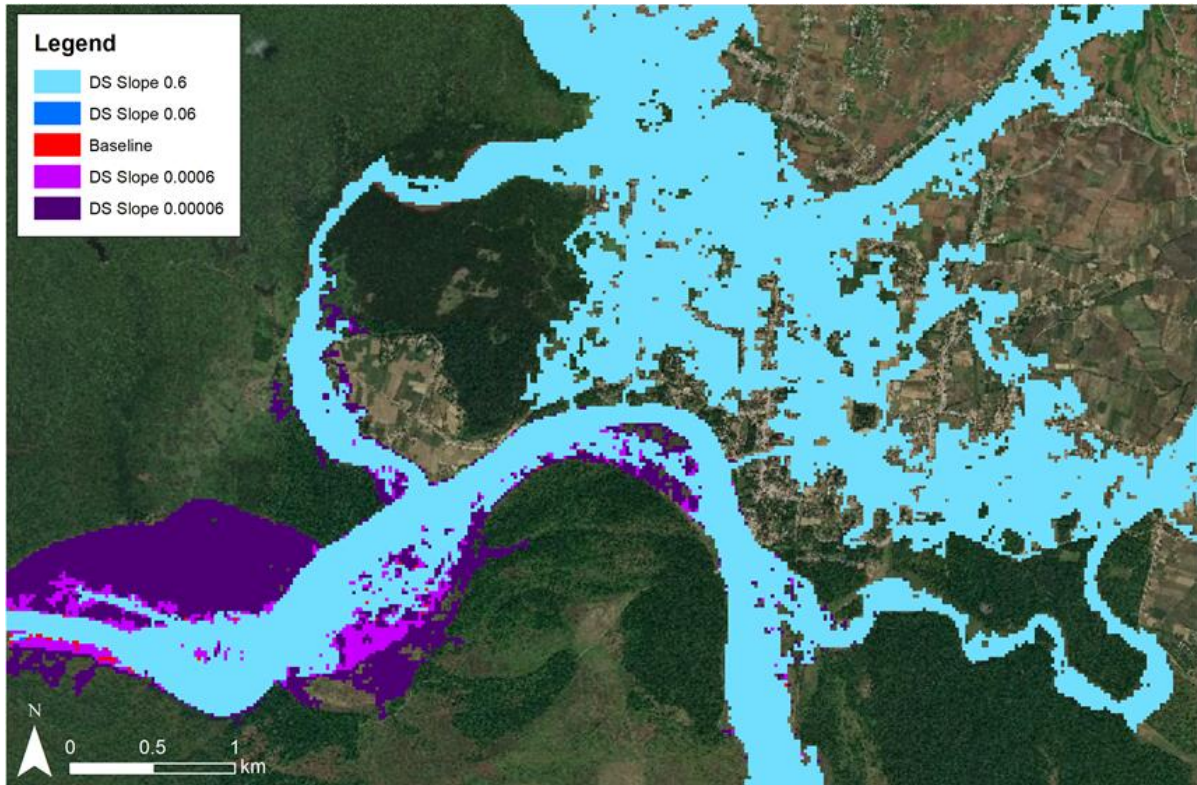
Appendix 7.27: The median flood extents of the 32 CRUM3 model inflow hydrographs from the channel friction value sensitivity analysis runs of the Sauraha LISFLOOD-FP model. The scenarios are layered in order of inundation extent with all cells representing an increased inundation extent visible.



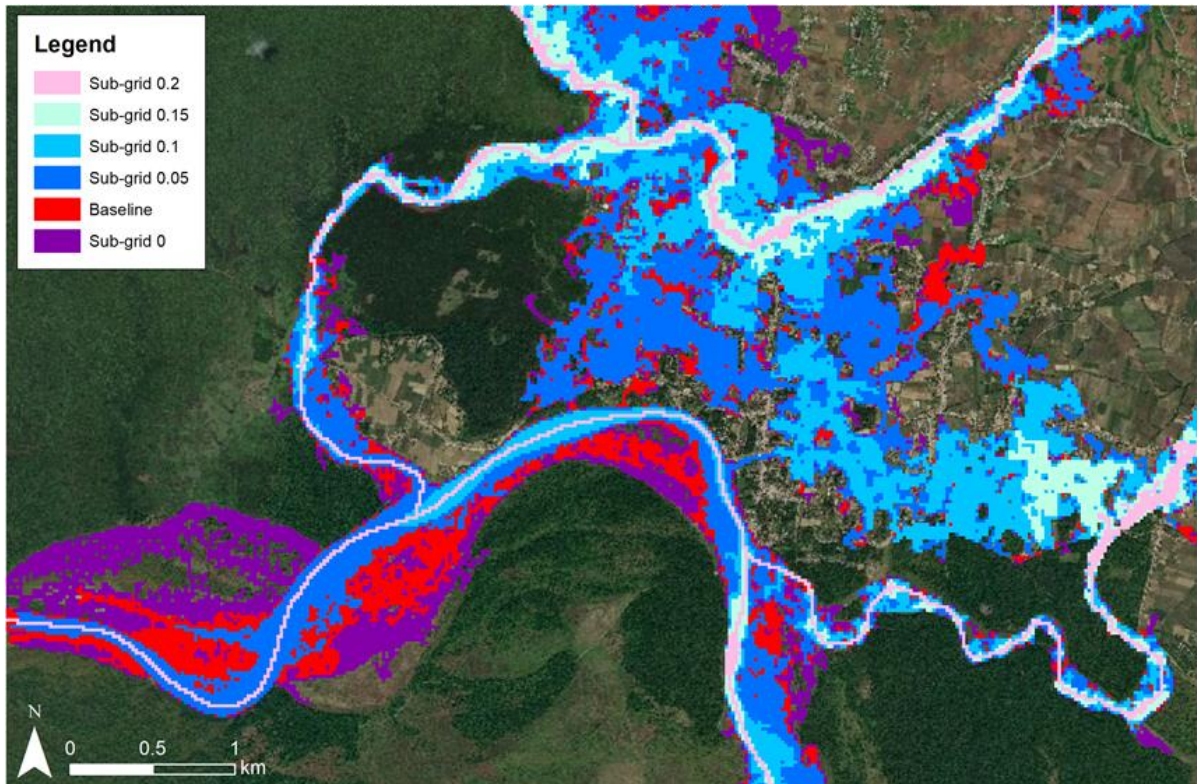
Appendix 7.28: The median flood extents of the 32 CRUM3 model inflow hydrographs from the floodplain friction value sensitivity analysis runs of the Sauraha LISFLOOD-FP model. The scenarios are layered in order of inundation extent with all cells representing an increased inundation extent visible.



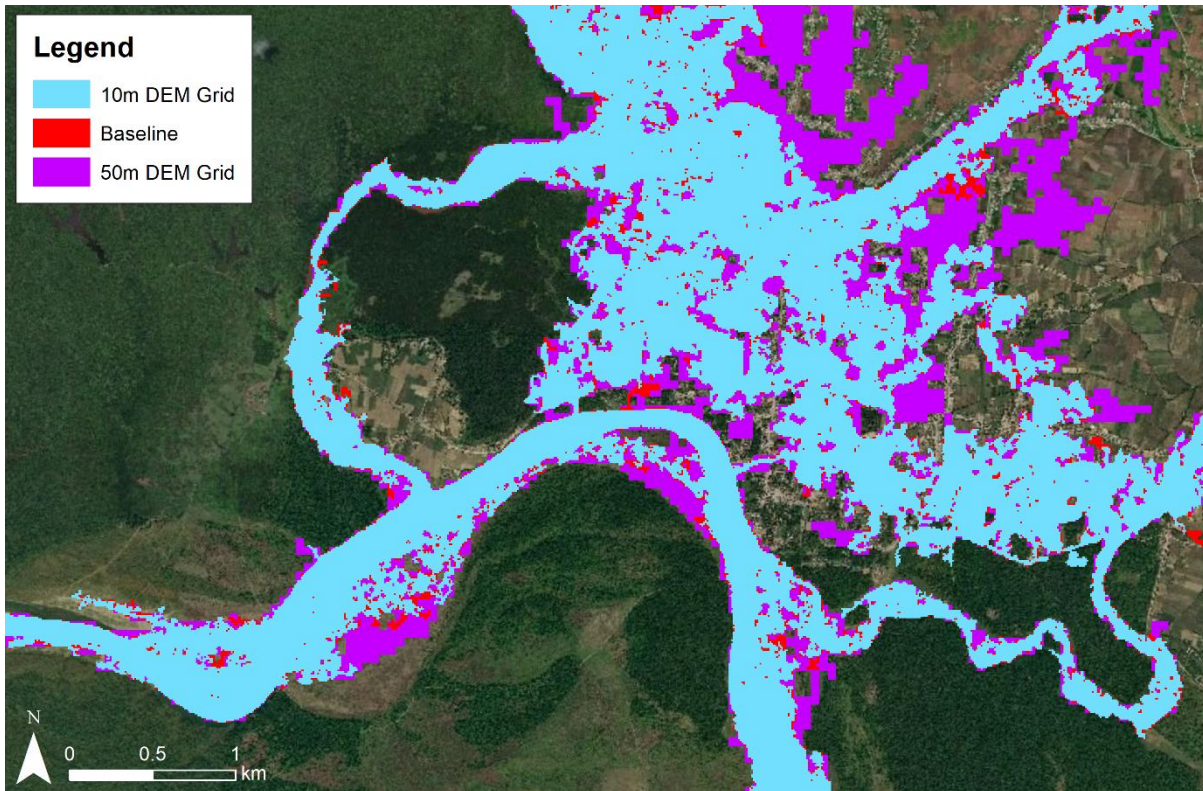
Appendix 7.29: The median flood extents of the 32 CRUM3 model inflow hydrographs from the downstream boundary slope value sensitivity analysis runs of the Sauraha LISFLOOD-FP model. The scenarios are layered in order of inundation extent with all cells representing an increased inundation extent visible.



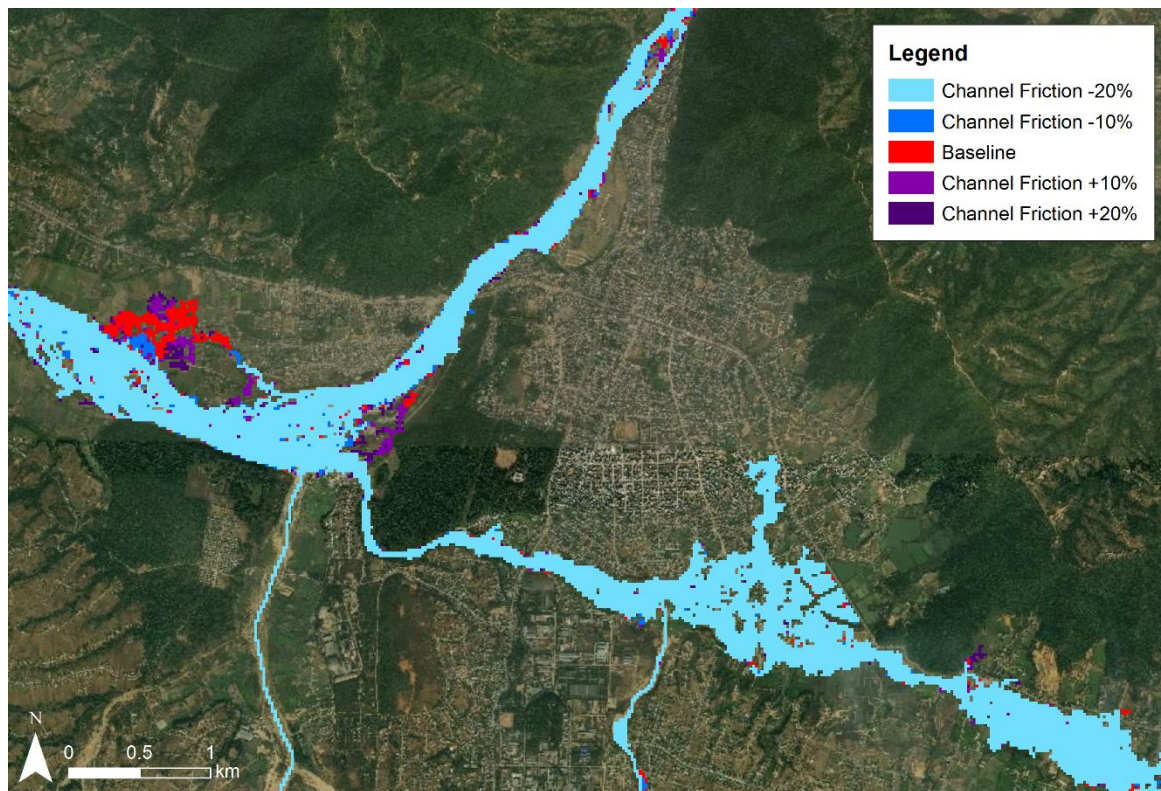
Appendix 7.30: The median flood extents of the 32 CRUM3 model inflow hydrographs from the sub-grid channel geometry parameter value sensitivity analysis runs of the Sauraha LISFLOOD-FP model. The scenarios are layered in order of inundation extent with all cells representing an increased inundation extent visible.



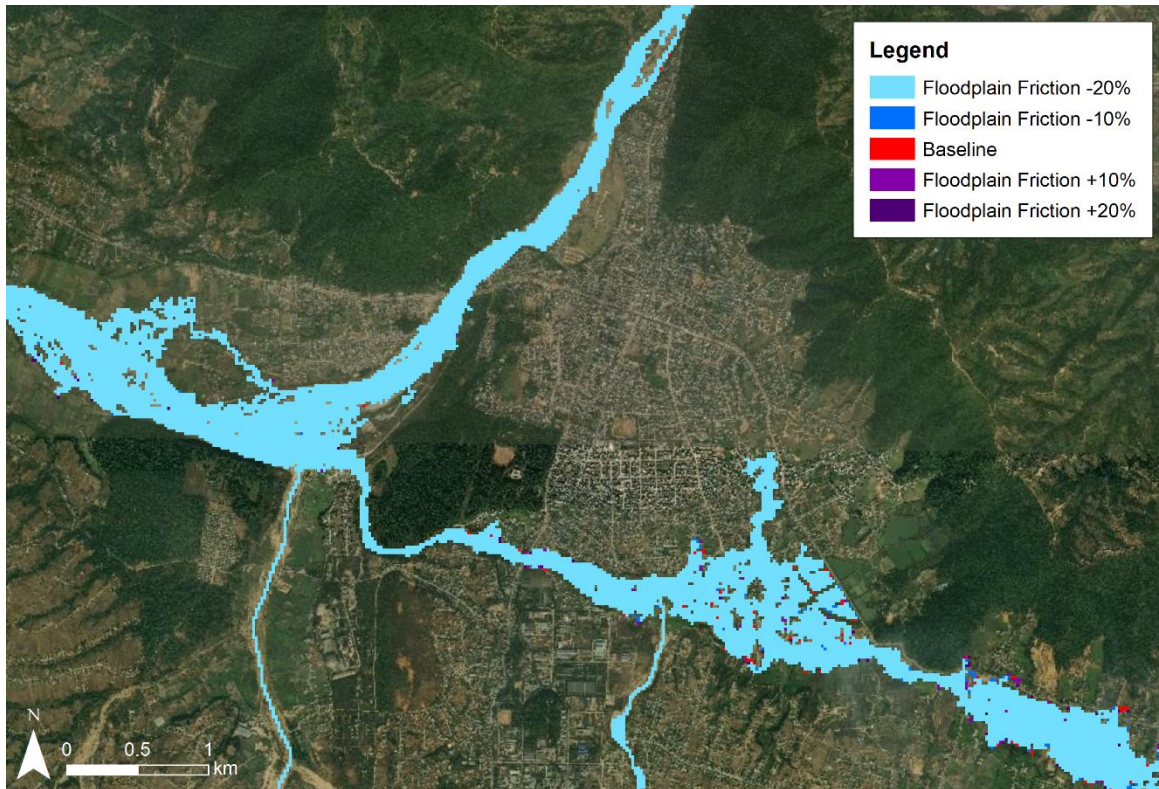
Appendix 7.31: The median flood extents of the 32 CRUM3 model inflow hydrographs from the model DEM grid resolution sensitivity analysis runs of the Sauraha LISFLOOD-FP model. The scenarios are layered in order of inundation extent with all cells representing an increased inundation extent visible.



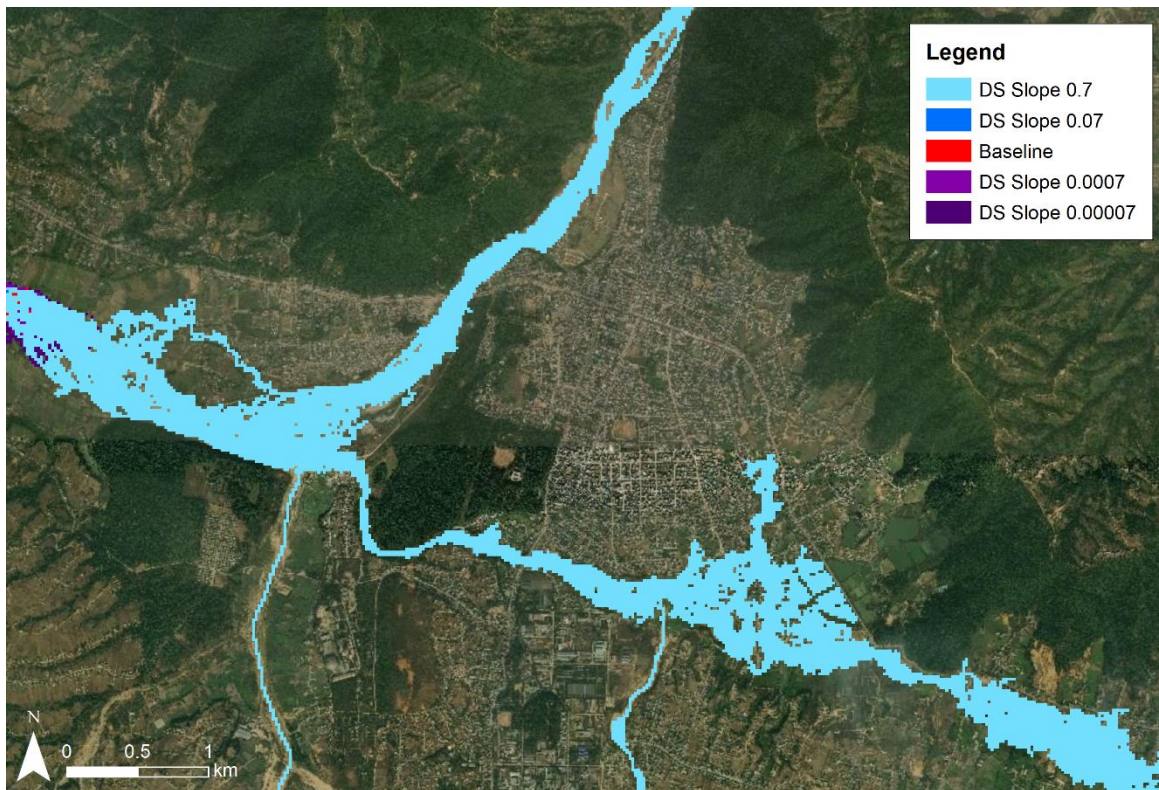
Appendix 7.32: The median flood extents of the 32 CRUM3 model inflow hydrographs from the channel friction value sensitivity analysis runs of the Hetauda LISFLOOD-FP model. The scenarios are layered in order of inundation extent with all cells representing an increased inundation extent visible.



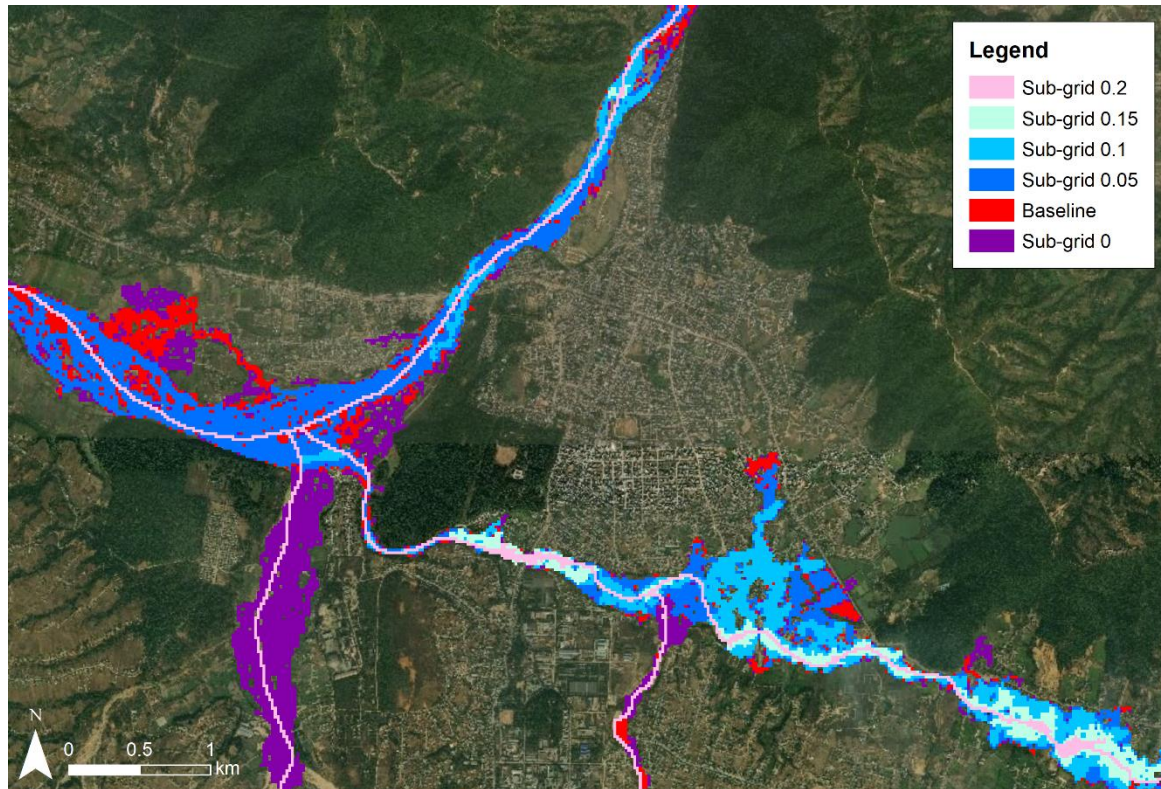
Appendix 7.33: The median flood extents of the 32 CRUM3 model inflow hydrographs from the floodplain friction value sensitivity analysis runs of the Hetauda LISFLOOD-FP model. The scenarios are layered in order of inundation extent with all cells representing an increased inundation extent visible.



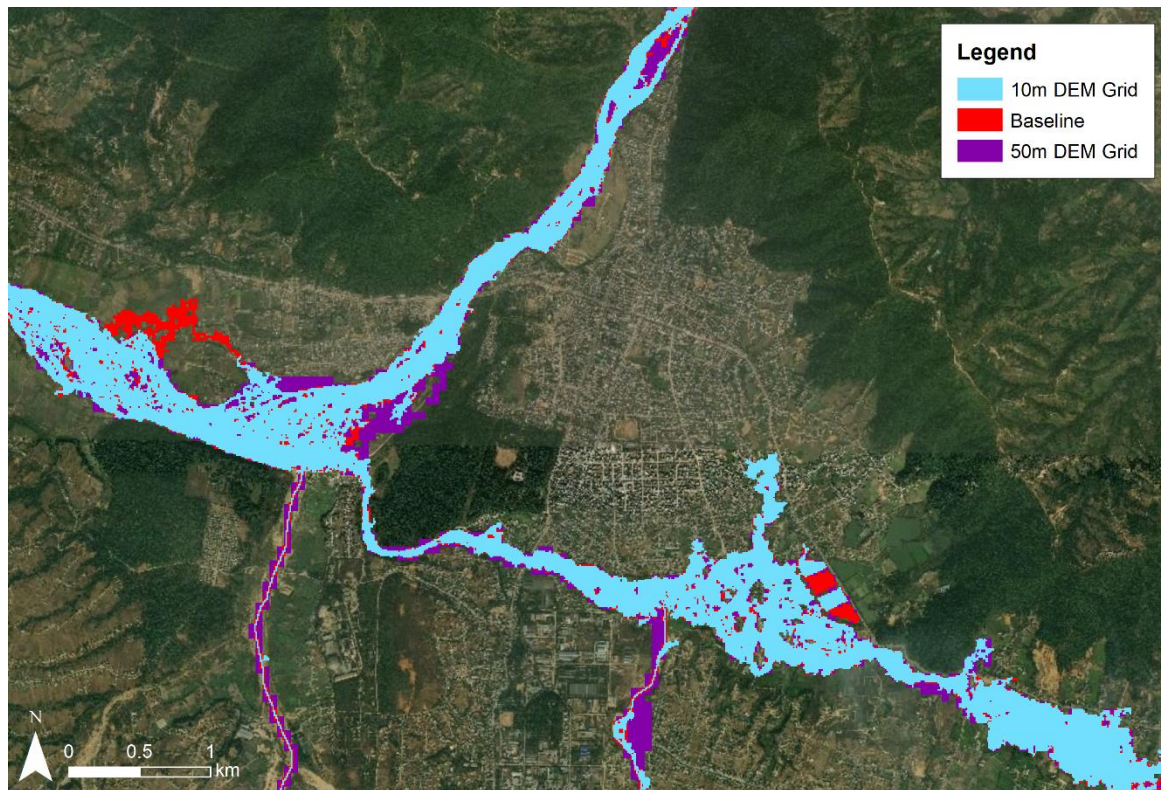
Appendix 7.34: The median flood extents of the 32 CRUM3 model inflow hydrographs from the downstream boundary slope value sensitivity analysis runs of the Hetauda LISFLOOD-FP model. The scenarios are layered in order of inundation extent with all cells representing an increased inundation extent visible.



Appendix 7.35: The median flood extents of the 32 CRUM3 model inflow hydrographs from the sub-grid channel geometry parameter value sensitivity analysis runs of the Hetauda LISFLOOD-FP model. The scenarios are layered in order of inundation extent with all cells representing an increased inundation extent visible.



Appendix 7.36: The median flood extents of the 32 CRUM3 model inflow hydrographs from the model DEM grid resolution sensitivity analysis runs of the Hetauda LISFLOOD-FP model. The scenarios are layered in order of inundation extent with all cells representing an increased inundation extent visible.



8 REFERENCES

- Abbasi, N. A., Xu, X., Lucas-Borja, M. E., Dang, W., & Liu, B. (2019). The use of check dams in watershed management projects: Examples from around the world. *Science of The Total Environment*, 676, 683–691. <https://doi.org/10.1016/j.scitotenv.2019.04.249>
- Abdelkareem, M. (2017). Targeting flash flood potential areas using remotely sensed data and GIS techniques. *Natural Hazards*, 85(1), 19–37. <https://doi.org/10.1007/s11069-016-2556-x>
- Abrahams, A. D., Parsons, A. J., & Wainwright, J. (1995). Effects of vegetation change on interrill runoff and erosion, Walnut Gulch, southern Arizona. *Geomorphology*, 13(1–4), 37–48.
- Abrahams, A.D., Parsons, A. J., & Hirsch, P. J. (1992). Field and laboratory studies of resistance to interrill overland flow on semi-arid hillslopes, southern Arizona. *Overland Flow: Hydraulics and Erosion Mechanics*, 1–23.
- Acharya, R. P., Maraseni, T. N., & Cockfield, G. (2019). Local Users and Other Stakeholders' Perceptions of the Identification and Prioritization of Ecosystem Services in Fragile Mountains: A Case Study of Chure Region of Nepal. *Forests*, 10(5), 421. <https://doi.org/10.3390/f10050421>
- Acreman, M., & Holden, J. (2013). How wetlands affect floods. *Wetlands*, 33(5), 773–786.
- Adhakari, B. R. (2013). Flooding and Inundation in Nepal Terai: Issues and Concerns. *Hydro Nepal: Journal of Water, Energy and Environment*, 12, 59–65. <https://doi.org/10.3126/hn.v12i0.9034>
- ADPC (Asian Disaster Preparedness Centre) (2010). *Nepal Hazard Risk Assessment Part 1*. Government of Nepal.
- Ampadu, B., Chappell, N. A., & Kasei, R. A. (2013). Rainfall-riverflow modelling approaches: Making a choice of data-based mechanistic modelling approach for data limited catchments: A review. *Canadian Journal of Pure and Applied Sciences*, 7(3), 2571–2580.
- Ameri, A. A., Pourghasemi, H. R., & Cerda, A. (2018). Erodibility prioritization of sub-watersheds using morphometric parameters analysis and its mapping: A comparison among TOPSIS, VIKOR, SAW, and CF multi-criteria decision making models. *Science of The Total Environment*, 613–614, 1385–1400. <https://doi.org/10.1016/j.scitotenv.2017.09.210>
- Andermann, C. (2011). *Climate, topography and erosion in the Nepal Himalayas* [PhD Thesis]. Université de Rennes.
- Andermann, C., Bonnet, S., & Gloaguen, R. (2011). Evaluation of precipitation data sets along the Himalayan front. *Geochemistry, Geophysics, Geosystems*, 12(7) Q07023.
- Andermann, C., Bonnet, S., Crave, A., Davy, P., Longuevergne, L., & Gloaguen, R. (2012a). Sediment transfer and the hydrological cycle of Himalayan rivers in Nepal. *Comptes Rendus Geoscience*, 344(11–12), 627–635. <https://doi.org/10.1016/j.crte.2012.10.009>
- Andermann, C., Longuevergne, L., Bonnet, S., Crave, A., Davy, P., & Gloaguen, R. (2012b). Impact of transient groundwater storage on the discharge of Himalayan rivers. *Nature Geoscience*, 5(2), 127–132. <https://doi.org/10.1038/ngeo1356>

- Apel, H., Merz, B., & Thielen, A. H. (2008). Quantification of uncertainties in flood risk assessments. *International Journal of River Basin Management*, 6(2), 149–162. <https://doi.org/10.1080/15715124.2008.9635344>
- Aquino, L. S., Timm, L. C., Reichardt, K., Barbosa, E. P., Parfitt, J. M. B., Nebel, A. L. C., & Penning, L. H. (2015). State-space approach to evaluate effects of land levelling on the spatial relationships of soil properties of a lowland area. *Soil and Tillage Research*, 145, 135–147.
- Archer, N. A. L., Bonell, M., Coles, N., MacDonald, A. M., Auton, C. A., & Stevenson, R. (2013). Soil characteristics and landcover relationships on soil hydraulic conductivity at a hillslope scale: A view towards local flood management. *Journal of Hydrology*, 497, 208–222. <https://doi.org/10.1016/j.jhydrol.2013.05.043>
- Arias-Hidalgo, M., Bhattacharya, B., Mynett, A. E., & van Griensven, A. (2013). Experiences in using the TMPA-3B42R satellite data to complement rain gauge measurements in the Ecuadorian coastal foothills. *Hydrology and Earth System Sciences*, 17(7), 2905–2915. <https://doi.org/10.5194/hess-17-2905-2013>
- Arnáez, J., Lana-Renault, N., Lasanta, T., Ruiz-Flaño, P., & Castroviejo, J. (2015). Effects of farming terraces on hydrological and geomorphological processes. A review. *CATENA*, 128, 122–134. <https://doi.org/10.1016/j.catena.2015.01.021>
- Arnaez, J., Lasanta, T., Errea, M. P., & Ortigosa, L. (2011). Land abandonment, landscape evolution, and soil erosion in a Spanish Mediterranean mountain region: The case of Camero Viejo. *Land Degradation & Development*, 22(6), 537–550.
- Arnold, J. G., & Allen, P. M. (1999). Automated methods for estimating baseflow and ground water recharge from streamflow records 1. *JAWRA Journal of the American Water Resources Association*, 35(2), 411–424.
- Aronica, G., Bates, P. D., & Horritt, M. S. (2002). Assessing the uncertainty in distributed model predictions using observed binary pattern information within GLUE. *Hydrological Processes*, 16(10), 2001–2016. <https://doi.org/10.1002/hyp.398>
- Asian Development Bank (2016). *Grant 0299-NEP: Water Resources Project Preparatory Facility. Final Report—Volume 3 East Rapti (1 of 9)*. Asian Development Bank.
- Bahadur, K. C. (2009). Improving Landsat and IRS image classification: Evaluation of unsupervised and supervised classification through band ratios and DEM in a mountainous landscape in Nepal. *Remote Sensing*, 1(4), 1257–1272.
- Baird, A. J. (1997). Overland flow generation and sediment mobilisation by water. *Arid Zone Geomorphology: Process, Form and Change in Drylands*, 165–184.
- Bartholmes, J., & Todini, E. (2005). Coupling meteorological and hydrological models for flood forecasting. *Hydrology and Earth System Sciences Discussions*, 9(4), 333–346.
- Bates, P. D., & De Roo, A. P. J. (2000). A simple raster-based model for flood inundation simulation. *Journal of Hydrology*, 236(1), 54–77. [https://doi.org/10.1016/S0022-1694\(00\)00278-X](https://doi.org/10.1016/S0022-1694(00)00278-X)

- Bates, P. D., Horritt, M. S., & Fewtrell, T. J. (2010). A simple inertial formulation of the shallow water equations for efficient two-dimensional flood inundation modelling. *Journal of Hydrology*, *387*(1), 33–45. <https://doi.org/10.1016/j.jhydrol.2010.03.027>
- Bates, P. D., Trigg, M. A., Neal, J. C., & Dabrowa, A. (2013). *LISFLOOD-FP User manual (Code release 5.9.6)*. School of Geographical Sciences, University of Bristol.
- Bathurst, J. C., Iroumé, A., Cisneros, F., Fallas, J., Iturraspe, R., Novillo, M. G., Urciuolo, A., Bièvre, B. de, Borges, V. G., Coello, C., Cisneros, P., Gayoso, J., Miranda, M., & Ramírez, M. (2011). Forest impact on floods due to extreme rainfall and snowmelt in four Latin American environments 1: Field data analysis. *Journal of Hydrology*, *400*(3–4), 281–291. <https://doi.org/10.1016/j.jhydrol.2010.11.044>
- Baugh, C. (2011). *The Impact of Climate Change upon the Snowmelt Hydrology of an Upland UK Catchment* [MRes Thesis]. Durham University.
- Bellin, N., van Wesemael, B., Meerkerk, A., Vanacker, V., & Barbera, G. G. (2009). Abandonment of soil and water conservation structures in Mediterranean ecosystems. *CATENA*, *76*(2), 114–121. <https://doi.org/10.1016/j.catena.2008.10.002>
- Benavidez, R., Jackson, B., Maxwell, D., & Paringit, E. (2016). Improving predictions of the effects of extreme events, land use, and climate change on the hydrology of watersheds in the Philippines. *Proceedings of the International Association of Hydrological Sciences*, *373*, 147–151. <https://doi.org/10.5194/piahs-373-147-2016>
- Bennett, N. D., Croke, B. F. W., Guariso, G., Guillaume, J. H. A., Hamilton, S. H., Jakeman, A. J., Marsili-Libelli, S., Newham, L. T. H., Norton, J. P., Perrin, C., Pierce, S. A., Robson, B., Seppelt, R., Voinov, A. A., Fath, B. D., & Andreassian, V. (2013). Characterising performance of environmental models. *Environmental Modelling & Software*, *40*, 1–20. <https://doi.org/10.1016/j.envsoft.2012.09.011>
- Beschta, R. L. (1998). Forest hydrology in the Pacific Northwest: Additional research needs. *JAWRA Journal of the American Water Resources Association*, *34*(4), 729–741.
- Beschta, R. L., Pyles, M. R., Skaugset, A. E., & Surfleet, C. G. (2000). Peakflow responses to forest practices in the western cascades of Oregon, USA. *Journal of Hydrology*, *233*(1–4), 102–120.
- Beven, K. (1989). Changing ideas in hydrology—The case of physically-based models. *Journal of Hydrology*, *105*(1–2), 157–172.
- Beven, K. (2005). *The Uncertainty Cascade in Flood Forecasting*. 9.
- Beven, K. (2006). A manifesto for the equifinality thesis. *Journal of Hydrology*, *320*(1–2), 18–36. <https://doi.org/10.1016/j.jhydrol.2005.07.007>
- Beven, K. (2009). *Environmental modelling: An uncertain future?* Routledge.
- Beven, K. J., & Kirkby, M. J. (1979). A physically based, variable contributing area model of basin hydrology/Un modèle à base physique de zone d'appel variable de l'hydrologie du bassin versant. *Hydrological Sciences Journal*, *24*(1), 43–69.
- Beven, K., & Binley, A. (1992). The future of distributed models: Model calibration and uncertainty prediction. *Hydrological Processes*, *6*(3), 279–298.

- Beven, K., & Binley, A. (2014). GLUE: 20 years on. *Hydrological Processes*, 28(24), 5897–5918. <https://doi.org/10.1002/hyp.10082>
- Beven, K., & Freer, J. (2001). Equifinality, data assimilation, and uncertainty estimation in mechanistic modelling of complex environmental systems using the GLUE methodology. *Journal of Hydrology*, 249(1–4), 11–29.
- Beven, K., & Lamb, R. (2017). The uncertainty cascade in model fusion. *Geological Society, London, Special Publications*, 408(1), 255–266. <https://doi.org/10.1144/SP408.3>
- Beven, K., Lamb, R., Leedal, D., & Hunter, N. (2015). Communicating uncertainty in flood inundation mapping: A case study. *International Journal of River Basin Management*, 13(3), 285–295. <https://doi.org/10.1080/15715124.2014.917318>
- Beven, K., Leedal, D., & McCarthy, S. (2014). *Framework for assessing uncertainty in fluvial flood risk mapping*. CIRIA.
- Bhatt, R. P. (2013). *Initial Environmental Examination for Construction of New Bank Protection Work and Spurs in Lothar of East Rapti*. Chitwan National Park Authority.
- Biancamaria, S., Bates, P. D., Boone, A., & Mognard, N. M. (2009). Large-scale coupled hydrologic and hydraulic modelling of the Ob river in Siberia. *Journal of Hydrology*, 379(1–2), 136–150.
- Binley, A., Beven, K., Calver, A., & Watts, L. G. (1991). Changing responses in hydrology: Assessing the uncertainty in physically based model predictions. *Water Resources Research*, 27(6), 1253–1261.
- Blazkova, S., & Beven, K. (2009). A limits of acceptability approach to model evaluation and uncertainty estimation in flood frequency estimation by continuous simulation: Skalka catchment, Czech Republic. *Water Resources Research*, 45(12).
- Blöschl, G., Reszler, C., & Komma, J. (2008). A spatially distributed flash flood forecasting model. *Environmental Modelling & Software*, 23(4), 464–478.
- Bodhinayake, W., & Cheng Si, B. (2004). Near-saturated surface soil hydraulic properties under different land uses in the St Denis National Wildlife Area, Saskatchewan, Canada. *Hydrological Processes*, 18(15), 2835–2850.
- Boelee, L., Lumbroso, D., Samuels, P. G., Stephens, E., & Cloke, H. (2017). *A review of the understanding of uncertainty in a flood forecasting system and the available methods of dealing with it*. HR Wallingford.
- Bonnifait, L., Delrieu, G., Le Lay, M., Boudevillain, B., Masson, A., Belleudy, P., Gaume, E., & Saulnier, G.-M. (2009). Distributed hydrologic and hydraulic modelling with radar rainfall input: Reconstruction of the 8–9 September 2002 catastrophic flood event in the Gard region, France. *Advances in Water Resources*, 32(7), 1077–1089.
- Bookhagen, B., & Burbank, D. W. (2010). Toward a complete Himalayan hydrological budget: Spatiotemporal distribution of snowmelt and rainfall and their impact on river discharge. *Journal of Geophysical Research*, 115(F3), F03019. <https://doi.org/10.1029/2009JF001426>
- Bracken, L. J., & Croke, J. (2007). The concept of hydrological connectivity and its contribution to understanding runoff-dominated geomorphic systems. *Hydrological Processes*, 21(13), 1749–1763.

- Breuer, L., Eckhardt, K., & Frede, H.-G. (2003). Plant parameter values for models in temperate climates. *Ecological Modelling*, *169*(2–3), 237–293.
- Bricker, S. H., Yadav, S. K., MacDonald, A. M., Satyal, Y., Dixit, A., & Bell, R. (2014). *Groundwater resilience Nepal: Preliminary findings from a case study in the Middle Hills*. British Geological Survey.
- Bronstert, A., Bárdossy, A., Bismuth, C., Buiteveld, H., Disse, M., Engel, H., Fritsch, U., Hundecha, Y., Lammersen, R., Niehoff, D., & Ritter, N. (2007). Multi-scale modelling of land-use change and river training effects on floods in the Rhine basin. *River Research and Applications*, *23*(10), 1102–1125. <https://doi.org/10.1002/rra.1036>
- Bruijnzeel, L. A. (2004). Hydrological functions of tropical forests: Not seeing the soil for the trees? *Agriculture, Ecosystems & Environment*, *104*(1), 185–228. <https://doi.org/10.1016/j.agee.2004.01.015>
- Brunner, G. W. (1995). *HEC-RAS River Analysis System. Hydraulic Reference Manual. Version 1.0*. Hydraulic Engineering Center, CA, USA. <https://apps.dtic.mil/docs/citations/ADA311952>
- Bruns, B., Bandaragoda, D. J., & Samad, M. (2002). *Integrated water-resources management in a river-basin context: Institutional strategies for improving the productivity of agricultural water management. Proceedings of the Regional Workshop, Malang, Indonesia January 15–19, 2001*.
- Butts, M. B., Payne, J. T., Kristensen, M., & Madsen, H. (2004). An evaluation of the impact of model structure on hydrological modelling uncertainty for streamflow simulation. *Journal of Hydrology*, *298*(1–4), 242–266.
- Calder, I. R., & Aylward, B. (2006). Forest and Floods: Moving to an Evidence-based Approach to Watershed and Integrated Flood Management. *Water International*, *31*(1), 87–99. <https://doi.org/10.1080/02508060608691918>
- Calder, I. R., Reid, I., Nisbet, T. R., & Green, J. C. (2003). Impact of lowland forests in England on water resources: Application of the Hydrological Land Use Change (HYLUC) model. *Water Resources Research*, *39*(11).
- Cammeraat, E. L. (2004). Scale dependent thresholds in hydrological and erosion response of a semi-arid catchment in southeast Spain. *Agriculture, Ecosystems & Environment*, *104*(2), 317–332.
- Canadell, J., Jackson, R. B., Ehleringer, J. B., Mooney, H. A., Sala, O. E., & Schulze, E.-D. (1996). Maximum rooting depth of vegetation types at the global scale. *Oecologia*, *108*(4), 583–595. <https://doi.org/10.1007/BF00329030>
- Carrillo, G., Troch, P. A., Sivapalan, M., Wagener, T., Harman, C., & Sawicz, K. (2011). Catchment classification: Hydrological analysis of catchment behaviour through process-based modelling along a climate gradient. *Hydrology & Earth System Sciences Discussions*, *8*(3).
- Castro, L. G., Libardi, P. L., & van Lier, J. (2002). Soil water dynamics in a Brazilian infiltration terrace under different management practices. *Sustainable Land Management-Environmental Protection-a Soil Physical Approach*, *35*, 191–198.
- Chalise, S. R., & Khanal, N. R. (2002). Recent extreme weather events in the Nepal Himalayas. *The Extremes of the Extremes: Extraordinary Floods*, *271*, 141–146.

Chappell, N. A., Hankin, B., Bielby, S., Tych, W., & Leeson, M. P. (2017). *Quantifying flood mitigation benefits of tree planting and related interventions in Wasdale*. Lancaster University.

Chappell, N. A., Vongtanaboon, S., Jiang, Y., & Tangtham, N. (2006). Return-flow prediction and buffer designation in two rainforest headwaters. *Forest Ecology and Management*, 224(1), 131–146. <https://doi.org/10.1016/j.foreco.2005.12.013>

Chaudhary, R. P., Uprety, Y., & Rimal, S. K. (2016). Deforestation in Nepal. In *Biological and Environmental Hazards, Risks, and Disasters* (pp. 335–372). Elsevier. <https://doi.org/10.1016/B978-0-12-394847-2.00020-6>

Chen, F., Zheng, J., Li, S., & Long, A. (2018). Effects of the Land Use and Check Dams on Flood in Upper Catchment of Fuping Hydrological Station by Hydrological Modelling. *Water Resources*, 45(4), 508–522.

Chok, N. S. (2010). *Pearson's versus Spearman's and Kendall's correlation coefficients for continuous data* [PhD Thesis]. University of Pittsburgh.

Chow, T. L., Rees, H. W., & Daigle, J. L. (1999). Effectiveness of terraces/grassed waterway systems for soil and water conservation: A field evaluation. *Journal of Soil and Water Conservation*, 54(3), 577–583.

Chow, V. T. (1959). *Open-channel hydraulics*. McGraw-Hill Book Co.

Clapp, R. B., & Hornberger, G. M. (1978). Empirical equations for some soil hydraulic properties. *Water Resources Research*, 14(4), 601–604.

Coffey, M. E., Workman, S. R., Taraba, J. L., & Fogle, A. W. (2004). Statistical procedures for evaluating daily and monthly hydrologic model predictions. *Transactions of the ASAE*, 47(1), 59.

Coulthard, T. J., Neal, J. C., Bates, P. D., Ramirez, J., Almeida, G. A. M. de, & Hancock, G. R. (2013). Integrating the LISFLOOD-FP 2D hydrodynamic model with the CAESAR model: Implications for modelling landscape evolution. *Earth Surface Processes and Landforms*, 38(15), 1897–1906. <https://doi.org/10.1002/esp.3478>

Crosetto, M., Tarantola, S., & Saltelli, A. (2000). Sensitivity and uncertainty analysis in spatial modelling based on GIS. *Agriculture, Ecosystems & Environment*, 81(1), 71–79.

Cunge, J. A. (1969). On the subject of a flood propagation computation method (Muskingum method). *Journal of Hydraulic Research*, 7(2), 205–230.

da Silva, R. M., Montenegro, S. M. G. L., & Santos, C. A. G. (2012). Integration of GIS and remote sensing for estimation of soil loss and prioritization of critical sub-catchments: A case study of Tapacurá catchment. *Natural Hazards*, 62(3), 953–970. <https://doi.org/10.1007/s11069-012-0128-2>

Dahal, R. K., & Hasegawa, S. (2008). Representative rainfall thresholds for landslides in the Nepal Himalaya. *Geomorphology*, 100(3–4), 429–443.

De Roo, A., Odijk, M., Schmuck, G., Koster, E., & Lucieer, A. (2001). Assessing the effects of land use changes on floods in the Meuse and Oder catchment. *Physics and Chemistry of the Earth, Part B: Hydrology, Oceans and Atmosphere*, 26(7–8), 593–599.

Department of Agriculture. (2000). *Soil Fertility Map of Chitwan Irrigation and East Rapti Irrigation Command Area of Chitwan District*. Consolidated Management Services Nepal Ltd.

DesInventar. (2019). *Disaster Information Management System: Nepal*. United Nations Office for Disaster Risk Reduction. Accessed on 04/07/2019. <https://www.desinventar.net/DesInventar/profiletab.jsp?countrycode=npl&continue=y>

Devkota, R. P. (2014). *Flood Adaptation Strategies under Climate Change in Nepal: A Socio-hydrological Analysis* [PhD Thesis]. University of Southern Queensland.

Dhakal, S. (2013). Flood hazard in Nepal and new approach of risk reduction. *International Journal of Landslide and Environment*, 1(1), 13–14.

Dhawan, B. D. (1993). Coping with Floods in Himalayan Rivers. *Economic and Political Weekly*, 28(18), 849–853.

Dhital, Y. P., Kayastha, R. B., & SS, E. (2011). Precipitation and discharge pattern analysis: A case study of Bagmati River basin, Nepal. *Journal of Flood Engineering*, 2(1), 49–60.

Di Baldassarre, G., Schumann, G., Bates, P. D., Freer, J. E., & Beven, K. J. (2010). Flood-plain mapping: A critical discussion of deterministic and probabilistic approaches. *Hydrological Sciences Journal*, 55(3), 364–376. <https://doi.org/10.1080/02626661003683389>

Diakakis, M. (2011). A method for flood hazard mapping based on basin morphometry: Application in two catchments in Greece. *Natural Hazards*, 56(3), 803–814. <https://doi.org/10.1007/s11069-010-9592-8>

Dijkshoorn, J. A., & Huting, J. R. M. (2009). *Soil and terrain database for Nepal. Report 2009/01*. ISRIC – World Soil Information.

Dingman, S. L. (1994). *Physical Hydrology*. Prentice Hall Inc., 7458.

Dixon, S. J., Sear, D. A., Odoni, N. A., Sykes, T., & Lane, S. N. (2016). The effects of river restoration on catchment scale flood risk and flood hydrology: The Effects of River Restoration on Catchment Scale Flood Risk. *Earth Surface Processes and Landforms*, 41(7), 997–1008. <https://doi.org/10.1002/esp.3919>

Domeneghetti, A., Vorogushyn, S., Castellarin, A., Merz, B., & Brath, A. (2013). Probabilistic flood hazard mapping: Effects of uncertain boundary conditions. *Hydrology and Earth System Sciences*, 17(8), 3127–3140. <https://doi.org/10.5194/hess-17-3127-2013>

Dottori, F., Baldassarre, G. D., & Todini, E. (2013). Detailed data is welcome, but with a pinch of salt: Accuracy, precision, and uncertainty in flood inundation modelling. *Water Resources Research*, 49(9), 6079–6085. <https://doi.org/10.1002/wrcr.20406>

El Kateb, H., Zhang, H., Zhang, P., & Mosandl, R. (2013). Soil erosion and surface runoff on different vegetation covers and slope gradients: A field experiment in Southern Shaanxi Province, China. *CATENA*, 105, 1–10. <https://doi.org/10.1016/j.catena.2012.12.012>

EM-DAT. (2019). *EM-DAT: The Emergency Events Database—Université catholique de Louvain*. Accessed on 11/04/2019. www.emdat.be

Emmett, W. W. (1970). *The hydraulics of overland flow on hillslopes* (Vol. 662). US Government Printing Office.

ESA. (2013, April 18). *ESA - Eduspace EN - Global Change—Landscape units of Nepal*. European Space Agency. https://www.esa.int/SPECIALS/Eduspace_Global_EN/SEMXXJQOSAKF_0.html

Euser, T., Winsemius, H. C., Hrachowitz, M., Fenicia, F., Uhlenbrook, S., & Savenije, H. H. G. (2013). A framework to assess the realism of model structures using hydrological signatures. *Hydrology and Earth System Sciences*, 17(5), 2013.

Evans, E. P., Ramsbottom, D. M., Wicks, J. M., Packman, J. C., & Penning-Rowsell, E. C. (2002). Catchment flood management plans and the modelling and decision support framework. *Proceedings of the Institution of Civil Engineers-Civil Engineering*, 150(5), 43–48.

Falter, D., Dung, N. V., Vorogushyn, S., Schröter, K., Hundecha, Y., Kreibich, H., Apel, H., Theisselmann, F., & Merz, B. (2016). Continuous, large-scale simulation model for flood risk assessments: Proof-of-concept. *Journal of Flood Risk Management*, 9(1), 3–21. <https://doi.org/10.1111/jfr3.12105>

Felder, G., Zischg, A., & Weingartner, R. (2017). The effect of coupling hydrologic and hydrodynamic models on probable maximum flood estimation. *Journal of Hydrology*, 550, 157–165.

Fensterseifer, C., Allasia, D. G., & Paz, A. R. (2016). Assessment of the TRMM 3B42 Precipitation Product in Southern Brazil. *JAWRA Journal of the American Water Resources Association*, 52(2), 367–375. <https://doi.org/10.1111/1752-1688.12398>

Fohrer, N., Haverkamp, S., Eckhardt, K., & Frede, H.-G. (2001). Hydrologic response to land use changes on the catchment scale. *Physics and Chemistry of the Earth, Part B: Hydrology, Oceans and Atmosphere*, 26(7–8), 577–582.

Foody, G. M. (2002). Status of land cover classification accuracy assessment. *Remote Sensing of Environment*, 80(1), 185–201. [https://doi.org/10.1016/S0034-4257\(01\)00295-4](https://doi.org/10.1016/S0034-4257(01)00295-4)

Fraser, A. (2019). *Modelling the potential for spatially distributed, natural flood-risk management techniques to mitigate flood risk at the catchment scale for a UK agricultural catchment* [MRes Thesis]. Durham University. <http://etheses.dur.ac.uk/12980/>

Freeman, T. G. (1991). Calculating catchment area with divergent flow based on a regular grid. *Computers & Geosciences*, 17(3), 413–422.

Freer, J. E., McMillan, H., McDonnell, J. J., & Beven, K. J. (2004). Constraining dynamic TOPMODEL responses for imprecise water table information using fuzzy rule based performance measures. *Journal of Hydrology*, 291(3–4), 254–277.

Freer, J., Beven, K. J., & Peters, N. (2003). Multivariate seasonal period model rejection within the generalised likelihood uncertainty estimation procedure. *Calibration of Watershed Models*, 69, 88.

García-Ruiz, J. M. (2010). The effects of land uses on soil erosion in Spain: A review. *Catena*, 81(1), 1–11.

García-Ruiz, J. M., & Lana-Renault, N. (2011). Hydrological and erosive consequences of farmland abandonment in Europe, with special reference to the Mediterranean region—A review. *Agriculture, Ecosystems & Environment*, 140(3–4), 317–338.

- Gardner, R. A. M., & Gerrard, A. J. (2002). Relationships between runoff and land degradation on non-cultivated land in the Middle Hills of Nepal. *The International Journal of Sustainable Development & World Ecology*, 9(1), 59–73.
- Gardner, R. A. M., & Gerrard, A. J. (2003). Runoff and soil erosion on cultivated rainfed terraces in the Middle Hills of Nepal. *Applied Geography*, 23(1), 23–45. [https://doi.org/10.1016/S0143-6228\(02\)00069-3](https://doi.org/10.1016/S0143-6228(02)00069-3)
- Gautam, D. K., & Dulal, K. (2013). Determination of threshold runoff for flood early warning in Nepalese Rivers. *IDRIM Journal*, 3(1), 126–136.
- Gautam, M. R., & Acharya, K. (2012). Streamflow trends in Nepal. *Hydrological Sciences Journal*, 57(2), 344–357. <https://doi.org/10.1080/02626667.2011.637042>
- Gerrard, A. J., & Gardner, R. A. M. (2000). The nature and management implications of landsliding on irrigated terraces in the Middle Hills of Nepal. *The International Journal of Sustainable Development & World Ecology*, 7(3), 229–235.
- Gerrard, J., & Gardner, R. (2002). Relationships Between Landsliding and Land Use in the Likhu Khola Drainage Basin, Middle Hills, Nepal. *Mountain Research and Development*, 22(1), 48–55. [https://doi.org/10.1659/0276-4741\(2002\)022\[0048:RBLALU\]2.0.CO;2](https://doi.org/10.1659/0276-4741(2002)022[0048:RBLALU]2.0.CO;2)
- Ghimire, C. P., Bruijnzeel, L. A., Lubczynski, M. W., & Bonell, M. (2014). Negative trade-off between changes in vegetation water use and infiltration recovery after reforesting degraded pasture land in the Nepalese Lesser Himalaya. *Hydrology and Earth System Sciences*, 18(12), 4933–4949.
- Ghimire, Chandra Prasad, Bonell, M., Bruijnzeel, L. A., Coles, N. A., & Lubczynski, M. W. (2013). Reforesting severely degraded grassland in the Lesser Himalaya of Nepal: Effects on soil hydraulic conductivity and overland flow production. *Journal of Geophysical Research: Earth Surface*, 118(4), 2528–2545.
- Ghimire, Chandra Prasad, Bruijnzeel, L. A., Bonell, M., Coles, N., Lubczynski, M. W., & Gilmour, D. A. (2014). The effects of sustained forest use on hillslope soil hydraulic conductivity in the Middle Mountains of Central Nepal. *Ecohydrology*, 7(2), 478–495.
- Ghimire, S. K., Higaki, D., & Bhattarai, T. P. (2013). Estimation of soil erosion rates and eroded sediment in a degraded catchment of the Siwalik Hills, Nepal. *Land*, 2(3), 370–391.
- Gilley, J. E., & Kottwitz, E. R. (1994). Maximum surface storage provided by crop residue. *Journal of Irrigation and Drainage Engineering*, 120(2), 440–449.
- Gilley, J. E., Kottwitz, E. R., & Wieman, G. A. (1992). Darcy-Weisbach roughness coefficients for gravel and cobble surfaces. *Journal of Irrigation and Drainage Engineering*, 118(1), 104–112.
- Gilmour, D. A., Bonell, M., & Cassells, D. S. (1987). The Effects of Forestation on Soil Hydraulic Properties in the Middle Hills of Nepal: A Preliminary Assessment. *Mountain Research and Development*, 7(3), 239. <https://doi.org/10.2307/3673199>
- Gobeyn, S., Van Wesemael, A., Neal, J., Lievens, H., Eerdenbrugh, K. V., De Vleeschouwer, N., Vernieuwe, H., Schumann, G. J.-P., Di Baldassarre, G., Baets, B. D., Bates, P. D., & Verhoest, N. E. C.

- (2017). Impact of the timing of a SAR image acquisition on the calibration of a flood inundation model. *Advances in Water Resources*, 100, 126–138. <https://doi.org/10.1016/j.advwatres.2016.12.005>
- Gonzalez-Sosa, E., Braud, I., Dehotin, J., Lassabatère, L., Angulo-Jaramillo, R., Lagouy, M., Branger, F., Jacqueminet, C., Kermadi, S., & Michel, K. (2010). Impact of land use on the hydraulic properties of the topsoil in a small French catchment. *Hydrological Processes*, 2382–2399. <https://doi.org/10.1002/hyp.7640>
- Google Earth. (2019). *Satellite imagery of the East Rapti catchment*. earth.google.com/web/
- Government of Nepal. (2010). *Nepal Hazard Risk Assessment*.
- Government of Nepal. (2017). *Nepal Flood 2017: Post Flood Recovery Needs Assessment*. Government of Nepal.
- Green, W. H., & Ampt, G. A. (1911). Studies on Soil Physics. *The Journal of Agricultural Science*, 4(1), 1–24.
- Grimaldi, S., Petroselli, A., Arcangeletti, E., & Nardi, F. (2013). Flood mapping in ungauged basins using fully continuous hydrologic–hydraulic modelling. *Journal of Hydrology*, 487, 39–47.
- Gupta, H. V., Sorooshian, S., & Yapo, P. O. (1998). Toward improved calibration of hydrologic models: Multiple and noncommensurable measures of information. *Water Resources Research*, 34(4), 751–763.
- Haigh, M., Rawat, J., & Bisht, H. (1990). Hydrological impact of deforestation in the central Himalaya. *Hydrology of Mountainous Areas (Proceedings of the Strbské Pleso Workshop, Czechoslovakia, June 1988)*. *IAHS Publications*, 190, 419–433.
- Hamilton, L. S., & Pearce, A. J. (1988). Soil and water impacts of deforestation. *Deforestation: Social Dynamics in Watersheds and Mountain Ecosystems*, 75–98.
- Hancock, G. R., Evans, K. G., Willgoose, G. R., Moliere, D. R., Saynor, M. J., & Loch, R. J. (2000). Medium-term erosion simulation of an abandoned mine site using the SIBERIA landscape evolution model. *Soil Research*, 38(2), 249–264. <https://doi.org/10.1071/sr99035>
- Hankin, B., Chappell, N. A., Page, T., Kipling, K., Whitling, M., & Burgess-Gamble, L. (2017). *Mapping the potential for Working with Natural Processes – user guide (SC150005)*. Environment Agency.
- Hankin, B., Metcalfe, P., Beven, K., & Chappell, N. A. (2019). Integration of hillslope hydrology and 2D hydraulic modelling for natural flood management. *Hydrology Research*, 50(6), 1535–1548.
- Hauke, J., & Kossowski, T. (2011). Comparison of Values of Pearson’s and Spearman’s Correlation Coefficients on the Same Sets of Data. *Quaestiones Geographicae*, 30(2), 87–93. <https://doi.org/10.2478/v10117-011-0021-1>
- He, Y., Wetterhall, F., Cloke, H. L., Pappenberger, F., Wilson, M., Freer, J., & McGregor, G. (2009). Tracking the uncertainty in flood alerts driven by grand ensemble weather predictions. *Meteorological Applications: A Journal of Forecasting, Practical Applications, Training Techniques and Modelling*, 16(1), 91–101.

- Heathwaite, A. L., Quinn, P. F., & Hewett, C. J. M. (2005). Modelling and managing critical source areas of diffuse pollution from agricultural land using flow connectivity simulation. *Journal of Hydrology*, 304(1–4), 446–461.
- Helton, J. C., & Davis, F. J. (2003). Latin hypercube sampling and the propagation of uncertainty in analyses of complex systems. *Reliability Engineering & System Safety*, 81(1), 23–69.
- Hlaing, K. T., Haruyama, S., & Aye, M. M. (2008). Using GIS-based distributed soil loss modeling and morphometric analysis to prioritize watershed for soil conservation in Bago river basin of Lower Myanmar. *Frontiers of Earth Science in China*, 2(4), 465–478. <https://doi.org/10.1007/s11707-008-0048-3>
- Holmgren, P. (1994). Multiple flow direction algorithms for runoff modelling in grid based elevation models: An empirical evaluation. *Hydrological Processes*, 8(4), 327–334.
- Hooijer, A., Klijn, F., Pedroli, G. B. M., & Van Os, A. G. (2004). Towards sustainable flood risk management in the Rhine and Meuse river basins: Synopsis of the findings of IRMA-SPONGE. *River Research and Applications*, 20(3), 343–357. <https://doi.org/10.1002/rra.781>
- Horritt, M. S. (2006). A methodology for the validation of uncertain flood inundation models. *Journal of Hydrology*, 326(1–4), 153–165. <https://doi.org/10.1016/j.jhydrol.2005.10.027>
- Horritt, M. S., & Bates, P. D. (2001). Effects of spatial resolution on a raster based model of flood flow. *Journal of Hydrology*, 253(1), 239–249. [https://doi.org/10.1016/S0022-1694\(01\)00490-5](https://doi.org/10.1016/S0022-1694(01)00490-5)
- Horritt, M. S., & Bates, P. D. (2002). Evaluation of 1D and 2D numerical models for predicting river flood inundation. *Journal of Hydrology*, 268(1), 87–99. [https://doi.org/10.1016/S0022-1694\(02\)00121-X](https://doi.org/10.1016/S0022-1694(02)00121-X)
- Howgate, O. R., & Kenyon, W. (2009). Community cooperation with natural flood management: A case study in the Scottish Borders. *Area*, 41(3), 329–340.
- Huffman, G. J., Adler, R. F., Bolvin, D. T., & Nelkin, E. J. (2010). The TRMM Multi-Satellite Precipitation Analysis (TMPA). In M. Gebremichael & F. Hossain (Eds.), *Satellite Rainfall Applications for Surface Hydrology* (pp. 3–22). Springer Netherlands. https://doi.org/10.1007/978-90-481-2915-7_1
- Huffman, G. J., Bolvin, D. T., Nelkin, E. J., Wolff, D. B., Adler, R. F., Gu, G., Hong, Y., Bowman, K. P., & Stocker, E. F. (2007). The TRMM Multisatellite Precipitation Analysis (TMPA): Quasi-Global, Multiyear, Combined-Sensor Precipitation Estimates at Fine Scales. *Journal of Hydrometeorology*, 8(1), 38–55. <https://doi.org/10.1175/JHM560.1>
- Huggett, R., & Cheesman, J. (2002). *Topography and the Environment*. Pearson Education.
- Hughes, D. A. (2006). Comparison of satellite rainfall data with observations from gauging station networks. *Journal of Hydrology*, 327(3–4), 399–410.
- Hunter, N. M., Bates, P. D., Horritt, M. S., De Roo, A. P. J., & Werner, M. G. F. (2005). Utility of different data types for calibrating flood inundation models within a GLUE framework. *Hydrology and Earth System Sciences Discussions*, 9(4), 412–430.
- Hurtrez, J.-E., Lucazeau, F., Lavé, J., & Avouac, J.-P. (1999). Investigation of the relationships between basin morphology, tectonic uplift, and denudation from the study of an active fold belt in the Siwalik

Hills, central Nepal. *Journal of Geophysical Research: Solid Earth*, 104(B6), 12779–12796. <https://doi.org/10.1029/1998JB900098>

Iacob, O., Brown, I., & Rowan, J. (2017). Natural flood management, land use and climate change trade-offs: The case of Tarland catchment, Scotland. *Hydrological Sciences Journal*, 62(12), 1931–1948. <https://doi.org/10.1080/02626667.2017.1366657>

ISET-International. (2015). *Urgent case for recovery: What we can learn from the August 2014 Karnali River floods in Nepal*. ISET.

Ives, J. D. (1987). The theory of Himalayan environmental degradation: Its validity and application challenged by recent research. *Mountain Research and Development*, 189–199.

Ives, J. D., & Messerli, B. (1989). *The Himalayan dilemma: Reconciling development and conservation*. Psychology Press.

Jackson, B. M. (2007). *Modelling water and solute transport within vegetated soils using a stochastic framework* [PhD Thesis]. Imperial College London (University of London). <http://hdl.handle.net/10044/1/1287>

Jackson, B. M., Pagella, T., Sinclair, F., Orellana, B., Henshaw, A., Reynolds, B., McIntyre, N., Wheeler, H., & Eycott, A. (2013). Polyscape: A GIS mapping framework providing efficient and spatially explicit landscape-scale valuation of multiple ecosystem services. *Landscape and Urban Planning*, 112, 74–88.

Jaquet, S., Shrestha, G., Kohler, T., & Schwilch, G. (2016). The Effects of Migration on Livelihoods, Land Management, and Vulnerability to Natural Disasters in the Harpan Watershed in Western Nepal. *Mountain Research and Development*, 36(4), 494–505. <https://doi.org/10.1659/MRD-JOURNAL-D-16-00034.1>

Juracek, K. E. (2000). *Estimation and comparison of potential runoff-contributing areas in Kansas using topographic, soil, and land-use information*. US Department of the Interior, US Geological Survey.

Kale, V. S., & Hire, P. S. (2004). Effectiveness of monsoon floods on the Tapi River, India: Role of channel geometry and hydrologic regime. *Geomorphology*, 57(3), 275–291. [https://doi.org/10.1016/S0169-555X\(03\)00107-7](https://doi.org/10.1016/S0169-555X(03)00107-7)

Kattelmann, R. (1987). Uncertainty in assessing Himalayan water resources. *Mountain Research and Development*, 279–286.

Kazakis, N., Kougias, I., & Patsialis, T. (2015). Assessment of flood hazard areas at a regional scale using an index-based approach and Analytical Hierarchy Process: Application in Rhodope–Evros region, Greece. *Science of the Total Environment*, 538, 555–563.

Khanal, N. R., & Watanabe, T. (2006). Abandonment of agricultural land and its consequences. *Mountain Research and Development*, 26(1), 32–40.

Khatri-Chhetri, T. B., Mishra, N. K., Tiwari, S. N., Shivakoti, G. P., & Shukla, A. (1987). *Lessons from inventory preparation of irrigation systems of Budhi Rapti River, Chitwan, Nepal*.

Kirkby, M. J. (1985). Hillslope hydrology. In *Hydrological Forecasting*. John Wiley and Sons.

- Kirkby, M., Bracken, L., & Reaney, S. (2002). The influence of land use, soils and topography on the delivery of hillslope runoff to channels in SE Spain. *Earth Surface Processes and Landforms*, 27(13), 1459–1473. <https://doi.org/10.1002/esp.441>
- Komi, K., Neal, J., Trigg, M. A., & Diekkrüger, B. (2017). Modelling of flood hazard extent in data sparse areas: A case study of the Oti River basin, West Africa. *Journal of Hydrology: Regional Studies*, 10, 122–132. <https://doi.org/10.1016/j.ejrh.2017.03.001>
- Kourgialas, N. N., & Karatzas, G. P. (2011). Flood management and a GIS modelling method to assess flood-hazard areas—A case study. *Hydrological Sciences Journal*, 56(2), 212–225. <https://doi.org/10.1080/02626667.2011.555836>
- Krause, P., Boyle, D. P., & Bäse, F. (2005). Comparison of different efficiency criteria for hydrological model assessment. *Advances in Geosciences*, 5, 89–97. <https://doi.org/10.5194/adgeo-5-89-2005>
- Lane, P. N. J., Best, A. E., Hickel, K., & Zhang, L. (2005). The response of flow duration curves to afforestation. *Journal of Hydrology*, 310(1), 253–265. <https://doi.org/10.1016/j.jhydrol.2005.01.006>
- Lane, S. N. (2017). Natural flood management: Natural flood management. *Wiley Interdisciplinary Reviews: Water*, 4(3), e1211. <https://doi.org/10.1002/wat2.1211>
- Lane, S. N., Brookes, C. J., Kirkby, M. J., & Holden, J. (2004). A network-index-based version of TOPMODEL for use with high-resolution digital topographic data. *Hydrological Processes*, 18(1), 191–201. <https://doi.org/10.1002/hyp.5208>
- Lane, S. N., Reaney, S. M., & Heathwaite, A. L. (2009). Representation of landscape hydrological connectivity using a topographically driven surface flow index. *Water Resources Research*, 45(8). <https://doi.org/10.1029/2008WR007336>
- Lasanta, T., Arnáez, J., Oserín, M., & Ortigosa, L. M. (2001). Marginal lands and erosion in terraced fields in the Mediterranean mountains. *Mountain Research and Development*, 21(1), 69–76.
- Lavé, J., & Avouac, J. P. (2001). Fluvial incision and tectonic uplift across the Himalayas of central Nepal. *Journal of Geophysical Research: Solid Earth*, 106(B11), 26561–26591. <https://doi.org/10.1029/2001JB000359>
- Legates, D. R., & McCabe, G. J. (1999). Evaluating the use of “goodness-of-fit” Measures in hydrologic and hydroclimatic model validation. *Water Resources Research*, 35(1), 233–241. <https://doi.org/10.1029/1998WR900018>
- Leh, M. D., & Chaubey, I. (2009). GIS-Based Predictive Models of Hillslope Runoff Generation Processes 1. *JAWRA Journal of the American Water Resources Association*, 45(4), 844–856.
- Lehning, M., Völksch, I., Gustafsson, D., Nguyen, T. A., Stähli, M., & Zappa, M. (2006). ALPINE3D: A detailed model of mountain surface processes and its application to snow hydrology. *Hydrological Processes: An International Journal*, 20(10), 2111–2128.
- Leopold, L. B., & Maddock, T. (1953). *The Hydraulic Geometry of Stream Channels and Some Physiographic Implications*. U.S. Government Printing Office.

- Leow, C. S., Abdullah, R., & Zakaria, N. A. (2011). Validating flood inundation map for hydrodynamic modelling of an ungauged catchment. *Sustainable Solutions for Global Crisis of Flooding, Pollution and Water Scarcity*, 607–614.
- Lesschen, J. P., Schoorl, J. M., & Cammeraat, L. H. (2009). Modelling runoff and erosion for a semi-arid catchment using a multi-scale approach based on hydrological connectivity. *Geomorphology*, 109(3), 174–183. <https://doi.org/10.1016/j.geomorph.2009.02.030>
- Li, H., Beldring, S., & Xu, C.-Y. (2014). Implementation and testing of routing algorithms in the distributed Hydrologiska Byråns Vattenbalansavdelning model for mountainous catchments. *Hydrology Research*, 45(3), 322–333. <https://doi.org/10.2166/nh.2013.009>
- Li, J., & Zeng, Q. (2002). A unified monsoon index. *Geophysical Research Letters*, 29(8), 115-1-115–4. <https://doi.org/10.1029/2001GL013874>
- Li, J., & Zeng, Q. (2003). A new monsoon index and the geographical distribution of the global monsoons. *Advances in Atmospheric Sciences*, 20(2), 299–302. <https://doi.org/10.1007/s00376-003-0016-5>
- Li, Y. M., Wang, K. Q., Liu, Z. Q., Wang, J. Y., & Zhou, X. (2006). Effect of Measure of Engineering Preparation to Soil Water in Yunnan Dry-Hot River Valley. *Journal of Soil and Water Conservation*, 1(2), 15–19.
- Li, Y., Zhang, Q., Yao, J., Werner, A. D., & Li, X. (2014). Hydrodynamic and Hydrological Modeling of the Poyang Lake Catchment System in China. *Journal of Hydrologic Engineering*, 19(3), 607–616. [https://doi.org/10.1061/\(ASCE\)HE.1943-5584.0000835](https://doi.org/10.1061/(ASCE)HE.1943-5584.0000835)
- Linde, A. H. T., Aerts, J. C. J. H., & Kwadijk, J. C. J. (2010). Effectiveness of flood management measures on peak discharges in the Rhine basin under climate change. *Journal of Flood Risk Management*, 3(4), 248–269. <https://doi.org/10.1111/j.1753-318X.2010.01076.x>
- Linke, S., Lehner, B., Ouellet Dallaire, C., Ariwi, J., Grill, G., Anand, M., Beames, P., Burchard-Levine, V., Maxwell, S., Moidu, H., Tan, F., & Thieme, M. (2019). Global hydro-environmental sub-basin and river reach characteristics at high spatial resolution. *Scientific Data*, 6(1), 283. <https://doi.org/10.1038/s41597-019-0300-6>
- Liu, X., Liu, F. M., Wang, X. X., Li, X. D., Fan, Y. Y., Cai, S. X., & Ao, T. Q. (2017). Combining rainfall data from rain gauges and TRMM in hydrological modelling of Laotian data-sparse basins. *Applied Water Science*, 7(3), 1487–1496. <https://doi.org/10.1007/s13201-015-0330-y>
- Liu, Y. B., Gebremeskel, S., De Smedt, F., Hoffmann, L., & Pfister, L. (2004). Simulation of flood reduction by natural river rehabilitation using a distributed hydrological model. *Hydrology and Earth System Sciences Discussions*, 8(6), 1129–1140.
- Liu, Y., & Pender, G. (2015). A flood inundation modelling using v-support vector machine regression model. *Engineering Applications of Artificial Intelligence*, 46, 223–231. <https://doi.org/10.1016/j.engappai.2015.09.014>
- López-Vicente, M., Poesen, J., Navas, A., & Gaspar, L. (2013). Predicting runoff and sediment connectivity and soil erosion by water for different land use scenarios in the Spanish Pre-Pyrenees. *Catena*, 102, 62–73.

- Luedeling, E., Nagieb, M., Wichern, F., Brandt, M., Deurer, M., & Buerkert, A. (2005). Drainage, salt leaching and physico-chemical properties of irrigated man-made terrace soils in a mountain oasis of northern Oman. *Geoderma*, 125(3), 273–285. <https://doi.org/10.1016/j.geoderma.2004.09.003>
- Luo, Y., Arnold, J., Allen, P., & Chen, X. (2012). Baseflow simulation using SWAT model in an inland river basin in Tianshan Mountains, Northwest China. *Hydrology and Earth System Sciences* 16, 4, 1259–1267.
- Maharjan, A., Bauer, S., & Knerr, B. (2013). *Migration for labour and its impact on farm production in Nepal*. Centre for the Study of Labour and Mobility Kathmandu, Nepal.
- Mahmoud, S. H., & Gan, T. Y. (2018). Multi-criteria approach to develop flood susceptibility maps in arid regions of Middle East. *Journal of Cleaner Production*, 196, 216–229.
- Manning, R. (1891). On the flow of water in open channels and pipes. *Institute of Civil Engineers of Ireland Transactions*, 20.
- Marks, D., Domingo, J., Susong, D., Link, T., & Garen, D. (1999). A spatially distributed energy balance snowmelt model for application in mountain basins. *Hydrological Processes*, 13(12–13), 1935–1959. [https://doi.org/10.1002/\(SICI\)1099-1085\(199909\)13:12/13<1935::AID-HYP868>3.0.CO;2-C](https://doi.org/10.1002/(SICI)1099-1085(199909)13:12/13<1935::AID-HYP868>3.0.CO;2-C)
- Mateo, C. M., Hanasaki, N., Komori, D., Tanaka, K., Kiguchi, M., Champathong, A., Sukhaphunnaphan, T., Yamazaki, D., & Oki, T. (2014). Assessing the impacts of reservoir operation to floodplain inundation by combining hydrological, reservoir management, and hydrodynamic models. *Water Resources Research*, 50(9), 7245–7266. <https://doi.org/10.1002/2013WR014845>
- MathWorks. (2018). *Latin Hypercube Design*. Lhsdesign - Latin Hypercube Design. Accessed on 15/2/2018. <https://uk.mathworks.com/help/stats/lhsdesign.html>
- Matplotlib. (2020). *matplotlib.pyplot.boxplot—Matplotlib 3.1.2 documentation*. https://matplotlib.org/3.1.1/api/_as_gen/matplotlib.pyplot.boxplot.html
- Mausser, W., & Bach, H. (2009). PROMET – Large scale distributed hydrological modelling to study the impact of climate change on the water flows of mountain watersheds. *Journal of Hydrology*, 376(3), 362–377. <https://doi.org/10.1016/j.jhydrol.2009.07.046>
- McIntyre, N., Wheeler, H., & Lees, M. (2002). Estimation and propagation of parametric uncertainty in environmental models. *Journal of Hydroinformatics*, 4(3), 177–198. <https://doi.org/10.2166/hydro.2002.0018>
- McMillan, H., & Brasington, J. (2008). End-to-end flood risk assessment: A coupled model cascade with uncertainty estimation. *Water Resources Research*, 44(3). <https://doi.org/10.1029/2007WR005995>
- McMillan, H., Freer, J., Pappenberger, F., Krueger, T., & Clark, M. (2010). Impacts of uncertain river flow data on rainfall-runoff model calibration and discharge predictions. *Hydrological Processes*, 24(10), 1270–1284. <https://doi.org/10.1002/hyp.7587>
- McMillan, H., Jackson, B., Clark, M., Kavetski, D., & Woods, R. (2011). Rainfall uncertainty in hydrological modelling: An evaluation of multiplicative error models. *Journal of Hydrology*, 400(1–2), 83–94.

- Meerkerk, A. L., Wesemael, B. van, & Bellin, N. (2009). Application of connectivity theory to model the impact of terrace failure on runoff in semi-arid catchments. *Hydrological Processes*, *23*(19), 2792–2803. <https://doi.org/10.1002/hyp.7376>
- Melching, C. S., Yen, B. C., & Wenzel, H. G. (1990). A reliability estimation in modeling watershed runoff with uncertainties. *Water Resources Research*, *26*(10), 2275–2286. <https://doi.org/10.1029/WR026i010p02275>
- Meng, J., Li, L., Hao, Z., Wang, J., & Shao, Q. (2014). Suitability of TRMM satellite rainfall in driving a distributed hydrological model in the source region of Yellow River. *Journal of Hydrology*, *509*, 320–332.
- Merz, B., Hall, J., Disse, M., & Schumann, A. (2010). Fluvial flood risk management in a changing world. *Natural Hazards and Earth System Science*, *10*(3), 509–527. <https://doi.org/10.5194/nhess-10-509-2010>
- Merz, J., Dangol, P. M., Dhakal, M. P., Dongol, B. S., & Weingartner, R. (2006). Rainfall amount and intensity in a rural catchment of the middle mountains, Nepal. *Hydrological Sciences Journal*, *51*(1), 127–143. <https://doi.org/10.1623/hysj.51.1.127>
- Metcalf, P. W. (2017). *Development of a modelling framework for integrated catchment flood risk management* [PhD Thesis]. Lancaster University.
- Metcalf, P., Beven, K., Hankin, B., & Lamb, R. (2017). A modelling framework for evaluation of the hydrological impacts of nature-based approaches to flood risk management, with application to in-channel interventions across a 29-km² scale catchment in the United Kingdom. *Hydrological Processes*, *31*(9), 1734–1748. <https://doi.org/10.1002/hyp.11140>
- Metz, J. J. (1991). A reassessment of the causes and severity of Nepal's environmental crisis. *World Development*, *19*(7), 805–820. [https://doi.org/10.1016/0305-750X\(91\)90134-4](https://doi.org/10.1016/0305-750X(91)90134-4)
- Meyles, E. W., Williams, A. G., Ternan, J. L., Anderson, J. M., & Dowd, J. F. (2006). The influence of grazing on vegetation, soil properties and stream discharge in a small Dartmoor catchment, southwest England, UK. *Earth Surface Processes and Landforms*, *31*(5), 622–631. <https://doi.org/10.1002/esp.1352>
- Milledge, D. G., Lane, S. N., Heathwaite, A. L., & Reaney, S. M. (2012). A Monte Carlo approach to the inverse problem of diffuse pollution risk in agricultural catchments. *Science of The Total Environment*, *433*, 434–449. <https://doi.org/10.1016/j.scitotenv.2012.06.047>
- Mogollón, B., Villamagna, A. M., Frimpong, E. A., & Angermeier, P. L. (2016). Mapping technological and biophysical capacities of watersheds to regulate floods. *Ecological Indicators*, *61*, 483–499. <https://doi.org/10.1016/j.ecolind.2015.09.049>
- Monteith, J. L. (1965). Evaporation and environment. *Symposia of the Society for Experimental Biology*, *19*, 205–234.
- Mora, B., Tsendbazar, N.-E., Herold, M., & Arino, O. (2014). Global Land Cover Mapping: Current Status and Future Trends. In I. Manakos & M. Braun (Eds.), *Land Use and Land Cover Mapping in Europe* (Vol. 18, pp. 11–30). Springer Netherlands. https://doi.org/10.1007/978-94-007-7969-3_2

- Moriasi, D. N., Arnold, J. G., Liew, M. W. V., Bingner, R. L., Harmel, R. D., & Veith, T. L. (2007). Model Evaluation Guidelines for Systematic Quantification of Accuracy in Watershed Simulations. *Transactions of the ASABE*, 50(3), 885–900. <https://doi.org/10.13031/2013.23153>
- Mosegaard, K., & Tarantola, A. (2002). Probabilistic approach to inverse problems. *International Geophysics Series*, 81(A), 237–268.
- Mulligan, M. (1996). Modelling the complexity of land surface response to climatic variability in Mediterranean environments. In M. G. Anderson & S. M. Brooks (Eds.), *Advances in hillslope processes*. John Wiley and Sons.
- Musleh, F. A., & Cruise, J. F. (2006). Functional Relationships of Resistance in Wide Flood Plains with Rigid Unsubmerged Vegetation. *Journal of Hydraulic Engineering*, 132(2), 163–171. [https://doi.org/10.1061/\(ASCE\)0733-9429\(2006\)132:2\(163\)](https://doi.org/10.1061/(ASCE)0733-9429(2006)132:2(163))
- Naden, P. (2013). Spatial Targeting of agri-environment measures for mitigating diffuse water pollution: Report of a workshop held on 16th July 2013. *Wallingford: Centre for Ecology and Hydrology. Coastal Erosion Risk Management Research and Development Programme*.
- Nash, J. E., & Sutcliffe, J. V. (1970). River flow forecasting through conceptual models part I—A discussion of principles. *Journal of Hydrology*, 10(3), 282–290.
- Neal, J., Schumann, G., & Bates, P. (2012). A subgrid channel model for simulating river hydraulics and floodplain inundation over large and data sparse areas. *Water Resources Research*, 48(11). <https://doi.org/10.1029/2012WR012514>
- Neal, J., Schumann, G., Fewtrell, T., Budimir, M., Bates, P., & Mason, D. (2011). Evaluating a new LISFLOOD-FP formulation with data from the summer 2007 floods in Tewkesbury, UK. *Journal of Flood Risk Management*, 4(2), 88–95. <https://doi.org/10.1111/j.1753-318X.2011.01093.x>
- Neal, J., Villanueva, I., Wright, N., Willis, T., Fewtrell, T., & Bates, P. (2012). How much physical complexity is needed to model flood inundation? *Hydrological Processes*, 26(15), 2264–2282. <https://doi.org/10.1002/hyp.8339>
- Nedkov, S., & Burkhard, B. (2012). Flood regulating ecosystem services—Mapping supply and demand, in the Etropole municipality, Bulgaria. *Ecological Indicators*, 21, 67–79. <https://doi.org/10.1016/j.ecolind.2011.06.022>
- Nepal, S. (2012). *Evaluating upstream downstream linkages of Hydrological Dynamics in the Himalayan Region* [PhD Thesis]. Friedrich-Schiller- University Jena.
- Nepal, S., Flügel, W.-A., & Shrestha, A. B. (2014). Upstream-downstream linkages of hydrological processes in the Himalayan region. *Ecological Processes*, 3(1), 19. <https://doi.org/10.1186/s13717-014-0019-4>
- Nepal, S., Zheng, H., Penton, D. J., & Neumann, L. E. (2015). Comparative performance of GR4JSG and J2000 hydrological models in the Dudh Koshi catchment of the Himalayan region. *MODSIM2015. MSSANZ*, 2395–2401.

- Neupane, R., & Shrestha, S. D. (2009). Hydrogeologic assessment and groundwater reserve evaluation in northwestern parts of Dun Valley aquifers of Chitwan, inner Terai. *Bulletin of the Department of Geology*, 12, 43-54
- Neupane, R. P., White, J. D., & Alexander, S. E. (2015). Projected hydrologic changes in monsoon-dominated Himalaya Mountain basins with changing climate and deforestation. *Journal of Hydrology*, 525, 216–230. <https://doi.org/10.1016/j.jhydrol.2015.03.048>
- Nguyen, P., Thorstensen, A., Sorooshian, S., Hsu, K., AghaKouchak, A., Sanders, B., Koren, V., Cui, Z., & Smith, M. (2016). A high resolution coupled hydrologic–hydraulic model (HiResFlood-UCI) for flash flood modelling. *Journal of Hydrology*, 541, 401–420. <https://doi.org/10.1016/j.jhydrol.2015.10.047>
- Nicholson, S. E., Some, B., Mccollum, J., Nelkin, E., Klotter, D., Berte, Y., Diallo, B. M., Gaye, I., Kpabeba, G., Ndiaye, O., Noukpozoukou, J. N., Tanu, M. M., Thiam, A., Toure, A. A., & Traore, A. K. (2003). Validation of TRMM and Other Rainfall Estimates with a High-Density Gauge Dataset for West Africa. Part I: Validation of GPCP Rainfall Product and Pre-TRMM Satellite and Blended Products. *Journal of Applied Meteorology*, 42, 18.
- Nikolopoulos, E. I., Anagnostou, E. N., Borga, M., Vivoni, E. R., & Papadopoulos, A. (2011). Sensitivity of a mountain basin flash flood to initial wetness condition and rainfall variability. *Journal of Hydrology*, 402(3–4), 165–178.
- Nisbet, T. R., & Thomas, H. (2008). Restoring floodplain woodland for flood alleviation. *Final Report for the Department for Environment, Food and Rural Affairs. Project SLD2316, DEFRA, London.*
- Nisbet, T. R., Silgram, M., Shah, N., Morrow, K., & Broadmeadow, S. (2011). Woodland for water: Woodland measures for meeting water framework directive objectives. *Forest Research Monograph*, 4, 156.
- NSET (National Society for Earthquake Technology). (2010). *Human death and other losses due to natural disasters (floods) in Nepal, 1971-2009* [Map]. NSET.
- O’Callaghan, J. F., & Mark, D. M. (1984). The extraction of drainage networks from digital elevation data. *Computer Vision, Graphics, and Image Processing*, 28(3), 323–344. [https://doi.org/10.1016/S0734-189X\(84\)80011-0](https://doi.org/10.1016/S0734-189X(84)80011-0)
- O’Connell, P. E., Ewen, J., O’Donnell, G., & Quinn, P. (2007). Is there a link between agricultural land-use management and flooding? *Hydrology and Earth System Sciences* 11(1), 96-107.
- O’Loughlin, F. E., Neal, J., Schumann, G. J. P., Beighley, E., & Bates, P. D. (2020). A LISFLOOD-FP hydraulic model of the middle reach of the Congo. *Journal of Hydrology*, 580, 124203. <https://doi.org/10.1016/j.jhydrol.2019.124203>
- Odoni, N. A., & Lane, S. N. (2010). Assessment of the impact of upstream land management measures on flood flows in Pickering Beck using overflow. *Project RMP55455: Slowing the Flow at Pickering.*
- Ojha, H. R., Shrestha, K. K., Subedi, Y. R., Shah, R., Nuberg, I., Heyojoo, B., Cedamon, E., Rigg, J., Tamang, S., Paudel, K. P., Malla, Y., & McManus, P. (2017). Agricultural land underutilisation in the hills of Nepal: Investigating socio-environmental pathways of change. *Journal of Rural Studies*, 53, 156–172. <https://doi.org/10.1016/j.jrurstud.2017.05.012>

- Orlandini, S., & Rosso, R. (1998). Parameterization of stream channel geometry in the distributed modeling of catchment dynamics. *Water Resources Research*, 34(8), 1971–1985. <https://doi.org/10.1029/98WR00257>
- Otukei, J. R., & Blaschke, T. (2010). Land cover change assessment using decision trees, support vector machines and maximum likelihood classification algorithms. *International Journal of Applied Earth Observation and Geoinformation*, 12, S27–S31.
- Owen, G. J., Perks, M. T., Benskin, C. M. H., Wilkinson, M. E., Jonczyk, J., & Quinn, P. F. (2012). Monitoring agricultural diffuse pollution through a dense monitoring network in the River Eden Demonstration Test Catchment, Cumbria, UK. *Area*, 44(4), 443–453. <https://doi.org/10.1111/j.1475-4762.2012.01107.x>
- Panthi, J., Dahal, P., Shrestha, M. L., Aryal, S., Krakauer, N. Y., Pradhanang, S. M., Lakhankar, T., Jha, A. K., Sharma, M., & Karki, R. (2015). Spatial and temporal variability of rainfall in the Gandaki River Basin of Nepal Himalaya. *Climate*, 3(1), 210–226.
- Papaoannou, G., Efstratiadis, A., Vasiliades, L., Loukas, A., Papalexiou, S. M., Koukouvinos, A., Tsoukalas, I., & Kossieris, P. (2018). An Operational Method for Flood Directive Implementation in Ungauged Urban Areas. *Hydrology*, 5(2), 24. <https://doi.org/10.3390/hydrology5020024>
- Pappenberger, F., Beven, K., Hunter, N. M., Bates, P. D., Gouweleeuw, B. T., Thielen, J., & De Roo, A. P. J. (2005). Cascading model uncertainty from medium range weather forecasts (10 days) through a rainfall-runoff model to flood inundation predictions within the European Flood Forecasting System (EFFS). *Hydrology and Earth System Sciences Discussions*, 9(4), 381–393.
- Pappenberger, F., Matgen, P., Beven, K., Henry, J. B., Pfister, L., & Fraipont, P. (2006). Influence of uncertain boundary conditions and model structure on flood inundation predictions. *Advances in Water Resources*, 29(10), 1430–1449. <https://doi.org/10.1016/j.advwatres.2005.11.012>
- Parsons, A. J., & Abrahams, A. D. (2009). Geomorphology of Desert Environments. In A. J. Parsons & A. D. Abrahams (Eds.), *Geomorphology of Desert Environments* (pp. 3–7). Springer Netherlands. https://doi.org/10.1007/978-1-4020-5719-9_1
- Pathak, P. C., Pandey, A. N., & Singh, J. S. (1985). Apportionment of rainfall in central Himalayan forests (India). *Journal of Hydrology*, 76(3–4), 319–332. [https://doi.org/10.1016/0022-1694\(85\)90140-4](https://doi.org/10.1016/0022-1694(85)90140-4)
- Patrikaki, O., Kazakis, N., Kougias, I., Patsialis, T., Theodossiou, N., & Voudouris, K. (2018). Assessing Flood Hazard at River Basin Scale with an Index-Based Approach: The Case of Mouriki, Greece. *Geosciences*, 8(2), 50. <https://doi.org/10.3390/geosciences8020050>
- Pattison, I. (2010). *Rural Land Management Impacts on Catchment Scale Flood Risk* [PhD Thesis]. Durham University. <http://etheses.dur.ac.uk/531/>
- Pattison, I., Lane, S. N., Hardy, R. J., & Reaney, S. M. (2014). The role of tributary relative timing and sequencing in controlling large floods. *Water Resources Research*, 50(7), 5444–5458. <https://doi.org/10.1002/2013WR014067>
- Paudel, K. P., Tamang, S., & Shrestha, K. K. (2014). Transforming Land and Livelihood: Analysis of Agricultural Land Abandonment in the Mid Hills of Nepal. *Journal of Forest and Livelihood*, 9.

- Pearson, C. (2016). *Modelling the potential impact of spatially targeted natural flood management at the landscape scale for a rural UK catchment*. [MRes Thesis]. Durham University.
- Pechlivanidis, I. G., Jackson, B. M., McIntyre, N. R., & Wheeler, H. S. (2011). Catchment scale hydrological modelling: A review of model types, calibration approaches and uncertainty analysis methods in the context of recent developments in technology and applications. *Global NEST Journal*, 13(3), 193–214.
- Pellicciotti, F., Buergi, C., Immerzeel, W. W., Konz, M., & Shrestha, A. B. (2012). Challenges and Uncertainties in Hydrological Modeling of Remote Hindu Kush–Karakoram–Himalayan (HKH) Basins: Suggestions for Calibration Strategies. *Mountain Research and Development*, 32(1), 39–50. <https://doi.org/10.1659/MRD-JOURNAL-D-11-00092.1>
- Penman, H. L. (1948). Natural evaporation from open water, bare soil and grass. *Proceedings of the Royal Society of London. Series A. Mathematical and Physical Sciences*, 193(1032), 120–145. <https://doi.org/10.1098/rspa.1948.0037>
- Perumal, M., & Sahoo, B. (2008). Volume Conservation Controversy of the Variable Parameter Muskingum–Cunge Method. *Journal of Hydraulic Engineering*, 134(4), 475–485. [https://doi.org/10.1061/\(ASCE\)0733-9429\(2008\)134:4\(475\)](https://doi.org/10.1061/(ASCE)0733-9429(2008)134:4(475))
- Petley, D. N., Hearn, G. J., Hart, A., Rosser, N. J., Dunning, S. A., Owen, K., & Mitchell, W. A. (2007). Trends in landslide occurrence in Nepal. *Natural Hazards*, 43(1), 23–44. <https://doi.org/10.1007/s11069-006-9100-3>
- Planet Team. (2017). *Planet Application Program Interface: In Space for Life on Earth*. <https://api.planet.com/>
- Ponce, V. M., & Lugo, A. (2001). Modeling Looped Ratings in Muskingum–Cunge Routing. *Journal of Hydrologic Engineering*, 6(2), 119–124. [https://doi.org/10.1061/\(ASCE\)1084-0699\(2001\)6:2\(119\)](https://doi.org/10.1061/(ASCE)1084-0699(2001)6:2(119))
- POST (Parliamentary Office of Science and Technology (UK)). (2014). *POSTNOTE: Catchment-wide flood management*. POST.
- Priestley, C. H. B., & Taylor, R. J. (1972). On the Assessment of Surface Heat Flux and Evaporation Using Large-Scale Parameters. *Monthly Weather Review*, 100(2), 81–92. [https://doi.org/10.1175/1520-0493\(1972\)100<0081:OTAOSH>2.3.CO;2](https://doi.org/10.1175/1520-0493(1972)100<0081:OTAOSH>2.3.CO;2)
- Prince, S. D., Haskett, J., Steininger, M., Strand, H., & Wright, R. (2013). NPP Cropland: Gridded Estimates for the Central USA, 1982–1996, R1. *ORNL DAAC*. <https://doi.org/10.3334/ORNLDAAC/612>
- Quinn, P., Beven, K., Chevallier, P., & Planchon, O. (1991). The prediction of hillslope flow paths for distributed hydrological modelling using digital terrain models. *Hydrological Processes*, 5(1), 59–79. <https://doi.org/10.1002/hyp.3360050106>
- Quinn, P., O'Donnell, G., Nicholson, A., Wilkinson, M., Owen, G., Jonczyk, J., Barber, N., Hardwick, M., & Davies, G. (2013). Potential use of Runoff Attenuation Features in small rural catchments for flood mitigation. *Newcastle University, Environment Agency, Royal Haskoning DHV, England*.

- Rahman, M., Bolisetti, T., & Balachandar, R. (2012). Hydrologic modelling to assess the climate change impacts in a Southern Ontario watershed. *Canadian Journal of Civil Engineering*, 39(1), 91–103. <https://doi.org/10.1139/l11-112>
- Rai, S. C., & Sharma, E. (1998). Comparative assessment of runoff characteristics under different land use patterns within a Himalayan watershed. *Hydrological Processes*, 12(13–14), 2235–2248.
- Razavi, S., Tolson, B. A., & Burn, D. H. (2012). Review of surrogate modeling in water resources. *Water Resources Research*, 48(7). <https://doi.org/10.1029/2011WR011527>
- Reaney, S. M. (in prep.). *Spatial targeting of natural flood risk management within river catchments: SCIMAP-Flood*.
- Reaney, S. M., & Pearson, C. (2016). *Spatial targeting of natural flood risk management within large river catchments: A nested approach of SCIMAP-Flood and CRUM3*. Durham University.
- Reaney, S. M., Bracken, L. J., & Kirkby, M. J. (2014). The importance of surface controls on overland flow connectivity in semi-arid environments: Results from a numerical experimental approach. *Hydrological Processes*, 28(4), 2116–2128. <https://doi.org/10.1002/hyp.9769>
- Reaney, S. M., Lane, S. N., Heathwaite, A. L., & Dugdale, L. J. (2011). Risk-based modelling of diffuse land use impacts from rural landscapes upon salmonid fry abundance. *Ecological Modelling*, 222(4), 1016–1029. <https://doi.org/10.1016/j.ecolmodel.2010.08.022>
- Rigon, R., Bancheri, M., Formetta, G., & de Lavenne, A. (2016). The geomorphological unit hydrograph from a historical-critical perspective. *Earth Surface Processes and Landforms*, 41(1), 27–37.
- Rimal, B., Keshtkar, H., Sharma, R., Stork, N., Rijal, S., & Kunwar, R. (2019). Simulating urban expansion in a rapidly changing landscape in eastern Tarai, Nepal. *Environmental Monitoring and Assessment*, 191(4), 255. <https://doi.org/10.1007/s10661-019-7389-0>
- Roberts, W. M., Gonzalez-Jimenez, J. L., Doody, D. G., Jordan, P., & Daly, K. (2017). Assessing the risk of phosphorus transfer to high ecological status rivers: Integration of nutrient management with soil geochemical and hydrological conditions. *Science of the Total Environment*, 589, 25–35.
- Rodríguez-Rincón, J. P., Pedrozo-Acuña, A., & Breña-Naranjo, J. A. (2015). Propagation of hydro-meteorological uncertainty in a model cascade framework to inundation prediction. *Hydrology and Earth System Sciences*, 19(7), 2981–2998. <https://doi.org/10.5194/hess-19-2981-2015>
- Rollason, E. (2018). *Re-evaluating participatory catchment management: Integrating mapping, modelling, and participatory action to deliver more effective risk management* [PhD Thesis]. Durham University. <http://etheses.dur.ac.uk/12857/>
- Rollason, E., Bracken, L. J., Hardy, R. J., & Large, A. R. G. (2018). The importance of volunteered geographic information for the validation of flood inundation models. *Journal of Hydrology*, 562, 267–280. <https://doi.org/10.1016/j.jhydrol.2018.05.002>
- Rollenbeck, R., & Bendix, J. (2011). Rainfall distribution in the Andes of southern Ecuador derived from blending weather radar data and meteorological field observations. *Atmospheric Research*, 99(2), 277–289.

- Romanowicz, R., & Beven, K. (2003). Estimation of flood inundation probabilities as conditioned on event inundation maps. *Water Resources Research*, *39*(3). <https://doi.org/10.1029/2001WR001056>
- Roughani, M., Ghafouri, M., & Tabatabaei, M. (2007). An innovative methodology for the prioritization of sub-catchments for flood control. *International Journal of Applied Earth Observation and Geoinformation*, *9*(1), 79–87. <https://doi.org/10.1016/j.jag.2006.06.001>
- Saghafian, B., & Khosroshahi, M. (2005). Unit Response Approach for Priority Determination of Flood Source Areas. *Journal of Hydrologic Engineering*, *10*(4), 270–277. [https://doi.org/10.1061/\(ASCE\)1084-0699\(2005\)10:4\(270\)](https://doi.org/10.1061/(ASCE)1084-0699(2005)10:4(270))
- Saghafian, B., Ghermezcheshmeh, B., & Kheirkhah, M. M. (2010). Iso-flood severity mapping: A new tool for distributed flood source identification. *Natural Hazards*, *55*(2), 557–570. <https://doi.org/10.1007/s11069-010-9547-0>
- Saghafian, B., Golian, S., Elmi, M., & Akhtari, R. (2013). Monte Carlo analysis of the effect of spatial distribution of storms on prioritization of flood source areas. *Natural Hazards*, *66*(2), 1059–1071.
- Saha, D., & Kukal, S. S. (2015). Soil Structural Stability and Water Retention Characteristics Under Different Land uses of Degraded Lower Himalayas of North-West India. *Land Degradation & Development*, *26*(3), 263–271. <https://doi.org/10.1002/ldr.2204>
- Sakai, H., Sakai, H., Yahagi, W., Fujii, R., Hayashi, T., & Upreti, B. N. (2006). Pleistocene rapid uplift of the Himalayan frontal ranges recorded in the Kathmandu and Siwalik basins. *Palaeogeography, Palaeoclimatology, Palaeoecology*, *241*(1), 16–27. <https://doi.org/10.1016/j.palaeo.2006.06.017>
- Salazar, S., Francés, F., Komma, J., Blume, T., Francke, T., Bronstert, A., & Blöschl, G. (2012). A comparative analysis of the effectiveness of flood management measures based on the concept of retaining water in the landscape; in different European hydro-climatic regions. *Natural Hazards and Earth System Sciences*, *12*(11), 3287–3306. <https://doi.org/10.5194/nhess-12-3287-2012>
- Samir, K. C. (2013). Community Vulnerability to Floods and Landslides in Nepal. *Ecology and Society*, *18*(1), art8. <https://doi.org/10.5751/ES-05095-180108>
- Sapkota, P., & Meilby, H. (1970). Modelling the growth of *Shorea robusta* using growth ring measurements. *Banko Janakari*, *19*(2), 25–32. <https://doi.org/10.3126/banko.v19i2.2982>
- Sastry, G., & Dhruva Narayana, V. V. (1986). Hydrologic responses of small watersheds to different land uses in Doon valley [India]. *Indian Journal of Agricultural Sciences (India)*, *56*(3), 194–197.
- Savage, J. T. S., Bates, P., Freer, J., Neal, J., & Aronica, G. (2016). When does spatial resolution become spurious in probabilistic flood inundation predictions? *Hydrological Processes*, *30*(13), 2014–2032. <https://doi.org/10.1002/hyp.10749>
- Savage, J. T. S., Pianosi, F., Bates, P., Freer, J., & Wagener, T. (2016). Quantifying the importance of spatial resolution and other factors through global sensitivity analysis of a flood inundation model. *Water Resources Research*, *52*(11), 9146–9163. <https://doi.org/10.1002/2015WR018198>
- Sawicz, K., Wagener, T., Sivapalan, M., Troch, P. A., & Carrillo, G. (2011). Catchment classification: Empirical analysis of hydrologic similarity based on catchment function in the eastern USA. *Hydrology and Earth System Sciences*, *15*(9), 2895–2911. <https://doi.org/10.5194/hess-15-2895-2011>

- Schaefli, B., & Gupta, H. V. (2007). Do Nash values have value? *Hydrological Processes*, 21(15), 2075–2080. <https://doi.org/10.1002/hyp.6825>
- Scott, H. D. (2000). *Soil physics: Agricultural and environmental applications*. Iowa State University Press.
- Seaborn. (2020). *seaborn.swarmplot—Seaborn 0.10.0 documentation*. <https://seaborn.pydata.org/generated/seaborn.swarmplot.html>
- Seeger, M., & Ries, J. B. (2008). Soil degradation and soil surface process intensities on abandoned fields in Mediterranean mountain environments. *Land Degradation & Development*, 19(5), 488–501.
- Shafii, M., & Tolson, B. A. (2015). Optimizing hydrological consistency by incorporating hydrological signatures into model calibration objectives. *Water Resources Research*, 51(5), 3796–3814. <https://doi.org/10.1002/2014WR016520>
- Shamir, E., Imam, B., Morin, E., Gupta, H. V., & Sorooshian, S. (2005). The role of hydrograph indices in parameter estimation of rainfall-runoff models. *Hydrological Processes*, 19(11), 2187–2207. <https://doi.org/10.1002/hyp.5676>
- Sharma, K. P., Vorosmarty, C. J., & Moore, B. (2000). Sensitivity of the Himalayan Hydrology to Land-Use and Climatic Changes. *Climatic Change*, 47(1), 117–139. <https://doi.org/10.1023/A:1005668724203>
- Sharma, R. H., & Awal, R. (2013). Hydropower development in Nepal. *Renewable and Sustainable Energy Reviews*, 21, 684–693. <https://doi.org/10.1016/j.rser.2013.01.013>
- Shilpakar, R. L., Bastiaanssen, W. G. M., & Molden, D. J. (2011). A remote sensing-based approach for water accounting in the East Rapti River Basin, Nepal. *Himalayan Journal of Sciences*, 7(9), 15–30. <https://doi.org/10.3126/hjs.v7i9.5785>
- Shilpakar, R.L. (2003). *Geo-information procedures for water accounting: A case study of the East Rapti River Basin, Nepal* [MSc Thesis]. International Institute for Geo-Information Science and Earth Observation (ITC), Enschede.
- Shrestha, A. B., & Bajracharya, S. R. (2013). Case studies on flash flood risk management in the Himalayas: In support of specific flash flood policies. *Case Studies on Flash Flood Risk Management in the Himalayas: In Support of Specific Flash Flood Policies*.
- Shrestha, A. B., Shah, S. H., & Karim, R. (2012). *Resource manual on flash flood risk management*. International Centre for Integrated Mountain Development.
- Shrestha, A. B., Wake, C. P., Dibb, J. E., & Mayewski, P. A. (2000). Precipitation fluctuations in the Nepal Himalaya and its vicinity and relationship with some large scale climatological parameters. *International Journal of Climatology*, 20(3), 317–327. [https://doi.org/10.1002/\(SICI\)1097-0088\(20000315\)20:3<317::AID-JOC476>3.0.CO;2-G](https://doi.org/10.1002/(SICI)1097-0088(20000315)20:3<317::AID-JOC476>3.0.CO;2-G)
- Shrestha, B. B. (2014). Debris Flow Characteristics and Effectiveness of Check Dams for Trapping Debris Flows in the Garjuwa Watershed, Nepal. *International Journal of Landslide and Environment*, 2(2), 15.

- Shrestha, D., Singh, P., & Nakamura, K. (2012). Spatiotemporal variation of rainfall over the central Himalayan region revealed by TRMM Precipitation Radar. *Journal of Geophysical Research: Atmospheres*, *117*(D22).
- Shrestha, M. B., Tamrakar, N. K., & Miyazaki, T. (2008). Morphometry and sediment dynamics of the Churiya River area, Siwalik Range in Nepal. *Boletín de Geología*, *30*(2), Article 2.
- Shrestha, N., Raes, D., Vanuytrecht, E., & Sah, S. K. (2013). Cereal yield stabilization in Terai (Nepal) by water and soil fertility management modeling. *Agricultural Water Management*, *122*, 53–62. <https://doi.org/10.1016/j.agwat.2013.03.003>
- Shrestha, P., & Barros, A. P. (2010). Joint spatial variability of aerosol, clouds and rainfall in the Himalayas from satellite data. *Atmospheric Chemistry & Physics*, *10*(17).
- Shukla, Y., & Mall, B. (2016). Enhancing Frontline Resilience: Transborder Community-Based Flood Early Warning System in India and Nepal. In *UNESCO Chair Conference on Technologies for Development (pp. 201-212)*. Springer.
- Singh, A. M. (2013). An Integrated Approach for Long Term Solutions of Flooding: A Study of the Eastern Chitwan Valley. *Hydro Nepal: Journal of Water, Energy and Environment*, *12*, 66–75.
- Singh, J., Knapp, H. V., Arnold, J. G., & Demissie, M. (2005). Hydrological Modeling of the Iroquois River Watershed Using HSPF and SWAT. *JAWRA Journal of the American Water Resources Association*, *41*(2), 343–360. <https://doi.org/10.1111/j.1752-1688.2005.tb03740.x>
- Singh, S. P., Adhikari, B. S., & Zobel, D. B. (1994). Biomass, Productivity, Leaf Longevity, and Forest Structure in the Central Himalaya. *Ecological Monographs*, *64*(4), 401–421. <https://doi.org/10.2307/2937143>
- Singh, V. P. (1997). Effect of spatial and temporal variability in rainfall and watershed characteristics on stream flow hydrograph. *Hydrological Processes*, *11*(12), 1649–1669. [https://doi.org/10.1002/\(SICI\)1099-1085\(19971015\)11:12<1649::AID-HYP495>3.0.CO;2-1](https://doi.org/10.1002/(SICI)1099-1085(19971015)11:12<1649::AID-HYP495>3.0.CO;2-1)
- Singh, V. P., & Woolhiser, D. A. (2002). Mathematical Modeling of Watershed Hydrology. *Journal of Hydrologic Engineering*, *7*(4), 270–292. [https://doi.org/10.1061/\(ASCE\)1084-0699\(2002\)7:4\(270\)](https://doi.org/10.1061/(ASCE)1084-0699(2002)7:4(270))
- Smith, K. A. (2012). *Evaluation of land management impacts on low flows in northern England* [MRes Thesis]. Durham University.
- Smith, P. J., Brown, S., & Dugar, S. (2016). *Community Based Early Warning Systems for flood risk mitigation in Nepal* [Preprint]. Hydrological Hazards. <https://doi.org/10.5194/nhess-2016-122>
- Sørensen, R., Zinko, U., & Seibert, J. (2006). On the calculation of the topographic wetness index: Evaluation of different methods based on field observations. *Hydrology and Earth System Sciences*, *13*.
- Sorooshian, S., & Gupta, V. K. (1995). Model calibration. In V. P. Singh (Ed.), *Computer models of watershed hydrology* (pp. 23–68). Water Resources Publications: Highlands Ranch, CO.
- Stavi, I., Fizik, E., & Argaman, E. (2015). Contour bench terrace (shich/shikim) forestry systems in the semi-arid Israeli Negev: Effects on soil quality, geodiversity, and herbaceous vegetation. *Geomorphology*, *231*, 376–382. <https://doi.org/10.1016/j.geomorph.2014.12.028>

- Stedinger, J. R., Vogel, R. M., Lee, S. U., & Batchelder, R. (2018). Appraisal of the generalized likelihood uncertainty estimation (GLUE) method. *Water Resources Research*. [https://doi.org/10.1029/2008WR006822@10.1002/\(ISSN\)1944-7973.ASSESS1](https://doi.org/10.1029/2008WR006822@10.1002/(ISSN)1944-7973.ASSESS1)
- Stehman, S. V., & Czaplewski, R. L. (1998). Design and Analysis for Thematic Map Accuracy Assessment. *Remote Sensing of Environment*, *64*(3), 331–344. [https://doi.org/10.1016/S0034-4257\(98\)00010-8](https://doi.org/10.1016/S0034-4257(98)00010-8)
- Su, F., Hong, Y., & Lettenmaier, D. P. (2008). Evaluation of TRMM Multisatellite Precipitation Analysis (TMPA) and Its Utility in Hydrologic Prediction in the La Plata Basin. *Journal of Hydrometeorology*, *9*(4), 622–640. <https://doi.org/10.1175/2007JHM944.1>
- Sulaiman, W. N. A., Heshmatpoor, A., & Rosli, M. H. (2010). Identification of flood source areas in Pahang river basin, Peninsular Malaysia. *EnvironmentAsia*, *3*, 73–78.
- Sulis, M., Paniconi, C., & Camporese, M. (2011). Impact of grid resolution on the integrated and distributed response of a coupled surface-subsurface hydrological model for the des Anglais catchment, Quebec. *Hydrological Processes*, *25*(12), 1853–1865. <https://doi.org/10.1002/hyp.7941>
- Tachikawa, T., Hato, M., Kaku, M., & Iwasaki, A. (2011). Characteristics of ASTER GDEM version 2. *2011 IEEE International Geoscience and Remote Sensing Symposium*, 3657–3660.
- Tadono, T., Ishida, H., Oda, F., Naito, S., Minakawa, K., & Iwamoto, H. (2014). Precise Global DEM Generation by ALOS PRISM. *ISPRS Annals of Photogrammetry, Remote Sensing and Spatial Information Sciences*, *II-4*, 71–76. <https://doi.org/10.5194/isprsannals-II-4-71-2014>
- Takaku, J., Tadono, T., & Tsutsui, K. (2014). Generation of High Resolution Global DSM from ALOS PRISM. *ISPRS - International Archives of the Photogrammetry, Remote Sensing and Spatial Information Sciences*, *XL-4*, 243–248. <https://doi.org/10.5194/isprsarchives-XL-4-243-2014>
- Takaku, J., Tadono, T., Tsutsui, K., & Ichikawa, M. (2016). Validation of "AW3D" global DSM generated from Alos Prism. *ISPRS Annals of the Photogrammetry, Remote Sensing and Spatial Information Sciences*, *3*, 25.
- Takeuchi, K., Ao, T., & Ishidaira, H. (1999). Introduction of block-wise use of TOPMODEL and Muskingum-Cunge method for the hydroenvironmental simulation of a large ungauged basin. *Hydrological Sciences Journal*, *44*(4), 633–646. <https://doi.org/10.1080/02626669909492258>
- Tamrakar, N. K., Maharjan, S., & Shrestha, M. B. (2008) Petrology of Rapti River san, Hetauda-Chitwan Dun Basin, Central Nepal; an example of recycled provenance. *Bulletin of the Department of Geology*, *11*, 23-30.
- Tang, Z., Zhang, H., Yi, S., & Xiao, Y. (2018). Assessment of flood susceptible areas using spatially explicit, probabilistic multi-criteria decision analysis. *Journal of Hydrology*, *558*, 144–158.
- Thomas, I. A., Jordan, P., Mellander, P.-E., Fenton, O., Shine, O., Ó hUallacháin, D., Creamer, R., McDonald, N. T., Dunlop, P., & Murphy, P. N. C. (2016). Improving the identification of hydrologically sensitive areas using LiDAR DEMs for the delineation and mitigation of critical source areas of diffuse pollution. *Science of The Total Environment*, *556*, 276–290. <https://doi.org/10.1016/j.scitotenv.2016.02.183>
- Thompson, M., Warburton, M., & Hatley, T. (2007). *Uncertainty: On a Himalayan Scale*. Himal Books.

- Thorne, C., Thorne, C. R., Evans, E. P., & Penning-Rowell, E. C. (2007). *Future Flooding and Coastal Erosion Risks*. Thomas Telford.
- Trlica, A., Hutyra, L. R., Schaaf, C. L., Erb, A., & Wang, J. A. (2017). Albedo, Land Cover, and Daytime Surface Temperature Variation Across an Urbanized Landscape: ALBEDO OF URBAN LANDSCAPE. *Earth's Future*, 5(11), 1084–1101. <https://doi.org/10.1002/2017EF000569>
- Tsendbazar, N. E. (2016). *Global land cover map validation, comparison and integration for different user communities* [PhD Thesis]. Wageningen University. <https://doi.org/10.18174/378336>
- Turner-Gillespie, D. F., Smith, J. A., & Bates, P. D. (2003). Attenuating reaches and the regional flood response of an urbanizing drainage basin. *Advances in Water Resources*, 26(6), 673–684. [https://doi.org/10.1016/S0309-1708\(03\)00017-4](https://doi.org/10.1016/S0309-1708(03)00017-4)
- UN OCHA. (2019). *Nepal: High Resolution Population Density Maps + Demographic Estimates - Humanitarian Data Exchange*. <https://data.humdata.org/dataset/nepal-high-resolution-population-density-maps-demographic-estimates>
- UNDP Nepal. (2009). *Community Based Disaster Management Practices, 2006-2008*. UNDP Nepal.
- Upreti, B. N. (1999). An overview of the stratigraphy and tectonics of the Nepal Himalaya. *Journal of Asian Earth Sciences*, 17(5–6), 577–606.
- van der Horst, D. (2007). Assessing the efficiency gains of improved spatial targeting of policy interventions; the example of an agri-environmental scheme. *Journal of Environmental Management*, 85(4), 1076–1087. <https://doi.org/10.1016/j.jenvman.2006.11.034>
- van Dijk, A. I. J. M., & Bruijnzeel, L. A. (2004). Runoff and soil loss from bench terraces. 1. An event-based model of rainfall infiltration and surface runoff. *European Journal of Soil Science*, 55(2), 299–316. <https://doi.org/10.1111/j.1365-2389.2004.00604.x>
- van Dijk, A. I. J. M., Bruijnzeel, L. A., Vertessy, R. A., & Ruijter, J. (2005). Runoff and sediment generation on bench-terraced hillsides: Measurements and up-scaling of a field-based model. *Hydrological Processes*, 19(8), 1667–1685. <https://doi.org/10.1002/hyp.5629>
- van Dijk, A. I. J. M., Noordwijk, M. V., Calder, I. R., Bruijnzeel, S. L. A., Schellekens, J., & Chappell, N. A. (2009). Forest–flood relation still tenuous – comment on ‘Global evidence that deforestation amplifies flood risk and severity in the developing world’ by C. J. A. Bradshaw, N.S. Sodi, K. S.-H. Peh and B.W. Brook. *Global Change Biology*, 15(1), 110–115. <https://doi.org/10.1111/j.1365-2486.2008.01708.x>
- Vojtek, M., & Vojteková, J. (2016). Flood hazard and flood risk assessment at the local spatial scale: A case study. *Geomatics, Natural Hazards and Risk*, 7(6), 1973–1992. <https://doi.org/10.1080/19475705.2016.1166874>
- Vrugt, J. A., & Sadegh, M. (2013). Toward diagnostic model calibration and evaluation: Approximate Bayesian computation. *Water Resources Research*, 49(7), 4335–4345.
- Wagener, T., & Kollat, J. (2007). Numerical and visual evaluation of hydrological and environmental models using the Monte Carlo analysis toolbox. *Environmental Modelling & Software*, 22(7), 1021–1033. <https://doi.org/10.1016/j.envsoft.2006.06.017>

- Wagener, T., Sivapalan, M., Troch, P., & Woods, R. (2007). Catchment Classification and Hydrologic Similarity. *Geography Compass*, 1(4), 901–931. <https://doi.org/10.1111/j.1749-8198.2007.00039.x>
- Wainwright, J., & Mulligan, M. (2004). Pointers for the future. *Environmental Modelling: Finding Simplicity in Complexity*, 389–396.
- Ward, E., Buytaert, W., Peaver, L., & Wheater, H. (2011). Evaluation of precipitation products over complex mountainous terrain: A water resources perspective. *Advances in Water Resources*, 34(10), 1222–1231. <https://doi.org/10.1016/j.advwatres.2011.05.007>
- WECS (Water and Energy Secretariat). (2011). *Water Resources of Nepal in the Context of Climate Change*. WECS.
- Wei, W., Chen, D., Wang, L., Daryanto, S., Chen, L., Yu, Y., Lu, Y., Sun, G., & Feng, T. (2016). Global synthesis of the classifications, distributions, benefits and issues of terracing. *Earth-Science Reviews*, 159, 388–403. <https://doi.org/10.1016/j.earscirev.2016.06.010>
- Werritty, A. (2006). Sustainable flood management: Oxymoron or new paradigm? *Area*, 38(1), 16–23. <https://doi.org/10.1111/j.1475-4762.2006.00658.x>
- Westerberg, I. K., Guerrero, J.-L., Younger, P. M., Beven, K. J., Seibert, J., Halldin, S., Freer, J. E., & Xu, C.-Y. (2011). Calibration of hydrological models using flow-duration curves. *Hydrology and Earth System Sciences*, 15(7), 2205–2227. <https://doi.org/10.5194/hess-15-2205-2011>
- Westoby, M. J., Brasington, J., Glasser, N. F., Hambrey, M. J., & Reynolds, J. M. (2012). ‘Structure-from-Motion’ photogrammetry: A low-cost, effective tool for geoscience applications. *Geomorphology*, 179, 300–314. <https://doi.org/10.1016/j.geomorph.2012.08.021>
- Wheaton, R. Z., & Monke, E. J. (2001). *Terracing as a ‘Best Management Practice’ for controlling erosion and protecting water quality*. Purdue University, Cooperative Extension Service.
- Wilcke, D., Zacharias, S., Jin, Z., & Sieker, F. (2006). *GIS-based Expert System for Land Use Planning as a Contribution to Flood Mitigation*. 1, 9.
- Willgoose, G. (2005). *User Manual for SIBERIA (Version 8.30)*. Telluric Research.
- Willmott, C. J. (1981). On the Validation of Models. *Physical Geography*, 2(2), 184–194. <https://doi.org/10.1080/02723646.1981.10642213>
- Wilson, M., Bates, P., Alsdorf, D., Forsberg, B., Horritt, M., Melack, J., Frappart, F., & Famiglietti, J. (2007). Modeling large-scale inundation of Amazonian seasonally flooded wetlands. *Geophysical Research Letters*, 34(15). <https://doi.org/10.1029/2007GL030156>
- Winsemius, H. C., Schaefli, B., Montanari, A., & Savenije, H. H. G. (2009). On the calibration of hydrological models in ungauged basins: A framework for integrating hard and soft hydrological information. *Water Resources Research*, 45(12). <https://doi.org/10.1029/2009WR007706>
- Winter, B., Schneeberger, K., Huttenlau, M., & Stötter, J. (2018). Sources of uncertainty in a probabilistic flood risk model. *Natural Hazards*, 91(2), 431–446. <https://doi.org/10.1007/s11069-017-3135-5>

- Wolock, D. M., & Price, C. V. (1994). Effects of digital elevation model map scale and data resolution on a topography-based watershed model. *Water Resources Research*, 30(11), 3041–3052. <https://doi.org/10.1029/94WR01971>
- Wright, N. G., Villanueva, I., Bates, P. D., Mason, D. C., Wilson, M. D., Pender, G., & Neelz, S. (2008). Case Study of the Use of Remotely Sensed Data for Modeling Flood Inundation on the River Severn, U.K. *Journal of Hydraulic Engineering*, 134(5), 533–540. [https://doi.org/10.1061/\(ASCE\)0733-9429\(2008\)134:5\(533\)](https://doi.org/10.1061/(ASCE)0733-9429(2008)134:5(533))
- Wulf, H., Bookhagen, B., & Scherler, D. (2010). Seasonal precipitation gradients and their impact on fluvial sediment flux in the Northwest Himalaya. *Geomorphology*, 118(1), 13–21. <https://doi.org/10.1016/j.geomorph.2009.12.003>
- Wünscher, T., Engel, S., & Wunder, S. (2008). Spatial targeting of payments for environmental services: A tool for boosting conservation benefits. *Ecological Economics*, 65(4), 822–833. <https://doi.org/10.1016/j.ecolecon.2007.11.014>
- WWF Nepal. (2013). *Chitwan-Annapurna landscape. A rapid assessment*. WWF, Hariyo Ban Program.
- Xiao, Y., Yi, S., & Tang, Z. (2017). Integrated flood hazard assessment based on spatial ordered weighted averaging method considering spatial heterogeneity of risk preference. *Science of the Total Environment*, 599, 1034–1046.
- Xu, Y. D., Fu, B. J., & He, C. S. (2013). Assessing the hydrological effect of the check dams in the Loess Plateau, China, by model simulations. *Hydrology and Earth System Sciences*, 17(6), 2185–2193. <https://doi.org/10.5194/hess-17-2185-2013>
- Yadav, M., Wagener, T., & Gupta, H. (2007). Regionalization of constraints on expected watershed response behaviour for improved predictions in ungauged basins. *Advances in Water Resources*, 30(8), 1756–1774. <https://doi.org/10.1016/j.advwatres.2007.01.005>
- Yan, K., Pappenberger, F., Umer, Y., Solomatine, D., & Baldassarre, G. D. (2014). Regional Versus Physically-Based Methods For Flood Inundation Modelling In Data Scarce Areas: An Application To The Blue Nile. *International Conference on Hydroinformatics*.
- Yang, D., Herath, S., & Musiak, K. (2001). Spatial resolution sensitivity of catchment geomorphologic properties and the effect on hydrological simulation. *Hydrological Processes*, 15(11), 2085–2099. <https://doi.org/10.1002/hyp.280>
- Yang, Y., Xiao, P., Feng, X., & Li, H. (2017). Accuracy assessment of seven global land cover datasets over China. *ISPRS Journal of Photogrammetry and Remote Sensing*, 125, 156–173. <https://doi.org/10.1016/j.isprsjprs.2017.01.016>
- Yazdi, J., & Salehi Neyshabouri, S. A. A. (2014). Adaptive surrogate modeling for optimization of flood control detention dams. *Environmental Modelling & Software*, 61, 106–120. <https://doi.org/10.1016/j.envsoft.2014.07.007>
- Yazdi, J., Sabbaghian Moghaddam, M., & Saghafian, B. (2018). Optimal Design of Check Dams in Mountainous Watersheds for Flood Mitigation. *Water Resources Management*, 32(14), 4793–4811. <https://doi.org/10.1007/s11269-018-2084-4>

- Yilmaz, K. K., Gupta, H. V., & Wagener, T. (2008). A process-based diagnostic approach to model evaluation: Application to the NWS distributed hydrologic model. *Water Resources Research*, 44(9). <https://doi.org/10.1029/2007WR006716>
- Zhang, L., Dawes, W. R., & Walker, G. R. (1999). *Predicting the effect of vegetation changes on catchment average water balance. Technical Report 99/12*. Cooperative Research Centre for Catchment Hydrology, CSIRO Land and Water.
- Zhang, W., & Montgomery, D. R. (1994). Digital elevation model grid size, landscape representation, and hydrologic simulations. *Water Resources Research*, 30(4), 1019–1028. <https://doi.org/10.1029/93WR03553>
- Zhang, Z., Jin, Q., Chen, X., Xu, C.-Y., Chen, S., Moss, E. M., & Huang, Y. (2016). Evaluation of TRMM Multisatellite Precipitation Analysis in the Yangtze River Basin with a Typical Monsoon Climate. *Advances in Meteorology*, 2016, Article ID 7329765. <https://doi.org/10.1155/2016/7329765>
- Zheng, D. L., Prince, S. D., & Wright, R. (2013). NPP Multi-Biome: Gridded Estimates for Selected Regions Worldwide, 1954-1998, R3. *ORNL DAAC*. <https://doi.org/10.3334/ORNLDAAC/614>
- Zischg, A. P., Felder, G., Mosimann, M., Röthlisberger, V., & Weingartner, R. (2018). Extending coupled hydrological-hydraulic model chains with a surrogate model for the estimation of flood losses. *Environmental Modelling & Software*, 108, 174–185. <https://doi.org/10.1016/j.envsoft.2018.08.009>
- Zocatelli, D., Borga, M., Zanon, F., Antonescu, B., & Stancalie, G. (2010). Which rainfall spatial information for flash flood response modelling? A numerical investigation based on data from the Carpathian range, Romania. *Journal of Hydrology*, 394(1–2), 148–161.
- Zokaib, S., & Naser, G. (2011). Impacts of land uses on runoff and soil erosion A case study in Hilkot watershed Pakistan. *International Journal of Sediment Research*, 26(3), 343–352.
- Zope, P. E., Eldho, T. I., & Jothiprakash, V. (2016). Impacts of land use–land cover change and urbanization on flooding: A case study of Oshiwara River Basin in Mumbai, India. *CATENA*, 145, 142–154. <https://doi.org/10.1016/j.catena.2016.06.009>